# AN INTRODUCTION TO SHOCK AND VIBRATION RESPONSE SPECTRA

## REVISION H

## BY TOM IRVINE

### VIBRATIONDATA

### NOVEMBER 27, 2023

_"If you want to find the secrets of the universe, think in terms of energy, frequency, and vibration."_

_- Nikola Tesla_

_____

_A vibration is a motion that can't make up its mind which way it wants to go._

_From a list of humorous quotes from fifth and sixth-grade students._

# 1  TOM IRVINE BACKGROUND



Tom Irvine earned B.S. and M.S. degrees in engineering science from Arizona State University, in 1985 and 1987, respectively.  He wandered into the specialty of vibration serendipitously and found that vibration's quirky traits were well-suited to his unconventional personality.

He worked at Orbital Sciences Corporation in Chandler, Arizona, for 11 years as a full-time employee, and 9 years as a consultant. He derived the shock and vibration levels and performed hands-on testing for the first Pegasus launch vehicle, which successfully flew in 1990. He has analyzed flight accelerometer data from Pegasus, numerous launch vehicles, and data from ground separation tests. He has posted hundreds of tutorials and software programs on his Vibrationdata website, covering shock, vibration, acoustics, structural dynamics, and signal processing.

He was later a scientist at Dynamic Concepts, Inc., in Huntsville, Alabama, where he worked on the NASA Space Launch System (SLS) vehicle.  He concurrently served as an industry representative for the NASA Engineering & Safety Center (NESC) Loads and Dynamics Technical Disciplines Team.  Following his NASA stint, he served as a senior technical fellow at Blue Origin.

He currently works at a large aerospace company.  Tom can be contacted via Email: tom@irvinemail.org

Readers are welcome to visit his blog:  https://vibrationdata.wordpress.com/

Tom either performed or verified the calculations in this e-book using his Vibrationdata Matlab GUI package which is freely available at the above blog link.   He hopes this book will help bridge the gap between shock and vibration analysis as taught in universities and as practiced in industry.

## 2   ACKNOWLEDGMENTS



Left to Right:  Turan Dirlik, Tom Irvine, Curtis Larsen

I have been blessed with many colleagues and mentors who have given me invaluable instruction and opportunities.  My Arizona State University adviser Dr. C.E. Wallace is foremost, as he enabled me to perform a hands-on vibration test project for my master's thesis.

Special thanks also to Phil Gray, Pat Grosserode, Bob Pinkham, Kent Hardy, Eric Osborne, Alex Hardt, Joe Clayton, Jeff Cianciatto and Dr. Curtis Larsen, each of whom I worked with or for at various times.

Kim Dahl inspired me to bundle my Matlab scripts together in a GUI package.  Alek Xu showed me how I could use Matlab's App Designer to streamline my package using tabs.

Stephen Hanly provided funding from enDAQ for the first edition of this ebook.

My conference colleagues have also taught me a great deal, including Turan Dirlik, David Smallwood, Howard Gaberson, Bryce Gardner, Isam Yunis, Alvar Kabe, Terry Scharton, Dennis Kern, Paul Blelloch, Daniel Kaufman, Ali Kolaini and Paul Bremner.

I endeavor to play these blessings forward to future generations.

Meanwhile like the Beatles, "I get by with the help of my friends."

# 3 ACRONYMS & VARIABLES

## 3.1 VARIABLES

| | | | | |
|---|---|---|---|---|
| A | 1. Amplitude<br>2. Cross-sectional area | | $I$ | 1. Area moment of inertia<br>2. Identity matrix |
| a | Acceleration | | $K_E$ | Kinetic energy |
| B | Bandwidth of an ideal rectangular filter | | k | 1. Stiffness<br>2. Wavenumber |
| b | Fatigue exponent | | L | Length |
| C | 1. Damping coefficient matrix<br>2. Crest factor | | M | 1. Mass matrix<br>2. Bending moment |
| c | 1. Damping coefficient<br>2. Speed of sound in the material | | m | mass |
| $C_L$ | Longitudinal wave speed | | $m_j$ | $j^{th}$ spectral moment for a PSD |
| $c_p$ | Bending wave phase speed | | N | Generalized displacement coordinates in the frequency domain |
| $c_g$ | Bending wave group speed | | n | 1. Number of octaves<br>2. Number of points<br>3. Frequency index<br>4. Number of rainflow cycles for a given amplitude |
| D | 1. Plate stiffness factor<br>2. Relative damage index | | | |
| d | Diameter | | | |
| E | Elastic modulus | | $P_E$ | Potential energy |
| F | Applied force in the frequency domain | | p | Probability density function |
| | | | $p_{dk}$ | Probability function Dirlik method |
| f | 1. Frequency<br>2. Applied force in the time domain | | Q | 1. Amplification factor<br>2. Eigenvector matrix |
| $f_n$ | Natural Frequency (Hz) | | q | 1. Eigenvector<br>2. Generalized displacement coordinate in the time domain |
| $f_r$ | Ring frequency | | | |
| $f_s$ | Strouhal frequency | | S | 1. Strouhal number<br>2. Dirlik amplitude independent variable |
| G, g | Gravity acceleration, 9.81 m/sec² | | | |
| G(f) | One-sided PSD | | s | Laplace variable |
| H | Transfer function | | | |
| h | 1. Impulse response function<br>2. Plate thickness | | T | Period or duration |

| | |
|---|---|
| t | Time |
| U | 1. Free stream air velocity<br>2. Displacement |
| u | Longitudinal displacement |
| V | Shear force |
| v | Velocity |
| W | Wavelet or damped sine amplitude |
| w | Hanning window function |
| X, x | Displacement amplitude |
| Y | 1. Amplitude<br>2. Beam transverse displacement |
| y | Base displacement amplitude |
| Z | 1. Plate transverse displacement<br>2. Scaled amplitude for rainflow cumulative probability density function |
| z | Relative displacement |

| | |
|---|---|
| | integral |
| $\phi$ | Phase angle |
| $\Omega$ | Eigenvalue matrix |
| $\omega$ | Angular frequency (rad/sec) |
| $\omega_d$ | Damped angular natural frequency |
| $\omega_n$ | Angular natural frequency |
| $\nu_{0^+}$ | Rate of zero up-crossings |
| $\nu_p$ | Expected peak rate |
| $\Delta f$ | Frequency step |
| $\Delta t$ | Time step |

| | |
|---|---|
| $\beta$ | Beam bending wavenumber |
| $\delta$ | 1. Logarithmic decrement0<br>2. Dirac Delta Function |
| $\eta$ | Loss factor |
| $\kappa$ | Kurtosis |
| $\lambda$ | Wavelength |
| $\mu$ | 1. Poisson ratio<br>2. Mean |
| $\xi$ | Viscous damping ratio |
| $\rho$ | 1. Mass density (mass/volume)<br>2. Frequency ratio |
| $\rho_L$ | Mass density (mass/length) |
| $\sigma$ | 1. Standard deviation<br>2. Stress |
| $\tau$ | Time delay in the convolution |

## 3.2 KEY ACRONYMS

| Nomenclature | Definition |
|---|---|
| ABSSUM | Absolute Sum |
| BPF | Blade Passing Frequency |
| CLA | Coupled Loads Analysis |
| DFT | Discrete Fourier Transform |
| DOF | Degree-of-freedom |
| ERM | Eccentric Rotating Mass |
| ESS | Environmental Stress Screening |
| FDS | Fatigue Damage Spectrum |
| FEA | Finite Element Analysis |
| FFT | Fast Fourier Transform |
| FRF | Frequency Response Function |
| LTM | Load Transformation Matrix |
| MAC | Mass Acceleration Curve |
| MDOF | Multi-degree-of-freedom |
| MPE | Maximum Predicted Environment |
| PSD | Power Spectral Density |
| PV | Pseudo Velocity |
| SDOF | Single-degree-of-freedom |
| SRS | Shock Response Spectrum |
| SRSS | Square-root-of-the-sum-of-the-squares |
| VRS | Vibration Response Spectrum |

# 4    INTRODUCTION

## 4.1 NATURAL FREQUENCY PHOTO GALLERY



Figure 4.1.  Mother Earth

The Earth experiences seismic vibration.  The fundamental natural frequency of the Earth is 309.286 micro Hertz, equivalent to a period of approximately 54 minutes [1].

The Earth also has a Schumann resonance at 7.83 Hz in its electromagnetic field.  The fundamental mode is a standing wave in the Earth–ionosphere cavity with a wavelength equal to the circumference of the Earth.

Figure 4.2.  IRVE 2 Launch & Free-Free Beam Analogy

A rocket vehicle behaves as a free-free beam during flight. The vehicle's body bending modes can be excited by wind gusts, aerodynamic buffeting, thrust offset, maneuvers, etc. The image shows the IRVE 2 launch from Wallops Island. The vehicle is a Black Brant 9 with a Terrier Mark 70 first stage. Flight accelerometer data showed that the fundamental bending frequency began at about 8 Hz and then swept up to 13 Hz as propellant mass was expelled.  Autopilot guidance and control algorithms need to account for the body bending mode to maintain stability.  Payloads can also be affected by the launch vehicle's bending modes.
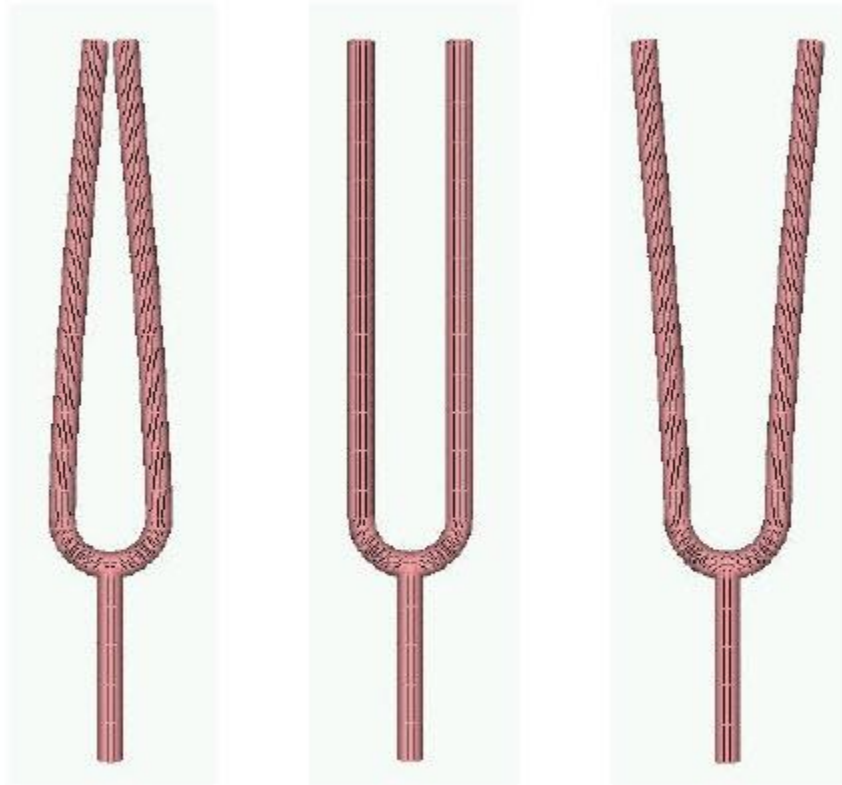
Figure 4.3. Tuning Fork, First Mode, A4 Note, Fundamental Frequency 440 Hz

The mode shape from a finite element model is shown exaggerated. The two tines undergo an in-plane bending mode, 180 degrees out-of-phase with one another. The stem also participates in this mode, but its displacement is so relatively small that it is not apparent in the figure.

## 4.2 SOME HISTORY

The Ancient Greek philosopher Pythagoras (570–495 BC) studied the vibration of stringed instruments and developed a theory of harmony. He first identified that the pitch of a musical note is in inverse proportion to the length of the string that produces it and that intervals between harmonious sound frequencies form simple numerical ratios.

The ancient Greeks believed that all objects were composed of some combination of the basic elements: earth, water, air, and fire. Aristotle (384–322 BC) attempted an explanation of earthquakes based on natural phenomena. He postulated that winds within the earth whipped

up the occasional shaking of the earth's surface.   He noted that earthquakes sometimes caused the water to burst forth in what would now be called a tsunami.

Galileo Galilei (1564-1642) performed numerous experiments with oscillating pendulums during the Renaissance.   He discovered that the period of swing of a pendulum was independent of its amplitude.  He used his pulse as a time measurement because there were no watches at that time.  Christiaan Huygens (1629-1695) successfully built a pendulum clock based on Galileo's work.

Robert Hooke (1635-1703) developed the law of linear spring stiffness.  This law has been generalized to the elasticity principle that strain in a body is proportional to the applied stress.

Sir Isaac Newton (1643-1727) derived his laws of motion, which are the foundation of mechanical vibration analysis.   He published his findings in a book known by its abbreviated title *Principia.*

Jacob Bernoulli, Daniel Bernoulli, and Leonhard Euler derived the equation of motion for beam vibration circa 1750.

Lord Rayleigh, John William Strutt, published *Theory of Sound* in two volumes during 1877-1878. Volume I covered harmonic vibrations, systems with one degree of freedom, vibrating systems in general, transverse vibrations of strings, longitudinal and torsional vibrations of bars, vibrations of membranes and plates, curved shells and plates, and electrical vibrations. Volume II covered aerial vibrations, vibrations in tubes, reflection and refraction - of plane waves, general equations, theory of resonators, Laplace's functions and acoustics, spherical sheets of air, the vibration of solid bodies, and facts and theories of audition.

The modern field of mechanical vibration analysis has been built upon the foundation of these authors' works and has further developed as the result of failures and disasters, as well as the need to design, analyze and test structures and components to withstand dynamic environments.  Vibration analysis is also important in other areas including semiconductor manufacturing, human exposure, energy harvesting, machine health monitoring, etc.

## 4.3 MECHANICAL FAILURES

### 4.3.1  Failure & Damage Photo Gallery
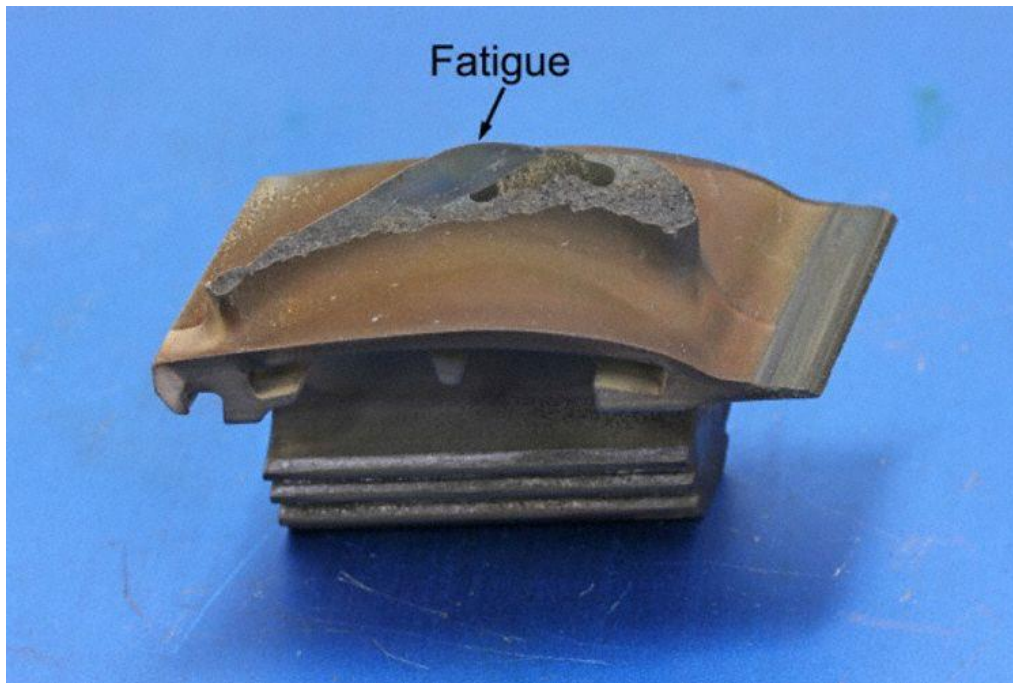


Figure 4.4.  Turbine Blade Failure due to High-Cycle Fatigue

A Qantas Boeing 747-400 aircraft was flying from Sydney to Singapore on May 9, 2011, when the crew noticed abnormalities from the aircraft's No. 4 engine during a climb.  The indications included an increase in both the exhaust gas temperature and vibration levels.  The plane continued to Singapore for a safe landing and disembarkation of the passengers and crew.

The Australian Transport Safety Bureau (ATSB) determined that the cause was a broken turbine blade. The jump in the exhaust gas temperature and vibration from the engine was "a direct result of the failure and separation of a single intermediate-pressure turbine blade", which fractured.

The ATSB said operators and maintainers of Rolls-Royce RB211-524 engines should be aware of the "potential for wear and degradation of the intermediate-pressure turbine blade interlocking shrouds."
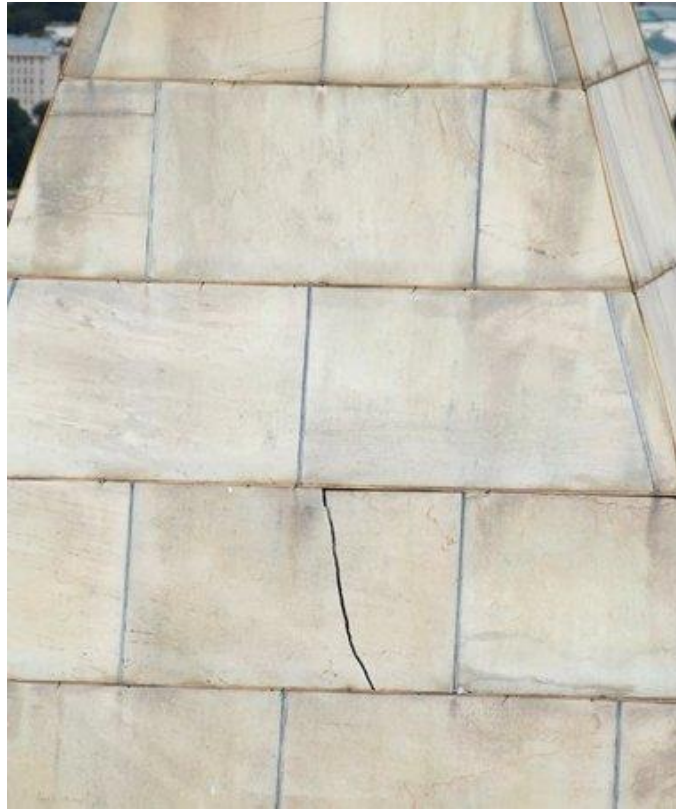
Figure 4.5.  Washington Monument Crack

A one-inch wide, four-foot long crack formed in the Washington Monument, near the top of the 555-foot obelisk, due to the Mineral, Virginia earthquake on August 23, 2011.
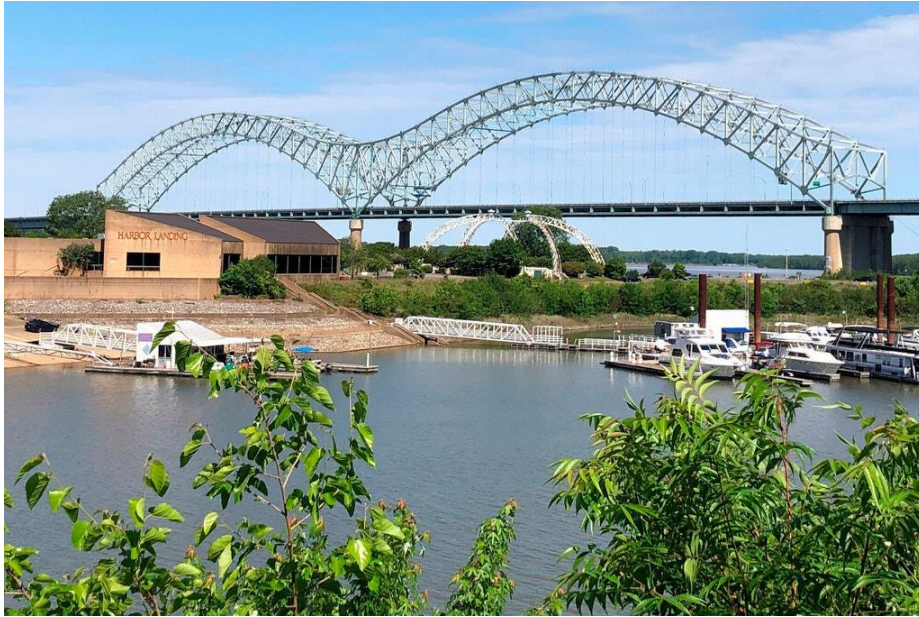
Figure 4.6.  Interstate 40 Bridge Crack

A crack in a steel beam forced the closure of the Interstate 40 Hernando DeSoto bridge that connects Arkansas and Tennessee over the Mississippi River at Memphis, on May 11, 2021.  A critical beam was fractured to the point of being nearly severed. Photos of the crack appear to show the two-foot-wide steel box beam broken nearly in two at a location near the bridge's center pier, on one end of the span on the Tennessee side of the bridge.

The crack was most likely a fatigue crack due to daily thermal contraction and expansion as well as the dynamic loads from the vehicle traffic.

Adel Abdelnaby, associate professor of engineering at University of Memphis said, "You know, usually I explain it to my students, imagine that's the truss and you have trucks driving on it and keeps on bending like this."

Abdelnaby studies and teaches bridge fatigue, which happens when tiny cracks in the metal form over time.

"You are subjecting steel to many cycles of stresses, millions of cycles. Every truck that passes by, that's one cycle. So, imagine how many cycles have been there since the 1970s," Abdelnaby explained.

The Hernando Desoto bridge opened in 1973. Abdelnaby said that bridges built during that era were not designed to handle such a high volume of traffic. Prior to its closure, 41,000 vehicles crossed this bridge every day. Thirty percent were commercial trucks.

Dr. Andrew Assadollahi, Department Chair of Civil and Environmental Engineering at Christian Brothers University, said: "Based on what I've seen of the photos while this member of the bridge is definitely an important member, it doesn't seem to be one of the main, load carrying girders of the entire bridge. But it's still a very important member."

Dr. Assadollahi said the reason why is because the loads on the bridge, like traffic or wind, are transmitted through structural members, then down to the foundation. "Anytime you have a member that has fractured or failed like this member has, the loads acting on the structure have to take a new path," he said.

"So if other members become over stressed then eventually that could lead to a major, major problem. So the decision to shut down the bridge when they did and to keep it shut down was definitely the right call, definitely."

Investigators eventually determined that the crack initiated due to a flawed weld, something that plagues similar bridges across the nation due to welding practices that are no longer acceptable today.  Note that the box beam was made from welded plates.

The bridge was repaired and reopened three months after the crack was detected.

As an aside, the bridge is also in the New Madrid Seismic zone. A sequence of earthquakes occurred in this zone in the winter of 1811-1812 that lasted for several months and included three very large earthquakes estimated to be between magnitude 7 and 8. The three largest quakes destroyed several settlements along the Mississippi River, caused minor structural damage as far away as Cincinnati, Ohio, and St. Louis, Missouri, and were felt as far away as Hartford, Connecticut, Charleston, South Carolina, and New Orleans, Louisiana.

Figure 4.7. Roller Coaster Pillar Crack

Fury 325 in Carowinds Amusement Park, North Carolina, is the tallest, fastest, longest "giga coaster" in North America, with a peak height of 325 feet and reaching 95 mph.  Jeremy Wagner, a park visitor, discovered this crack in a support pillar on June 30, 2023.

Gary Kilpatrick, a North Carolina-based engineer and amusement park ride expert, said that the crack could have been caused by several factors, such as issues with a welded area, a defect in the material, or fatigue stress from the ride.

"When these machines go through this cycle of stress over and over again, that's what we as engineers call fatigue stresses and over time if you have a problem in some area, it will manifest itself in a form of a failure like that," said Kilpatrick.

The engineer said if the crack was left unnoticed, it could have caused fatigue and overload on other parts of the ride.

Note that voids and other defects can occur in welds, causing stress concentration where cracks can initiate.  Cracks can also form during or soon after the welding process.  The heating expansion and cooling contraction of the materials create "residual stress" which can exceed the material strength.  Cracks relieve stress.  Cyclical loading then causes the preexisting cracks to grow.

The amusement park's location near Charlotte has only minor seismic activity. Earthquake induced damage is unlikely.

### 4.3.2   Historical Failures

Railcar axles were failing under repeated "low level" cyclic stress, in the mid-nineteenth century.    These stresses puzzled engineers because the levels were much lower than the material yield stress. The Versailles rail accident occurred on May 8, 1842, after the leading locomotive broke an axle, and the carriages behind piled into it and caught fire causing many deaths.   This prompted German scientist August Wöhler to develop the S-N curves used in fatigue analysis.  The term "fatigue" was chosen to describe the "tired metal" in the axles.

The collapse of the Tacoma Narrows Bridge "Galloping Gertie" was captured on film on November 7, 1940.  This failure is often referred to as the classic "resonant vibration" failure. But it was more properly a "self-excited" or "flutter" response, as discussed in Section 7.

### 4.3.3   Aerospace and Other Industries

Aerospace has myriad examples of potential vibration problems.  Helicopters may undergo "ground resonance" before takeoff.  Launch vehicles may have pogo oscillations in liquid engine propulsion systems.  Solid rocket boosters may have thrust oscillations.  Both high-performance aircraft and launch vehicles must withstand random vibration due to turbulent boundary layers and shock waves as they accelerate through the transonic velocity and encounter the maximum dynamic pressure condition.

Ships, automobiles, machine tools, buildings, nuclear reactors, and other mechanical systems and structures all have their vibration concerns and failure modes.

### 4.3.4   Failure Modes



Figure 4.8.  Mountain Bike Frame Fatigue Crack in Welded Joint

There are many types of potential failure modes including yielding, buckling, ultimate stress, fatigue, fretting, fastener loosening, and loss of sway space.  Engineers must understand these hazards so that the components, systems, and structures may be designed and tested accordingly.

Resonant excitation is often a factor in these failures.  Engineers thus have a responsibility to identify equipment natural frequencies through analysis and testing.  The natural frequency is the frequency at which the system would oscillate if it were given an initial displacement and then allowed to vibrate freely.   Resonance occurs when the excitation frequency is at or near the system's natural frequency.  Damping values, mode shapes, effective modal mass, and other dynamic parameters are also needed for this analysis.

### 4.3.5   Malfunctions
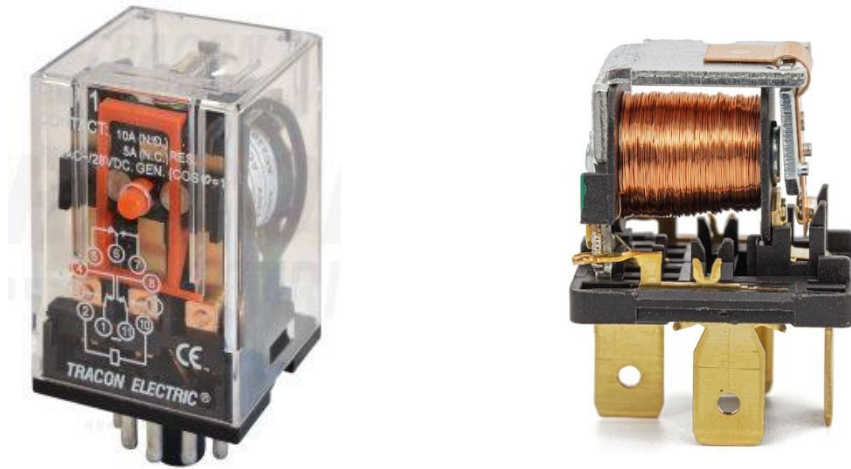


Figure 4.9.  Two Electromagnetic Relays

Electromagnetic relays and switches may experience "contact chatter" during shock and vibration.  One chatter example is a closed relay which intermittently opens in response to base excitation.  This does not represent a "hard failure" but may adversely affect system performance or cause other types of failures.  The relay may even undergo a "change of state" requiring a reset.

Relays that are used in launch avionics must withstand liftoff and ascent vibration, as well as pyrotechnic shock.

In addition, relays are used in nuclear power plant equipment to control pumps, valves, circuit breakers, etc.  The relays must withstand seismic excitation, particularly if they are part of circuits needed for safe plant shutdown.  Electrical switches and relays should thus be powered and monitored during dynamic testing.

Likewise, closed valves can leak under dynamic environments and should be monitored accordingly.

## 4.4 MACHINE HEALTH MONITORING



Figure 4.10.  Vibration Monitoring for Predictive Maintenance

Machines, pumps, and other equipment with reciprocating or rotating parts may experience vibration due to blade passing frequencies, gear mesh frequencies, magnetostriction motor hum, shaft misalignment, rotating imbalance, bearing defects, part loosens, etc.   In addition, fluid-handling machines, like fans and pumps will experience broadband turbulence.

Some vibration is normal.   But excessive vibration may cause accelerated wear and premature failure.  Equipment manufacturers should provide acceptable limits in terms of amplitude and frequency.   The amplitude specification may be in terms of displacement, velocity, or acceleration.

Vibration monitoring is thus needed to reduce maintenance costs, extend life, and improve safety.   Machine vibration can be measured with accelerometers which are permanently mounted on the machine and monitored continuously with a wireless network.    Or a technician may use a handheld device with an accelerometer that can be temporarily mounted to the machine via a magnetic base, as a periodic check.  A good practice is to take baseline measurements when the machine is new and operating properly.

## 4.5 VIBRATION ENERGY HARVESTING
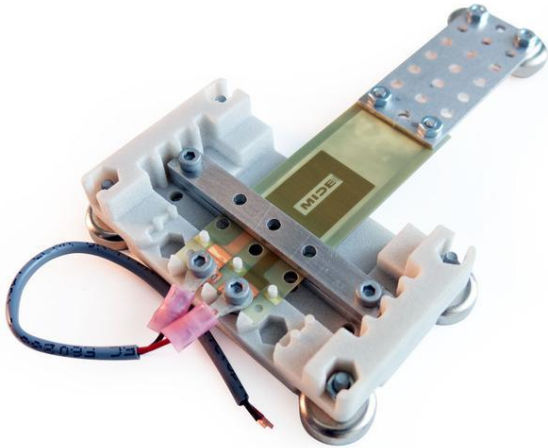


Figure 4.11.  Cantilever Piezoelectric Energy Harvesting Kit

Piezoelectric transducers or electromagnetic induction devices can be used to convert ambient vibration energy to electrical current to charge batteries or to power wireless sensor networks. As an example, consider a cooling pump in a factory.  The pump's vibration could be used to power its health monitoring sensor.

Piezoelectric crystals are asymmetric. The asymmetry in the unit cell of the material sets up the mechanism whereby deforming the crystal leads to a small potential difference.   The piezoelectric harvesters are typically cantilever beam structures.  A mass may be added to the free end of the beam to tune the device to the source's dominant vibration frequency.   Note that steady vibration with a dominant frequency is best suited for harvesting.  Outputs of 10 to 50 milliwatts are possible, depending on the vibration amplitude and frequency.

Another potential benefit of an energy harvesting device is that it removes energy from a system, thus providing some damping that can extend the system's life.

# 5   HUMAN VIBRATION

## 5.1 BODILY NATURAL FREQUENCIES
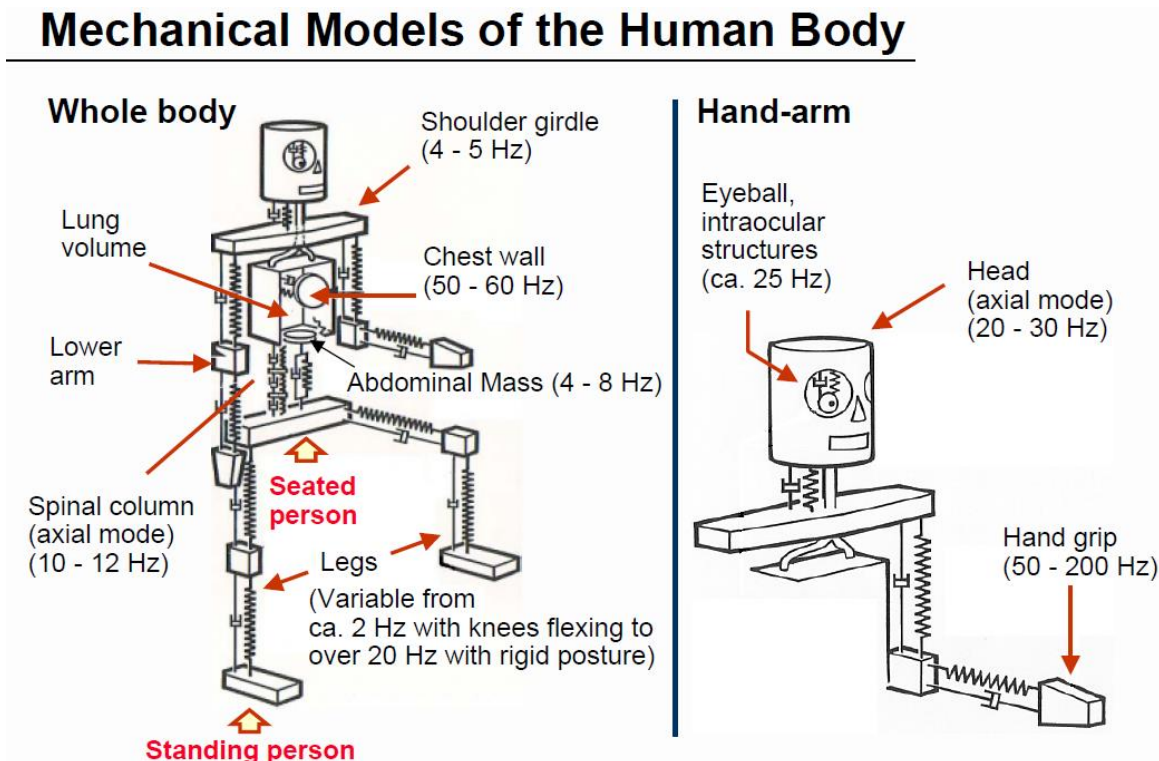


Figure 5.1.  Human Body Natural Frequencies (courtesy of Brüel & Kjær)

There are also biomedical concerns for the case where humans are exposed to vibration. Operators of farm equipment, busses, and trains may suffer spinal damage due to long-term exposure.  The human spinal column's natural frequency is 10 to 12 Hz.  Each organ and bodily part has its natural frequency.  Whole body vibration is addressed in ISO 2631 [2].  Hand-arm vibration is another concern for operators of power tools.

## 5.2 MOTION SICKNESS

### 5.2.1  Introduction
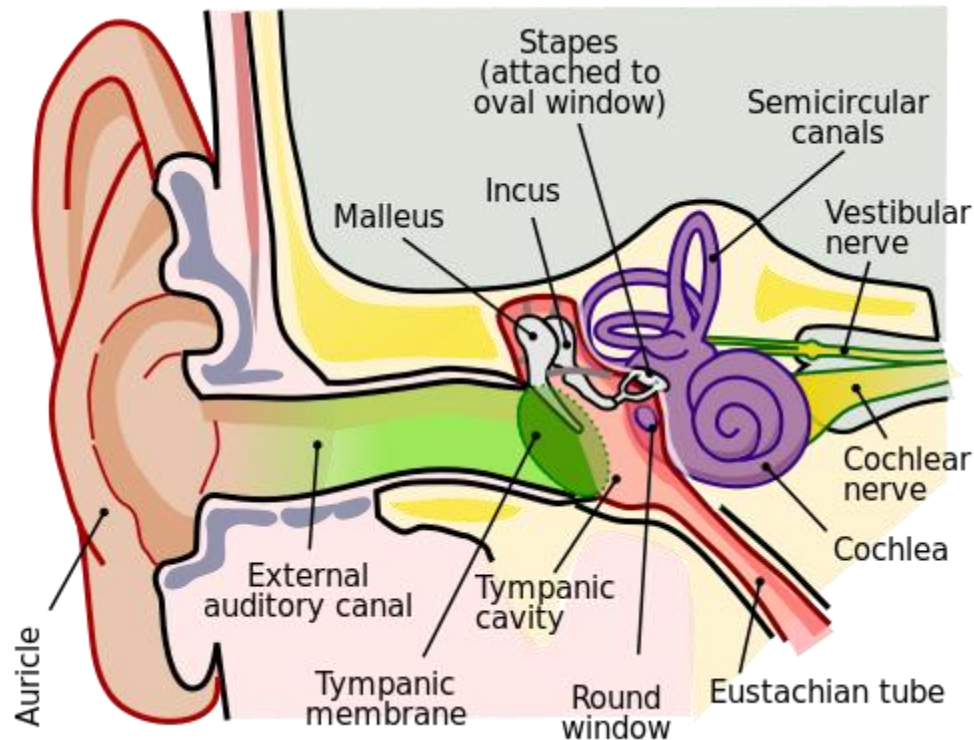
Figure 5.2.  Human Ear (Wikipedia)

Passengers in aircraft, amusement park rides, automobiles, ships, and spacecraft may experience motion sickness.  Occupants in tall buildings with a height greater than 50 meters may also experience this condition.  An individual's likelihood of becoming nauseated in response to vibration from these sources depends on many factors such as age, gender, previous motion experience, visual reference frame, head movement, etc.  The symptoms of motion sickness include dizziness, sweating, and vomiting.  Furthermore, dehydration may result from vomiting.

Motion sickness is caused by very low frequency vibration in the domain from 0.1 Hz to 0.5 Hz. M.J. Griffin [3] wrote in the Handbook of Human Vibration:

> Motion sickness occurs with motions of low frequencies at which the posture of the torso does not greatly alter the amount of translational motion transmitted to the upper parts of the body: transmissibility for vertical excitation is very near to unity at frequencies below 1 Hz in all persons.

### 5.2.2  Physiological Causes

Three sensory systems appear to have a role in motion sickness: visual, vestibular, and somatosensory.  The role of sight is straightforward.  Some individuals even become nauseated while viewing films with excessive motion, or while training in a car simulator.   The vestibular system consists of the cavities and semicircular canals in the ear.   Hair cells in the cavities detect translational movement. The semicircular canals sense rotational movement of the head.   Somatosensory organs are spread throughout the body.  These organ sense force and displacements.   One theory is that these systems may provide the brain with conflicting information during motion or even apparent motion, thus causing illness.

### 5.2.3  Ships

M.J. Griffin cited a study where 5% of the passengers on a ship experienced vomiting while the ship underwent a 0.2 m/sec^2 acceleration amplitude during a 3-hour voyage.   The corresponding amplitude would have been approximately 25 cm (10 inches) peak-to-peak, assuming a 0.2 Hz sinusoidal frequency.

The probability for motion sickness also depends on the direction of the oscillations.  The vertical and pitch axes are worst-case translational and rotational axes respectively in ships. Note that the vertical motion in ships is partly caused by pitch oscillation. The problem of seasickness can be reduced to some extent by locating passengers at the center of the ship.  Unfortunately, the principal vertical acceleration frequency of most large ships is close to 0.2 Hz, which is within the domain of maximum human sensitivity.

### 5.2.4  Automobiles

The fundamental frequency of a passenger car is typically 1.0 to 1.5 Hz.  Fortunately, this domain is at least one octave above the 0.1 Hz to 0.5 Hz domain of human sensitivity.  Researchers have thus found that the vertical oscillation of an automobile does not tend to correlate with carsickness.  Rather, carsickness tends to result from horizontal oscillations of the vehicle.   Furthermore, horizontal oscillations can be of greater magnitude in the horizontal

axis than in the vertical axis, over the domain of sensitivity.  Horizontal oscillations tend to be most severe during braking maneuvers and during travel down a winding road.


### 5.2.5   Aircraft
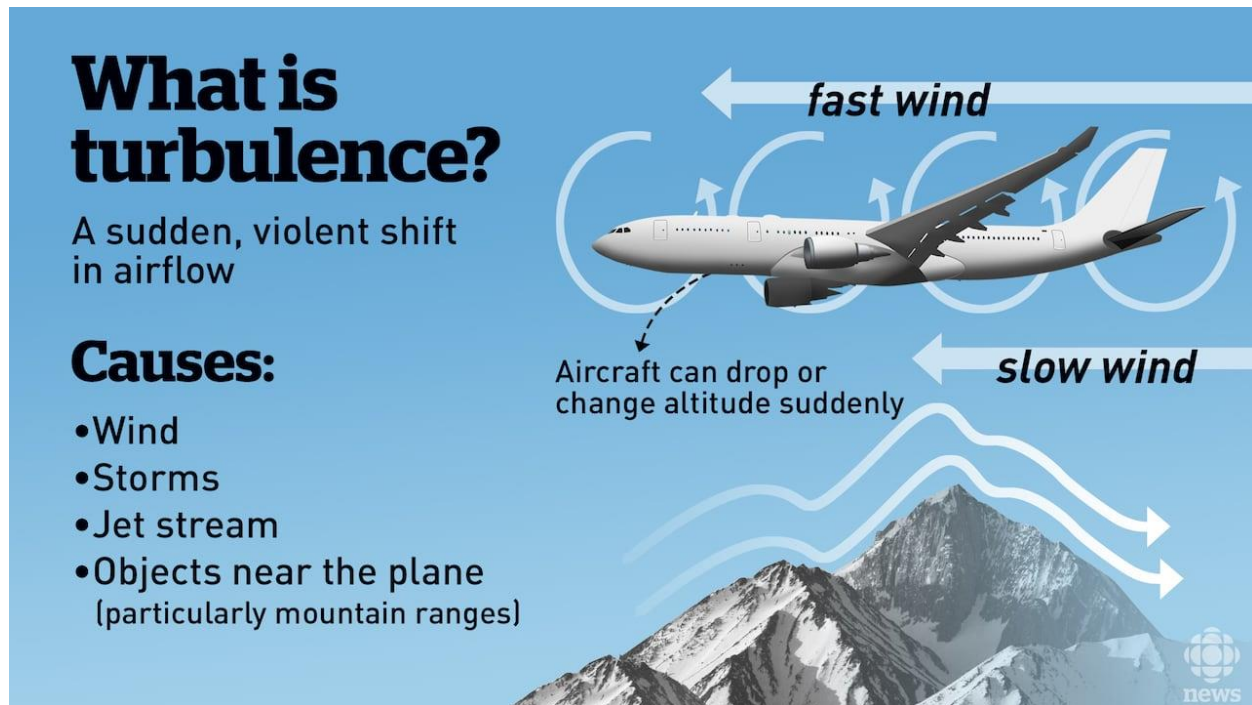


Figure 5.3.  Aircraft Turbulence (John Fraser/CBC)


Motion sickness in aircraft is most likely to occur during turbulence.  Passenger aircraft fly at high altitudes to avoid areas of turbulent airflow.  The incidence of airsickness is thus reduced. On the other hand, military pilots flying maneuvers in high-performance aircraft may be more likely to experience nausea.


### 5.2.6   Tall Buildings

The vibration modes of a building may be excited by wind.  The wind excitation mechanism is oncoming turbulence, as well as possible vortex shedding in the wake.    The buildings may sway back and forth or even twist in response to the wind.    The swaying problem is particularly severe at the top floors of the building.  The twisting problem is most severe at the building's corners.  Fortunately, a structure can be stabilized by active, semi-active, or passive control systems to dampen the movement.   For example, the Citicorp Tower in New York City

has a fundamental frequency of 0.15 Hz, which is within the sensitivity domain. The Tower has a "tuned mass damper" system that counteracts vibration at this frequency, however.

5.2.7   Sopite Syndrome

Sopite syndrome is a response to prolonged motion exposure. Drowsiness and mood changes are the primary characteristics of the syndrome. The sopite syndrome can exist in isolation from more apparent symptoms such as nausea, can last long after nausea has subsided, and can debilitate some individuals.  The sopite syndrome has been attributed to motion-induced drowsiness such as that experienced by a baby when rocked.

The effects of the sopite syndrome may range from minor physical inconveniences to hazardous conditions. People who operate automobiles, airplanes, etc., may experience impaired motor function due to the motions of the vehicle.

The symptoms often persist for a time after the motional stimulus has ceased.

5.2.8   Whole Body Vibration as Exercise



Figure 5.4.  Whole Body Vibration, Base Excitation

The vibrating plate transmits energy to the person's body forcing muscles to contract and relax dozens of times each second.

Advocates claim that the benefits include:

- weight loss
- fat burning
- improved flexibility
- enhanced blood flow
- reduced bone mass loss
- reduced muscle soreness after exercise
- decrease of the stress hormone cortisol

But some doctors caution that further research is needed.

# 6 VIBRATION EXCITATION SOURCES

## 6.1 SOURCE CHARACTERIZATION

Engineers must also determine the characteristics of the shock or vibration excitation so that they can properly analyze and test the affected components or structures. Design modifications can then be made to avoid dynamic coupling between the excitation frequencies and the structure's natural frequencies. The excitation sources can be grouped into four types.

## 6.2 INITIAL DISPLACEMENT OR VELOCITY

A common example is a guitar string which is given an initial displacement and then suddenly released. Another is the Pegasus drop transient which is discussed in Section 15.8. An initial velocity example is a drop shock test machine.

## 6.3 APPLIED FORCE

Wind, acoustic pressure, and ocean currents impacting structures are all cases of applied force. So is footfall excitation on a pedestrian bridge. Shafts with rotating imbalance also impart an applied force within a machine. Another example is the force from a hammer striking an object. Impulse hammers are used to purposely excite a structure in modal testing to identify the structure's natural frequencies, damping ratios, and mode shapes. The force may also be applied by a small shaker attached to the structure via a stinger rod.

## 6.4 BASE EXCITATION

Seismic excitation is a classic example of base excitation. Another is an automobile traveling over a speed bump or down a washboard road. Aircraft and launch vehicle avionics components are subjected to base excitation from their mounting structures during flight. These components are tested on large shaker tables to verify that they can withstand flight vibration before installation into the vehicle.

## 6.5 SELF-EXCITED VIBRATION

Self-excited vibration is a special case where the alternating force that sustains the motion is created or controlled by the motion itself.  This source type is also referred to as negative damping.  Airfoil and bridge flutter are two examples in this category.  See the Tacoma Narrows Bridge failure in Section 7.  The pogo oscillation in a launch vehicle with liquid engines is another case.

## 6.6 SOURCE PHOTO GALLERY, INITIAL DISPLACEMENT



Figure 6.1.  Spring-Action Teeter Totter Natural Frequency

The author gave the teeter-totter an initial displacement, without human riders, and recorded the damped sine oscillation with an Android smartphone accelerometer app.

The natural frequency was 2.1 Hz with 0.6% damping, as determined via a damped-sine curve-fit. The frequency would decrease with riders.
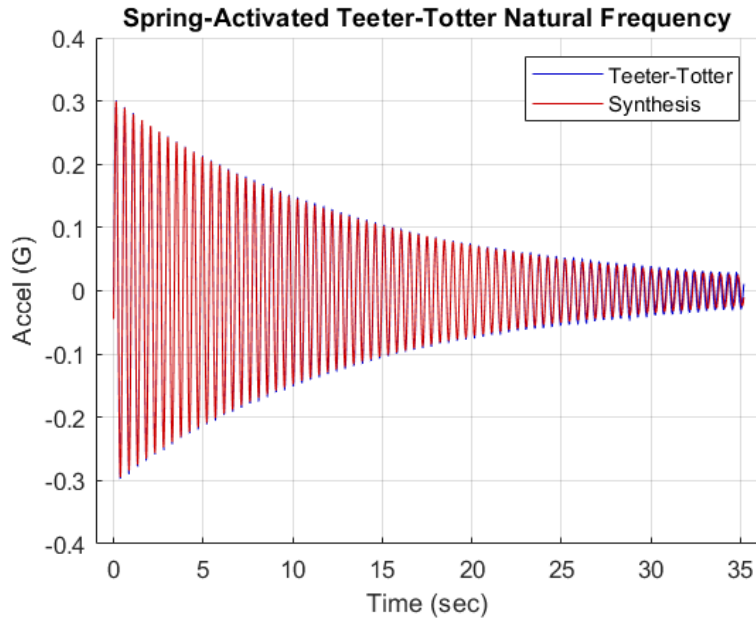
Figure 6.2.  Teeter-Totter Free Vibration

## 6.7 SOURCE PHOTO GALLERY, BASE EXCITATION



Figure 6.3.  Washboard Road, Base Excitation

Corrugations or ripples can form on gravel and dirt roads with dry, granular road materials, with repeated traffic.  This washboard pattern creates an uncomfortable ride for the occupants of traversing vehicles and hazardous driving conditions for vehicles that travel too fast to maintain traction and control due to decreased contact between the tires and the road.

There are four primary causes of this pattern:

1. Drivers' acceleration, speed & braking habits
2. Lack of moisture
3. Poor quality of gravel
4. Lack of crown on the surface

Furthermore, grading can be used to remove potholes and washboards.   But the road grader may worsen the washboards if its speed is too fast or if its blade is set improperly.

Note that a vehicle's suspension system distributes the shock and energy of road irregularities with a bouncing rhythm called harmonic oscillation.  The wheels exert extra force on the road at each downstroke, causing the road particles to either pack or displace at regular intervals. Once a pattern of ruts starts to establish itself, it becomes self-reinforcing due to forced

oscillation. The next vehicle hits the same irregularities in the road and bounces at the same rate, causing the pattern to become more and more defined. Forced oscillation overcomes minor variations in oscillation rate that might otherwise arise due to differences in car weight.
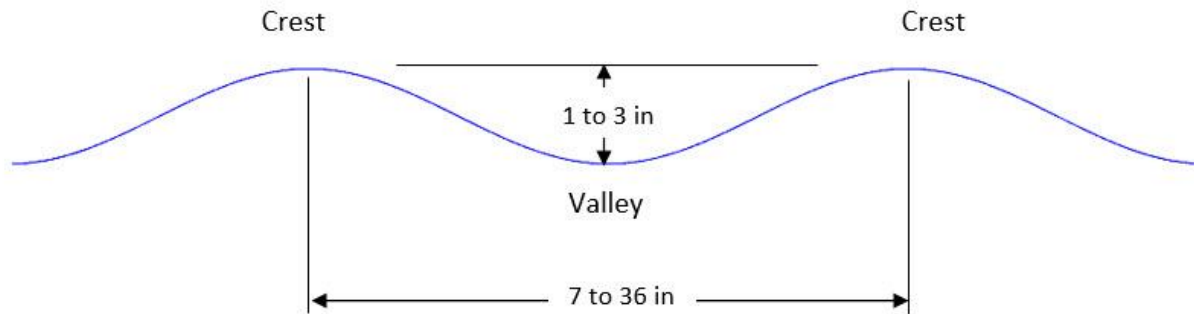


Figure 6.4.  Typical Washboard Road Geometry

Another critical part of the feedback loop is the driver.  Depending on the speed, the downstroke exerted by the car wheels may meet the road at a point where a bump is ramping upwards causing the car to respond with a high displacement.  Instinctively, most drivers slow to a speed at which the downstrokes coincide with the troughs between bumps, reinforcing the pattern.

The resulting road-induced vibration may damage shock absorbers and other suspension components.  Bolts may loosen.  Fatigue cracks may form in metal panels and parts.  Worn tie rod ends, worn-out bushings, and CV joints are also possible.

A mitigation strategy for drivers is to use a lower tire pressure to increase the contact area between the tires and the road.  Drivers can also turn off the vehicle's Automatic Braking System (ABS) since conventional brakes work better in loose material.

Figure 6.5.  Speed Bump (left) and Hump (Right)

Speed Bumps are designed to:

- Improve pedestrian safety
- Reinforce stop signs in parking lots
- Reduce the risk of accidents on private residential streets, driveways, and parking lots

Speed bumps are specifically made to slow drivers down to between 2 to 5 mph.

Speed Humps are designed to:

- Slow traffic on public roads such as schools, hospitals, and anywhere reduced vehicle speeds are desired
- Be gentle enough so that emergency vehicles do not need to slow down in industrial areas or areas with heavy truck traffic where high speeds can lead to an overturned vehicle

Speed humps are specifically designed to slow vehicles to between 10 to 15 mph.

Figure 6.6. Loma Prieta Earthquake 1989, Base Excitation

The earthquake caused the Cypress Viaduct to collapse, resulting in 42 deaths. The Viaduct was a raised freeway that was part of the Nimitz freeway in Oakland, which is Interstate 880. The Viaduct had two traffic decks. Resonant vibration caused 50 of the 124 spans of the Viaduct to collapse. The reinforced concrete frames of those spans were mounted on weak soil. As a result, the natural frequency of those spans coincided with the excitation frequency of the earthquake ground motion. The Viaduct structure thus amplified the ground motion. The spans suffered increasing vertical motion. Cracks formed in the support frames. Finally, the upper roadway collapsed, slamming down on the lower road. The remaining spans which were mounted on firm soil withstood the earthquake.
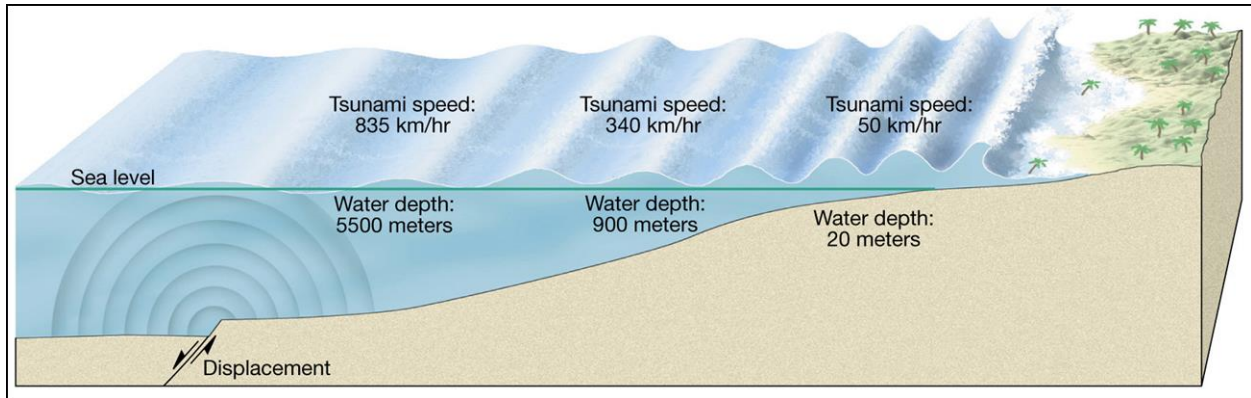
Figure 6.7.  Tsunami from Earthquake, Base Excitation

Tsunamis are formed due to ocean floor displacement. This most frequently occurs as a result of movement along a subducting plate.



Figure 6.8.  Cruise Ship Pool Slosh, Base Excitation

The water sloshing is due to base excitation from the ship's pitching motion.

By Ka23 13 - Own work, CC BY-SA 4.0, https://commons.wikimedia.org/w/index.php?curid=62275141

Figure 6.9.  Shaker Table Testing, Lateral Base Excitation

A small satellite is mounted to a slip table which is driven by a large electromagnetic shaker. The purpose of the test is to verify that the satellite can withstand the flight vibration that will be imparted by the launch vehicle.  The test can also be used to verify the parts and workmanship, including solder joints, fasteners, etc.

Figure 6.10.  Shaker Table Testing, Vertical Base Excitation


An equipment rack is mounted via wire rope isolators to an expander head which is mounted in turn on an electromagnetic shaker.

The damping can be very nonlinear, particularly depending on displacement amplitude.

The flexing of wire rope involves both Coulombic and viscous damping. At very low vibration levels, the wire strands stick together and little sliding occurs. The damping is low and the behavior is viscous.

With higher displacements, Coulomb damping predominates as the wires break free and start to slide against each other, absorbing large amounts of energy.

At large displacements, the bending and stretching of the wire strands overshadows the sliding friction and viscous behavior again starts to show.

The damping contribution is important, but the wire rope isolators' main effect is to reduce the fundamental frequency of the system.
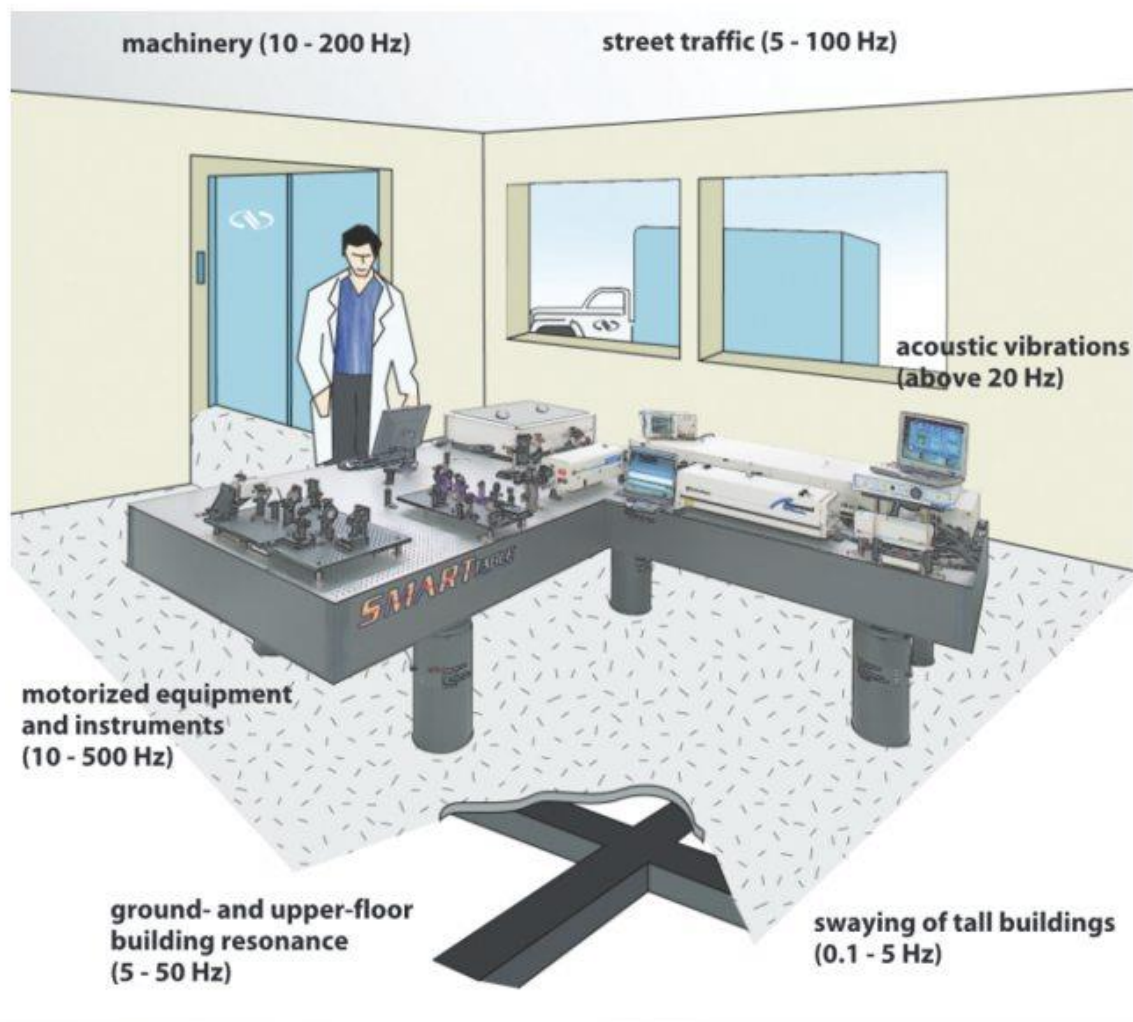
Figure 6.11.  Optical Bench, Base Excitation (Newport image)

Laser holography and electronic microscopes are sensitive to vibration.  All of the sources in the image represent base excitation to the benchtop except for airborne sound.

Pneumatic isolators are built into the bench legs to filter out external vibration above a certain frequency.  In addition, tuned mass dampers may be added to the table to control the benchtop's response at one or more of its natural frequencies.

The benchtop itself is constructed from honeycomb sandwich material for stiffness and stability purposes.  (Section 14).

## 6.8 SOURCE PHOTO GALLERY, APPLIED FORCE
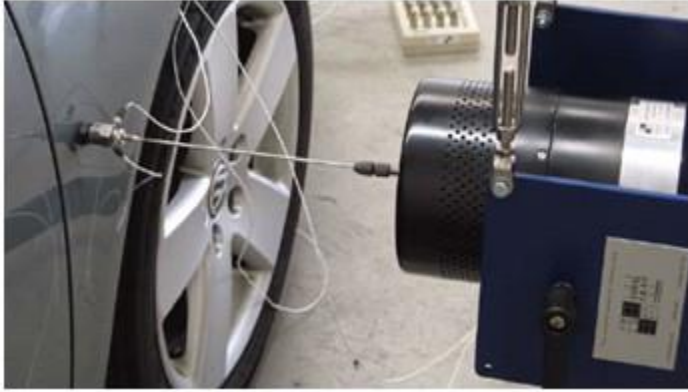


(Image courtesy of the Modal Shop)

A small shaker applies a force excitation to an automobile fender via a stinger rod. The applied force and resulting acceleration at the input point are measured by an impedance head transducer. Response accelerometers may be mounted at various locations on the vehicle.

Figure 6.12. Automobile Modal Test, Applied Force



Figure 6.13. Thumper Truck, Applied Force

A thumper truck is a vehicle-mounted ground impact system that can be used to provide a seismic source to perform both reflection and refraction seismic surveys for oil, natural gas, and mineral exploration. A heavy weight is raised by a hoist at the back of the truck and dropped about three meters, to impact the ground. The resulting ground waveforms are measured with geophones. Some thumpers use a technology called "Accelerated Weight Drop" (AWD), where

high-pressure gas is used to accelerate a heavy-weight Hammer (5,000 kg) to hit a base plate coupled to the ground.



Figure 6.14.  Space Shuttle Orbiter Ku-Band Antenna Dithering, Applied Force to Orbiter

The Ku-band antenna is the disk below the lower Atlantis decal.  Dither is a vibration employed in some mechanical systems to avoid stiction and to ensure smooth motion.  Stiction is short for static friction.  The antenna was dithered via a command signal at a frequency of 17 Hz to maintain its ability to smoothly search for Tracking and Data Relay Satellite System (TDRSS) satellites.  There was a concern that the antenna's resulting vibration would interfere with sensitive microgravity experiments such as crystal growth.

Figure 6.15.  Honeywell Inertial Navigation System Dithering, Applied Force

The Inertial Navigation System (INS) has Ring Laser Gyros (RLGs).    Each gyro has a dither frequency.  The unit shown above has dither frequencies at 526, 573, and 620 Hz.

One of the inherent difficulties of the laser gyro is the problem of frequency "lock-in." [4]  The laser gyro measures turning rate by sensing frequency differences. When the rate of turn is very small and thus the frequency difference between the two beams is also small, there is a tendency for the two frequencies to couple together, or "lock-in," and a zero turning rate is indicated.

Lock-in limits the accuracy of the laser gyro at important low turn rates. Fortunately, there are several ways to overcome the problem of lock-in. A common approach is to "dither," or vibrate, the gyroscope, either mechanically or electromagnetically. This dithering of the laser gyroscope adds to the complexity, weight, and size of the device, and, in the case of mechanical dithering, adds moving mechanical parts.

Figure 6.16.  Space Shuttle & Ares I Solid Rocket Boosters, Applied Pressure

Solid rocket boosters have elongated internal combustion cavities which act as organ pipes. Vortex shedding within the hot exhaust gases drives standing pressure waves inside these cavities.  These pressure waves have a fundamental thrust oscillation frequency with integer harmonics.  The cavities can be modeled as closed-closed pipes because the nozzle throat diameter is relatively small compared to the cavity diameter.  The Space Shuttle boosters' thrust oscillation frequency was 15 Hz.  The Ares I vehicle was projected to have a 12 Hz oscillation, but this vehicle was canceled before what would have been its first flight.  Note that the speed of sound in the internal hot exhaust gas is about 3500 ft/sec.

Figure 6.17.  Titan II Gemini Vehicle, Pogo Oscillation

Rocket vehicles with liquid engines, such as the Titan II, may experience combustion instability, which causes excessive vibration forces.  This is a potential source of self-excited vibration, whereby the elastic vehicle structure and the propulsion system form a closed-loop feedback system.

There are several types of combustion instability vibration effects. A common effect is "Pogo," which is similar to Pogo stick motion. In this case, a low-frequency oscillation in the combustion chamber, or propellant feed system, excites the longitudinal vibration mode of the entire rocket vehicle, or some other structural mode.  This may create a cyclical energy exchange between the vibration mode and the propulsion system oscillation.  The problem may also be initiated when a wind gust or some other perturbation excites the vibration mode.  This vibration in turn causes an oscillation in the propulsion system, which further excites the vibration.

Placing accumulators in the fuel and oxidant lines to damp out the pressure fluctuations solves this Pogo problem. The accumulator contains a volume of gas that acts like a soft spring to reduce the propellant frequency to well below that of critical structural frequencies.  The accumulator volume must be carefully selected to meet this goal.
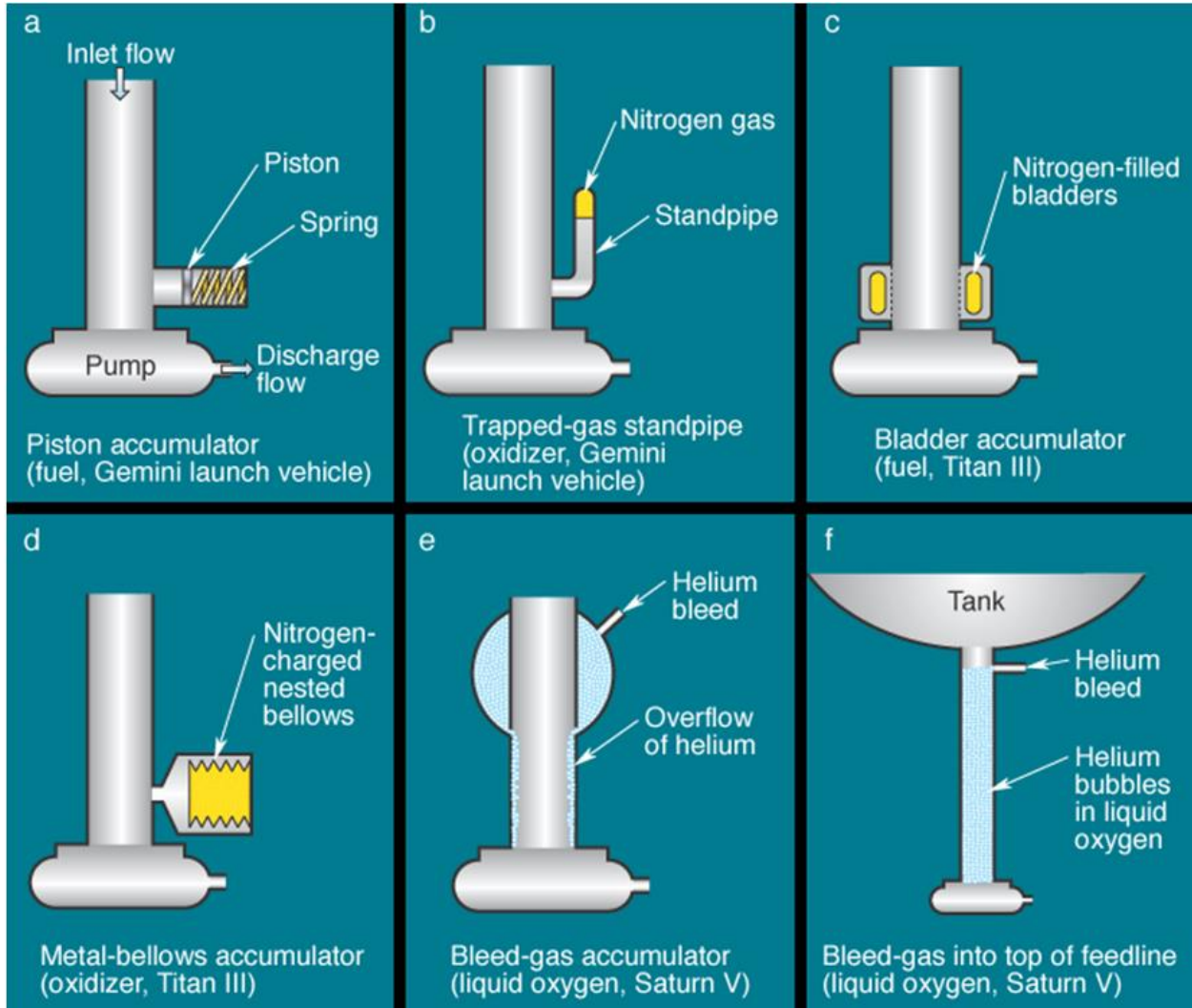
Figure 6.18.  Pogo Oscillation Mitigation Devices

Image courtesy of the Aerospace Corporation.

# 7 TACOMA NARROWS BRIDGE FAILURE

## 7.1 BRIDGE INTRODUCTION



Figure 7.1.  Torsional Mode of the Tacoma Narrows Bridge

The Tacoma Narrows Bridge failure is an example of self-excited vibration of such importance that it warrants its own section in this document.  The original Tacoma Narrows Bridge was opened to traffic on July 1, 1940.  It was located in Washington State, near Puget Sound.

The Tacoma Narrows Bridge was the third-longest suspension bridge in the United States at the time, with a length of 5939 feet including approaches.  Its two supporting towers were 425 feet high.  The towers were 2800 feet apart.

Before this time, most bridge designs were based on trusses, arches, and cantilevers to support heavy freight trains.  Automobiles were obviously much lighter.  Suspension bridges were both more elegant and economical than railway bridges.  The suspension design thus became favored for automobile traffic.  Unfortunately, engineers did not fully understand the forces acting upon bridges.  Neither did they understand the response of the suspension bridge design to these forces.

Furthermore, the Tacoma Narrows Bridge was built with shallow plate girders instead of the deep stiffening trusses of railway bridges. Note that the wind can pass through trusses. Plate girders, on the other hand, present an obstacle to the wind. As a result of its design, the Tacoma Narrows Bridge experienced rolling undulations that were driven by the wind. It thus acquired the nickname "Galloping Gertie."

## 7.2 BRIDGE COLLAPSE



Figure 7.2. Tacoma Narrows Bridge Collapse

Strong winds caused the bridge to collapse on November 7, 1940. Initially, 35 mph winds excited the bridge's transverse vibration mode, with an amplitude of 1.5 feet. This motion lasted 3 hours. The wind then increased to 42 mph. In addition, a support cable at mid-span snapped, resulting in an unbalanced loading condition. The bridge response thus changed to a 0.2 Hz torsional vibration mode, with an amplitude of up to 28 feet. The torsional mode is shown in Figure 7.1.

The torsional mode shape was such that the bridge was effectively divided into two halves. The two halves vibrated out-of-phase with one another. In other words, one half rotated clockwise, while the other rotated counterclockwise. The two half spans then alternate polarities.

One explanation of this is the "law of minimum energy." A suspension bridge may either twist as a whole, or divide into half spans with opposite rotations. Nature prefers the two half-span option since this requires less wind energy. The dividing line between the two half-spans is

called the "nodal line."  Ideally, no rotation occurs along this line.  The bridge collapsed during the excitation of this torsional mode.  Specifically, a 600-foot length of the center span broke loose from the suspenders and fell a distance of 190 feet into the cold waters below.  The failure is shown in Figure 7.2.

## 7.3 BRIDGE FAILURE THEORIES

### 7.3.1  Candidates

The fundamental weakness of the Tacoma Narrows Bridge was its extreme flexibility, both vertically and in torsion.   This weakness was due to the shallowness of the stiffening girders and the narrowness of the roadway, relative to its span length.  Engineers still debate the exact cause of its collapse, however.  Three theories are:

1.  Random turbulence
2.  Periodic vortex shedding
3.  Aerodynamic instability (negative damping)

These theories are taken from Reference [5].  Aerodynamic instability is the leading candidate.

### 7.3.2  Random Turbulence

An early theory was that the wind pressure simply excited the natural frequencies of the bridge.  This condition is called "resonance."  The problem with this theory is that resonance is a very precise phenomenon, requiring the driving force frequency to be at, or near, one of the system's natural frequencies to produce large oscillations.  The turbulent wind pressure, however, would have varied randomly with time.  Thus, turbulence would seem unlikely to have driven the observed steady oscillation of the bridge.

### 7.3.3  Vortex Shedding

Theodore von Karman, a famous aeronautical engineer, was convinced that vortex shedding drove the bridge oscillations.  A diagram of vortex shedding around a spherical body is shown in Figure 7.3.  Von Karman showed that blunt bodies such as bridge decks could also shed periodic vortices in their wakes.

A problem with this theory is that the natural vortex shedding frequency was calculated to be 1 Hz, as shown in Section 7.4. This frequency is also called the "Strouhal frequency." The torsional mode frequency, however, was 0.2 Hz. This frequency was observed by Professor F. B. Farquharson, who witnessed the collapse of the bridge. The calculated vortex shedding frequency was five times higher than the torsional frequency. It was thus too high to have excited the torsional mode frequency.

In addition to "von Karman" vortex shedding, a flutter-like pattern of vortices may have formed at a frequency coincident with the torsional oscillation mode. Whether these flutter vortices were a cause or an effect of the twisting motion is unclear.



Figure 7.3. Vortex Shedding around a Spherical Body

### 7.3.4   Aerodynamic Instability

Aerodynamic instability is a self-excited vibration. In this case, the alternating force that sustains the motion is created or controlled by the motion itself. The alternating force disappears when the motion disappears. This phenomenon is also modeled as free vibration with negative damping.

Airfoil flutter and transmission line galloping are related examples of this instability. Further explanations of instability are given in References [6], [7], and [8].

The following scenario shows how aerodynamic instability may have caused the Tacoma Narrows Bridge to fail. For simplicity, consider the motion of only one span half. Assume that

the wind direction was not perfectly horizontal, perhaps striking the bridge span from below, as shown in Figure 7.4.
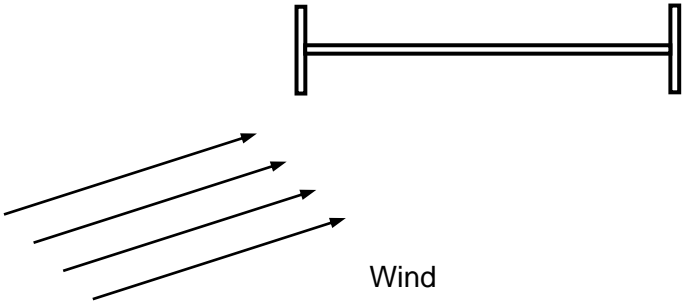


Figure 7.4.  Span at Initial Rest Position

Thus, the bridge is initially at an angle-of-attack relative to the wind.  Aerodynamic lift is generated because the pressure below the span is greater than the pressure above.  This lift force effectively places a torque, or moment, on the bridge.  The span then begins to twist clockwise as shown in the next figure.  Specifically, the windward edge rotates upward while the leeward edge rotates downward.
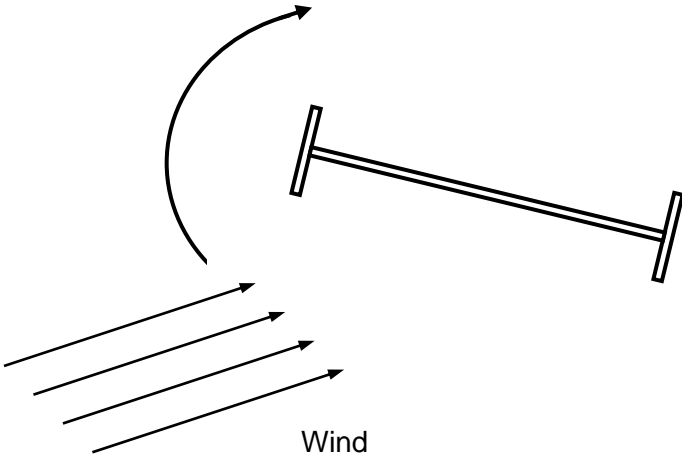


Figure 7.5.  Span Rotates Clockwise
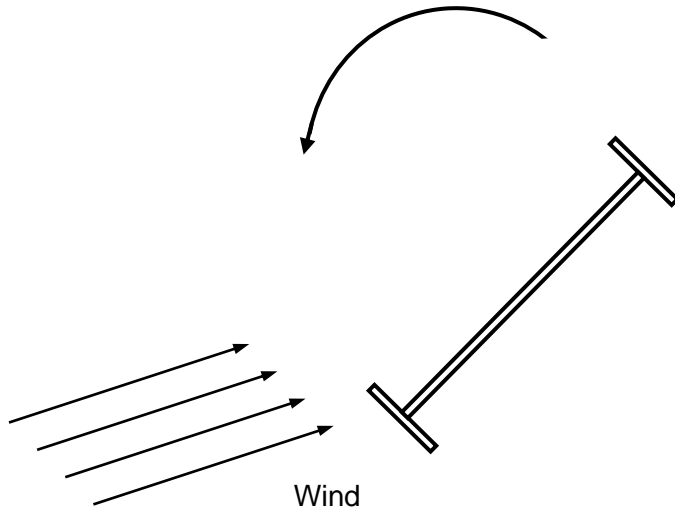
Figure 7.6.  Span Rotates Counterclockwise

The span has rotational stiffness, however.  Thus, elastic strain energy builds up as the span rotates.  Eventually, the stiffness moment overcomes the moment from the lift force.  The span then reverses its course, now rotating counterclockwise.

The span's angular momentum will not allow it to simply return to its initial rest position, however.  The reason is that there is little or no energy dissipation mechanism.  Thus, the span overshoots its initial rest position.  In fact, it overshoots to the extent that the wind now strikes the span from above as shown in Figure 7.6.  The wind's lift force now effectively places a counterclockwise moment on the span.

Once again, strain energy builds up in the span material.  Eventually, the stiffness moment exceeds the moment from the wind's lift force.  The span thus reverses course, now rotating clockwise.  Again, it overshoots its rest position.  The cycle of oscillation begins anew from the position shown in Figure 7.4, except that the span now has rotational velocity as it passes through the original rest position.

The cycles of oscillation continue repetitively.

Note that the wind force varies as a function of the span angle during the cycle.  The wind force may also vary with the angular velocity.  The wind force is not a function of time, however.

Eventually, one or two failure modes occur.  One possibility is that the span experiences fatigue failure due to an excessive number of stress reversals.  The other is that the angular displacement increased in an unstable manner until the material is stressed beyond its yield point, and then beyond its ultimate stress limit.

These two failure modes can be interrelated.  For example, accumulated fatigue effectively lowers the yield and ultimate stress limits.  Regardless, the bridge collapses.

As a final note, the aerodynamic instability oscillation is not a resonant oscillation since the wind does not have a forcing frequency at, or near, the bridge's torsional mode frequency. Some physics and engineering textbooks mistakenly cite the Tacoma Narrows Bridge as an example of resonance.  This problem is discussed in Reference [9]. Nevertheless, the bridge's collapse remains the most famous structural failure due to vibration.

## 7.4 BRIDGE'S STROUHAL FREQUENCY

The original Tacoma Narrows Bridge collapsed in 1940.  It experienced severe torsional oscillations driven by a 42 mph wind. The fundamental weakness of the Tacoma Narrows Bridge was its extreme flexibility, both vertically and in torsion.   This weakness was due to the shallowness of the stiffening girders and the narrowness of the roadway, relative to its span length. A cross-section of the bridge is shown in Figure 7.7.
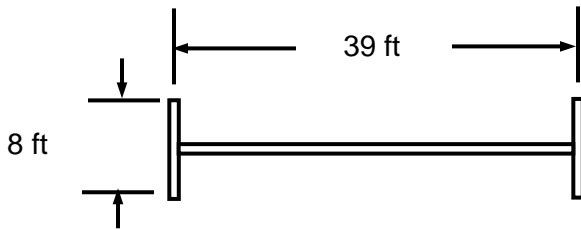


Figure 7.7.  Cross-section of Tacoma Narrows Bridge Span

The Strouhal number for the bridge cross-section is S=0.11 according to Reference [9]. Furthermore, the characteristic dimension is the girder height of 8 ft, which may be substituted for the diameter.  The Strouhal frequency for a 42 mph (61.6 ft/sec) wind is thus

$$ f_S = S\,U/D \tag{7.1} $$

$$ f_S = 0.11\,(61.1 \text{ ft/sec})/(8 \text{ ft}) = 0.84 \text{ Hz} \tag{7.2} $$

The Strouhal frequency is rounded to 1 Hz in Reference [9].  On the other hand, the bridge's torsional oscillation was observed to be 0.2 Hz.  The Strouhal frequency was thus at least two octaves greater than the torsional mode frequency.  Billah and Scanlan thus argue in Reference [9] that the Karman vortex shedding could not have driven the torsional mode oscillation.  They argue instead that an aerodynamic instability resulted in a self-excited oscillation, which caused the failure.  Several decades after the failure, the matter is not completely settled.

## 7.5 REPLACEMENT BRIDGE
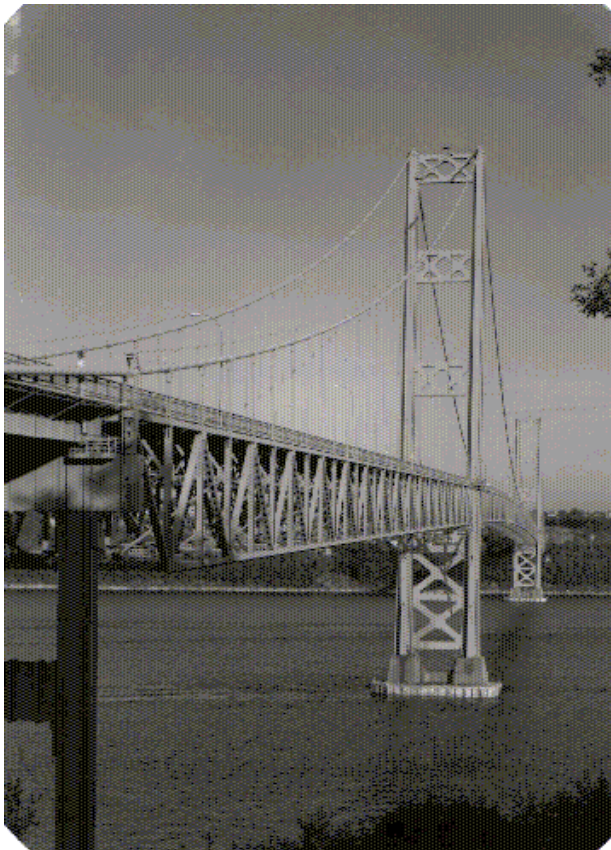


A new Tacoma Narrows Bridge was built in 1950.  The new bridge has truss girders that allow the wind to pass through.  It also has increased torsional stiffness because it was thicker and wider.  Furthermore, wind tunnel testing was performed to verify the design of the new bridge before its construction.  A similar bridge was later built alongside the new bridge in the figure to ease traffic flow, with one-way traffic on each bridge.

Figure 7.8.  New Tacoma Narrows Bridge

## 8.1 FREE VIBRATION MODEL
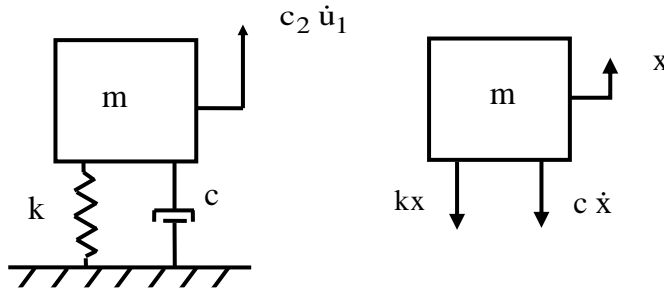


Figure 8.1.  Single-degree-of-Freedom System, Spring-Mass Model

The mass value is $m$.  The viscous damping coefficient is $c$.  The spring stiffness from Hooke's law is $k$.  The displacement is $x$.  The velocity is $\dot{x}$.  The equation of motion is derived using Newton's law.

$$\sum F = m\ddot{x} \tag{8.1}$$

$$m\ddot{x} = -kx - c\dot{x} \tag{8.2}$$

$$m\ddot{x} + c\dot{x} + kx = 0 \tag{8.3}$$

The resulting equation of motion is a second-order, ordinary differential equation, linear, homogenous with constant coefficients.  The angular natural frequency in radians/sec is

$$\omega_n = \sqrt{k/m} \tag{8.4}$$

The natural frequency in Hz is

$$f_n = \omega_n \, / \, (2\pi) \tag{8.5}$$

The natural frequency is the frequency at which the system would oscillate if it were given an initial displacement and then allowed to vibrate freely. It is also the frequency at which an energy exchange occurs between kinetic and potential energy.

As an example, consider an SDOF system with m= 5 lbm and k=20000 lbf/in. Calculate the natural frequency with the proper unit conversion.

$$\omega_n = \sqrt{\frac{20000 \text{ lbf/in}}{(5 \text{ lbm})\left(\frac{1 \text{ lbf sec}^2/\text{in}}{386 \text{ lbm}}\right)}} = 1243 \text{ rad/sec} \tag{8.6}$$

$$f_n = 1243 \text{ rad/sec} / (2\pi) \sim 200 \text{ Hz} \tag{8.7}$$

The period T is the inverse of the natural frequency.

$$T = 1 / f_n \tag{8.8}$$

Furthermore, the damping coefficient divided by mass can be represented as

$$c/m = 2\,\xi\,\omega_n \tag{8.9}$$

The corresponding amplification factor is

$$Q = 1/(2\,\xi) \tag{8.10}$$

The damped natural frequency is

$$\omega_d = \omega_n \sqrt{1 - \xi^2} \tag{8.11}$$

The free vibration solution to equation (8.3) can be found using a Laplace transform and applying the initial displacement and velocity per Reference [10]. The resulting displacement is

$$x(t) = \exp(-\xi\,\omega_n t)\left\{ x(0)\cos(\omega_d t) + \left[\frac{\dot{x}(0) + \xi\,\omega_n x(0)}{\omega_d}\right]\sin(\omega_d t) \right\} \tag{8.12}$$

The resulting time history is a damped sinusoid, similar to the Pegasus drop transient flight accelerometer data shown later in this document in Figure 15.14.

## 8.2 CONSERVATION OF ENERGY METHOD

The conservation of energy method is based on the time derivative of the total energy of an undamped system.

$$\frac{d}{dt}(K_E + P_E) = 0 \tag{8.13}$$

Apply this method to the SDOF system in Figure 8.1 to derive the equation of motion.

$$\frac{d}{dt}\left(\frac{1}{2}m\dot{x}^2 + \frac{1}{2}kx^2\right) = 0 \tag{8.14}$$

$$m\dot{x}\ddot{x} + kx\dot{x} = 0 \tag{8.15}$$

Dividing through by the velocity term yields the equation of motion for the undamped SDOF system.

$$m\ddot{x} + kx = 0 \tag{8.16}$$

## 8.3 RAYLEIGH METHOD

The Rayleigh method can be used to determine the fundamental frequency of an undamped system by setting the maximum kinetic energy $K_E$ to the maximum potential energy $P_E$.

$$[\,K_E\,]_{max} = [\,P_E\,]_{max} \tag{8.17}$$

The kinetic energy for the SDOF system in Figure 8.1 is

$$K_E = \frac{1}{2}m\dot{x}^2 \tag{8.18}$$

The potential energy for the SDOF system is

$$P_E = \frac{1}{2}kx^2 \tag{8.19}$$

Assume a displacement of

$$x(t) = A \sin(\omega_n t) \tag{8.20}$$

The corresponding velocity is

$$\dot{x}(t) = A \omega_n \cos(\omega_n t) \tag{8.21}$$

The energy terms become

$$K_E = \frac{1}{2} m \omega_n{}^2 A^2 \cos^2(\omega_n t) \tag{8.22}$$

$$P_E = \frac{1}{2} k A^2 \sin^2(\omega_n t) \tag{8.23}$$

Substitute the two energy terms into equation (8.17).

$$\frac{1}{2} m \omega_n{}^2 A^2 = \frac{1}{2} k A^2 \tag{8.24}$$

Algebraic simplification yields the expected natural frequency

$$\omega_n = \sqrt{k/m} \tag{8.25}$$

## 8.4 NATURAL FREQUENCY EXAMPLE

An avionics component is modeled as a solid mass per Figure 8.1. The goal is to mount the component via elastomeric isolator bushings so that the natural frequency is 30 Hz. The isolators will filter out high-frequency vibration energy from the base excitation. Calculate the required isolator stiffness using equation (8.4).

$$k = m \omega_n{}^2 = (2\pi f_n)^2 m \tag{8.26}$$

$$k = \left( 2\pi \left( 30 \frac{\text{cycles}}{\text{sec}} \right) \right)^2 (5 \text{ lbm}) \left( \frac{1 \text{ lbf sec}^2/\text{in}}{386 \text{ lbm}} \right) = 460 \frac{\text{lbf}}{\text{in}} \tag{8.27}$$

The stiffness $k$ in equation (8.27) is the total isolator stiffness. Now assume that the component will be mounted via four isolators in parallel. The individual isolator stiffness would then be 115 lbf/in. The next step would be to determine whether isolators with that stiffness value are commercially available. Otherwise, some adjustment or compromise would be needed.

## 8.5 OCTAVE RULE

A one-octave increase in frequency means that the higher frequency is twice the lower frequency. Conversely, the lower frequency is one-half the higher one. The number of octaves $n$ between any two frequencies $f_1$ and $f_2$ is

$$n = \log_2(f_2/f_1)$$

(8.28)

Note that a piano keyboard has steps of one-twelfth octave counting both the black and white keys.

The octave rule-of-thumb in mechanical vibration analysis states that there should be at least a one-octave separation between two frequencies to mitigate dynamic coupling. For example, consider an SDOF system subjected to a harmonic force or base excitation. The system's natural frequency should be tuned to less than one-half or greater than twice the excitation frequency.

Isolation or low tuning would be the case where the system's natural frequency was at most one-half the excitation frequency. High tuning occurs when the natural frequency is at least twice the excitation frequency. The system is said to be hard-mounted if the natural frequency is significantly greater than the excitation frequency.

As another example, consider two SDOF systems that are to be joined together. The respective natural frequencies should be separated by one octave before mounting one system with another. The Pegasus launch vehicle in Section 15.8 has a natural frequency of about 10 Hz. The payload's natural frequency should be high-tuned to 20 Hz or more to reduce dynamic coupling effects. Note that tuning below 5 Hz is a poor choice due to the possibility of high relative displacement of the payload within the vehicle fairing, as well as possible interference with the autopilot control algorithm stability. Further information about this frequency requirement can be found in the Pegasus Payload User Guide.

**Middle C** (near C4)

A0 27.5 — A0# 29.135
B0 30.868
C1 32.703 — C1# 34.648
D1 36.708 — D1# 38.891
E1 41.203
F1 43.654 — F1# 46.249
G1 48.999 — G1# 51.913
A1 55.000 — A1# 58.270
B1 61.735
C2 65.406 — C2# 69.296
D2 73.416 — D2# 77.782
E2 82.407
F2 87.307 — F2# 92.499
G2 97.999 — G2# 103.83
A2 110.00 — A2# 116.54
B2 123.47
C3 130.81 — C3# 138.59
D3 146.83 — D3# 155.56
E3 164.81
F3 174.61 — F3# 185.00
G3 196.00 — G3# 297.65
A3 220.00 — A3# 233.08
B3 246.94
C4 261.63 — C4# 277.18
D4 293.66 — D4# 311.13
E4 329.63
F4 349.23 — F4# 369.99
G4 392.00 — G4# 415.30
A4 440.00 — A4# 466.16
B4 493.88
C5 523.25 — C5# 554.37
D5 587.33 — D5# 622.25
E5 659.25
F5 698.46 — F5# 739.99
G5 783.99 — G5# 830.61
A5 880.00 — A5# 932.33
B5 987.77
C6 1046.5 — C6# 1108.7
D6 1174.7 — D6# 1244.5
E6 1318.5
F6 1396.9 — F6# 1480.0
G6 1568.0 — G6# 1661.2
A6 1760.0 — A6# 1864.7
B6 1979.5
C7 2093.0 — C7# 2217.5
D7 2349.3 — D7# 2489.0
E7 2637.0
F7 2793.8 — F7# 2960.0
G7 3136.0 — G7# 3322.4
A7 3520.0 — A7# 3729.3
B7 3951.1
C8 4186.0

## Piano Keyboard

The number beside each key is the fundamental frequency in units of cycles per second, or Hertz.

## Octaves

The A4 key has a frequency of 440 Hz. Note that A5 has a frequency of 880 Hz. The A5 key is thus one octave higher than A4 since it has twice the frequency.

## Overtones

An overtone is a higher natural frequency for a given string. The overtones are "harmonic" if each occurs at an integer multiple of the fundamental frequency. A note's first overtone is one octave higher than its fundamental frequency.

## Musical Scale

The modern musical scale can be traced to Pythagoras of Samos. Pythagoras was a Greek philosopher and mathematician, who lived from approximately 560 to 480 BC. He and his followers believed that all relations could be reduced to numerical relations. This conclusion stemmed from observations in music, mathematics, and astronomy. Pythagoras studied the sound produced by vibrating strings. He subjected two strings to equal tension. He then divided one string exactly in half. When he plucked each string, he discovered that the shorter string produced a pitch that was one octave higher than the longer string.

Figure 8.2. Piano Keyboard

## 8.6 SOME MATHEMATICS

### 8.6.1 Complex Variables

Complex variables with real and imaginary components are used extensively in signal analysis and structural dynamics. The imaginary component is expressed as a scale factor applied to $j = \sqrt{-1}$ .

Let $C$ be a complex variable with real component $A$ and imaginary component $B$.

$$C = A + j\,B \tag{8.29}$$

The variable $C$ is a vector in the complex, Euclidean plane. The magnitude is the norm.

$$|C| = \sqrt{A^2 + B^2} \tag{8.30}$$

The phase angle $\phi$ is

$$\phi = \arctan\,(B/A) \tag{8.31}$$

### 8.6.2 Euler's Equation

Euler's equation is a complex exponential function used for Fourier transforms and for structural modal response.

$$\exp(\pm\,j\alpha) = \cos(\alpha) \pm j\,\sin(\alpha) \tag{8.32}$$

Complex exponentials can simplify trigonometry because they are easier to manipulate than their sinusoidal components.

# 9 TWO-DEGREE-OF-FREEDOM SYSTEMS

## 9.1.1 Grounded Two-DOF System, Equation of Motion
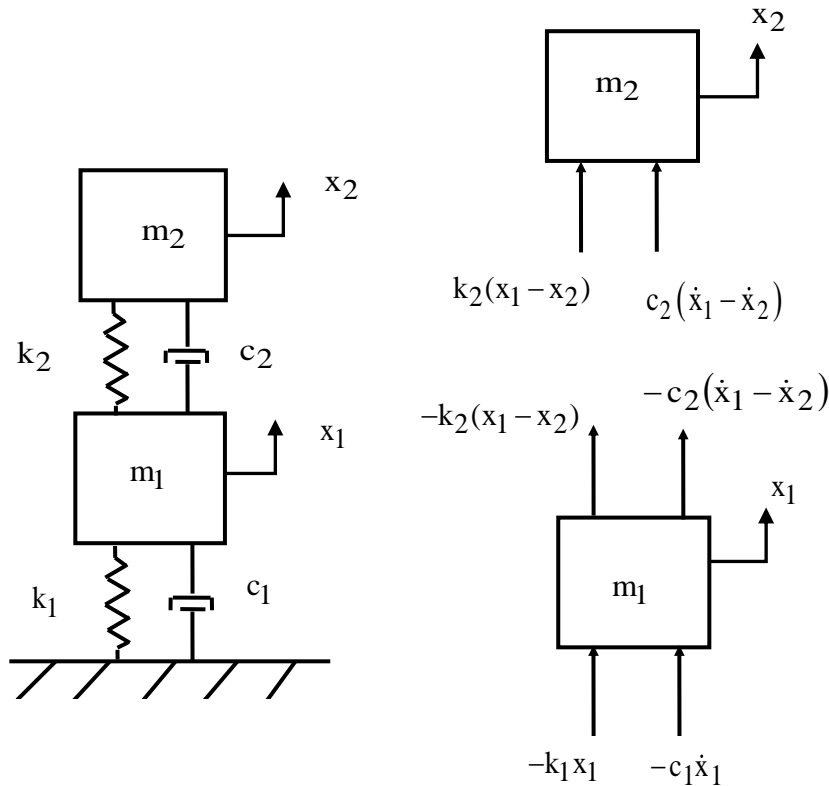


Figure 9.1.  Two-Degree-of-Freedom System, Spring-Mass Model

Newton's law can be applied to the system in Figure 9.1 to derive the equations of motion.  The steps are omitted for brevity.  The resulting pair of ordinary differential equations can be represented in matrix form and are coupled via the damping and stiffness matrices.

$$\begin{bmatrix} m_1 & 0 \\ 0 & m_2 \end{bmatrix} \begin{bmatrix} \ddot{x}_1 \\ \ddot{x}_2 \end{bmatrix} + \begin{bmatrix} c_1 + c_2 & -c_2 \\ -c_2 & c_2 \end{bmatrix} \begin{bmatrix} \dot{x}_1 \\ \dot{x}_2 \end{bmatrix} + \begin{bmatrix} k_1 + k_2 & -k_2 \\ -k_2 & k_2 \end{bmatrix} \begin{bmatrix} x_1 \\ x_2 \end{bmatrix} = \begin{bmatrix} 0 \\ 0 \end{bmatrix} \tag{9.1}$$

A shorthand form is

$$M\ddot{\bar{x}} + C\dot{\bar{x}} + K\bar{x} = \bar{0} \tag{9.2}$$

The matrices and vectors are

$$M = \begin{bmatrix} m_1 & 0 \\ 0 & m_2 \end{bmatrix}, \; C = \begin{bmatrix} c_1 + c_2 & -c_2 \\ -c_2 & c_2 \end{bmatrix}, \; K = \begin{bmatrix} k_1 + k_2 & -k_2 \\ -k_2 & k_2 \end{bmatrix}, \; \bar{x} = \begin{bmatrix} x_1 \\ x_2 \end{bmatrix} \tag{9.3}$$

Consider the undamped, homogeneous form of equation (9.2).

$$M\ddot{\bar{x}} + K\bar{x} = \bar{0} \tag{9.4}$$

### 9.1.2  Grounded Two-DOF System, Eigenvalues & Vectors

Seek a harmonic solution of the form

$$\bar{x} = \bar{q}\exp(j\omega t) \tag{9.5}$$

$$\dot{\bar{x}} = j\omega\bar{q}\exp(j\omega t) \tag{9.6}$$

$$\ddot{\bar{x}} = -\omega^2\bar{q}\exp(j\omega t) \tag{9.7}$$

The $\bar{q}$ vector is the generalized coordinate vector.   The undamped, homogeneous equation is transformed through substitution and algebraic manipulation into the generalized eigenvalue problem.

$$\{K - \omega^2 M\}\,\bar{q} = \bar{0} \tag{9.8}$$

The eigenvalues $\omega^2$ can be found by setting the determinant equal to zero.

$$\det\{K - \omega^2 M\} = 0 \tag{9.9}$$

There is an eigenvalue for each degree-of-freedom.  Each angular natural frequency is then calculated from the square root of the respective eigenvalue.  The corresponding eigenvectors represent orthogonal mode shapes.  The eigenvector for each mode is found via

$$\{K - \omega_i^2 M\}\,\bar{q} = \bar{0}\,, \qquad i = 1,2 \tag{9.10}$$

An eigenvector matrix Q can be formed.  The eigenvectors are inserted in column format.

$$Q = [ \quad \bar{q}_1 \quad | \quad \bar{q}_2 \quad ] = \begin{bmatrix} q_{11} & q_{12} \\ q_{21} & q_{22} \end{bmatrix}$$

<div align="right">(9.11)</div>

The coefficient $q_{ij}$ represents the modal displacement of mass i for mode j.

Each eigenvector can be multiplied by an arbitrary scale factor.  A mass-normalized eigenvector matrix $\widehat{Q}$ can be calculated such that the following orthogonality relations are obtained.

$$\widehat{Q}^T M \widehat{Q} = I$$

<div align="right">(9.12)</div>

$$\widehat{Q}^T K \widehat{Q} = \Omega$$

<div align="right">(9.13)</div>

The superscript T represents matrix transpose.  The identity matrix is I, a diagonal matrix of ones.  The diagonal matrix of eigenvalues $\Omega$.

## 9.1.3  Grounded Two-DOF System Example, Free Vibration

Now define a modal coordinate $\eta(t)$ in terms of the normalized eigenvector matrix such that the displacement vector is

$$\bar{x} = \widehat{Q} \, \bar{\eta} = \begin{bmatrix} \hat{q}_{11} & \hat{q}_{12} \\ \hat{q}_{21} & \hat{q}_{22} \end{bmatrix} \bar{\eta}$$

<div align="right">(9.14)</div>

Substitute equation (9.14) into equation (9.2).

$$M \widehat{Q} \, \bar{\ddot{\eta}} + C \widehat{Q} \, \bar{\dot{\eta}} + K \widehat{Q} \, \bar{\eta} = \bar{0}$$

<div align="right">(9.15)</div>

Premultiply by the transpose of the normalized eigenvector matrix.

$$\widehat{Q}^T M \widehat{Q} \, \bar{\ddot{\eta}} + \widehat{Q}^T C \widehat{Q} \, \bar{\dot{\eta}} + \widehat{Q}^T K \widehat{Q} \, \bar{\eta} = \widehat{Q}^T \bar{0}$$

<div align="right">(9.16)</div>

The orthogonality relationships yield

$$I \ddot{\bar{\eta}} + \hat{Q}^T C \hat{Q} \, \dot{\bar{\eta}} + \Omega \bar{\eta} = \bar{0} \tag{9.17}$$

Furthermore, the following simplifying assumption is made for the damping matrix.[1]

$$\hat{Q}^T C \hat{Q} = \begin{bmatrix} 2\xi_1\omega_1 & 0 \\ 0 & 2\xi_2\omega_2 \end{bmatrix} \tag{9.18}$$

The equation of motion can now be written as

$$\begin{bmatrix} 1 & 0 \\ 0 & 1 \end{bmatrix}\begin{bmatrix} \ddot{\eta}_1 \\ \ddot{\eta}_2 \end{bmatrix} + \begin{bmatrix} 2\xi_1\omega_1 & 0 \\ 0 & 2\xi_2\omega_2 \end{bmatrix}\begin{bmatrix} \dot{\eta}_1 \\ \dot{\eta}_2 \end{bmatrix} + \begin{bmatrix} \omega_1^2 & 0 \\ 0 & \omega_2^2 \end{bmatrix}\begin{bmatrix} \eta_1 \\ \eta_2 \end{bmatrix} = \begin{bmatrix} 0 \\ 0 \end{bmatrix} \tag{9.19}$$

The two equations are now uncoupled in terms of the modal coordinates. The modal displacement for free vibration response to initial conditions is found via Laplace transforms as shown in Reference [11]. The modal displacement for DOF i is

$$\eta_i(t) = \exp(-\xi_i \omega_i t)\left\{ \eta_i(0)\cos(\omega_{d,i}\, t) + \frac{1}{\omega_{d,i}}[\dot{\eta}_i(0) + \xi\omega_i\eta(0)]\sin(\omega_{d,i}\,t)\right\} \tag{9.20}$$

The damped angular natural frequency is

$$\omega_{d,i} = \omega_i\sqrt{1 - \xi_i^2} \tag{9.21}$$

The physical displacement can then be found by substituting equation (9.20) into (9.14). The physical displacements can be expressed in terms of the eigenvector coefficients and modal coordinates as

$$x_1(t) = \hat{q}_{11}\eta_1(t) + \hat{q}_{12}\eta_2(t) \tag{9.22}$$

$$x_2(t) = \hat{q}_{21}\eta_1(t) + \hat{q}_{22}\eta_2(t) \tag{9.23}$$

---

[1] "All models are wrong, but some are useful."  - George E. P. Box

The modal displacement initial conditions are required for the complete solution. These can be found from the following transformations.

$$\bar{x}(0) = \hat{Q}\,\bar{\eta}(0) \tag{9.24}$$

$$\hat{Q}^{\mathrm{T}} M\,\bar{x}(0) = \hat{Q}^{\mathrm{T}} M\,\hat{Q}\,\bar{\eta}(0) \tag{9.25}$$

$$\hat{Q}^{\mathrm{T}} M\,\hat{Q} = I \tag{9.26}$$

$$\bar{\eta}(0) = \hat{Q}^{\mathrm{T}} M\,\bar{x}(0) \tag{9.27}$$

Similarly,

$$\dot{\bar{\eta}}(0) = \hat{Q}^{\mathrm{T}} M\,\dot{\bar{x}}(0) \tag{9.28}$$

## 9.1.4  Grounded Two-DOF System, Participation Factors & Effective Modal Mass

The participation factors and effective modal masses are indicators of how excitable the modes are given uniform base excitation to the given system.  Some modes are more readily excited than others, and some cannot be excited at all for this excitation type.

The system's generalized mass matrix $\hat{m}$ is given by

$$\hat{m} = \hat{Q}^{\mathrm{T}} M\,\hat{Q} \tag{9.29}$$

Again, the generalized mass will be the identity matrix if the eigenvectors are mass normalized. Let $\bar{r}$ be the influence vector which represents the displacements of the masses resulting from the static application of a unit ground displacement. Define a coefficient vector $\bar{L}$ as

$$\bar{L} = Q^{\mathrm{T}} M\,\bar{r} \tag{9.30}$$

The modal participation factor matrix $\Gamma_i$ for mode $i$ is

$$\Gamma_i = \bar{L}_i / \hat{m}_{ii} \tag{9.31}$$

The effective modal mass $m_{eff, i}$ for mode $i$ is

$$m_{eff, i} = \bar{L}_i{}^2 / \hat{m}_{ii} \qquad (9.32)$$

### 9.1.5  Two-DOF System Example, Response to Initial Displacement

The system in Figure 9.1 has the following parameters.

Table 9.1.  Grounded Two-DOF System, Parameters

| Variable | Value |
|----------|-------|
| $m_1$ | 2 lbm |
| $m_2$ | 1 lbm |
| $k_1$ | 150 lbf/in |
| $k_2$ | 100 lbf/in |
| $x_1$ | 0.01 in |
| $x_2$ | 0.005 in |

Assume 5% damping for each mode.  The initial velocity is zero for each mass.

Apply the mass and stiffness values from Table 9.1 into equation (9.1) to form the following matrices.

$$M = \begin{bmatrix} 2/386 & 0 \\ 0 & 1/386 \end{bmatrix}, \ K = \begin{bmatrix} 250 & -100 \\ -100 & 100 \end{bmatrix} \qquad (9.33)$$

The 1/386 factor is needed to convert lbm to lbf sec^2/in.  The eigenvalues and vectors are found by inserting these matrices into equations (9.9) and (9.10).   The results are shown in the following table.

Table 9.2.  Grounded Two-DOF System Modal Parameters

| Mode | Angular Natural Frequency (rad/sec) | Natural Frequency (Hz) | Participation Factor | Modal Mass Ratio |
|------|-------------------------------------|------------------------|----------------------|------------------|
| 1    | 125.25                              | 20.0                   | 0.085                | 0.935            |
| 2    | 266.72                              | 42.5                   | -0.022               | 0.065            |

The mass-normalized mode shapes in matrix format are

$$\hat{Q} = \begin{bmatrix} 8.93 & -10.64 \\ 15.05 & 12.63 \end{bmatrix} \tag{9.34}$$

The response time histories for the initial conditions are shown in Figure 9.2.
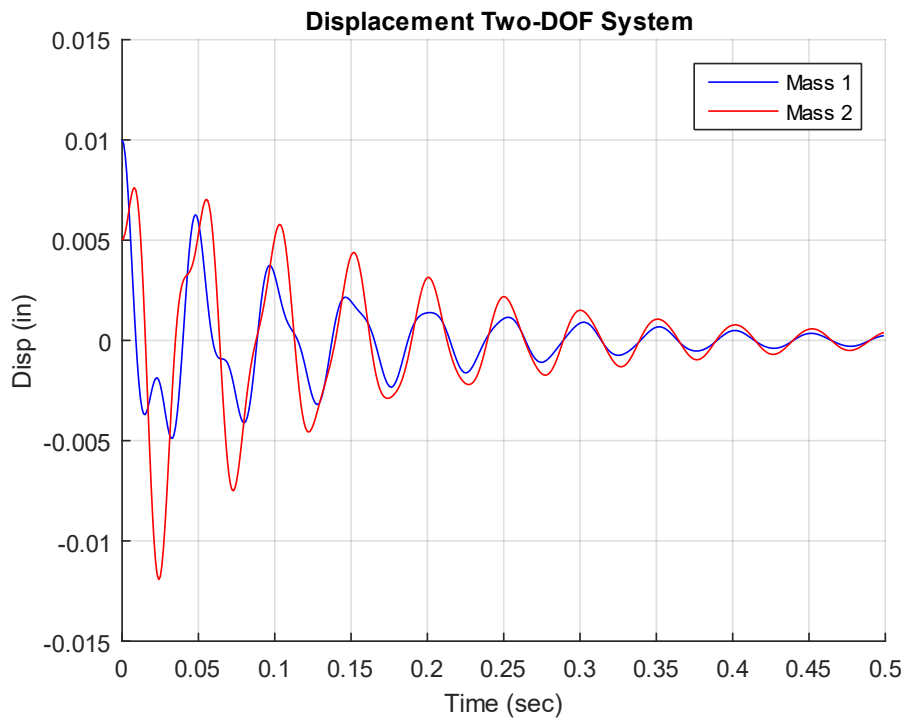


Figure 9.2.  Grounded, Two-DOF System, Response to Initial Displacement

## 9.1.6 Semi-definite, Two-DOF System

### 9.1.6.1 Semi-definite, Two-DOF System Equation of Motion
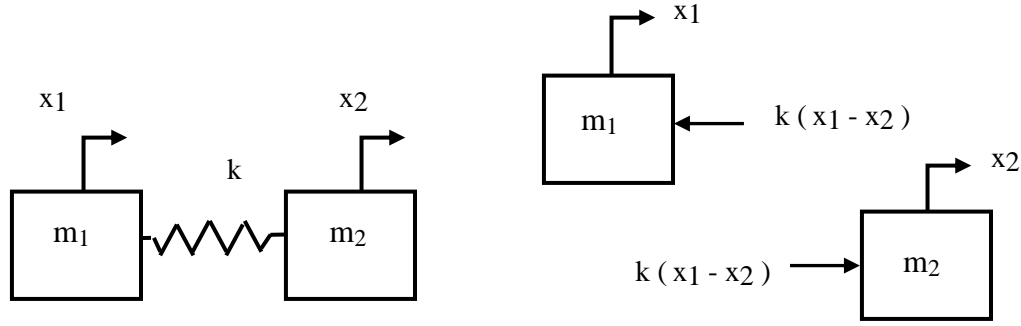


Figure 9.3. Ungrounded, Two-DOF System

Consider the system in Figure 9.3. This system could represent a simple, two-node finite element model of a rod's longitudinal vibration. A characteristic of this system is that the fundamental mode is a rigid-body mode at zero frequency. Both masses move in unison for the rigid-body mode. Newton's law can be applied to the system to derive the equations of motion. The steps are omitted for brevity. The resulting pair of ordinary differential equations can be represented in matrix form.

$$\begin{bmatrix} m_1 & 0 \\ 0 & m_2 \end{bmatrix} \begin{bmatrix} \ddot{x}_1 \\ \ddot{x}_2 \end{bmatrix} + \begin{bmatrix} k & -k \\ -k & k \end{bmatrix} \begin{bmatrix} x_1 \\ x_2 \end{bmatrix} = \begin{bmatrix} 0 \\ 0 \end{bmatrix} \tag{9.35}$$

The eigenvalues and vectors are found using the method shown in Section 9.1.2. Each angular natural frequency is then calculated from the square root of the respective eigenvalue.

$$\omega_1 = 0 \tag{9.36}$$

$$\omega_2 = \sqrt{\frac{k(m_1 + m_2)}{m_1 m_2}} \tag{9.37}$$

The mass-normalized eigenvectors, representing the mode shapes, are

$$\bar{q}_1 = \frac{1}{\sqrt{m_1 + m_2}} \begin{bmatrix} 1 \\ 1 \end{bmatrix} \tag{9.38}$$

$$\bar{q}_2 = \frac{1}{\sqrt{m_1 m_2 (m_1 + m_2)}} \begin{bmatrix} m_2 \\ m_1 \end{bmatrix} \tag{9.39}$$

Again, the two masses move in unison for the first mode. They move 180 degrees out-of-phase for the second mode. The semi-definite system is revisited in Section 17.3.3.

### 9.1.6.2 Semi-definite, Two-DOF System Example

Consider the system in Figure 9.3 with the values in Table 9.3.

Table 9.3. Semi-definite, Two-DOF System, Parameters

| Variable | Value |
|----------|-------|
| $m_1$ | 2 lbm |
| $m_2$ | 1 lbm |
| $k$ | 2000 lbf/in |

The mass and stiffness matrices are

$$M = \begin{bmatrix} 2/386 & 0 \\ 0 & 1/386 \end{bmatrix}, \quad K = \begin{bmatrix} 2000 & -2000 \\ -2000 & 2000 \end{bmatrix} \tag{9.40}$$

The 1/386 factor is needed to convert lbm to lbf sec^2/in.

The eigenvalues and vectors are found by inserting these matrices into equations (9.9) and (9.10). The angular natural frequencies are

$$\omega_1 = 0 \tag{9.41}$$

$$\omega_2 = 1076 \text{ rad/sec} \ (171.3 \text{ Hz}) \tag{9.42}$$

The mass-normalized eigenvectors in column format are

$$Q = [ \ \bar{q}_1 \ | \ \bar{q}_2 \ ] = \begin{bmatrix} 11.343 & -8.021 \\ 11.343 & 16.042 \end{bmatrix} \tag{9.43}$$

The total mass sum is 3 lbm (0.00777 lbf sec^2/in) which is also the effective modal mass of the rigid-body modes. The second mode has zero effective modal mass.

# 10 STATE SPACE METHOD

## 10.1 INTRODUCTION
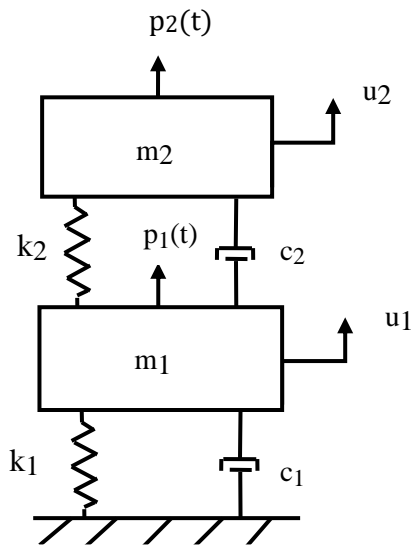


Figure 10.1.  Two-DOF System with Dashpots

Structural dynamics systems can be represented in terms of mass, damping, and stiffness matrices.  Each of these matrices may be coupled depending on the model complexity, degrees-of-freedom, etc.   The mass and stiffness matrices in the assembled equation of motion may be uncoupled using the normal modes for the undamped system.  This approach gives real natural frequencies and real mode shapes.

Damping effects can be included in forced response analyses by implicitly assuming that the damping matrix can be diagonalized into modal damping coefficients by the undamped modes.  But systems with dashpots in general have damping matrices that cannot be uncoupled in this manner.

The state-space method is useful for modal and forced response analysis of systems with discrete dashpot damping.  This approach yields complex natural frequencies and mode shapes, with real and imaginary components.
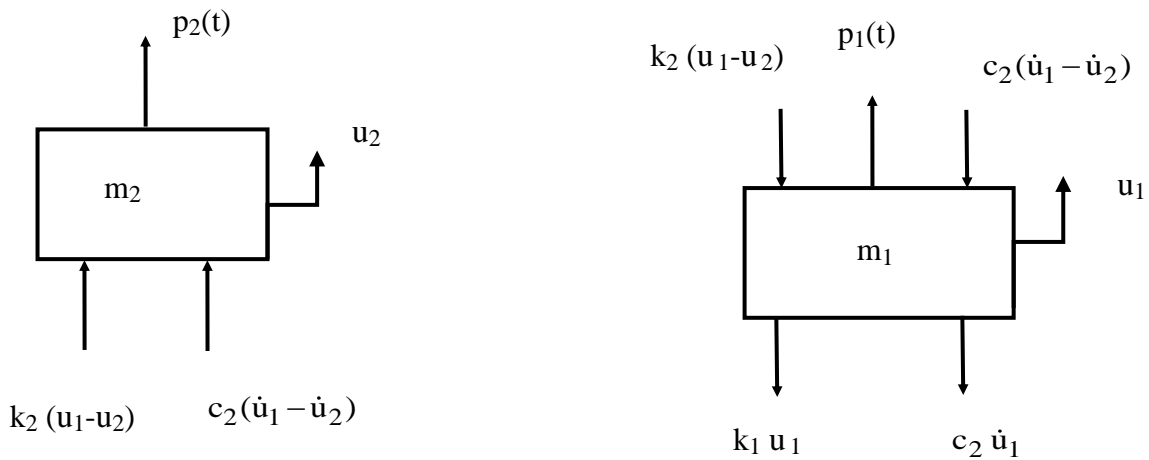
Figure 10.2. Free-Body Diagrams

Determine the equation of motion for mass 2.

$$\sum F = m_2 \; \ddot{u}_2 \tag{10.1}$$

$$m_2 \; \ddot{u}_2 = p_2(t) + k_2 \; (u_1 - u_2) + c_2 \; (\dot{u}_1 - \dot{u}_2) \tag{10.2}$$

$$m_2 \; \ddot{u}_2 + c_2(\dot{u}_2 - \dot{u}_1) + k_2(u_2 - u_1) = p_2(t) \tag{10.3}$$

Determine the equation of motion for mass 1.

$$\sum F = m_1 \ddot{u}_1 \tag{10.4}$$

$$m_1 \; \ddot{u}_1 = p_1(t) - k_1 u_1 - k_2 \; (u_1 - u_2) - c_1 \dot{u}_1 - c_1(\dot{u}_1 - \dot{u}_2) \tag{10.5}$$

$$m_1 \; \ddot{u}_1 + c_1 \dot{u}_1 + c_2(\dot{u}_1 - \dot{u}_2) + k_1 u_1 + k_2(u_1 - u_2) = p_1(t) \tag{10.6}$$

$$m_1 \; \ddot{u}_1 + (c_1 + c_2)\dot{u}_1 - c_2 \dot{u}_2 + (k_1 + k_2)u_1 - k_2 u_2 = p_2(t) \tag{10.7}$$

The equations of motion in matrix form are

$$\begin{bmatrix} m_1 & 0 \\ 0 & m_2 \end{bmatrix} \begin{bmatrix} \ddot{u}_1 \\ \ddot{u}_2 \end{bmatrix} + \begin{bmatrix} c_1 + c_2 & -c_2 \\ -c_2 & c_2 \end{bmatrix} \begin{bmatrix} \dot{u}_1 \\ \dot{u}_2 \end{bmatrix} + \begin{bmatrix} k_1 + k_2 & -k_2 \\ -k_2 & k_2 \end{bmatrix} \begin{bmatrix} u_1 \\ u_2 \end{bmatrix} = \begin{bmatrix} p_1(t) \\ p_2(t) \end{bmatrix} \qquad (10.8)$$

The equations can be represented as

$$M\ddot{u} + C\dot{u} + Ku = P \qquad (10.9)$$

where

$$M = \begin{bmatrix} m_1 & 0 \\ 0 & m_2 \end{bmatrix}, \quad C = \begin{bmatrix} c_1 + c_2 & -c_2 \\ -c_2 & c_2 \end{bmatrix}, \quad K = \begin{bmatrix} k_1 + k_2 & -k_2 \\ -k_2 & k_2 \end{bmatrix}$$

$$u = \begin{bmatrix} u_1 \\ u_2 \end{bmatrix}, \quad P = \begin{bmatrix} p_1(t) \\ p_2(t) \end{bmatrix}$$

The dimensions of the mass, damping, and stiffness matrices are (N x N), where N is the number of degrees-of-freedom. N = 2 for the example in this paper.

Let

$$z(t) = \begin{Bmatrix} u(t) \\ v(t) \end{Bmatrix}, \quad \dot{z}(t) = \begin{Bmatrix} v(t) \\ \dot{v}(t) \end{Bmatrix} \qquad (10.10)$$

The vector $v$ is defined as the effective velocity vector by the momentum equality.

$$Mv(t) = M\dot{u}(t) \qquad (10.11)$$

The equations can be expressed in the state-space format as

$$\begin{bmatrix} C & M \\ M & 0 \end{bmatrix} \begin{bmatrix} v \\ \dot{v} \end{bmatrix} + \begin{bmatrix} K & 0 \\ 0 & -M \end{bmatrix} \begin{bmatrix} u \\ v \end{bmatrix} = \begin{bmatrix} p(t) \\ 0 \end{bmatrix} \qquad (10.12)$$

The state-space equations can be simplified as

$$A\dot{z} + Bz = F(t) \tag{10.13}$$

where

$$A = \begin{bmatrix} C & M \\ M & 0 \end{bmatrix}, \quad B = \begin{bmatrix} K & 0 \\ 0 & -M \end{bmatrix}, \quad F(t) = \begin{bmatrix} p(t) \\ 0 \end{bmatrix}$$

The dimensions of the A and B matrices are (2N x 2N).

The A and B matrices are not positive definite. The eigenvalues and vectors are either real or complex, with real and imaginary components. This implies that the modes are not synchronous. There is a phase lag such that different degrees-of-freedom do not simultaneously reach their corresponding peaks and valleys.

The free vibration problem is

$$A\dot{z} + Bz = 0 \tag{10.14}$$

The previous equation represents a homogeneous set of ordinary differential equations with constant coefficients. The solution can be expressed as

$$z(t) = \psi \exp(\lambda t) = \begin{Bmatrix} \psi_u \\ \psi_v \end{Bmatrix} \exp(\lambda t) = \begin{Bmatrix} \psi_u \\ \lambda \psi_u \end{Bmatrix} \exp(\lambda t) \tag{10.15}$$

$$\dot{z}(t) = \lambda \psi \exp(\lambda t) = \lambda \begin{Bmatrix} \psi_u \\ \psi_v \end{Bmatrix} \exp(\lambda t) = \lambda \begin{Bmatrix} \psi_u \\ \lambda \psi_u \end{Bmatrix} \exp(\lambda t) \tag{10.16}$$

where $\lambda$ is a scalar and $\psi$ is a 2N vector

The corresponding generalized eigenvector problem is

$$\lambda A \psi \exp(\lambda t) + B \psi \exp(\lambda t) = 0 \tag{10.17}$$

$$[\lambda A + B]\psi = 0 \tag{10.18}$$

The solution to this problem yields a set of 2N eigenvalues $\lambda_i$, i=1, 2, ... , 2N.

It also gives corresponding eigenvectors $\psi_i$, i=1, 2, ... , 2N.

The eigenvalues are found via

$$\det[\lambda A + B] = 0 \tag{10.19}$$

The eigenvalues must either be real for complex conjugate pairs because the coefficient matrices are real.   Real eigenvalues indicate very high damping leading to overdamped modes.

Furthermore, eigenvalues with complex conjugate pairs have corresponding eigenvectors which are complex conjugates.

Consider i and j pairings of the generalized eigenvalue problem.

$$[\lambda_i A + B]\psi_i = 0 \tag{10.20}$$

$$[\lambda_j A + B]\psi_j = 0 \tag{10.21}$$

Premultiply each eigenvalue problem by $\psi^T$ such that

$$\psi_j^{\;T}[\lambda_i A + B]\psi_i = 0 \tag{10.22}$$

$$\psi_j^{\;T}[\lambda_j A + B]\psi_j = 0 \tag{10.23}$$

A and B are both symmetric matrices thus

$$\psi_i^{\;T}[\lambda_i A + B]\psi_j = 0 \tag{10.24}$$

Subtract equation (10.24) from equation (10.22).

$$\psi_i^{T}[(\lambda_j - \lambda_i)A]\psi_j = 0 \tag{10.25}$$

$$(\lambda_j - \lambda_i)\psi_i^{T}A\psi_j = 0 \tag{10.26}$$

For $\lambda_j \neq \lambda_i$,

$$\psi_i^{T}A\,\psi_j = 0 \quad , \quad i, j = 1, 2, \dots, 2N \tag{10.27}$$

By substitution, for $\lambda_j \neq \lambda_i$,

$$\psi_i^T B \psi_j = 0 \quad , \quad i, j = 1, 2, \ldots, 2N \qquad (10.28)$$

The previous two equations are orthogonality relationships.

The complex eigenvector modal matrix is

$$\psi = [\psi_1 \quad \psi_2 \quad \ldots \quad \psi_{2N}] \qquad (10.29)$$

The orthogonality relationships yield the following modal diagonal terms $a_r$ and $b_r$.

$$\psi^T A \psi = \text{diag}(a_r) \qquad (10.30)$$

$$\psi^T B \psi = \text{diag}(b_r) \qquad (10.31)$$

The eigenvalues are

$$\lambda_r = -b_r/a_r \qquad (10.32)$$

The complex eigenvalues have the following relationships to the natural frequency $\omega_r$ and damping ratio $\xi_r$,

$$\lambda_r = \alpha_r + j\beta_r = -\xi_r \omega_r + j\omega_r \sqrt{1 - \xi_r^2} \qquad (10.33)$$

$$\omega_r = \sqrt{\alpha_r^2 + \beta_r^2} \qquad (10.34)$$

$$\xi_r = \omega_r/a_r \qquad (10.35)$$

## 10.3  FREQUENCY RESPONSE FUNCTION DERIVATION

The non-homogeneous state-space equation can be expressed as

$$A\dot{\bar{z}} + B\bar{z} = \bar{P} \tag{10.36}$$

where

$$A = \begin{bmatrix} C & M \\ M & 0 \end{bmatrix}, \quad B = \begin{bmatrix} K & 0 \\ 0 & -M \end{bmatrix}, \quad \bar{z} = \begin{Bmatrix} u \\ \dot{u} \end{Bmatrix}, \quad \bar{P} = \begin{bmatrix} p \\ 0 \end{bmatrix} \tag{10.37}$$

The 2N complex eigenvectors are

$$\psi = \begin{Bmatrix} \Psi_u \\ \Psi_v \end{Bmatrix} = \begin{Bmatrix} \Psi_u \\ \lambda\Psi_u \end{Bmatrix} \tag{10.38}$$

Now define a generalize coordinate $\eta(t)$ such that

$$\bar{z} = \psi\bar{\eta} \tag{10.39}$$

$$A\psi\dot{\bar{\eta}} + B\psi\bar{\eta} = \bar{P} \tag{10.40}$$

Premultiply by the transpose of the eigenvector matrix.

$$\psi^T A\psi\dot{\bar{\eta}} + \psi^T B\psi\bar{\eta} = \psi^T\bar{P} \tag{10.41}$$

Recall

$$\psi^T A\psi = \text{diag}(a_r) \tag{10.42}$$

$$\psi^T B\psi = \text{diag}(b_r) \tag{10.43}$$

The individual modal equation is thus

$$a_r\dot{\eta}_r + b_r\eta_r = \psi_r^T\bar{P} \tag{10.44}$$

$$\dot{\eta}_r + \frac{b_r}{a_r}\eta_r = \frac{1}{a_r}\psi_r^T\bar{P} \tag{10.45}$$

$$\lambda_r = -b_r/a_r \tag{10.46}$$

$$\dot{\eta}_r - \lambda_r\eta_r = \frac{1}{a_r}\psi_r^T\bar{P} \tag{10.47}$$

Take the Laplace transform

$$L\{\dot{\eta}_r - \lambda_r\eta_r\} = L\left\{\frac{1}{a_r}\psi_r^T\bar{P}\right\} \tag{10.48}$$

$$s\hat{\eta}_r(s) - \eta_r(0) - \lambda_r\hat{\eta}_r(s) = \frac{1}{a_r}\psi_r^T\widehat{P}(s) \tag{10.49}$$

$$[s - \lambda_r]\hat{\eta}_r(s) - \eta_r(0) = \frac{1}{a_r}\psi_r^T\widehat{P}(s) \tag{10.50}$$

For zero initial conditions,

$$[s - \lambda_r]\hat{\eta}_r(s) = \frac{1}{a_r}\psi_r^T\widehat{P}(s) \tag{10.51}$$

$$\hat{\eta}_r(s) = \frac{1}{a_r[s - \lambda_r]}\psi_r^T\widehat{P}(s) \tag{10.52}$$

$$\hat{\eta}(s) = \sum_{r=1}^{2N}\frac{1}{a_r[s - \lambda_r]}\psi_r^T\widehat{P}(s) \tag{10.53}$$

Change from the Laplace to the frequency domain with $s = j\omega$.

$$\hat{\eta}(\omega) = \sum_{r=1}^{2N} \frac{1}{a_r[j\omega - \lambda_r]} \psi_r^T \hat{P}(\omega) \tag{10.54}$$

Recall

$$\bar{z} = \psi\bar{\eta} \tag{10.55}$$

The Fourier transform equivalent for the frequency domain is

$$\hat{Z}(\omega) = \psi\hat{\eta}(\omega) \tag{10.56}$$

$$\hat{Z}(\omega) = \sum_{r=1}^{2N} \frac{1}{a_r[j\omega - \lambda_r]} \psi_r \psi_r^T \hat{P}(\omega) \tag{10.57}$$

Recall

$$\hat{Z}(\omega) = \left\{ \begin{matrix} \hat{U}(\omega) \\ j\omega\hat{U}(\omega) \end{matrix} \right\} \tag{10.58}$$

$$\psi = \left\{ \begin{matrix} \psi_u \\ \psi_v \end{matrix} \right\} = \left\{ \begin{matrix} \psi_u \\ \lambda\psi_u \end{matrix} \right\} \tag{10.59}$$

$$\hat{P}(\omega) = \left\{ \begin{matrix} \hat{p}(\omega) \\ 0 \end{matrix} \right\} \tag{10.60}$$

$$\hat{U}(\omega) = \sum_{r=1}^{2N} \frac{1}{a_r[j\omega - \lambda_r]} (\psi_u)_r (\psi_u)_r^T \hat{p}(\omega) \tag{10.61}$$

$$\hat{U}(\omega) = H(\omega)\hat{p}(\omega) \tag{10.62}$$

78

$$H(\omega) = \sum_{r=1}^{2N} \frac{1}{a_r[j\omega - \lambda_r]} (\psi_u)_r (\psi_u)_r^T \qquad (10.63)$$

The receptance function (displacement/force) at coordinate i due to a harmonic force excitation only at coordinate k is

$$H_{ik}(\omega) = \sum_{r=1}^{2N} \frac{1}{a_r[j\omega - \lambda_r]} (\psi_u)_{ir} (\psi_u)_{kr} \qquad (10.64)$$

Note the reciprocity principle.

$$H_{ik}(\omega) = H_{ki}(\omega) \qquad (10.65)$$

The mobility function (velocity/force) at coordinate i due to a harmonic force excitation only at coordinate k is

$$H_{v,ik}(\omega) = j\omega \sum_{r=1}^{2N} \frac{1}{a_r[j\omega - \lambda_r]} (\psi_u)_{ir} (\psi_u)_{kr} \qquad (10.66)$$

The accelerance function (acceleration/force) at coordinate i due to a harmonic force excitation only at coordinate k is

$$H_{a,ik}(\omega) = -\omega^2 \sum_{r=1}^{2N} \frac{1}{a_r[j\omega - \lambda_r]} (\psi_u)_{ir} (\psi_u)_{kr} \qquad (10.67)$$

## 10.4  EXAMPLE
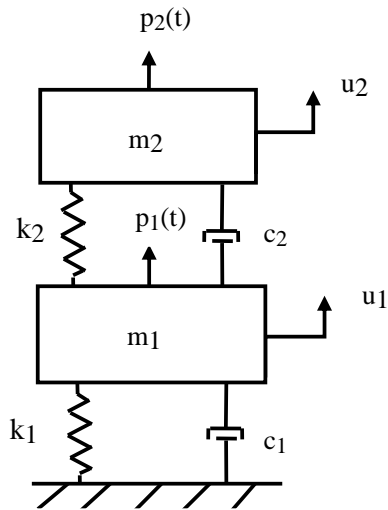


Figure 10.3.  Two-DOF System with Dashpots

The system in the above figure is analyzed via a Matlab script.  Note that the mass matrix is divided by 386 to convert lbm to lbf sec^2/in.   The mass, damping, and stiffness matrices are

$$
M = \begin{bmatrix} 0.0052 & 0 \\ 0 & 0.0026 \end{bmatrix}, \quad C = \begin{bmatrix} 0.4398 & -0.161 \\ -0.161 & 0.161 \end{bmatrix}, \quad K = \begin{bmatrix} 2500 & -1000 \\ -1000 & 1000 \end{bmatrix}
$$

(10.68)

The state-space matrices are

$$
A = \begin{bmatrix} C & M \\ M & 0 \end{bmatrix} = \begin{bmatrix} 0.4398 & -0.161 & 0.0052 & 0 \\ -0.161 & 0.161 & 0 & 0.0026 \\ 0.0052 & 0 & 0 & 0 \\ 0 & 0.0026 & 0 & 0 \end{bmatrix}
$$

(10.69)

$$
B = \begin{bmatrix} K & 0 \\ 0 & -M \end{bmatrix} = \begin{bmatrix} 2500 & -1000 & 0 & 0 \\ -1000 & 1000 & 0 & 0 \\ 0 & 0 & -0.0052 & 0 \\ 0 & 0 & 0 & -0.0026 \end{bmatrix}
$$

(10.70)

The eigenvalues, eigenvectors, and lambda ratios of the state space system are shown in the following tables. The complex values are in Matlab syntax where $i = \sqrt{-1}$.

Table 10.1. Eigenvalues and Natural Frequencies

| Complex | Magnitude (rad/sec) | Natural Frequency (Hz) |
|---|---|---|
| -14.13 - 396.1i | 396.3 | 63.08 |
| -14.13 + 396.1i | 396.3 | 63.08 |
| -59.38 - 841.4i | 843.5 | 134.2 |
| -59.38 + 841.4i | 843.5 | 134.2 |

Table 10.2. Eigenvectors

| Mode 1 | Mode 2 | Mode 3 | Mode 4 |
|---|---|---|---|
| -0.0001 + 0.0015i | -0.0001 - 0.0015i | -0.0001 + 0.0010i | -0.0001 - 0.0010i |
| -0.0001 + 0.0025i | -0.0001 - 0.0025i | 0.0001 - 0.0012i | 0.0001 + 0.0012i |
| 0.5908 + 0.0052i | 0.5908 - 0.0052i | 0.8397 - 0.0052i | 0.8397 + 0.0052i |
| 0.9963 + 0.0037i | 0.9963 - 0.0037i | -0.9953 - 0.0047i | -0.9953 + 0.0047i |

Table 10.3. Lambda Ratios

| r | $\lambda_r$ |
|---|---|
| 1 | -14.13 - 396.1i |
| 2 | -14.13 + 396.1i |
| 3 | -59.38 - 841.4i |
| 4 | -59.38 + 841.4i |

The frequency response function (FRF) magnitudes are plotted in the following figures.
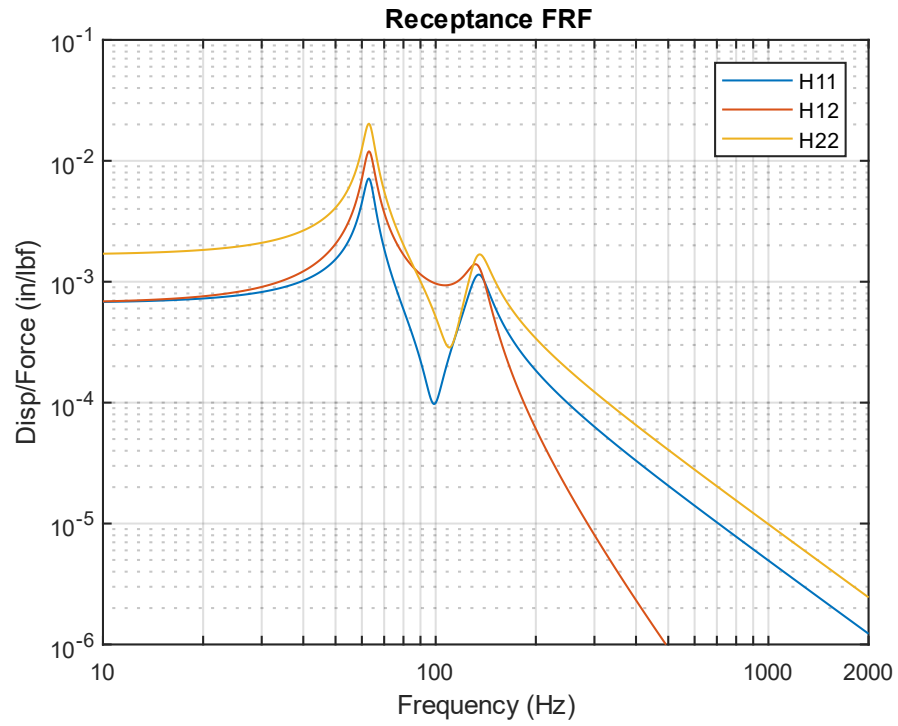
Figure 10.4.  State Space Receptance
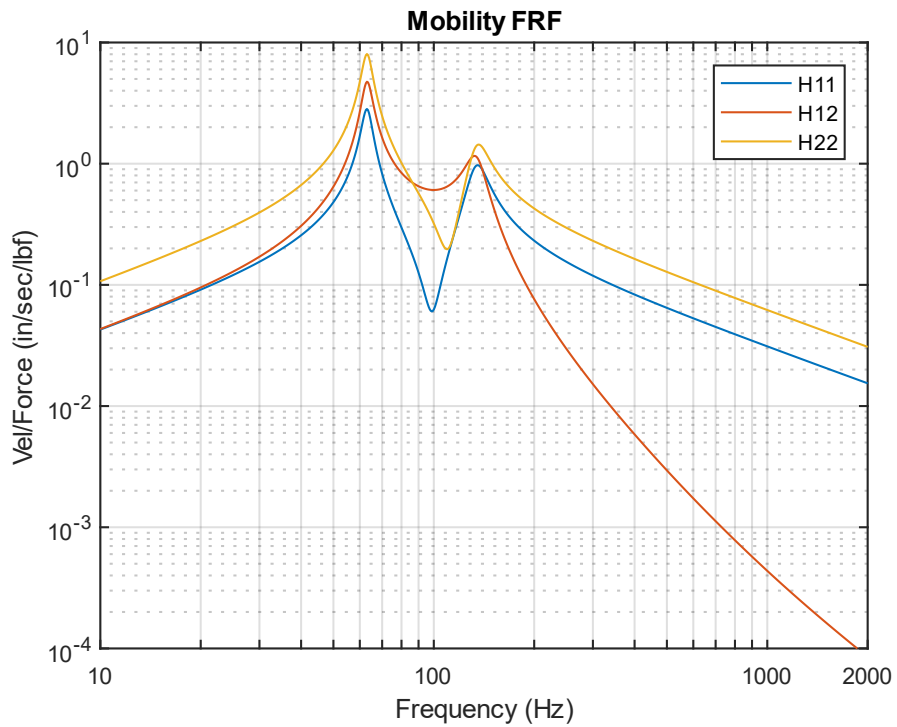


Figure 10.5.  State Space Mobility
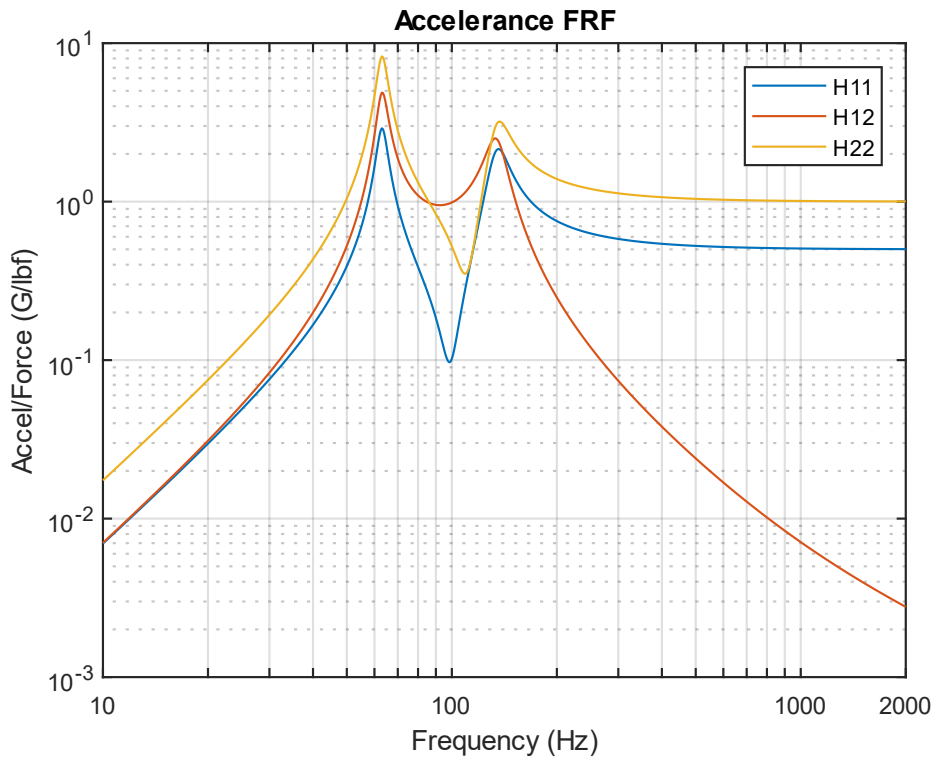
Figure 10.6.  State Space Accelerance

# 11 CONTINUOUS SYSTEMS WITH LONGITUDINAL VIBRATION

## 11.1 ROD LONGITUDINAL NATURAL FREQUENCY

### 11.1.1 One-Dimensional Longitudinal Vibration Equation of Motion
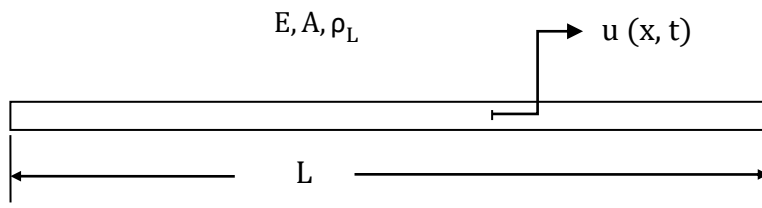


Figure 11.1.  Slender Rod

The longitudinal displacement $u(x, t)$ in a rod in undamped free vibration is governed by the second-order, partial differential equation

$$\frac{\partial}{\partial x}\left[EA(x)\frac{\partial u}{\partial x}\right] = \rho_L(x)\frac{\partial^2 u}{\partial t^2} \tag{11.1}$$

The term $EA(x)$ is the product of the elastic modulus and cross-sectional area.  The equation for a uniform rod is

$$\frac{\partial^2 u}{\partial x^2} = \left(\frac{\rho}{E}\right)\frac{\partial^2 u}{\partial t^2} \tag{11.2}$$

Note that

$$\rho = \rho_L \,/\, A \tag{11.3}$$

Equation (11.2) is a common formula for one-dimensional wave propagation.  Similar equations govern the propagation of sound in a pipe and the torsional vibration in a shaft.  Note that a wave is a phenomenon in which physical energy propagates through space relative to a medium.  Wave propagation is discussed throughout this document, as shown for seismic waves in Section 26.6.1 for example.

The method of separation of variables can be applied to equation (11.2) as

$$u(x, t) = U(x) \exp(j\omega t) \tag{11.4}$$

$$\frac{\partial}{\partial t} u(x, t) = j\omega U(x) \exp(j\omega t) \tag{11.5}$$

$$\frac{\partial^2}{\partial t^2} u(x, t) = -\omega^2 U(x) \exp(j\omega t) \tag{11.6}$$

Substitute equations (11.4) and (11.6) into (11.2). The resulting spatial equation after some simplification is

$$\frac{d^2}{dx^2} U(x) + \omega^2 \left(\frac{\rho}{E}\right) U(x) = 0 \tag{11.7}$$

Longitudinal waves are non-dispersive. The group and phase wave speeds are equal. The wave speed is calculated from the elastic modulus and mass density.

$$C_L = \sqrt{E/\rho} \tag{11.8}$$

The speed of sound is related to the frequency and wavelength by

$$C_L = f\lambda \tag{11.9}$$

The spatial equation can be expressed as

$$\frac{d^2}{dx^2} U(x) + \frac{\omega^2}{C_L^2} U(x) = 0 \tag{11.10}$$

The spatial solution is

$$U(x) = a_1 \sin\left(\frac{\omega x}{C_L}\right) + a_2 \cos\left(\frac{\omega x}{C_L}\right) \tag{11.11}$$

The $a_i$ values in the previous equation are coefficients that depend on the boundary conditions.

The boundary condition for a fixed left end is

$$U(0) = 0 \qquad\qquad (11.12)$$

The boundary condition for a free left end is

$$\frac{d}{dx}U(x)|_{x=0} = 0 \qquad\qquad (11.13)$$

The same boundary conditions could be applied at the right end. The longitudinal natural frequencies are given in Table 11.1.

Table 11.1.  Longitudinal Beam or Rod Natural Frequencies

| Configuration | Natural Frequencies | Mode Shapes |
|---|---|---|
| Fixed-Free | $f_n = \dfrac{(2n-1)}{4}\dfrac{C_L}{L}, n = 1,2,3\dots$ | $U(x) = \sin\left(\dfrac{(2n-1)\pi x}{2L}\right)$ |
| Free-Free | $f_n = \dfrac{n}{2}\dfrac{C_L}{L}, n = 1,2,3\dots$ | $U(x) = \cos\left(\dfrac{n\pi x}{L}\right)$ |
| Fixed-Fixed | $f_n = \dfrac{n}{2}\dfrac{C_L}{L}, n = 1,2,3\dots$ | $U(x) = \sin\left(\dfrac{n\pi x}{L}\right)$ |

The mode shapes are normalized to a value of one.  Note that the Free-Free beam also has a rigid-body mode at zero frequency.   Further solution details are given in Reference [12].  Also, longitudinal vibration is revisited in Section 29.2.

The previous method of separation of variables is a modal solution approach.  As an alternative, a wave solution can be applied to equation (11.2) as

$$u(x, t) = A \sin(kx - \omega t - \phi) \qquad\qquad (11.14)$$

The wavenumber $k$ is related to the angular frequency, longitudinal wave speed, and wavelength as

$$k = \omega \,/\, c \, = 2\,\pi\,/\,\lambda \qquad\qquad (11.15)$$

## 11.1.2 Rod Longitudinal Vibration Energy Formulas

Natural frequency and mode shapes can also be derived from a rod's energy terms via the Rayleigh-Ritz or finite element method.  The following formulas are given for reference.

The total strain or potential energy $P_E$ of a uniform rod is

$$P_E = \frac{1}{2} \int_0^L EA \left(\frac{dU}{dx}\right)^2 dx \tag{11.16}$$

The total kinetic energy $K_E$ of a uniform rod is

$$K_E = \frac{1}{2} \omega_n^2 \int_0^L \rho_L U^2 \, dx \tag{11.17}$$

## 11.1.3 Beam Longitudinal Vibration Example
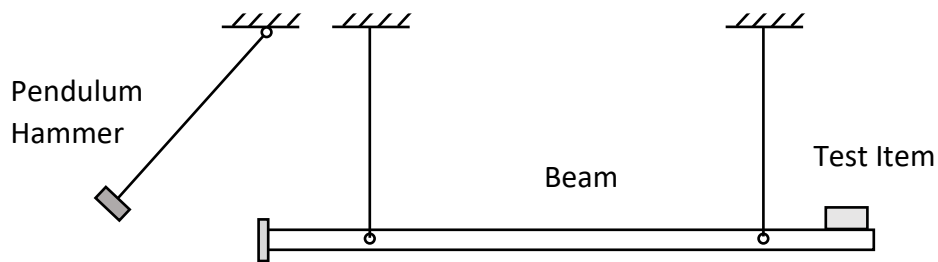


Figure 11.2.    Longitudinal Beam for Shock Testing

The suspended beam can be idealized as a free-free beam for longitudinal vibration.    The pendulum hammer is raised to some initial angular displacement and then released.    The hammer strikes the beam's end plate on the left end, delivering a force impulse.    The longitudinal modes of the beam amplify the input energy and deliver a base input shock pulse to the test article mounted near the right end.

Bai and Thatcher described this shock test method in Reference [13]. This method is still used today, although the pendulum hammer is often replaced by a pneumatic gun firing a projectile into the beam's end plate.

The goal was to choose the beam length so that its fundamental frequency would match the "knee frequency" of a shock response spectrum specification at 2000 Hz. (Further information on this type of specification is given in Section 26.) The length for an aluminum beam to meet this goal is calculated as

$$L = \frac{1}{2}\frac{C_L}{f_n} = \frac{200{,}000 \text{ in/sec}}{2(2000 \text{ cyles/sec})} = 50 \text{ in} \approx 4 \text{ ft} \tag{11.18}$$

Note that the longitudinal wave speed in aluminum is about 200,000 in/sec. Steel also has this approximate wave speed.

## 11.2  COIL SPRING SURGE
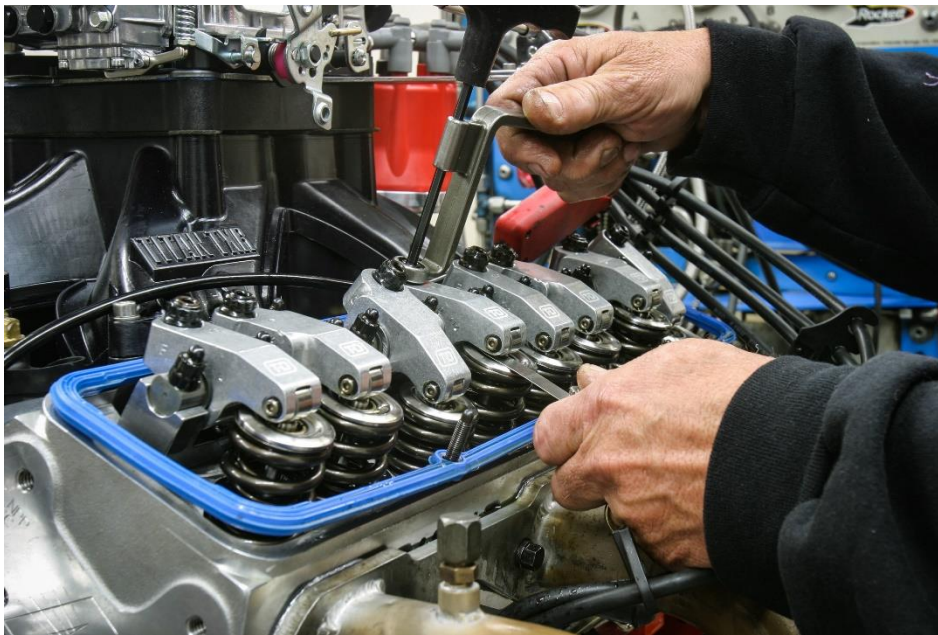


Figure 11.3.  Automotive Valve Springs & Lifters

Spring surge is another form of longitudinal vibration, which arises because springs have both stiffness and inertia properties. This is in contrast to the usual simplifying assumption in vibration analysis that springs are massless. Springs used in high-speed machinery must have natural frequencies well in excessive of the frequency of motion that they control. Otherwise, the spring itself may resonate, resulting in a loss of engine performance or even catastrophic failure. This can occur in automotive value springs when the engine camshaft RPM speed is increased well above the normal operating speed. Race car engines are at particular risk for this problem. Spring surge is also a potential concern when coil springs are used as isolation mounts for equipment.

The following spring natural frequencies are taken from Reference [14]. Note the similarities with the longitudinal rod formulas in Table 11.1.
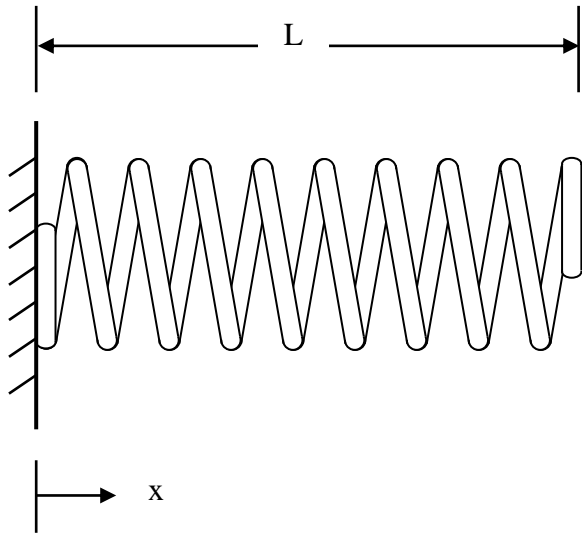


Figure 11.4. Fixed-Free Spring

The fundamental frequency of the fixed-free spring is

$$f_n = \frac{(2n-1)}{4}\sqrt{\frac{k}{\rho_L L}} \quad , n = 1,2,3 \tag{11.19}$$

Its corresponding normalized mode shape is

$$U(x) = \sin\left(\frac{(2n-1)\pi x}{2L}\right) \tag{11.20}$$

The wave speed in the spring is

$$C_L = \sqrt{k\,L\,/\rho_L}$$ (11.21)

The wave speed equation applies to other spring boundary conditions as well.
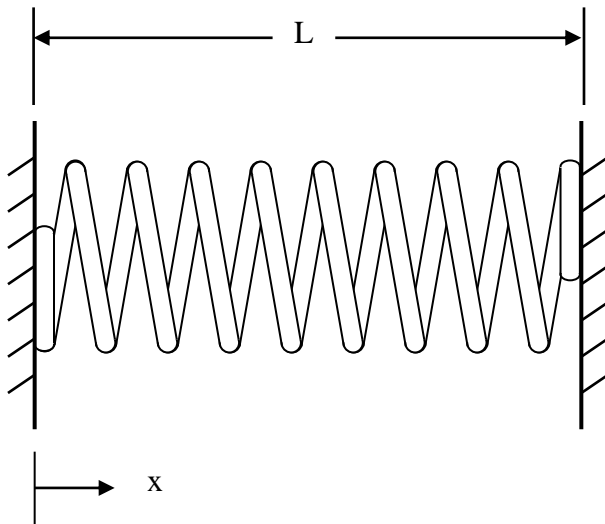


Figure 11.5.  Fixed-Fixed Spring

The fundamental frequency of the fixed-fixed spring is

$$f_n = \frac{n}{2}\sqrt{\frac{k}{\rho_L\,L}} \quad , n = 1,2,3$$ (11.22)

The corresponding normalized mode shape is

$$U(x) = \sin\left(\frac{n\pi x}{L}\right)$$ (11.23)

Note that the Fixed-Fixed and Free-Free cases have the same natural frequency equation.
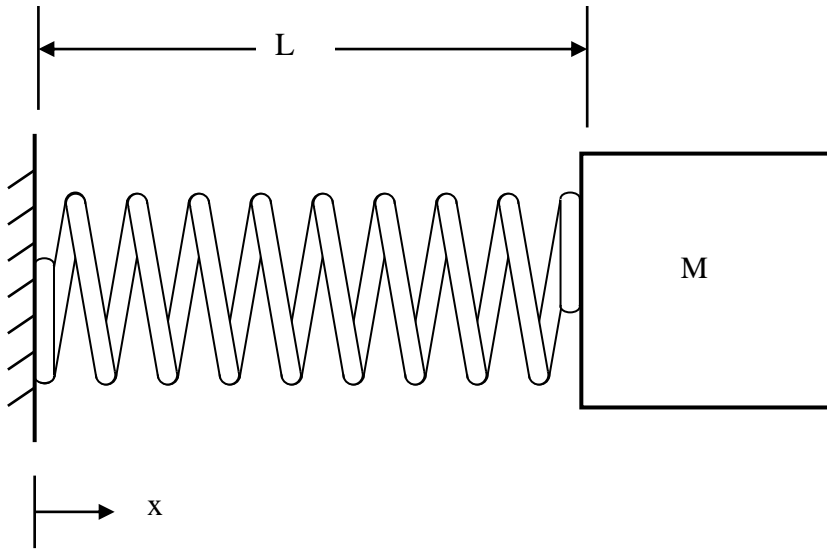
Figure 11.6. Spring with End Mass

The simplified fundamental frequency formula for a spring with and end mass M is

$$f_n = \frac{1}{2\pi} \sqrt{\frac{k}{M + 0.33\,\rho_L\,L}} \qquad (11.24)$$

A more rigorous formula is

$$f_n = \frac{\lambda_n}{2\pi} \sqrt{\frac{k}{\rho_L\,L}} \;,\quad \cot(\lambda_n) = \left(\frac{M}{\rho_L\,L}\right)\lambda_n\,, \qquad n = 1,2,3, \dots \qquad (11.25)$$

The corresponding mode shape is

$$U(x) = \sin(\lambda_n\,x/L)\,,\quad n = 1, 2, 3, \dots \qquad (11.26)$$
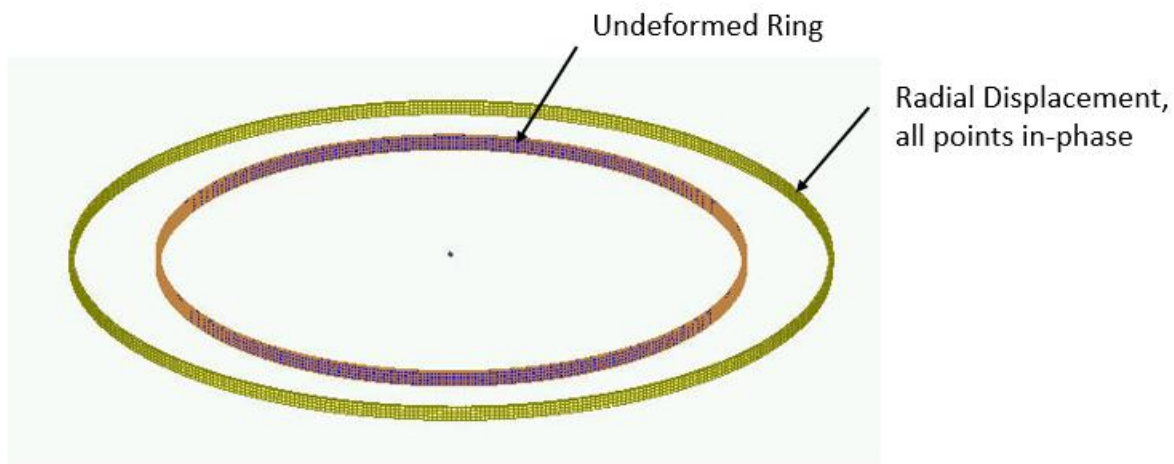
Figure 11.7  Ring Mode from Finite Element Model

Consider a thin ring with a rectangular cross-section and with completely free boundary conditions. The ring frequency corresponds to the mode in which all points move radially outward together and then radially inward together.   This is the first extension mode.  It is analogous to a longitudinal mode in a rod. The ring frequency is the frequency at which the longitudinal wavelength in the skin material is equal to the vehicle circumference.

$$f_r = \frac{C_L}{\pi d} \qquad (11.27)$$

The ring frequency is an important concept for launch vehicles.  The front end of a launch vehicle is typically composed of cylindrical shell segments which house avionics components and the payload.  These shells tend to have notable vibration responses at their respective ring frequencies due to external acoustic environments and stage separation shock events. Furthermore, there is a rule-of-thumb in statistical energy analysis (SEA) that a cylinder tends to behave as a flat plate above its ring frequencies.  This is a simplifying assumption.  Also, note that the ring frequency is an idealized concept for a cylindrical shell.  In practice, cylindrical shells tend to have a high modal density near the ring frequency.

Consider an aluminum launch vehicle cylindrical shell with a diameter of 60 inches.  Again, the longitudinal wave speed in aluminum is approximately 200,000 in/sec.  The ring frequency is

$$f_r = (200{,}000 \text{ in/sec})/(\pi\, 60 \text{ in }) = 1060 \text{ Hz} \qquad (11.28)$$

# 12 BERNOULLI-EULER BEAMS

### 12.1.1 Beam Equations
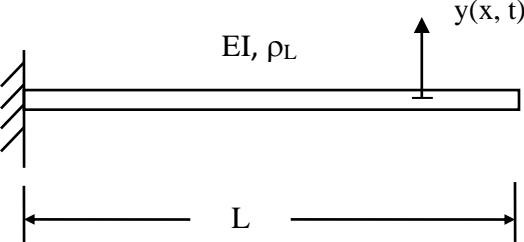


Figure 12.1.  Cantilever or Fixed-Fixed Beam
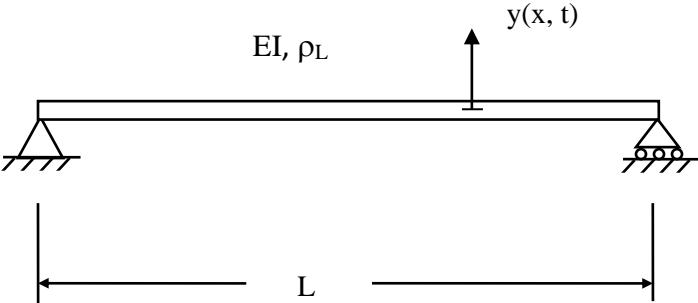


Figure 12.2.  Simply-Supported or Pinned-Pinned Beam

The governing equation for beam bending free vibration is a fourth-order, partial differential equation.

$$-\frac{\partial^2}{\partial x^2}\left[EI(x)\frac{\partial^2 y}{\partial x^2}\right] = \rho_L \frac{\partial^2 y}{\partial t^2}$$

(12.1)

The term $EI(x)$ is the stiffness which is the product of the elastic modulus and area moment of inertia.  The equation for a uniform beam is

$$-EI\,\frac{\partial^4 y}{\partial x^4} = \rho_L \frac{\partial^2 y}{\partial t^2}$$

(12.2)

The method of separation of variables can be applied as

$$y(x, t) = Y(x)\exp(j\omega t) \tag{12.3}$$

$$\frac{\partial}{\partial t} y(x, t) = j\omega\, Y(x)\, \exp(j\omega t) \tag{12.4}$$

$$\frac{\partial^2}{\partial t^2}\, y(x, t) = -\omega^2\, Y(x)\, \exp(j\omega t) \tag{12.5}$$

Substitution into equation (12.2) leads to the spatial ordinary differential equation.

$$\frac{d^4}{dx^4} Y(x) + \omega^2 \left(\frac{\rho_L}{EI}\right) Y(x) = 0 \tag{12.6}$$

Define the wavenumber β as

$$\beta^4 = \omega^2 \left(\frac{\rho_L}{EI}\right) \tag{12.7}$$

The differential equation can be expressed as

$$\frac{d^4}{dx^4} Y(x) + \beta^2 Y(x) = 0 \tag{12.8}$$

The spatial solution has the form

$$Y(x) = a_1\sinh(\beta x) + a_2\cosh(\beta x) + a_3\sin(\beta x) + a_4\cos(\beta x) \tag{12.9}$$

Substitute the spatial solution into the differential equation.

$$\beta^4\{a_1\sinh(\beta x) + a_2\cosh(\beta x) + a_3\sin(\beta x) + a_4\cos(\beta x)\}$$

$$-\omega^2 \left(\frac{\rho_L}{EI}\right)\{a_1\sinh(\beta x) + a_2\cosh(\beta x) + a_3\sin(\beta x) + a_4\cos(\beta x)\} = 0 \tag{12.10}$$

Equation (12.10) is satisfied by the wavenumber relationship in equation (12.7), which gives credibility to the assumed spatial solution. The $a_i$ values in equations (12.9) and (12.10) are coefficients that depend on the boundary conditions discussed in 12.1.2. The spatial solution gives eigen function modes shapes. It also gives eigenvalue roots from which the natural frequencies are calculated.

The eigenvalues are represented as $\beta_L$. The angular natural frequencies $\omega_n$ are

$$\omega_n = \beta_n^2 \sqrt{EI/\rho_L}$$

(12.11)

## 12.1.2 Common Boundary Conditions

### 12.1.2.1 Cantilever Beam

Recall the cantilever or fixed-free beam in Figure 12.1. The displacement and slope at the fixed end are both zero.

$$Y(0) = 0 \ , \quad \frac{d}{dx} Y(0) = 0$$

(12.12)

The moment and shear force at the free end are both zero.

$$M = \left[ EI(x) \frac{d^2}{dx^2} Y(x) \right]\Big|_{x=L} = 0 \ , \quad M = \frac{d}{dx}\left[ EI(x) \frac{d^2}{dx^2} Y(x) \right]\Big|_{x=L} = 0$$

(12.13)

Application of these boundary conditions to the spatial displacement in equation (12.9) and its derivatives yields the following equation for finding the $a_i$ coefficients.

$$\begin{bmatrix} \sin(\beta L) + \sinh(\beta L) & \cos(\beta L) + \cosh(\beta L) \\ \cos(\beta L) + \cosh(\beta L) & -\sin(\beta L) + \sinh(\beta L) \end{bmatrix} \begin{bmatrix} a_1 \\ a_2 \end{bmatrix} = \begin{bmatrix} 0 \\ 0 \end{bmatrix}$$

(12.14)

By inspection, equation (12.14) can only be satisfied if $a_1 = 0$ and $a_2 = 0$. Set the determinant of the matrix to zero to obtain a nontrivial solution. This yields the following transcendental equation for finding the roots by the Newton-Raphson method. Multiple roots satisfy the equation. A subscript is thus added.

$$\cos(\beta_n L)\cosh(\beta_n L) = -1 \qquad (12.15)$$

The fundamental root for the cantilever beam is $\beta_n L = 1.87510$. The natural frequencies can be found by substituting each root into equation (12.11).

12.1.2.2 Pinned-Pinned Beam

Recall the pinned-pinned beam in Figure 12.2. The boundary conditions at the left end of the pinned-pinned beam are

$$Y(0) = 0 , \quad M = \left[ EI(x) \, \frac{d^2}{dx^2} Y(x) \right]\Bigg|_{x=0} = 0 \qquad (12.16)$$

The boundary conditions at the right end are similar.

Application of these boundary conditions to the spatial displacement in equation (12.9) and its derivatives yields the following equation for finding the $a_i$ coefficients.

$$\begin{bmatrix} \sinh(\beta L) & \sin(\beta L) \\ \sinh(\beta L) & -\sin(\beta L) \end{bmatrix} \begin{bmatrix} a_1 \\ a_2 \end{bmatrix} = \begin{bmatrix} 0 \\ 0 \end{bmatrix} \qquad (12.17)$$

By inspection, the previous equation can only be satisfied if $a_1 = 0$ and $a_2 = 0$. Set the determinant of the matrix to zero to obtain a nontrivial solution. This yields the following transcendental equation. Multiple roots satisfy the equation. A subscript is thus added.

$$\sin(\beta_n L)\sinh(\beta_n L) = 0 \qquad (12.18)$$

The equation is satisfied if

$$\beta_n L = n\,\pi , \ n=1,2,3, \dots \qquad (12.19)$$

The natural frequencies can be found by substituting each root into equation (12.11).

### 12.1.3 Beam Bending Fundamental Frequencies

The solutions to the beam equation for various boundary conditions are derived in Reference [15].   A summary of beam formulas is given in Table 12.1.  Note that the free-free beam also has a rigid-body mode with zero frequency.

Table 12.1  Beam Bending Fundamental Frequencies

| Configuration | Fundamental Frequency |
|---|---|
| Cantilever (Fixed-Free) | $\dfrac{1}{2\pi}\left(\dfrac{3.5156}{L^2}\right)\sqrt{EI/\rho_L}$ |
| Cantilever with end mass | $\dfrac{1}{2\pi}\sqrt{\dfrac{3EI}{(0.2235 m_{beam} + m_{end})L^3}}$ |
| Pinned-Pinned | $\dfrac{\pi}{2\,L^2}\sqrt{EI/\rho_L}$ |
| Free-Free & Fixed-Fixed | $\dfrac{1}{2\pi}\left(\dfrac{22.373}{L^2}\right)\sqrt{EI/\rho_L}$ |
| Fixed-Pinned | $\dfrac{1}{2\pi}\left(\dfrac{15.418}{L^2}\right)\sqrt{EI/\rho_L}$ |

The pinned-pinned beam has harmonics as follows.

$$f_n = \frac{\pi}{2}\left(\frac{n}{L}\right)^2\sqrt{EI/\rho_L} \quad, \quad n = 1,2,3, \dots \tag{12.20}$$

The beam bending frequencies for other configurations have non-integer harmonics.  The free-free beam's higher modal frequencies are shown in the following table.  The free-free formulas also apply to the fixed-fixed beam.  The fixed-free beam higher modal frequencies are shown in the table thereafter.

Table 12.2  Free-Free & Fixed-Fixed Beam Bending Frequencies, Elastic Modes

| Mode | Natural Frequency (Hz) |
|------|------------------------|
| $f_1$ | $= \dfrac{1}{2\pi}\left(\dfrac{22.373}{L^2}\right)\sqrt{EI/\rho_L}$ |
| $f_2$ | $= 2.757\, f_1$ |
| $f_3$ | $= 5.404\, f_1$ |
| $f_4$ | $= 8.402\, f_1$ |

Table 12.3  Fixed-Free Beam Bending Frequencies, Elastic Modes

| Mode | Natural Frequency (Hz) |
|------|------------------------|
| $f_1$ | $= \dfrac{1}{2\pi}\left(\dfrac{3.5156}{L^2}\right)\sqrt{EI/\rho_L}$ |
| $f_2$ | $= 6.268\, f_1$ |
| $f_3$ | $= 17.456\, f_1$ |
| $f_4$ | $= 34.386\, f_1$ |

## 12.1.4 Beam Bending Participation Factors & Effective Modal Mass

Again, the mode shapes $Y_n(x)$ and their corresponding mode shapes are found by applying the boundary conditions to the displacement shape in equation (12.9).  The participation factors and effective modal mass are then

$$\Gamma_n = \int_0^L \rho_L Y_n(x)dx \qquad\qquad (12.21)$$

$$m_{eff,\,n} = \frac{\left[\int_0^L \rho_L Y_n dx\right]^2}{\int_0^L \rho_L [Y_n(x)]^2 dx} \qquad\qquad (12.22)$$

## 12.1.5 Bending Wave Speed & Wavelength



**Traveling Bending Wave Packet Simulation**
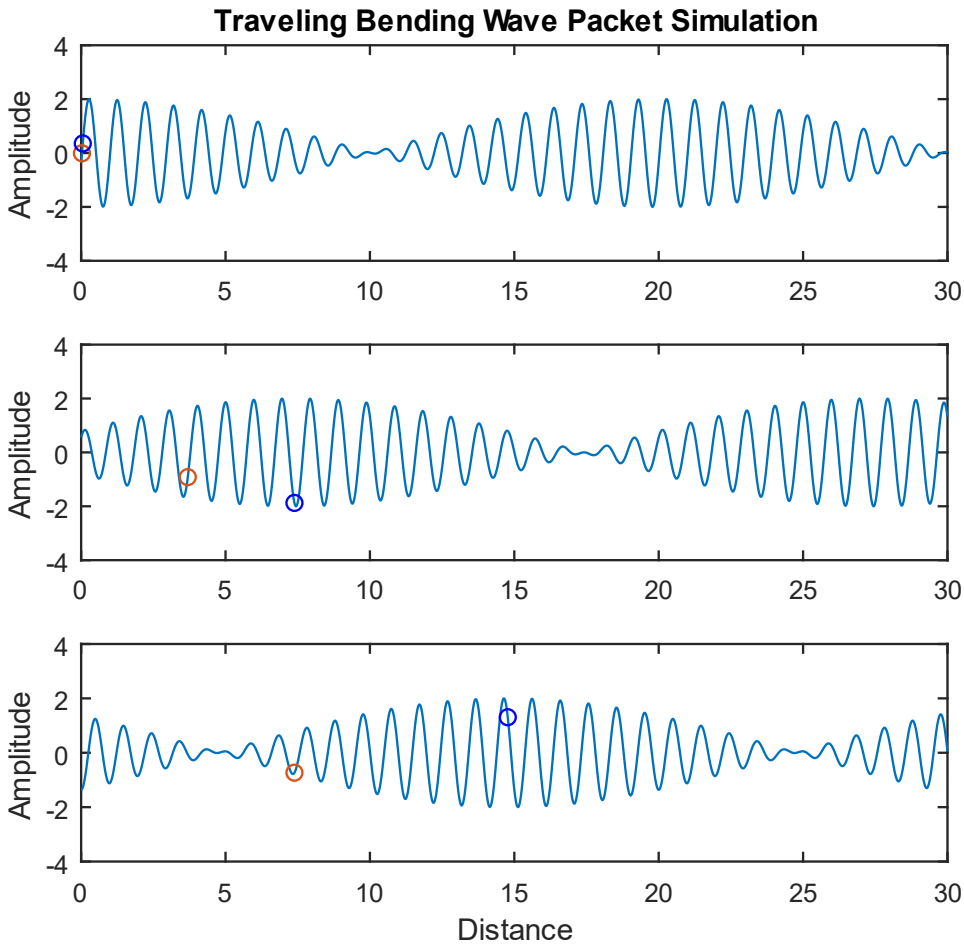
Figure 12.3.  Traveling Bending Wave Packet Dispersion, Snapshots at Three Different Times

Both the red and blue circles oscillate in the vertical axis in Figure 12.3.  The red circle travels at the phase velocity.  The blue circle propagates twice as fast at the group velocity and is always at or near the positive or negative peak in the wave packet.   The phase speed is the more important of the two speeds for vibroacoustics analyses where the bending waves are excited by the external sound field, or vice versa.

Bending waves are dispersive as a result of the governing fourth-order partial differential equation.  The wave speed varies with the angular natural frequency.  The phase speed for a given frequency is

$$c_p = \sqrt{\omega}\ [EI/\rho_L]^{1/4} \tag{12.23}$$

The group speed is twice the phase speed.

$$c_g = 2\, c_p \qquad\qquad\text{(12.24)}$$

Demonstrating bending wave propagation in terms of these two speeds is best done with animation, but the still images in Figure 12.3 may be useful. Furthermore, the phase speed is related to the frequency and bending wavelength by

$$c_p = f\,\lambda \qquad\qquad\text{(12.25)}$$

## 12.1.6 Beam Bending Energy Formulas

Natural frequency and mode shapes can also be derived from a beam's energy terms via the Rayleigh-Ritz or finite element method. The following formulas are given for reference.

The total strain or potential energy $P_E$ of a uniform beam is

$$P_E = \frac{1}{2} \int_0^L EI \left(\frac{d^2 y}{dx^2}\right)^2 \, dx \qquad\qquad\text{(12.26)}$$

The total kinetic energy $K_E$ of a uniform beam is

$$K_E = \frac{1}{2}\omega_n^2 \int_0^L \rho(y)^2 \, dx \qquad\qquad\text{(12.27)}$$

## 12.1.7 Beam Example, Wind Chime



Figure 12.4.  Author's Wind Chimes

The wind chimes in the figure are made from anodized aluminum.  The tallest one is 34.7 inches long, 1.25-inch diameter, and 0.094-inch wall thickness.  The chimes are like free-free beams undergoing bending vibration when struck.  The vibration then generates sound waves at discrete frequencies matching the bending frequencies.   The fundamental frequency of the tallest chime is calculated via the following steps.

The tallest wind chime was struck separately from the others.  The resulting sound was recorded and analyzed.  The sound tone represented bending modes.  The theoretical value agrees closely with the measured frequency of 244 Hz.  A comparison of the first four measured modal frequencies and their respective theoretical values is given in Table 12.4.

There are two orthogonal planes where transverse vibration occurs.  Each mode actually represents a pair of modes.  The pair should ideally have the same frequency but may be slightly different due to manufacturing and material imperfections, as well as two holes in each for the connecting cord.

$$I = \frac{\pi}{64}[d_o^4 - d_i^4] = \frac{\pi}{64}[(1.25 \text{ in})^4 - (1.16 \text{ in})^4] = 0.0574 \text{ in}^4 \qquad (12.28)$$

$$\rho_L = \left(0.1 \frac{\text{lbm}}{\text{in}^3}\right)\left(\frac{1 \text{ lbf sec}^2/\text{in}}{386 \text{ lbm}}\right)\left(\frac{\pi}{4}\right)[(1.25 \text{ in})^2 - (1.16 \text{ in})^2]$$
$$= 8.84e - 05 \frac{\text{lbf sec}^2}{\text{in}^2} \qquad (12.29)$$

$$f_n = \frac{1}{2\pi}\left[\frac{22.373}{(34.7 \text{ in})^2}\right]\sqrt{\left(1.0e + 07 \frac{\text{lbf}}{\text{in}^2}\right)(0.0574 \text{ in}^4) \Big/ 8.84e - 05 \frac{\text{lbf sec}^2}{\text{in}^2}}$$
$$= 238 \text{ Hz} \qquad (12.30)$$

Table 12.4. Tallest Chime Elastic Mode Natural Frequencies

| Mode | Calculated (Hz) | Measured (Hz) | Musical Note |
|------|-----------------|---------------|--------------|
| 1    | 238             | 244           | B            |
| 2    | 657             | 664           | E            |
| 3    | 1288            | 1273          | D#           |
| 4    | 2127            | 2050          | C            |
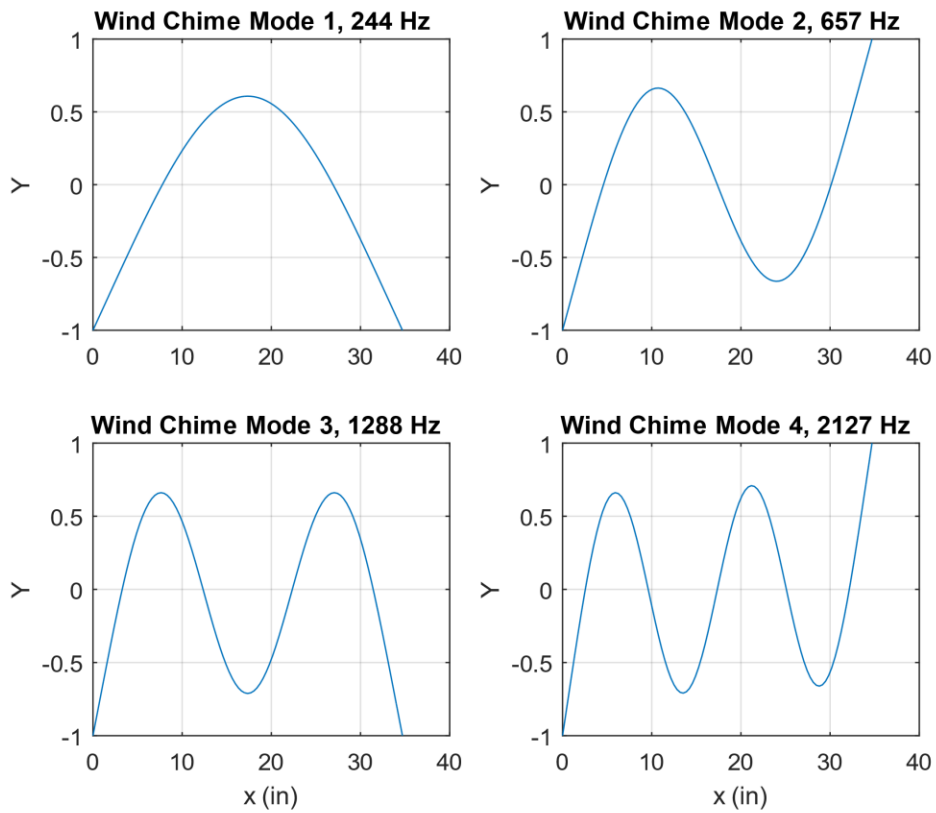
Figure 12.5.  Wind Chime Elastic Mode Shapes

The Y-axis represents transverse displacement which has been normalized to have a maximum absolute value of one.    The points where each curve crosses the zero baseline are nodal points.
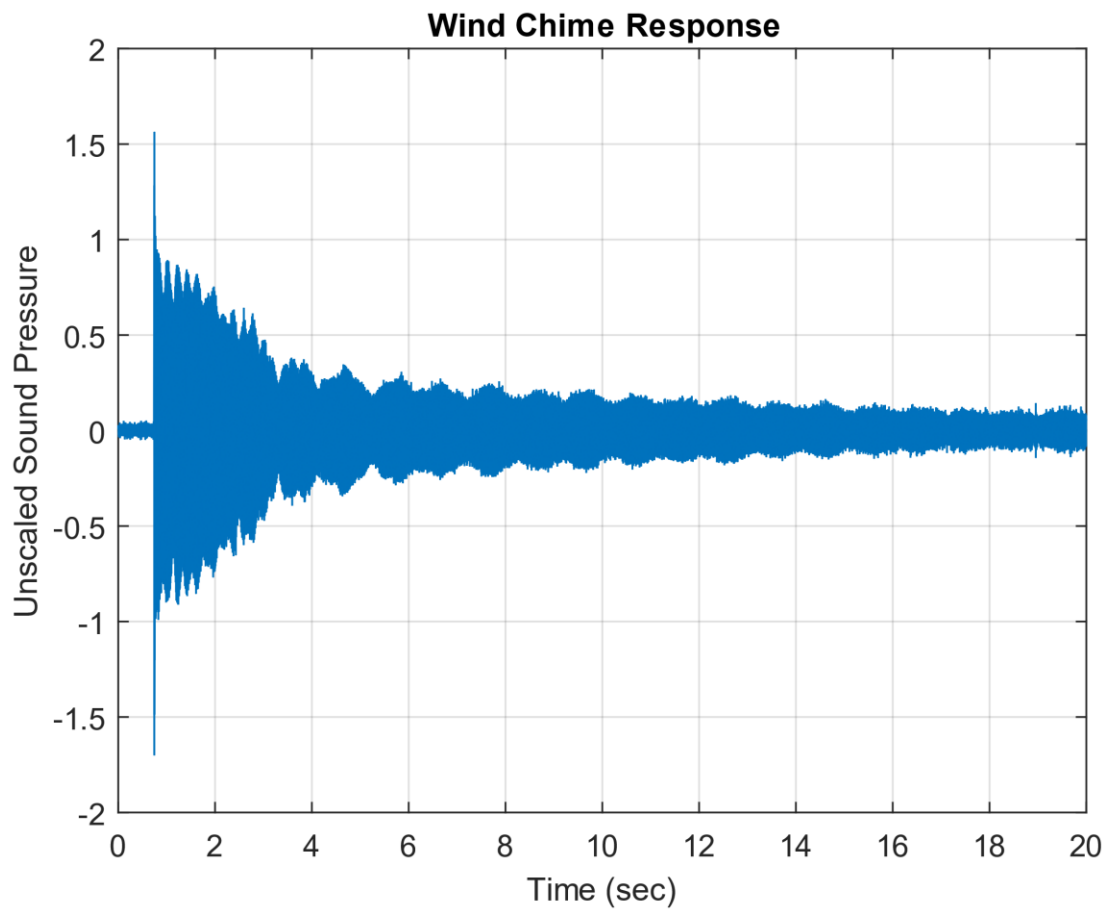
Figure 12.6.  Tallest Wind Chime Time History

The time history shows some beat frequency effect because each mode is a pair of orthogonal modes with closely-spaced frequencies.
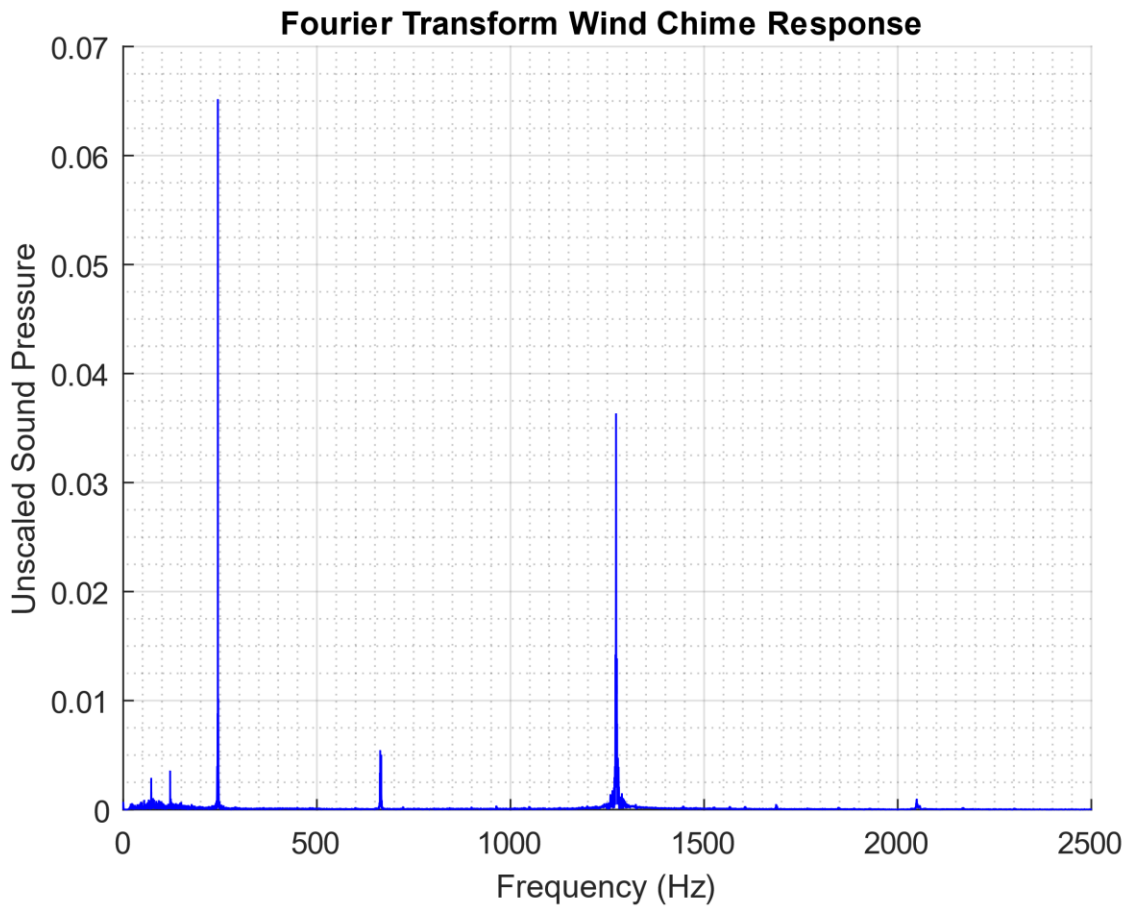
Figure 12.10.  Tallest Wind Chime Fourier Transform

The highest response is at the fundamental bending mode at 244 Hz.  The fourth bending mode at 2050 Hz is barely excited.  Note that Fourier transforms are covered in Section 23.

# 13 THIN PLATE VIBRATION

## 13.1.1 Rectangular Plate, Bending Vibration

### 13.1.1.1 Rectangular Plate Equations
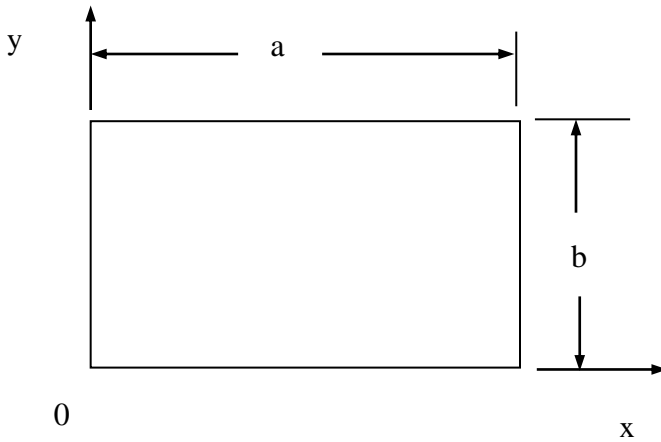


Figure 13.1.  Rectangular Plate

The fourth-order governing equation of motion for the out-of-plane displacement is

$$D\left(\frac{\partial^4 z}{\partial x^4} + 2\frac{\partial^4 z}{\partial x^2\,\partial y^2} + \frac{\partial^4 z}{\partial y^4}\right) + \rho h \frac{\partial^2 z}{\partial t^2} = 0 \tag{13.1}$$

The plate stiffness factor is

$$D = \frac{Eh^3}{12(1 - \mu^2)} \tag{13.2}$$

The kinetic energy in the plate is

$$K_E = \frac{\rho h\, \Omega^2}{2} \int_0^b \int_0^a Z^2\, dxdy \tag{13.3}$$

The potential or strain energy in the plate is

$$P_E = \frac{D}{2} \int_0^b \int_0^a \left\{ \left(\frac{\partial^2 Z}{\partial x^2}\right)^2 + \left(\frac{\partial^2 Z}{\partial y^2}\right)^2 + 2\mu \left(\frac{\partial^2 Z}{\partial x^2}\right)\left(\frac{\partial^2 Z}{\partial y^2}\right) + 2(1-\mu)\left(\frac{\partial^2 Z}{\partial x\, \partial y}\right)^2 \right\} dxdy \tag{13.4}$$

Assume a harmonic displacement response for the partial differential equation (13.1).

$$z(x, y, t) = Z(x, y)\exp(j\omega t) \tag{13.5}$$

Substitution of the assumed response leads to the spatial equation

$$D\left(\frac{\partial^4 Z}{\partial x^4} + 2\frac{\partial^4 Z}{\partial x^2\, \partial y^2} + \frac{\partial^4 Z}{\partial y^4}\right) - \rho h\omega^2\, Z = 0 \tag{13.6}$$

The modal solution for most boundary conditions requires an approximation method such as the Rayleigh-Ritz or finite element method. Further information on plate vibration solutions is given in Reference [16].

13.1.1.2 Rectangular Plate, Simply-Supported along All Edges

The case of a plate with simply-supported boundary conditions on all four edges can be solved exactly. The boundary conditions for this plate are

$$Z(x, y) = 0, \quad M_x(x, y) = 0 \quad \text{for } x=0, a \tag{13.7}$$
$$Z(x, y) = 0, \quad M_y(x, y) = 0 \quad \text{for } y=0, b \tag{13.8}$$

The displacement and bending moment along each edge is equal to zero.

Assume the following displacement function which satisfies the boundary conditions, where m and n are indices. The mass-normalized modes shapes for the plate are

$$Z_{mn} = \frac{2}{\sqrt{\rho abh}} \sin\left(\frac{m\pi x}{a}\right) \sin\left(\frac{n\pi y}{b}\right)$$

(13.9)

The angular natural frequencies are

$$\omega_{mn} = \sqrt{\frac{D}{\rho h}} \left[\left(\frac{m\pi}{a}\right)^2 + \left(\frac{n\pi}{b}\right)^2\right]$$

(13.10)

### 13.1.1.3 Rectangular Plate Example

Consider a rectangular circuit board made from G10 material. The modulus of elasticity is 2.7e+06 lbf/in^2 with a Poisson ratio of 0.12. The dimensions of the circuit board are 4 in x 2 in x 0.063 in. The board is simply-supported about its perimeter. Assume that the electronic components do not add any stiffness.

The board has a uniform mass distribution. The total mass is 0.113 lbm. This includes the G10 board and the electronic components. The mass per area is

$$\rho h = 0.0141 \ \text{lbm/in}^2 = 3.65e - 05 \ \text{lbf sec}^2/\text{in}^3$$

(13.11)

The circuit board stiffness factor is

$$D = \frac{(2.7e + 06 \ \text{lbf/in}^2)(0.063 \ \text{in})^3}{12(1 - 0.12^2)} = 57.1 \ \text{lbf in}$$

(13.12)

The fundamental angular natural frequency is

$$\omega_{mn} = \sqrt{\frac{57.1 \ \text{lbf in}}{3.65e - 05 \ \text{lbf sec}^2/\text{in}^3}} \left[\left(\frac{\pi}{4 \ \text{in}}\right)^2 + \left(\frac{\pi}{2 \ \text{in}}\right)^2\right] = 3875 \ \text{rad/sec}$$

(13.13)

The fundamental frequency is equivalent to 613.7 Hz. The mode shape is shown in Figure 13.2.
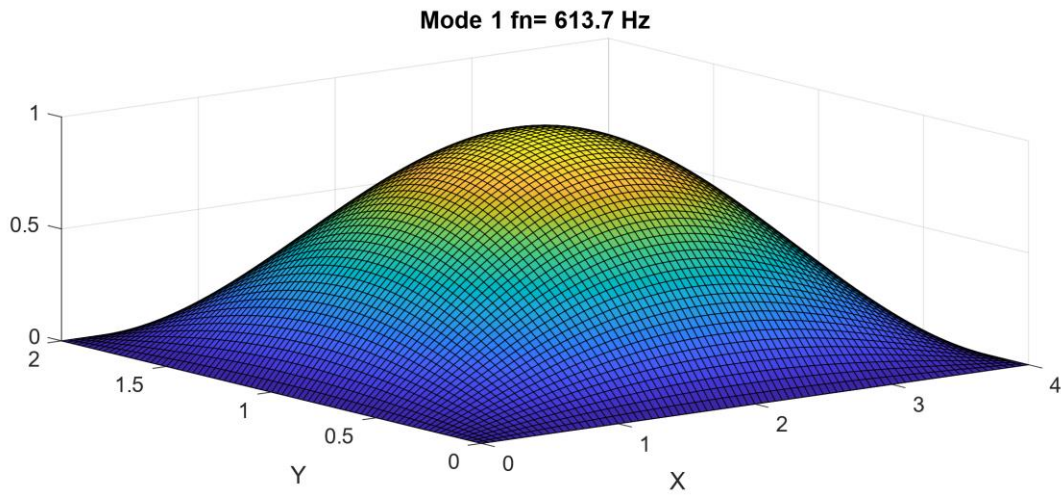
Figure 13.2.  Circuit Board, Fundamental Bending Mode Shape


## 13.1.2 Circular Plate, Bending Vibration

### 13.1.2.1 Circular Plate Equations
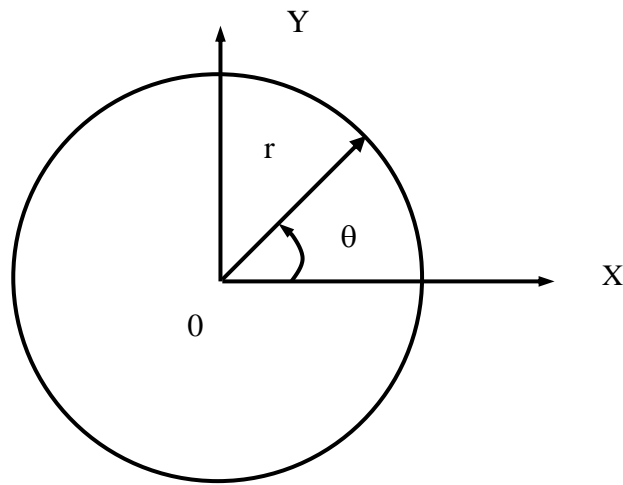


Figure 13.3.  Circular Plate

The governing fourth-order spatial equation of motion for the out-of-plane displacement is

$$\nabla^4\, Z(r,\Theta) - \beta^4\, Z(r,\Theta) = 0 \tag{13.14}$$

The biharmonic operator is

$$\nabla^4 = \nabla^2\nabla^2 = \left(\frac{\partial^2}{\partial r^2} + \frac{1}{r}\frac{\partial}{\partial r} + \frac{1}{r^2}\frac{\partial^2}{\partial\Theta^2}\right)\left(\frac{\partial^2}{\partial r^2} + \frac{1}{r}\frac{\partial}{\partial r} + \frac{1}{r^2}\frac{\partial^2}{\partial\Theta^2}\right) \tag{13.15}$$

The wave number is

$$\beta = \sqrt{\omega}\left[\frac{\rho h}{D}\right]^{1/4} \tag{13.16}$$

The kinetic energy in the plate is

$$K_E = \frac{\rho h\,\omega^2}{2}\int_0^{2\pi}\int_0^R Z^2\, r dr\, d\Theta \tag{13.17}$$

The potential or strain energy in the plate is

$$P_E = \frac{D}{2}\int_0^{2\pi}\int_0^R \left\{\left(\frac{\partial^2 Z}{\partial r^2} + \frac{1}{r}\frac{\partial Z}{\partial r} + \frac{1}{r^2}\frac{\partial^2 Z}{\partial\Theta^2}\right)^2 - 2(1-\mu)\frac{\partial^2 Z}{\partial r^2}\left(\frac{1}{r}\frac{\partial Z}{\partial r} + \frac{1}{r^2}\frac{\partial^2 Z}{\partial\Theta^2}\right)\right.$$
$$\left. + 2(1-\mu)\left[\frac{\partial}{\partial r}\left(\frac{1}{r}\frac{\partial Z}{\partial\Theta}\right)\right]^2\right\} r\, dr\, d\Theta$$

$$\tag{13.18}$$

The solution of equation (13.14) proceeds by assuming the separation of the spatial variables.

$$Z(r,\theta) = R(r)\Theta(\theta) \tag{13.19}$$

Further information on this solution method is given in Reference [16].

13.1.2.2 Circular Plate, Simply-Supported

The boundary conditions for the simply-supported plate are

$$Z(a, \theta) = 0 \tag{13.20}$$

$$M_r = 0 \quad \text{at} \quad r = a \tag{13.21}$$

The mass-normalized, fundamental mode shape is

$$Z_{00} = \frac{1.945}{\sqrt{m}} \{ J_0(2.2215 \, r/a) - 0.03686 \, I_0(2.2215 \, r/a) \} \tag{13.22}$$

Note that $I_0$ and $J_0$ in equation (13.22) are Bessel functions. This fundamental mode shape is sometimes referred to as an "oil can" mode.

The corresponding fundamental frequency is

$$\omega_{00} = \frac{4.979}{a^2} \sqrt{\frac{D}{\rho h}} \quad , \quad \text{for } \mu = 0.33 \tag{13.23}$$

A characteristic equation for variable mode numbers and Possion ratios is given in Reference [16]. The roots of this equation determine the numerical coefficient on the righthand side of equation (13.23).

13.1.2.3 Circular Plate Example, Simply-Supported

Assume a 48-inch diameter, 0.5-inch thick, aluminum circular plate, with a simply-supported circumference. Calculate the fundamental frequency and mode shape. The plate stiffness factor is

$$D = \left[ \frac{(10e + 06 \, \text{lbf/in}^2)(0.5 \, \text{in})^3}{12(1 - 0.33^2)} \right] = 1.169e + 05 \, \text{lbf in} \tag{13.24}$$

The mass per area is

$$\rho h = (0.000259 \text{ lbf sec}^2/\text{in}^4)(0.5 \text{ in}) = 1.295e - 04 \text{ lbf sec}^2/\text{in}^3 \qquad (13.25)$$

The angular natural frequency is

$$\omega_{00} = \frac{4.979}{(24 \text{ in})^2} \sqrt{\frac{1.169e + 05 \text{ lbf in}}{1.295e - 04 \text{ lbf sec}^2/\text{in}^3}} = 259.7 \text{ rad/sec} \qquad (13.26)$$

The angular frequency is equivalent to 41.33 Hz.
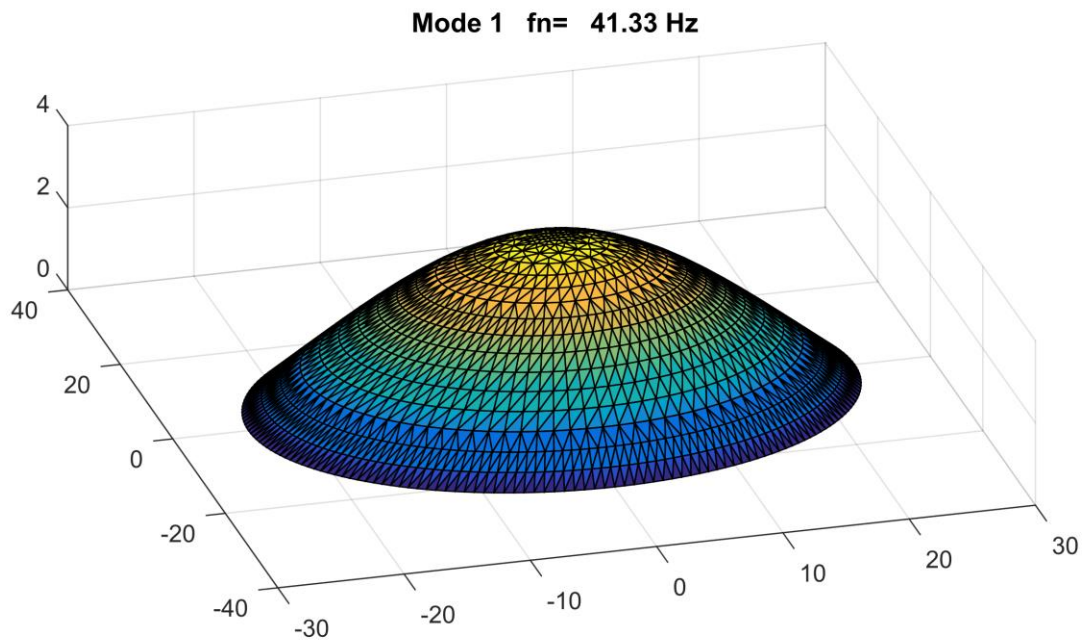


Figure 13.4.  Circular Plate Fundamental Mode Shape

## 14.1 HONEYCOMB SANDWICH PLATE CHARACTERISTICS
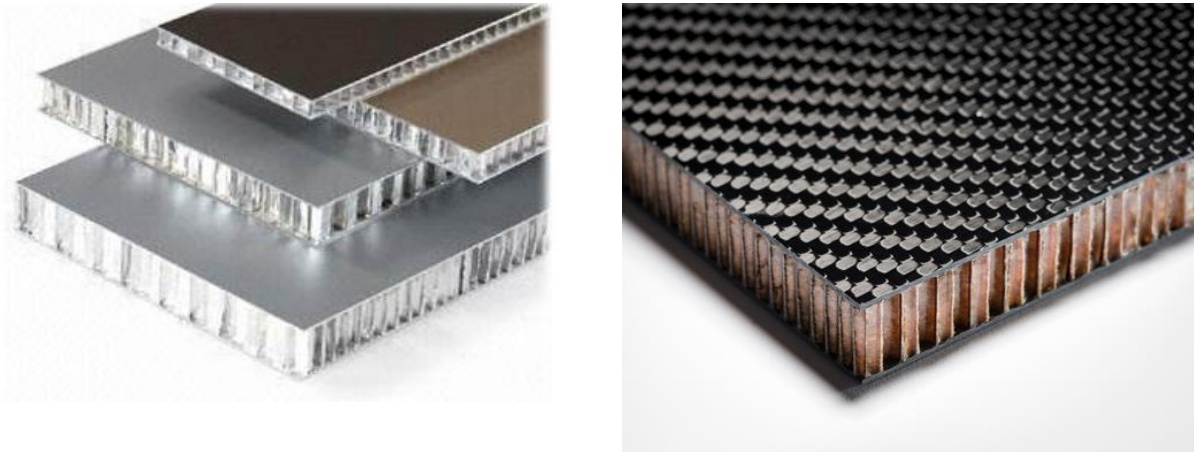


Figure 14.1.   Sample Honeycomb Sandwich Plates
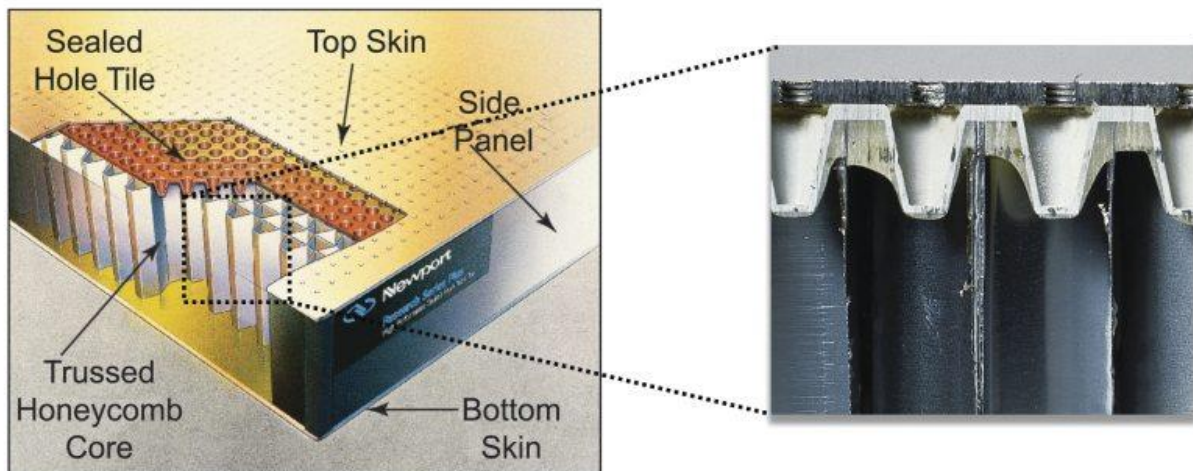


Figure 14.2.   Optical Bench (Newport image)

Optical tables provide a rigid platform for high-precision optical experiments and systems. They are designed to eliminate errors caused by relative motion between optical components in the beam path.

Figure 14.3.   Honeycomb Panel, Aircraft Cabin Floor

The strength-to-weight ratio of honeycomb composite panels is high in comparison to rib-stiffened aluminum panels used in previous generations of aircraft.  However, the high stiffness and low weight can result in supersonic wave propagation at relatively low frequencies, which adversely affects the acoustical performance at these frequencies.   The poor acoustical performance of these types of structures can increase the cabin noise levels to which the passengers and crew are exposed.



Figure 14.4.   Honeycomb Sandwich Structure, Boeing 747 Fore Flap
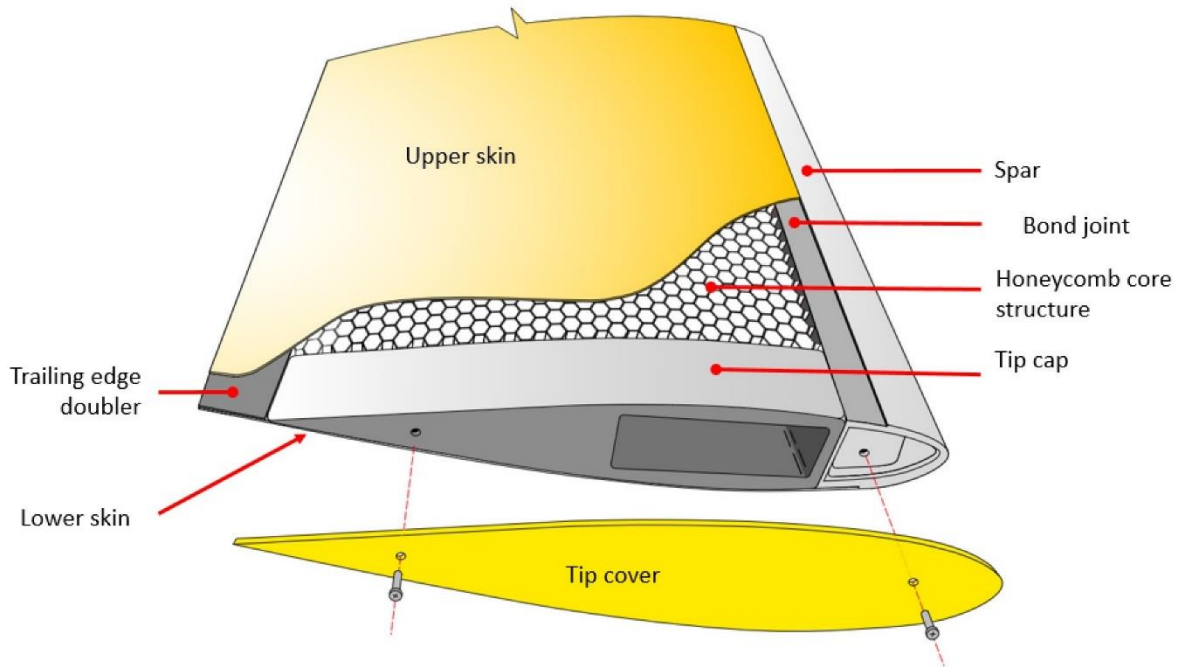
Figure 14.5.   Robinson R44 Helicopter Main Rotor Blade
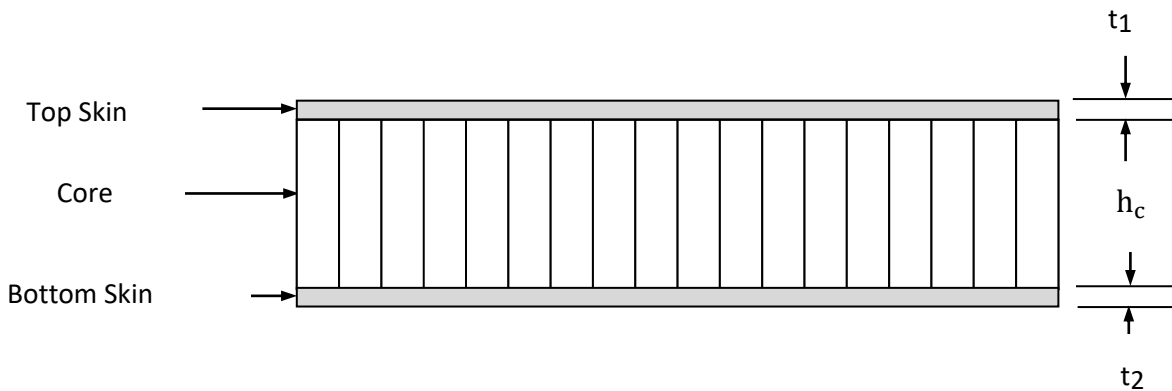


Figure 14.6.  Honeycomb Sandwich Geometry

Honeycomb sandwich structures are designed to have a high stiffness-to-mass ratio.   The stiff, strong face sheets carry the bending loads, while the core resists shear loads. The face sheets are typically made from aluminum or carbon fiber with epoxy resin. The honeycomb core material is usually aluminum for aerospace applications.   Other core materials include Nomex aramid or Kevlar para-aramid fiber sheets saturated with a phenolic resin.  In addition, closed-cell foams such as Rohacell are substituted for honeycomb in some sandwich panel designs.
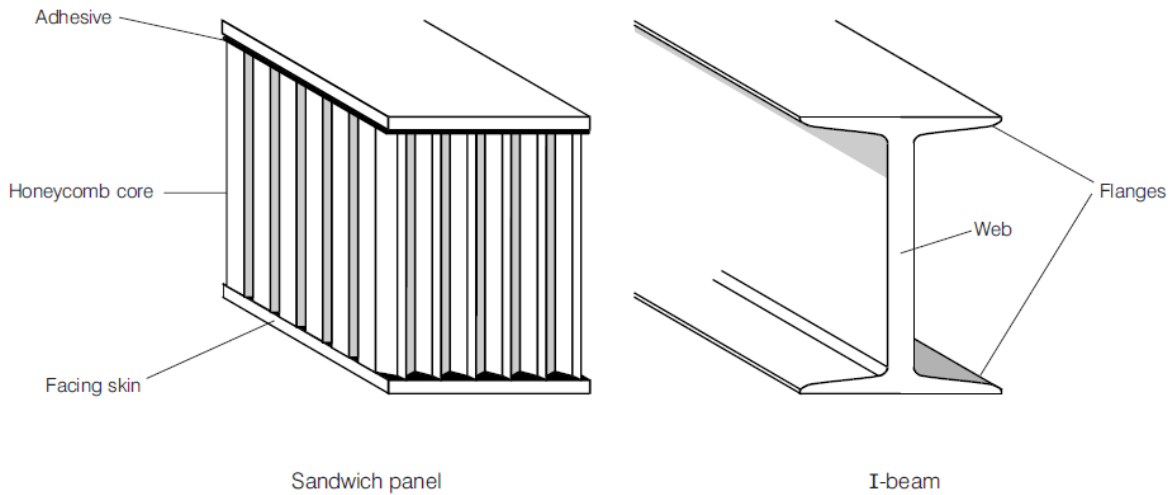
Figure 14.7.  I-beam Analogy

The facing skins of a sandwich panel can be compared to the flanges of an I-beam, as they carry the bending stresses to which the beam is subjected. With one facing skin in compression, the other is in tension for bending.  Similarly, the honeycomb core corresponds to the web of the I-beam.  The core resists the shear loads and increases the stiffness of the structure by holding the facing skins apart.
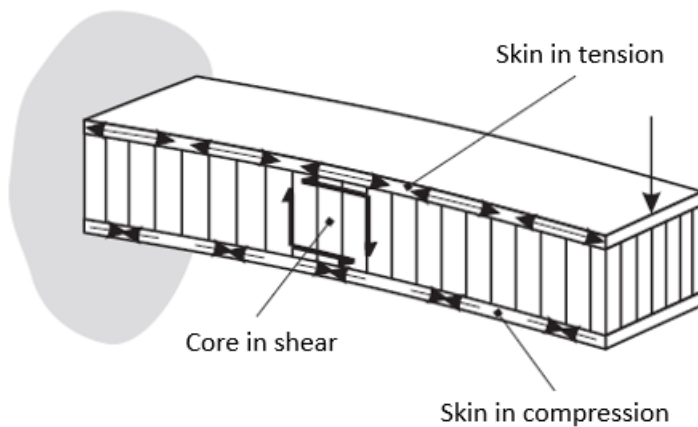


Figure 14.8.  Honeycomb Beam in Bending, Static Load

The stiff, strong face sheets carry the bending & in-plane loads. The core resists transverse shear loads.  Total Deflection = Bending Deflection + Shear Deflection
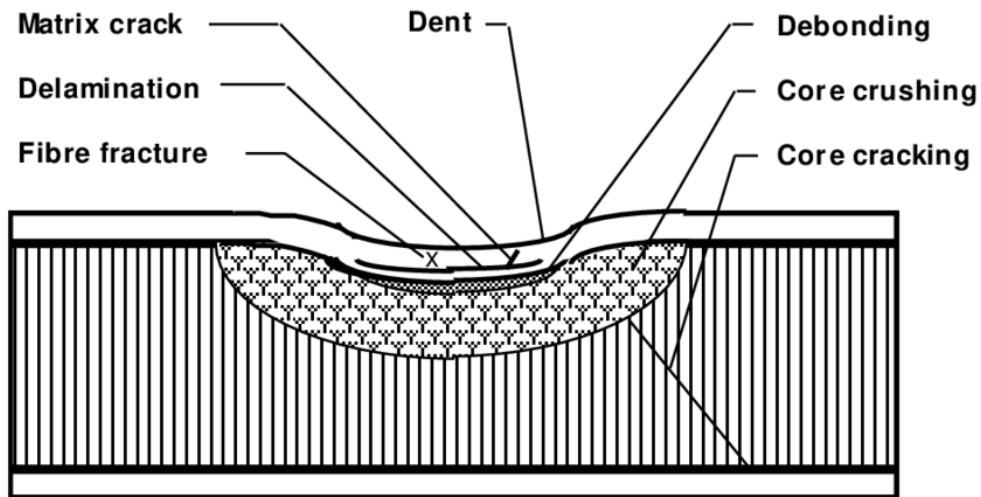
Figure 14.9.  Local Compression (Robin Olsson Image)
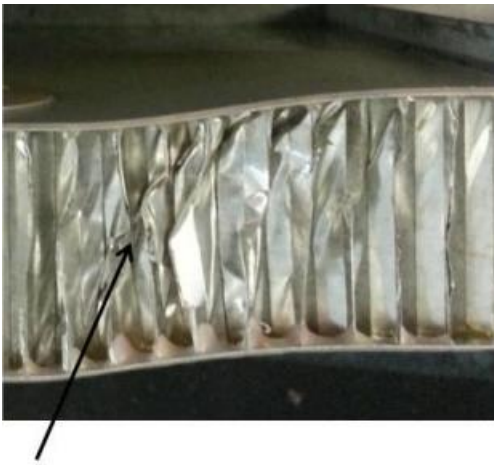


Figure 14.10.  Shear Buckling (Andrew L. Lyford Image)

Shear buckling occurs because in a tall honeycomb panel the core in the middle of the panel is no longer well supported by the face sheet and can buckle due to shear loads, particularly near the edge of the panel.
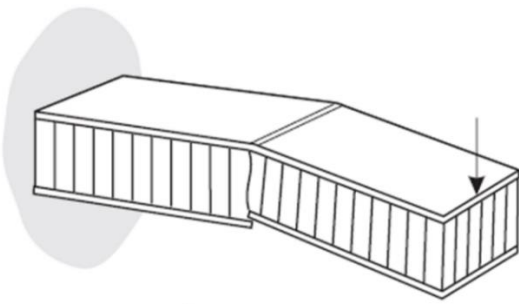
Skin Compression Failure
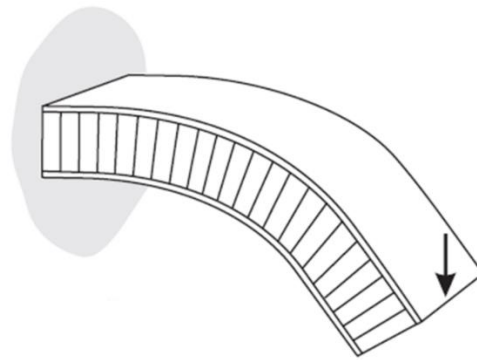
Excessive Deflection

Panel Buckling
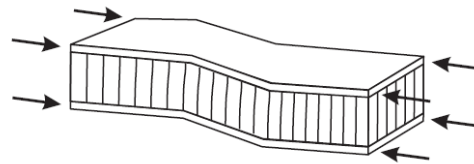
Shear Crimping
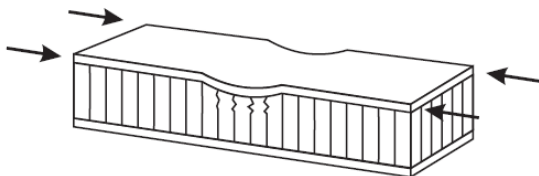
Skin Compression
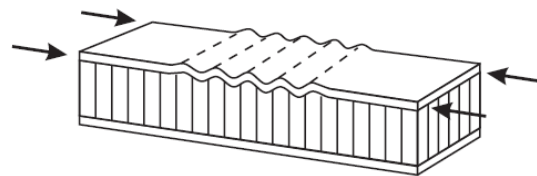
Intra Cell Buckling

Figure 14.11.  Various Failure Modes

## 14.3 HONEYCOMB SANDWICH DYNAMIC PROPERTIES

Table 14.1.  Honeycomb Sandwich Plate Normal Modes

| Frequency Domain | Characteristics |
|---|---|
| Low | Bending of the entire structure as if were a thick plate |
| Mid | Transverse shear strain in the honeycomb core governs the behavior |
| High | The structural skins act in bending as if disconnected |

The modal response of honeycomb sandwich plates has the characteristic shown in Table 14.1. The lower natural frequencies may be calculated using the plate formulas in Sections 13.1.1 and 13.1.2 by properly accounting for the material and geometric properties.

Assume

1. The skin elastic modulus is much greater than the core modulus.
2. Each skin has the same material.
3. Each skin is "thin" relative to the core.

The honeycomb sandwich plate bending stiffness from Reference [17] is

$$D = \left[\frac{E_f}{1-\mu^2}\right]\left[\frac{t_1 t_2\, h^2}{t_1 + t_2}\right] \ , \ \ h = h_c + \frac{1}{2}[t_1 + t_2] \tag{14.1}$$

The elastic modulus of each skin or face sheet is $E_f$.

## 14.4 TRANSITION FREQUENCIES

The transition for global bending-to-shear motion is considered to occur at the frequency at which the global bending phase speed equals the core shear speed, as an idealization

Assume uniform face sheet thickness:    $t_f = t_1 = t_2$

The global stiffness factor B is

$$B = \frac{E t_f (h_c + t_f)^2}{2(1 - \mu^2)} \tag{14.2}$$

The global bending-to-shear transition frequency $\omega_1$ is

$$\omega_1 = \frac{G_c h_c}{\sqrt{B\mu}} \tag{14.3}$$

where $G_c$ is the core shear modulus

The transition frequency $\omega_2$ for shear-to-face sheet bending motion is considered to occur at the frequency at which the core shear speed equals the face sheet bending phase speed

$$B_f = \frac{E_f t_f^3}{12(1 - \mu^2)} \tag{14.4}$$

$$\omega_2 = \frac{G_c h_c}{\sqrt{2B_f \mu}} \tag{14.5}$$

## 14.5  HONEYCOMB SANDWICH PLATE EXAMPLE, PART I

A suborbital rocket vehicle has a circular bulkhead made from honeycomb.  The material is aluminum for both the core and skins.  The bulkhead properties are shown in Table 14.2. Calculate the fundamental frequency of the bare bulkhead.

Table 14.2  Bulkhead Parameters

| Parameter | Value |
|---|---|
| Boundary Condition | Simply Supported |
| Diameter | 40 inch |
| Core Thickness | 1.0 inch |
| Thickness of Each Skin | 0.063 inch |
| Total Thickness | 1.125 inch |
| Skin Elasticity | 10.0e+06 lbf/in^2 |
| Core Elasticity | Negligible |
| Skin Density | 0.10 lbm/in^3 |
| Core Density | 0.01 lbm/in^3 |
| Poisson's Ratio | 0.3 |

The plate stiffness is calculated in two steps.

$$h = 1.0 \text{ in} + \frac{1}{2}[\,0.063 \text{ in} + 0.063 \text{ in}] = 1.063 \text{ in} \tag{14.6}$$

$$D = \left[\frac{10e + 06 \text{ lbf/in}^2}{1 - 0.33^2}\right]\left[\frac{(0.063 \text{ in})(0.063 \text{ in})\,(1.063 \text{ in})^2}{0.063 \text{ in} + 0.063 \text{ in}}\right] = 3.99e + 05 \text{ lbf in}$$

$$\tag{14.7}$$

The total skin mass is

$$m_{skin} = 2\left(\frac{\pi}{4}\right)(40 \text{ in})^2(0.063 \text{ in})(0.1 \text{ lbm/in}^3) = 15.83 \text{ lbm} \tag{14.8}$$

The core mass is

$$m_{core} = \left(\frac{\pi}{4}\right)(40 \text{ in})^2(1 \text{ in})(0.01 \text{ lbm/in}^3) = 12.57 \text{ lbm} \tag{14.9}$$

The total bulkhead mass is

$$m_{total} = 15.83 \text{ lbm} + 12.57 \text{ lbm} = 28.4 \text{ lbm} \tag{14.10}$$

The total mass per area is

$$\rho_A = \frac{28.4 \text{ lbm}}{(\pi/4)(40 \text{ in})^2} = 0.0226 \text{ lbm/in}^2 = 5.854e - 05 \text{ lbf sec}^2/\text{in}^3 \tag{14.11}$$

The angular fundamental frequency of the bare bulkhead for $\mu=0.33$ is

$$\omega_{00} = \frac{4.979}{(20 \text{ in})^2}\sqrt{\frac{3.99e + 05 \text{ lbf in}}{5.854e - 05 \text{ lbf sec}^2/\text{in}^3}} = 1028 \text{ rad/sec} \tag{14.12}$$

The angular frequency is equivalent to 164 Hz.  The mode shape is qualitatively similar to that in Figure 13.4.

## 14.6  HONEYCOMB SANDWICH PLATE EXAMPLE, PART II

Now assume that 100 lbm of avionics components are added to the bulkhead and that this nonstructural mass is spread uniformly across the bulkhead.  Neglect the geometry and stiffness of the avionics.  Repeat the natural frequency calculation.

The total mass per area is

$$\rho_A = \frac{(100 + 28.4)\text{ lbm}}{(\pi/4)(40\text{ in})^2} = 0.1022\text{ lbm/in}^2 = 2.647\text{e} - 04\text{ lbf sec}^2/\text{in}^3 \qquad (14.13)$$

The angular fundamental frequency of the mass-loaded bulkhead for μ=0.33 is

$$\omega_{00} = \frac{4.979}{(20\text{ in})^2}\sqrt{\frac{3.99\text{e} + 05\text{ lbf in}}{2.647\text{e} - 04\text{ lbf sec}^2/\text{in}^3}} = 483.3\text{ rad/sec} \qquad (14.14)$$

The equivalent frequency is 76.9 Hz.


## 14.7  AIRCRAFT FUSELAGE HONEYCOMB PANEL ACOUSTICS

The strength-to-weight ratio of honeycomb composite panels is high in comparison to rib-stiffened aluminum panels used in previous generations of aircraft. However, the high stiffness and low weight can result in supersonic wave propagation at relatively low frequencies, which adversely affects the acoustical performance at these frequencies.  The poor acoustical performance of these types of structures can increase the cabin noise levels to which the passengers and crew are exposed.

## 14.8  HONEYCOMB PANEL VENT HOLES
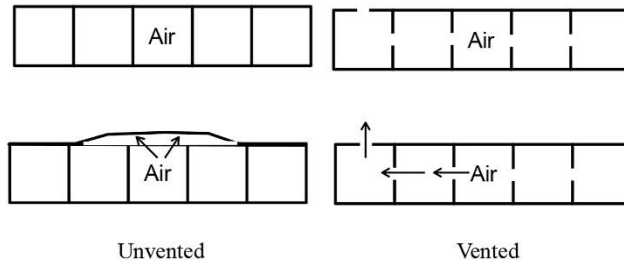


Figure 14.12.  Unvented & Vented Panels

Honeycomb sandwich structures are used in a wide variety of critical structures in Air Force space systems. These include payload fairings (shrouds) for launch vehicles, adapters for mounting satellite payloads, solar array substrates, antennas, and equipment platforms.

Since 1964, there have been several known or suspected failures of honeycomb structures, which have been costly. These failures have been attributed to the lack of venting in the panel design manufacture. On the other hand, based on available information, vented honeycomb sandwich panels never have experienced failure during flight.

Honeycomb sandwich panels that are not vented will contain air (and possibly volatiles, including moisture) which causes a pressure differential during the launch into orbit. If heating also is involved, the internal pressure will rise further. In any case, each unvented honeycomb cell acts as a tiny pressure vessel imposing stresses on the skin-to-core bonds. If these stresses are high enough, panel failure (i.e., skin-to-core debonding) will occur. Certain defects introduced during panel manufacture would make failure more likely.

# 15 DAMPING

## 15.1 DAMPING GALLERY



Figure 15.1. Atlas V Launch Vehicle

Launch vehicles must withstand ground winds and potential vortex-shedding effects. A vehicle may be on its pad for ten days or so before launch.

Wind gusts can oscillate near a natural resonance of the launch vehicle creating excessive motion that exceeds structural design limits. Damping controls the response at resonance.

A wind damper is typically mounted between the vehicle and its tower for tall vehicles. The damper is modeled as a dashpot for structural dynamics analysis.

Figure 15.2.  Shock Absorber for Seismic Isolation of Taipei City Hospital

The shock absorbers are viscous dampers, designed to limit the building's lateral response in the event of an earthquake.  The absorbers were installed as a seismic retrofit.

Figure 15.3. Truck Shock Absorber

An automotive shock absorber is a damper that has a piston that moves inside a sealed, oil-filled cylinder with the up-and-down movement of the wheel. Some dampers have an extra chamber containing gas, to further slow the piston movement.

## 15.2  DAMPING METRICS

The following metrics are demonstrated by example throughout this document. The viscous damping ratio is defined in terms of the damping coefficients as

$$\xi = c/c_r \tag{15.1}$$

The critical damping coefficient is

$$c_r = 2 \sqrt{k\,m} \tag{15.2}$$

The amplification factor is

$$Q = 1 / (2\,\xi) \tag{15.3}$$

The amplification factor can be calculated from measured frequency response function data via the half-power method.

$$Q = f / \Delta f \tag{15.4}$$

where f is the peak center frequency and Δf is the difference between the two -3 dB points on either side of the peak.

The logarithmic decrement is

$$\delta = \frac{2\,\pi\,\xi}{\sqrt{1-\xi^2}}$$

## 15.3  FOUR DAMPING CATEGORIES

The four damping types are summarized in Table 15.1.  The description is for the free vibration of a single-degree-of-freedom system due to initial displacement or velocity.

Table 15.1.  Damping Types

| Type | Value | Response Description |
|------|-------|----------------------|
| Undamped | $\xi=0$ | Simple harmonic motion, sinusoidal response |
| Underdamped | $0<\xi<1$ | Damped sine response with exponential decay |
| Critically damped | $\xi=1$ | Border between the overdamped and underdamped cases |
| Overdamped | $\xi>1$ | Sum of two decaying exponentials with no oscillation |

The first three of these types are shown by examples in Figure 15.4.  The underdamped type is emphasized throughout this document.
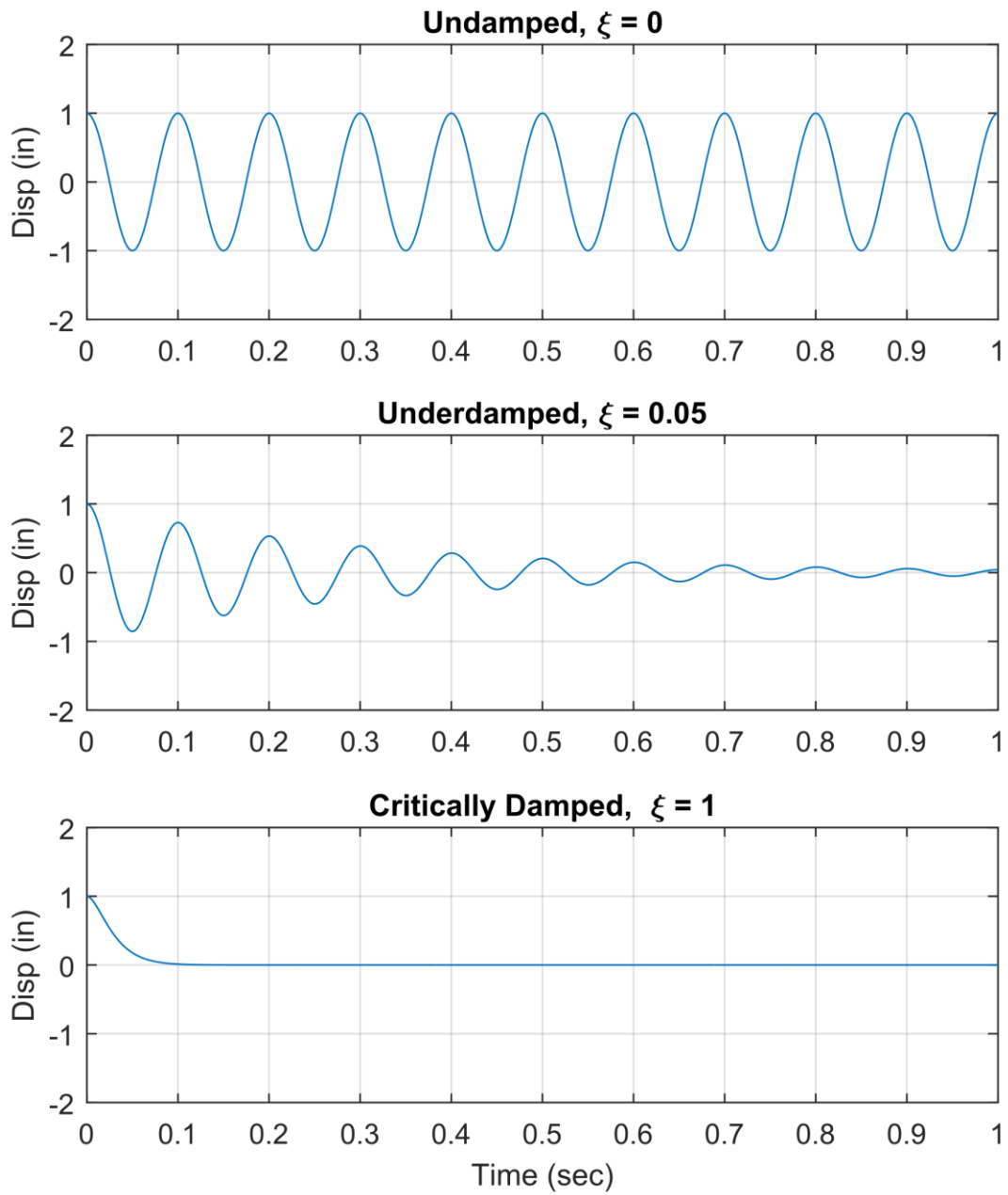
Figure 15.4. SDOF Response to Initial Displacement for Three Damping Cases

## 15.4 DAMPING MECHANISMS

Damping occurs as vibration energy is converted to heat, sound, or some other loss mechanism. Damping is needed to limit the structural resonant response. Common sources are:

1. viscous effects
2. Coulomb damping, dry friction
3. Structural damping, hysteresis, complex stiffness
4. aerodynamic drag
5. acoustic radiation
6. air pumping at joints
7. boundary damping

The dominant source for assembled structures is usually joint friction. This damping mechanism may be nonlinear due to joint microslip effects. The damping value tends to increase at higher excitation levels.

Damping may also decrease as the natural frequency increases, such that the amplification factor increases with the natural frequency. The equation per Reference [18] for approximating Q for an electronic system subjected to a sine base input is

$$Q = A \left( \frac{f_n}{( G_{in} )^{0.6}} \right)^{0.76}$$ 
(15.6)

where

| | |
|---|---|
| $A$ | = 1.0 for beam-type structures<br>= 0.5 for plug-in PCBs or perimeter-supported PCBs<br>= 0.25 for small electronic chassis or electronic boxes |
| $G_{in}$ | Sine Base Input (G) |

**Beam structures:** several electronic components with some interconnecting wires or cables.

**PCB:** printed circuit board well-populated with an assortment of electronic components.

**Small electronic chassis:** 8-30 inches in its longest dimension, with a bolted cover to provide access to various types of electronic components such as PCBs, harnesses, cables, and connectors.

CIRCUIT BOARD FUNDAMENTAL FREQUENCY  Q vs fn
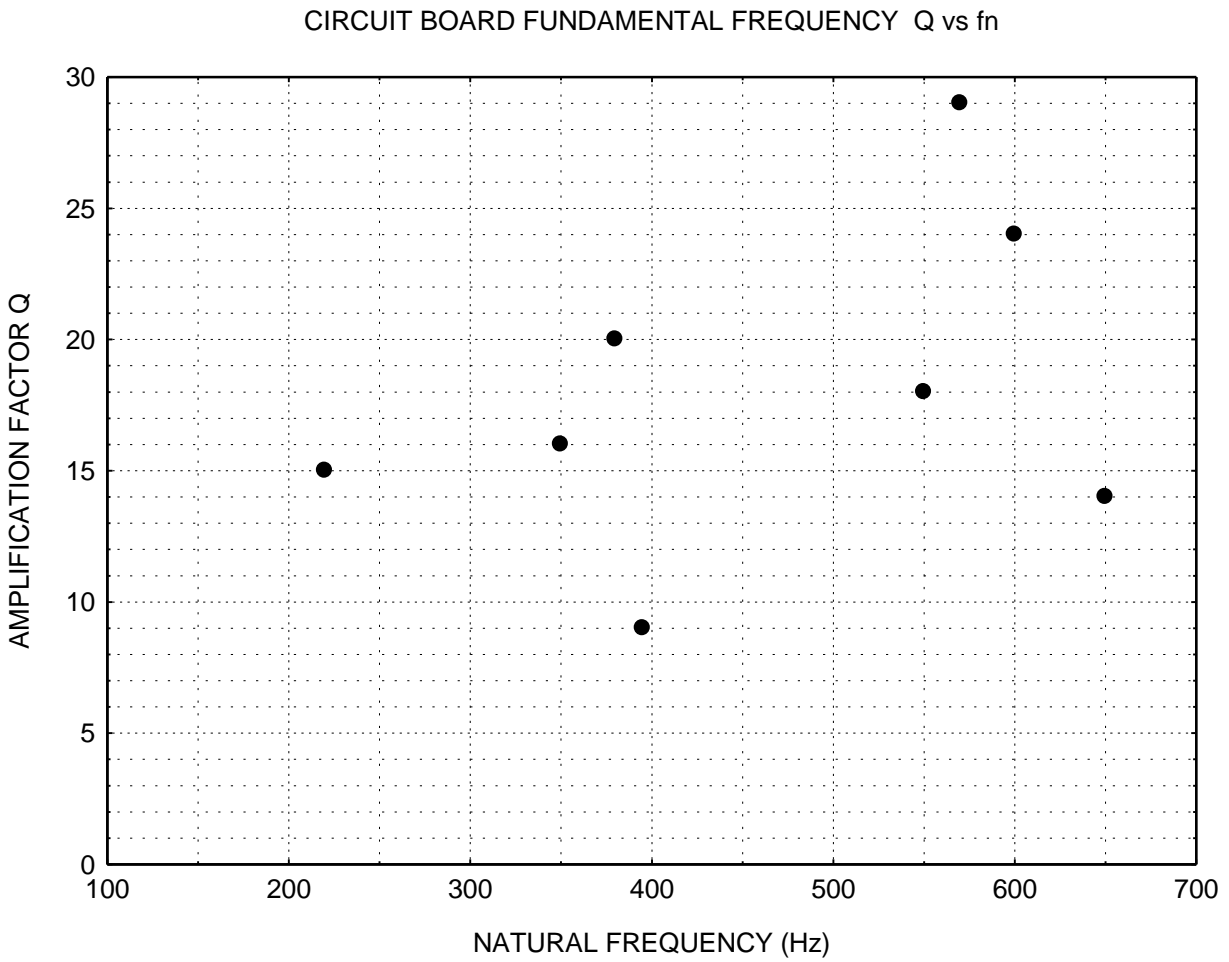
Figure 15.5. Avionics Circuit Board Amplification Factors, Author's Experimental Results

The results were measured from shaker table test data.  The half-power method was used to estimate the Q factors from the transmissibility functions.   The Q range is 9 to 29.
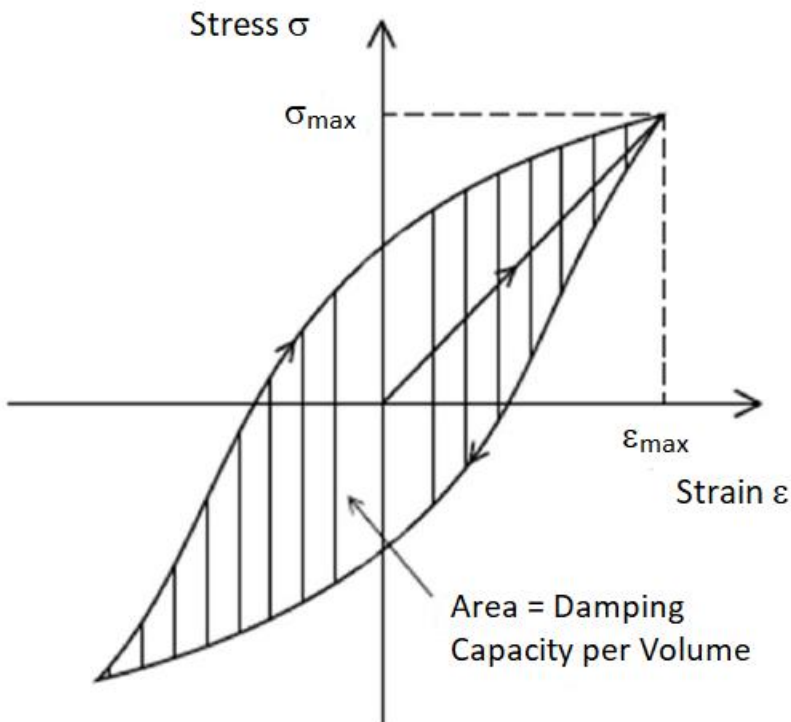
Figure 15.6. Structural Damping in Stress-Strain Curve Format

Internal friction and heat generation in the material cause a deviation from perfect elasticity, resulting in the hysteresis loop in the stress-strain curve. The structural damping is proportional to the displacement and is independent of frequency. Structural damping is modeled as an imaginary component of the stiffness, thus rendering the total stiffness as a complex variable.[2] Unfortunately, the resulting equation of motion can only be solved in the frequency domain and not the time domain. The workaround is to approximate structural damping as viscous damping, which effectively assumes a resonant response.

Structural damping is represented by the loss factor $\eta$. The assumed relationship between the loss factor and viscous damping ratio $\xi$ is

$$\eta \approx 2\xi \qquad\qquad (15.7)$$

---

[2] The elastic modulus is likewise complex due to hysteresis.

## 15.6  DAMPING LAYER MATERIALS

Commercial vendors offer various layered materials to provide vibration damping and to reduce sound radiation.  The two main types are extensional damping and constraint layer damping configurations.  These are passive damping methods.
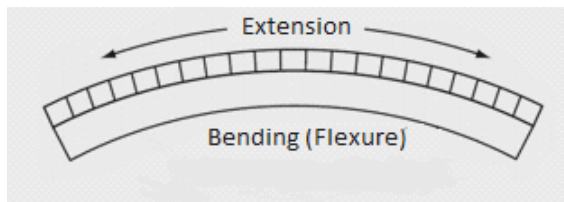


Figure 15.7.  Extensional Viscoelastic Damping Layer (aka Free-layer Damping)

The polymer material, shown as the top layer in the above figure, may be in the form of an adhesive layer or a paste compound that is applied to the surface with a trowel.  Energy is dissipated by extension and compression of the damping material under flexural stress from the bottom base structure. Damping increases with the damping layer thickness.
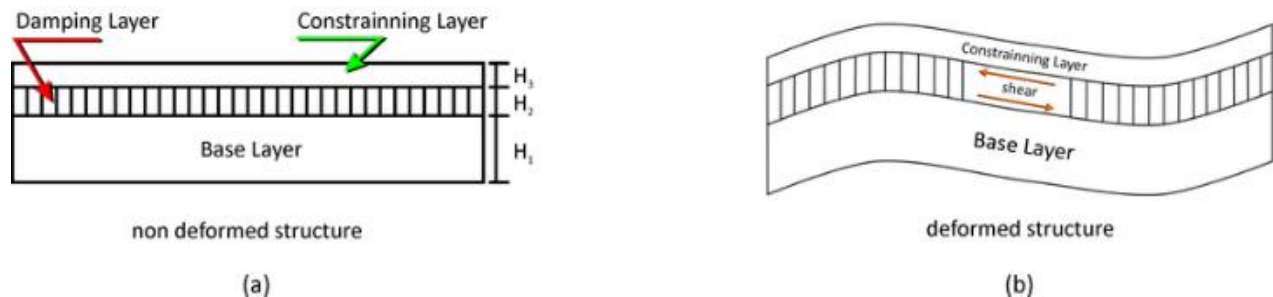


Figure 15.8.  Constraint Layer Damping

The soft viscoelastic damping layer undergoes shear deformation which dissipates some of the kinetic energy by converting it to heat.  The constraining layer is typically made from aluminum or steel sheet metal and is much stiffer than the middle damping layer.

## 15.7 HUNTSVILLE, ALABAMA PEDESTRIAN BRIDGE DAMPING



Figure 15.9. University Drive Pedestrian Bridge



Figure 15.10. Slam Stick X, Triaxial Accelerometer & Data Logger, Shown on Bookshelf

The bridge in Figure 15.9 is near the University of Alabama in Huntsville. The author walked to the center of the bridge and mounted the triaxial accelerometer in Figure 15.10 on the deck floor using double-sided tape. He was the only person on the bridge. The ambient vibration response of the bridge was negligibly low in each of the axes, while he remained standing. The wind was very light on this day. The author then jumped up and down on the bridge to excite its vibration modes. The response in the vertical axis was significant. The response in each of the lateral axes remained negligibly low.
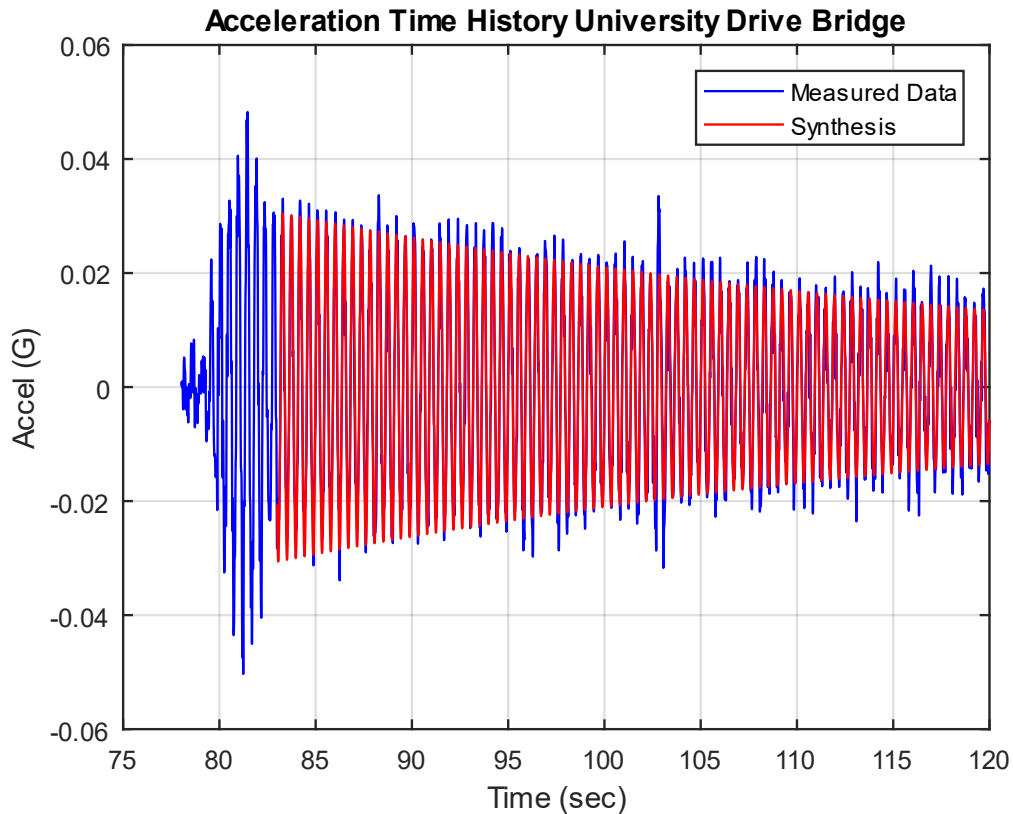
Figure 15.11. Signal Identification via Damped Sine Curve-fit

The jumps were performed near the 80-second mark. The accelerometer data was band-passed filtered from 1 to 20 Hz. The response after 82 seconds represents the free vibration decay. A damped sine curve-fit synthesis was performed on the vertical acceleration time history as shown in Figure 15.11, using trial-and-error with convergence. The bridge's fundamental frequency is 2.2 Hz with 0.16% damping using the viscous model. The damping ratio is very low. But note that the fundamental frequency and damping may be nonlinear. A pedestrian's vertical forces correspond to each footfall and typically occur at 2.0 Hz. This is very close to the bridge's 2.2 Hz natural frequency.

Also, note that there is a potential for pedestrians to synchronize their steps with the bridge motion and with one another. This behavior is instinctive rather than deliberate. Pedestrians find that walking in synchronization with the motion of a bridge is more comfortable, even if the oscillation amplitude is initially very small. This cadence makes their interaction with the movement of the bridge more predictable and helps them maintain their balance. But the synchronization also causes the pedestrians' gait to reinforce the bridge's oscillation in a resonance-like manner. These sorts of problems occurred after the opening of the London Millennium Bridge in 2000. Both passive and tuned mass dampers were added to the bridge for

vibration control.    Retrofitting the University Drive Bridge with dampers is unnecessary due to its low pedestrian traffic volume.    But this could be an interesting project for the nearby engineering students.

## 15.8  PEGASUS LAUNCH VEHICLE DAMPING

### 15.8.1  Drop Transient



Figure 15.12. Pegasus Launch Vehicle, Drop & Stage 1 Burn
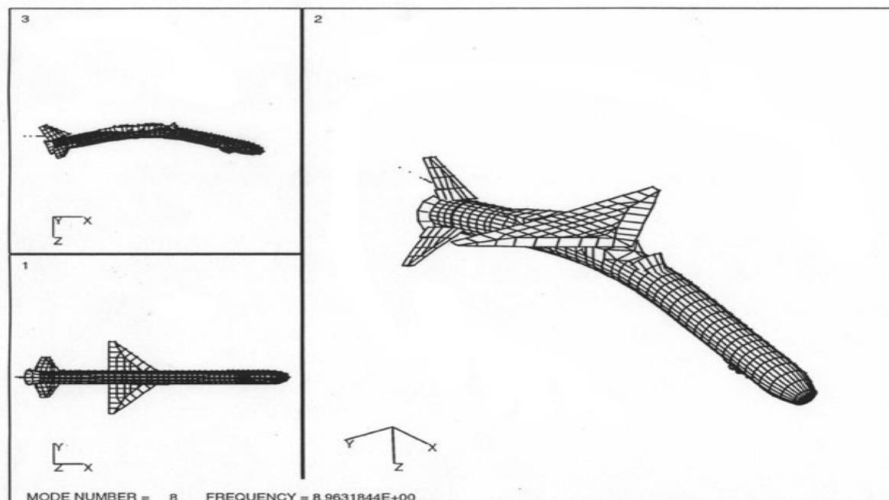


Figure 15.13.   Pegasus Fundamental Bending Mode Shape, Exaggerated

A modified L-1011 aircraft carries the Pegasus vehicle up to an altitude of nearly 40,000 ft and a speed of Mach 0.8, as shown in Figure 15.12.  Pegasus is suspended underneath the aircraft by hooks, where it develops an initial displacement due to gravity.  The strain energy is suddenly released at the onset of the drop transient, causing Pegasus to oscillate nearly as a free-free beam.  This is a significant "coupled loads" event for the payload which is enclosed in the fairing

at the front end of the vehicle.  The Pegasus' first stage then ignites.  The payload is eventually delivered into a low earth orbit.   A certain Pegasus/payload configuration was analyzed via a finite element modal analysis.  The resulting wire mesh model of the fundamental bending mode is shown in Figure 15.13.  Note that this was a different Pegasus configuration than that represented by the flight data in Figure 15.14.

## 15.8.2 Drop Transient Damped Sine Curve-fit
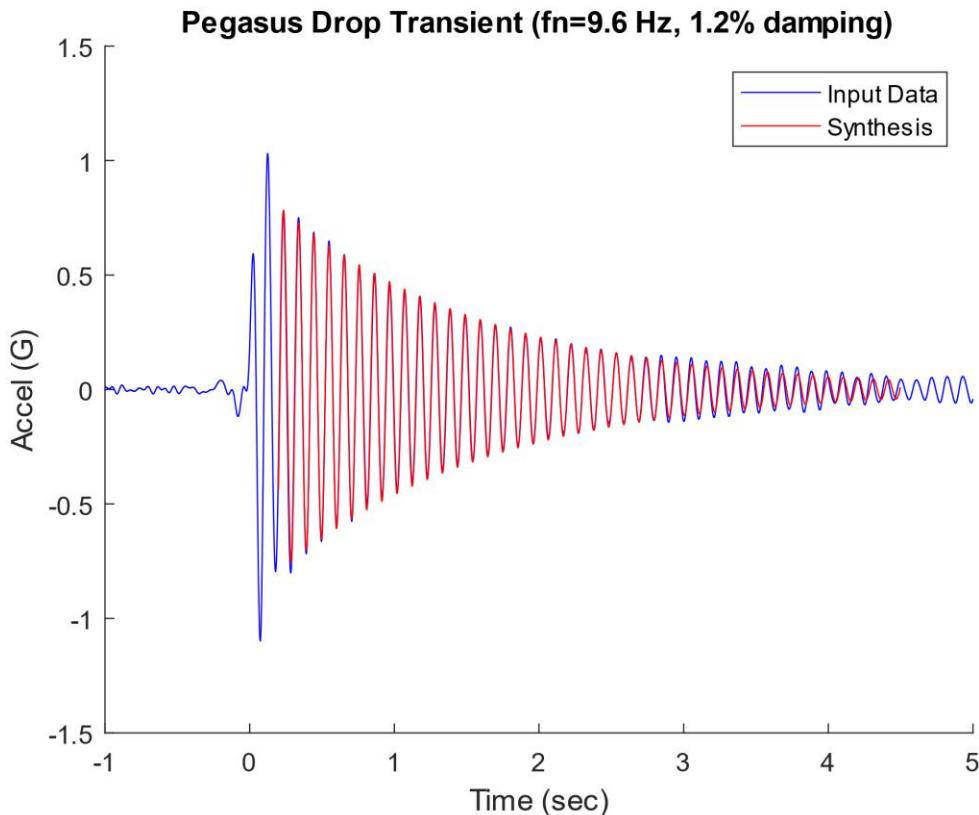


Figure 15.14.  Pegasus Drop Transient, Flight Accelerometer Data, Free Vibration Response

The data was measured in the transverse axis at the payload interface.  The response is nearly a textbook-quality damped sinusoid, with exponential decay.   The natural frequency and damping ratio are identified via a synthesized damped sine curve-fit using the viscous model.

### 15.8.3 Drop Transient Logarithmic Decrement Method
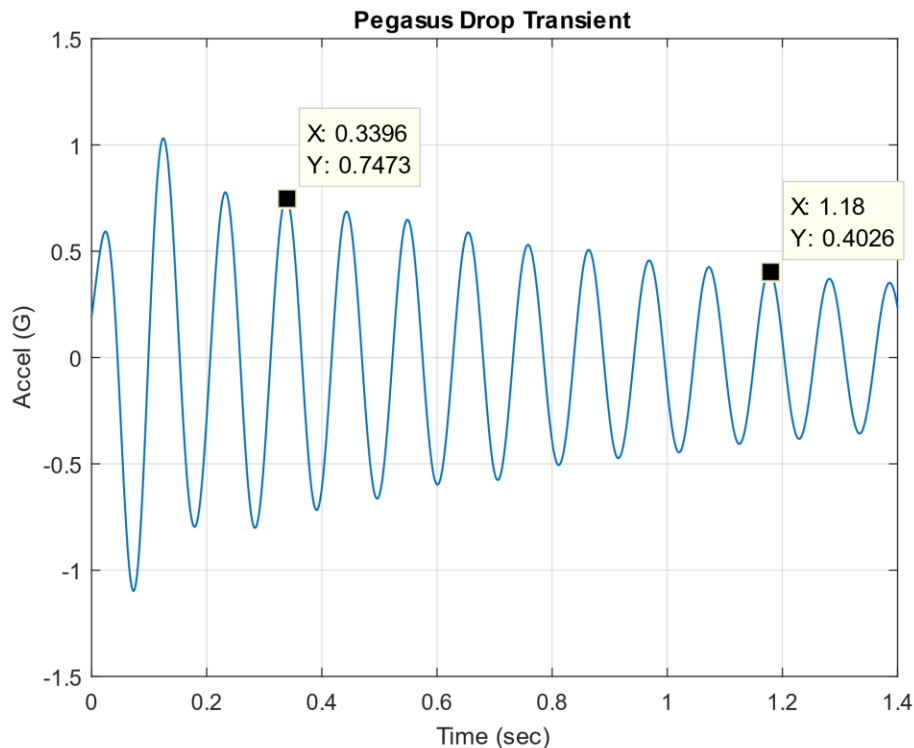


Figure 15.15.  Pegasus Drop Transient, Flight Accelerometer Data, Logarithmic Decrement

The logarithmic decrement for a starting peak and a peak n cycles later is

$$\delta = \frac{1}{n} \ln \left( \frac{x_o}{x_n} \right) \qquad (15.8)$$

The logarithmic decrement for the two peaks shown in Figure 15.15 is

$$\delta = \frac{1}{8} \ln \left( \frac{0.7473}{0.4026} \right) = 0.0773 \qquad (15.9)$$

The logarithmic decrement value is equivalent to 1.2% damping in agreement with the previous damped sine curve-fit.    The logarithmic decrement method has been included for historical reasons.  The damped sine curve-fit method is more robust.

## 15.8.4  Douglas C-47 Propeller Natural Frequencies & Damping



Figure 15.16.  Douglas C-47 at Fort Moore, GA Airborne Training School

This plane was used for paratrooper drops throughout WW II.  It is the military version of the DC-3 aircraft.  The C-47 was powered by two Pratt & Whitney R-1830-90C Twin Wasp 14-cylinder air-cooled radial piston engines, 1,200 hp (890 kW) each.  Each engine had three propeller blades.  The propeller hub frequencies were 2700 rpm (45 Hz) and 2325 rpm (38.75 Hz) for takeoff and cruise respectively.

The author tapped his fist against one of the blades and recorded the blade response with his Smartphone's accelerometer app, with the Smartphone pressed against the blade.  The resulting acceleration response is shown in the following figure.  A damped sine curve-fit was used to extract the natural frequencies and damping ratios of the first four modes.
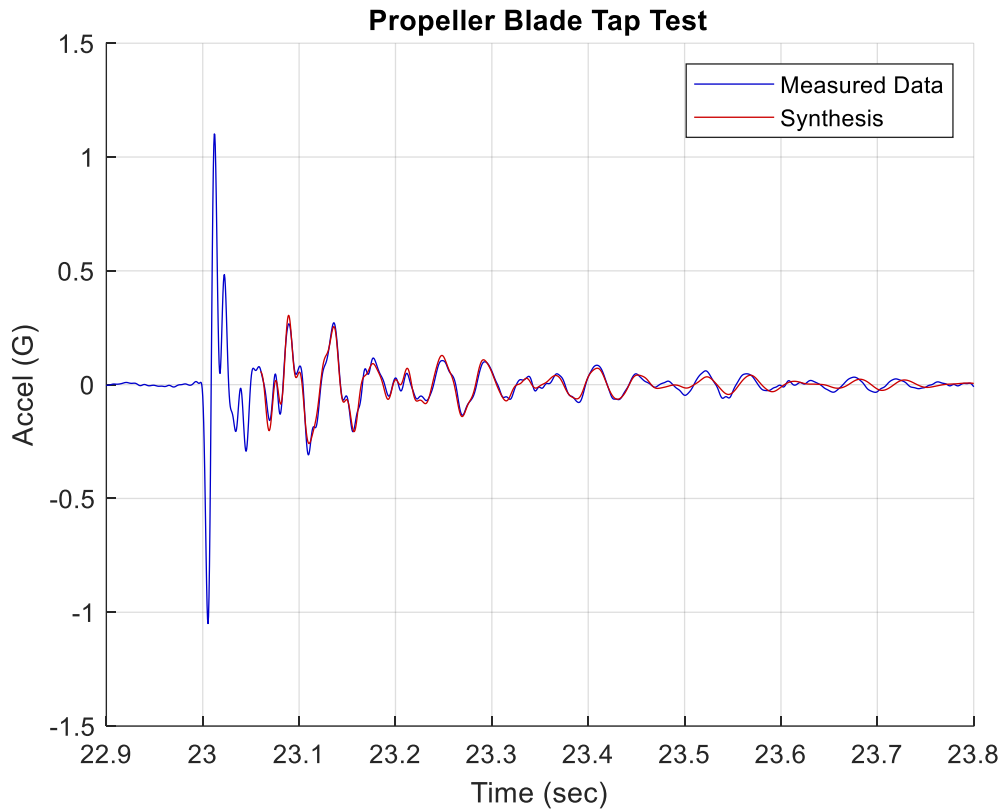
Figure 15.17.  Douglas C-47 Propeller Blade Tap Test Result

The Synthesis curve is the damped sine curve-fit.

Table 15.2.  Natural Frequency & Damping Result

| Mode | Natural Freq (Hz) | Damping |
|---|---|---|
| 1 | 18.4 | 2.6% |
| 2 | 25.3 | 2.9% |
| 3 | 64.4 | 2.2% |
| 4 | 80.7 | 2.3% |

Note that rotation adds stiffness.  So, the natural frequencies would increase by some amount as the engines were running.

## 15.9 TRANSAMERICA BUILDING DAMPING



The Transamerica Pyramid is built from a steel frame, with a truss system at the base. The height is 850 ft (260 m). Reference [19] gives natural frequency and damping as obtained in the 1989 Loma Prieta earthquake and from ambient vibration. The ambient vibration was presumably due to wind, low-level micro-tremors, mechanical equipment, outside street traffic, etc.

The results in the table below show non-linear behavior with an increase in damping during the severe earthquake relative to the benign ambient vibration.

Figure 15.18. Transamerica Pyramid

Table 15.3.  Transamerica Pyramid, Modal Parameters

| Direction | Loma Prieta Earthquake | | Ambient Vibration | |
|---|---|---|---|---|
| | fn (Hz) | Damping | fn (Hz) | Damping |
| North-South | 0.28 | 4.9% | 0.34 | 0.8% |
| East-West | 0.28 | 2.2% | 0.32 | 1.4% |

## 15.10  NASA DAMPING REFERENCES

Table 15.4.  Excerpt from NASA SP-8050, Structural Vibration Prediction

| Type of Structure | Percent of Critical Viscous Damping | Remarks |
|---|---|---|
| Homogeneous-element configurations (machined brackets, solid beams, welded construction) | 1 to 2 | Damping factor depends on stress levels induced during vibration |
| Riveted or bolted structures | 3 to 10 | Damping cause by friction at joints significantly reduces the vibration amplification |
| Laminated plastics | 4 to 10 | Phenolic laminate |
| Honeycomb-core panels | 3 to 6 | Damping factor depends on method of fabrication (brazed versus adhesive bond) and on acoustic radiation |
| Vibration-isolated components | 10 to 20 | Damping factor depends on the isolator design |
| Nonviscous fluids | 0.5 | Frequency < 5 Hz |
|  | 1.0 | 5 Hz $\leq$ Frequency $\leq$ 15 Hz |
|  | 1.5 | Frequency > 15 Hz |

Figure 15.19.  Saturn V / Apollo

Table 15.5.  Excerpt from NASA SP-8079, Structural Interaction with Control Systems

| Vehicle | Vibration Mode | Frequency (Hz) | Damping Ratio |
|---|---|---|---|
| Saturn V / Apollo | First | 1.0 | 0.005 |
| | Second | 1.7 | 0.007 |
| | Third | 2.3 | 0.006 |
| | Fourth | 3.0 | 0.010 |

The damping values were measured during a modal test.

## 15.11 COULOMB DAMPING
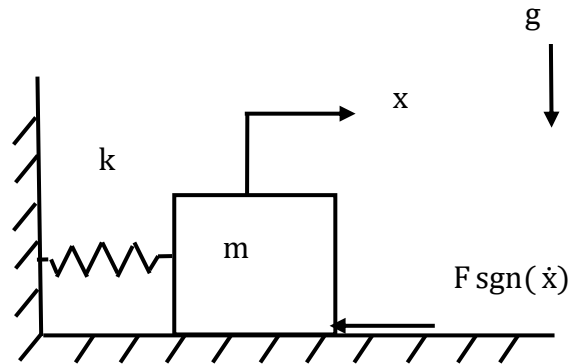


Figure 15.20.  SDOF System, Coloumb Damping

Coulomb damping is dry friction damping due to sliding contact.  Consider the free vibration response of a single-degree-of-freedom system subjected to Coulomb damping.  The motion is nonlinear.  The damping force $F$ is

$$F = \mu \, mg \tag{15.10}$$

where

$\mu$ = kinetic friction coefficient

m = mass

g = acceleration of gravity

Assume that the friction coefficient is constant for simplicity.
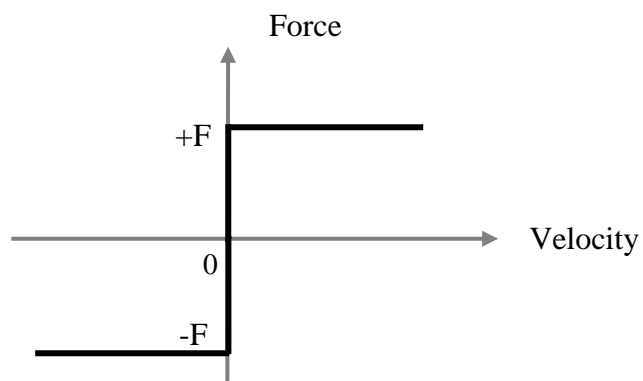


Figure 15.21.  Coulomb Force vs. Velocity

The governing equation of motion for the displacement x is

$$m\ddot{x} + kx = -F\,\text{sgn}(\dot{x}) \tag{15.11}$$

The $\text{sgn}(\dot{x})$ function represents the sign of $\dot{x}$.

As an alternative, the governing equation can be written as

$$m\ddot{x} + kx = -F\frac{\dot{x}}{|\dot{x}|} \tag{15.12}$$

The governing equation is solved in a piecewise-linear manner.

Assume that initial displacement $x(0)$ is

$$x(0) > F/k \tag{15.13}$$

Also assume that the initial velocity is zero.

Consider the equation of motion for negative velocity.

$$m\ddot{x} + kx = F \quad \text{for} \quad \dot{x} < 0 \tag{15.14}$$

$$\ddot{x} + \left(\frac{k}{m}\right)x = \left(\frac{F}{m}\right) \tag{15.15}$$

The natural frequency $\omega_n$ is

$$\omega_n{}^2 = \left(\frac{k}{m}\right) \tag{15.16}$$

Let

$$E = \left(\frac{F}{m}\right) \tag{15.17}$$

$$\ddot{x} + \omega_n^2 x = E \tag{15.18}$$

The equation is solved using Laplace transforms.

$$x(t) = \frac{F}{k} + \left[x(0) - \frac{F}{k}\right]\cos\omega_n t \quad \text{for } \dot{x} < 0 \tag{15.19}$$

$$\dot{x}(t) = -\omega_n\left[x(0) - \frac{F}{k}\right]\sin\omega_n t \quad \text{for } \dot{x} < 0 \tag{15.20}$$

The velocity equals zero at

$$t = \frac{\pi}{\omega_n} \tag{15.21}$$

The displacement at this time is

$$x\left(\frac{\pi}{\omega_n}\right) = \frac{F}{k} + \left[-x(0) + \frac{F}{k}\right] \tag{15.22}$$

$$x\left(\frac{\pi}{\omega_n}\right) = \frac{2F}{k} - x(0) \tag{15.23}$$

Consider the equation of motion for positive velocity.

$$m\ddot{x} + kx = -F \quad \text{for } \dot{x} > 0 \tag{15.24}$$

The initial displacement term must be reset to the last displacement for negative velocity. Furthermore, a phase angle must be added to the argument in the cosine term.

$$x(t) = \frac{-F}{k} + \left[\left[\frac{2F}{k} - x(0)\right] + \frac{F}{k}\right]\cos(\omega_n t + \pi) \qquad \text{for } \dot{x} > 0 \qquad\qquad (15.25)$$

$$x(t) = \frac{-F}{k} + \left[\frac{3F}{k} - x(0)\right]\cos(\omega_n t + \pi) \qquad \text{for } \dot{x} > 0 \qquad\qquad (15.26)$$

$$\dot{x}(t) = -\omega_n\left[\frac{3F}{k} - x(0)\right]\sin(\omega_n t + \pi) \qquad\qquad (15.27)$$

The first negative displacement peak thus has an amplitude that is $2\,F/k$ less than the initial displacement in terms of absolute values. The pattern continues such that the envelope has a linear decay. The velocity returns to zero for

$$t = \frac{2\pi}{\omega_n} \qquad\qquad (15.28)$$

$$x\left(\frac{2\pi}{\omega_n}\right) = \frac{-F}{k} - \left[\frac{3F}{k} - x(0)\right] \qquad\qquad (15.29)$$

$$x\left(\frac{2\pi}{\omega_n}\right) = x(0) - \frac{4F}{k} \qquad\qquad (15.30)$$

Each consecutive positive peak is thus $4\,F/k$ lower than the previous positive peak. The process is then repeated.
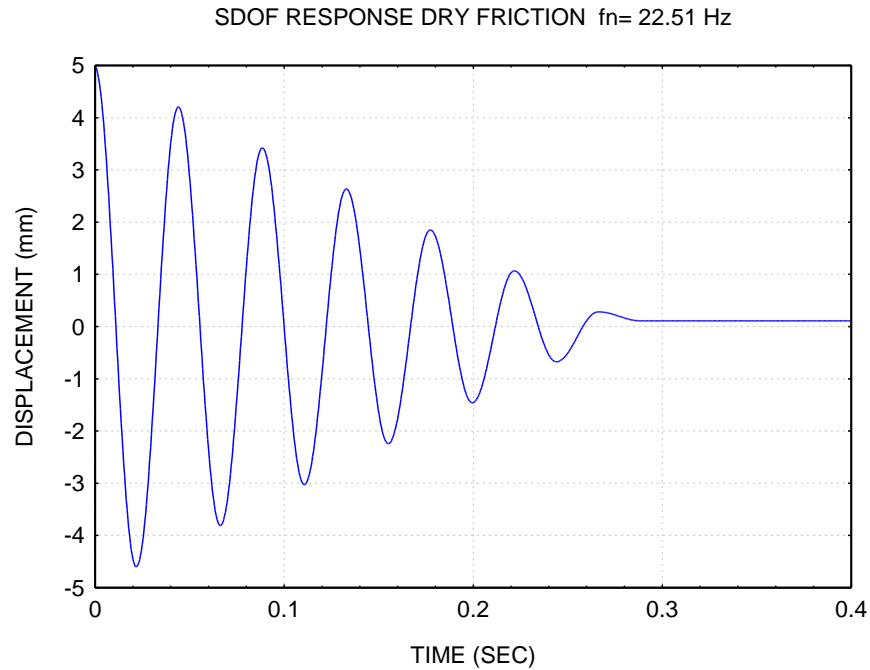
Figure 15.22.  SDOF Response, Dry Friction, Initial Displacement

A single-degree-of-freedom system has

   mass = 1 kg

   stiffness = 20,000 N/m

   kinetic friction coefficient = 0.4

   initial displacement = 5 mm

The resulting displacement is shown in the above figure.

The displacement converges to $F/k$, where $F = \mu \, mg$.

Depending on the initial displacement, the displacement may also converge to $-F/k$.

## 15.12 PIEZOELECTRIC DAMPING
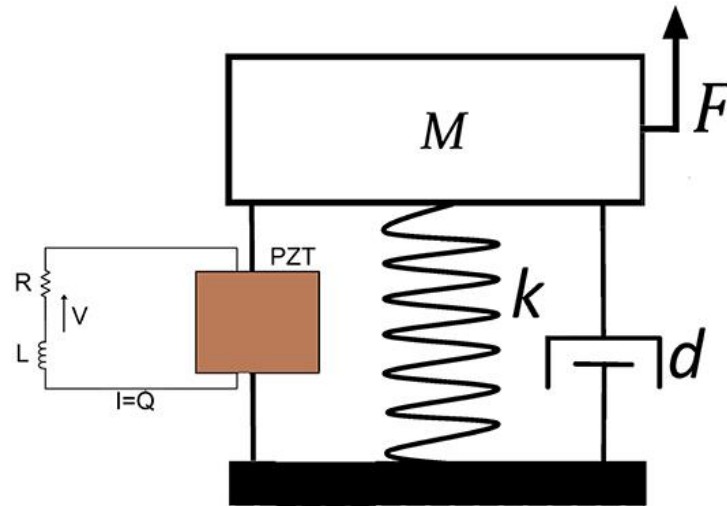


Figure 15.23. SDOF System with Piezoelectric Shunt Damping

Piezoelectric shunt damping systems reduce structural vibration by shunting an attached piezoelectric transducer with an electrical impedance. Current impedance designs result in a coupled electrical resonance at the target modal frequencies.

Piezoelectric transducers (PZTs), in conjunction with appropriate circuitry, can be used as a mechanical energy dissipation device. If a simple resistor is placed across the terminals of the PZT, the PZT will act as a viscoelastic damper. If the network consists of a series inductor–resistor R–L circuit, the passive network combined with the inherent capacitance of the PZT creates a damped electrical resonance. The resonance can be tuned so that the PZT acts as a tuned vibrational energy absorber.

# 16 SINUSOIDAL VIBRATION

## 16.1 DESCRIPTIVE STATISTICS
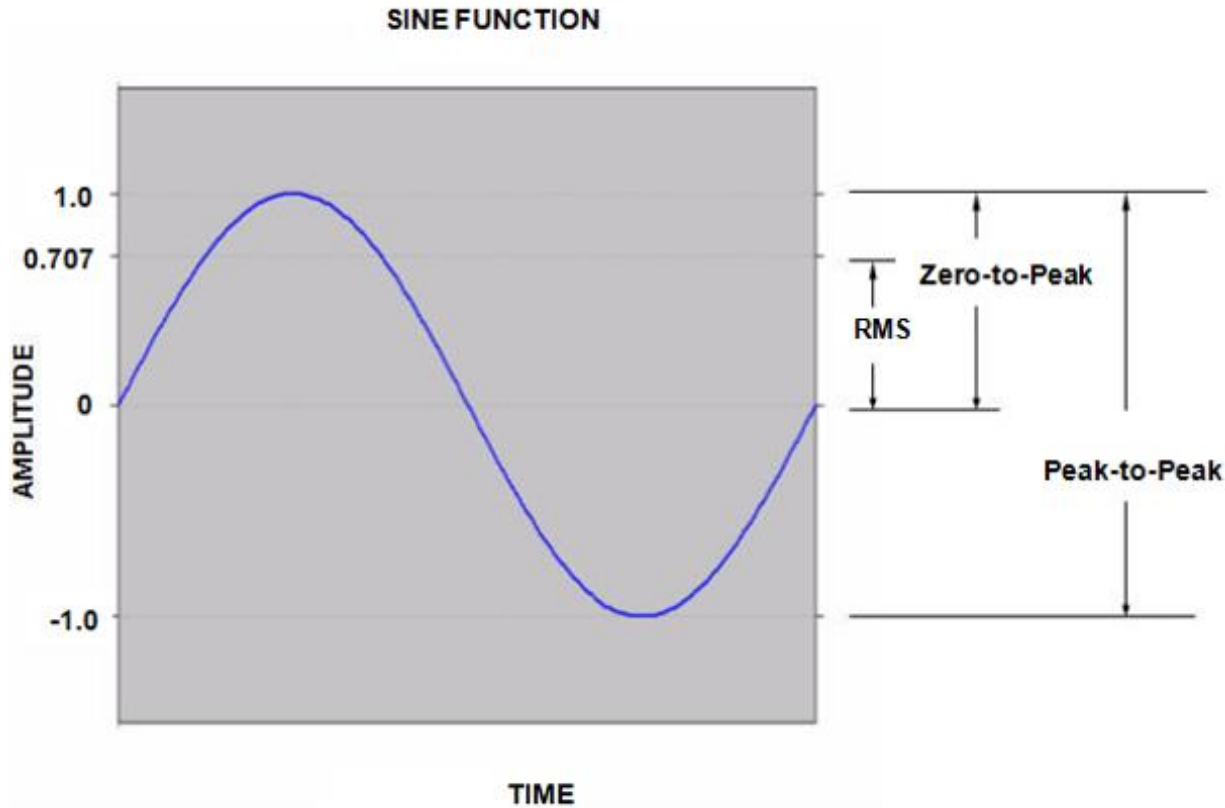


Figure 16.1.  Sine Function, One-Cycle

A sine function is characterized by its frequency and amplitude.  The frequency is the inverse of the period, where the period is the duration of one cycle.  The amplitude may be represented by any of the three parameters shown on the right-hand side. The zero-to-peak and RMS amplitudes for sinusoidal oscillations are related by

$$A_{Peak} = \sqrt{2}\, A_{RMS} \qquad\qquad (16.1)$$

Note that

$$A_{RMS}{}^2 = A_{mean}{}^2 + A_{1\sigma}{}^2 \qquad\qquad (16.2)$$

where $A_{1\sigma}$ is the standard deviation

The RMS value is thus equal to the standard deviation for the case of zero mean. A pure sine function always has zero mean.
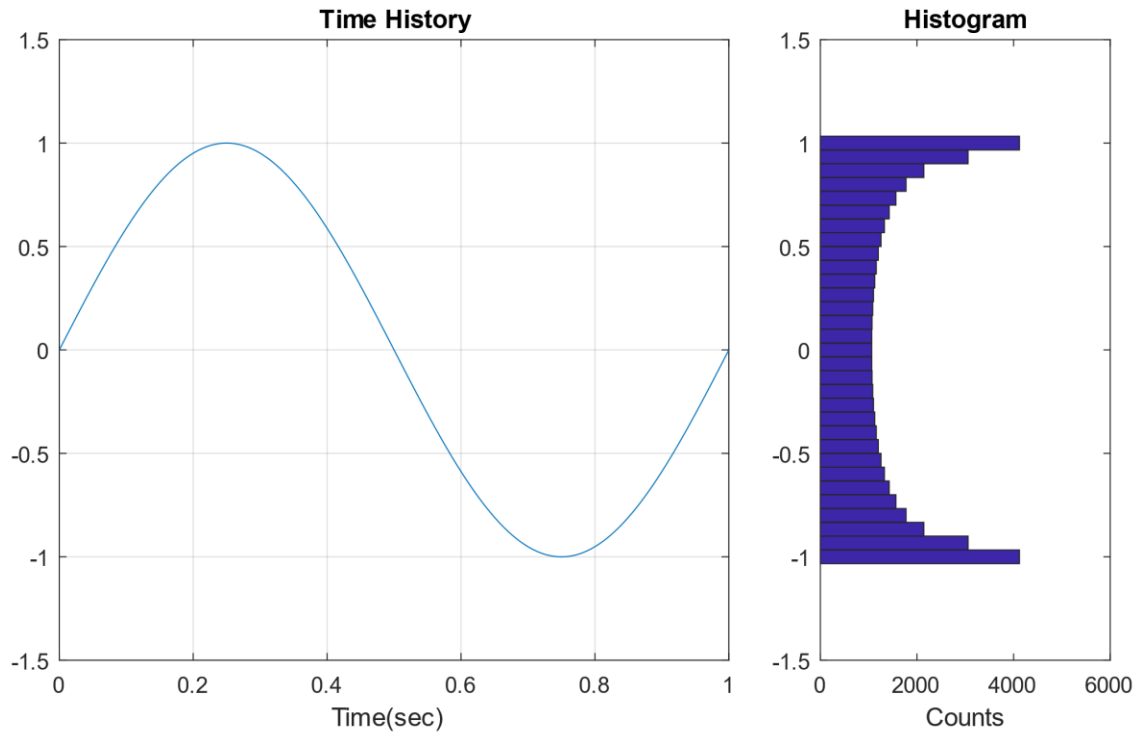


Figure 16.2.   Sine Function & Histogram

A sine function and its corresponding histogram are shown in Figure 16.2. The histogram divides the amplitude points into bins and then counts the points in each bin. The number of points in each bin is then plotted as a bar graph. Some of the histograms in this document are turned 90 degrees clockwise and shown adjacent to the corresponding time history for educational purposes.

A sine function has a bathtub histogram. The amplitude tends to dwell at either the peak or valley with a fairly rapid transition in between. Histograms are important for fatigue analysis.

Now let $x(t)$ be a sinusoidal displacement function.  The displacement equation is

$$x(t) = X \sin(\omega t) \qquad\qquad (16.3)$$

where

X    is the zero-to-peak amplitude

The corresponding velocity $v(t)$ is

$$v(t) = \omega X \cos(\omega t) \qquad\qquad (16.4)$$

The acceleration $a(t)$ is

$$a(t) = -\omega^2 X \sin(\omega t) \qquad\qquad (16.5)$$

Table 16.1.  Peak Values Referenced to Peak Displacement

| Parameter | Value |
|---|---|
| displacement | $X$ |
| Velocity | $\omega X$ |
| acceleration | $\omega^2 X$ |

Table 16.2.  Peak Values Referenced to Peak Acceleration

| Parameter | Value |
|---|---|
| acceleration | $A$ |
| Velocity | $A / \omega$ |
| displacement | $A / \omega^2$ |

Let $A$ be the peak acceleration.

$$A = \omega^2 X \qquad\qquad (16.6)$$

Conversely,

$$X = A/\omega^2 \qquad\qquad (16.7)$$

## 16.2  SINE TESTING

Table 2 has enormous consequences for vibration testing. Commercial shaker tables, such as those in Figure 6.9 and Figure 6.10, are typically limited to a few inches of peak-to-peak displacement unless they are large-scale tables specifically designed for earthquake simulation. Vibration tests are usually specified in terms of acceleration. The test specification starting frequency is typically 10 to 20 Hz to limit the displacement.

## 16.3  SAMPLE SINE CALCULATIONS

Astronaut Michael Collins wrote [20]:

> The first stage of the Titan II vibrated longitudinally so that someone riding on it would be bounced up and down as if on a pogo stick. The vibration was at a relatively high frequency, about 11 cycles per second, with an amplitude of plus or minus 5 Gs in the worst case.

The equivalent angular frequency for 11 Hz is 69.1 rad/sec. Calculate the corresponding displacement $X$ using equation (16.7).

$$X = (5\ G\ )(386\ \text{in/sec}^2\ /\ G)\ /\ (\ 69.1\ \text{rad/sec})^2 = 0.40\ \text{inch zero-to-peak} \qquad (16.8)$$

M.J. Griffin [3] cited a study where 5% of the passengers on a ship experienced vomiting while the ship underwent a 0.2 m/sec^2 acceleration amplitude during a 3 hour. Assume a 0.2 Hz frequency (1.26 rad/sec^2). Calculate the displacement.

$$X = (0.2\ \text{m/sec\textasciicircum2})(100\ \text{cm/m})\ /\ (\ 1.26\ \text{rad/sec})^2 = 12.7\ \text{cm zero-to-peak} \qquad (16.9)$$
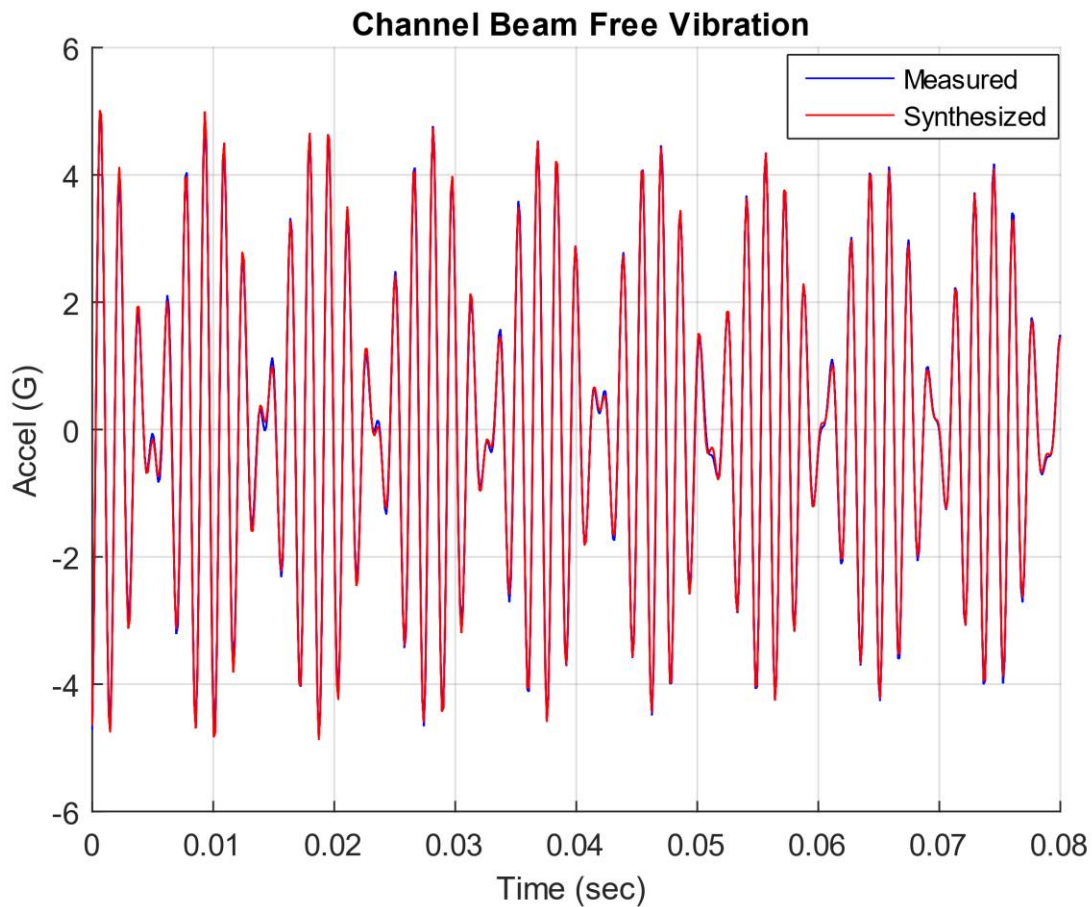
Figure 16.3.  Channel Beam Free Vibration Response at Free End to Force Impulse

Consider the case of two closely-space vibration frequencies generating sound.  The envelope of the two signals oscillates at a frequency that is the difference between the two frequencies. This beat frequency is detected by the human hearing and brain system, but it is a psychoacoustic effect that does not affect the mechanical hardware.

A channel beam was mounted in a horizontal, cantilever configuration.  The free end was struck with an impulse hammer in the vertical axis.  The resulting acceleration time history at the free end is shown in Figure 16.3.   A synthesized damped sine curve-fit yielded natural frequencies at 583 and 691 Hz.  The beat frequency is the difference which is 108 Hz.
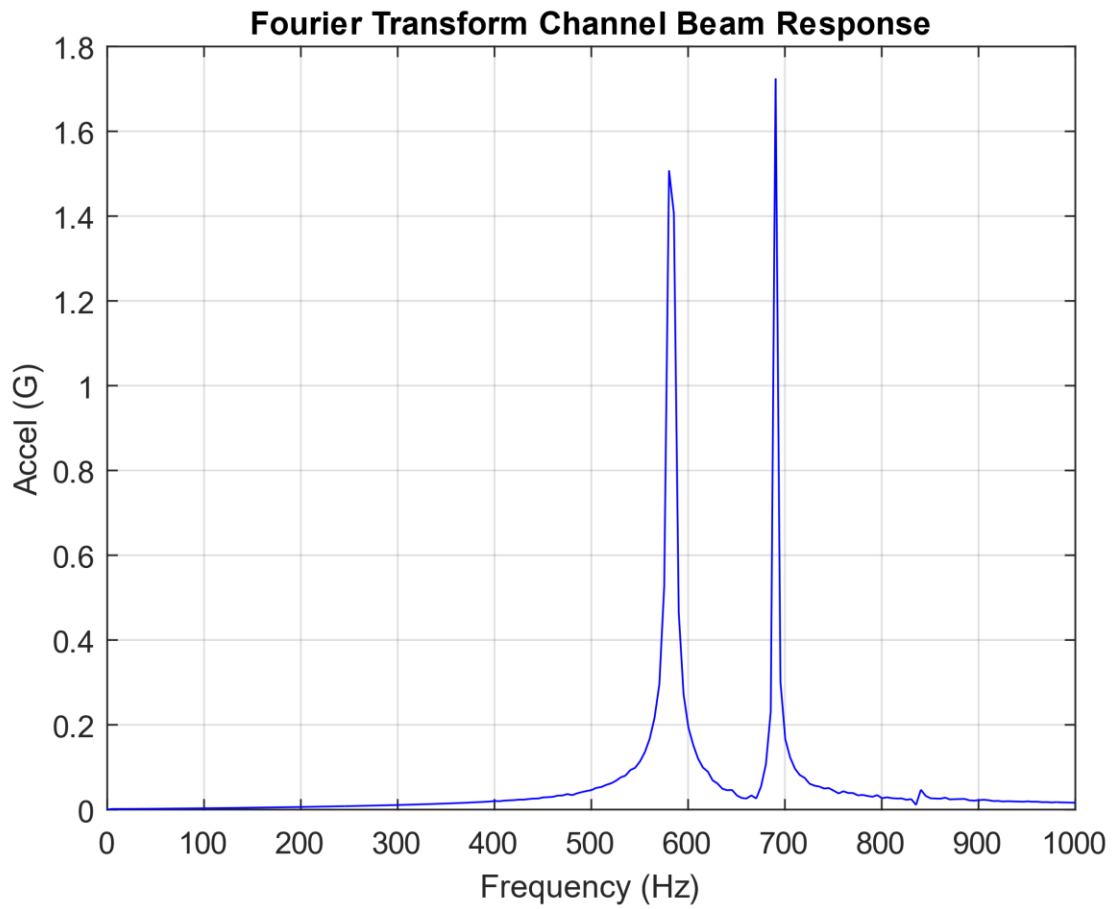
Figure 16.4.  Channel Beam Free Vibration Response Fourier Transform

A Fourier transform of the beat frequency data is shown in Figure 16.4.  Peaks occur at 583 and 691 Hz but not at the 108 Hz beat frequency.  Fourier transforms are covered in Section 23.

# 17 DYNAMIC MODELS FOR EXTERNAL EXCITATION

## 17.1  TWO MODELS

There are two basic SDOF spring-mass models used for external excitation in shock and vibration analysis.  One is the applied force model, and the other is the base excitation model. An introduction to these types and images was given in Section 6.  The purpose of this section is to demonstrate solution methods for each of these types in both the time and frequency domains.

## 17.2  APPLIED FORCE

### 17.2.1  SDOF Response Equations

The applied force model and its free-body diagram are
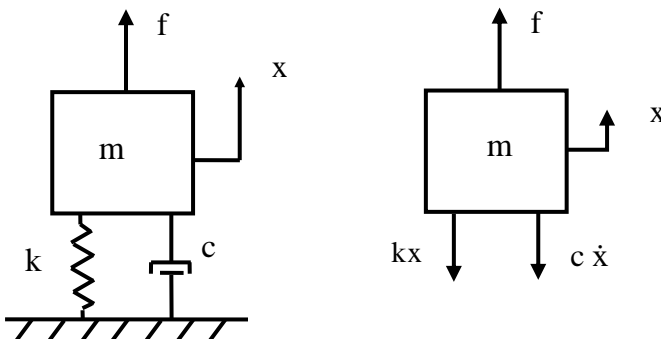


Figure 17.1.  Single-degree-of-freedom Model, Applied Force

The equation of motion for applied force $F$ is derived using Newton's law.

$$\sum F = m\ddot{x} \tag{17.1}$$

$$m\ddot{x} = f(t) - kx - c\dot{x} \tag{17.2}$$

$$m\ddot{x} + c\dot{x} + kx = f(t) \tag{17.3}$$

$$\ddot{x} + 2\,\xi\,\omega_n\,\dot{x} + \omega_n{}^2 x = \frac{1}{m} f(t) \tag{17.4}$$

The resulting equation of motion is non-homogenous.   It can be solved via Laplace transforms if the force is deterministic such as a sine function.  A convolution integral is needed if the force varies arbitrarily with time.   The resulting displacement for an applied force i

$$x(t) = \frac{1}{m\omega_d} \int_0^t f(\tau)\,\exp[-\xi\,\omega_n(t-\tau)]\sin[\omega_d(t-\tau)]d\tau \tag{17.5}$$

The displacement convolution integral has an embedded impulse response function.

$$h_d(t) = \frac{1}{m\omega_d} [\exp(-\xi\,\omega_n t)][\sin(\omega_d t)] \tag{17.6}$$

The Laplace transform of the impulse response function is the steady-state frequency response function (FRF).

$$H_d(s) = \frac{1}{m}\left[\frac{1}{s^2 + 2\,\xi\,\omega_n\,s + \omega_n{}^2}\right] \tag{17.7}$$

This FRF can be represented in the frequency domain by setting $s = j\,\omega,$ where $j = \sqrt{-1}$ .

$$H_d(\omega) = \frac{1}{m}\left[\frac{1}{(\omega_n{}^2 - \omega^2) + j\,2\,\xi\,\omega_n\,\omega}\right] \tag{17.8}$$

The FRF in equation (17.8) is the Fourier transform of the impulse response function in equation (17.6).  Fourier transforms are covered in Section 23.   An equivalent FRF is

$$H_d(\omega) = \frac{1}{k}\left[\frac{\omega_n{}^2}{(\omega_n{}^2 - \omega^2) + j\,2\,\xi\,\omega_n\,\omega}\right] \tag{17.9}$$

Equations (17.8) and (17.9) are called "receptance" and give the displacement per unit force at a given excitation frequency $\omega$.

The velocity and acceleration FRFs are calculated from the displacement FRF as follows.

$$H_v(\omega) = j\omega \, H_d(\omega) \qquad \text{(mobility)} \tag{17.10}$$

$$H_a(\omega) = -\omega^2 \, H_d(\omega) \qquad \text{(accelerance)} \tag{17.11}$$

The convolution integral in equation (17.5) can be solved in the time domain via a digital recursive relationship [21], [22]. The resulting displacement is

$$x_i = 2\exp(-\xi\,\omega_n\Delta t)\cos(\omega_d\Delta t)\,x_{i-1} \quad - \exp(-2\xi\,\omega_n\Delta t)\,x_{i-2}$$

$$+\,\frac{\Delta t}{m\,\omega_d}\,\exp(-\xi\,\omega_n\Delta t)\sin(\omega_d\Delta t)\,f_{i-1}$$

$$\tag{17.12}$$

The previous displacement equation is sufficiently accurate for most cases. A more accurate but more complex displacement equation is

$$x_i = 2\exp(-\xi\,\omega_n\Delta t)\cos(\omega_d\Delta t)\,x_{i-1} \quad - \exp(-2\xi\,\omega_n\Delta t)\,x_{i-2}$$

$$+ \left\{ (A\,f_i + B\,f_{i-1} + C\,f_{i-2})/(m\,\omega_d{}^3\Delta t) \right\}$$

where $\quad A = A_1 + A_2 + \omega_n\Delta t \quad , \quad B = B_1 + B_2 + B_3 \quad , \quad C = C_1 + C_2$

$$A_1 = 2\xi\,[\exp(-\xi\,\omega_n\Delta t)\cos(\omega_d\Delta t) - 1]$$

$$A_2 = \frac{\omega_n}{\omega_d}\left[2\xi^2 - 1\right]\exp(-\xi\,\omega_n\Delta t)\sin(\omega_d\Delta t)$$

$$B_1 = -2\omega_n\Delta t\,\exp(-\xi\,\omega_n\Delta t)\cos(\omega_d\Delta t)$$

$$B_2 = 2\xi\,[1 - \exp(-2\,\xi\,\omega_n\Delta t)]$$

$$B_3 = -2\,\frac{\omega_n}{\omega_d}\left[2\xi^2 - 1\right]\exp(-\xi\,\omega_n\Delta t)\sin(\omega_d\Delta t)$$

$$C_1 = (2\xi + \omega_n\Delta t)\exp(-2\xi\,\omega_n\Delta t)$$

$$C_2 = \exp(-\xi\,\omega_n\Delta t)\left[\frac{\omega_n}{\omega_d}\left[2\xi^2 - 1\right]\sin(\omega_d\Delta t) - 2\xi\cos(\omega_d\Delta t)\right]$$

$$\tag{17.13}$$

The velocity is

$$\dot{x}_i = 2\exp(-\xi\omega_n\Delta t)\cos(\omega_d\Delta t)\,\dot{x}_{i-1} \quad -\exp(-2\xi\omega_n\Delta t)\,\dot{x}_{i-2}$$

$$+\frac{1}{m\omega_n{}^2\Delta t}\{\,U\,f_i\ +V\,f_{i-1}\ +W\,f_{i-2}\,\}$$

where

$$U = \exp(-\xi\,\omega_n\Delta t)\left[-\cos(\omega_d\Delta t)-\frac{\xi\omega_n}{\omega_d}\sin(\omega_d\Delta t)\right]+1$$

$$V = \exp(-2\xi\,\omega_n\Delta t)+2\exp(-\xi\,\omega_n\Delta t)\left[\frac{\xi\omega_n}{\omega_d}\sin(\omega_d\Delta t)\right]-1$$

$$W = \exp(-\xi\,\omega_n\Delta t)\left[\cos(\omega_d\Delta t)-\frac{\xi\omega_n}{\omega_d}\sin(\omega_d\Delta t)\right]-\exp(-2\xi\,\omega_n\Delta t)$$

$$(17.14)$$

The acceleration is

$$\ddot{x}_i = 2\exp(-\xi\,\omega_n\Delta t)\cos(\omega_d\Delta t)\,\ddot{x}_{i-1} \quad -\exp(-2\xi\,\omega_n\Delta t)\,\ddot{x}_{i-2}$$

$$+\frac{1}{m\,\omega_d\,\Delta t}\exp(-\xi\,\omega_n\Delta t)\sin(\omega_d\Delta t)\{\,f_i-2\,f_{i-1}+\,f_{i-2}\,\}$$

$$(17.15)$$

The transmitted force from the mass to the ground $f_T$ is

$$f_{T,i} = 2\exp(-\xi\omega_n\Delta t)\cos(\omega_d\Delta t)\,f_{T,i-1}$$

$$-\exp(-2\xi\omega_n\Delta t)\,f_{T,i-2}$$

$$+\left\{1 - \left(\frac{1}{\omega_d\Delta t}\right)\exp(-\xi\omega_n\Delta t)\,\sin(\omega_d\Delta t)\right\}f_i$$

$$+\left\{2\exp(-\xi\omega_n\Delta t)\left[-\cos(\omega_d\Delta t) + \left(\frac{1}{\omega_d\Delta t}\right)\sin(\omega_d\Delta t)\right]\right\}f_{i-1}$$

$$+\left\{\exp(-2\xi\omega_n\Delta t) - \left(\frac{1}{\omega_d\Delta t}\right)\exp(-\xi\omega_n\Delta t)\sin(\omega_d\Delta t)\right\}f_{i-2}$$

(17.16)

Equations (17.13) through (17.16) are "ramp invariant" digital recursive filtering relationships.

Alternate methods for numerically solving equation (17.4) include the Runge-Kutta and Newmark-beta methods. The Runge-Kutta method may be unstable for stiff systems, however, which are common in vibroacoustics analysis.

## 17.2.2 Input & Response Example, Applied Force

The single-degree-of-freedom system in Figure 17.1 has a mass of 20 kg, stiffness of 78960 N/m, natural frequency of 10 Hz, and an amplification factor Q=10 for this example. It is excited into resonance by a 20 N applied force sinusoidal excitation at 10 Hz. The exact response can be calculated via a Laplace transform solution. The result is shown in Figure 17.2.
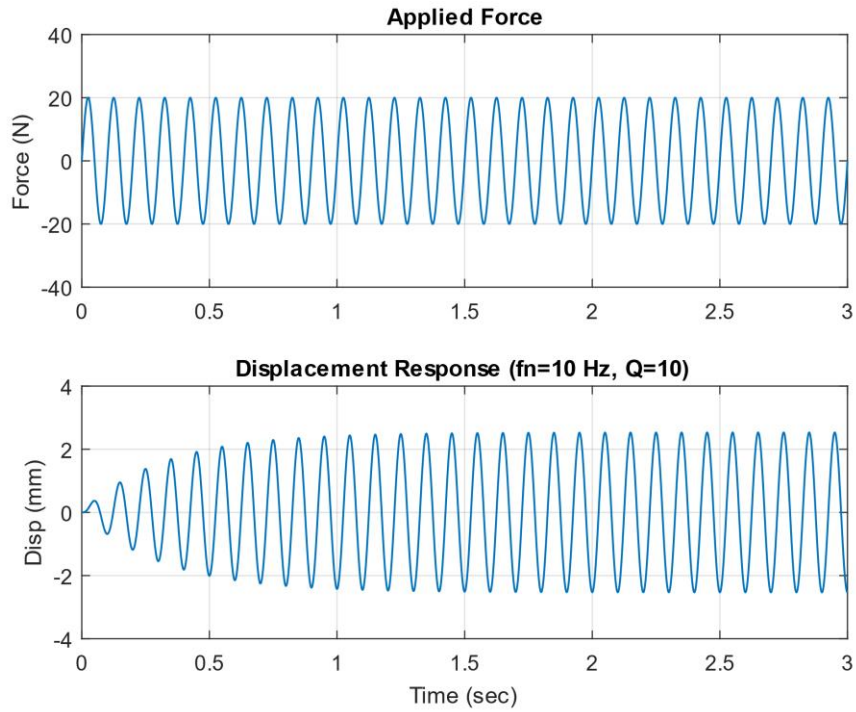
Figure 17.2.  Sine Applied Force & Response


The peak response is 2.53 mm.  Note that the following ratio is approximately equal to the Q value.

$$\left| \frac{kx}{F} \right| = \left| \frac{(78960 \text{ N/m})(0.00253)}{10 \text{ N}} \right| \approx 10 \tag{17.17}$$
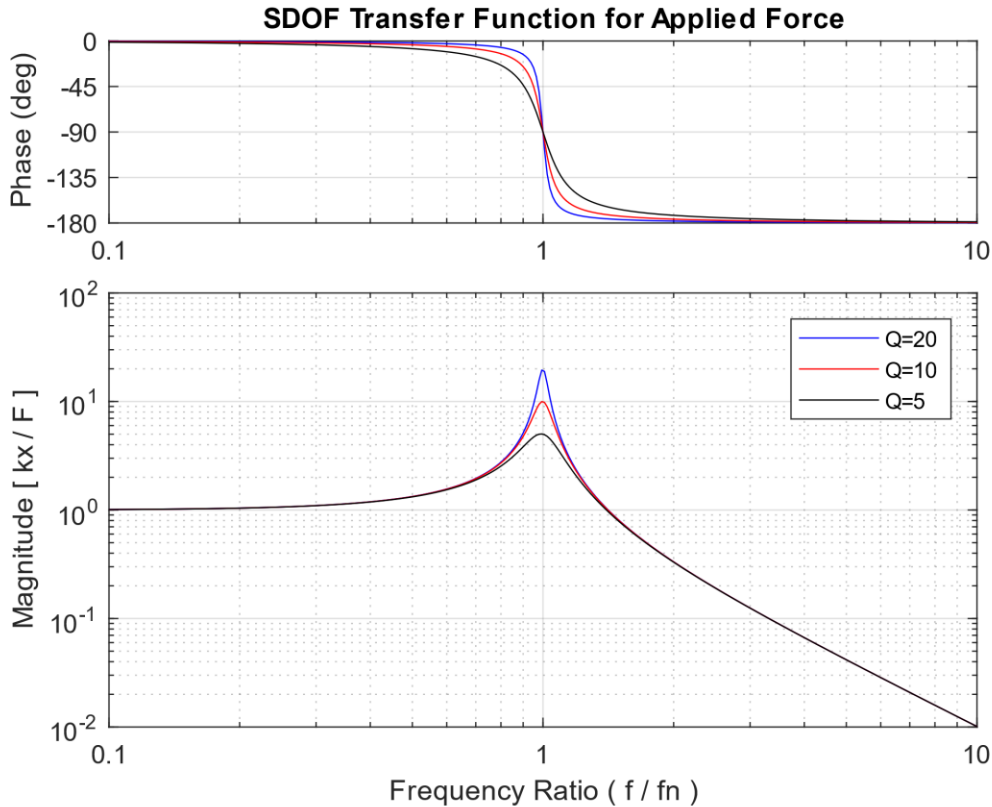
Figure 17.3.  Transfer Function for Steady-State Force Excitation

The response calculation could be repeated for several frequency and amplification factor cases to determine the maximum steady-state response for each case. The transfer function represents the displacement divided by the applied force as normalized by the stiffness such that the magnitude is unitless.  The transfer function magnitude is

$$\left| \frac{kx}{F} \right| = \frac{1}{\sqrt{(1 - \rho^2)^2 + (2\xi\rho)^2}} \quad , \qquad \rho = f/f_n \tag{17.18}$$

The phase angle by which the displacement lags the force is

$$\theta = \arctan\left( \frac{2\xi\rho}{1 - \rho^2} \right) \tag{17.19}$$

The applied force transfer function in Figure 17.3 can roughly be divided into three zones. The function is controlled by stiffness at the low-frequency ratio end. Its magnitude converges to the simple static Hooke's law as the frequency ratio approaches zero. The function is controlled by damping for frequency ratios at or near the resonance condition where the ratio is equal to 1. The function is controlled by mass at higher ratios, above √2.

### 17.2.3 Six Transfer Functions for Applied Force and Response

Recall equation (17.8). The following equation represents the ratio of displacement to force in terms of their respective Fourier transforms.

$$\frac{X(\omega)}{F(\omega)} = H_d(\omega) \tag{17.20}$$

Similar frequency response ratios can be formed for the velocity and acceleration responses relative to force. Inverses of these functions can also be taken. The names of these transfer functions are given in Table 17.1 and Table 17.2.

Table 17.1. Transfer Function Nomenclature

| Displacement / Force | Velocity / Force | Acceleration / Force |
|---|---|---|
| Admittance, Compliance, Receptance | Mobility | Accelerance, Inertance |

Table 17.2. Reciprocal Transfer Function Nomenclature

| Force / Displacement | Force / Velocity | Acceleration / Force |
|---|---|---|
| Dynamic Stiffness | Mechanical Impedance | Apparent Mass, Dynamic Mass |

Furthermore, the receptance frequency response function can be modeled in terms of a block diagram. Similar diagrams could be drawn for the other transfer functions.
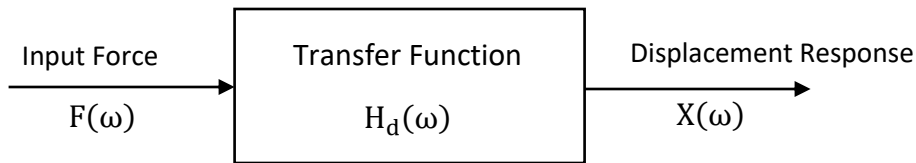
Figure 17.4.  FRF Diagram with Input & Output

## 17.2.4 Helicopter Ground Resonance
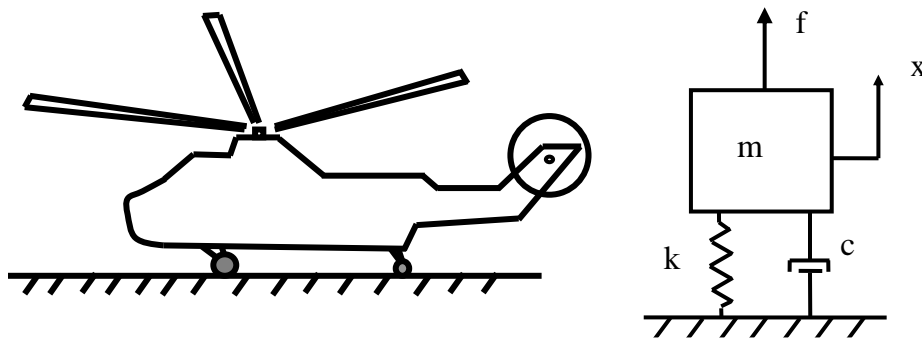


Figure 17.5.   Helicopter Preparing for Takeoff and SDOF System Analogy

A sketch of a generic helicopter is shown in Figure 17.5.  The helicopter may be modeled as a single-degree-of-freedom system excited by an applied force.

A new helicopter design must undergo thorough testing to ensure the reliability of the design with respect to vibration. It may encounter severe vibration while it is on the ground, preparing for takeoff.   A similar problem may occur immediately after landing.

Many helicopters have fully articulated rotor systems.  The advancing blades flap upward and the retreating blades flap downward to maintain uniform lift during forward flight. A helicopter with a fully-articulated rotor has some measure of an unbalanced rotational force, which causes an oscillating force.  This force may excite one of the helicopter's natural frequencies, as the

rotor accelerates to its full operating speed before takeoff. This condition is called resonant excitation.

John O. Emmerson wrote in Reference [23]:

> In the mid-1950s, the emerging helicopter introduced a frightening problem called ground resonance. A perfectly sound production helicopter firmly supported on its landing gear with the rotor turning at or near flight rpm would suddenly initiate a "tramping" on the gear and then, almost immediately, completely disintegrate. The Sikorsky company, which was leading the pack in developing the helicopter, quickly gathered the most data on these ground-based disasters and thus shouldered the lion's share of corrective understanding and action. The company established that the lead/lag pivots on the rotor blades, the pylon elastic stiffness, and the elastic components of the landing gear, including the tire and shock struts, all working together as a single structural entity, had an unfortunate resonant frequency near the rotor operating rpm. The engineers were able to show that a fearless pilot, entering the resonant phase, could save the day by pulling up the collective pitch control and unloading the landing gear (i.e., getting airborne). Lowering the resonant frequency and adding damping offered a permanent solution.
>
> Today, all of us in the helicopter development business, with the apprehension borne of substantial ignorance, approach initial ground whirl testing of each new helicopter with tremulous respect for the demon of ground resonances.

Modern helicopters avoid ground resonance by using dampers on the blades and the landing gear. The landing gear may have shock-absorbing struts.

Figure 17.6.   TH-55 Osage, Military Version of the Hughes 269A



Figure 17.7.   TH-55 Osage, Destroyed by Ground Resonance

An intact TH-55 helicopter is shown in Figure 17.6.  A similar TH-55 helicopter was destroyed by ground resonance in March 1967, at Ft. Wolters, TX, as shown in Figure 17.7.

## 17.2.5 Isolation Mounting to Attenuate Force Transmitted to Ground



Figure 17.8.   Pump Mounted to Floor via Inertial Frame & Springs

The primary goal of machinery isolation is to attenuate the vibration energy flow from a machine to adjoining areas. This is accomplished most effectively by "tuning," which is the process of separating the machine operating frequency from any of its structural frequencies. Consider the fundamental structural frequency to be the isolated spring-mass system frequency for simplicity.

The frequency separation should satisfy the "octave rule" as a minimum requirement. A one-octave separation means that the higher frequency is twice the value of the lower frequency.

A case of "low tuning" exists if the isolation frequency is at least one octave below the machine operating frequency.

A case of "high tuning" exists if the isolation frequency is at least one octave above the machine operating frequency.

Measurement of the floor's natural frequency should be considered for either of these methods because there is dynamic coupling between the machine and a non-rigid floor.

*Low Tuning*

Certain conditions must be satisfied for low tuning to be effective.

1. The machine's operating frequency should be above 4 Hz (240 rpm)
2. The soft support should not cause manufacturing problems in the case of a machine tool.
3. Machine start-up and shutdown transients should not cause excessive deflections or velocities.
4. The support must withstand both the static and dynamic forces of the machine.
5. The isolation frequency should be at least one octave below the machine operating frequency.

There are numerous methods for implementing low tuning. The most common methods are summarized in the following table.

Table 17.3.  Low-Tuning Methods

| Method | Isolation Frequency Domain | Notes |
|---|---|---|
| Hard-mount to Floor | 2 to 3 Hz | This is only practical if the floor natural frequency is 2 to 3 Hz. Typically, a floor has a natural frequency greater than 8 Hz, however. |
| Helical Steel Springs | 4 to 10 Hz | Springs have linear stiffness. Separate damping elements may be required. |
| Air Cushions | 0.5 to 3 Hz | Air cushions are very effective, but the air pressure must be maintained. |
| Rubber Mat or Mounts | 5 to 10 Hz | Rubber has nonlinear stiffness. It usually provides good damping, however. |
| Stabilizing Mass with Isolation Springs | 4 to 10 Hz | See Note below |

Note:   A stabilizing mass is often required for precision machine tools.  The stabilizing mass should be greater than the machine mass.  A higher stabilizing mass allows stiffer springs to be used to maintain a given isolated frequency.  Stiffer springs reduce the machine's own vibration amplitude per equation (17.18).
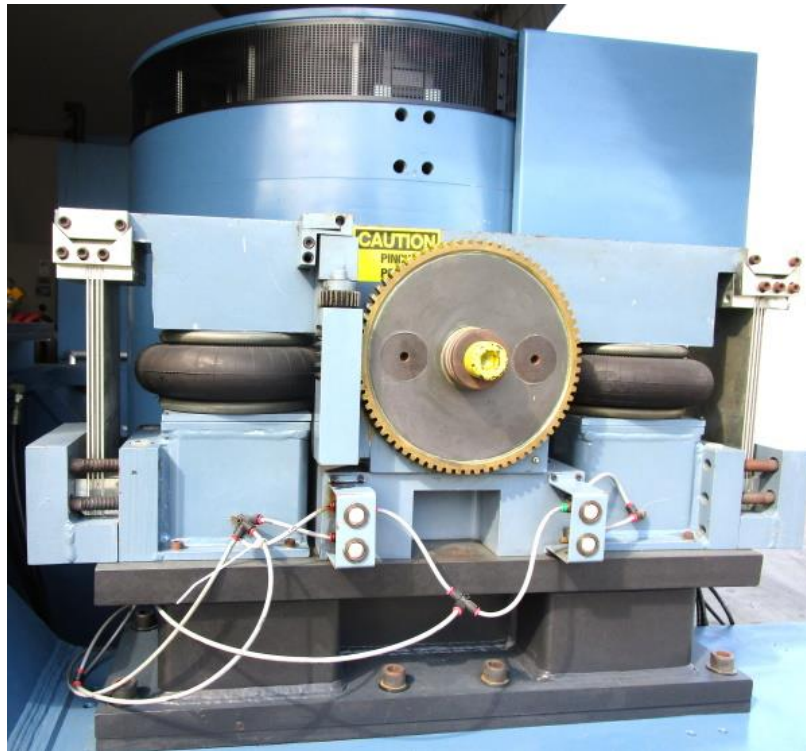


Figure 17.9.   Vibration Shaker with Black Air Cushion Mounts

*High Tuning*

High tuning is used for situations where low tuning is impractical. For example, high tuning might be used for a case where the vibration amplitude of a machine tool needed to be limited so that it could maintain precise tolerances.

High tuning requires a rigid connection between the machine and the floor. The floor's natural frequency effectively becomes the isolation frequency.

The floor natural frequency must be at least one octave higher than the machine operating frequency to achieve high tuning.

## 17.2.6 Two-Degree-of-Freedom System Subjected to Applied Forces

### 17.2.6.1 Two-Degree-of-Freedom System Equations of Motion, Time Domain
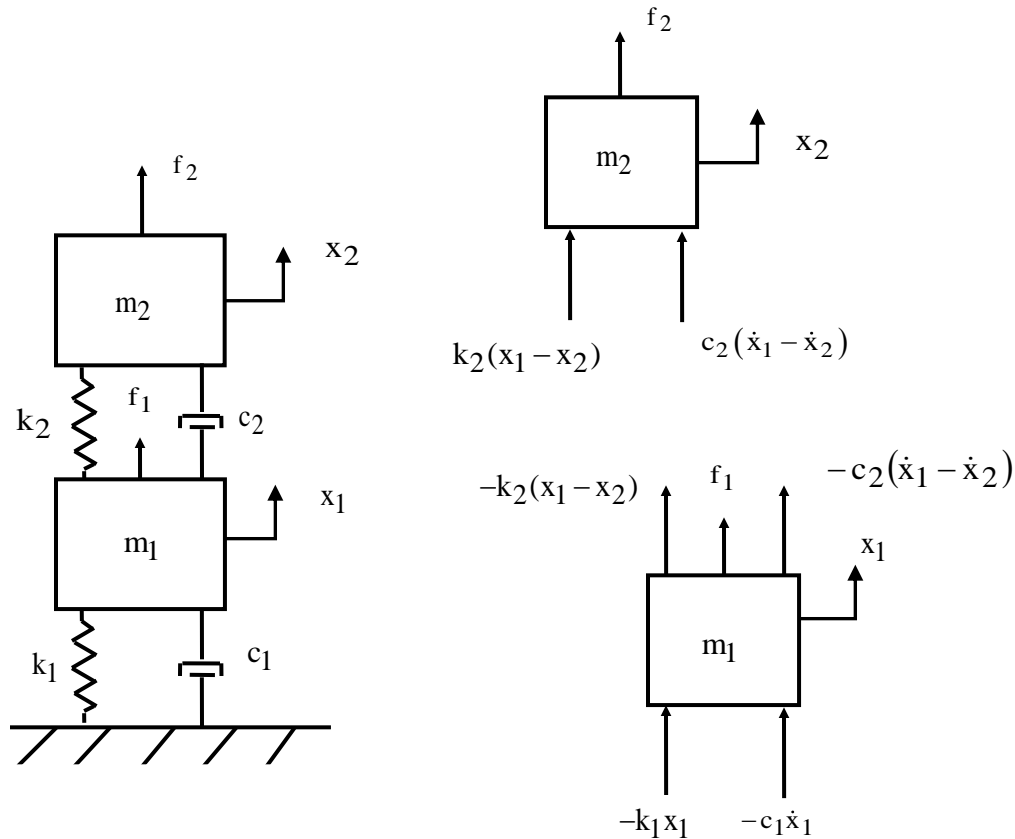


Figure 17.10.   Two-DOF System with External Forces

Recall the grounded, two-DOF system from Section 9.1.1.  It is shown again in Figure 17.10 with added forces.   The coupled equations of motion are

$$\begin{bmatrix} m_1 & 0 \\ 0 & m_2 \end{bmatrix} \begin{bmatrix} \ddot{x}_1 \\ \ddot{x}_2 \end{bmatrix} + \begin{bmatrix} c_1 + c_2 & -c_2 \\ -c_2 & c_2 \end{bmatrix} \begin{bmatrix} \dot{x}_1 \\ \dot{x}_2 \end{bmatrix} + \begin{bmatrix} k_1 + k_2 & -k_2 \\ -k_2 & k_2 \end{bmatrix} \begin{bmatrix} x_1 \\ x_2 \end{bmatrix} = \begin{bmatrix} f_1 \\ f_2 \end{bmatrix} \tag{17.21}$$

Note that each of the coefficient matrices is symmetric.  This is typical for linear structural dynamics systems.

A shorthand form of equation (17.4) is

$$M\ddot{\bar{x}} + C\dot{\bar{x}} + K\bar{x} = \bar{f} \qquad (17.22)$$

The matrices and vectors are

$$M = \begin{bmatrix} m_1 & 0 \\ 0 & m_2 \end{bmatrix}, \qquad C = \begin{bmatrix} c_1 + c_2 & -c_2 \\ -c_2 & c_2 \end{bmatrix}, \qquad K = \begin{bmatrix} k_1 + k_2 & -k_2 \\ -k_2 & k_2 \end{bmatrix},$$

$$\bar{f} = \begin{bmatrix} f_1 \\ f_2 \end{bmatrix}, \qquad \bar{x} = \begin{bmatrix} x_1 \\ x_2 \end{bmatrix} \qquad (17.23)$$

The natural frequencies and mode shapes are found from the undamped, homogeneous equation as was shown in Section 9.1.1. Now define a modal coordinate η(t) in terms of the normalized eigenvector matrix $\widehat{Q}$ such that the displacement vector is

$$\bar{x}(t) = \widehat{Q}\,\bar{\eta}(t) = \begin{bmatrix} \hat{q}_{11} & \hat{q}_{12} \\ \hat{q}_{21} & \hat{q}_{22} \end{bmatrix} \bar{\eta}(t) \qquad (17.24)$$

Repeat the steps in Section 9.1.1 with the added force term.

$$\widehat{Q}^T M \widehat{Q}\,\ddot{\bar{\eta}} + \widehat{Q}^T C \widehat{Q}\,\dot{\bar{\eta}} + \widehat{Q}^T K \widehat{Q}\,\bar{\eta} = \widehat{Q}^T \bar{f} \qquad (17.25)$$

The orthogonality relationships yield

$$I\ddot{\bar{\eta}} + \widehat{Q}^T C \widehat{Q}\,\dot{\bar{\eta}} + \Omega\,\bar{\eta} = \widehat{Q}^T \bar{F} \qquad (17.26)$$

The equation of motion can now be written with the modal damping simplification as

$$\begin{bmatrix} 1 & 0 \\ 0 & 1 \end{bmatrix}\begin{bmatrix} \ddot{\eta}_1 \\ \ddot{\eta}_2 \end{bmatrix} + \begin{bmatrix} 2\xi_1\omega_1 & 0 \\ 0 & 2\xi_2\omega_2 \end{bmatrix}\begin{bmatrix} \dot{\eta}_1 \\ \dot{\eta}_2 \end{bmatrix} + \begin{bmatrix} \omega_1{}^2 & 0 \\ 0 & \omega_2{}^2 \end{bmatrix}\begin{bmatrix} \eta_1 \\ \eta_2 \end{bmatrix} = \begin{bmatrix} \hat{q}_{11} & \hat{q}_{12} \\ \hat{q}_{21} & \hat{q}_{22} \end{bmatrix}\begin{bmatrix} f_1 \\ f_2 \end{bmatrix}$$
$$(17.27)$$

The two equations are now uncoupled in terms of the modal coordinates. Now consider the case where the forcing functions are deterministic time domain functions. The modal displacement for the response to the harmonic forces can be found via Laplace transforms. Alas, the resulting modal displacement equations even for sinusoidal forces are too unwieldy for inclusion in this book but are given in Reference [24]. The physical displacements are then found via equation (17.24). The solution for the case of arbitrary forces can be calculated using

the ramp invariant digital recursive filtering relationship in Reference [21].   See also equations (17.12) through (17.15).

### 17.2.6.2 Two-Degree-of-Freedom System, Time Domain Example

The system in Figure 17.10 has the parameters previously shown in Table 9.1, with 5% damping for each mode.  Its natural frequencies are again 20.0 and 42.5 Hz.   The mass-normalized mode shapes in matrix format are

$$\widehat{Q} = \begin{bmatrix} 8.93 & -10.64 \\ 15.05 & 12.63 \end{bmatrix}$$

(17.28)

It is subjected to a single sinusoidal force applied to the top mass, with zero initial conditions. The amplitude is 1 lbf.  The forcing frequency is 20.0 Hz, which is the same as the fundamental frequency.  The results are shown in Figure 17.11.  Now consider the steady-state amplitude ratios between the mass responses.   The responses are very nearly in proportion to the eigenvector coefficients in the first column of equation (17.28).   The response of mass 2 is thus nearly (15.05/8.93) times greater than that of mass 1.  The measured ratio is slightly inexact became the 20.0 Hz excitation also excites the 42.5 Hz mode, but the second mode's participation can be considered negligibly low due to the greater than one-octave frequency separation.

The analysis is repeated with the forcing frequency at 42.5 Hz, as shown in Figure 17.12.  The steady-state response of mass 2 is nearly (12.63/10.64) times that of mass 1, per the second column of equation (17.28).    The negative sign in the second column indicates that the responses are 180 degrees out-of-phase with one another.
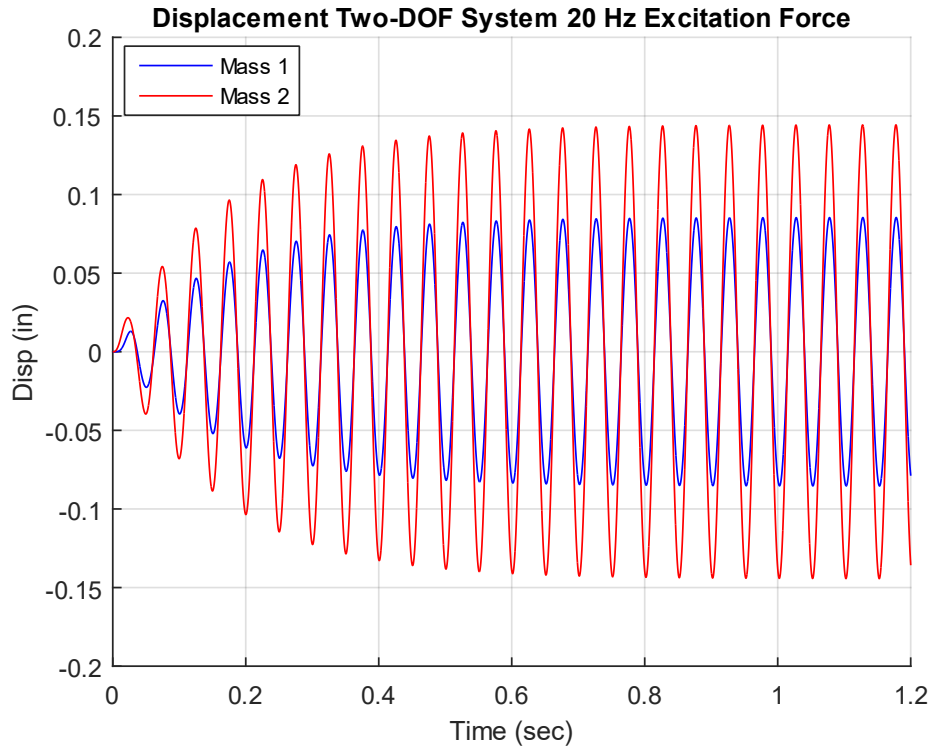
Figure 17.11.   Displacement Responses to 20.0 Hz Excitation
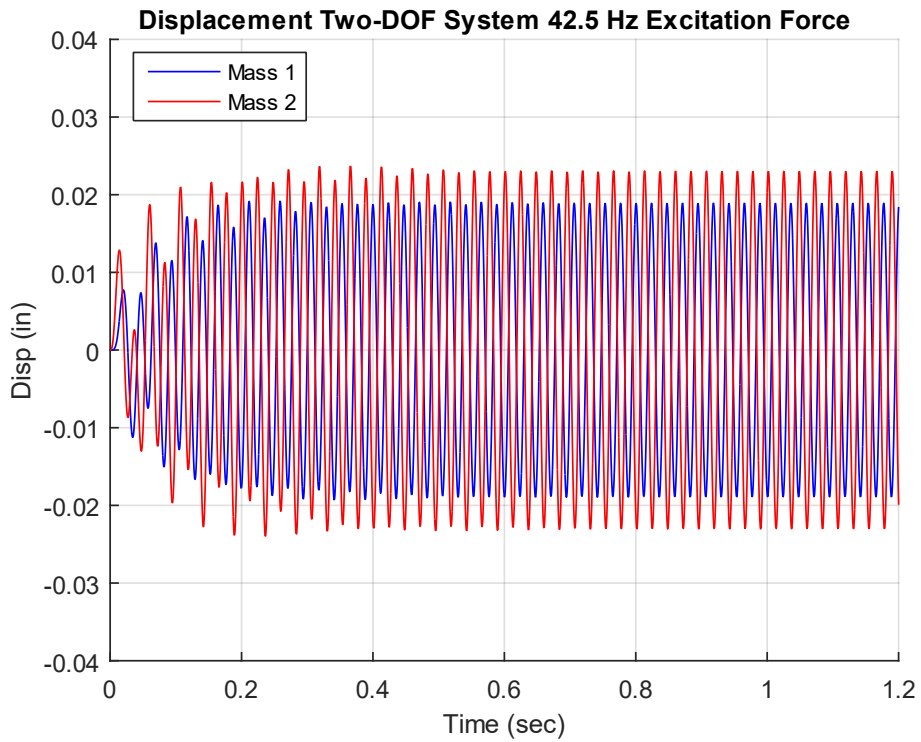


Figure 17.12.   Displacement Responses to 42.5 Hz Excitation

17.2.6.3 Two-Degree-of-Freedom System Equations of Motion, Frequency Domain

Equation (17.27) can be used in the frequency domain for the case of steady-state harmonic forces.  Define force and modal displacement coordinates as follows

$$\bar{f}(t) = \bar{F}\exp(j\omega t) \tag{17.29}$$

$$\bar{\eta}(t) = \bar{N}\exp(j\omega t) \tag{17.30}$$

Substitute these harmonic terms into Equation (17.27).  This process is akin to taking a Fourier transform of the equation.  The result for modal displacement ｉafter simplification is

$$[(\omega_i{}^2 - \omega^2) + j(2\xi_i\,\omega_i\,\omega)]N_i = \hat{q}_{1i}F_1 + \hat{q}_{2i}F_2 \tag{17.31}$$

$$N_i = \frac{\hat{q}_{1i}\,F_1 + \hat{q}_{2i}\,F_2}{(\omega_i{}^2 - \omega^2) + j(2\xi_i\,\omega_i\,\omega)} \tag{17.32}$$

The modal displacement equation can be generalized to a system with n degrees-of-freedom as

$$N_i = \sum_{p=1}^{n}\left\{\frac{\hat{q}_{pi}\,F_p}{(\omega_i{}^2 - \omega^2) + j(2\xi_i\,\omega_i\,\omega)}\right\} \tag{17.33}$$

The physical displacements are then found from

$$\bar{X}(\omega) = \hat{Q}\,\bar{N}(\omega) = \begin{bmatrix}\hat{q}_{11} & \hat{q}_{12} \\ \hat{q}_{21} & \hat{q}_{22}\end{bmatrix}\bar{N}(\omega) \tag{17.34}$$

The physical displacement at degree-of-freedom k is

$$X_k = \sum_{i=1}^{n}\hat{q}_{ki}\,N_i \tag{17.35}$$

The principle of linear superposition holds in this case. The displacement can be calculated for an individual force. Then the total displacement is the sum of the displacements for the individual forces.

Assume that the only force acting on the system is at DOF p. The modal displacement at DOF i is

$$N_i = \frac{\hat{q}_{pi}\, F_p}{(\omega_i{}^2 - \omega^2) + j\,(2\,\xi_i\,\omega_i\,\omega)} \tag{17.36}$$

The physical displacement at DOF k for the single force case is

$$X_k = \sum_{i=1}^{n} \left\{ \frac{\hat{q}_{ki}\, \hat{q}_{pi}\, F_p}{(\omega_i{}^2 - \omega^2) + j\,(2\,\xi_i\,\omega_i\,\omega)} \right\} \tag{17.37}$$

The receptance function for the single force applied becomes

$$H_{d,kp}(\omega) = \frac{X_k}{F_p} = \sum_{i=1}^{n} \left\{ \frac{\hat{q}_{ki}\, \hat{q}_{pi}}{(\omega_i{}^2 - \omega^2) + j\,(2\,\xi_i\,\omega_i\,\omega)} \right\} \tag{17.38}$$

The numerator in the series shows the relationship between the receptance function and the mass-normalized eigenvector terms.

## 17.2.7 Two-Degree-of-Freedom System, Frequency Domain Example
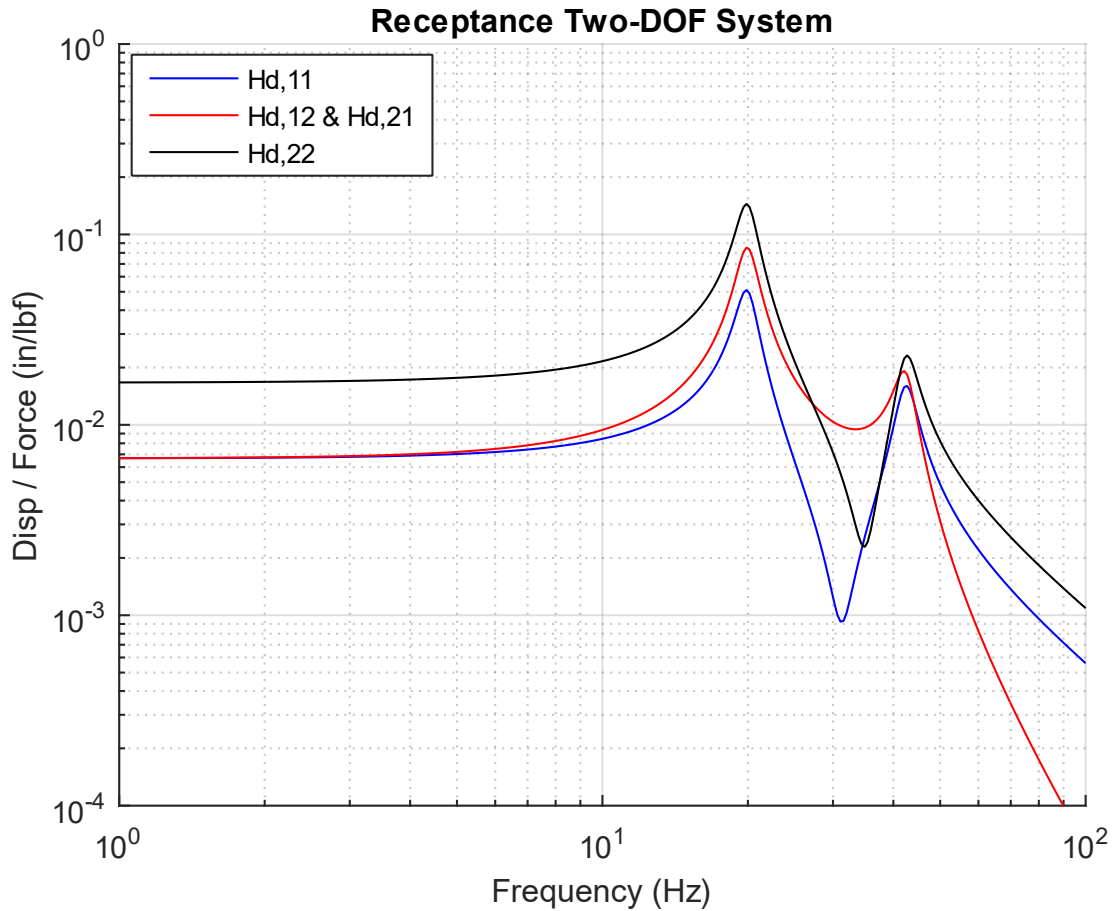


Figure 17.13.   Two-DOF System Receptance FRF

The system in Figure 17.10 has the parameters previously shown in Table 9.1, with 5% damping for each mode.  Its natural frequencies are again 20.0 and 42.5 Hz.   Its receptance frequency response function from equation (17.38) is given in Figure 17.13 for four permutations.  The first index in the legend is the response location.  The second is the applied force location, where each location is a degree-of-freedom.  The phase angles could also be plotted but are omitted for brevity.

## 17.3 BASE EXCITATION

### 17.3.1 SDOF Response Equations

This case is also referred to as support motion or seismic excitation.  The base excitation model and its free-body diagram are
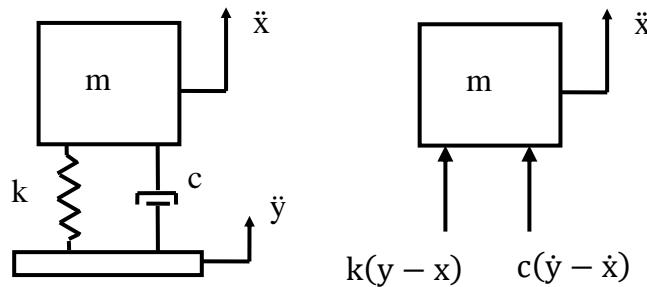


Figure 17.14.  Single-degree-of-freedom Model, Base Excitation

The base displacement is $y$, and the base velocity is $\dot{y}$.  The equation of motion for base excitation is derived using Newton's law.

$$\sum F = m\ddot{x} \tag{17.39}$$

$$m\ddot{x} = c(\dot{y} - \dot{x}) + k(y - x) \tag{17.40}$$

The challenge with the previous equation is that the base displacement and base velocity are usually unknown, but the base acceleration is known.  The workaround is to define a relative displacement $z$ as

$$z = x - y \tag{17.41}$$

Through substitution and algebraic manipulation, the following ordinary differential equation is derived in terms of relative displacement.

$$m(\ddot{z} + \ddot{y}) \ = \ -c\dot{z} - kz \qquad (17.42)$$

$$m\ddot{z} + c\dot{z} \ + kz \ = \ -m\ddot{y} \qquad (17.43)$$

The resulting equation of motion is non-homogenous.  The $m\ddot{y}$ term on the right-hand side can be regarded as an inertial force.  The equation for base excitation can be further simplified as

$$\ddot{z} + (c/m)\dot{z} \ + (k/m)z \ = \ -\ddot{y} \qquad (17.44)$$

$$\ddot{z} + 2\xi\omega_n\dot{z} \ + \ \omega_n{}^2 z \ = \ -\ddot{y} \qquad (17.45)$$

$$\ddot{z} = -2\xi\omega_n\dot{z} - \ \omega_n{}^2 z \ - \ddot{y} \qquad (17.46)$$

The absolute acceleration is then calculated as

$$\ddot{x} = \ddot{z} + \ddot{y} \qquad (17.47)$$

$$\ddot{x} = -2\xi\omega_n\dot{z} - \ \omega_n{}^2 z \qquad (17.48)$$

The above equation set can be solved via Laplace transforms if the base acceleration is deterministic such as a sine function.  A convolution integral is needed if the excitation varies arbitrarily with time.   The resulting relative displacement equation for acceleration base excitation for the case of zero initial conditions is

$$z(t) = - \int_0^t \ddot{y}(\tau)\, h(t - \tau)\, d\tau \qquad (17.49)$$

The relative displacement convolution integral has an embedded impulse response function with respect to a velocity impulse.

$$h(t) = \frac{1}{\omega_d} \ [\exp(-\xi\,\omega_n t)][\sin(\omega_d t)] \qquad (17.50)$$

$$z(t) = -\frac{1}{\omega_d} \ \int_0^t \ddot{y}(\tau)\, \exp[-\xi\,\omega_n(t - \tau)]\sin[\omega_d(t - \tau)]d\tau \qquad (17.51)$$
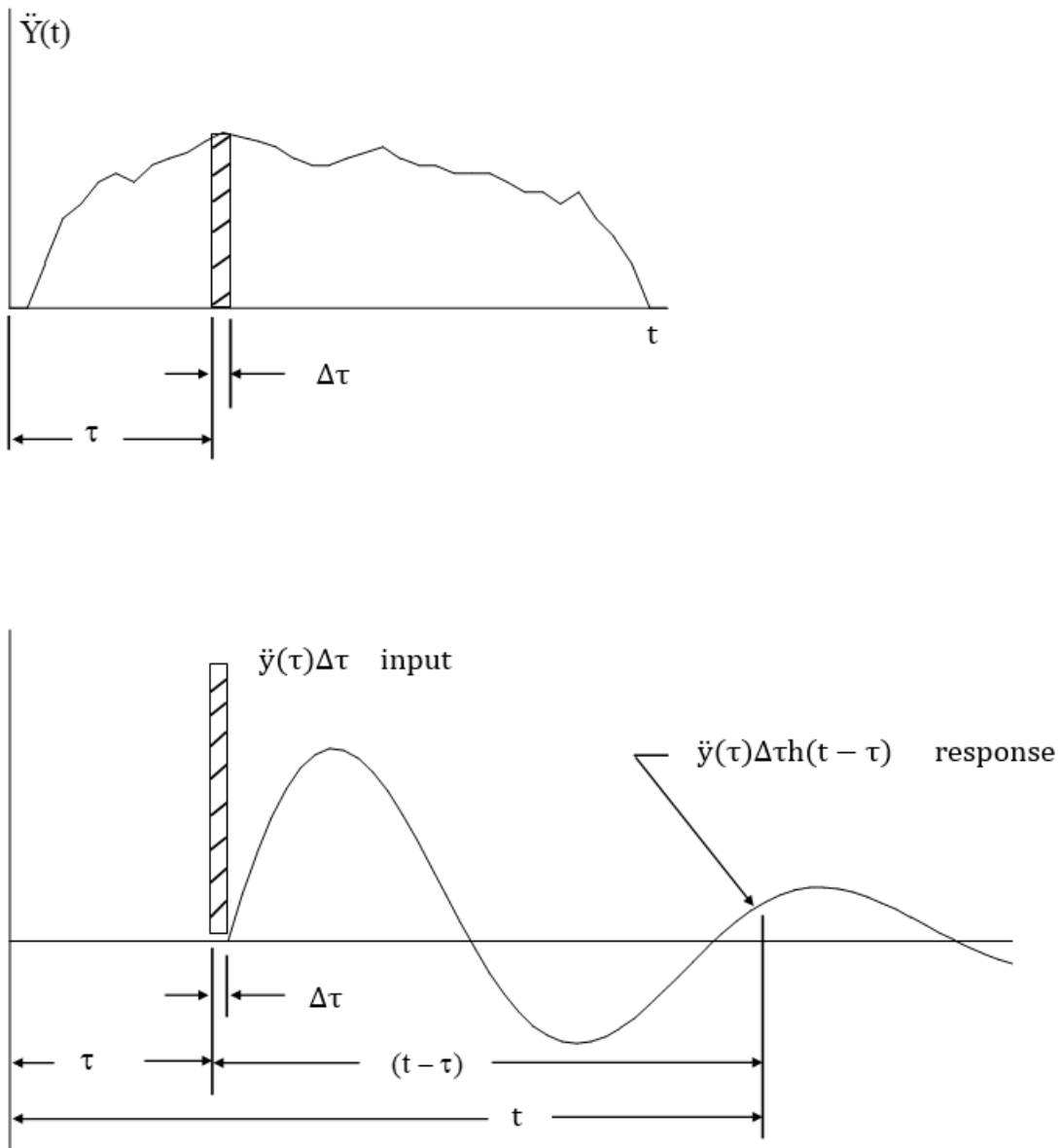
Figure 17.15. Single-degree-of-freedom Model, Arbitrary Base Input and Response

The total relative displacement is found by summing the response to each velocity impulse $\ddot{y}(\tau_i)\Delta\tau_i$.

$$z(t_m) = -\frac{1}{\omega_d} \sum_{i=1}^{m} \ddot{y}(\tau_i) \exp[-\xi \omega_n (t_m - \tau_i)] \sin[\omega_d (t_m - \tau_i)] \Delta \tau_i \qquad (17.52)$$

Note that the principle of superposition holds because the system is linear. The series form changes to the integral form in equation (17.51) as an infinitesimally small interval is taken.

Equation (17.46) can also be solved in the frequency domain. Time and frequency domain analyses should yield the same results per Parseval's theorem.

The Laplace transform of the impulse response function is the steady-state transmissibility function for relative displacement.

$$H_z(s) = \left[ \frac{1}{s^2 + 2\,\xi\,\omega_n\,s + \omega_n{}^2} \right] \qquad (17.53)$$

This transmissibility function can be represented in the frequency domain by setting $s = j\,\omega$, where $j = \sqrt{-1}$.

$$H_z(\omega) = \left[ \frac{1}{(\omega_n{}^2 - \omega^2) + j\,2\,\xi\,\omega_n\,\omega} \right] \qquad (17.54)$$

The relative displacement transmissibility function in equation (17.54) is the Fourier transform of the impulse response function in equation (17.50). Fourier transforms are covered in Section 23.

The absolute acceleration response convolution integral is

$$\ddot{x}(t) = \frac{1}{\omega_d} \int_0^t \ddot{y}(\tau) \exp[-\xi\,\omega_n(t-\tau)]\{(\omega_d{}^2 - \xi^2\omega_n{}^2)\sin[\omega_d(t-\tau)]$$
$$+ 2\xi\omega_n\omega_d\cos[\omega_d(t-\tau)]\}\,d\tau \qquad (17.55)$$

The convolution integral is computationally inefficient, however. An alternative is to use the Smallwood ramp invariant digital recursive filtering relationship [25]. The recursive filtering algorithm is fast and is the numerical engine used in almost all shock response spectrum software. It is also accurate assuming that the data has a sufficiently high sample rate and is free from aliasing.

The algorithm is discussed further in Section 26.5. The embedded acceleration impulse response function in the convolution integral is

$$h_a(t) = \frac{1}{\omega_d} \exp[-\xi\,\omega_n(t-\tau)]\{(\omega_d{}^2 - \xi^2\omega_n{}^2)\sin[\omega_d(t-\tau)] + 2\xi\omega_n\omega_d\cos[\omega_d(t-\tau)]\}$$

$$(17.56)$$

The Laplace transform of the impulse response function is the steady-state transmissibility function for absolute acceleration.

$$H_a(s) = \left[\frac{2\,\xi\,\omega_n\,s + \omega_n{}^2}{s^2 + 2\,\xi\,\omega_n\,s + \omega_n{}^2}\right]$$

$$(17.57)$$

The transmissibility function in the frequency domain is

$$H_a(\omega) = \left[\frac{\omega_n{}^2 + j\,2\,\xi\,\omega_n\,\omega}{(\omega_n{}^2 - \omega^2) + j\,2\,\xi\,\omega_n\,\omega}\right]$$

$$(17.58)$$

## 17.3.2  Input & Response Example, Base Excitation

The single-degree-of-freedom system in Figure 17.14 has a natural frequency of 10 Hz and an amplification factor Q=10 for this example.  It is excited into resonance by a 1 G sinusoidal base excitation at 10 Hz.  The exact response can be calculated via a Laplace transform solution.  The result is shown in Figure 17.16.
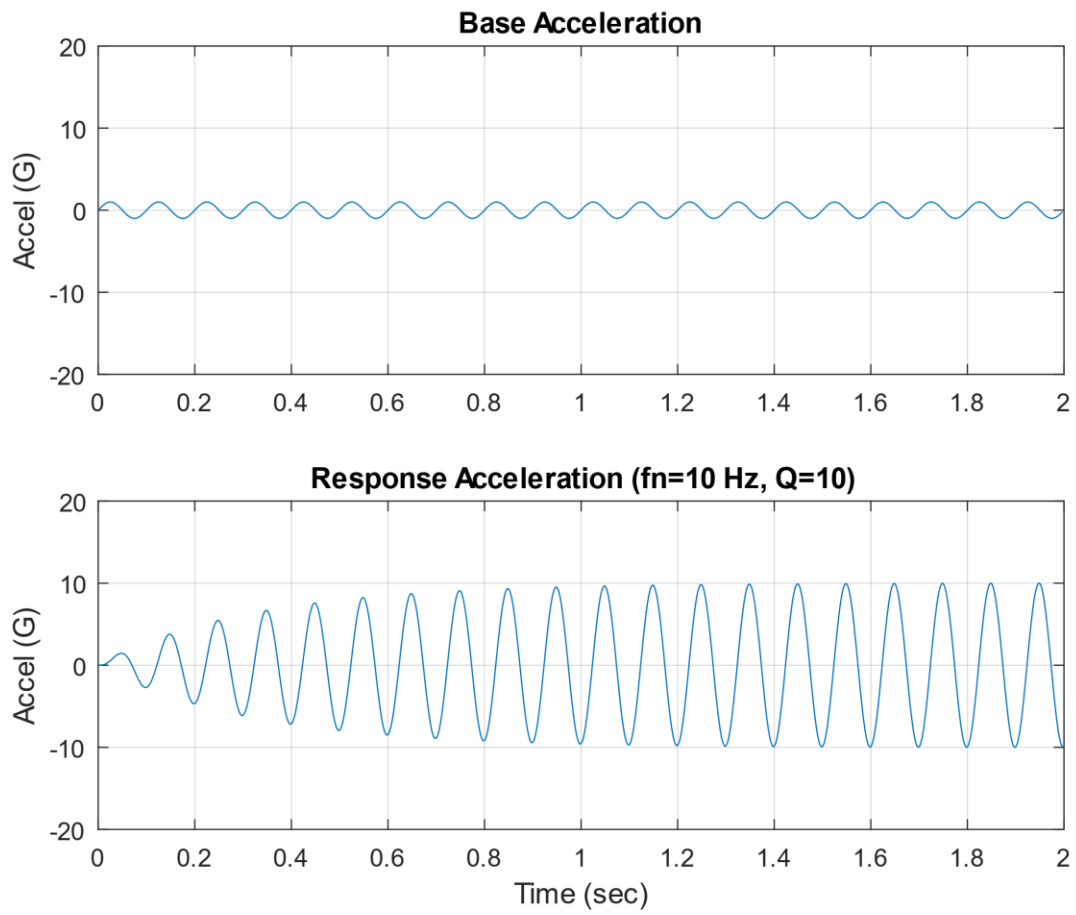
Figure 17.16.  Sine Base Input & Response
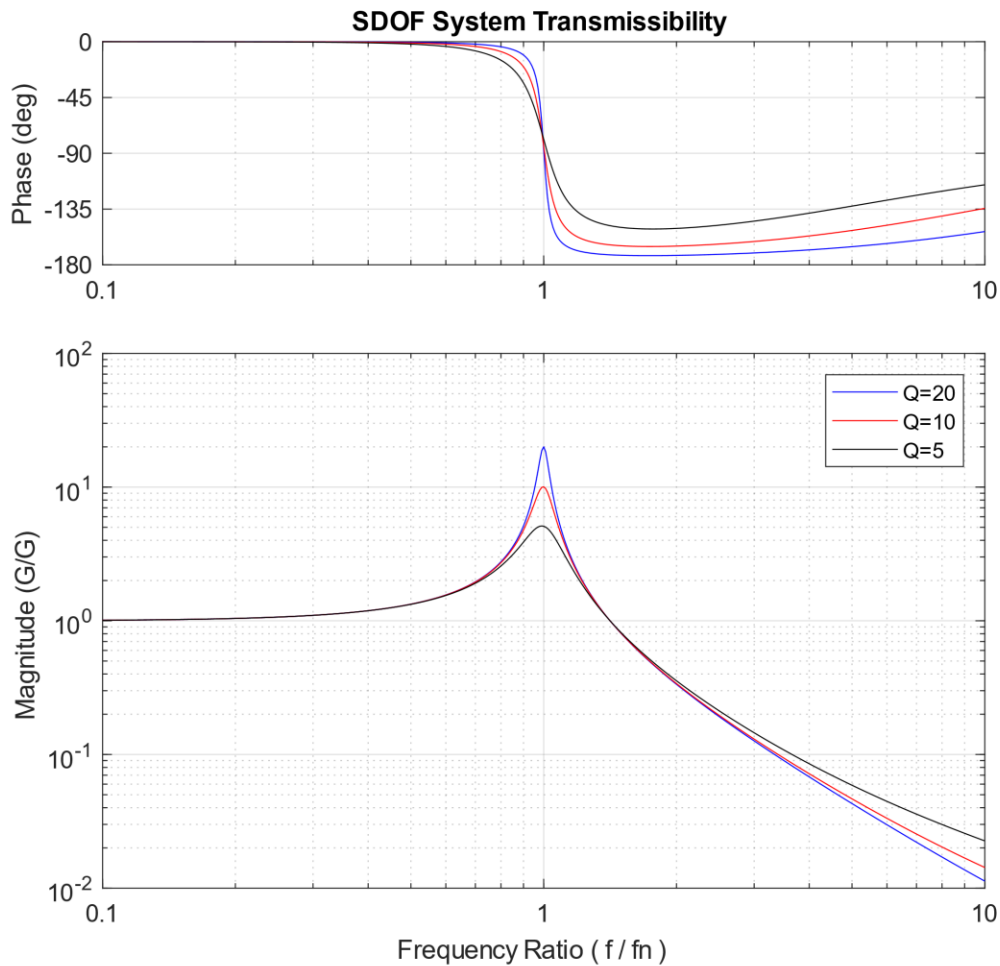
Figure 17.17.  Transmissibility Function for Steady-State Sine Base Input

The response calculation could be repeated for several frequency and amplification factor cases to determine the maximum steady-state response for each case.  The transmissibility results for three amplification factor cases are shown in Figure 17.17.    The frequency ratio is the excitation frequency f divided by the natural frequency fn.    The magnitude is the steady response divided by the input amplitude.   The transmissibility magnitude tends to unity gain when the excitation frequency is much less than the natural frequency.   Resonant amplification occurs when the frequency ratio is at or very near one.   Isolation occurs when the excitation frequency is greater than √2 times the natural frequency.

Note that the Q value is approximately equal to the peak transmissibility at resonance in Figure 17.17.  Also, the resonant time domain response in Figure 17.16 reached a steady-state peak of Q times the base input.   This suggests that sine vibration testing could be a way for measuring

the amplification factor and its corresponding damping ratio by noting the peak response either in the frequency or time domain.  But this simple relationship should be considered only for the special case of a single-degree-of-freedom system.  Multi-degree-of-freedom systems and continuous systems have responses that depend on damping as well as on mode shape parameters.

Consider a cantilever beam subjected to base excitation exciting its fundamental bending mode.  An accelerometer is mounted on the beam's free end and another at its midpoint.  The peak response at the free end will be higher than that at the midpoint due to the respective location-dependent modal gain factors.  The half-power bandwidth method is a much more reliable damping identification method for measured response data from this beam and general structures.  This method would yield the same damping value from either of the two accelerometer data results.  See the examples in Sections 20.4 and 20.5.

The transmissibility function plotted in Figure 17.17 was introduced in Section 17.3.  The magnitude $H(\rho)$ can be represented as

$$| H(\rho) | = \sqrt{\frac{1 + (2\xi\rho)^2}{(1 - \rho^2)^2 + (2\xi\rho)^2}} \ , \qquad \rho = f/f_n \qquad\qquad (17.59)$$

The phase angle by which the response lags the input is

$$\phi = \arctan\left[\frac{2\xi\,\rho^3}{1 + \rho^2(4\xi^2 - 1)}\right] \qquad\qquad (17.60)$$

## 17.3.3 Alternate Base Excitation Method using Seismic Mass
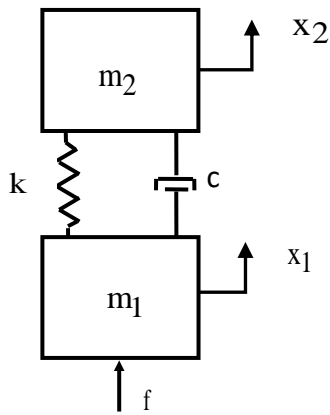


Figure 17.18. Seismic Mass for Base Excitation, Semi-definite System

Recall the semi-definite system in Section 9.1.6 and the two-DOF system subjected to an applied force in Section 17.2.6. A hybrid of these systems can be configured for base excitation by setting the bottom mass to a value vastly larger than the top mass by a factor of, say, 1e+04. Then an external force is applied to the base to produce the desired acceleration. This approach is unnecessary for SDOF system base excitation but becomes very useful for complex, multi-degree-of-freedom systems. The equation of motion is

$$\begin{bmatrix} m_1 & 0 \\ 0 & m_2 \end{bmatrix} \begin{bmatrix} \ddot{x}_1 \\ \ddot{x}_2 \end{bmatrix} + \begin{bmatrix} c & -c \\ -c & c \end{bmatrix} \begin{bmatrix} \dot{x}_1 \\ \dot{x}_2 \end{bmatrix} + \begin{bmatrix} k & -k \\ -k & k \end{bmatrix} \begin{bmatrix} x_1 \\ x_2 \end{bmatrix} = \begin{bmatrix} f \\ 0 \end{bmatrix} = \begin{bmatrix} m_1 \ddot{y} \\ 0 \end{bmatrix} \qquad (17.61)$$

The hybrid equation is solved using the methods in Section 17.2.6. There is a rigid-body mode at zero frequency. The second modal frequency is

$$\omega_2 = \sqrt{\frac{k(m_1+m_2)}{m_1 m_2}} \qquad (17.62)$$

The second modal frequency becomes

$$\omega_2 \approx \sqrt{k/m_2} \quad , \text{ for } m_1 \gg m_2 \qquad (17.63)$$

The second frequency is essentially equal to the top mass and the spring as a single-degree-of-freedom system.

Repeat the example in Section 17.3.2.  The natural frequency was 10 Hz in this example with Q=10.  The use of the seismic mass method requires explicit knowledge of the mass and stiffness values, as shown in the example in Table 17.4.  The top mass is excited into resonance by a 1 G sinusoidal base excitation at 10 Hz via an equivalent 1e+05 lbf force applied to the bottom, seismic mass.  The acceleration response is shown in Figure 17.19.  The result is the same as that in Figure 17.16 with the response time histories in both plots reaching 10 G steady-state.

Table 17.4.  Seismic Mass, Hybrid System, Parameters

| Variable | Value |
|----------|-------|
| $m_1$ | 1.0e+05 lbm |
| $m_2$ | 10 lbm |
| $k_1$ | 102.2 lbf/in |
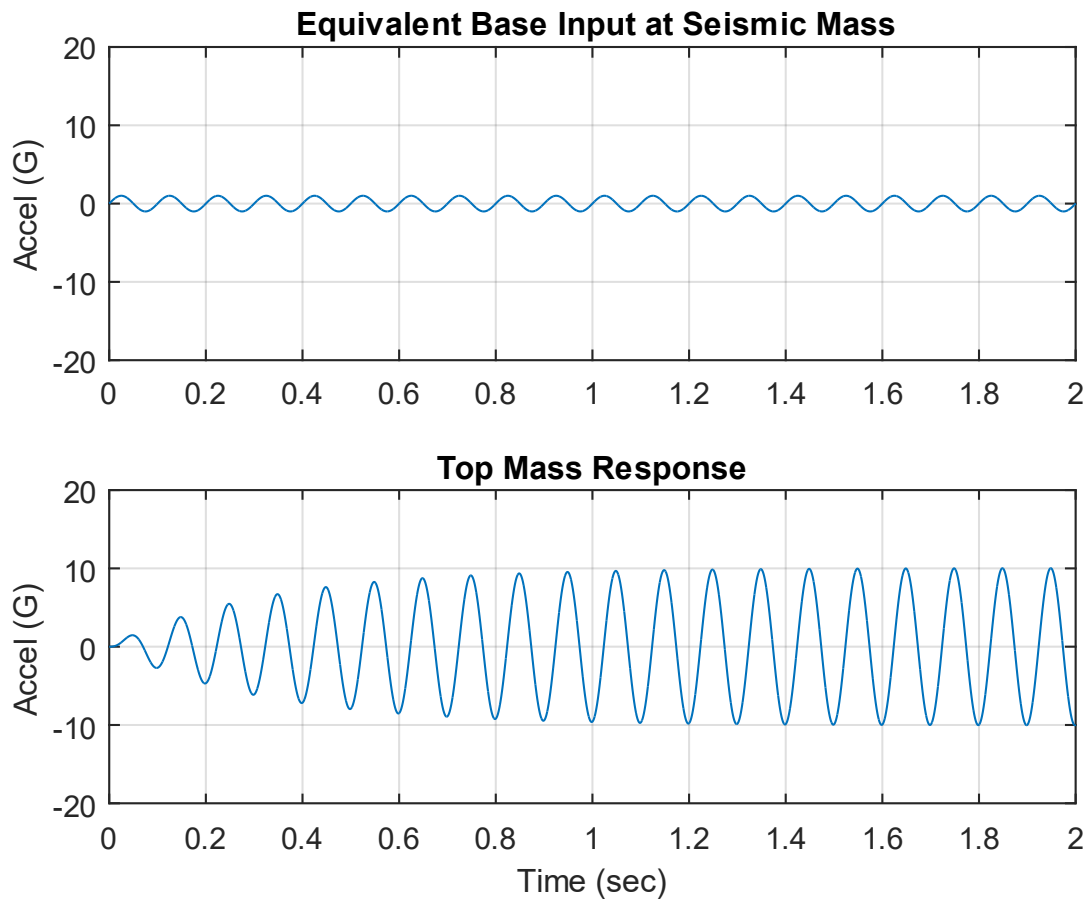
Figure 17.19. Sine Base Input & Response, Seismic Mass Method

Note that in some cases it may be necessary to ground the seismic mass with a very soft spring for numerical stability purposes, such that the fundamental frequency is just slightly above the zero frequency but is still much less than the frequency in equation (17.63).

### 17.3.4 Two-DOF Response Equations, Time Domain
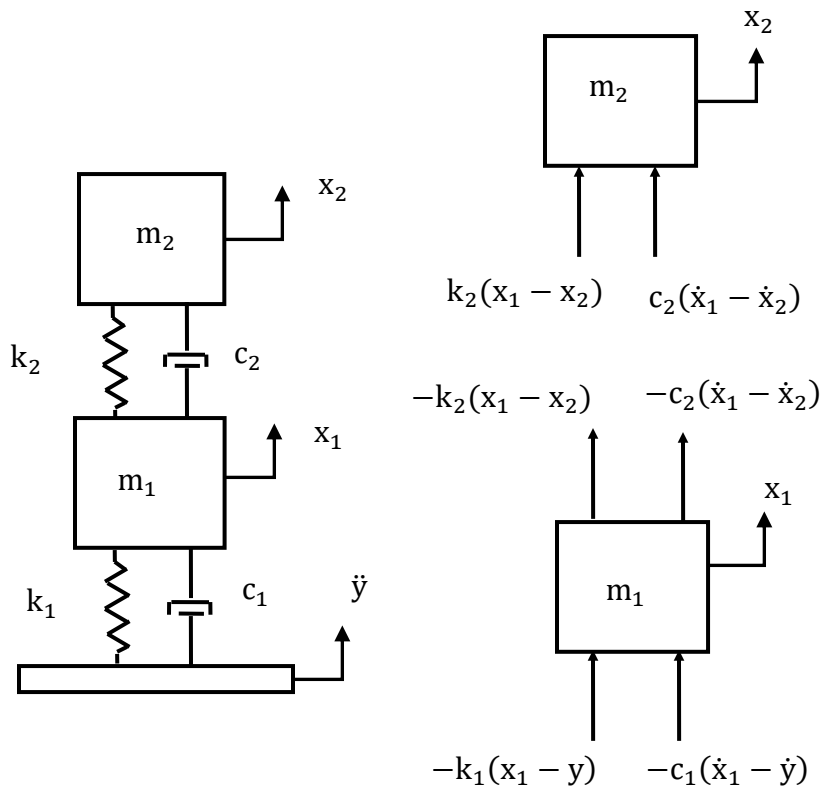


Figure 17.20. Two-DOF System Subjected to Base Excitation

Consider the system in Figure 17.20, which is sometimes referred to as two-stage isolation per Reference [26]. The equation of motion can be derived using Newton's law.

$$\begin{bmatrix} m_1 & 0 \\ 0 & m_2 \end{bmatrix} \begin{bmatrix} \ddot{x}_1 \\ \ddot{x}_2 \end{bmatrix} + \begin{bmatrix} c_1 + c_2 & -c_2 \\ -c_2 & c_2 \end{bmatrix} \begin{bmatrix} \dot{x}_1 \\ \dot{x}_2 \end{bmatrix} + \begin{bmatrix} k_1 + k_2 & -k_2 \\ -k_2 & k_2 \end{bmatrix} \begin{bmatrix} x_1 \\ x_2 \end{bmatrix} = \begin{bmatrix} c_1\dot{y} + k_1 y \\ 0 \end{bmatrix} \tag{17.64}$$

The familiar challenge with equation (17.64) is that the base displacement and base velocity are usually unknown, but the base acceleration is known. The workaround is to define a relative displacement z such that

$$z_i = x_i - y \tag{17.65}$$

Substitution of the relative displacements into (17.64) yields the following equation after algebraic manipulation.

$$\begin{bmatrix} m_1 & 0 \\ 0 & m_2 \end{bmatrix} \begin{bmatrix} \ddot{x}_1 \\ \ddot{x}_2 \end{bmatrix} + \begin{bmatrix} c_1 + c_2 & -c_2 \\ -c_2 & c_2 \end{bmatrix} \begin{bmatrix} \dot{x}_1 \\ \dot{x}_2 \end{bmatrix} + \begin{bmatrix} k_1 + k_2 & -k_2 \\ -k_2 & k_2 \end{bmatrix} \begin{bmatrix} x_1 \\ x_2 \end{bmatrix} = - \begin{bmatrix} m_1 \ddot{y} \\ m_2 \ddot{y} \end{bmatrix} \qquad (17.66)$$

The natural frequencies and modes shapes are calculated using the method from Section 9.1.2. The modal decoupling process is essentially the same as that in Section 17.2.6, with the force vector changed to

$$\bar{F} = - \begin{bmatrix} m_1 \ddot{y} \\ m_2 \ddot{y} \end{bmatrix} \qquad (17.67)$$

The relative displacement is represented in terms of the mass-normalized eigenvector matrix and the modal displacement.

$$\bar{z}(t) = \widehat{Q}\ \bar{\eta}(t) = \begin{bmatrix} \hat{q}_{11} & \hat{q}_{12} \\ \hat{q}_{21} & \hat{q}_{22} \end{bmatrix} \bar{\eta}(t) \qquad (17.68)$$

The uncoupled equations of motion are

$$\begin{bmatrix} 1 & 0 \\ 0 & 1 \end{bmatrix} \begin{bmatrix} \ddot{\eta}_1 \\ \ddot{\eta}_2 \end{bmatrix} + \begin{bmatrix} 2\xi_1 \omega_1 & 0 \\ 0 & 2\xi_2 \omega_2 \end{bmatrix} \begin{bmatrix} \dot{\eta}_1 \\ \dot{\eta}_2 \end{bmatrix} + \begin{bmatrix} \omega_1{}^2 & 0 \\ 0 & \omega_2{}^2 \end{bmatrix} \begin{bmatrix} \eta_1 \\ \eta_2 \end{bmatrix} = - \begin{bmatrix} \hat{q}_{11} & \hat{q}_{12} \\ \hat{q}_{21} & \hat{q}_{22} \end{bmatrix} \begin{bmatrix} m_1 \ddot{y} \\ m_2 \ddot{y} \end{bmatrix} \qquad (17.69)$$

The modal displacement can be calculated via Laplace transforms for a deterministic base acceleration. Modal accelerations can be calculated by twice differentiating the modal displacements.

A ramp invariant digital filtering relationship can be used for a base excitation which varies arbitrarily with time. Such equations are available for direct calculation of both the modal displacement and acceleration. The filtering equations are taken from Reference [21] given the virtual force and displacement characteristics of equation (17.69), rather than the SDOF formulas for base excitation given in References [25], [27].

The physical relative displacement can then be calculated by applying the modal displacements to equation (17.68). The physical relative acceleration can then be determined from the modal acceleration via the same eigenvector matrix transformation in equation (17.68). The physical absolute acceleration is then found by adding the base acceleration to the physical relative acceleration.

## 17.3.5 Two-DOF Response Equations, Time Domain Example

The system in Figure 17.20 has the parameters previously shown in Table 9.1 with 5% damping for each mode.  Its natural frequencies are again 20.0 and 42.5 Hz.  It is subjected to sinusoidal base excitation, with zero initial conditions.  The base acceleration amplitude is 1 G with a frequency of 20.0 Hz, which is the same as the fundamental frequency as shown in Figure 17.21. The analysis is repeated with the excitation frequency at 42.5 Hz in Figure 17.22.
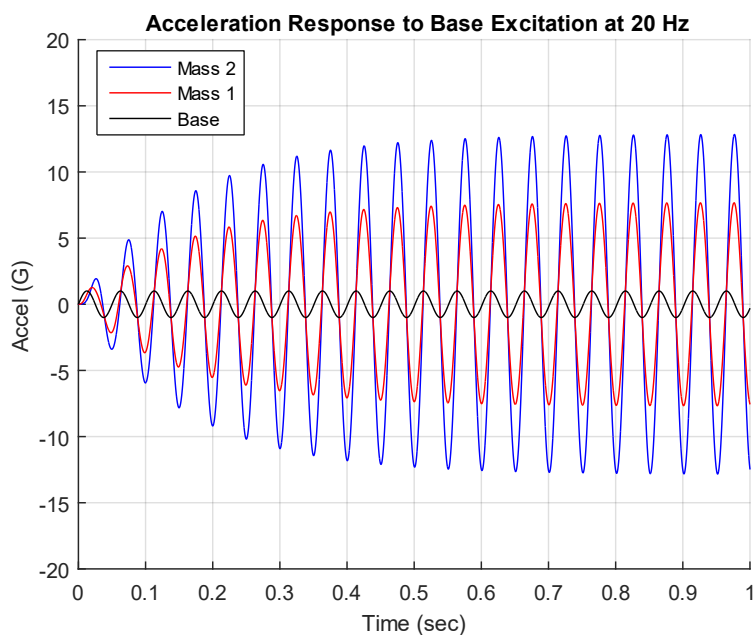


Figure 17.21.   Acceleration Responses to 20.0 Hz Excitation
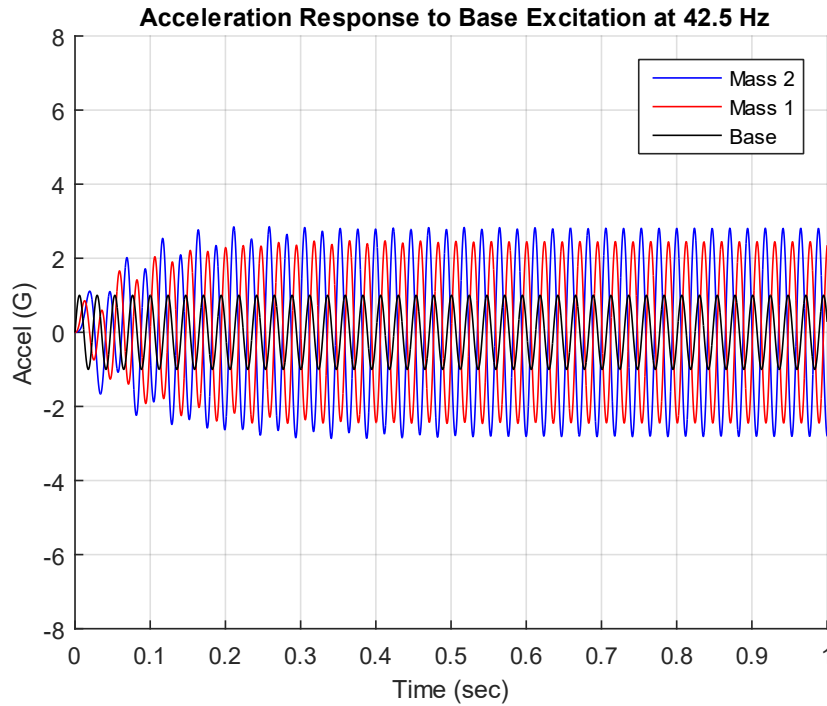
Figure 17.22.   Acceleration Responses to 42.5 Hz Excitation

The responses are 180 degrees out-of-phase with one another.

### 17.3.6 Two-DOF Response Equations, Frequency Domain

Equation (17.69) can be used in the frequency domain for the case of steady-state harmonic base excitation.  Define base acceleration and modal displacement coordinates as follows

$$\ddot{\bar{y}}\,(t) = \overline{Y}_A \exp\,(j\omega t) \tag{17.70}$$

$$\bar{\eta}\,(t) = \overline{N} \exp\,(j\omega t) \tag{17.71}$$

Substitute these harmonic terms into Equation (17.69).  The result for modal displacement $i$ after simplification is

$$[(\omega_i^2 - \omega^2) + j\,2\,\xi_i\,\omega_i\omega]N_i = -(\hat{q}_{1i}\,m_1 + \hat{q}_{2i}\,m_2)\,Y_A \tag{17.72}$$

$$N_i = \frac{-(\hat{q}_{1i}\,m_1 + \hat{q}_{2i}\,m_2)\,Y_A}{(\omega_i^2 - \omega^2) + j\,2\,\xi_i\,\omega_i\omega} \tag{17.73}$$

The physical relative displacements are then found from

$$\bar{Z}(\omega) = \hat{Q}\,\bar{N}(\omega) = \begin{bmatrix} \hat{q}_{11} & \hat{q}_{12} \\ \hat{q}_{21} & \hat{q}_{22} \end{bmatrix}\bar{N}(\omega) \tag{17.74}$$

The physical relative displacement at degree-of-freedom $k$ is

$$Z_k = \sum_{i=1}^{2}\hat{q}_{ki}\,N_i = -Y_A\sum_{i=1}^{2}\left\{\frac{\hat{q}_{ki}(\hat{q}_{1i}\,m_1 + \hat{q}_{2i}\,m_2)}{(\omega_i^2 - \omega^2) + j\,2\,\xi_i\,\omega_i\omega}\right\} \tag{17.75}$$

The transmissibility function relating physical relative displacement to base excitation is

$$H_{rd}(\omega) = \frac{Z_k}{Y_A} = -\sum_{i=1}^{2}\left\{\frac{\hat{q}_{ki}(\hat{q}_{1i}\,m_1 + \hat{q}_{2i}\,m_2)}{(\omega_i^2 - \omega^2) + j\,2\,\xi_i\,\omega_i\omega}\right\} \tag{17.76}$$

The transmissibility function relating physical relative acceleration to base excitation is

$$H_{ra}(\omega) = \omega^2\sum_{i=1}^{2}\left\{\frac{\hat{q}_{ki}(\hat{q}_{1i}\,m_1 + \hat{q}_{2i}\,m_2)}{(\omega_i^2 - \omega^2) + j\,2\,\xi_i\,\omega_i\omega}\right\} \tag{17.77}$$

The transmissibility function relating physical absolute acceleration to base excitation is

$$H_{aa}(\omega) = 1 + \omega^2\sum_{i=1}^{2}\left\{\frac{\hat{q}_{ki}(\hat{q}_{1i}\,m_1 + \hat{q}_{2i}\,m_2)}{(\omega_i^2 - \omega^2) + j\,2\,\xi_i\,\omega_i\omega}\right\} \tag{17.78}$$

## 17.3.7 Two-DOF Response Equations, Frequency Example
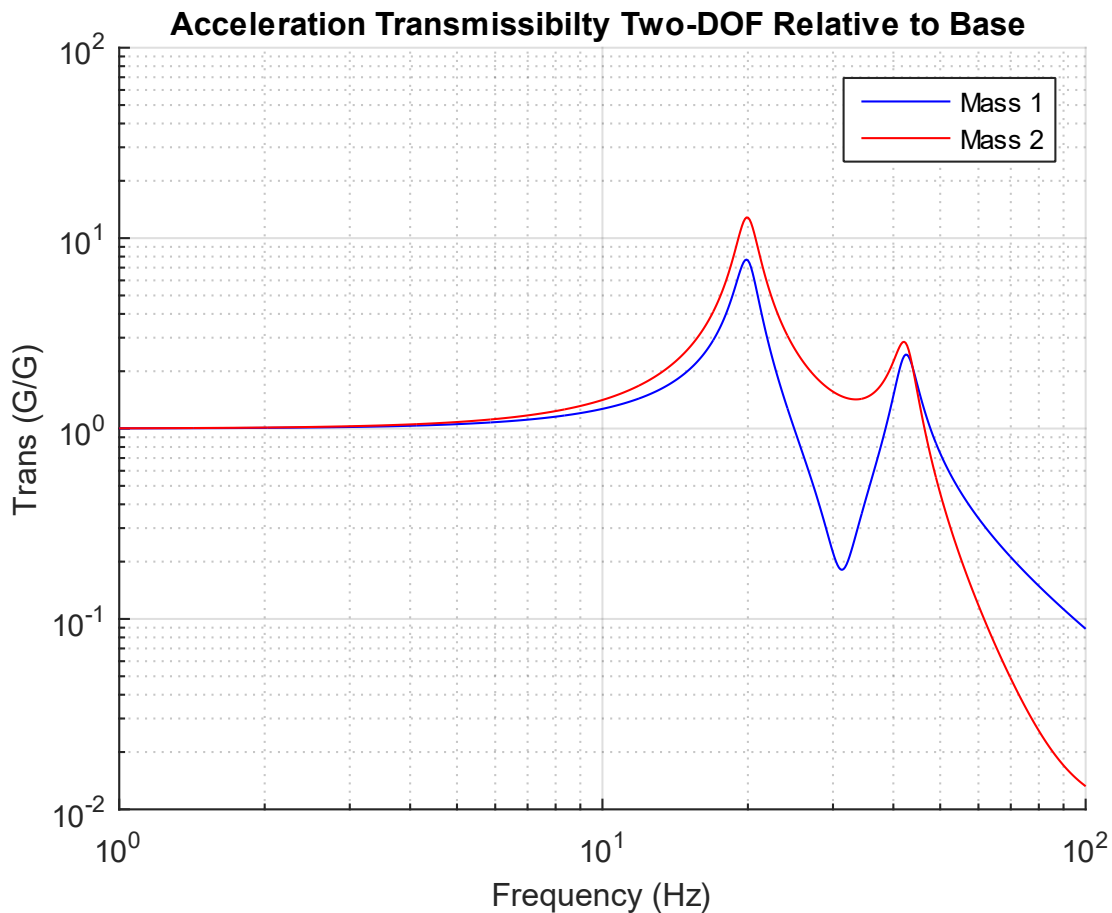


Figure 17.23.  Two-DOF System Transmissibility

The system in Figure 17.20 has the parameters previously shown in Table 9.1, with 5% damping for each mode.  Its natural frequencies are again 20.0 and 42.5 Hz.  The transmissibility function for each mass relative to the base is given in

Figure 17.23 as calculated per equation (17.78).  The damping could be determined by applying the half-power bandwidth method to the curves if this were measured data.

## 18.1 SDOF SYSTEM, ROTATING IMBALANCE



| M | total mass |
|---|---|
| m | eccentric mass representing the unbalance |
| c | viscous damping coefficient |
| k | stiffness |
| x | absolute displacement of the non-rotating mass |
| e | eccentricity radius |
| $\omega$ | rotational angular frequency |
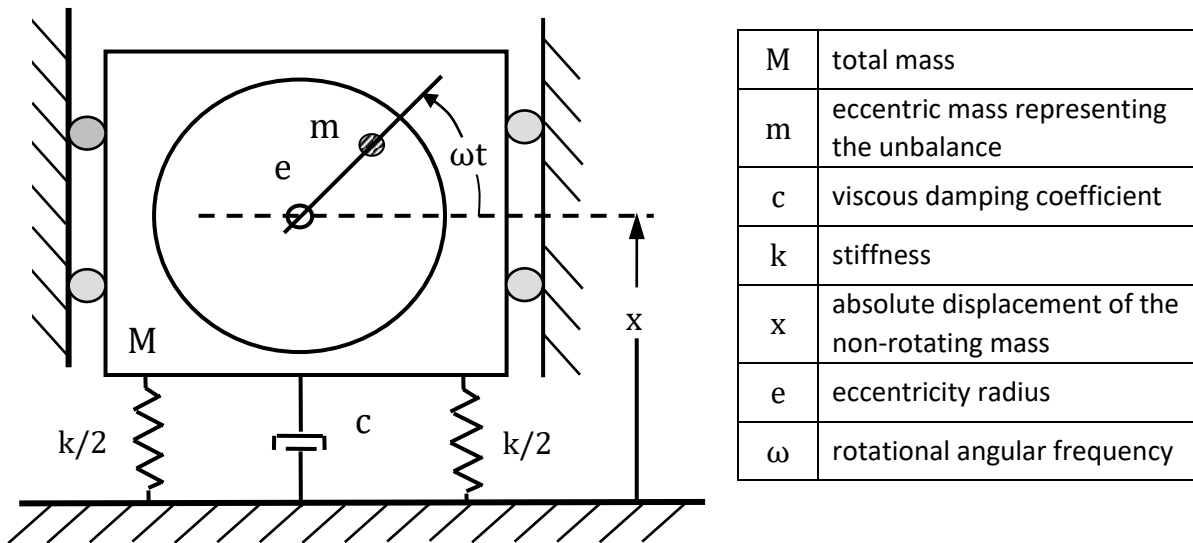
Figure 18.1.  SDOF System with Rotating Imbalance Force

Rotating unbalance in machinery is an example of an applied centripetal force.  Model a machine with rotating unbalance as a single-degree-of-freedom system.  The free body diagram is essentially the same one as in Figure 17.1 and is omitted for brevity.

The forcing function is

$$f(t) = m\omega^2 e \sin(\omega t) \qquad (18.1)$$

The equation of motion is

$$M\ddot{x} + c\dot{x} + kx = m\omega^2 e \sin(\omega t) \qquad (18.2)$$

The steady-state displacement magnitude X is

$$| X | = \frac{e\, \rho^2}{\sqrt{(1 - \rho^2)^2 + (2\xi\rho)^2}} \quad , \qquad \rho = f/f_n \qquad\qquad (18.3)$$

The phase angle is the same as equation (17.19).

Unbalance can cause several problems in machinery, such as excessive vibration, noise, wear, heat, and reduced efficiency.  Bearings are particularly vulnerable to vibration.

## 18.2  ECCENTRIC MASS VIBRATORS

Rotating imbalance can also have productive uses as shown in this section.
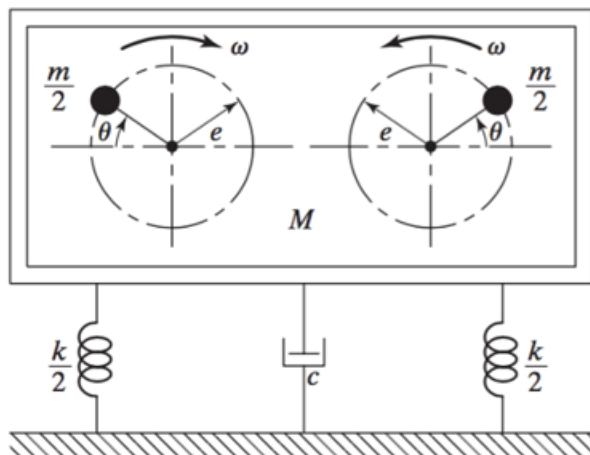


Figure 18.2.  Shaker with Two Counter-Rotating Eccentric Masses

A conceptual vibration shaker for test purposes is shown.

Both single and double mass eccentric mass shakers have been used to excite civil engineering structures for modal test purposes.  These shakers are also used for other purposes such as fruit harvesting and pile driving.

Figure 18.3.  Commercial, Tractor-Mounted Tree Trunk Shaker, Apple Harvesting

Two clamp arms from the apparatus grip the trunk.  Each arm has an eccentric mass shaker.  This method is fast but can damage the tree.

Figure 18.4.  Vibratory Hammer Suspended from Crane Boom for Pile Driving

The vibratory hammer has four internal rotating eccentric masses and is used.  The force is transmitted vertically from the vibrator, through the clamped pile, and into the ground.  The vibration reduces the friction between the pile and the ground.  The pile is driven by a combination of the vibrator's weight and the transmitted force.  This vibratory method is more efficient than the traditional impact method.

Figure 18.5.  Eccentric Mass Vibrator Mounted Externally on Hopper

The transmitted vibration allows bulk materials to flow more readily through the hopper by reducing friction between the material and the hopper's inner surfaces.  Kinetic friction is less than static friction.



Figure 18.6.  Small Vibration Motors

In addition, Eccentric Rotating Mass (ERM) motors are commonly used in cell phones, video game controllers, massage chairs, vibration exercise plates, etc.  An ERM designed to provide tactile feedback is an example of a "haptic" motor.  ERMs typically operate on DC voltage.  A typical cell phone ERM operates between 100 and 200 Hz depending on the model.

Consider users who commonly set their phones to vibration mode.  Some have developed a condition called "phantom vibration syndrome" or "vibranxiety." This is a condition whereby users mistakenly answer their phones although nobody has actually called. The condition may result from neurological or psychological factors and may be triggered by sound and vibration sources external to the phone.

Jeffrey Janata is the director of the behavioral medicine program at University Hospitals in Cleveland. He explained:

> You come armed with this template that leads you to be attentive to sensations that represent a cell phone vibrating. And it leads you to over-incorporate non-vibratory sensations and attribute them to the idea that you're receiving a phone call. When cell phone users regularly experience sensations, such as vibrating, their brains become wired to those sensations. Neurological connections that have been used or formed by the sensation of vibrating are easily activated. They're over-solidified, and similar sensations are incorporated into that template. They become a habit of the brain.

This condition results from neuroplasticity of the brain's ability to form new connections in response to changes in the environment.

Alejandro Lleras is a sensation and perception professor at the University of Illinois at Urbana-Champaign. He adds that learning to detect rings and vibrations is part of a perceptual learning process.

> When we learn to respond to a cell phone, we're setting perceptual filters so that we can pick out that (ring or vibration), even under noisy conditions. As the filter is created, it is imperfect, and false alarms will occur. Random noise is interpreted as a real signal, when in fact, it isn't.

Others claim that this syndrome is due to the user's anticipation of important calls or even wishful thinking. Christine Rosen is a senior editor of "The New Atlantis," a journal of technology and society. She speculated that phantom cell phone vibrations are psychosomatic.

> Cell phone users talk about the reassurance of being constantly connected. It signals to everyone around you that you are part of another community.  So you are not just a stranger in a public space, but you are a person who is in demand and who can demand the attention of someone else.

## 18.4  TURBINE ENGINE BLADE-OFF TEST



Figure 18.7.  Rolls Royce Engine Blade-off Test

The engine blade-off test is performed to make sure that the engine can survive a fan, compressor or turbine blade breaking off within the engine, without fragments being ejected through the outside enclosure of the engine.  This is a containment requirement.

A fan blade is deliberately detached during the test using an explosive device while the engine is running at maximum thrust. The test does not require that the engine continues to operate after the blade failure.  The resulting blade loss causes a rotating imbalance force which can induce moderate to severe structural vibration.

For an actual flight occurrence, the engine would be shut down. But there is no means of stopping the engine from continuing to rotate while there is sufficient airflow through the fan section to drive the engine.  So it would continue to "windmill" without producing any thrust. The rotating imbalance vibration would persist under these conditions.

## 19.1 INTRODUCTION

Vibration can be a cause or an effect of bearing defects or failure. The vibration generates an accompanying sound.
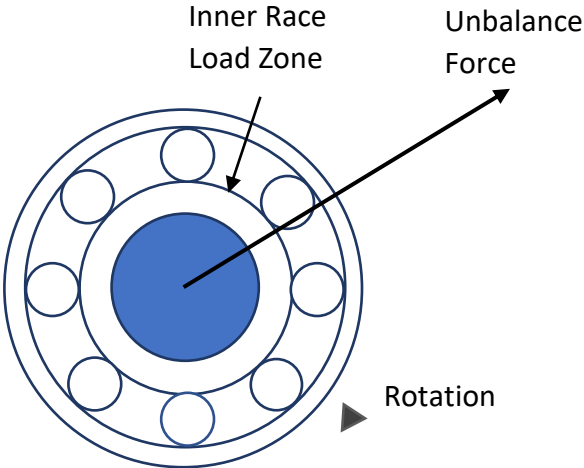


Figure 19.1. Bearing Load due to Unbalance Force
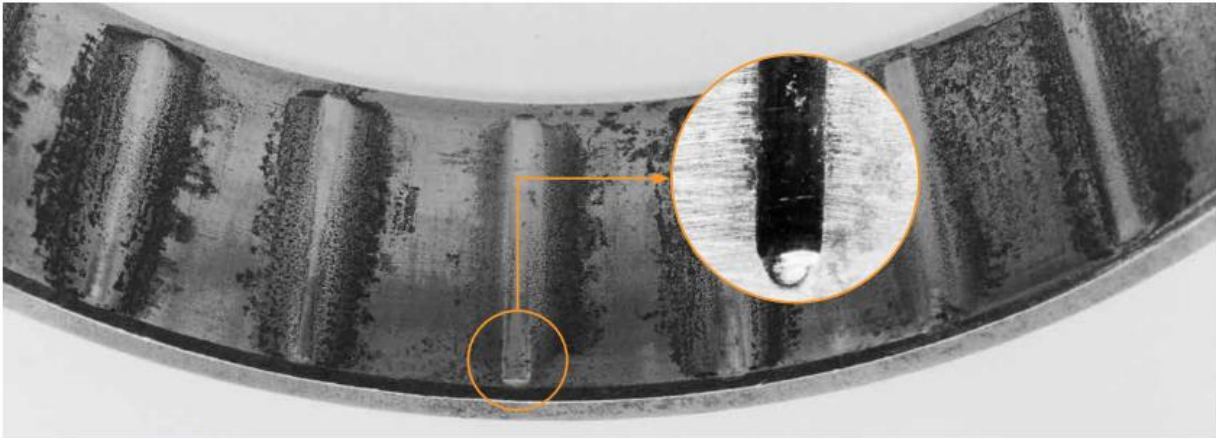


Figure 19.2. False Brinelling in Tapered Roller Bearing Outer Ring (Timken image)

Bearing vibration wears away the surface texture.  This is a form of fretting.[3]  The vibration may be along the bearing's longitudinal axis while the bearing is otherwise stationary.  The depressions caused by false brinelling will have the same spacing as the rolling elements under this "static" condition.   The incoming vibration may be due to a nearby powered machine.

Roller bearings also exhibit false brinelling when they encounter very small reversing angular oscillations (less than one complete rotation of the rolling element).    This oscillation may prevent the flow of lubrication to some spots.
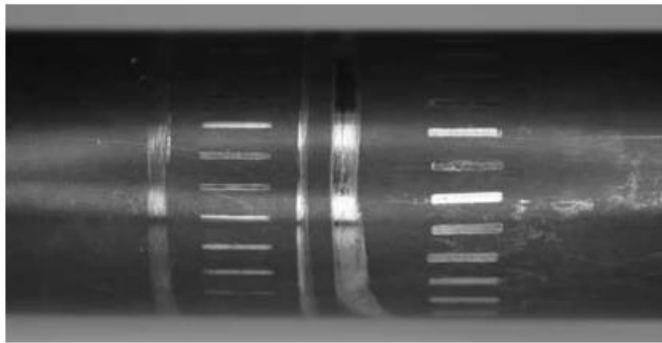


Figure 19.3.   False Brinelling on a Shaft where a Cylindrical Bearing was Mounted (Timken image)

## 19.2  BEARING DEFECTS FREQUENCY MANIFESTATION

Signs of pending bearing failure will appear in the Fourier transforms of accelerometer data as measured on the machine.  A 0.1 in/sec velocity magnitude at a specific bearing frequency indicates a significant bearing deference per Reference [28].

Bearings can fail due to improper lubrication, contamination, shaft misalignment or rotating imbalance, excessive preload or overload, heat, stray electrical currents, manufacturing defects, improper installation, etc.

The contamination may be from dirt particles, metal shavings, other foreign objects, or moisture.

High temperatures can cause the lubricant to degrade.  Overheated bearings can seize.

---

[3]  Often referred to as "fretting corrosion" because it produces fine, metallic particles that can oxidize, like rust.

Electricity passing through a bearing will result in arcing and burning. This results in pitting and cratering if currents are large enough. Even a low current can create small burns that create fluting over time wherever the current passes through. This fluting can cause melting, early spalling, and excessive noise.

Excessive load repeated over time can cause metal fatigue. Rolling elements create a wave in contacting material as they roll. This constantly rolling load puts the material in rapidly alternating tension and compression, which will cause damage over time.



Figure 19.4.  Premature Bearing Failures (Image courtesy of Evolution Magazine from SKF)

Some typical examples of premature bearing failure from (a) paper machines, (b) compressors, (c) low-speed and (d) high-speed stages of a wind turbine gearbox

A bearing failure can be associated with any of the following frequencies.

- **BPFO (Ball Pass Frequency Outer)** or outer race failing frequency. Corresponds physically to the number of balls or rollers that pass through a given point of the outer race each time the shaft makes a complete turn.

- **BPFI (Ball Pass Frequency Inner)** or inner race failing frequency. Corresponds physically to the number of balls or rollers that pass through a given point of the inner track each time the shaft makes a complete turn.

- **BSF (Ball Spin Frequency)** or rolling element failing frequency. Corresponds physically to the number of turns that a bearing ball or roller makes each time the shaft makes a complete turn.  A defect on a rolling element will generate a frequency at 2x BSF.

- **FTF (Fundamental Train Frequency)** or cage failing frequency. Corresponds physically to the number of turns that makes the bearing cage each time the shaft makes a complete turn.



$$P_D = \frac{D_1 + D_2}{2}$$

$$N_B = \text{Number of balls}$$

$$\beta = \text{Contact angle}$$

$$\text{BPFO} = \text{RPM}\frac{N_B}{2}\left(1 - \frac{B_D}{P_D}\cos(\beta)\right) \qquad \text{BPFI} = \text{RPM}\frac{N_B}{2}\left(1 + \frac{B_D}{P_D}\cos(\beta)\right)$$

$$\text{BSF} = \text{RPM}\frac{P_D}{B_D}\left[1 - \left(\frac{B_D}{P_D}\cos(\beta)\right)^2\right] \qquad \text{FTF} = \text{RPM}\frac{1}{2}\left(1 - \frac{B_D}{P_D}\cos(\beta)\right)$$
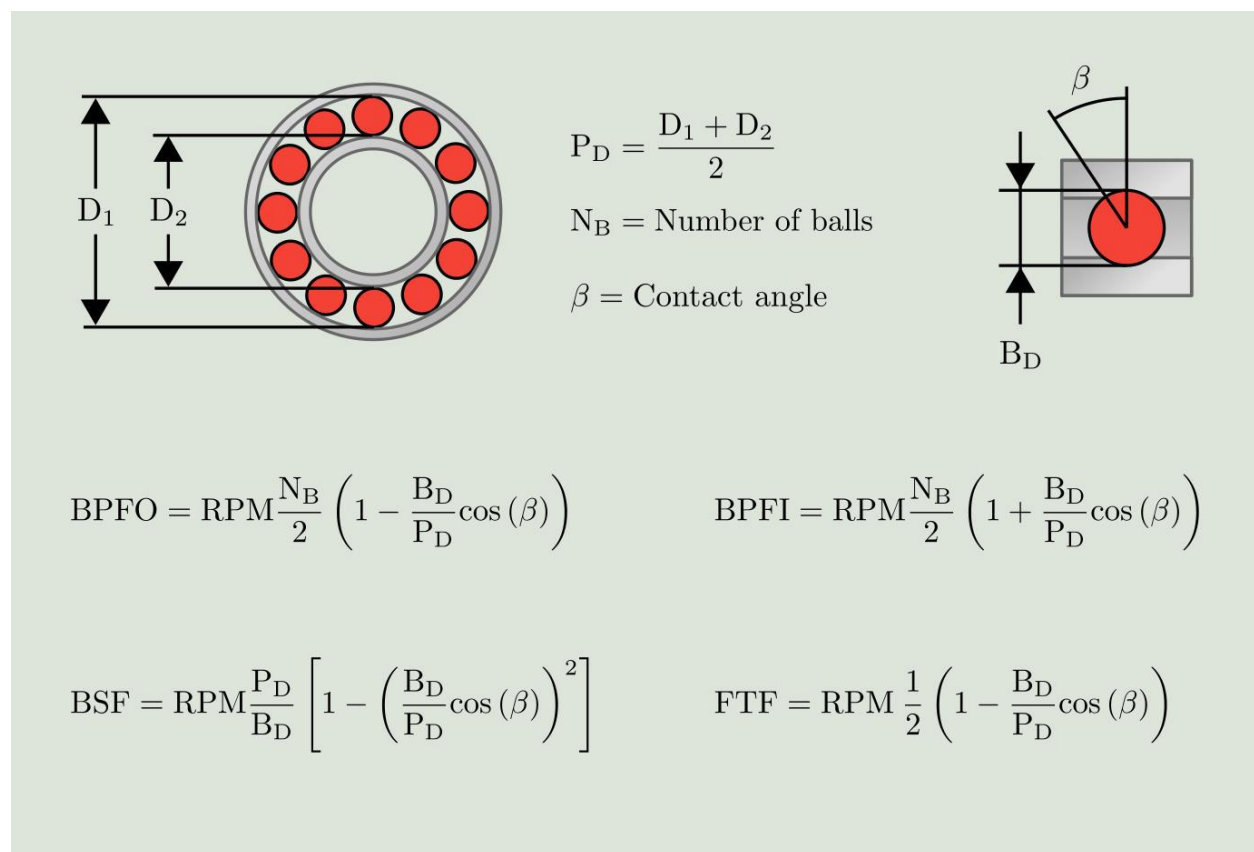
Figure 19.5.  Bearing Frequencies (Power-MI image)

In cases where the bearing physical parameters are unknown, empirical formulas are available to determine the failing frequencies of the bearing races and the cage as a function of the number of rolling elements and the rotating speed:

$$BPFO = 0.4 \times N_B \times RPM \qquad\qquad (19.1)$$

$$BPFI = 0.6 \times N_B \times RPM \qquad\qquad (19.2)$$

$$FTF = 0.4 \times RPM \qquad\qquad (19.3)$$

$N_B$ is the number of balls. Most ball bearings have between 7 and 15 balls with the majority falling between 9 and 11.

The results for these variables can be divided by 60 to convert RPM to Hz.

Bearing defects may also manifest as high-frequency shock pulses in the accelerometer time history, particularly if there is metal-to-metal contact due to a lack of lubrication. Potential defects in the rolling elements or raceways include indentations, spalls, cracks, and flaking. The shock pulses could represent each ball encountering a defect in one of the raceways.

## 19.3 BEARING FAULTS, FOUR STAGES
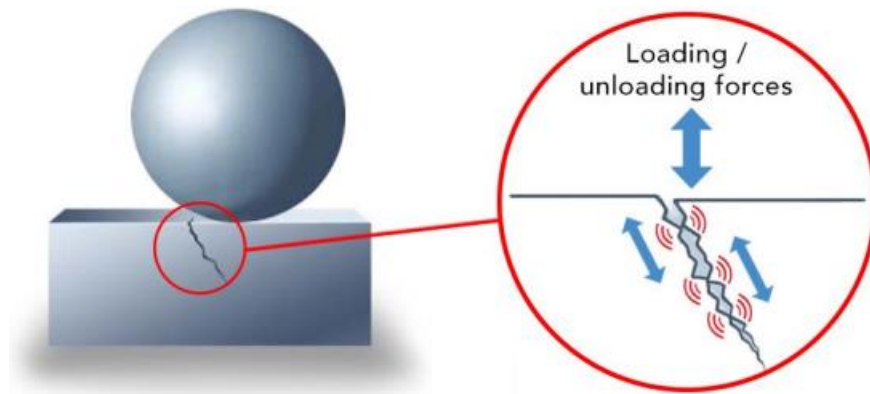


Figure 19.6.  Bearing Frequencies (SPM image)

Typical early bearing failure behavior in Stages 1 and 2 for a crack in which microscopic parts rub against each other. When the bearing passes a crack, the loading and unloading forces create friction between microscopic metal parts, which in turn emits elastic waves. This process causes the crack to grow.

Bearing faults are categorized into four stages, based on the types of frequencies produced by rolling elements impacting defects in the inner or outer races.

Table 19.1.  Fault Stages

| Stage | Characteristics |
|---|---|
| 1 | Small pits appear in the bearing race. Metal-to-metal impacts of rolling elements appear at ultrasonic frequencies in the Fourier spectrum, at 20 to 60 kHz. |
| 2 | Defects start to ring at the bearing's natural frequencies. This generally occurs between 500 and 2000 Hz. These natural frequencies may be resonances of either bearing support structures or components of the bearings themselves such as races or rolling elements. Sideband frequencies also start to appear above and below these frequencies.  A magnetically mounted accelerometer's natural frequency may be excited into resonance. <br><br> Repair should be scheduled for critical machines at this stage. |
| 3 | Levels increase at bearing defect frequencies and harmonics appear on the spectrum. As this stage progresses, defect frequency harmonics and sidebands increase. If the bearing is removed, defects can be clearly seen in the raceways. Bearings at this stage should be replaced both in critical and non-critical machinery at this stage. |
| 4 | The noise floor is raised at all frequencies, creating a random, broadband spectrum. Amplitudes of both high-frequency noise floor and high-frequency spectral peaks may decrease at some point.  In some cases, the spectral peaks will fall below the broadband noise floor.  These are signs that the bearing is about to fail. |

# 20 SINE SWEEP TESTING, SHAKER TABLE

## 20.1 SINE SWEEP INTRODUCTION
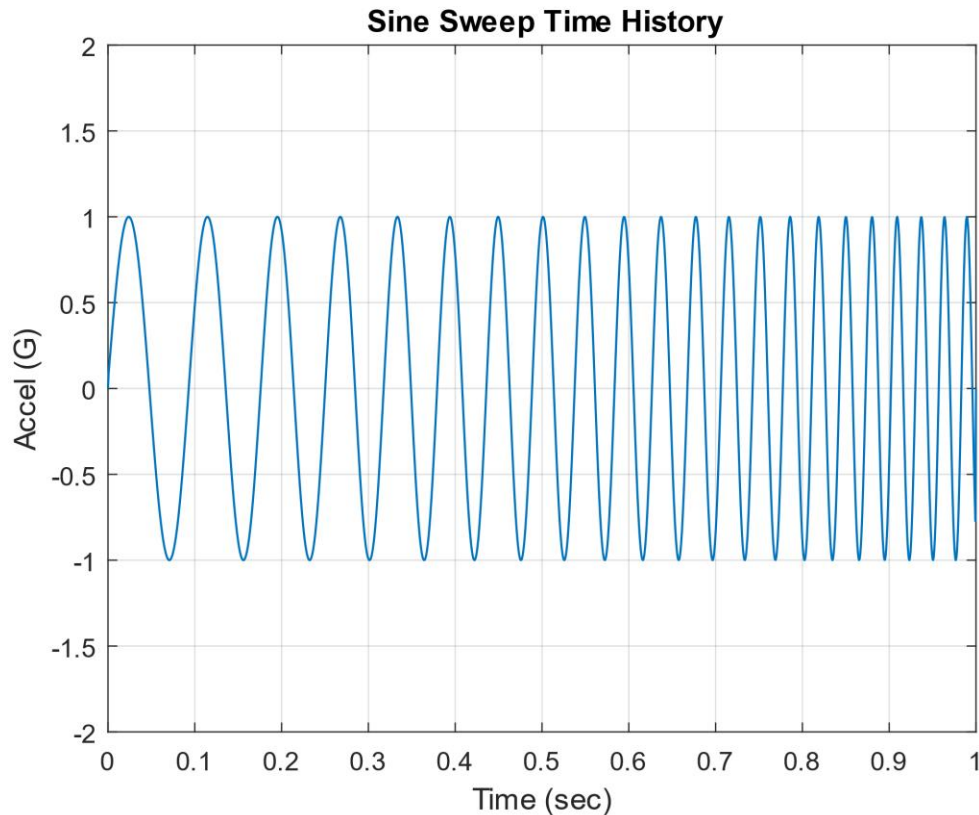


**Figure 20.1.** Sample Sine Sweep Time History with Very Brief Duration for Educational Purposes Only

Structures and components may be mounted on shaker tables, similar to those in Figure 6.9 and Figure 6.10, and subject to sine sweep base excitation (see Section 32). The essence of a sine sweep test is that the base excitation input consists of a single frequency at any given time. The frequency itself, however, varies with time. The sine sweep test may begin at a low frequency and then sweep to a high frequency, or vice-versa. Some specifications require several cycles, where one cycle is defined as from low to high frequency and then from high back to low frequency.

The specification might require either a linear or a logarithmic sweep rate. The sweep will spend greater time at the lower frequency end if the sweep is logarithmic. The example in

Figure 20.1 had a logarithmic sweep rate and a constant amplitude. Nevertheless, the specification might require that the amplitude vary with frequency.

Some potential shaker sine sweep test objectives are

1. Identify natural frequencies and amplification factors or damping ratios
2. Perform sine sweep before and after random vibration test to determine if any parts loosened, etc.
3. Check for linearity of stiffness and damping by varying the input amplitude
4. Workmanship screen for defective parts and solder joints
5. Represent an actual environment such as a rocket motor oscillation
6. NASA/GSFC typically uses sine sweep vibration for spacecraft testing
7. NASA-STD-7002 requires 5 to 50 Hz sine sweep for payloads with amplitude 1.25 times the flight limit load and sweep rate of 4 octaves/min

RTCA DO-160F, Environmental Conditions and Test Procedures for Airborne Equipment, requires a sine sweep before and after a random vibration PSD test. The instructions are to perform a 0.5 G peak sinusoidal scan from 10 to 2000 Hz at a sweep rate not exceeding 1.0 octave/min to determine natural frequencies and amplification factors from response accelerometers. Shifts in natural frequencies may indicate damage.

## 20.2 SINE SWEEP TIME DOMAIN EQUATIONS

### 20.2.1 Linear Sweep Rate

The normalized amplitude function for a linear sweep is

$$Y(t) = \sin\left\{\pi\left[(f_2 - f_1)\left(\frac{t}{T}\right) + f_1\right]\right\}$$

(20.1)

The test duration is $T$. The starting and ending frequencies are $f_1$ and $f_2$, respectively.

## 20.2.2 Logarithmic Sweep Rate

The normalized amplitude function for a logarithmic sweep is

$$Y(t) = \sin\left\{2\pi\left[\frac{f_1\left(-1+2^{Rt}\right)}{R\ln(2)}\right]\right\}$$
(20.2)

The sweep rate in octaves per time is R. Recall the octave formula in Section 8.5. A typical sweep rate is 1 octave/minute for sine sweep tests intended for natural frequency identification.

## 20.2.3 Sweep Type Comparison
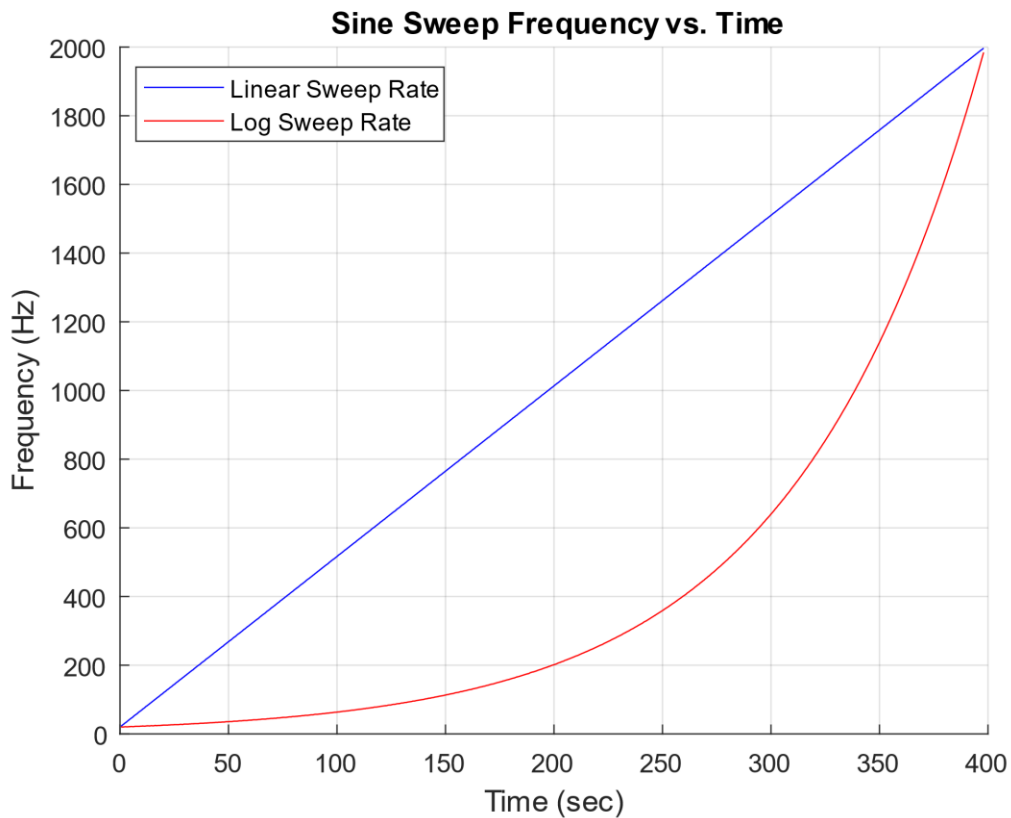


Figure 20.2.  Sweep Rate Comparison Example

A comparison of the frequency-time variation for two sweep rate types is shown in Figure 20.2. The sweeps were performed over the frequency domain from 20 to 2000 Hz over a 400-second duration. This is equivalent to a rate of 1 octave/minute for the logarithmic sweep.

## 20.3  SINE SWEEP SPECIFICATION EXAMPLE

A vendor has a product that must withstand sinusoidal vibration with an amplitude of 12 G, over the frequency domain from 10 Hz to 2000 Hz, with a logarithmic sweep rate.

The shaker table has a displacement limit of 1.0-inch peak-to-peak, or 0.5-inch zero-to-peak. Recall that the displacement limit is a constraint at low frequencies. How should the test be specified? The answer is to use a specification with two amplitude segments as shown in Figure 20.3. The first segment is a constant displacement ramp, 0.5-inch zero-to-peak. The second segment is a constant acceleration plateau at 12 G.
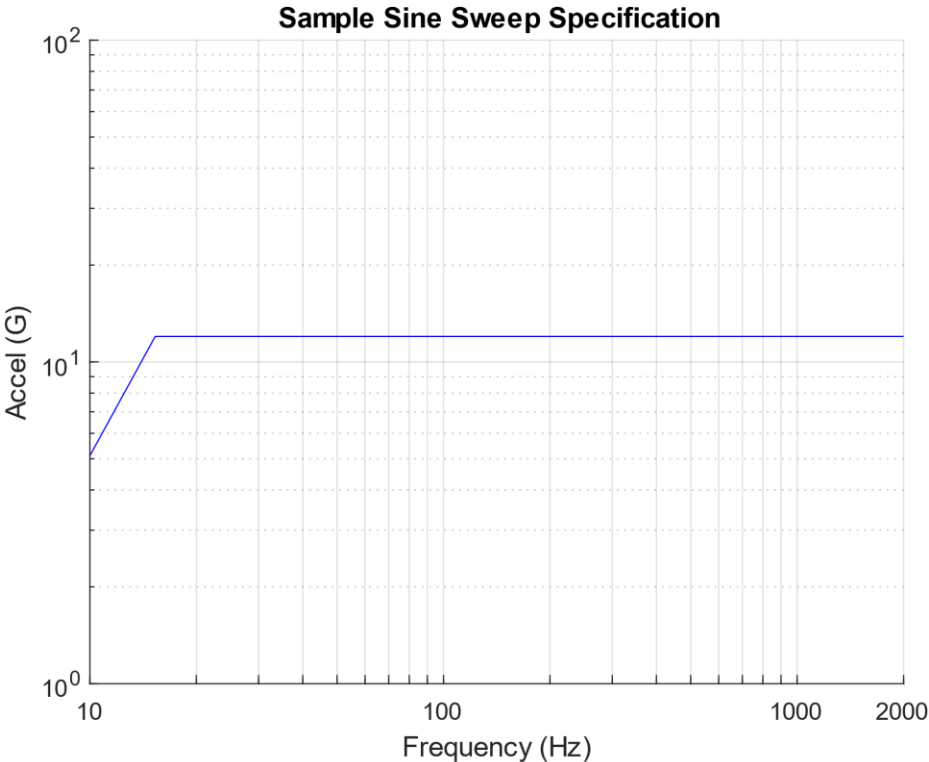


Figure 20.3.  Sample Sine Sweep Specification

The cross-over frequency is calculated from the square root of the ratio of the peak acceleration to the peak displacement. The respective peaks should be in zero-to-peak format.

$$f_{cross} = \frac{1}{2\pi} \sqrt{\frac{\ddot{X}_{peak}}{X_{peak}}} \qquad (20.3)$$

The cross-over frequency for the specification in Figure 11.2 is

$$f_{cross} = \frac{1}{2\pi} \sqrt{\frac{12\ G\ \left(386\ \frac{in/sec^2}{G}\right)}{0.5\ in}} = 15.3\ Hz \qquad (20.4)$$

This is the frequency at which the 12 G acceleration corresponds to a 0.5 in zero-to-peak displacement. It is the knee frequency in Figure 20.3.

## 20.4 SINE SWEEP INPUT & RESPONSE EXAMPLE, SDOF SYSTEM

The SDOF system in Figure 17.14 has a natural frequency of 40 Hz and an amplification factor of Q=10. It is subjected to a base input of 1 G from 10 to 80 Hz, with a logarithmic rate of 1 octave/min. The input and response time histories are shown in Figure 20.4. The peak response is 10 times the peak input acceleration. This corresponds to Q=10, but this is the special of an SDOF system excited into resonance. A better method for damping identification is the half-power bandwidth method, which is particularly needed for multi-degree-of-freedom and continuous systems due to modal gain factors.

A transmissibility function can be made relating the response to the input in the frequency domain. This is done by tracking the frequency in terms of the zero-crossing rate. The result is shown in Figure 20.5 along with the half-power bandwidth damping calculation.

Each of the data points in Figure 20.5 is an approximation constrained by the resolution and plot cursor limitations. The points at 37.85 and 41.91 Hz are each half-power points, 3 dB less than the resonant peak. The amplification factor is the frequency difference between the half-power points divided by the center frequency.

$$Q = \frac{f}{\Delta f} = \frac{40.05\ Hz}{(41.91 - 37.85)\ Hz} = 9.86 \approx 10 \qquad (20.5)$$

Recall that Q=10 corresponds to 5% damping.
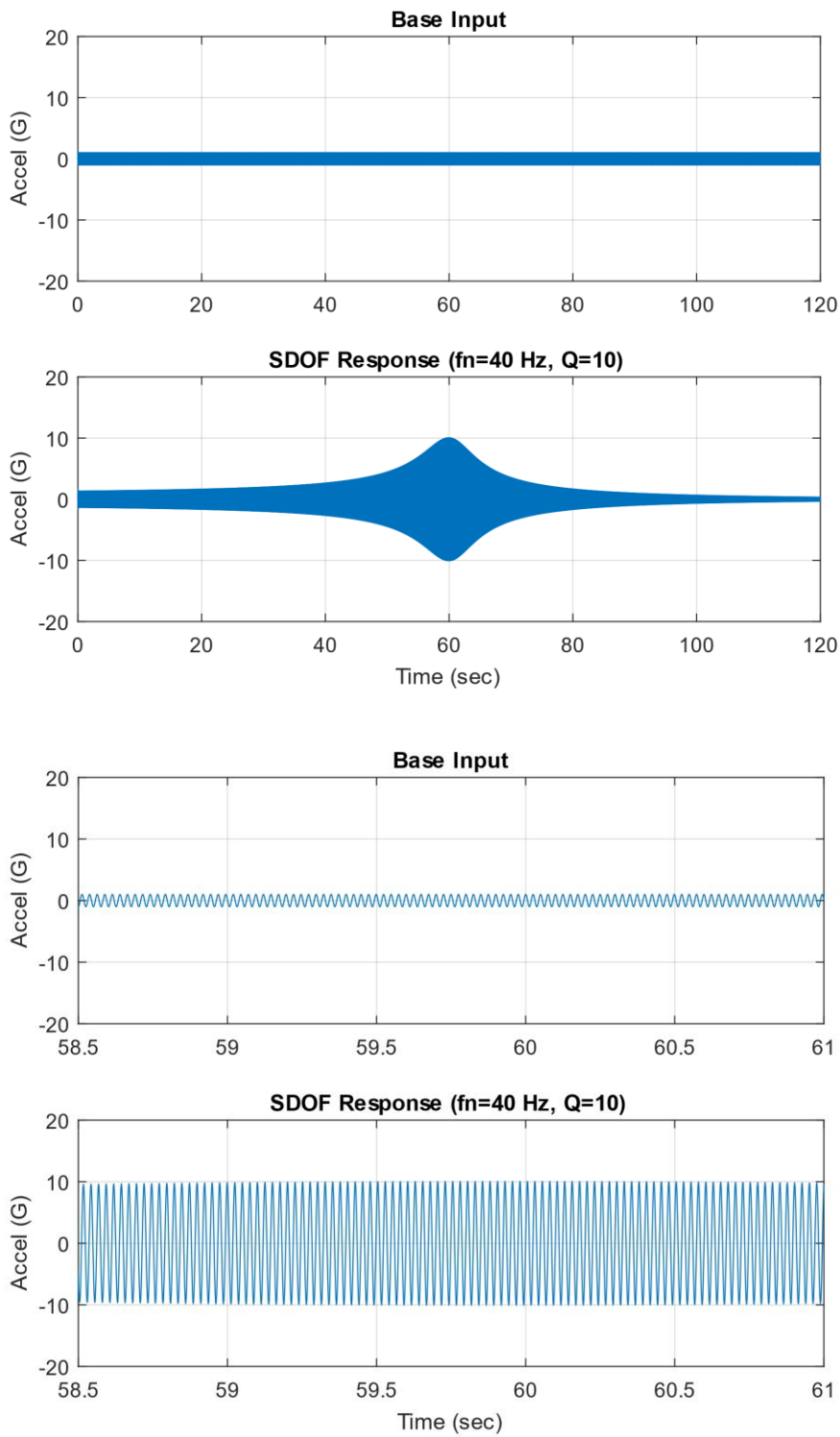
Figure 20.4.  Sine Sweep Input & Response, Total Duration & Close-up Views
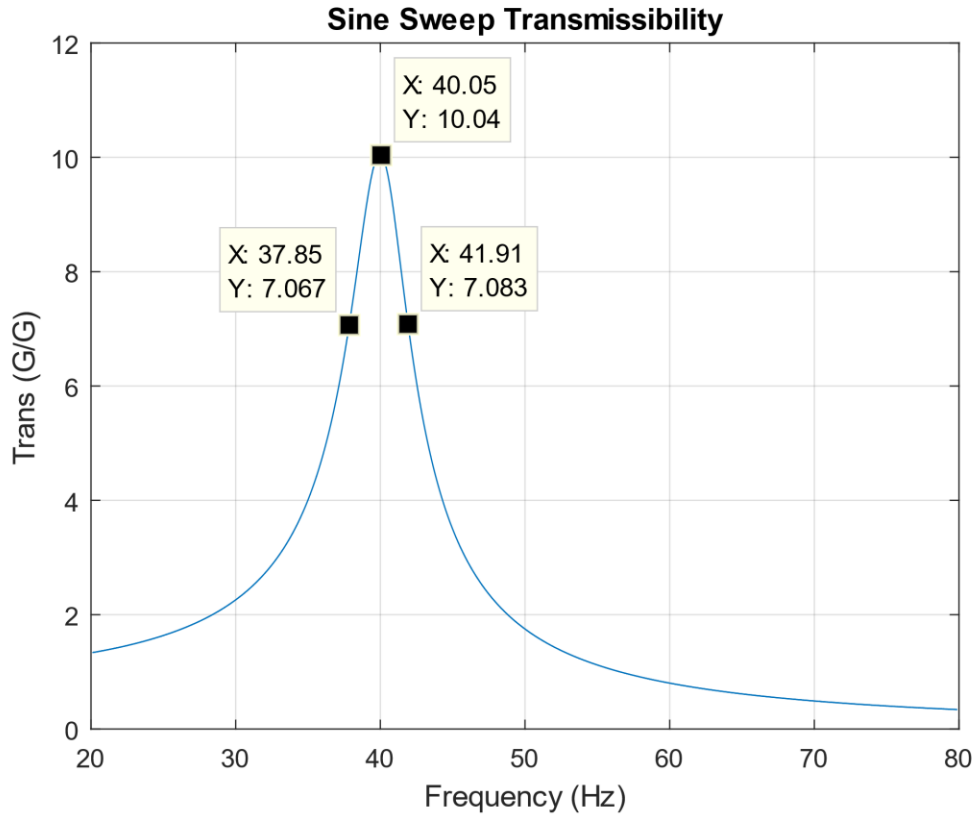
Figure 20.5.  SDOF Transmissibility Function from Input & Response Time Histories

## 20.5  SINE SWEEP INPUT & RESPONSE EXAMPLE, CONTINUOUS BEAM
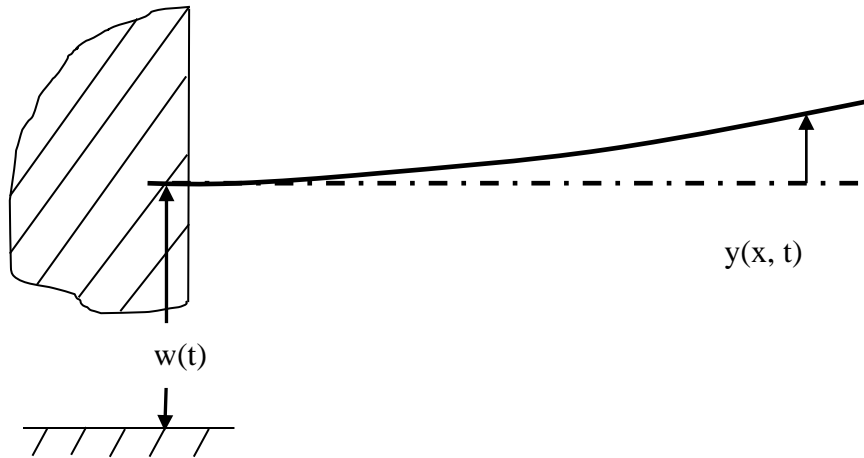


Figure 20.6.  Cantilever Beam, Base Excitation

Table 20.1.  Cantilever Beam Parameters

| Material | Aluminum |
|---|---|
| Length | 24 inch |
| Cross-section | Circular, 1-inch diameter |
| Area Moment of Inertia | 0.04909 in^4 |
| Elastic Modulus | 1.0e+07 lbf/in^2 |
| Mass/Length | 0.0785 lbm/in (2.035e-04 lbf sec^2/in^2) |
| Amplification Factor | Q=10 for all modes |

Consider the cantilever beam in Figure 20.6 with the properties in Table 20.1.  The fundamental frequency of the cantilever beam using the formula in Table 12.3.

$$f_1 = \frac{1}{2\pi} \left[ \frac{3.5156}{(24 \text{ in})^2} \right] \sqrt{\frac{(1.0e + 07 \text{ lbf/in}^2)(0.04909 \text{ in}^4)}{2.035e - 04 \text{ lbf sec}^2/\text{in}^2}} = 47.7 \text{ Hz} \qquad (20.6)$$

The first four natural frequencies and their associated parameters are shown in the following table.

Table 20.2.  Cantilever Beam Modal Parameters

| Mode | Natural Frequency (Hz) | Participation Factor | Modal Mass Ratio |
|------|------------------------|----------------------|------------------|
| 1 | 47.7 | 2.99E-03 | 0.646 |
| 2 | 299 | 9.20E-04 | 0.198 |
| 3 | 837 | 3.16E-04 | 0.068 |
| 4 | 1641 | 1.62E-04 | 0.035 |
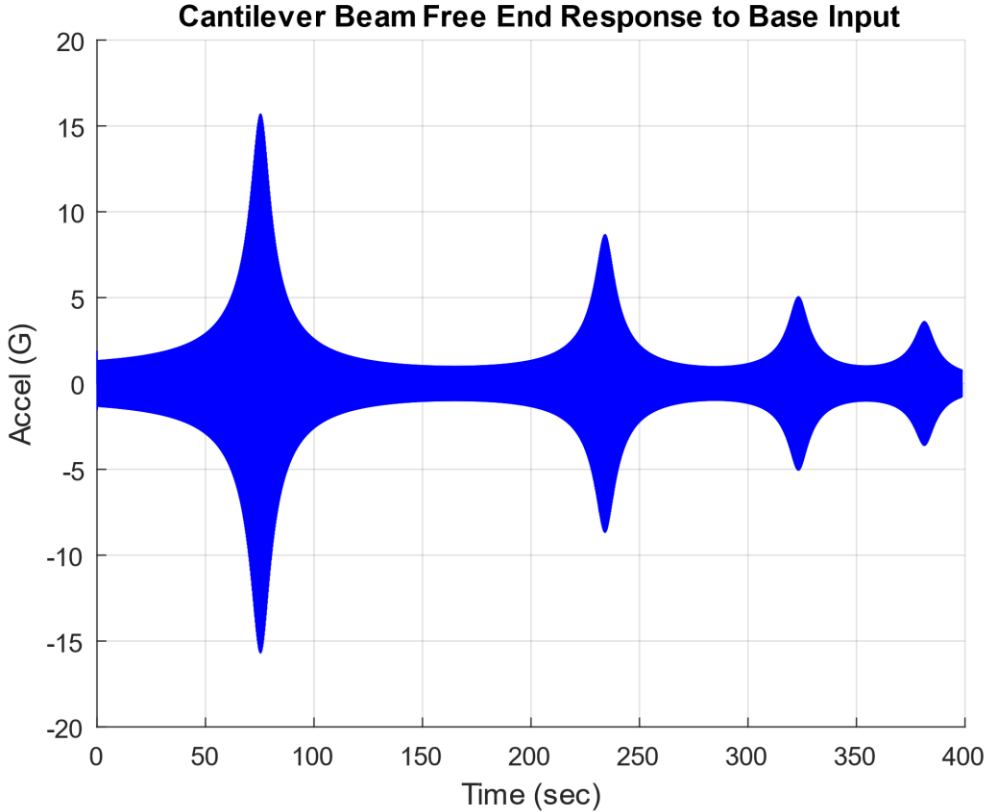


Figure 20.7.  Cantilever Beam Response Time History at Free End

The cantilever beam is subjected to a 1 G sine sweep from 20 to 2000 Hz at a logarithmic rate of 1 octave/minute. The acceleration response is shown in Figure 20.7, as calculated using Reference [29]. The corresponding transmissibility function is shown in the following figure.



**Cantilever Beam Free End Response to Base Input**
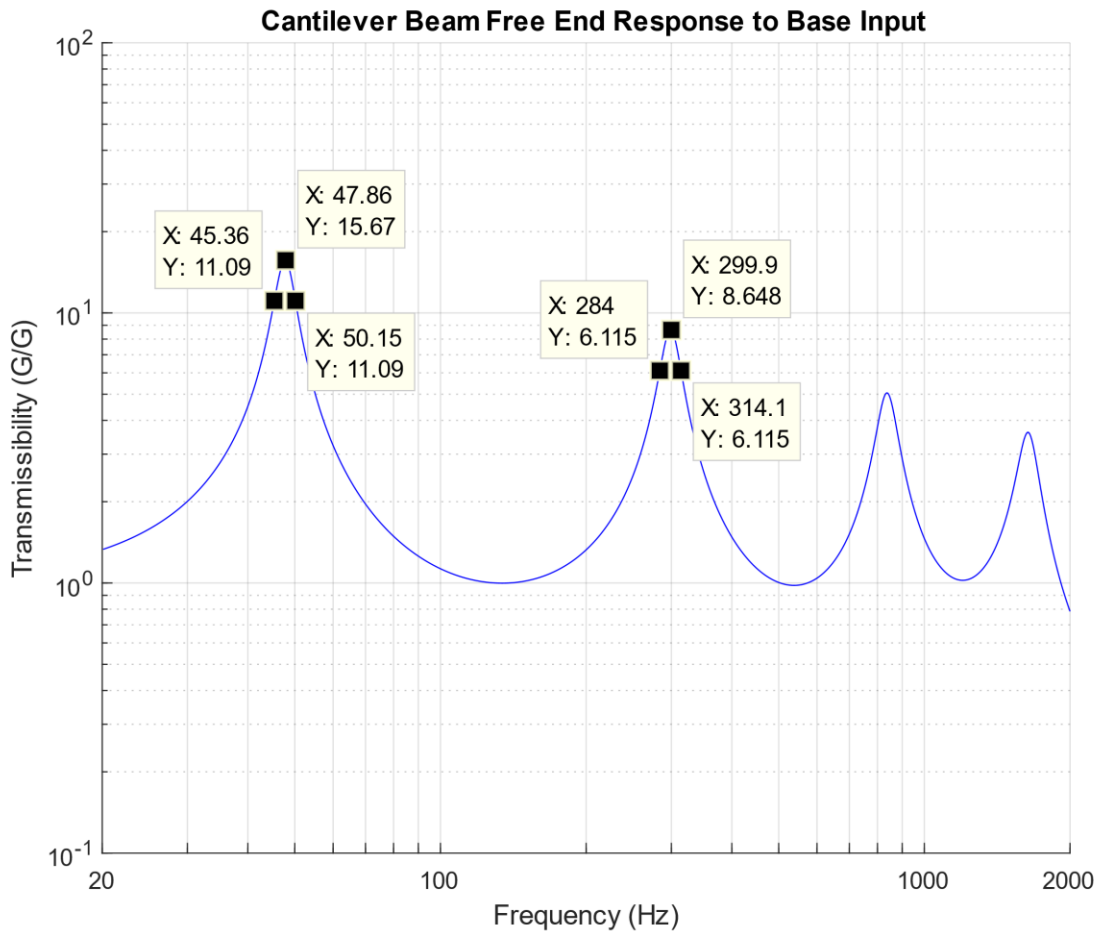
Figure 20.8. Cantilever Beam Transmissibility at Free End

Again, each of the modes had an amplification factor of 10, but each of the four peaks in Figure 20.8 has an amplitude other than 10. The peaks depend on both the amplification factor and the mode shape parameters. Nevertheless, the half-power bandwidth method can be used to extract the proper amplification values as shown for the first and second modes in the following equations.

The amplification factor for the first bending mode is

$$Q = \frac{f}{\Delta f} = \frac{47.86 \text{ Hz}}{(50.15 - 45.36) \text{ Hz}} \approx 10 \tag{20.7}$$

The amplification factor for the second bending mode is

$$Q = \frac{f}{\Delta f} = \frac{299.9 \text{ Hz}}{(314.1 - 284) \text{ Hz}} \approx 10 \tag{20.8}$$

The half-power bandwidth calculation could be repeated for the third and fourth modes.

# 21  RANDOM VIBRATION

## 21.1  RANDOM EXCITATION SOURCES



**Flight Accelerometer Data, Suborbital Launch Vehicle**
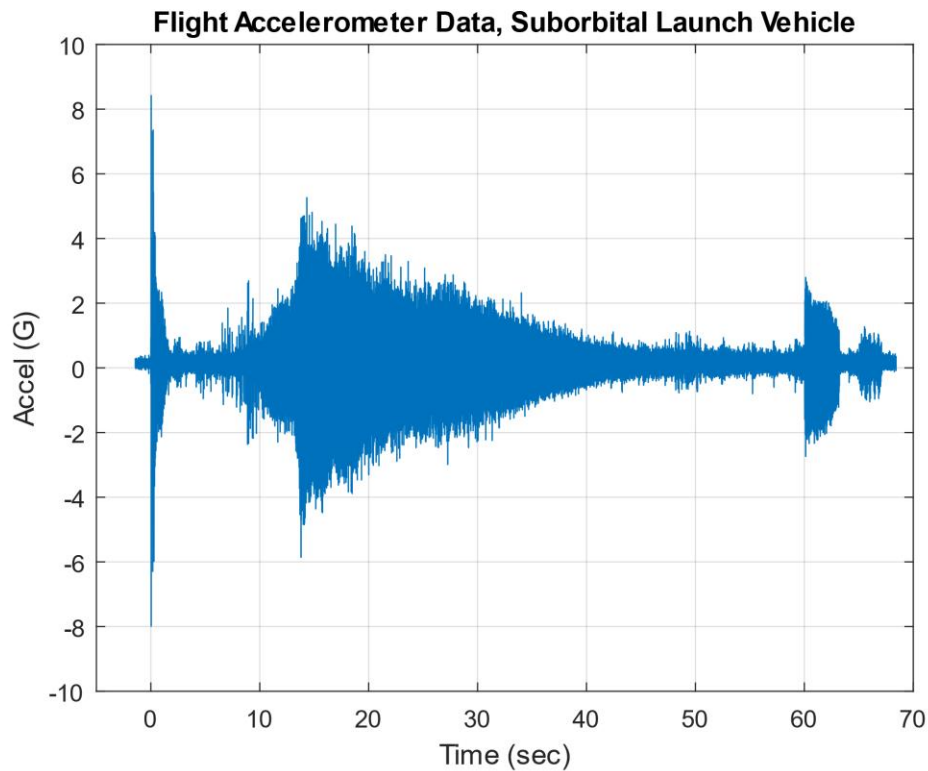
Figure 21.1.  Nonstationary Flight Accelerometer Data

The liftoff acoustic event occurs during the first two seconds.  The vibration then tapers down to a lower lever during the subsonic portion of the flight.  The envelope then increases as the vehicle accelerates through the transonic velocity and encounters its maximum dynamic pressure condition in the 10 to 20-second segment. The level then gradually decreases throughout the remainder of the first stage burn. Some transient events occur beginning at 60 seconds due to the attitude control system and other sources.

Consider the following vibration sources:

1. Turbulent airflow passing over an aircraft wing
2. Oncoming turbulent wind against a building
3. Rocket vehicle liftoff acoustics
4. Earthquake excitation of a building

One common characteristic of these examples is that the motion varies randomly with time. Thus, the amplitude cannot be expressed in terms of a "deterministic" mathematical function.

Dave Steinberg wrote [18]:

> The most obvious characteristic of random vibration is that it is nonperiodic. A knowledge of the past history of random motion is adequate to predict the probability of occurrence of various acceleration and displacement magnitudes, but it is not sufficient to predict the precise magnitude at a specific instant.

Random vibration analysis is thus a matter of probability and statistics. The parameters include: mean, standard deviation, histogram, power spectral density, etc. Stationary random vibration is where the key statistical parameters remain constant over time. The goal of most shaker table vibration tests is to apply a stationary base input to the test unit. This would be the case where the specification was a power spectral density. But real-world vibration tends to be nonstationary as shown in Figure 21.1.

## 21.2 STATISTICAL PARAMETERS

The mean value $\mu$ of the time history is calculated as

$$\mu = \frac{1}{n} \sum_{i=1}^{n} Y_i \tag{21.1}$$

where $Y_i$ is the instantaneous amplitude and $n$ is the total number of points.

The variance $\sigma^2$ of the time history is

$$\sigma^2 = \frac{1}{n} \sum_{i=1}^{n} [Y_i - \mu]^2 \tag{21.2}$$

The root-mean-square value $Y_{RMS}$ of the time history is

$$Y_{RMS} = \sqrt{\frac{1}{n}\sum_{i=1}^{n} Y_i{}^2}$$

(21.3)

A normal distribution is symmetric about its mean value, but some time histories may have skewed histograms. The skewness $\gamma$ is calculated as

$$\gamma = \frac{1}{n\sigma^3}\sum_{i=1}^{n}[Y_i - \mu]^3$$

(21.4)

Kurtosis is a measure of the "tailedness" of the histogram. The kurtosis $\kappa$ is calculated as

(21.5)

$$\kappa = \frac{1}{n\sigma^4}\sum_{i=1}^{n}[Y_i - \mu]^4$$

Sinusoidal time histories have $\kappa$ =1.5. Broadband random, stationary, Gaussian time histories have $\kappa$ =3.0. Time histories with higher kurtosis values usually have higher sigma peaks than those expected from a Gaussian distribution.

Recall

$$Y_{RMS}{}^2 = \mu^2 + \sigma^2$$

(21.6)

The RMS and standard deviation values are equal in the case of zero mean.

The crest factor is the ratio of the absolute peak divided by the RMS.

$$C = A_{peak} / A_{RMS}$$

(21.7)

The denominator on the right-hand side may be replaced by the standard deviation for the case of zero mean. The crest factor for pure sine vibration is always $\sqrt{2}$. The crest factor for random vibration is typically assumed to be 3, but higher crest factors can occur even for closed-loop stationary broadband vibration tests performed on shaker tables [30].

Now consider an SDOF system subjected to a stationary Gaussian broadband random applied force or base excitation. The expected crest factor $C_e$ per Reference [31] is

$$C_e = \sqrt{2 \ln(f_n T)} + \frac{0.5772}{\sqrt{2 \ln(f_n T)}}$$

(21.8)

The 0.5772 number is the Euler's constant to the precision shown. Note that equation (21.8) can be extended to a multi-degree-of-freedom response by replacing the natural frequency with the positive-slope zero-crossing frequency.

## 21.3 RANDOM VIBRATION HISTOGRAMS

Again, the histogram divides the time history amplitude points into bins and then counts the points in each bin. Stationary random vibration tends to have a Gaussian or Normal distribution, also known as a bell curve.[4] This function represents the distribution of the instantaneous points for the random vibration environment, which may either be broadband or narrowband. White noise is a special case of broadband vibration which is presented later in this document. The Gaussian histogram can be normalized as a probability density function such that the total area under the curve is equal to one. These functions are useful in vibration analysis for estimating peak responses and fatigue damage.
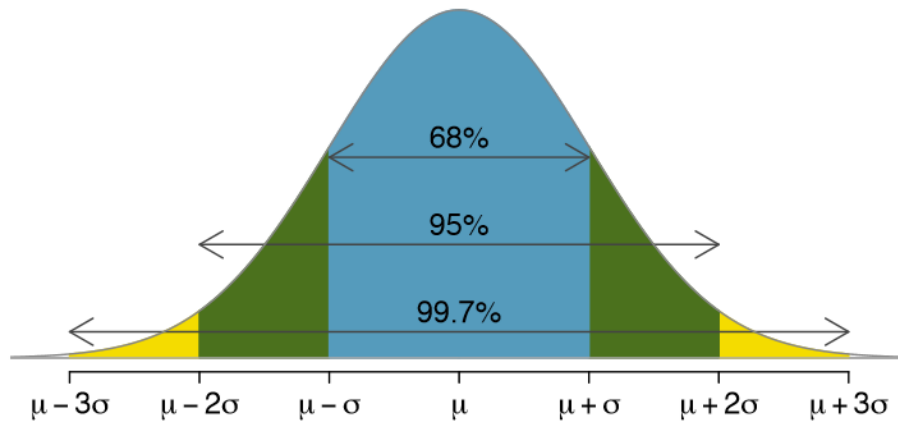


Figure 21.2. Gaussian Probability Density Function

---

[4] Stationary random vibration would have a non-Gaussian distribution if the data was skewed or had a kurtosis other than 3, for example. But non-Gaussian distributions are more common with nonstationary random vibration.

Again, the mean value is µ and the standard deviation is σ. The mean value in random vibration is usually zero, either because the vibrating object has zero net displacement or because the accelerometer signal has been AC coupled.

The Gaussian distribution equation is

$$p(x) = \frac{1}{\sqrt{2\pi\sigma^2}} \exp\left(\frac{-(x-\mu)^2}{2\sigma^2}\right)$$ (21.9)

The probability that the variable $x$ will be between any two given limits is obtained by integrating the area under the curve, which requires the gamma function. Probability examples are shown in Table 21.1 and Table 21.2. The probability of exceedance for absolute values above 3σ seems negligibly low but is still significant given that random time history may have over one million points.

Table 21.1. Gaussian Distribution, Probability of Occurrence between Limits

| Statement | Probability Ratio | Percent |
|---|---|---|
| -σ < x < +σ | 0.6827 | 68.27% |
| -2σ < x <+2σ | 0.9545 | 95.45% |
| -3σ < x < +3σ | 0.9973 | 99.73% |
| -4σ < x < +4σ | 0.999937 | 99.9937% |

Table 21.2. Gaussian Distribution, Probability of Occurrence outside Limits

| Statement | Probability Ratio | Percent |
|---|---|---|
| \| x \| > σ | 0.3173 | 31.73% |
| \| x \| > 2σ | 0.0455 | 4.55% |
| \| x \| > 3σ | 0.0027 | 0.27% |
| \| x \| > 4σ | 6.33425e-05 | 6.33425e-03% |
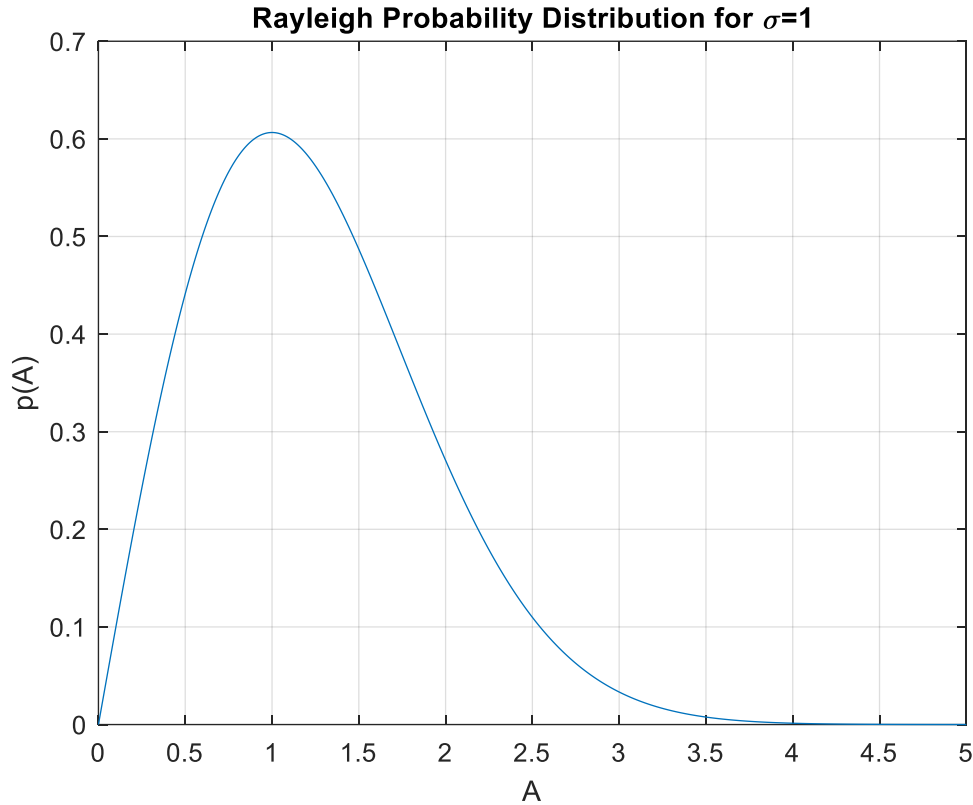
Figure 21.3. Rayleigh Distribution

The Rayleigh distribution is a continuous probability density function for a positive-valued random variable with the equation

$$p(A) = \frac{A}{\sigma^2} \exp\left(\frac{-A^2}{2\sigma^2}\right), \quad A > 0 \tag{21.10}$$

The X-axis represents a scale factor times the standard deviation, as denoted by $A$ which is used to denote the absolute value of x.

The area under the curve from zero to a given $A$ value represents the probability of occurrence. The total area under the curve is one.   The probability of exceeding the $A$ value is one minus the area as shown in Table 21.3.  The probability that a given peak will be within zero and $1\sigma$ is 39.35%.  The probability of exceeding $1\sigma$ is 60.65%.

An SDOF response time history can be reduced to a subset of points representing local peaks.  A peak occurs at a point where the initial slope has the opposite polarity of the ending slope.   A

peak can be negative or positive regardless of whether it is a local minimum or maximum.  The peak distribution will tend to be a Rayleigh distribution for random excitation, whether by an applied force or base input. Characterizing the distribution is important for fatigue analysis.


Table 21.3.  Rayleigh Distribution, Probability of Occurrence Outside Limits

| $\lambda$ | Prob [ $A > \lambda\sigma$ ] |
|:---:|:---:|
| 0.5 | 88.25 % |
| 1.0 | 60.65 % |
| 1.5 | 32.47 % |
| 2.0 | 13.53 % |
| 2.5 | 4.39 % |
| 3.0 | 1.11 % |
| 3.5 | 0.22 % |
| 4.0 | 0.034 % |


Thus, 1.11% of the peaks will be above 3$\sigma$ for a signal whose peaks follow the Rayleigh distribution.

Figure 21.4.  White Light Passing through Prism

White light passed through a prism produces a spectrum of colors.  White noise is a type of analogous random vibration. White noise and pink noise are two special cases of random vibration.

White noise is a random signal which has a constant power spectrum for a constant frequency bandwidth.  The bandwidth is normally given in units of Hertz.  White noise is analogous to white light, which is composed of a continuous spectrum of colors.  Static noise over a non-operating TV or radio station channel tends to be white noise.  In addition, Commercial white noise generators are designed to produce soothing random noise which masks household noise as a sleep aid.

Pink noise is a random signal which has a constant power spectrum for each octave band.  This noise is called pink because the low frequency or "red" end of the spectrum is emphasized.  Pink noise is used in acoustics to measure the frequency response of an audio system in a particular room.  It can thus be used to calibrate an analog graphic equalizer.  Waterfalls and ocean waves may generate pink-like noise.

## 21.5 WHITE NOISE INPUT & RESPONSE EXAMPLE
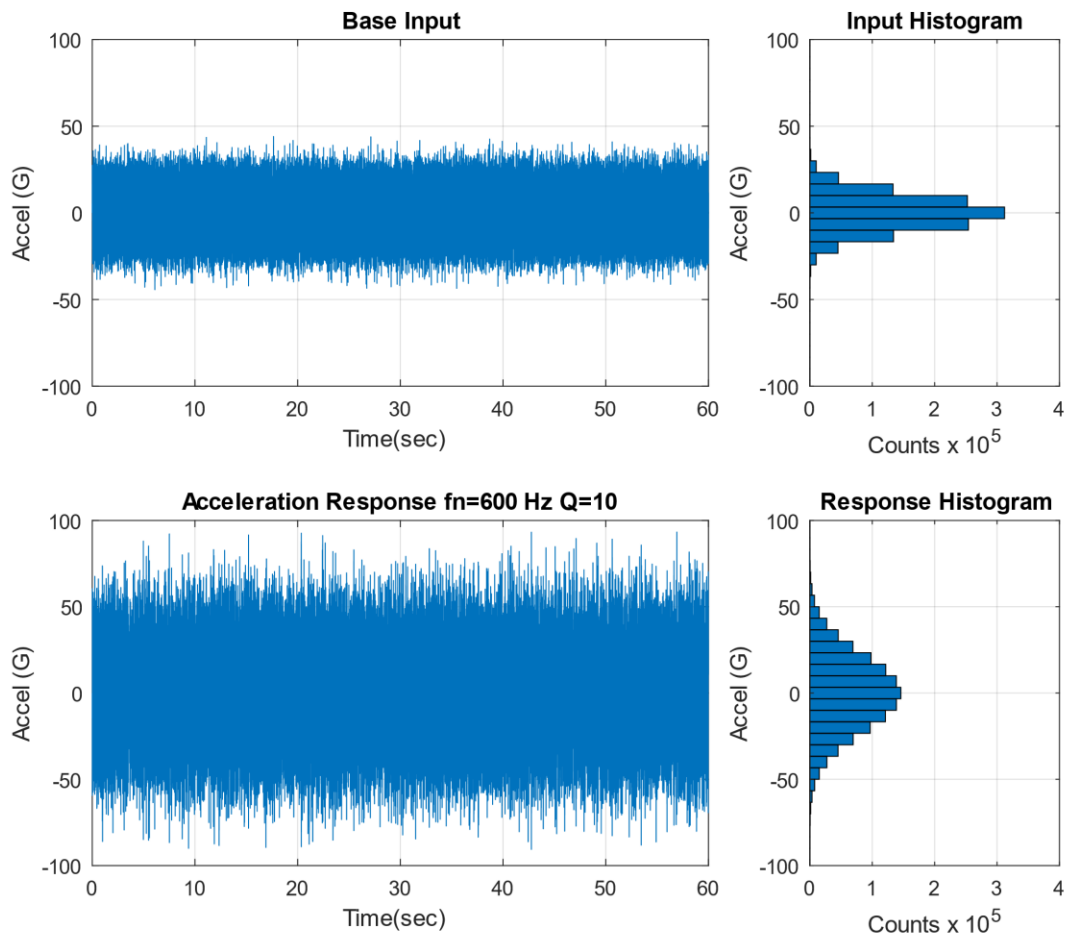


Figure 21.5.  White Noise Base Input Time History and SDOF Response with Histograms

Stationary white noise base input excitation is applied to the SDOF model in Figure 17.14.  The system has a natural frequency of 600 Hz and an amplification factor of Q equal to 10, or 5% damping.  The input time history is shown in Figure 21.5, with a Gaussian distribution and a standard deviation of 10 G.  The response is calculated using the Smallwood ramp invariant digital recursive filtering relationship [25].  The response likewise has a Gaussian distribution.
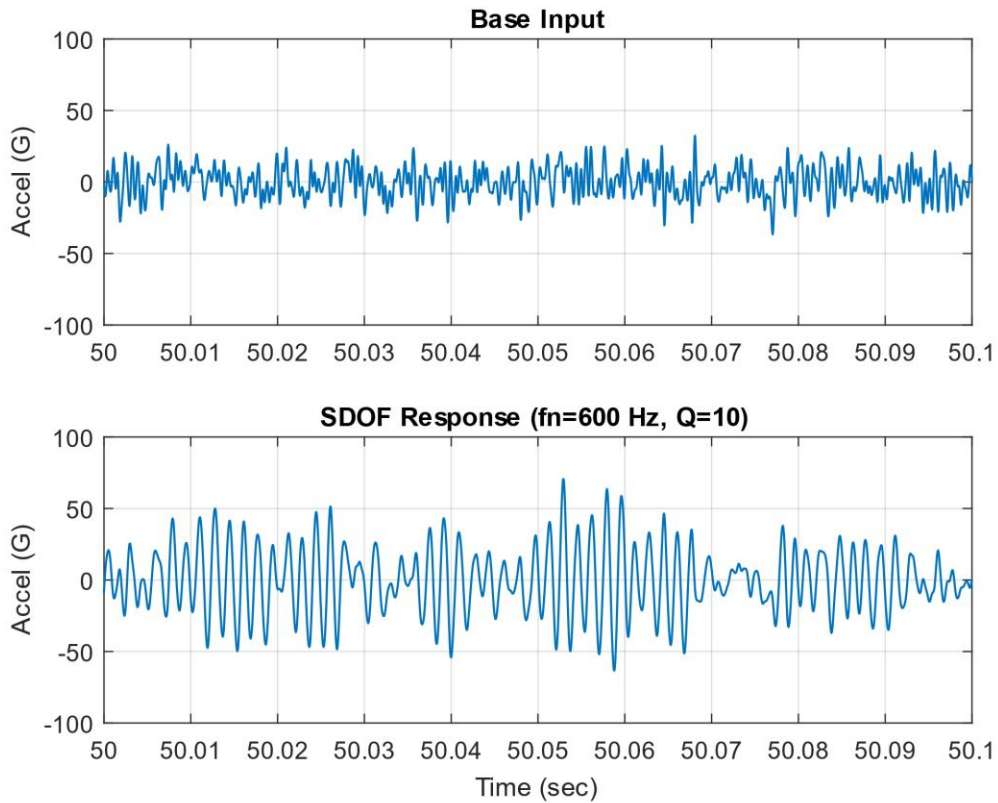
Figure 21.6.  SDOF Response to White Noise Base Input, Close-up View

Table 21.4.  SDOF Response to White Noise Statistics

| Parameter | Value | Parameter | Value |
|-----------|-------|-----------|-------|
| Mean | 0 G | Kurtosis | 3.0 |
| Std Dev | 21.8 G | Crest Factor | 4.28 |
| RMS | 21.8 G | Maximum | 93.3 G |
| Skewness | 0 | Minimum | -90.6 G |

A brief segment from the input and response is given in Figure 21.6.  The white noise input is broadband random.  The response tends to vibrate at 600 Hz natural frequency, but the amplitude envelope varies randomly with time.  The response is narrowband random.  The response statistics for the entire duration are given in Table 21.4.

The response mean is zero. The RMS and standard deviation values are thus equal per equation (17) and have a value of 21.8 G. The highest input absolute peak is 93.3 G. The ratio of the peak relative to the standard deviation is called the "crest factor," which is 4.28 in this example. This value can also be represented as 4.28σ. A common assumption is that the crest factor is 3σ, which is three times the standard deviation. But 4σ and 5σ peaks are common in stationary random vibration.
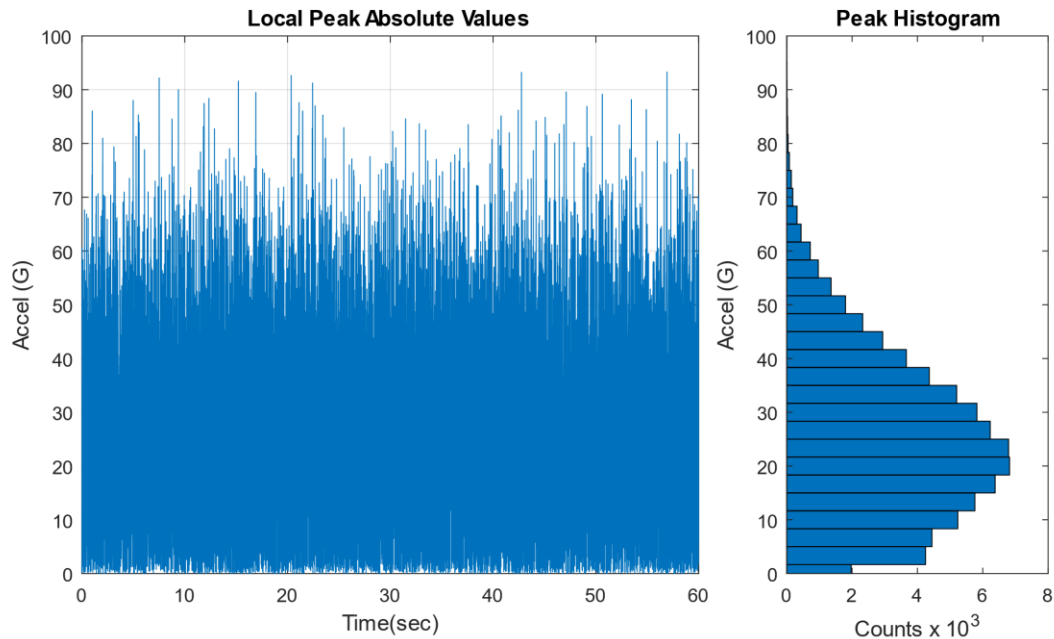


Figure 21.7. SDOF Response to White Noise, Absolute Peak Values with Histogram

The histogram of the absolute local peaks has a Rayleigh distribution.

The expected crest factor for the sample problem is

$$C_e = \sqrt{2 \ln[(600 \text{ Hz})(60 \text{ sec})]} + \frac{0.5772}{\sqrt{2 \ln[(600 \text{ Hz})(60 \text{ sec})]}} = 4.71 \qquad (21.11)$$

The crest factor for the sample problem was 4.28, which is 10% lower than the expected value.

## 21.6 CREST FACTOR STUDY

As a numerical experiment, the white noise synthesis and response calculation steps for the previous example were repeated 20,000 times. A crest factor was calculated for each trial. A histogram of the crest factor is shown in Figure 21.8. The histogram has a shape somewhat similar to a Rayleigh distribution, but further investigation is needed to properly characterize it. The crest factors ranged from 4.14 to 6.62, with a mean of 4.76. This experimental mean value was 1.1% higher than the theoretical 4.71 value. Again, stationary random vibration time histories with Gaussian distributions typically have peaks ranging from $4\sigma$ to $5\sigma$, but higher crest values may also occur. This is true both for broadband inputs and narrowband responses. Designing structures and components for $3\sigma$ vibration loads is thus insufficient, even though this is a common rule-of-thumb.
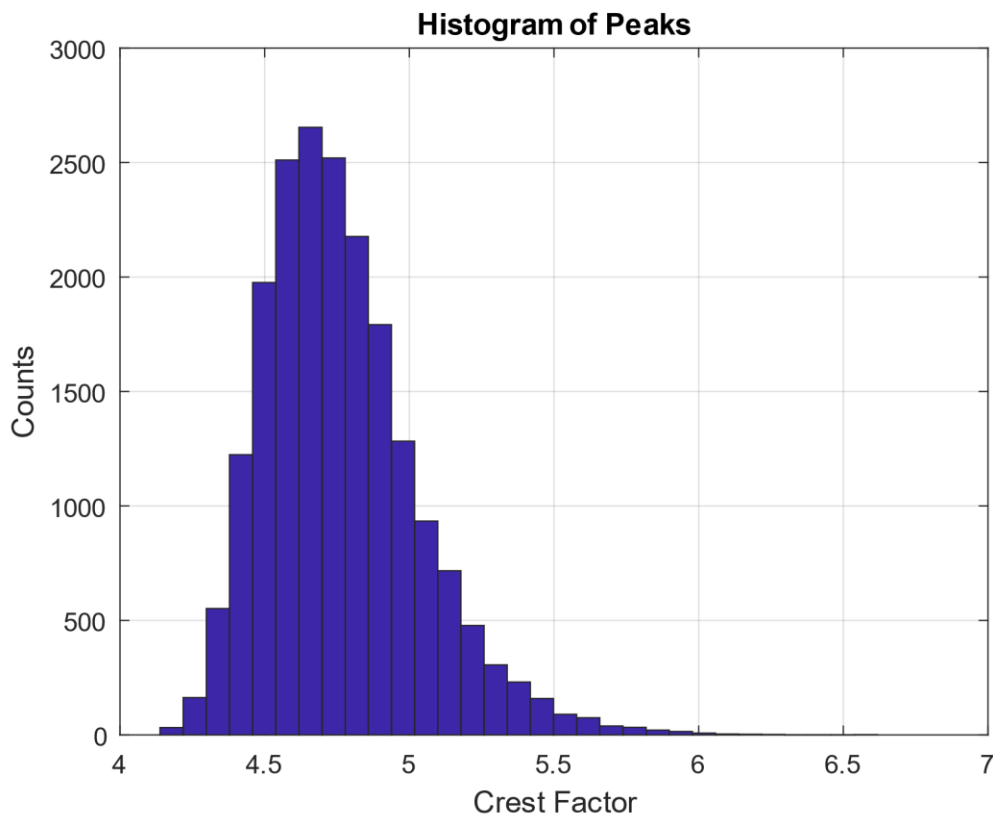


Figure 21.8. Histogram of Response Peaks for 20,000 Trials

## 21.7 EQUIVALENT STATIC LOADS FOR RANDOM VIBRATION

A particular engineering design problem is to determine the equivalent static load for equipment subjected to base excitation random vibration. The goal is to determine peak response values. The resulting peak values may be used in a quasi-static analysis, or perhaps in a fatigue calculation. The following table shows some design, analysis, and test levels in terms of the response standard deviation.

Table 21.5. Equivalent Static Loads

| Refer. | Author | Design, Analysis, Test Response Level | Qualifying Statements |
|--------|--------|---------------------------------------|------------------------|
| [32] | Himelblau, et al | 3σ | However, the response may be non-linear and non-Gaussian |
| [33] | Fackler | 3σ | 3σ is the usual assumption for the equivalent peak sinusoidal level |
| [34] | Luhrs | 3σ | Theoretically, any large acceleration may occur |
| [35] | NASA | 3σ for STS Payloads<br><br>2σ for ELV Payloads | Minimum Probability Level Requirements |
| [36] | McDonnell Douglas | 4σ | Equivalent Static Load |
| [30] | Scharton & Pankow | 5σ | Shaker test data |
| [37] | DiMaggio, Sako, Rubin | Equation (21.8) truncated to first term on right side | Rayleigh distribution |
| [31] | Ahlin | Equation (21.8) | Rayleigh distribution |

The Ahlin method Equation (21.8) is the preferred method in this document because it realistically accounts for peaks greater than 3σ depending on the product of the natural frequency and duration.

But the equivalent static load approach is questionable because static deflection shapes differ from dynamic fundamental mode shapes. Note that beam bending stress is proportional to the second derivative of the modal displacement.

Consider a continuous beam with uniform geometry and material properties. The bending moment M is

$$M = EI \frac{d^2Y}{dx^2} \qquad (21.12)$$

The Y variable is the transverse static or dynamic deflection shape in either the time or frequency domain and referenced to a particular point along the length.

The outer fiber bending stress σ from the flexure formula is

$$\sigma = \frac{M \, \hat{c}}{I} \qquad (21.13)$$

The distance from the beam's neutral axis to the outer fiber is $\hat{c}$.

Thus, any difference between the static and dynamic displacement mode shapes will be amplified as the second derivative is taken. The equivalent static stress will thus have some error. The best approach is to treat dynamic excitation as a dynamic problem.

## 21.8  NON-GAUSSIAN RANDOM VIBRATION

Stationary Gaussian random time histories can be generated in closed-loop shaker table tests. But time histories measured in the field usually depart from the Gaussian ideal.  A theoretical example is shown in **Figure 21.9**.    Nevertheless, the response of an SDOF system to a non-Gaussian random input will have some tendency to be Gaussian due to the "central limit theorem," as shown in **Figure 21.9**.

The central limit theorem in probability theory establishes that, in some situations, when independent random variables are added, their properly normalized sum tends toward a normal distribution even if the original variables themselves are not normally distributed.
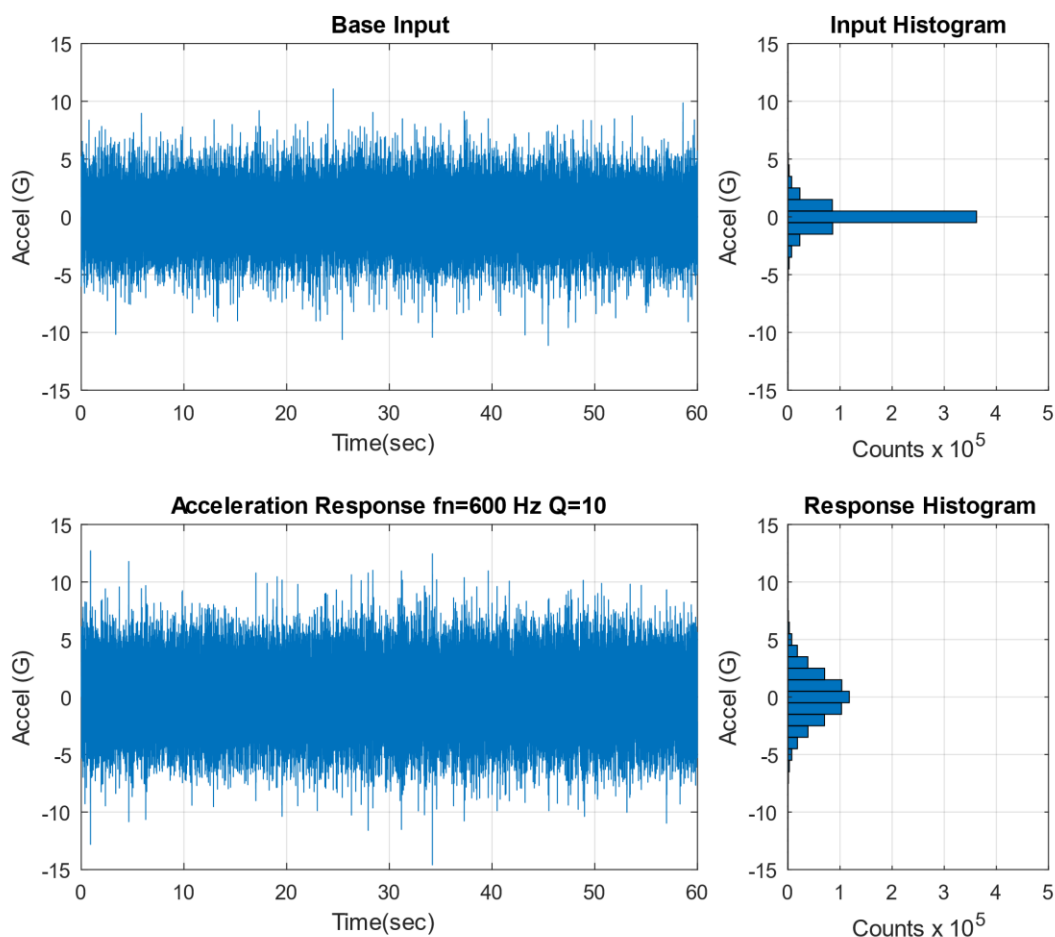


Figure 21.9.  Non-Gaussian Broadband Random Time History & Response

The base input has standard deviation=1.0, kurtosis=9.3, and crest factor=11.1.  The response statistics are shown in **Table 21.6**.

Table 21.6.  SDOF Response to Non-Gaussian Time History

| Parameter | Value | | Parameter | Value |
|-----------|-------|---|-----------|-------|
| Mean | 0 G | | Kurtosis | 3.5 |
| Std Dev | 2.12 G | | Crest Factor | 6.9 |
| RMS | 2.12 G | | Maximum | 12.7 G |
| Skewness | 0 | | Minimum | -14.6 G |

## 21.9  BENFORD'S LAW

Benford's law, also known as the Newcomb–Benford law, the law of anomalous numbers, or the first-digit law, is an observation that in many real-life sets of numerical data, the leading digit is likely to be small.[5] In sets that obey the law, the number 1 appears as the leading significant digit about 30% of the time, while 9 appears as the leading significant digit less than 5% of the time. If the digits were distributed uniformly, they would each occur about 11.1% of the time.

The occurrence frequency of the leading digit is somehow logarithmic.

Not every data set satisfies Benford's law.  Benford's law tends to be best suited to:

1. Quantitative, random data
2. Data that are measured rather than assigned
3. Ranges over orders of magnitudes
4. Not artificially restricted by minimums or maximums
5. Mixed populations
6. Larger datasets are better

As an experiment, the author generated two million points in Matlab to simulate a stationary signal with randomly-varying amplitude and with normal distribution. The mean value was zero. The standard deviation was one million.  A histogram was made of the first digit of each

---

[5]  Benford's law is used as a tool to investigate fraud in tax returns, financial reports, election results, etc.  The concept is that faked data sets would tend to have an even distribution of first digits.

absolute instantaneous amplitude point. The objective was to determine whether the first digit histogram would match the Benford pattern. The results of the normal random signal was similar to Benford but with some variation as shown in the table below.

In addition, the nonstationary flight accelerometer data from an unmanned, suborbital launch vehicle in Figure 21.1 was analyzed. The data had 453,250 points. The amplitude was multiplied by one million to achieve the desired multiple orders of magnitude effect. The nonstationary results had good agreement with Benford.

Table 21.7.  Benford's Law Applied to Random Vibration

| First Digit | Benford Histogram | Normal Random Signal Histogram | Nonstationary Flight Data Histogram |
|---|---|---|---|
| 1 | 30.1% | 36.0% | 33.7% |
| 2 | 17.6% | 12.9% | 19.2% |
| 3 | 12.5% | 8.7% | 12.1% |
| 4 | 9.7% | 8.1% | 8.4% |
| 5 | 7.9% | 7.8% | 6.6 |
| 6 | 6.7% | 7.3% | 5.7% |
| 7 | 5.8% | 6.9% | 5.1% |
| 8 | 5.1% | 6.5% | 4.7% |
| 9 | 4.6% | 6.0% | 4.5% |

Further research is needed to determine whether this Benford comparison is useful for mechanical vibration analysis.  But an informal Internet search revealed several research papers where Benford's law has been used to extract useful information from seismic signals. Meanwhile scientists studying astronomy and nature have found plentiful examples of Benford's law in their various data sets.

## 21.10  HALT/HASS TESTING WITH NON-GAUSSIAN RANDOM VIBRATION
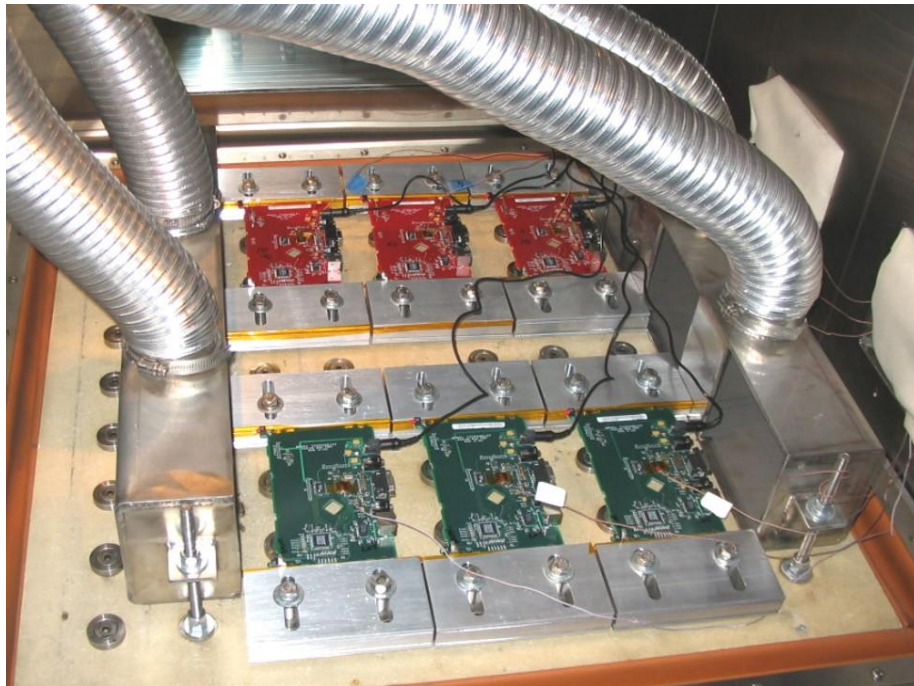


Figure 21.10.  HALT/HASS Testing of Circuit Boards, Combined Thermal Cycling and Vibration

Highly Accelerated Life Testing (HALT) is a process for the ruggedization of preproduction products.  Highly Accelerated Stress Screening (HASS) is the production screen for products once they have been characterized in HALT, typically performed on 100% of units per lot.  The random vibration environment is nonstationary, non-Gaussian vibration with high kurtosis.  The overall GRMS of the vibration is controlled, but the spectral content is uncontrolled.  The thermal cycling and vibration may be applied separately or simultaneously depending on the test phase.    Note that HALT/HASS is the offspring of the classical Environmental Stress Screening (ESS) process.

Figure 21.11.  HALT/HASS Chamber Vibration Impactors

The underside of the chamber is connected to hammer impactors which create a repetitive shock time history.
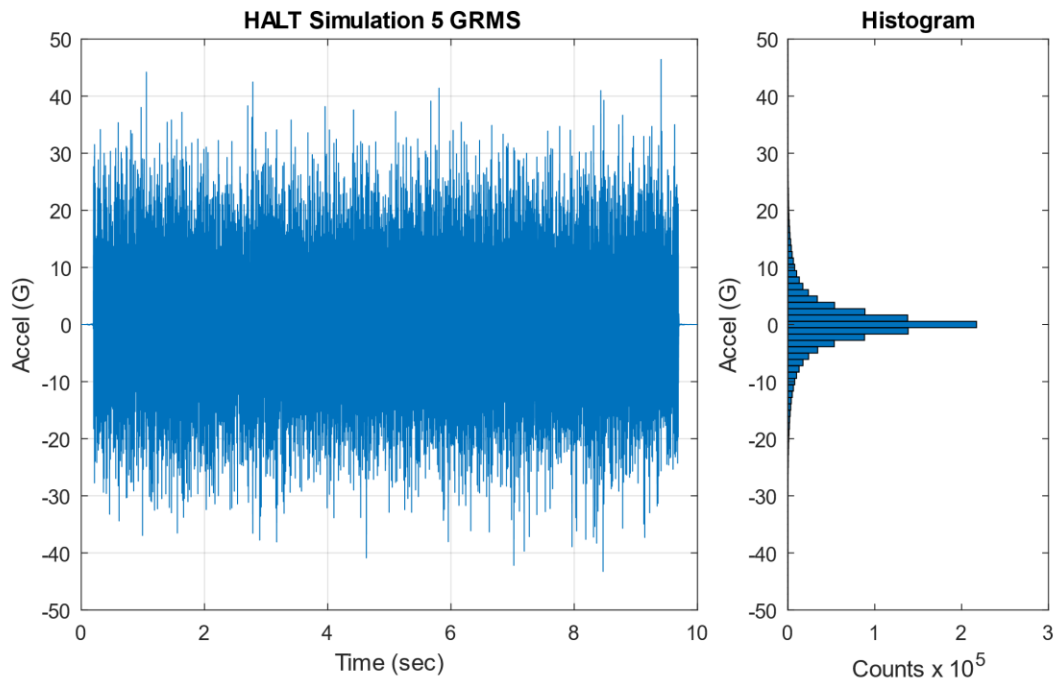
Figure 21.12.  HALT Time History Simulation with Histogram

A time history was synthesized to represent a typical HALT chamber vibration environment, as shown in Figure 21.12.  The kurtosis is 8.9 and the crest factor is 9.3.  The time history appears stationary, but the close-up view in Figure 21.13 reveals that it is composed of a series of transient pulses.
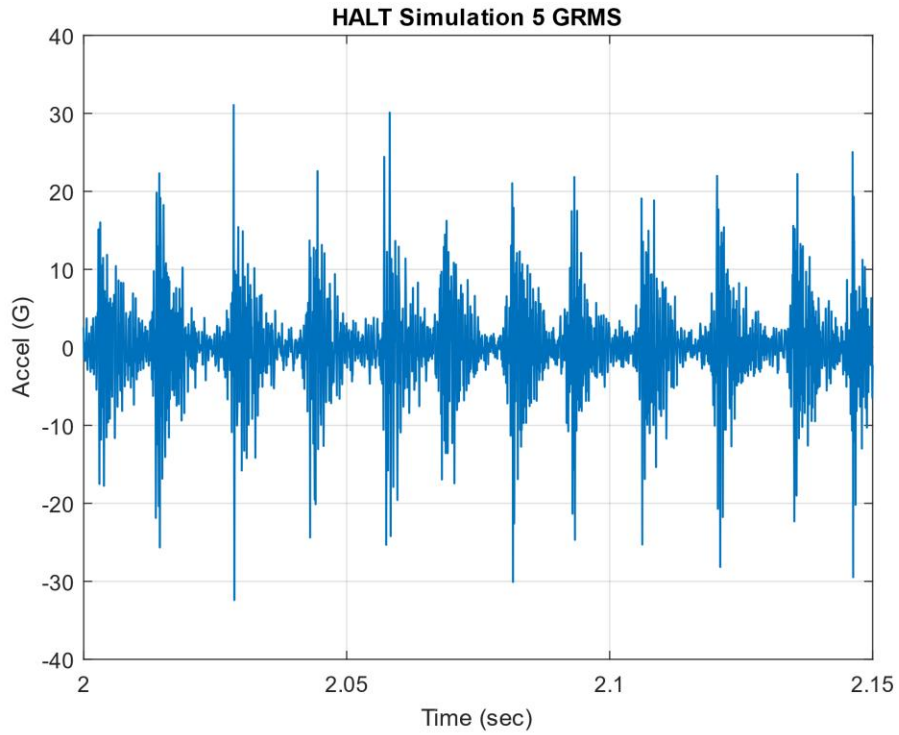
Figure 21.13.  HALT Time History Simulation, Close-up View

The vibration is a series of repetitive shock pulses due to the hammer strikes underneath the table.
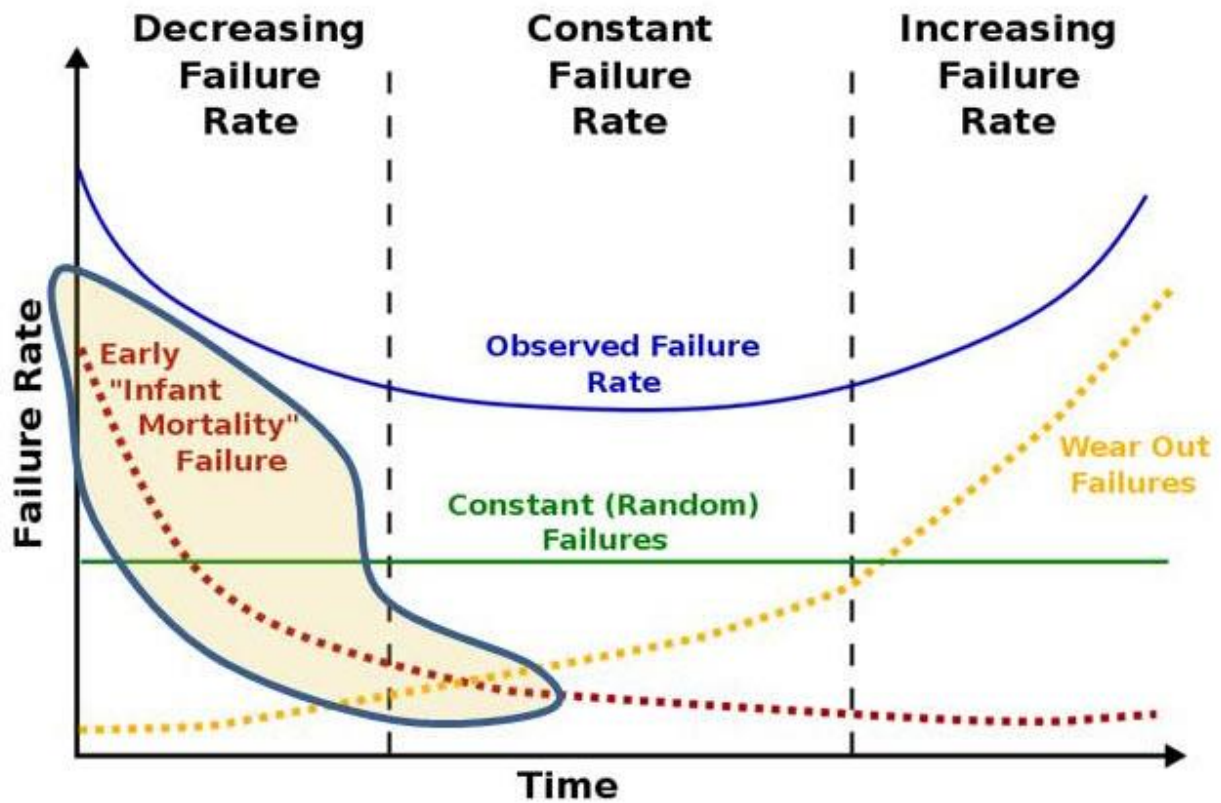
Figure 21.14.  Electronics Life Cycle Bathtub Curve

A successful screening process for mass-produced electronics will precipitate latent defects to eliminate the "infant mortality" failures shown in Figure 21.14.  The defects could be bad solder joints, loose connectors or screws, bent clamps, flawed pieces parts, etc.  An example of a bad solder joint is shown in Figure 21.15.
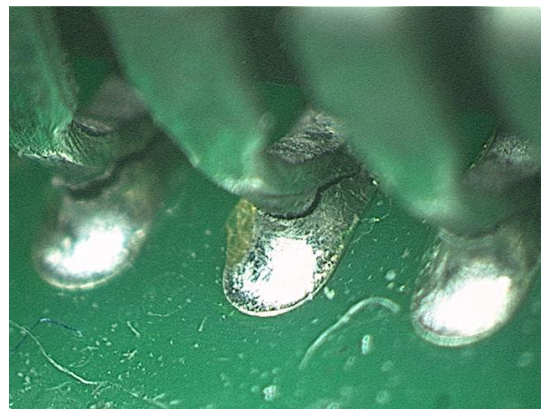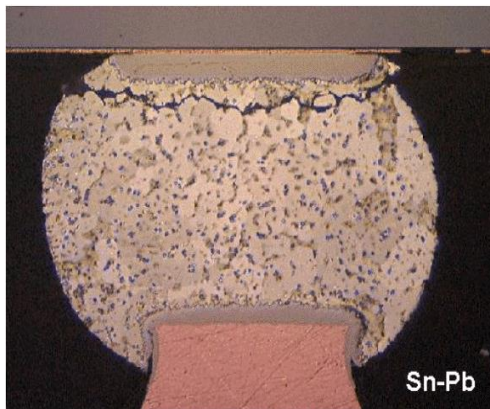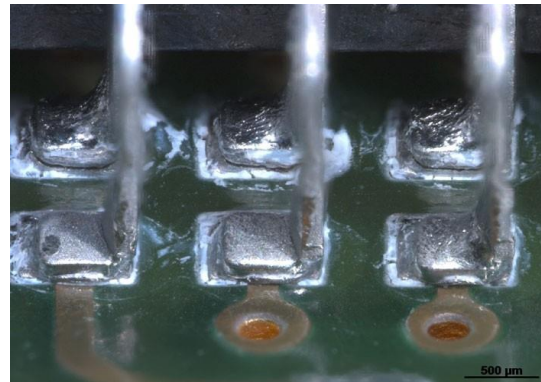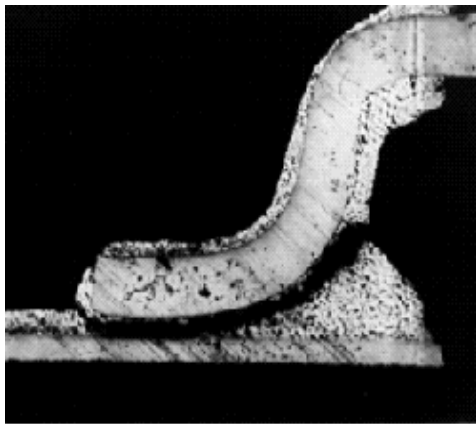
Figure 21.15.  Cracked Solder Joints

The purpose of subjecting electronic components to HALT/HASS is to uncover flaws such as bad solder joints.   The electronic components can be powered and monitored before, during, and after the tests to verify that they are functional.

# 22 SAMPLE RATE & ALIASING

## 22.1 DATA COLLECTION ACCURACY

The wagon wheel or stroboscopic effect is an optical illusion in which a spoked wheel appears to rotate at a different speed than its true rotation. The wheel can appear to rotate more slowly than the true rotation, appear stationary, or even appear to rotate in the opposite direction from the true rotation. The wagon-wheel effect is seen in film or television depictions of stagecoaches or wagons in Western movies, but the effect may also be seen in videos of helicopter rotors and aircraft propellers.

This optical illusion is a form of aliasing. It can occur in a video recording where the frame rate is too slow relative to the rotational or oscillation frequency of the moving object. A similar problem can occur when accelerometer data is digitized unless precautions are taken.

Engineers collect accelerometer data in a variety of settings both in the field and in lab tests. The accelerometers measure the data in analog form. The accelerometer may have an integral mechanical low-pass filter. Furthermore, the signal conditioning unit may have an analog low-pass filter. Low pass filtering of the *analog* signal is necessary to prevent aliasing. Eventually, the data is passed through an analog-to-digital converter.

The proper low pass frequency and sampling rate must be selected to ensure that the digitized data is accurate. There are three rules-of-thumb which must each be met.

## 22.2  FIRST REQUIREMENT

The first requirement is that the sampling rate must be greater than the maximum analysis frequency.  Industry guidelines are summarized in Table 22.1, where

$$(minimum\ sampling\ rate) \geq (\ N\ )(\ maximum\ analysis\ frequency\ ) \tag{22.1}$$

Table 22.1.  Sample Rate First Requirement

| Analysis Type | N |
|---|---|
| Frequency Domain | 2 |
| Time Domain | 10 |

The frequency domain requirement is based on the need for at least two time-domain coordinates per cycle to resolve a sine wave. The frequency domain analysis thus extends up to the Nyquist frequency which is one-half the sample rate.   Note that some conservative references specify an N of 2.5 or even 2.56 for frequency domain calculations.

A sampling rate of 100 kHz is thus required for a shock response spectrum (SRS) analysis extending to 10 kHz.  The SRS function is covered in Section 26.  Recall that the SRS is calculated in the time domain.

The IES Handbook for Dynamic Data Acquisition and Analysis [38] gives the following guidelines:

> Unlike other spectral quantities evolving from the discrete Fourier transform computations, the SRS is essentially a time domain quantity.  Hence, the digital sampling rate given by $R_s = 1/\Delta t$ introduces errors beyond those associated with aliasing about the Nyquist frequency.  Thus, $R_s$ must be high enough to accurately describe the response of the SRS oscillators. To minimize potential error, it is recommended that the SRS computations be performed with a sampling rate of $R_s \geq 10\ f_h$, where $f_h$ is the highest natural frequency of the SRS computation.

## 22.3  SECOND REQUIREMENT

Shannon's sampling theorem states that a sampled time signal must not contain components at frequencies above the Nyquist frequency.

Again, the Nyquist frequency is equal to one-half the sampling rate.  Shannon's theorem applies to frequency domain analysis.

Thus, the second requirement is that the sampling rate must be greater than the maximum frequency present in the source energy at the measurement location.  This requirement is independent of the maximum analysis frequency.

The guidelines are summarized in Table 22.2, where

$$(\text{minimum sampling rate}) \geq (\,M\,)(\,\text{maximum frequency in source energy}\,) \qquad (22.2)$$

Table 22.2.  Sample Rate Second Requirement

| Analysis Type | M |
|---|---|
| Frequency Domain | 2 |
| Time Domain | 10 |

Note the similarity between Table 22.1 and Table 22.2.

## 22.4  THIRD REQUIREMENT

The analog low pass filter cutoff frequency should be at least 1.5 times greater than the maximum analysis frequency of interest.  It should also be less than 0.6 times the Nyquist frequency for conservatism.  These recommendations come from Allan Piersol and the IES Handbook for Dynamic Data Acquisition and Analysis.

## 22.5  ANTI-ALIASING FILTER

| Accelerometer | | Signal Conditioner & Low pass Filter | | Analog-to-Digital Converter |
|---|---|---|---|---|
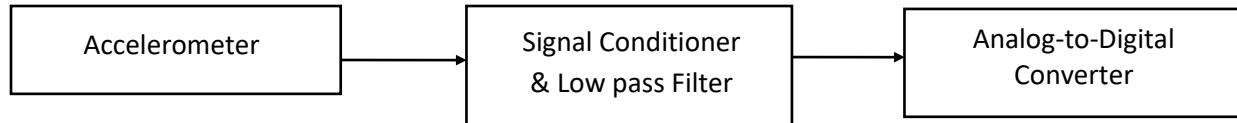
Figure 22.1.  Data Acquisition Flow Chart

The challenge is that the maximum frequency in the source energy may be unknown, which is the usual case for field data.  The solution is to use an analog low-pass filter before digitization.  This filter is also referred to as an anti-aliasing filter.   The filter cut-off frequency is typically set at, or slightly above, the maximum analysis frequency.

The IES Handbook for Dynamic Data Acquisition and Analysis gives the following guidelines.

Let

$f_c$    be the cutoff frequency

$f_N$    be the Nyquist frequency

- A low-pass anti-aliasing filter with a cutoff rate of at least 60 dB/octave should be used for the analog-to-digital conversion of all dynamic data.

- With a 60 dB/octave cutoff rate, the half-power point cutoff frequency of the filter should be set at $f_c \leq 0.6 \ f_N$.

- If the anti-aliasing filter has a more rapid cutoff rate, a higher cutoff frequency can be used, but the bound $f_c \leq 0.8 \ f_N$ should never be exceeded.

## 22.6 COMPLIANT DATA ACQUISTION SETUP EXAMPLES

The following tables show values typical for aerospace shock and vibration.

| Table 22.3.  Vibration, Frequency Domain | |
|---|---|
| Parameter | Frequency (kHz) |
| Maximum Analysis | 2 |
| Sample Rate | 10 |
| Nyquist | 5 |
| Analog Low-pass Filter | 3 |

| Table 22.4.  Pyrotechnic Shock, Time Domain | |
|---|---|
| Parameter | Frequency (kHz) |
| Maximum Analysis | 10 |
| Sample Rate | 100 |
| Nyquist | 50 |
| Analog Low-pass Filter | 30 |
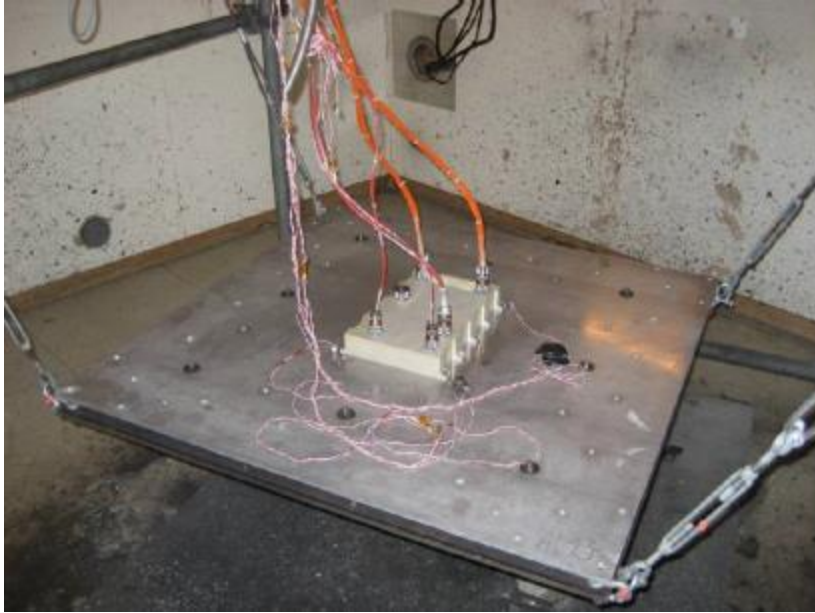
Figure 22.2. Pyrotechnic Shock Test of an Avionics Component

Mild detonating cord is the source shock and is coiled on the underside of the plate. Accelerometers are mounted on the plate to record the shock level. The component is powered and monitored during the test. The source shock may have energy components exceeding 100 kHz. The use of an analog anti-aliasing filter is critical. Otherwise, high-frequency energy will be erroneously folded down to lower frequencies in the shock response spectrum.

## 22.7 ALIASING EXAMPLE
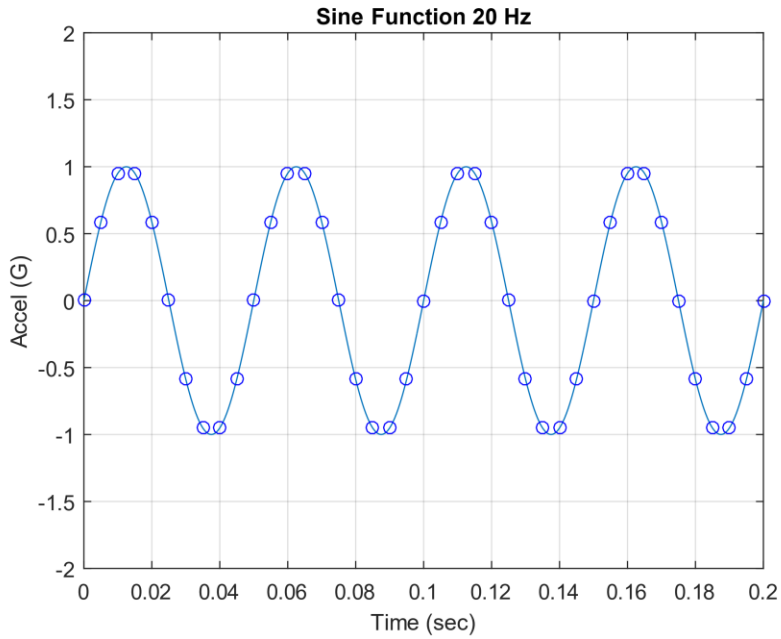


Figure 22.3.  A 20 Hz Sine Function Sampled at 200 Hz

There are 10 points per period.  The Nyquist frequency is 100 Hz.
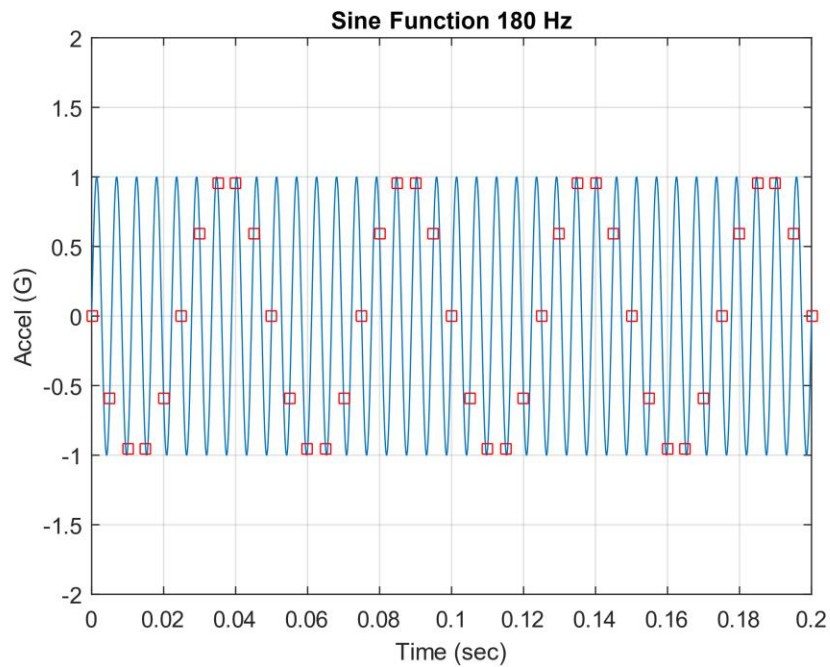


Figure 22.4.  A 180 Hz Sine Function Samples at 200 Hz

The red markers show that there are 1.11 points per 180 Hz cycle.  The Nyquist frequency is 100 Hz. Aliasing occurs!
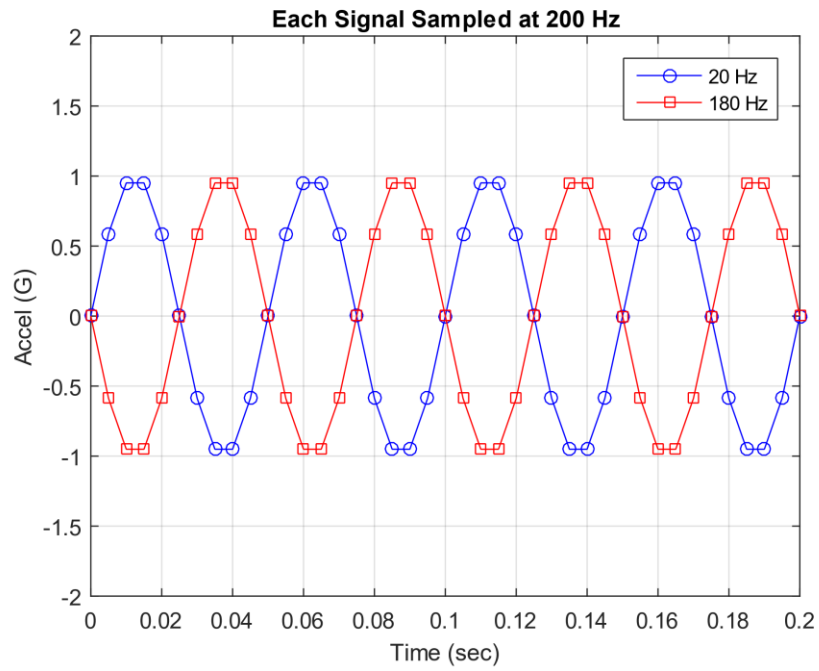


Figure 22.5.  Two Signals Digitized at 200 Hz

The two signals both appear as 20 Hz although only one truly is.
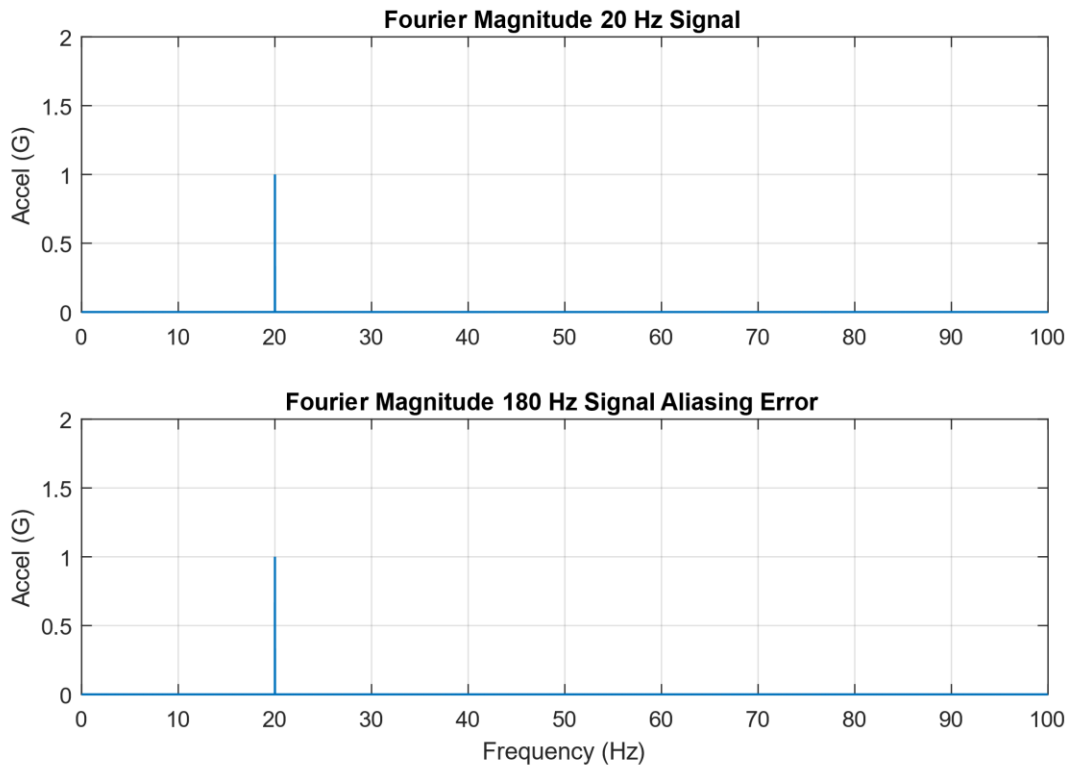
Figure 22.6.  Fourier Magnitude of Each Signal Sampled at 200 Hz

The 180 Hz signal is folded about the Nyquist frequency which is 100 Hz.  The resulting energy is deposited at 20 Hz.  Fourier transforms are covered in Section 23.

As an example, consider a pyrotechnic shock test with a time domain maximum analysis frequency of 10 kHz.  The sample rate should be at least 100 kHz.  The Nyquist frequency is 50 kHz.  Assume a low pass filter with a 60 dB/octave cutoff rate.  The maximum cutoff frequency should thus be 30 kHz.   These are values to satisfy basic requirements.  A better approach would be to set the sample rate at 250 kHz or more if the measurement is going to be in the "near field" relative to the source.  This higher sample rate can be readily achieved in a ground test, but not in flight where the telemetry bandwidth is limited.

As another example, consider a vibration test with a maximum analysis frequency of 2 kHz in the time domain.  The sample rate should be at least 20 kHz.  The Nyquist frequency is 10 kHz. The maximum cutoff frequency should thus be 6 kHz.

# 23 FOURIER TRANSFORMS

## 23.1 TEXTBOOK FOURIER TRANSFORM

The Fourier transform is a method for identifying the spectral content of a time history. This transform has already been used previously in this document, including for the channel beam vibration response in Figure 16.3 and Figure 16.4. This section will give background equations starting with the rarefied mathematician approach and finishing with the practical engineering version.

The textbook Fourier transform $X(f)$ for a continuous time series $x(t)$ is defined as

$$X(f) = \int_{-\infty}^{\infty} x(t) \exp\left(-j\, 2\pi\, f\, t\right) dt \tag{23.1}$$

Note that $j = \sqrt{-1}$ .

And both the time and frequency domains are considered to extend from minus to plus infinity in their respective spheres.

There is also an inverse Fourier transform defined as

$$x(t) = \int_{-\infty}^{\infty} X(f) \exp\left(+j\, 2\pi\, f\, t\right) df \tag{23.2}$$

As an aside, the corresponding Euler's equation is

$$\exp(\pm j\, 2\, \pi\, f\, t) = \cos(2\, \pi\, f\, t) \pm j \sin(2\, \pi\, f\, t) \tag{23.3}$$

There are several impractical quirks begat from this transform and inverse pair. One is that a signal as simple as a pure sine function will have a spectral component at a negative of its true frequency, as shown in Figure 23.1. How is an engineer to design and test for a negative frequency? In addition, measured time histories have a distinct start and stop time with a finite duration. Next, integration is analogous to multiplication. Assume that $x(t)$ represents an acceleration time history. The resulting Fourier transform from equation (23.1) would return a transform with amplitude dimension [acceleration-time]. What would this be? Velocity?

The last peculiarity is that measured time histories are strictly real. The resulting Fourier transform of a measured signal from equation (23.1) would be complex, with real and imaginary components. Now take this Fourier transform and insert it into the inverse formula in (23.2). The resulting time history will be complex. Fortunately, this concern is easily resolved because the imaginary components will all be zero.
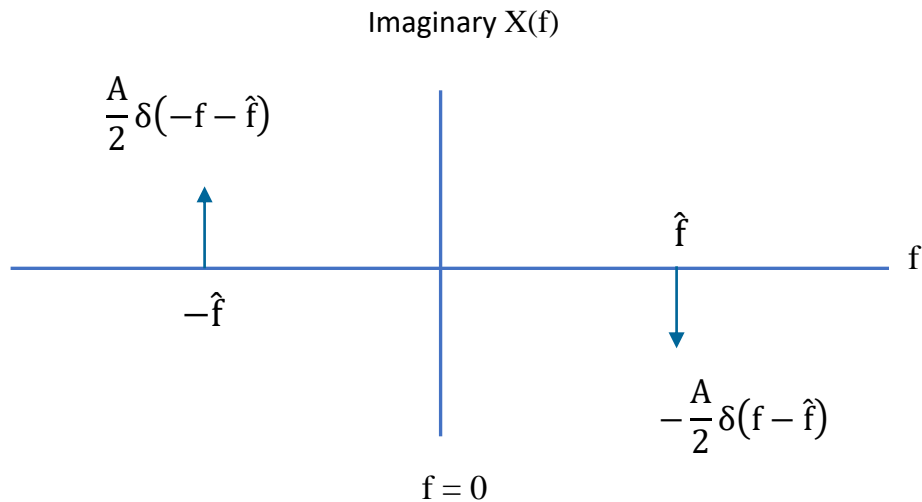


Figure 23.1. Mathematicians' Fourier Transform of a Sine Function

The time history behind the imagery Fourier transform equation (23.1) is

$$x(t) = A \sin(2 \pi \hat{f} t) \qquad (23.4)$$

The real Fourier transform is omitted because it is zero for a pure sine function with zero phase angle. The symbol $\delta$ represents the Dirac delta function, a mathematical oddity unsuitable for engineering design and test purposes.

Note the following traits for any given signal:

1. The real Fourier transform is symmetric about the f=0 line.
2. The imaginary Fourier transform is anti-symmetric about the f=0 line.

## 23.1.1 Discrete Fourier Transform

The discrete Fourier transform rectifies some, but not all, impracticalities of the textbook Fourier transform. Engineers collect data using data acquisition systems which return digitized outputs for measured analog inputs. The integral in equation (23.1) thus needs to be exchanged for a series, which is easily done. The resulting discrete Fourier transform is

$$X_k = \frac{1}{N} \sum_{n=0}^{N-1} \left\{ x_n \exp\left(-j\frac{2\pi}{N}nk\right) \right\} \quad , \text{for } k = 0, 1, \dots, N-1 \tag{23.5}$$

Its corresponding inverse is

$$x_n = \sum_{k=0}^{N-1} \left\{ X_k \exp\left(+j\frac{2\pi}{N}nk\right) \right\} \quad , \text{for } n = 0, 1, \dots, N-1 \tag{23.6}$$

Eureka! Equation (23.5) does away with negative frequencies. The starting frequency will now be zero. Also, the Fourier transform amplitude dimension will now be the same as that of the time history. The time domain dimension of acceleration will thus carry directly over to the Fourier transform. And both the time and frequency domain functions may now be defined over finite domains. Alas, this discrete pair will need further tweaking before the equations are ready for practical use, but progress has been made.

Recall the beloved sine function from equation (23.4). Set its amplitude at 1 G and its frequency at 1 Hz. Digitize it with a sample rate of 32 samples per second with a 512-second duration. The frequency step in the Fourier transform will be (1/512) Hz. The imaginary discrete Fourier transform is shown in Figure 23.2.
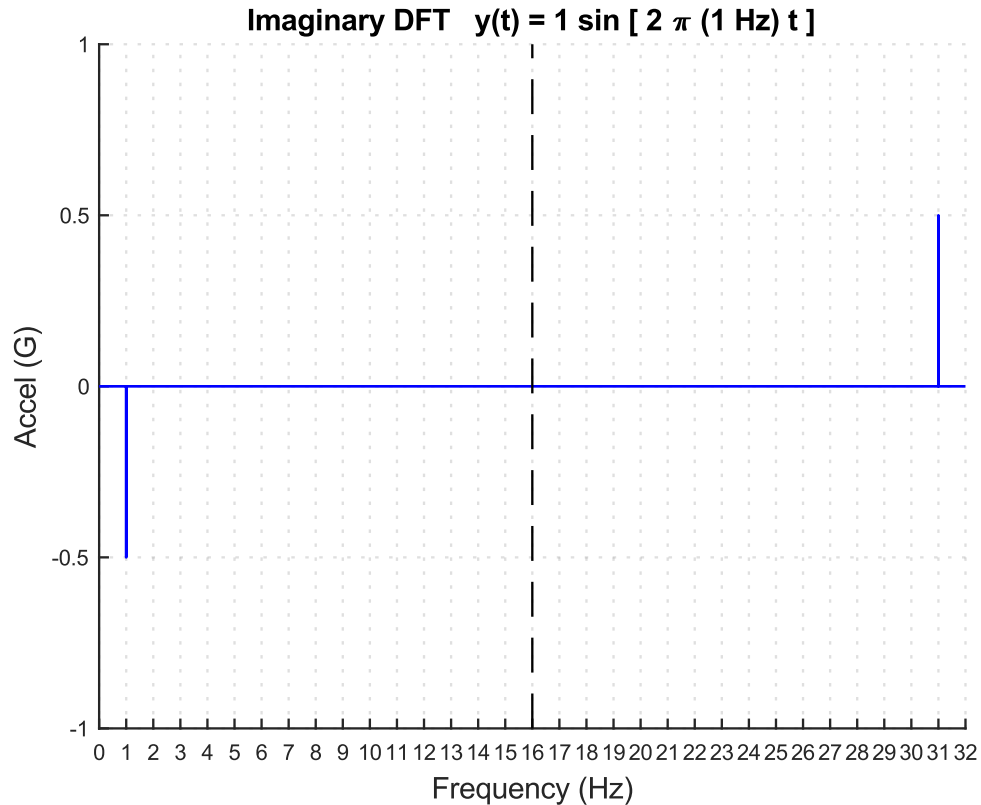
**Figure 23.2.  Discrete Fourier Transform of a Sine Function**

The sine function has a frequency of 1 Hz.  Again, the Fourier transform of a pure sine function is imaginary and antisymmetric.  The antisymmetric reflection occurs at about 16 Hz which is the Nyquist frequency, one-half the sample rate.  Does the discrete Fourier transform imply that a hypothetical component subjected to this environment needs to be designed and tested for 31 Hz as well as 1 Hz?  How would the peak at 31 Hz change if the sample rate were increased to 64 samples per second?  Is this some manifestation of Heisenberg's uncertainty principle?  And why is the absolute amplitude at 1 Hz equal to 0.5 but the sine function amplitude is 1?

The discrete Fourier transform in equation (23.5) will not be abandoned.  It reappears in certain calculations such as going back and forth between impulse response functions and transfer functions, convolution applications, inverse Fourier transforms, etc.   These intermediate concepts will be covered in a future document.  But a more practical transform is needed presently.

## 23.1.2 Useful Discrete Fourier Transform

Sidestepping the quandaries raised in the previous section, let us modify the discrete Fourier transform into a practical tool. Henceforth, the Fourier transform will only be shown up to the Nyquist frequency. And the Fourier transform will be represented in terms of magnitude rather than real and imaginary components. The phase may also be shown with magnitude if needed. And the amplitudes at all nonzero frequencies will be doubled. A more elegant way of expressing this is that the energy components above the Nyquist frequency will be folded about the Nyquist frequency to lower frequencies. The energy at 31 Hz in Figure 23.2 would thus be deposited at 1 Hz. Note that the spectral magnitude at zero frequency is a special case since it remains the simple mean value of the signal.

The full amplitude Fourier transform up to the Nyquist frequency is

$$
X_k = \begin{cases} \dfrac{1}{N} \left| \displaystyle\sum_{n=0}^{N-1} x_n \right|, & \text{for } k = 0 \\[2em] \dfrac{2}{N} \left| \displaystyle\sum_{n=0}^{N-1} x_n \exp\left(-j\dfrac{2\pi}{N} nk\right) \right|, & \text{for } k = 1, \dots \dfrac{N}{2} - 1 \end{cases}
$$

(23.7)
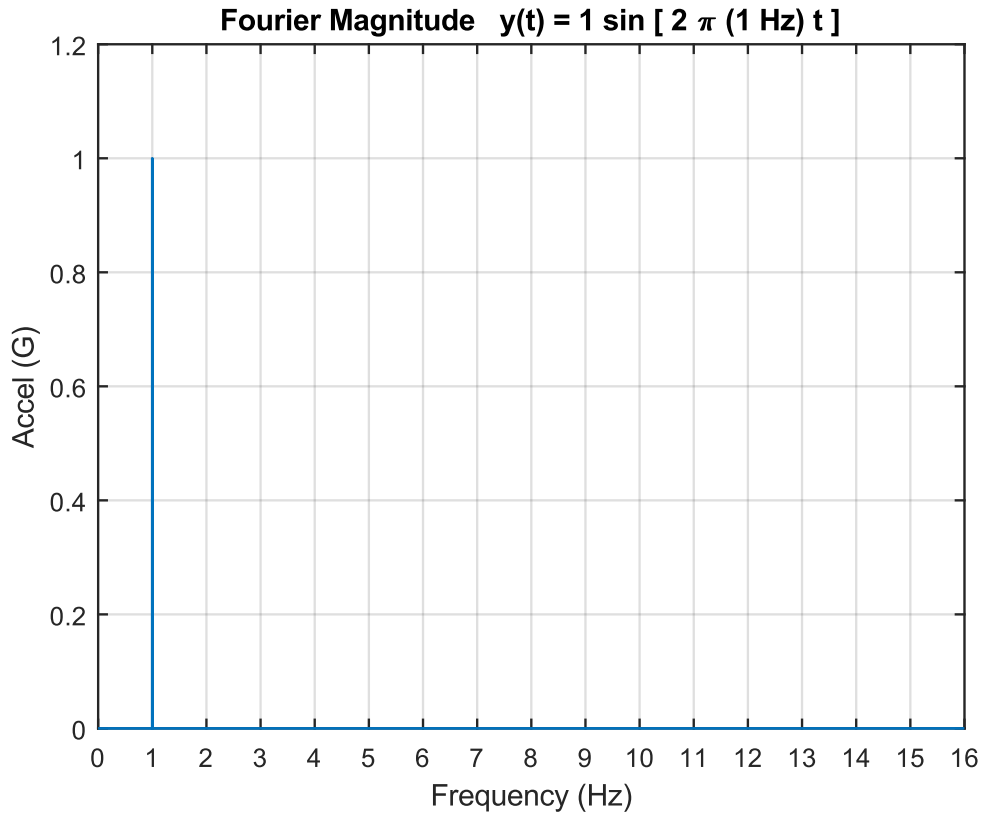
Figure 23.3.  Full Amplitude, Discrete Fourier Transform of a Sine Function, Up to Nyquist Frequency

The beloved sine function's Fourier magnitude is plotted in the above figure using equation (23.6).  A clean spectral peak of 1 G appears at 1 Hz.  The phase angle is omitted because it would only be valid at the sinusoid's own frequency.  It would be noise at other frequencies.  There is a need for phase angle in other situations, such as modal testing, comparing the lag from input to response, etc.

## 23.2  LEAKAGE & HANNING WINDOW

### 23.2.1  Leakage Error

There are several error sources associated with the Fourier transform, including "leakage," which is a smearing of energy throughout the frequency domain.  Leakage results when both of the following conditions are present:

1.  The signal is taken over a finite duration
2.  The signal is "non-periodic" in the time record

Both these conditions are usually present in engineering data, so leakage is common. For example, leakage occurs if a Fourier transform is calculated for a non-integral number of sine function cycles.
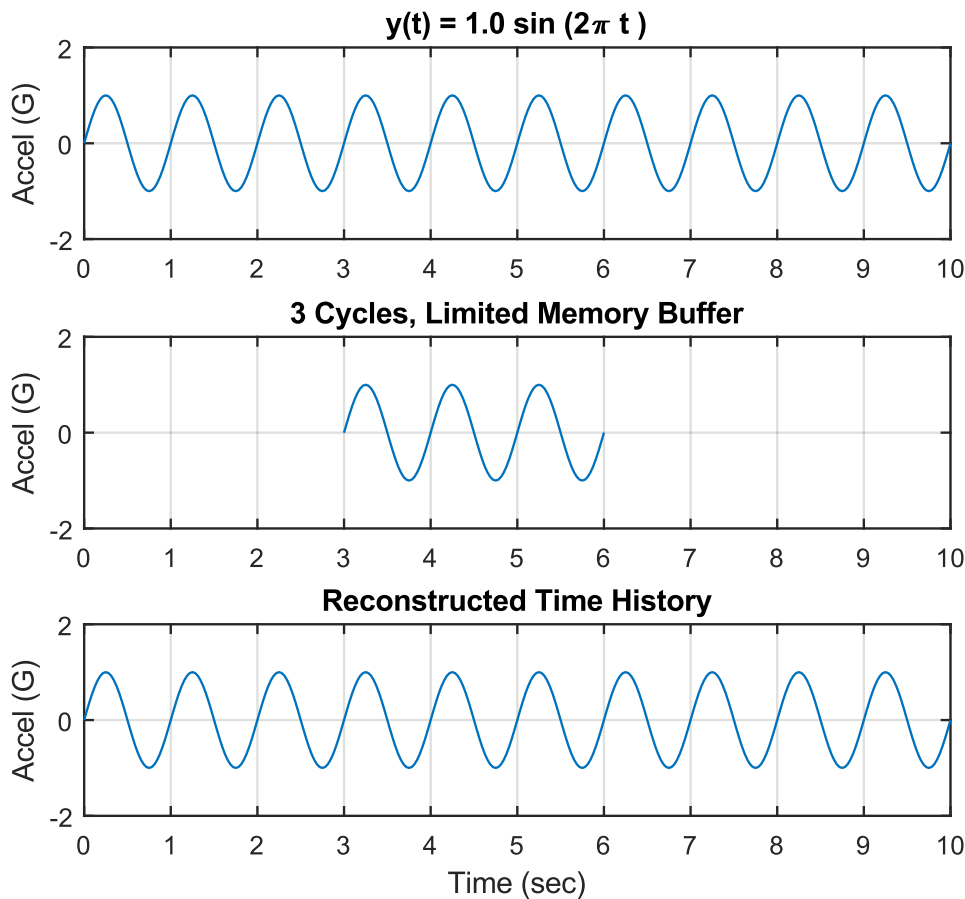


Figure 23.4. Sine Function and Memory Buffer Example 1

Consider that a data acquisition system is used to monitor a sine function over a 10-second duration. The sine function has an amplitude of 1 G and a frequency of 1 Hz, as shown in the top subplot. The sample rate is 32 samples per second. Now assume that the data acquisition system has a limited memory buffer and measures only three cycles as shown in the middle subplot. Note that the time history amplitude is zero at the start and end of the record, with an integer number of cycles. In essence, the Fourier transform will correctly assume that the original signal is a series of three-cycle segments as shown in the bottom subplot, such that no leakage occurs as shown in Figure 23.6.
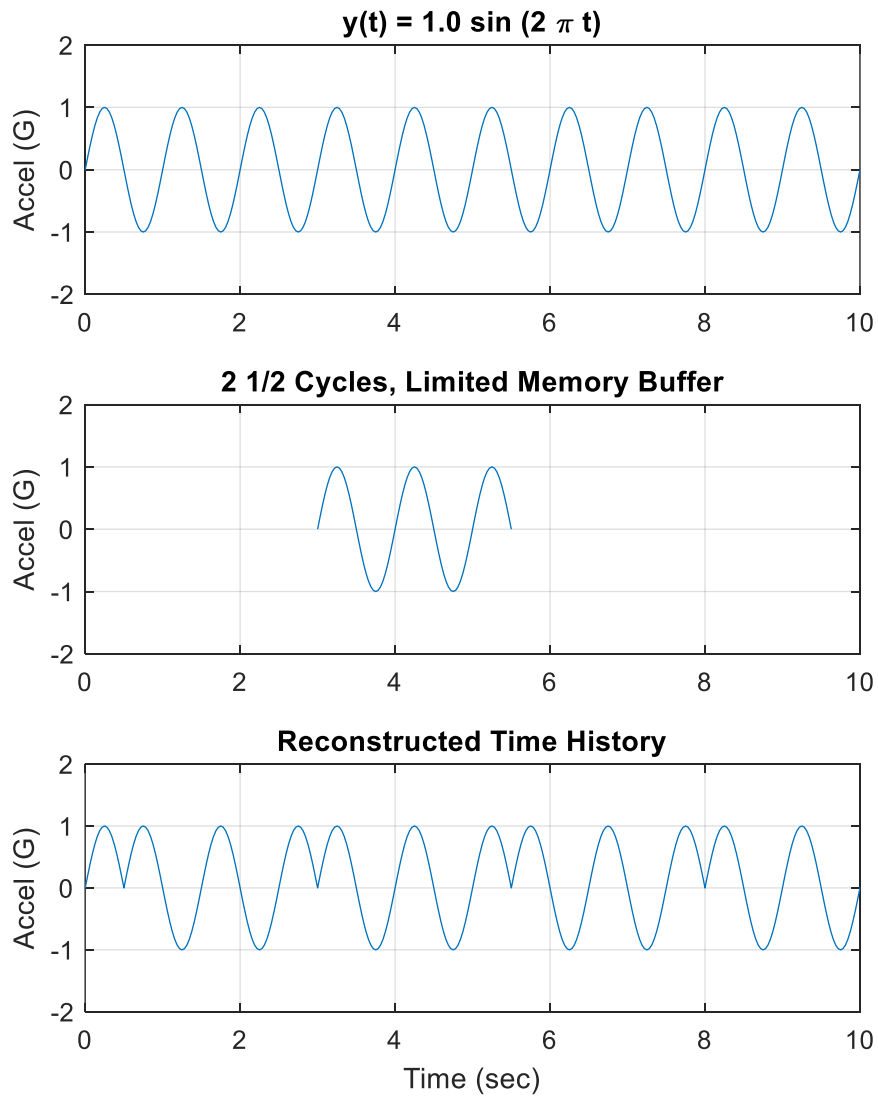
Figure 23.5.   Sine Function and Memory Buffer Example 2

Repeat the previous example but with a tighter memory buffer that only measures 2 1/2 cycles as shown in the middle subplot.  Leakage will occur due to the non-integer number of cycles. The Fourier transform will assume that the original signal is a distorted series of these segments as shown in the bottom subplot, as shown in Figure 23.6.
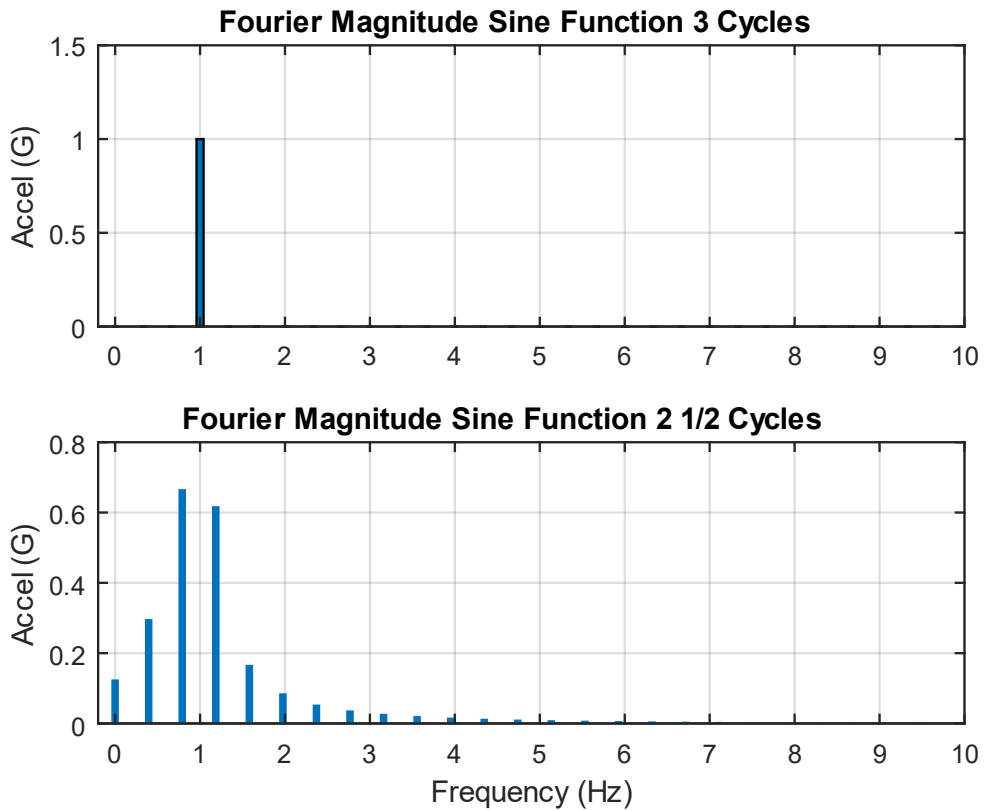
Figure 23.6.   Fourier Magnitude Comparison, Both Examples

The top subplot shows a clean spectral line at 1 Hz for the case of three whole cycles.  The bottom subplot shows that the energy is smeared across several bands as a result of leakage error from the non-integer number of cycles.

On a related note, the top subplot has a spectral line available at exactly 1 Hz.  But the bottom subplot lacks a line at 1 Hz and instead has lines at 0.8 and 1.2 Hz.   Recall that the frequency step is the inverse of the duration.  The three-cycle spectral increment is thus 0.333 Hz, whereas the two-and-a-half cycle step is 0.4 Hz.

## 23.2.2 Hanning Window
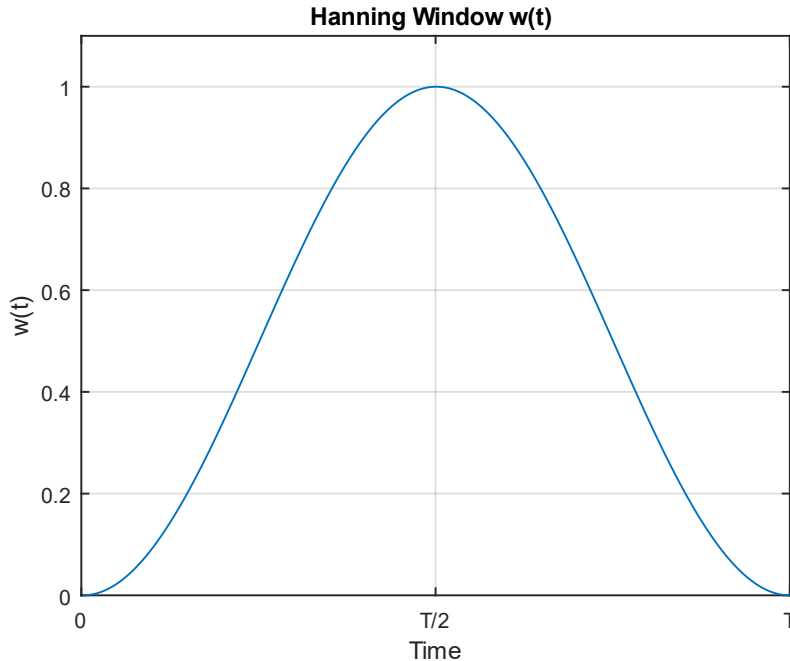


Figure 23.7.  Hanning Window

The leakage error can be reduced by subjecting the time history to an appropriate window. Two common types of windows are the rectangular window and the Hanning window.

The rectangular, or flat, window leaves the time history data unmodified and is equivalent to no window at all.   A rectangular window is appropriate for transient data or nonstationary data, including the type of shock time histories presented in Section 26.  It does not reduce leakage.

One of the most common windows is the Hanning window or the cosine squared window.  It works best with stationary data.   This window tapers the time history data so that the amplitude envelope decreases to zero at both the beginning and end of the time segment.  The Hanning window $w(t)$ can be defined the is plotted in Figure 23.7.

$$w(t) = 1 - \cos^2\left(\frac{\pi t}{T}\right), 0 \leq t \leq T \tag{23.8}$$

A normalization factor of the square root of (8/3) may be applied to the Hanned data to compensate for lost energy, to maintain the original overall RMS level.
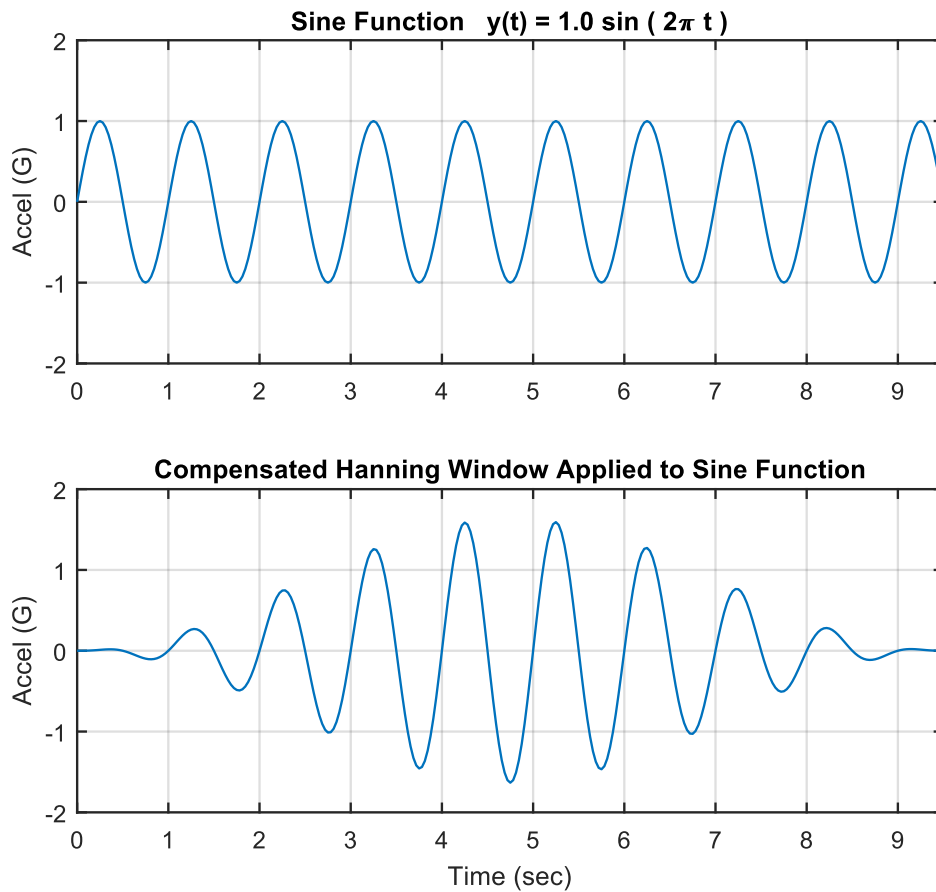
Figure 23.8.  Sample Sine Function, with Non-Integer Number of Cycles

A sine function before and after the Hanning window application is shown in Figure 23.8.  The non-integer number of cycles will cause a leakage error which is mitigated by the Hanning window although not eliminated.  The Fourier transforms of each are shown in Figure 23.9.
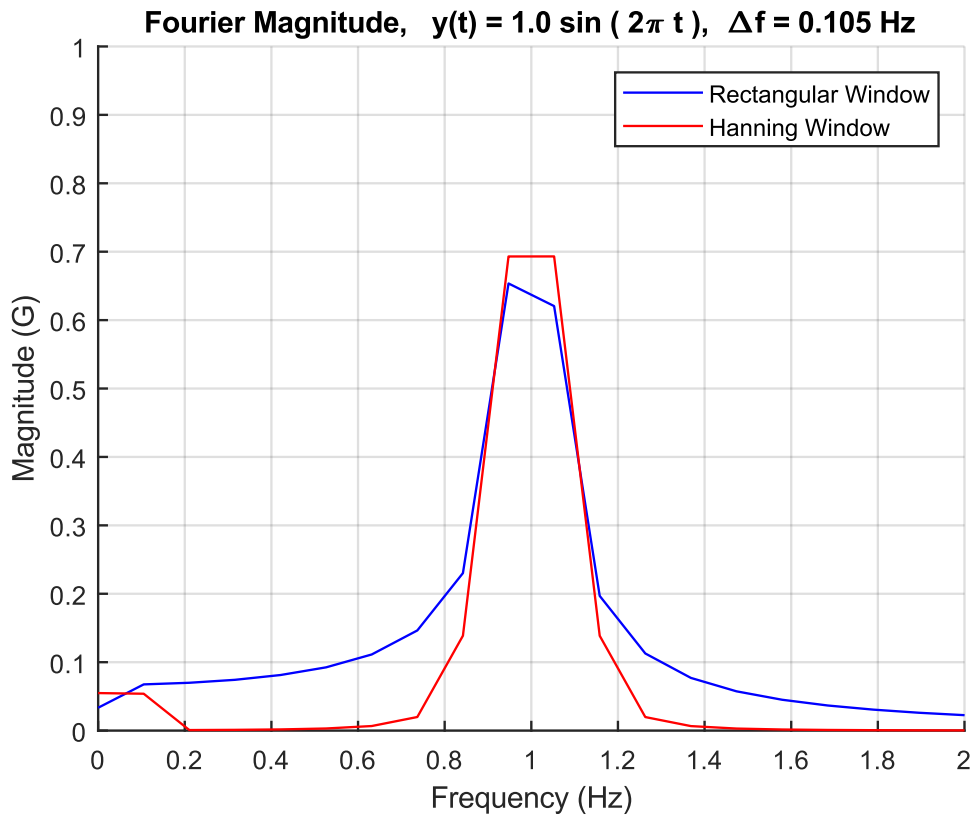
**Figure 23.9.** Fourier Spectra, Sine Function Before and After Hanning Window

Ideally, the Fourier transform would have a single, discrete line at 1 Hz with an amplitude of 1 G. A challenge is that there are spectral lines available at 0.945 Hz and 1.05 Hz but none at 1.0 Hz. Both the rectangular and Hanning Fourier transforms have some leakage errors as a result. The rectangular window produces more leakage error than the Hanning window. Thus, the Hanning window is recommended for stationary data.

## 23.3 FAST FOURIER TRANSFORM

### 23.3.1 FFT History

A fast Fourier transform (FFT) is an algorithm that computes the discrete Fourier transform (DFT) of a sequence using shortcuts made possible by symmetries in the exponential weighting functions. Carl Friedrich Gauss developed the FFT in unpublished work in 1805 to interpolate the orbit of asteroids Pallas and Juno from sample observations.

James Cooley of IBM and John Tukey of Princeton University independently rediscovered and popularized Gauss' FFT algorithm in 1965. The method is based on a time series with several points equal to $2^N$, where N is an integer.

Charles Rader, Leo Bluestein, and others have since published algorithms that allow FFT calculations of time histories with arbitrary lengths.

Software for these methods is available in FFTW, which is a free C subroutine library for computing the DFTs in one or more dimensions, of arbitrary input size, and of both real and complex data. https://www.fftw.org/

A Matlab FFT script is posted at:

https://www.mathworks.com/matlabcentral/fileexchange/127334-fft-one-sided-full-amplitude-discrete-fourier-transform

Matlab uses the FFTW library for its DFT calculations.
https://www.mathworks.com/help/matlab/ref/fft.html

### 23.3.2 Cooley-Tukey FFT Characteristics

The discrete Fourier transform requires a tremendous amount of calculations for digital signals with large numbers of points. A time history with M coordinates would require $M^2$ complex multiplication steps. The discrete Fourier transform can be carried out by a Fast Fourier transform (FFT) method, however. The method is based on a time series with several points equal to $2^N$, where N is an integer. The FFT requires $M \log_2 M$ complex multiplication steps, where $M = 2^N$.

Suitable Record Lengths for the FFT Calculation include:

2, 4, 8, 16, 32, 64, 128, 256, 512, 1024, 2048, 4196, 8192, 16384, 32768, 65536, 131072, 262144, 524288, 1048576, 2097152, . . . , $2^N$ .

### 23.3.3 Cooley-Tukey FFT Example

Now consider a time history with 1,000,000 points. A regular Fourier transform would require $10^{12}$ complex multiplication steps. On the other hand, an FFT would only require approximately $2(10^7)$ steps. Thus, the FFT achieves the calculation in 1/50,000th of the time.

The above example is not quite correct. Again, the FFT is based on a time series with $2^N$ coordinates. Note that $2^{19}$ = 524,288 and $2^{20}$ = 1,048,576. But a time history with 1,000,000 points falls between these two cases.

There are some options for dealing with a time history that is not an integer power of 2. One option is to truncate the time history. This should be acceptable if the data is stationary. In the above example, the time history would thus be truncated to 524,288 points. The second option is to pad the time history with trailing zeroes to bring its length to an integer power of 2. A problem with this option is that it artificially reduces the amplitude of the Fourier transform spectral lines. A third option is to carefully perform linear interpolation on the data so that its length becomes $2^N$. Or the problem can be circumvented altogether by configuring the data acquisition system to collect exactly $2^N$ points. This was a feature of some vintage systems.

Again, additional FFT algorithms have been developed that can handle time histories of arbitrary length such that truncation or zero-padding is no longer needed.

### 23.3.4 Cooley-Tukey FFT Algorithm

The Fourier transform requires multiplying the time points by complex weighting functions. These functions have a certain symmetry for the case of time series with $2^N$ points. The calculation can thus be simplified by taking advantage of this symmetry using concepts such as the unit circle and the butterfly algorithm. A few introductory steps are given here. Define a weighting factor $W^n$.

$$W^n = \exp\left(-j\frac{2\pi n}{N}\right) \tag{23.9}$$

The discrete Fourier transform becomes

$$X_k = \frac{1}{N} \sum_{n=0}^{N-1} \left\{ x_n \, W^{nk} \right\} \quad , \text{for } k = 0, 1, \dots , N-1 \tag{23.10}$$

The matrix representation is

$$\begin{bmatrix} X(0) \\ X(1) \\ X(2) \\ \vdots \\ X(N-1) \end{bmatrix} = \frac{1}{N} \begin{bmatrix} W^0 & W^0 & W^0 & \dots & W^0 \\ W^0 & W^1 & W^2 & \dots & W^{(N-1)} \\ W^0 & W^2 & W^4 & \dots & W^{2(N-1)} \\ \vdots & \vdots & \vdots & \ddots & \vdots \\ W^0 & W^{(N-1)} & W^{2(N-1)} & \dots & W^{(N-1)(N-1)} \end{bmatrix} \begin{bmatrix} x(0) \\ x(1) \\ x(2) \\ \vdots \\ x(N-1) \end{bmatrix} \tag{23.11}$$

Note that the weighting matrix in equation (23.11) is symmetric and that

$$W^0 = 1 \tag{23.12}$$

The Fourier transform equation in matrix form simplifies to

$$\begin{bmatrix} X(0) \\ X(1) \\ X(2) \\ \vdots \\ X(N-1) \end{bmatrix} = \frac{1}{N} \begin{bmatrix} 1 & 1 & 1 & \dots & 1 \\ 1 & W^1 & W^2 & \dots & W^{(N-1)} \\ 1 & W^2 & W^4 & \dots & W^{2(N-1)} \\ \vdots & \vdots & \vdots & \ddots & \vdots \\ 1 & W^{(N-1)} & W^{2(N-1)} & \dots & W^{(N-1)(N-1)} \end{bmatrix} \begin{bmatrix} x(0) \\ x(1) \\ x(2) \\ \vdots \\ x(N-1) \end{bmatrix} \tag{23.13}$$

The weights can be arranged geometrically as shown in Figure 23.10.
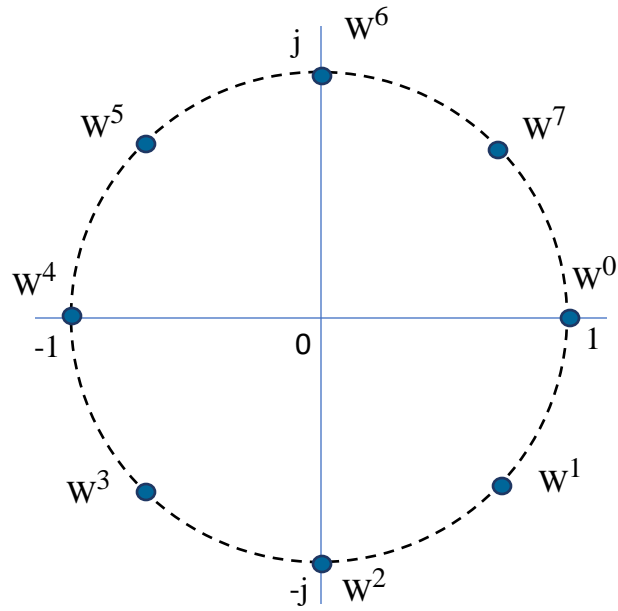
Figure 23.10. Unit Circle for N=8, Polar Coordinates with Real and Imaginary Axes

The units circle shows some emerging symmetries. The real part of $W^1$ is equal to that of $W^7$. The imaginary part of $W^1$ is equal to that of $W^3$. Additional symmetries can be identified by noting that some values are the negative of others. Further development of the FFT algorithm is beyond the scope of this document but is given in References [39] and [40].

Figure 23.11.   Transformer Utility Box

Magnetic fields from alternating currents induce vibration in certain materials, such as iron, steel, and ferrite alloys.  This effect is called magnetostriction.   Transformer hum is a common example of magnetostriction.   This hum is a potential nuisance, and it is an energy loss mechanism.
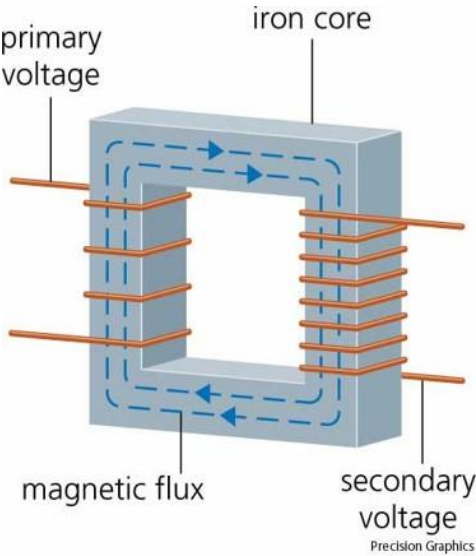


Figure 23.12.   Step-up Transformer

A basic transformer has two sets of windings, the primary and the secondary. Certain transformers may have secondary windings or taps. The primary connects to the power source. The secondary connects to the load usually at a lower voltage. The windings are wrapped around a core, which may be iron or ferrite, depending on the design requirements. An iron core may be laminated with layers of iron and non-conducting material stacked together. A laminated iron core is used to reduce the creation of eddy currents in the iron core that would dissipate the energy being transferred from the primary coil to the secondary coil in the form of heat.

An alternating current is input to the primary winding. The current produces a magnetic flux or magnetic lines of force in the core. The resulting magnetic field induces an alternating current in the secondary winding. The number of turns on each winding determines the output voltage from the transformer. The output voltage from the secondary is proportional to the ratio of the turns on the windings.
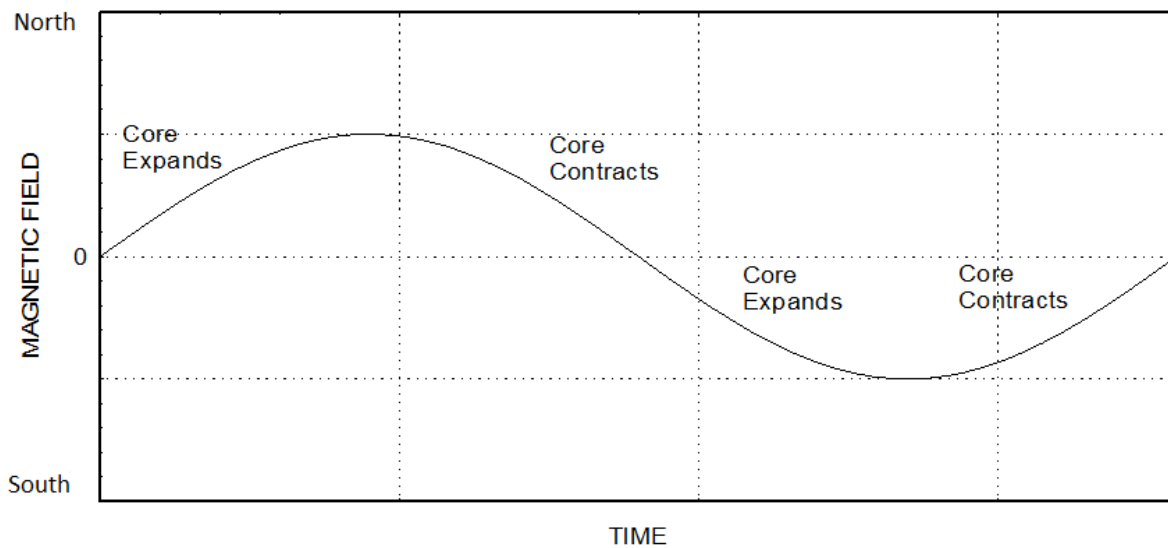


Figure 23.13. Magnetostriction Cycle

The magnetic field stresses the core material. The stress causes the core volume to expand regardless of the polarity. The core contracts to its equilibrium volume as the magnetic flux returns to zero. The material expands and contracts twice per each magnetic cycle, as shown in the above figure. The core thus vibrates at 120 Hz in response to the changing magnetic field from 60 Hz AC power. The deformation amplitude may be so small that it is imperceptible to the unaided human eye. Nevertheless, it may be large enough to generate a hum. The hum frequency is 120 Hz, with integer harmonics. A hypothetical strain gage mounted on the core would output a rectified version of the above curve.
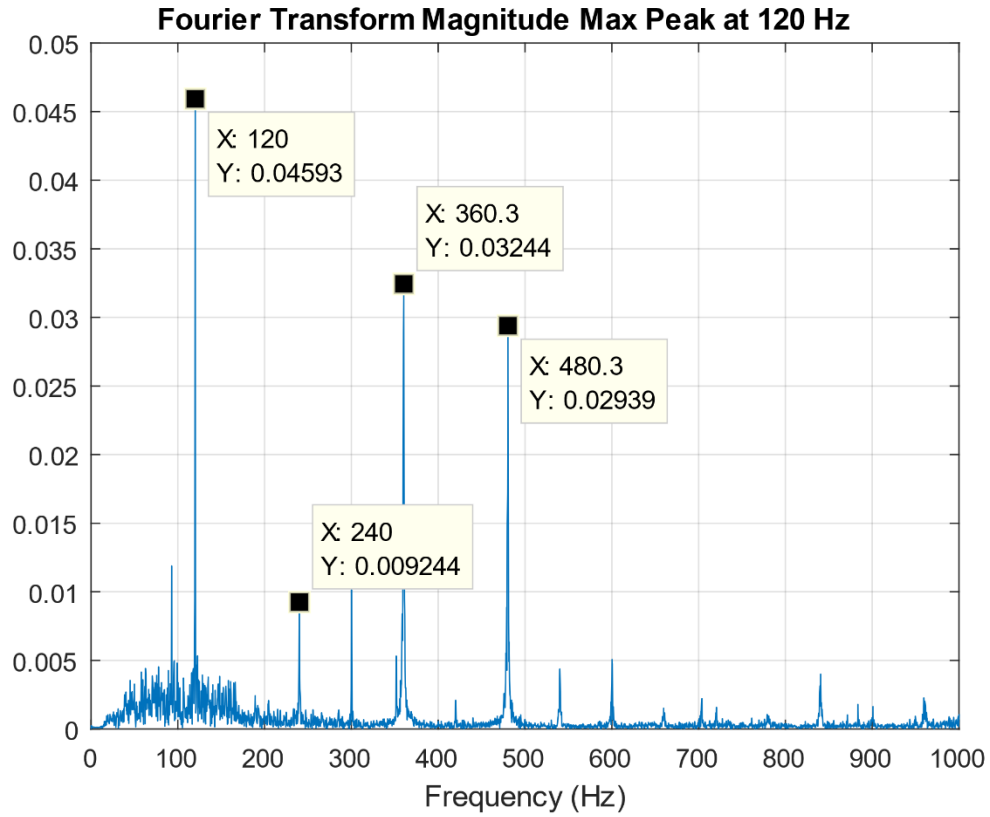
Figure 23.14.  Transformer Hum Fourier Spectra

The Fourier magnitude from a sound output of the transformer in Figure 23.11 is shown in Figure 23.14, with its 120 Hz peak and integer harmonics.

Figure 23.15.   Apache AH-64 Helicopter

The Apache is a twin-engine army attack helicopter, as shown in Figure 23.15.  It entered service with the US Army in 1984.

Helicopter noise consists of a complex mixture of sounds. The repeating impulse noise from the rotor blades is the dominant source of distinct spectral tones. The fundamental tone occurs at a characteristic frequency depending on the number of blades and their rotation speed. The blade-passing frequency (BPF) is the shaft rotation frequency times the number of rotor blades. Noise occurs at the BPF as well as at integer harmonics.  Both the main rotor and the tail rotor generate this type of noise.

Rotor-vortex interaction noise is another source. This source is also referred to as blade-vortex interaction (BVI) noise. This source is significant in descent or level flight at low and medium velocities. Vortices form in the wake of the blades. A given rotor blade can run into the tip vortex shed by a preceding blade. This causes a distinctive type of noise: the annoying "blade-slap" of helicopters with slow-turning rotors, or a sharp fluttering noise for rotorcraft with fast-turning rotors.

Furthermore, the velocity at the tips of the advancing blades in high-speed forward flight may approach Mach 1.  Shock waves begin to form at this condition, leading to shock-induced flow separation. The shock waves and turbulent flow generate further noise. This source is referred to as high-speed impulsive (HSI) noise.  In addition, most helicopters are powered by turbine engines. Engine and gearbox noise consists of distinct spectral peaks as well as broadband random noise.  A segment of an acoustic time history from an Apache flyover is shown in Figure 23.16.  The signal is a summation of sine tones, mostly from the main and tail rotor blade passing frequencies.
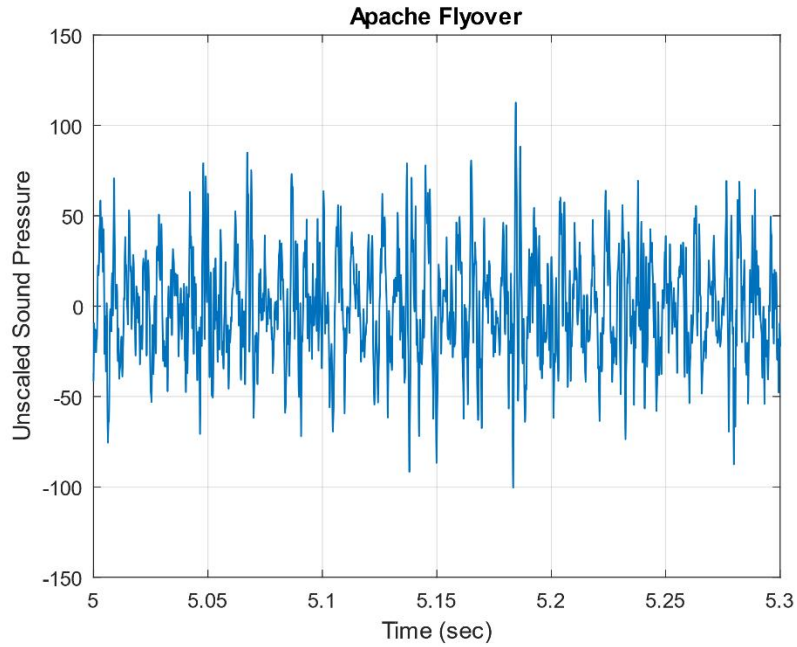
Figure 23.16.  Apache Flyover Acoustic Time History
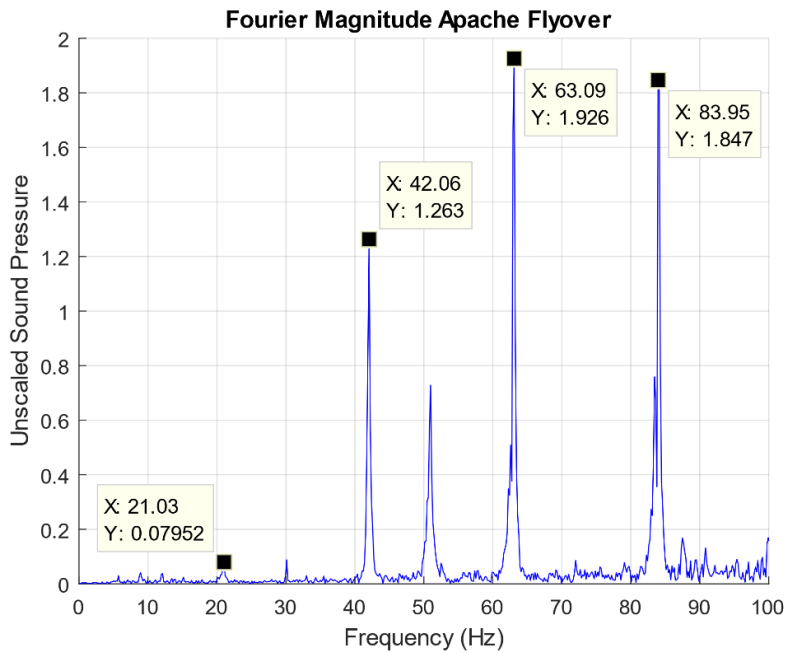


Figure 23.17.  Apache Flyover Acoustic Fourier Spectra with Main Rotor BPFs Identified

The measured blade passing frequency is 21 Hz with integer harmonics.  The Apache's main rotor has four blades.  The apparent main hub frequency is thus 5.25 Hz. The actual main hub frequency is $\cong 4.84$ Hz per published data in Reference [41].  The apparent frequency is higher due to a Doppler shift with the Apache flying toward the microphone.
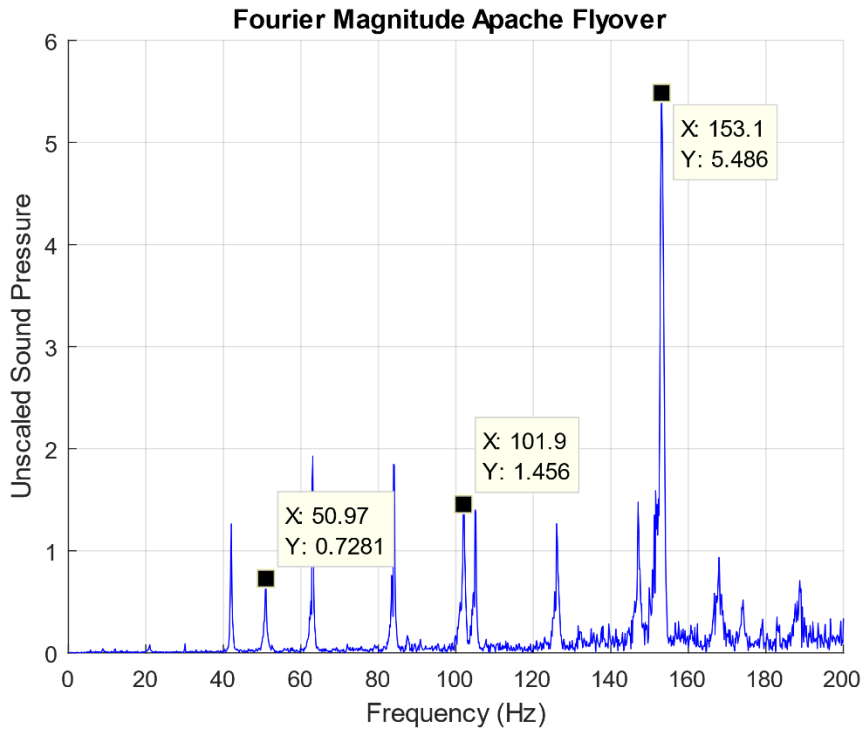


Figure 23.18.  Apache Flyover Acoustic Fourier Spectra with Tail Rotor BPFs Identified

The Apache tail rotor has four blades. The blades, however, are not oriented 90° (perpendicular) from each other as in most helicopters. Specifically, one set in front of the other at a 55° angle. The supplementary angle is 125°. This unusual arrangement is required because the two sets of blades use a "Delta-Hinge" which allows the blades to simultaneously flap and feather. The four blades appear to behave as two for the tail rotor blade pass frequency.

The purpose of this design is to render the blades more efficient and to reduce noise.  The main rotor hub and the tail rotor hub are driven by the same source. Thus, there is a fixed ratio between the spin rates of each rotor.  The tail rotor spin rate is about 4.86 times higher than the main rotor rate per Reference [41].  Again, the measured, Doppler-shifted, main rotor spin rate is 5.25 Hz or 315 rpm. The tail rotor spin rate is 25.5 Hz, or 1530 rpm, per the fixed ratio. The unique configuration of the blades yields a 2X blade passing frequency at 51 Hz. The blades behave as two pairs rather than as four individual blades. Tail rotor integer harmonics of this

frequency occur at 102, 153, and 204 Hz.  Recall that 153 Hz was the dominant peak in the Fourier transform in Figure 23.17, due to the tail rotor's interaction with the main rotor wake.

## 23.6  TURBOPROP ENGINE



Figure 23.19.  Bombardier Q400 Aircraft

The author once flew from Spokane to Seattle, Washington on an Alaska/Horizon Air Bombardier Q400 aircraft, similar to the one in Figure 23.19.  He made an audio recording using his Android phone.  The Fourier magnitude is shown in Figure 23.20.

This model aircraft has two Pratt & Whitney Canada PW150A turboprop engines.  The PW150A engine/propeller rotation rate during takeoff and climb is 1020 RPM but is throttled back at cruise altitude to 850 RPM, or 14.17 Hz.
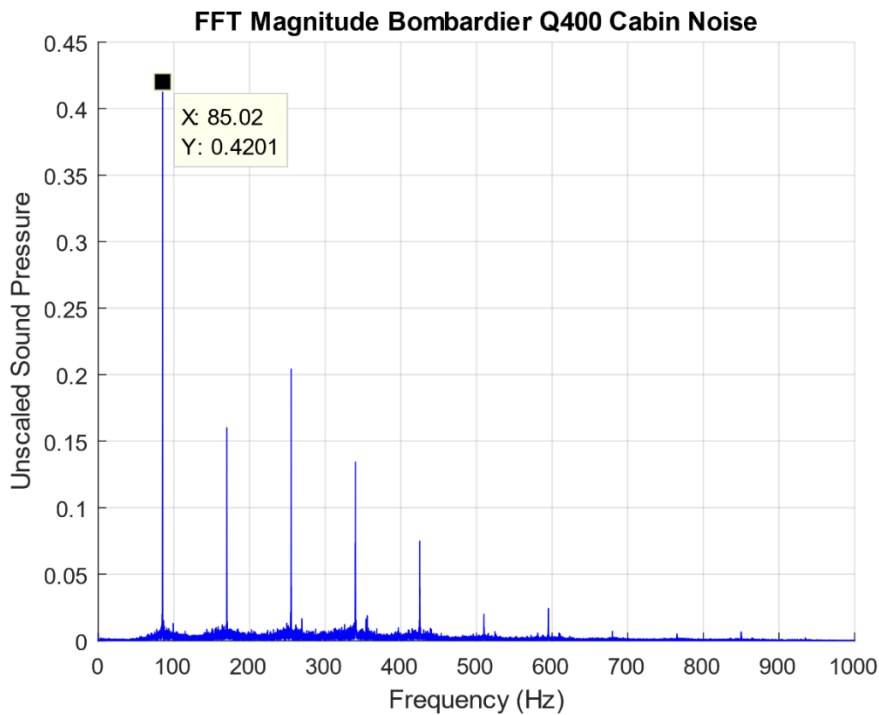


Figure 23.20.  Turboprop Engine Noise Fourier Spectra

There are six blades on each engine, so the blade passing frequency is 85 Hz. This frequency and its integer harmonics are clearly visible in the spectral analysis.

## 23.7 WATERFALL FFT

### 23.7.1 Introduction

A waterfall FFT is a 3D plot with axes of time, frequency, and amplitude. It is useful for visualizing how spectral peak amplitudes and frequencies change with time. A spectrogram is a related 2D plot that shows this same data but with amplitude represented in terms of contour colors.

### 23.7.2 Solid Rocket Motor Example
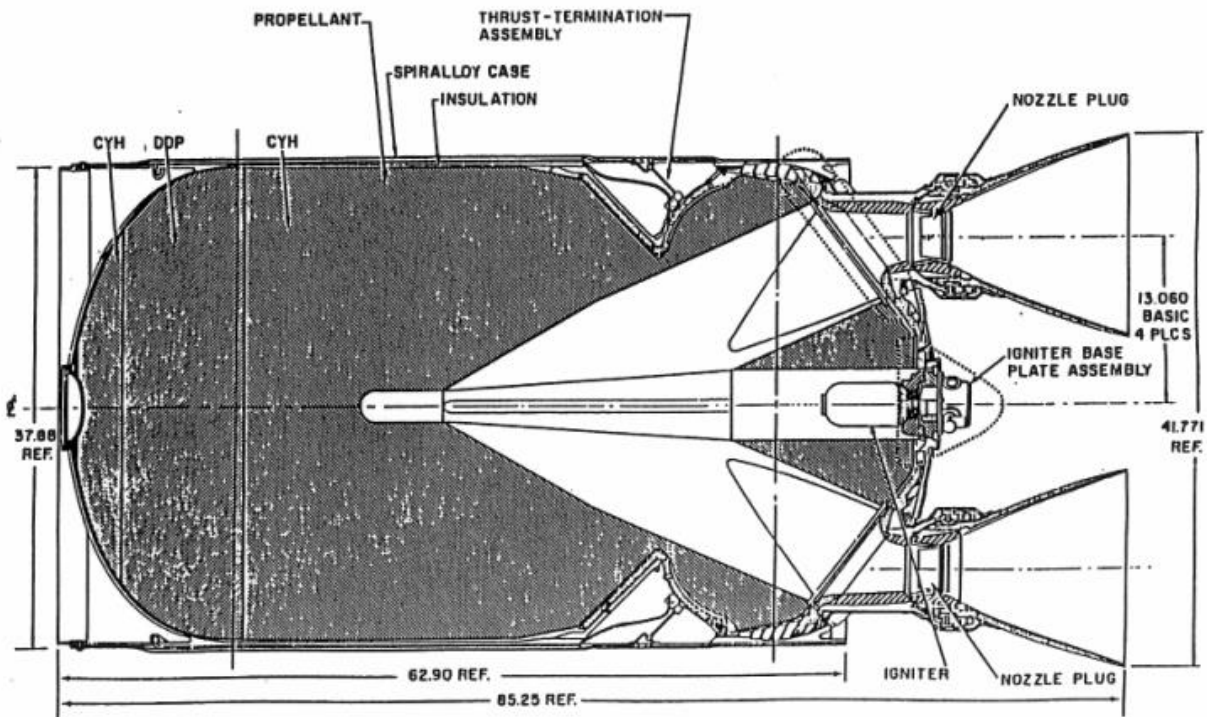


Figure 23.21.  Solid Rocket Motor

Solid rocket motors may have standing pressure oscillations that form in the combustion chamber cavities, caused by vortex-shedding and other effects.  This condition is called

"Resonant Burn" or "Thrust Oscillation." The sinusoidal oscillation frequency may sweep downward as the cavity volume increases due to the conversion of propellant to exhaust gas. A typical upper-stage motor susceptible to this problem is shown in Figure 23.21. Flight data from an accelerometer mounted on a bulkhead adjacent to this motor during its resonance burn is shown in Figure 23.22. The sinusoidal character is apparent in the close-up view.
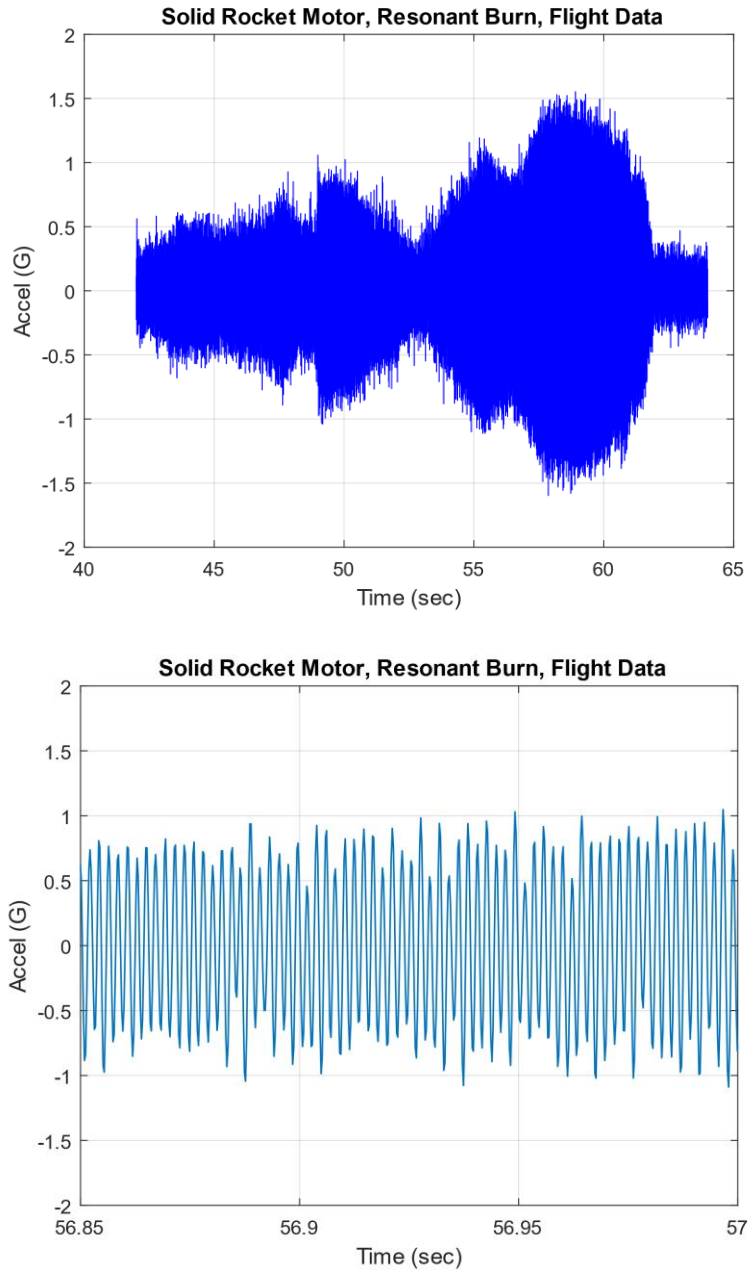


Figure 23.22. Solid Motor Resonance Burn, Accelerometer Data, Full and Close-up Views
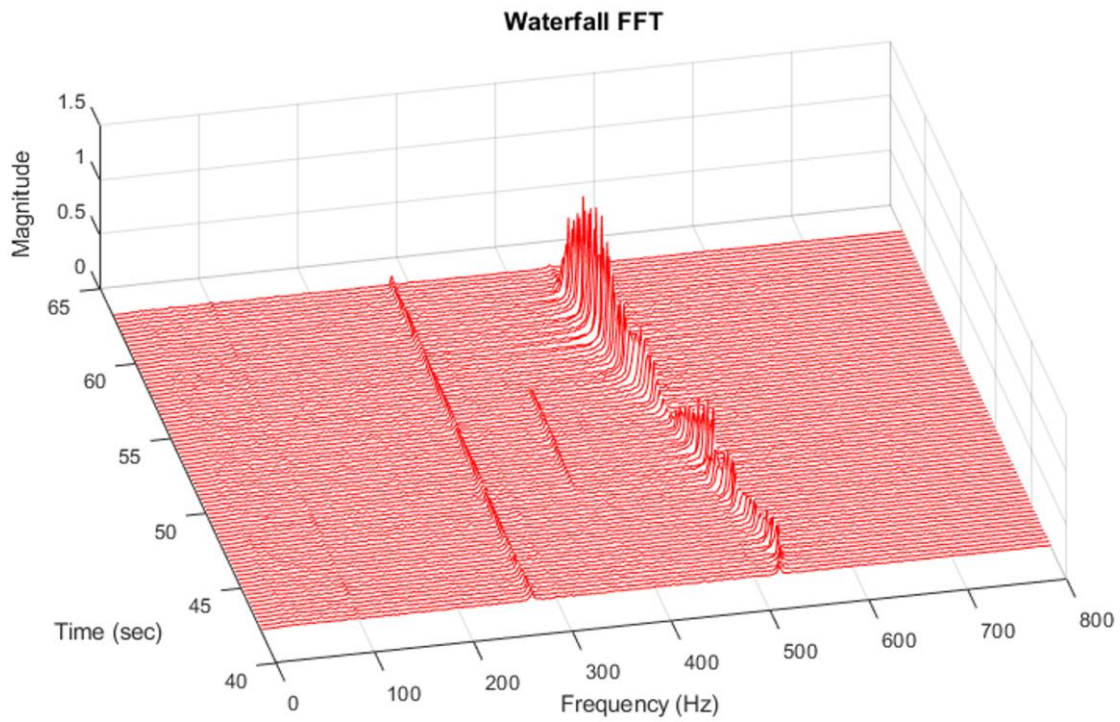
Figure 23.23.  Solid Motor Resonance Burn, Accelerometer Data, Waterfall FFT

The resonant burn spectral peaks begin at 520 Hz and then sweep downward to 450 Hz.  The corresponding amplitude varies with both frequency and time probably due to structural resonance effects as measured by the bulkhead accelerometer.  The causes of peaks at 280 and 350 Hz are unknown.

### 23.7.3 Seaplane Acoustics



Figure 23.24.  De Havilland Canada DHC-3 Otter Seaplane
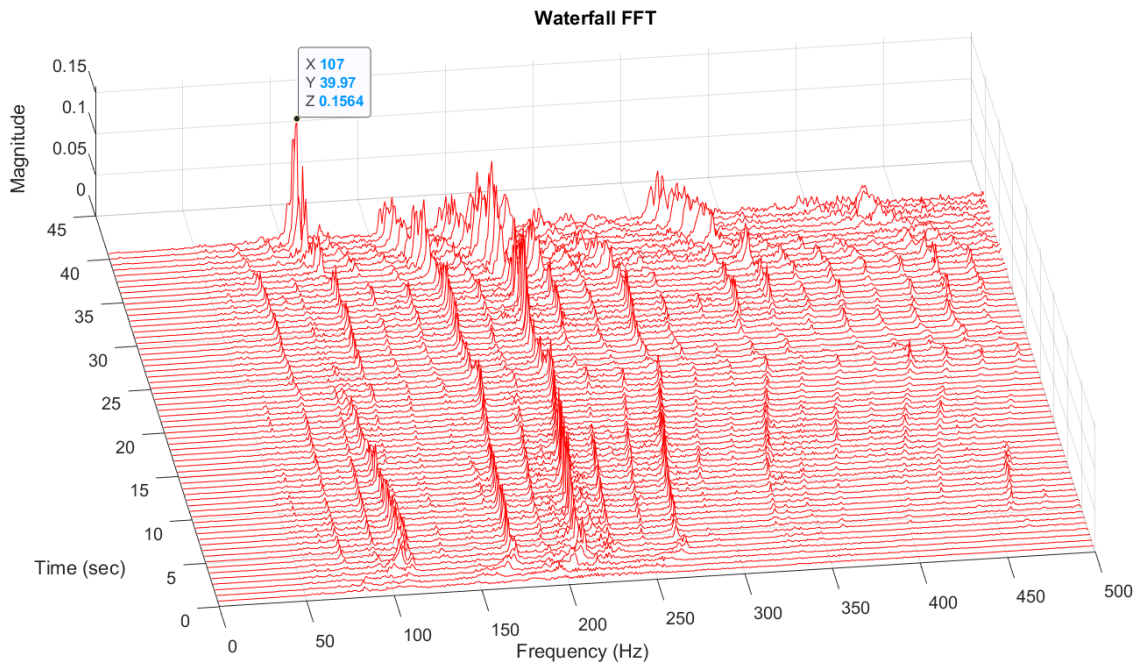


Figure 23.25.  Seaplane, Unscaled Acoustic Data, Waterfall FFT

The aircraft in Figure 23.24 is powered by a single Pratt & Whitney R-1340 Wasp, 600 hp, air-cooled, radial engine with a propeller hub speed of 2250 rpm (35.7 Hz). This aircraft is used for tours and transportation, operated by Harbour Air. The image is extracted from a video taken from Vancouver's Stanley Park. The author took the video of the takeoff using an Android Smartphone, then extracted the audio track and calculated the waterfall FFT.

The spectral peaks in Figure 23.25 have frequency shifts due to the Doppler effect. The 107 Hz spectral peak is due to the blade passing frequency.   The aircraft engine has three blades, resulting in 3 x 35.7 Hz =107 Hz.

### 23.7.4 Wind Chime Acoustics
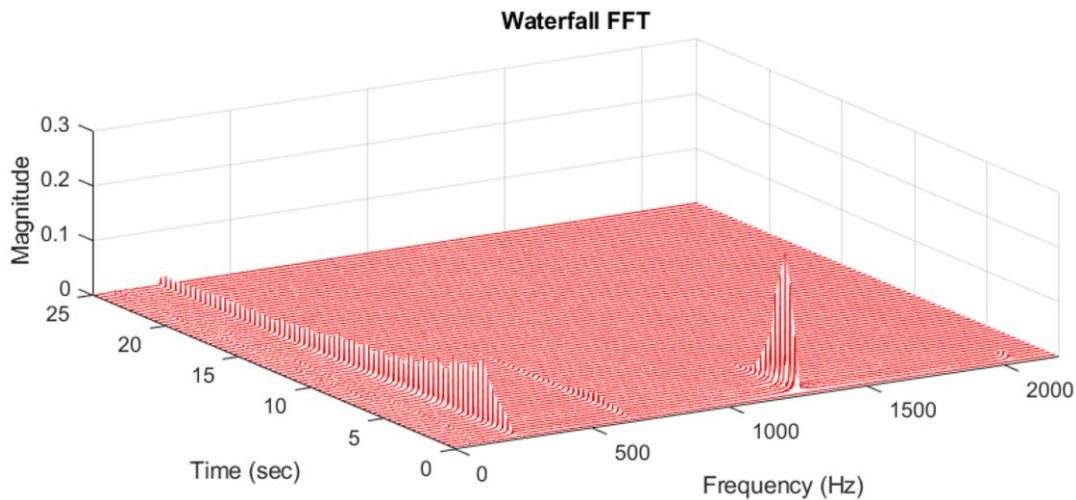


Figure 23.26.   Wind Chime, Unscaled Sound Pressure, Waterfall FFT

Recall the wind chime example from Section 12.1.7.  The bending frequencies for the tallest chime were 238, 657, 1288, and 2127 Hz.  A waterfall of the chime's sounding is shown in Figure 23.26.  The fundamental tone is very persistent with low damping.  The second mode makes a very small contribution.  The third mode initially has the highest generated sound, but the tone decays quickly.  The fourth mode's spectral peaks are barely visible in the plot.

## 23.8  WHITE NOISE FOURIER TRANSFORM

The Fourier transform is an excellent tool for resolving both the frequency and amplitude of a pure sinusoidal signal, aside from leakage concerns.  Alas, it is a poor choice for random vibration.  This is the motivation for representing random vibration in terms of power spectral density as presented in Section 24.  The problem with the Fourier transform approach for random vibration relates to the dependence of the amplitude on the frequency resolution as shown in the following example.   Consider a stationary white noise signal.  An engineer may choose the entire signal or a representative segment for the Fourier transform calculation.  A longer segment duration gives a finer frequency resolution.  There would thus be more points in the Fourier transform magnitude to represent the signal's energy.   The corresponding amplitude of each point would be, on average, lower than if a shorter segment were used with a wider frequency resolution and fewer points.
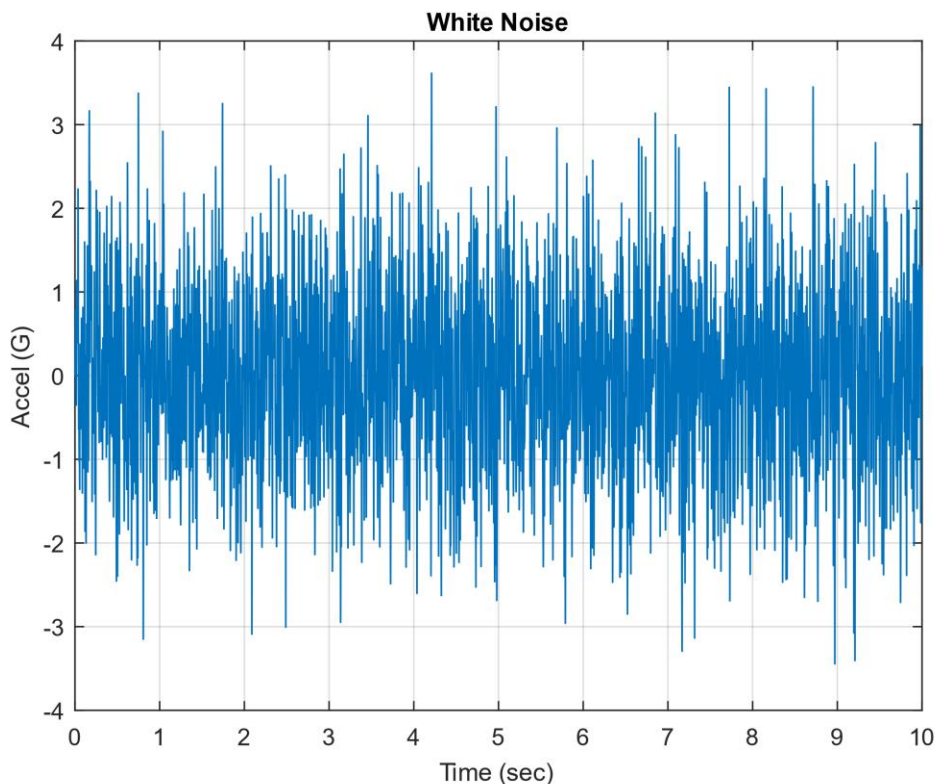


Figure 23.27.   White Noise Time History

A stationary white noise signal is shown in Figure 23.27.  The standard deviation of the entire time history is 1 G.  The standard deviation of the segment from 0 to 1 second is also 1 G, approximately.  Separate Fourier transforms are taken from the entire duration and for the 0 to 1-second segment, as shown in Figure 23.28.
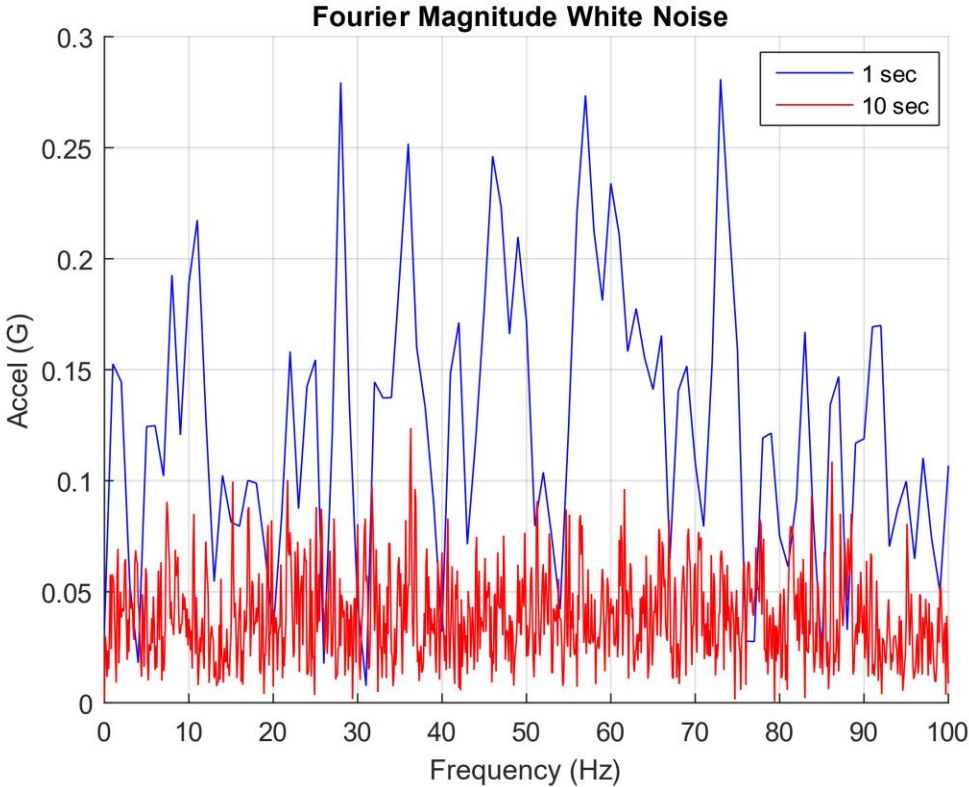


Figure 23.28.   White Noise Fourier Transform

Each curve represents a standard deviation of 1 G, equivalent to 1 GRMS given zero mean.  The overall GRMS value can be calculated by taking the "square root of the sum of the squares" from each curve.  The blue curve has fewer points, by a factor of one-tenth, to carry the energy than the red curve.  The blue curve's average amplitude is thus higher than the denser red curve.

# 24  POWER SPECTRAL DENSITY

## 24.1  DECIBELS & SLOPES

### 24.1.1 Differences

Power spectral density functions are sometimes specified in terms of decibels.  The dB difference between two levels A & B in units of $G^2$ or $G^2$/Hz is

$$\Delta dB = 10 \log ( A / B ) \qquad\qquad (24.1)$$

A 6 dB increase would quadruple a $G^2$/Hz level.  A 6 dB decrease would reduce the $G^2$/Hz level by a ratio of one-fourth.

The dB difference between two levels C & D in units of G or GRMS is

$$\Delta dB = 20 \log ( C / D ) \qquad\qquad (24.2)$$

A 6 dB increase would double a G level.  A 6 dB decrease would reduce the G level by a ratio of one-half.

### 24.1.2 Slopes

Consider a frequency domain plot with a straight-line segment in log-log format with coordinates  $(f_1, y_1)$ and $(f_2, y_2)$ .  The slope N between the coordinate pair is

$$N = \frac{\log[y_2/y_1]}{\log[f_2/f_1]} \qquad\qquad (24.3)$$

The line equation for this pair is

$$y(f) = y_1 \, (f^N/f_1^N) \qquad\qquad (24.4)$$

The dB/octave slope for units of $G^2$ or $G^2/Hz$ is

$$\Delta dB \, / \, oct = 10 \, N \log 2 \qquad (24.5)$$

The dB/octave slope is for units of G or GRMS is

$$\Delta dB \, / \, oct = 20 \, N \log 2 \qquad (24.6)$$

## 24.2  PSD SPECIFICATIONS
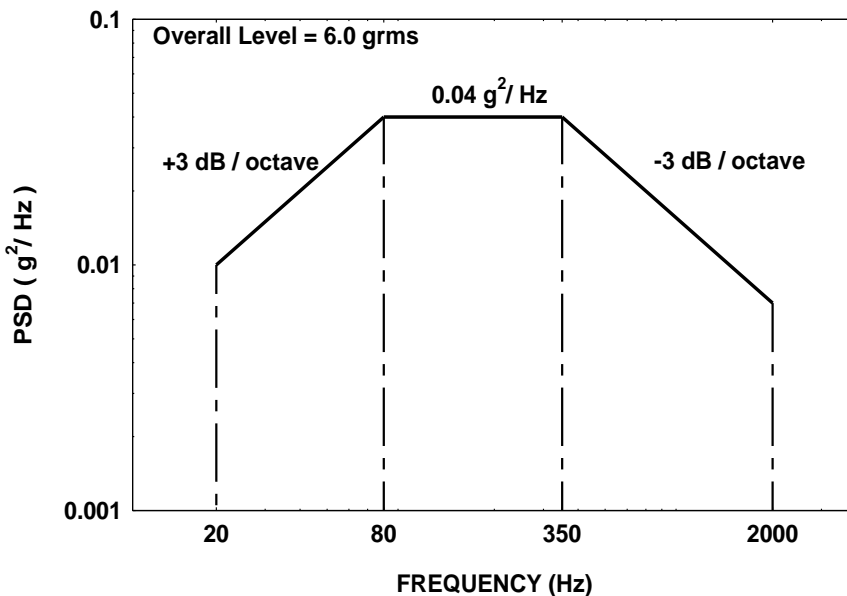


Figure 24.1.   Navmat P-9492 Acceleration PSD

The power spectral density in Figure 24.1 is taken from Reference [42].   The lowercase g convention is carried over from this source, but uppercase G is used elsewhere in the present document.   This level is intended as a base input for a shaker table test (see Section 32) to screen components for parts and workmanship defects.   It is representative of similar levels found in various military and NASA standards.   The Y-axis unit is more properly $grms^2/Hz$.   The specification consists of three straight-line segments in log-log format.   The overall grms value is the "square root of the area under the curve."   The integration approach is to take the $grms^2$ area under each of the three segments.   Then sum the areas and take the square root.   This

requires special integration formulas due to the log-log format which depend on the slope from equation (24.3).

The area $a_i$ for a segment is

$$a_i = \begin{cases} \left[\dfrac{y_i}{f_i^N}\right]\left[\dfrac{1}{N+1}\right]\left[f_{i+1}^{N+1} - f_i^{N+1}\right], & \text{for } N \neq -1 \\[4mm] [y_i f_i]\left[\ln\left(\dfrac{f_{i+1}}{f_i}\right)\right], & \text{for } N = -1 \end{cases}$$

(24.7)

The overall level for m total segments is then

$$a_{RMS} = \sqrt{\sum_{i=1}^{m} a_i}$$

(24.8)

Performing these steps for the Navmat P-9492 specification in Figure 24.1 requires some preliminary work because the specification did not explicitly give the first and last amplitudes. The first coordinate amplitude is 0.01 g²/Hz by inspection of the graph. Identifying the last coordinate amplitude requires a two-step calculation. The slope is

$$N = \frac{-3\text{ dB}}{10 \log 2} \approx -1.0$$

(24.9)

The final coordinate amplitude is

$$y = \left[\frac{0.04\text{ G}^2/\text{Hz}}{(350\text{ Hz})^{-1}}\right][2000\text{ Hz}]^{-1} \approx 0.007\text{ G}^2/\text{Hz}$$

(24.10)

The final amplitude is whimsically referred to as "Bond." The overall grms calculation is summarized in Table 24.1.

Table 24.1.  Navmat P-9492 Overall Level Calculation

| Frequency Domain | Slope N | grms$^2$ |
|---|---|---|
| 20 to 80 | 1 | 1.5 |
| 80 to 350 | 0 | 10.8 |
| 350 to 2000 | -1 | 24.4 |
| | Total | 36.7 |

The overall level is the square root of 36.7 grms$^2$ which is 6.06 grms.

## 24.3  PSD INTEGRATION IN THE FREQUENCY DOMAIN

An acceleration PSD has a corresponding velocity PSD and a displacement PSD.

Let

APSD   =   Acceleration PSD
VPSD   =   Velocity PSD
DPSD   =   Displacement PSD

The integration formulas are

$$\text{VPSD}(\omega) = \text{APSD}(\omega) / \omega^2 \tag{24.11}$$

$$\text{DPSD}(\omega) = \text{APSD}(\omega) / \omega^4 \tag{24.12}$$

The resulting velocity and displacement PSDs for the Navmat specification are shown in Figure 24.2 and Figure 24.3, respectively.  These plots are useful to determine whether a given acceleration PSD test can be performed on a certain shaker table given the table's velocity and displacement limits.
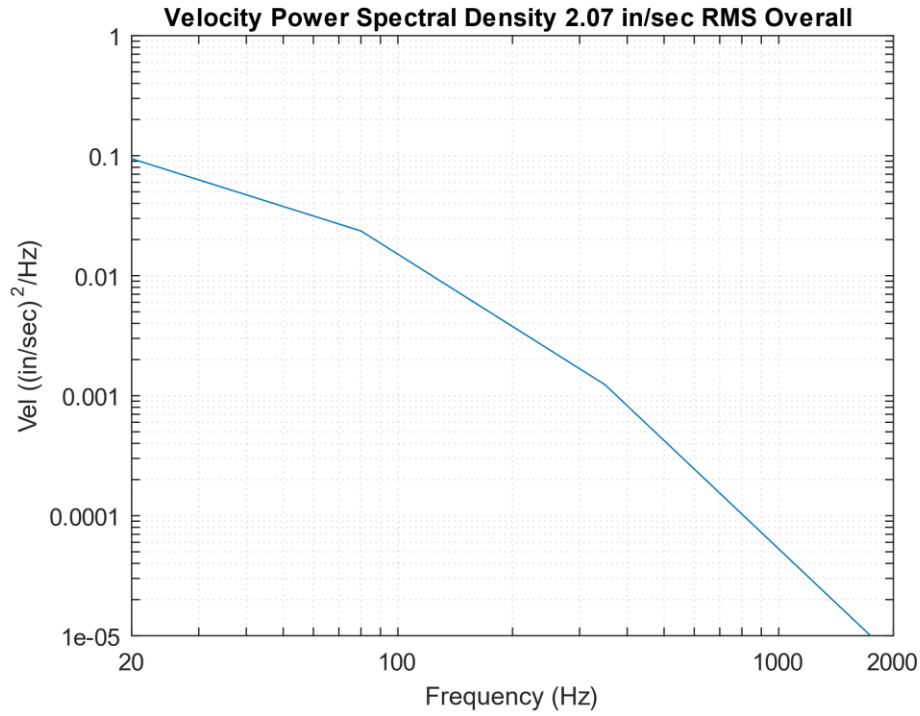
Figure 24.2.   Navmat P-9492 Velocity PSD
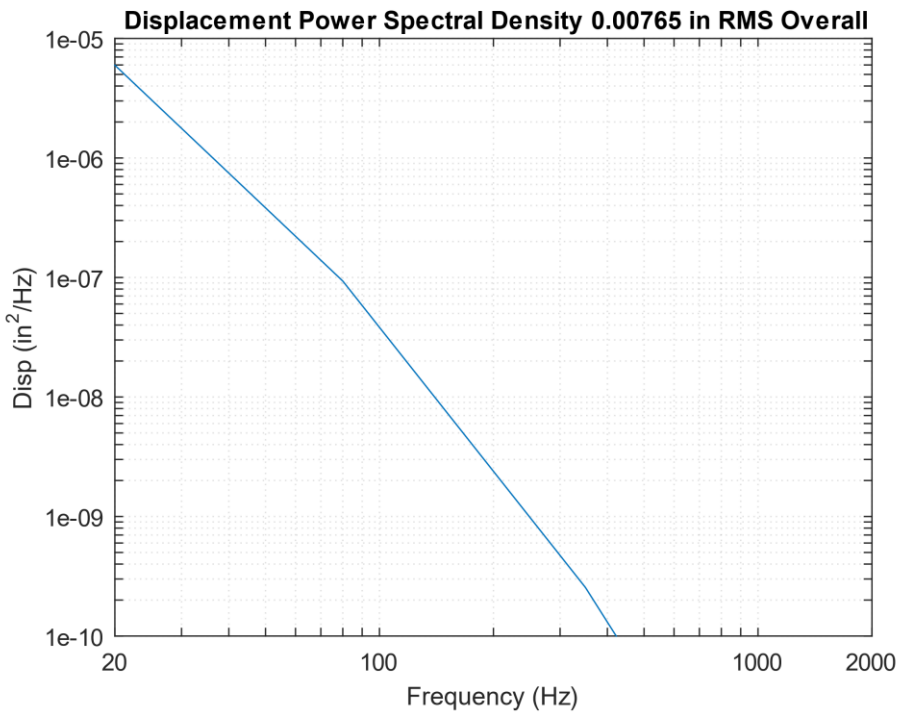


Figure 24.3.   Navmat P-9492 Displacement PSD

## 24.4  PSD CALCULATION METHODS

Power spectral density functions of measured data may be calculated via three methods:

1. Measuring the RMS value of the amplitude in successive frequency bands, where the signal in each band has been bandpass filtered
2. Taking the Fourier transform of the autocorrelation function
3. Taking the limit of the Fourier transform $X(f)$ times its complex conjugate divided by its period T as the period approaches infinity.

The filtering option is the most instructive method and is covered in Section 30.  The autocorrelation option is the Wierner-Khintchine approach and is omitted from this document. A modified form of the third option is covered in this section and is the preferred method for computational efficiency.

The one-sided power spectral density function $X_{PSD}(f)$ is calculated from the discrete Fourier transform $X(f)$ as

$$X_{PSD}(f) = \lim_{\Delta f \to 0} \left[ \frac{1}{2} \frac{X(f)X^*(f)}{\Delta f} \right] \qquad (24.13)$$

The Fourier transform in the equation extends from zero frequency to the Nyquist frequency, which is one-half the sample rate.  Each Fourier transform has its amplitude dimension in terms of the peak.  The one-half factor is needed to convert the amplitude from peak$^2$/Hz to rms$^2$/Hz.

The frequency step is finite in practice and is the inverse of the total measured duration.

$$\Delta f = 1 \, / \, T \qquad (24.14)$$

This frequency step is the smallest sine wave frequency that can be resolved, where this sine wave has one period equal to the total duration.  The frequency step is linked to the number of statistical-degrees-of-freedom.  The reliability of the power spectral density data is proportional to the number of degrees.  A wider $\Delta f$ gives greater PSD confidence in terms of smoothing the spectral components.

The number of degrees $N_{dof}$ is defined as

$$N_{dof} = 2 \, B \, T \qquad (24.15)$$

The variable $B$ is the bandwidth of an ideal rectangular filter.   It is equal to the frequency step $\Delta f$ for an ideal rectangular filter.  The $BT$ product is unity and the number of DOF is always equal to two for a given record assuming a rectangular filter.   This number may be increased for a given record by subdividing it into a set of small segments, where each segment has two degrees.  The total number of degrees is then equal to twice the number of segments.  This subdivision approach tends to smooth the PSD.  The penalty, however, is that the frequency resolution widens as the record is subdivided which could smear narrow peaks.  These tradeoffs are shown by example in the following table.

Table 24.2.  Time History with 4096 Samples Taken over 16 Seconds, Rectangular Filter

| Number of Records NR | Number of Time Samples per Record | Period of Each Record $T_i$ (sec) | Frequency Resolution $B_i = 1 / T_i$ (Hz) | DOF per Record $= 2B_i T_I$ | Total DOF |
|---|---|---|---|---|---|
| 1 | 4096 | 16 | 0.0625 | 2 | 2 |
| 2 | 2048 | 8 | 0.125 | 2 | 4 |
| 4 | 1024 | 4 | 0.25 | 2 | 8 |
| 8 | 512 | 2 | 0.5 | 2 | 16 |
| 16 | 256 | 1 | 1 | 2 | 32 |
| 32 | 128 | 0.5 | 2 | 2 | 64 |
| 64 | 64 | 0.25 | 4 | 2 | 128 |

Note that the final PSD is the arithmetic average if the individual record PSDs if more than one record is used.

Additional rows could be added to the above table but are omitted for brevity.  Selecting the optimum processing strategy for a given time history is a matter of engineering judgment.  Continuing with the table example, a frequency step of 4 Hz with 128 DOF might be a good choice for demonstrating that the broadband base input for a shaker table test complied with the specified PSD's tolerance bands.   On the other hand, a narrow frequency resolution from the first or second row may be needed if the purpose of analyzing the PSD is to identify lightly-damped, low-frequency resonant peaks.

Recall that a rectangular filter leaves the time history data unmodified. Leakage error may be a concern, however, as discussed in Section 23.2. A Hanning window can be applied to each data segment to reduce leakage, but it is a non-ideal filter that reduces the number of DOF. The key to applying the Hanning window is to subdivide the data into overlapping segments. Nearly 90% of the DOF are recovered with a 50% overlap, as shown in Figure 24.4.
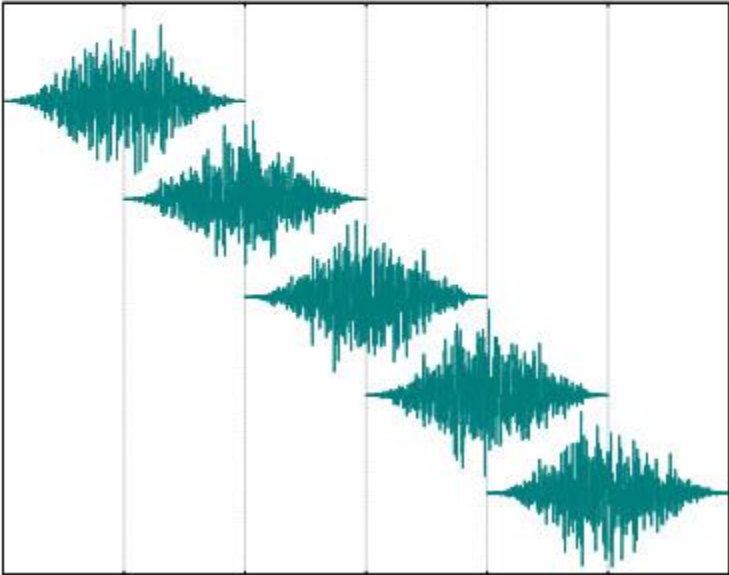


Figure 24.4. White Noise and Subdivision into Overlapped Segments with Hanning Windows

## 24.5  PSD CALCULATION EXAMPLES

### 24.5.1  Matlab Scripts

A Matlab script for calculating the power spectral density of a time history is given at:

https://www.mathworks.com/matlabcentral/fileexchange/127339-power-spectral-density-psd-of-a-time-history

A script for synthesizing a time history for an acceleration PSD specification is given at:

https://www.mathworks.com/matlabcentral/fileexchange/127399-synthesize-a-time-history-for-an-acceleration-psd

### 24.5.2 White Noise PSD

Recall the white noise time history in Figure 23.27.  A PSD is calculated for this signal with a Hanning window and 50% overlap for each of the two frequency resolution cases.  The PSDs are shown in Figure 24.5.
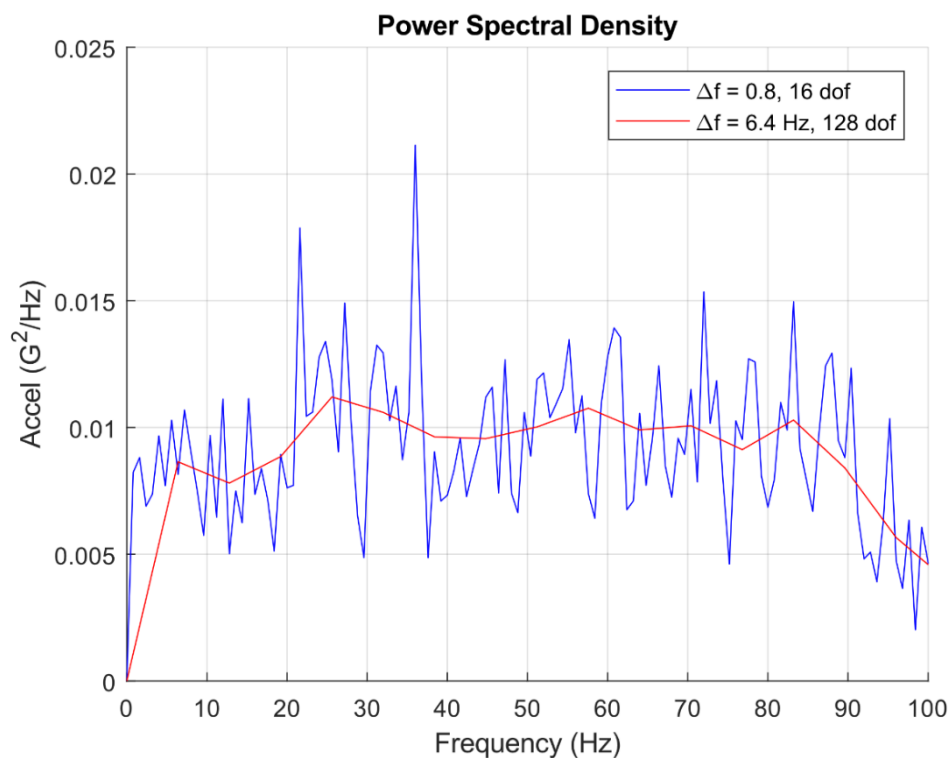


Figure 24.5.   White Noise PSDs

The blue curve has a finer frequency resolution and more variation than the red curve.  The red curve is smoother due to its wider frequency resolution and higher DOF number.  The red curve effectively averages the PSD points into wider bands.  Note that pure white noise would have a flat PSD curve.  The time history in  Figure 23.27 departs from this ideal because it was taken over a short, 10-second duration.  It was also band-limited via low-pass filtering such that it has a roll-off beginning at about 85 Hz.  Filtering is covered in Section 30.

### 24.5.3 Taurus Auto PSD



Figure 24.6.   2003 Ford Taurus Auto

The author mounted an accelerometer in his auto's console as shown in Figure 24.6.   The vehicle was driven on a highway at 65 mph.  An accelerometer time history from this road test is given in Figure 24.7.  The PSD is shown in Figure 24.8, with a narrow frequency resolution to aid in spectral peak identification.  The fundamental mode damping is calculated via the half-power bandwidth method in Figure 24.9.
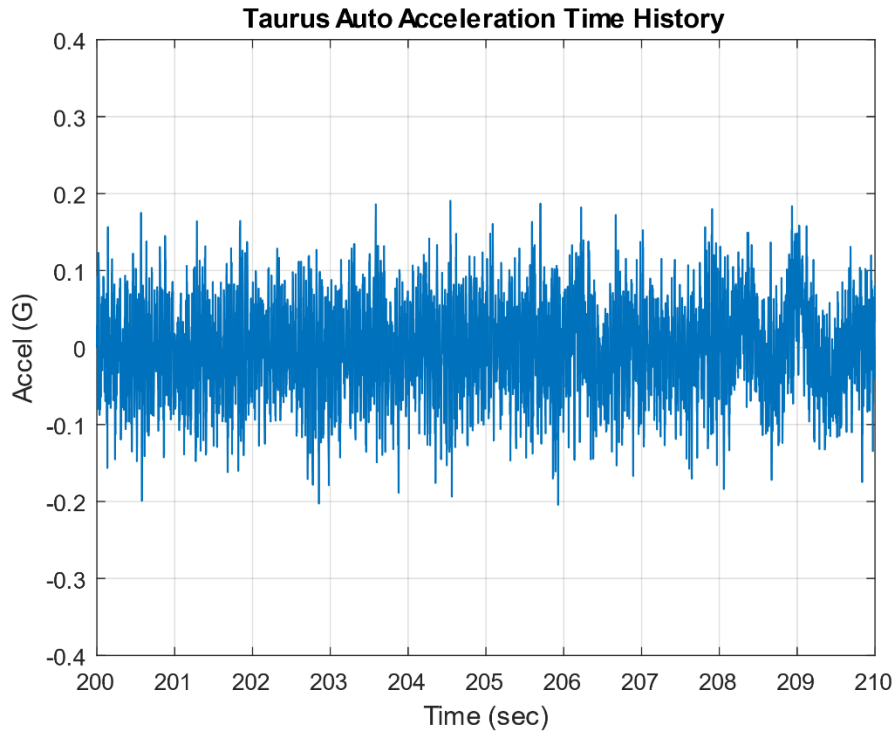
Figure 24.7.   Taurus Time History
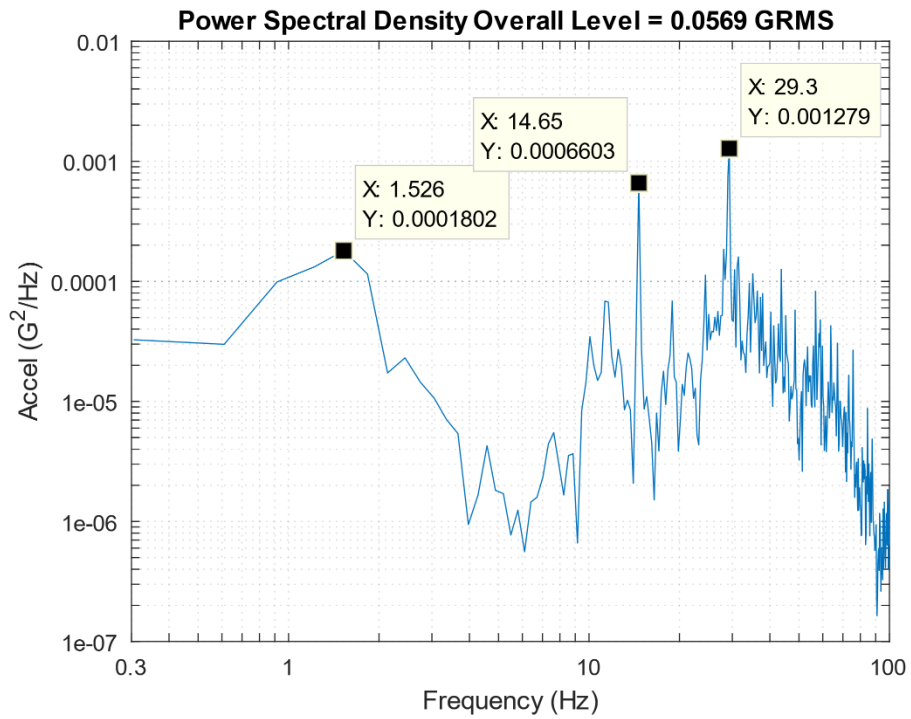


Figure 24.8.   Taurus PSD, Δf=0.3 Hz, 6 Statistical DOF
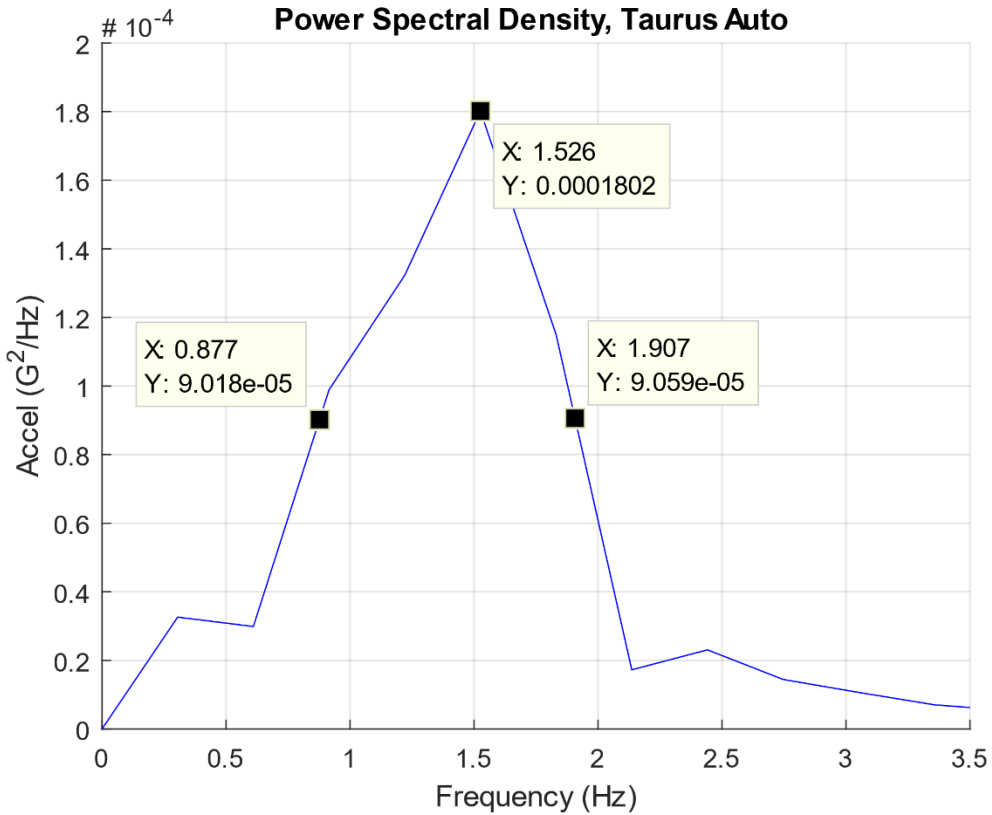
Figure 24.9.   Taurus PSD, Half-Power Bandwidth

$$Q = \frac{f}{\Delta f} = \frac{1.5 \text{ Hz}}{(1.9 - 0.88) \text{ Hz}} \approx 1.5 \quad (33\% \text{ damping}) \qquad (24.16)$$

The Taurus auto spring-mass Frequency is 1.5 Hz with 33% damping, which is typical damping for shock absorbers.  Common automobile natural frequencies are given in Table 24.3.

Table 24.3.  Automobile Spring-Mass Frequencies

| Vehicle | Fundamental Frequency |
|---|---|
| Passenger Car | 1 to 1.5 Hz |
| Sports Car | 2 to 2.5 Hz |
| Hummer | 4.5 Hz |

The spectral peaks in Figure 24.8 at 14.6 and 29.1 Hz can be explained as tire imbalance frequencies per the following calculation steps.

a.  Assume a 25-inch tire outer diameter at 65 mph.
b.  Circumference = $\pi$ (25 inch) = 78.5 inch
c.  65 mph = 1144 in/sec
d.  Speed/Circumference = (1144 in/sec) / 78.5 in = 14.6 Hz
e.  2X harmonic = 29.1 Hz

## 24.5.4 Tire Imbalance
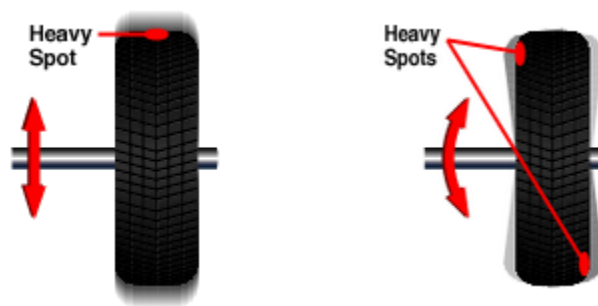


Figure 24.10.  Tire Imbalance (Discount Tire image)

Static imbalance (left image) occurs when there is a heavy or light spot in the tire that prevents the tire from rolling evenly and causing the tire and wheel to undergo an up-and-down motion.

Dynamic Imbalance (right image) occurs when there is unequal weight on one or both sides of the tire/wheel assembly's lateral centerline, thus creating a side-to-side wobble or wheel shimmy.

A vehicle generally vibrates from an unbalanced tire at speeds greater than 45 mph.

Some common symptoms of tire imbalance include:

- Vibration in the steering wheel, floorboard, or seat that increases with speed
- Poor fuel economy
- Uneven and faster than usual treadwear
- Difficulty steering smoothly
- Premature wear of shocks, springs, bearings, and other wheel assembly components
- Loud tire noise while driving

## 24.6  PSD TIME HISTORY SYNTHESIS

Table 24.4.  Time History Synthesis Steps to Meet PSD Specification

| Step | Description |
|------|-------------|
| 1 | Generate a white noise time history |
| 2 | Take the FFT |
| 3 | Scale the FFT amplitude per the PSD for each frequency |
| 4 | The time history is the inverse FFT |
| 5 | Use integration, polynomial trend removal, fade in and out, and differentiation so that the corresponding mean velocity and mean displacement are both zero |
| 6 | Scale the time history so that its GRMS value matches the specification's overall GRMS value |
| 7 | Take a PSD of the synthesized time history to verify that it matches the PSD specification |

The method for synthesizing a time history to satisfy a PSD is shown in Table 24.4. These steps are used to synthesize an acceleration time history to satisfy the Navmat P-9492 specification. The resulting broadband random time history is shown in Figure 24.11, with its normal distribution histogram.  It began as white noise but was modified such that the final time history is no longer white noise.  Its final, corresponding PSD is shaped and defined over a finite frequency domain, as shown in Figure 24.12.  White noise would have a flat PSD in contrast.
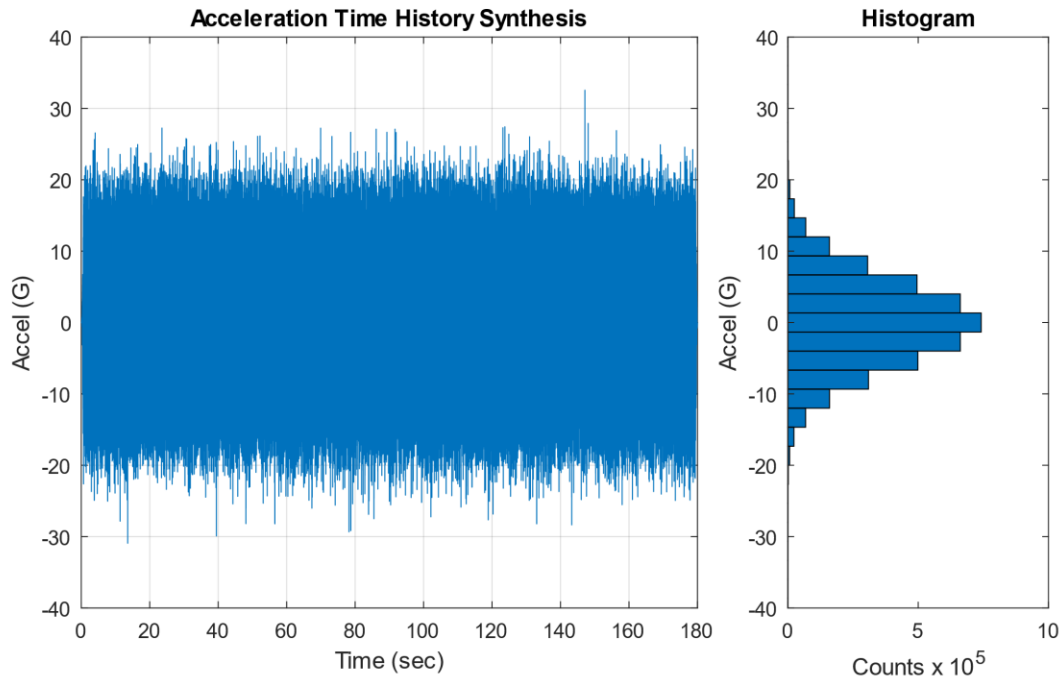
Figure 24.11.   Acceleration Time History and Histogram

Table  24.5.   Acceleration Time History Statistics

| Parameter | Value | | Parameter | Value |
|-----------|-------|---|-----------|-------|
| Mean | 0 G | | Kurtosis | 3.01 |
| Std Dev | 6.06 G | | Crest Factor | 5.375 |
| RMS | 6.06 G | | Maximum | 32.56 G |
| Skewness | 0.011 | | Minimum | -30.93 G |
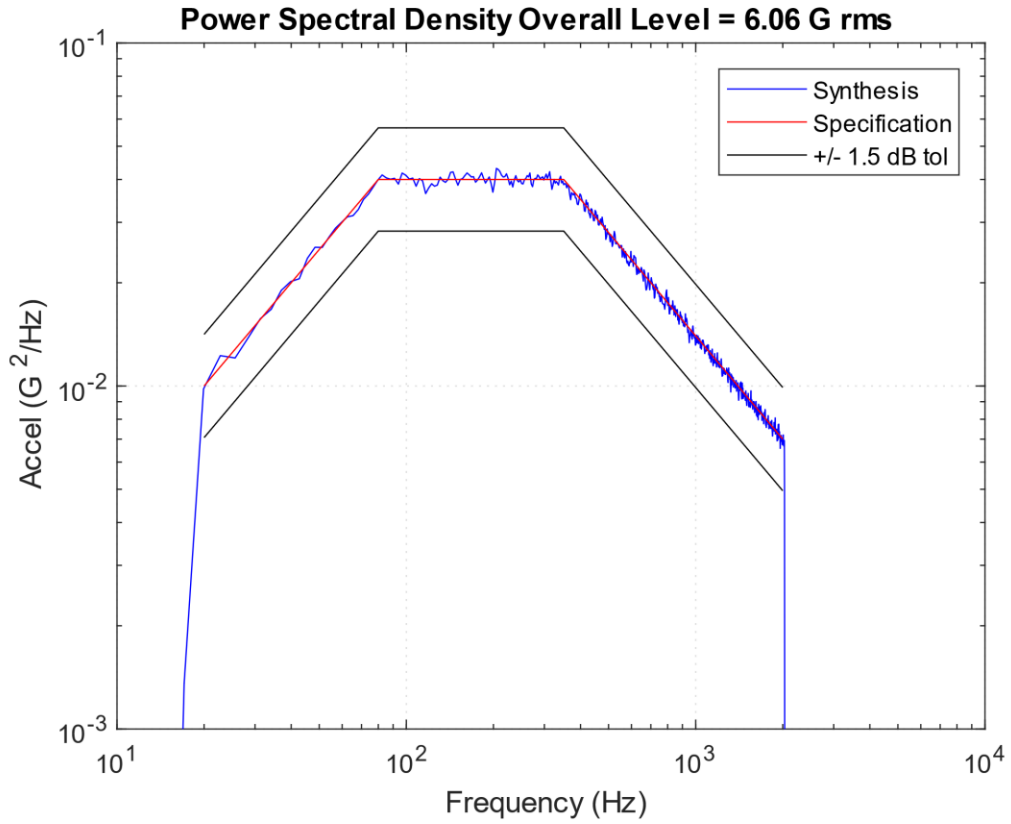
Figure 24.12.   PSD Verification

The synthesized time history satisfies the specification well within the tolerance bands.  The frequency step is 2.84 Hz with 1024 statistical DOF.
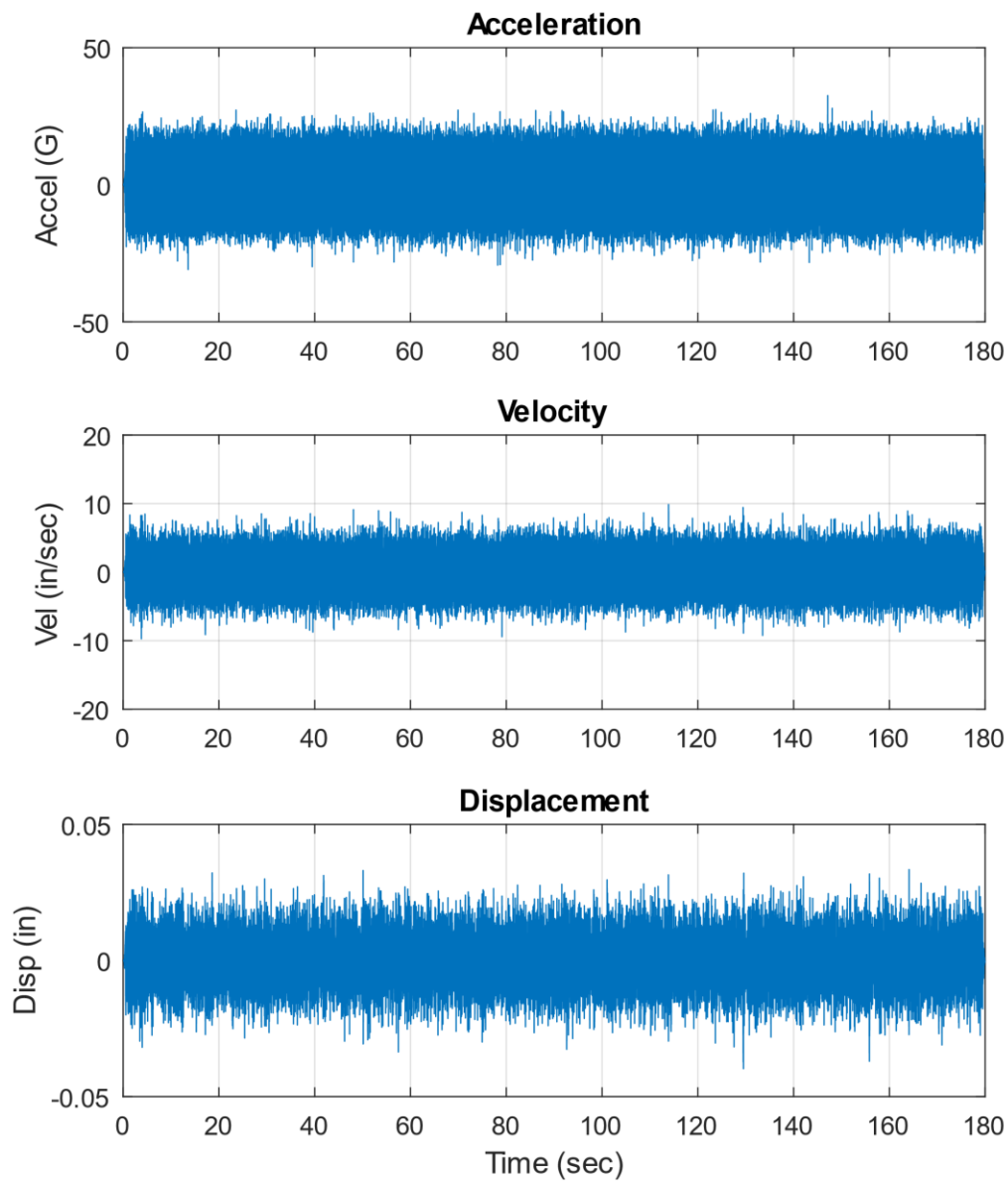
Figure 24.13. Synthesized Time History, Acceleration, Velocity, and Displacement

Each of the three response time histories has a stable oscillation about its zero baseline. Each also has a brief fade in and out, which could be seen in a close-up view of the start and finish.

Now assume an SDOF system with (fn=200 Hz, Q=10) subjected to the Navmat P-9492 PSD base input, using the model in Figure 17.14. Solve for the acceleration response in the time domain using the synthesized base input. The numerical engine is the Smallwood ramp invariant digital recursive relationship. The response time history is shown in Figure 24.14.
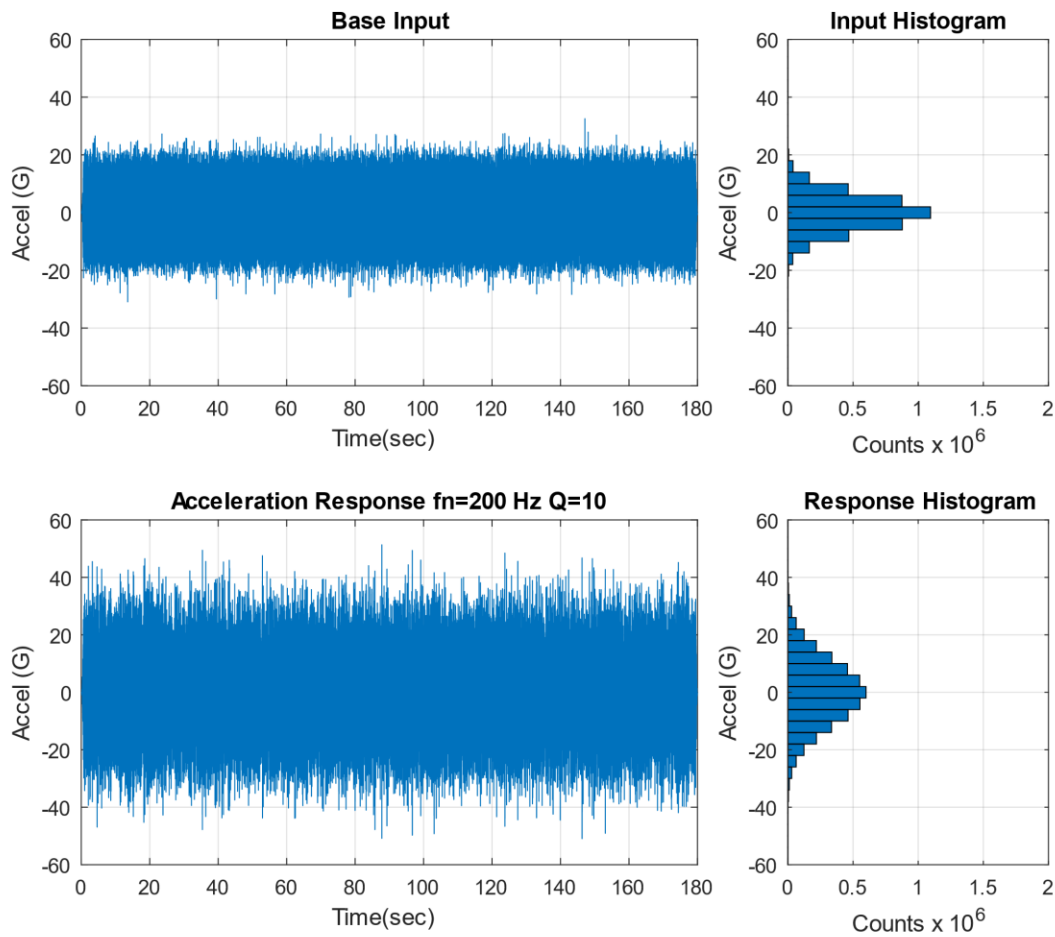
Figure 24.14.   SDOF Response to Synthesized Base Input

Table  24.6.   Acceleration Response Time History Statistics

| Parameter | Value | Parameter | Value |
|-----------|-------|-----------|-------|
| Mean | 0 G | Kurtosis | 3.02 |
| Std Dev | 11.3 G | Crest Factor | 4.548 |
| RMS | 11.3 G | Maximum | 51.36 G |
| Skewness | 0.003 | Minimum | -50.95 G |

The overall response of 11.3 GRMS is very close to the theoretical values from the frequency domain methods which will be shown in Sections 24.7 and 24.8.  The theoretical crest factor for this case per equation (21.11) is 4.71, slightly higher than the 4.548 value in the table.

The time domain synthesis method could whimsically be referred to as a Rube Goldberg approach, after the famous inventor and cartoonist.
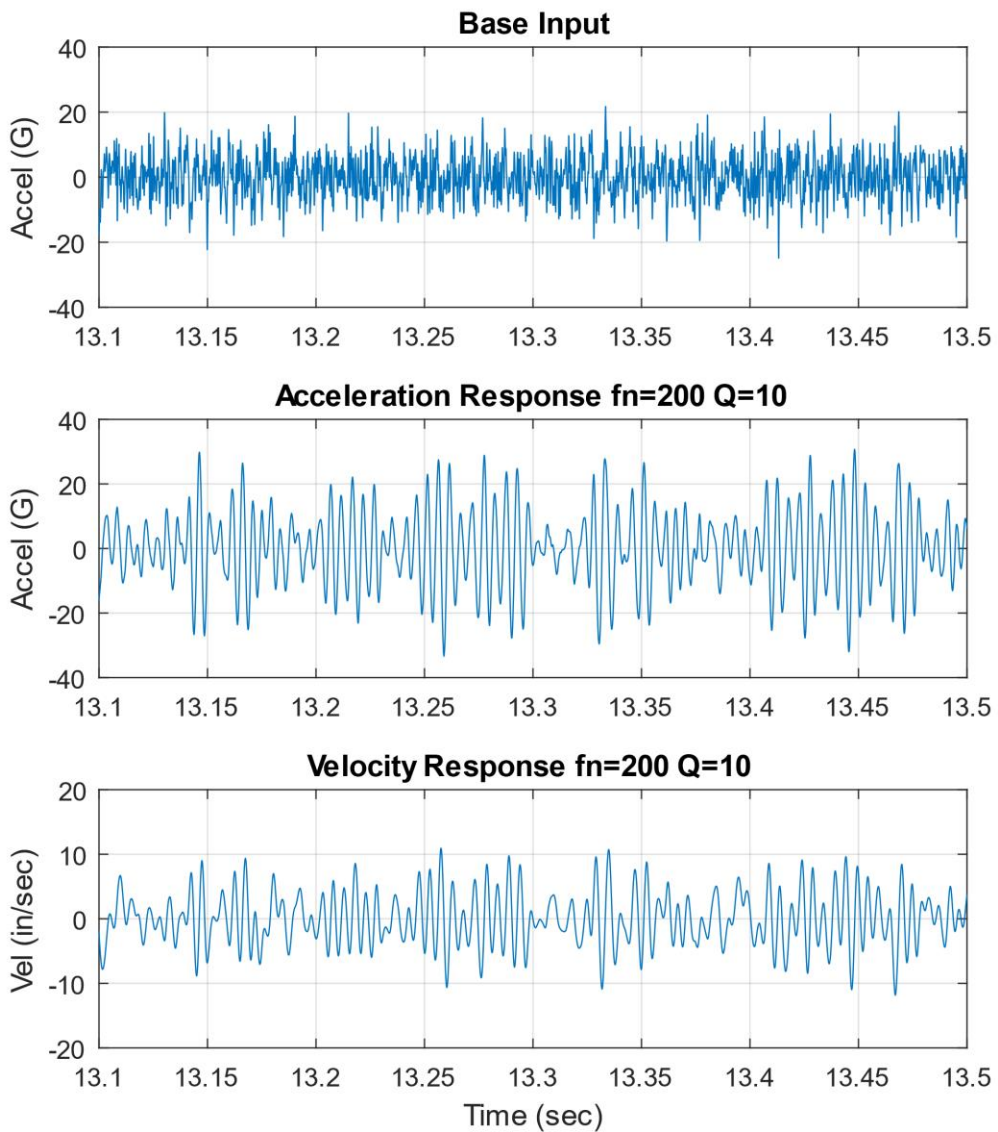


Figure 24.15.   Input and Response Acceleration including Response Velocity, Close-up View

The base input is broadband random vibration.  The response acceleration and velocity time histories are narrowband random.  The SDOF system prefers to oscillate at its natural frequency.  The positive slope zero cross rate is 199.6 Hz.
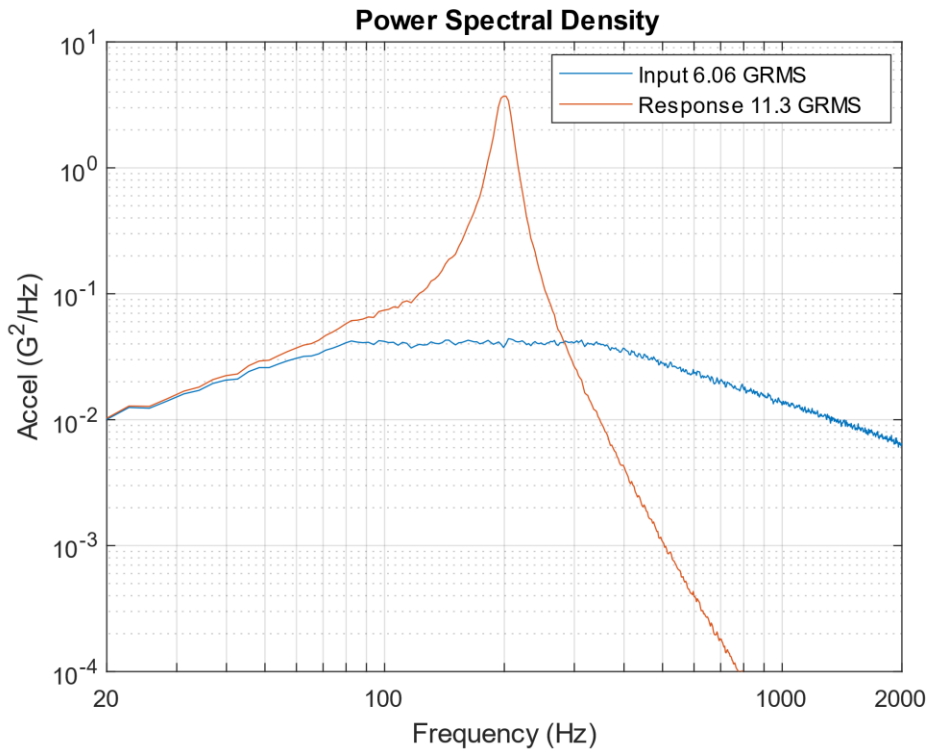
Figure 24.16.    Input and Response PSDs for Navmat P-9492 Synthesis

The response PSD tracks the input at the low-frequency end with nearly unity gain.  The resonant response occurs at and near the 200 Hz natural frequency.  The energy above √2 times the natural frequency is attenuated.  Compare Figure 24.16 with the same set of PSD curves derived from the frequency domain method which will be shown in Figure 24.19.
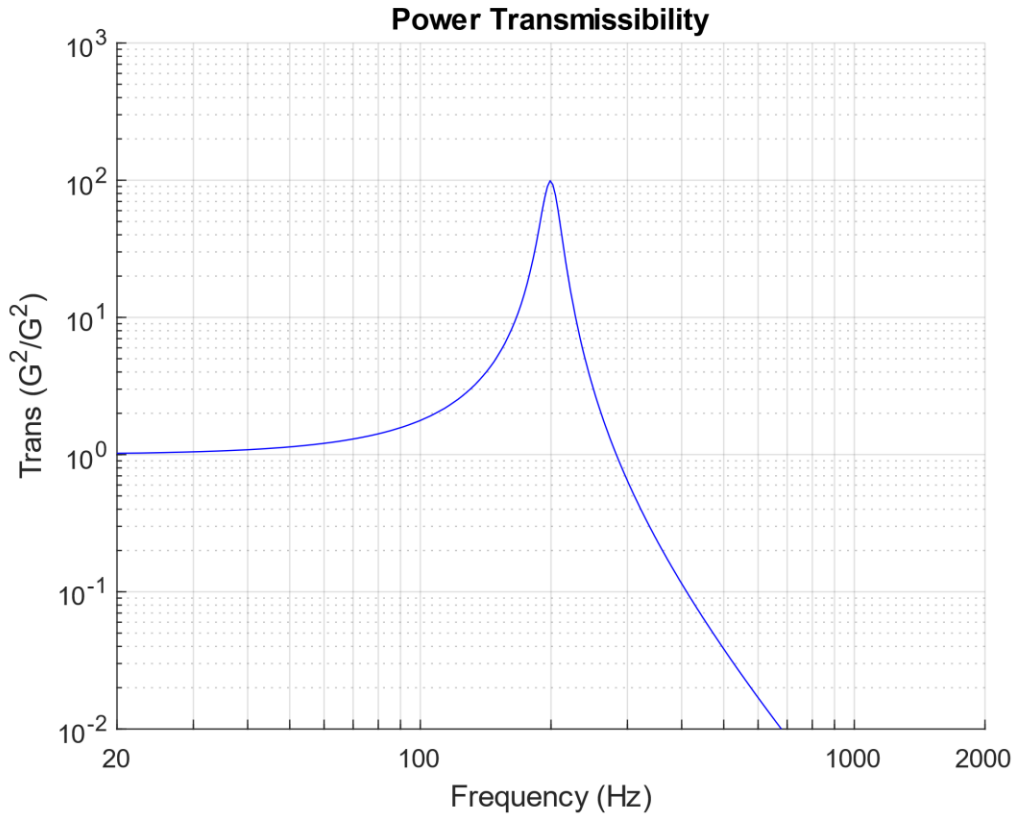
Figure 24.17.   Power Transmissibility for Input and Response PSDs

The peak power transmissibility reaches nearly 100 $G^2/ G^2$ at 200 Hz which is equivalent to $Q^2$ where Q=10.  But this is a special case of an SDOF system subjected to base excitation.  A more robust method for estimating the Q value, as if this were experimental data, is to use the half-power bandwidth method shown in Figure 24.18.

**Power Transmissibility**

X: 199.4
Y: 99.13

X: 188.9
Y: 49.69

X: 209.6
Y: 49.49
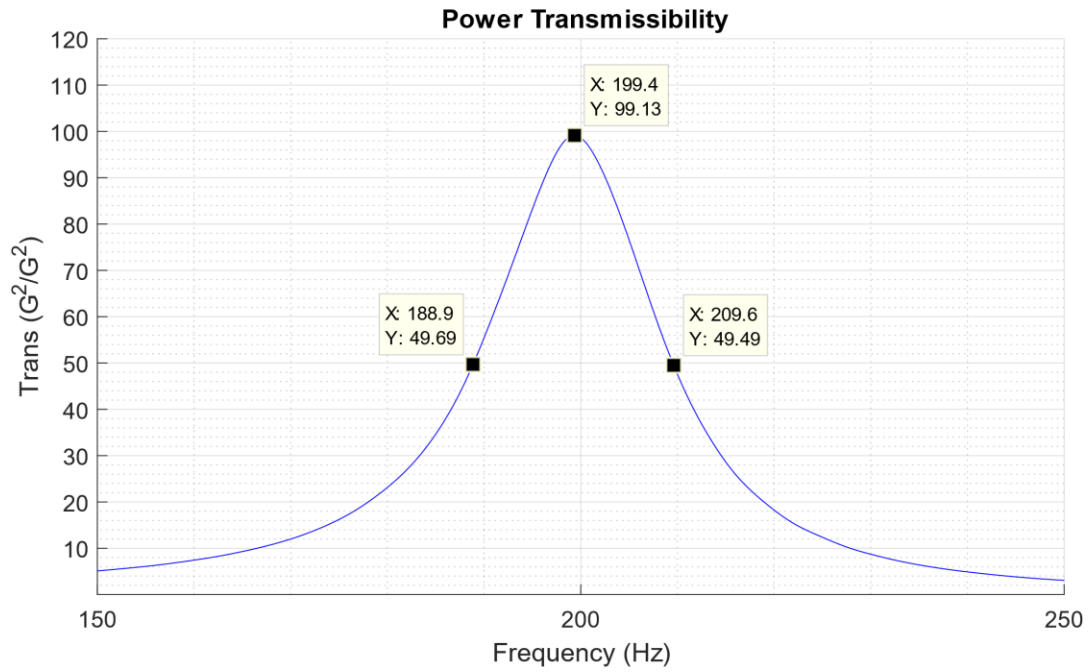
Figure 24.18.   Power Transmissibility with Half-Power Bandwidth Points

The half-power bandwidth method yields the following amplification factor.

$$Q = \frac{f}{\Delta f} = \frac{199.4 \text{ Hz}}{(209.6 - 188.9) \text{ Hz}} = 9.63 \approx 10 \qquad (24.17)$$

## 24.7 MILES EQUATION FOR BASE EXCITATION

Consider an SDOF system subjected to base excitation where the input PSD is white noise over the frequency domain from 0 to infinity Hz, using the model in Figure 17.14. The resulting acceleration $\ddot{x}_{GRMS}$ can be determined by the Miles equation from Reference [18]. The constant power spectral density amplitude is represented by $A$ with unit of ($G^2$/ Hz).

$$\ddot{x}_{GRMS}(f_n, Q) = \sqrt{\frac{\pi}{2} f_n \, Q \, A} \tag{24.18}$$

An equivalent form is

$$\ddot{x}_{GRMS}(f_n, \xi) = \sqrt{\frac{\pi}{4\xi} f_n \, Q \, A} \tag{24.19}$$

The Miles equation is widely used due to its simplicity, but its assumption of white noise over an infinite domain does not exist in physical reality. A rule of thumb states that it may be used as long as the input PSD is flat within one octave on either side of the natural frequency. In practice, this rule is used with some compromise.

Assume an SDOF system with (fn=200 Hz, Q=10) subjected to the Navmat P-9492 PSD base input. The overall response is

$$\ddot{x}_{GRMS}(f_n, Q) = \sqrt{\frac{\pi}{2} (200 \text{ Hz}) \, (10) \, (0.04 \text{ G}^2/\text{Hz})} = 11.2 \text{ GRMS} \tag{24.20}$$

A more robust method for performing the response calculation is given in Section 24.8.

## 24.8  GENERAL METHOD FOR BASE EXCITATION

Real-world PSD specifications are shaped and have lower and upper-frequency limits. Miles' equation cannot account for a PSD with ramps and plateaus. The problem is exacerbated if the PSD is from narrowband measured data with peaks and dips. These practical characteristics can be readily accounted for by applying the power transmissibility function to the base input PSD and then by doing a point-by-point multiplication to calculate the response PSD. The overall response is then the square root of the area under the response PSD curve.

Recall the SDOF transmissibility function from equation (17.59).

$$| H(\rho) | = \sqrt{\frac{1 + (2\xi\rho)^2}{(1 - \rho^2)^2 + (2\xi\rho)^2}} \ , \qquad \rho = f/f_n \tag{24.21}$$

The power transmissibility is equal to the transmissibility squared. The response PSD is calculated from the power transmissibility to the input PSD.

$$X_{PSD}(f) = \left[ \frac{1 + (2\xi\rho)^2}{(1 - \rho^2)^2 + (2\xi\rho)^2} \right] Y_{PSD}(f) \tag{24.22}$$

$$\ddot{x}_{GRMS}(f_n, \xi) = \sqrt{\sum_{i=1}^{N} \left[ \frac{1 + (2\xi\rho)^2}{(1 - \rho^2)^2 + (2\xi\rho)^2} \right] Y_{PSD}(f_i) \Delta f_i} \ , \qquad \rho = f_i/f_n$$

$$\tag{24.23}$$

Equation (24.23) is cumbersome but is readily implemented via a software program. It does not appear to have a name in the literature but is referred to as the "general method" in this document.

**Power Spectral Density fn=200 Hz Q=10**
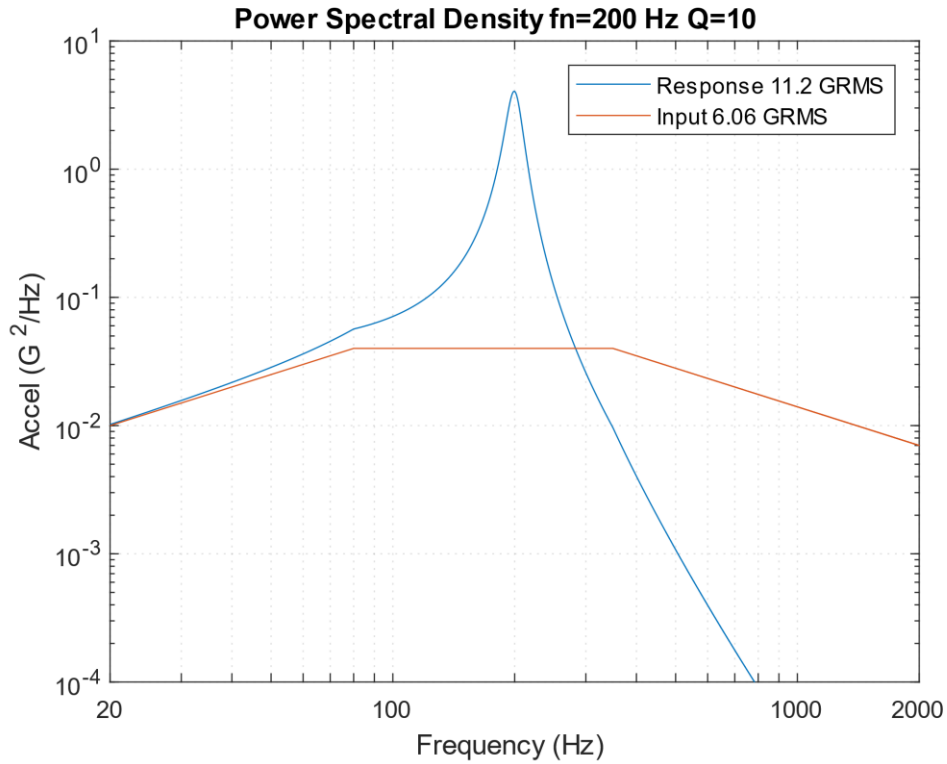
Figure 24.19.   General Method SDOF Response to Navmat P-9492 Base Input PSD

Repeat the example of an SDOF system with (fn=200 Hz, Q=10) subjected to the Navmat P-9492 PSD base input using the general method.  The overall response in Figure 24.19 agrees with the Miles result.  It is also very close to the time domain overall response in Table  24.6. The general method would yield a more accurate result if the natural frequency fell on either of the input PSD slopes.

Compare Figure 24.19 with the same set of PSD curves derived from the time domain synthesis in Figure 24.16.

# 25 VIBRATION RESPONSE SPECTRUM

## 25.1 RESPONSE SPECTRUM BASICS
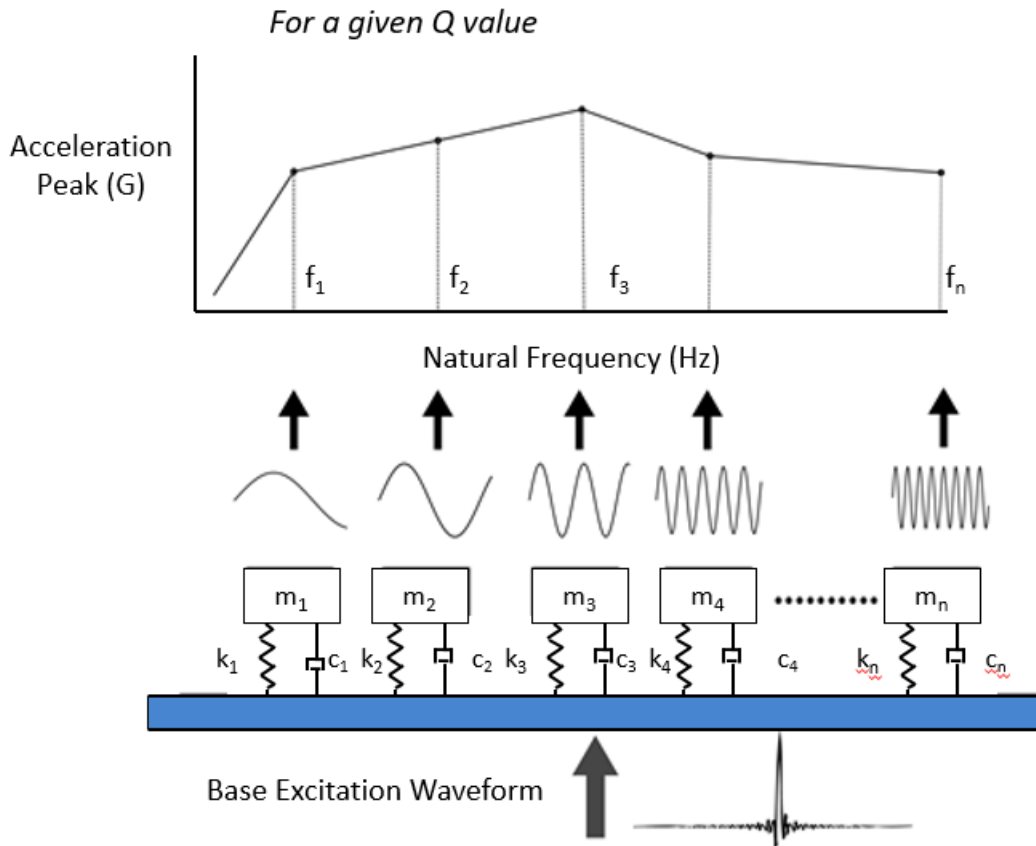


Figure 25.1. Response Spectrum Concept

A *Response Spectrum* is a plot of a chosen response metric, as a function of oscillator frequency, of an array of single-degree-of-freedom (SDOF) damped oscillators subjected to the same base excitation. The base input may be either a time history or a PSD. The SDOF systems are arranged in order of ascending natural frequency. Each system is independent of the others. The base input is independent with no mass-loading effect from the oscillators.

## 25.2  VRS BASICS

The vibration response spectrum overall level is calculated using equation (24.23) by varying the natural frequency for a given Q value.  It can be plotted in terms of the overall 1-sigma, 3-sigma, and peak values as a function of natural frequency.  The GRMS and 1-sigma values are taken to be equal because the mean is assumed to be zero.  The expected peak value, or crest factor, is calculated from equation (21.8) and is the only of three response metrics that depends on duration.

The vibration response spectrum is demonstrated in the following example.  First calculate the SDOF response to the Navmat P-9492 PSD base input for natural frequencies at 100, 200, and 300 Hz, with Q=10, using the model in Figure 17.14.
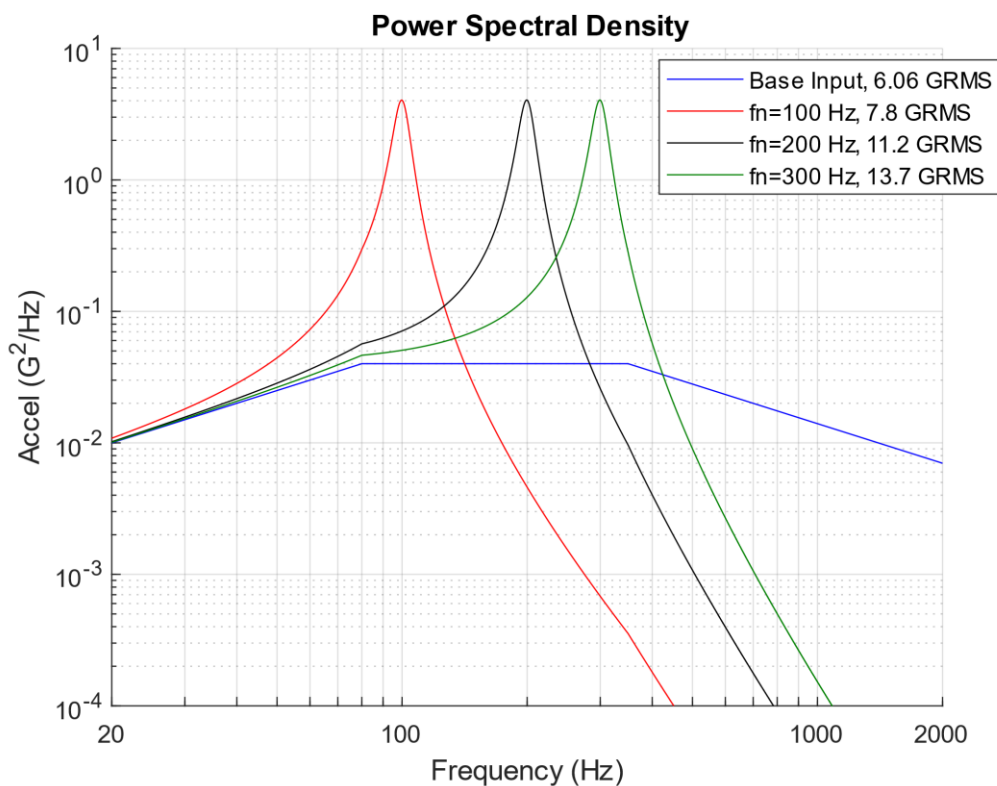


Figure 25.2.  SDOF Response to Navmat P-9492 Base Input PSD for Three Natural Frequencies
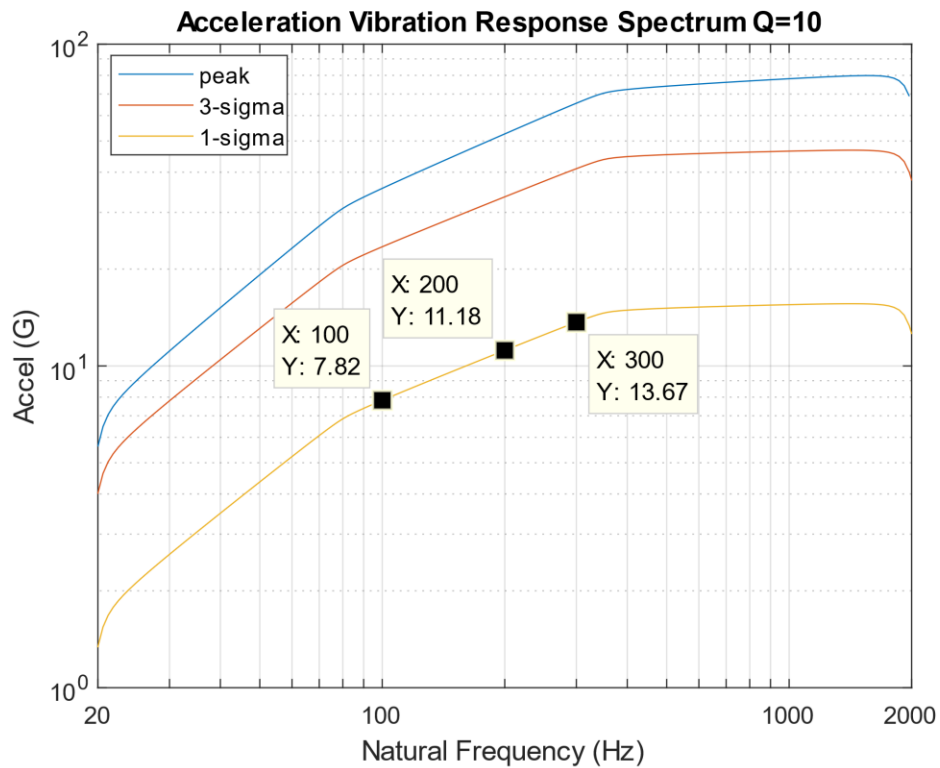
Figure 25.3.  Vibration Response Spectrum of Navmat P-9492 Base Input PSD

The calculation of the response PSDs in Figure 25.2 could be repeated for a larger set of natural frequencies.  This process can be automated via a software program.  The resulting VRS is shown in Figure 25.3.  Figure 25.2 legend's three coordinates are shown explicitly in the plot.  A duration of 180 seconds is assumed, but this only affects the peak curve.   The peak curve shows that peaks up to 4 and 5-sigma may occur over the duration.
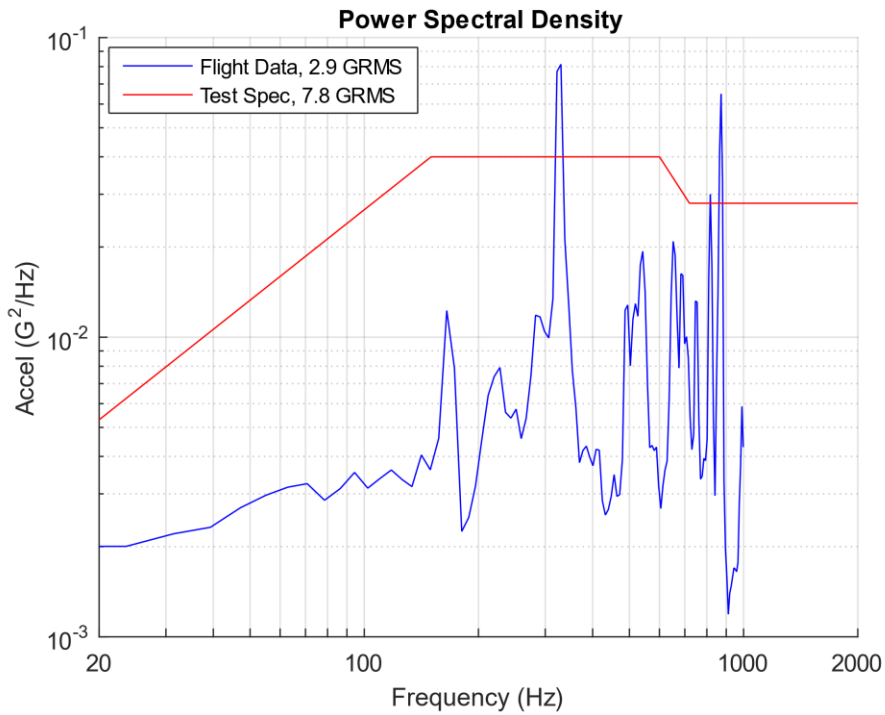
Figure 25.4.   PSD Comparison

The following example is actual case history.  A launch vehicle avionics component was tested to the red curve in Figure 25.4.   The blue curve represents the flight data from an accelerometer mounted adjacent to the component.  The flight data has three peaks that exceeded the test level.  Was the component under-tested?  The natural frequency of the component is unknown but could have been at any of the three exceedance peaks.  Assume that each curve represents the same duration for simplicity.
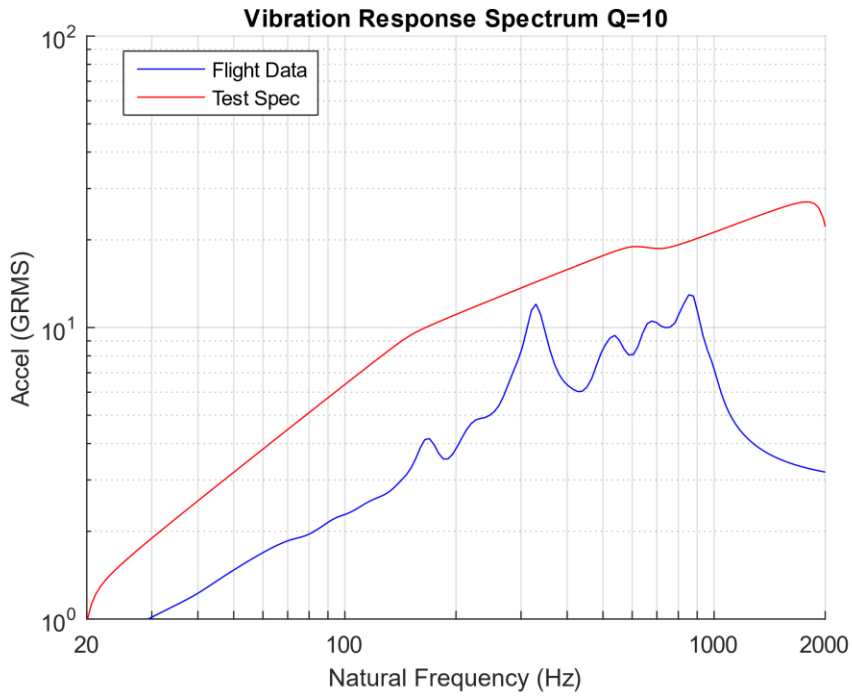
Figure 25.5.  Vibration Response Spectrum Comparison

The test level was 8.6 dB higher than the flight data in terms of overall level.  The vibration response spectrum comparison shows that the component would have a higher response to the test level than to the flight level across the entire natural frequency spectrum from 20 to 2000 Hz.   The component test level enveloped the flight data with margin to spare.

## 25.4  PSD ENVELOPE DERIVATION VIA VRS

The vibration response spectrum can also be used as an indirect method for deriving a PSD envelope for a measured environment.  The PSD envelope will have a few coordinates in log-log format as a simplification.  The goal is to derive the least PSD possible that will still envelop the measured PSD in terms of the respective VRS curves.  This allows for some peak clipping as demonstrated in the following example for an actual case history.  There are some industry rules of thumb for peak clipping, but the VRS is a more thorough approach.
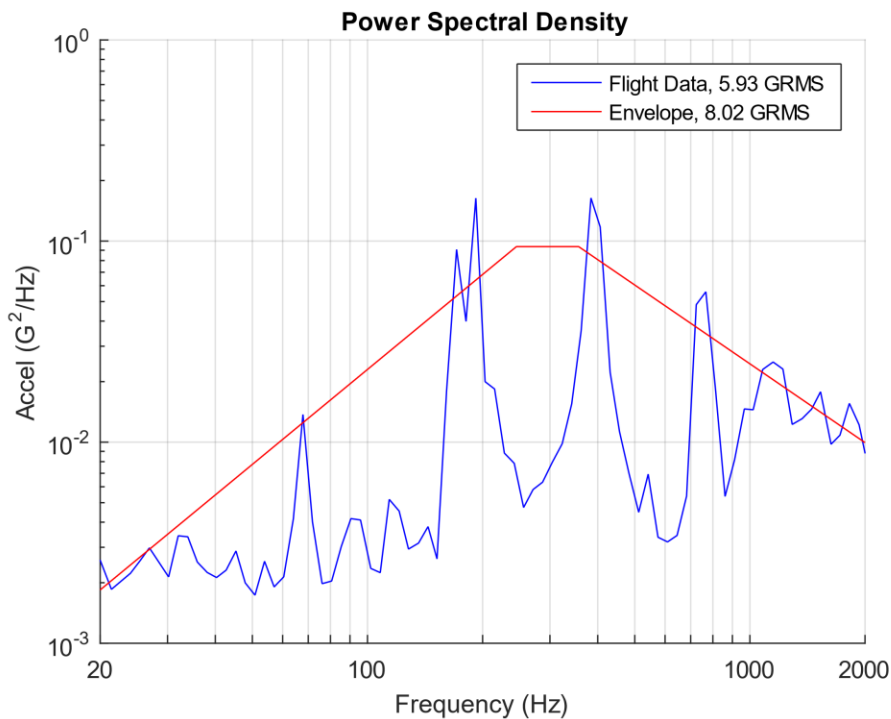


Figure 25.6.   Suborbital Launch Vehicle Flight PSD and Envelope

The flight data from a launch vehicle's internal bulkhead location is shown in Figure 25.6.  The spectral peaks were unexpected.  A realization was later made that a small access cover had been prematurely jettisoned at liftoff.  The result was that the cylindrical module housing the bulkhead became a large whistle.  This was an anomaly that could be corrected for the next flight in this vehicle series.  Nevertheless, it presented an opportunity to develop the enveloping method.  The following example proceeds assuming the whistle condition would be

repeated.  The proposed envelope is shown with the flight data in Figure 25.6.  The VRS justification for the envelope is given in Figure 25.7.  Assume the flight and envelope duration are the same for simplicity.  The envelope derivation process uses trial-and-error with random number generation, along with some convergence routines.
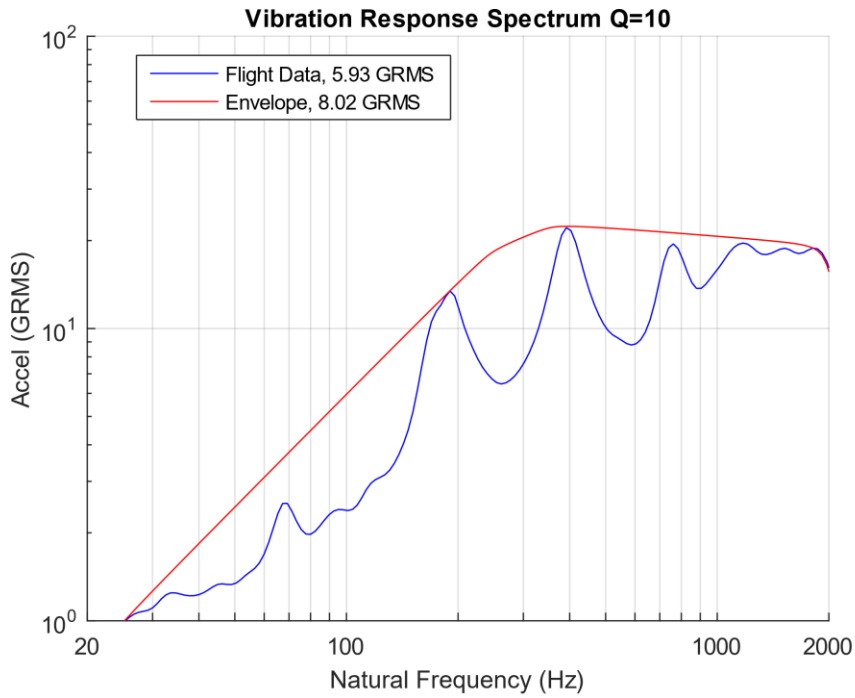


Figure 25.7.   Vibration Response Spectrum Comparison

# 26 SHOCK TESTING & ANALYSIS

## 26.1 SHOCK ISOLATOR PHOTO GALLERY





Basement columns
supporting base isolators

Base Isolator

Figure 26.1  Building Isolation, Bhuj Hospital, Gujarat Province, India

The isolators are Lead Rubber Bearings (LRB) which are stiff and strong in the vertical direction but flexible in the horizontal direction.
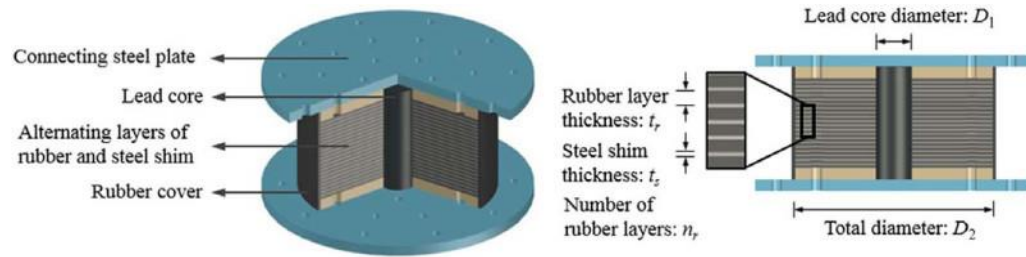
Figure 26.2  Typical LRB Design for Buildings and Bridges



Figure 26.3.  Titan II Missile Silo,
Launch Control Room

The missile control room is mounted underground via huge isolation springs. A typical spring is shown in the background. The purpose is to isolate the control room from mechanical shock and vibration in the event of a nuclear strike above the launch site. The springs allow 18 inches of relative displacement. The control room could thus carry out a retaliatory strike, as ordered by the U.S. president.  This site is located south of Tucson, Arizona. It has been decommissioned and is now a museum.

Figure 26.4.  Typical Isolators for Small Equipment and Avionics Boxes

Avionics components may be mounted via isolators to reduce the shock and vibration energy transmitted from the mounting location to the component itself.  The isolators are typically made from a rubber-like elastomeric or thermoplastic material.
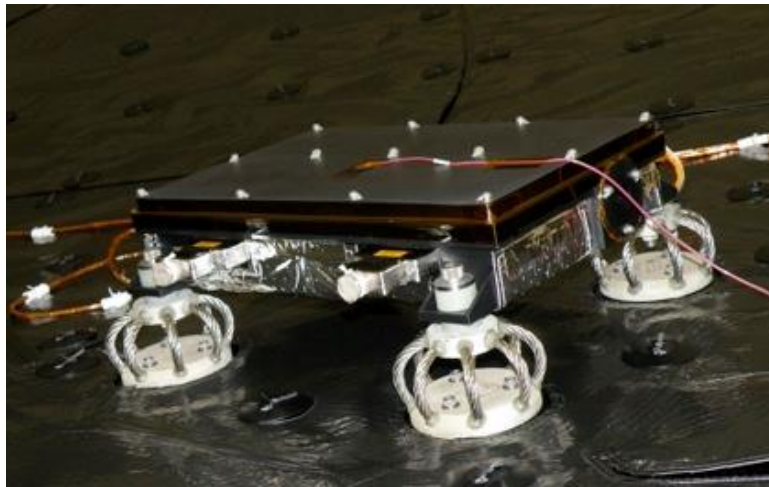


Figure 26.5.  Sensor Electronics, Wire Rope Isolators (NASA/JPL photo)

The source shock energy is attenuated as it propagates to avionics mounting locations through the launch vehicle's material and joints.  The input shock to a component can be mitigated by mounting the component as far away from the source device as possible.

Another effective attenuation technique is to mount the component via elastomeric bushings or wire rope isolators.  The NASA Mars Science Laboratory Sensor Support Electronics unit is mounted on isolators as shown.
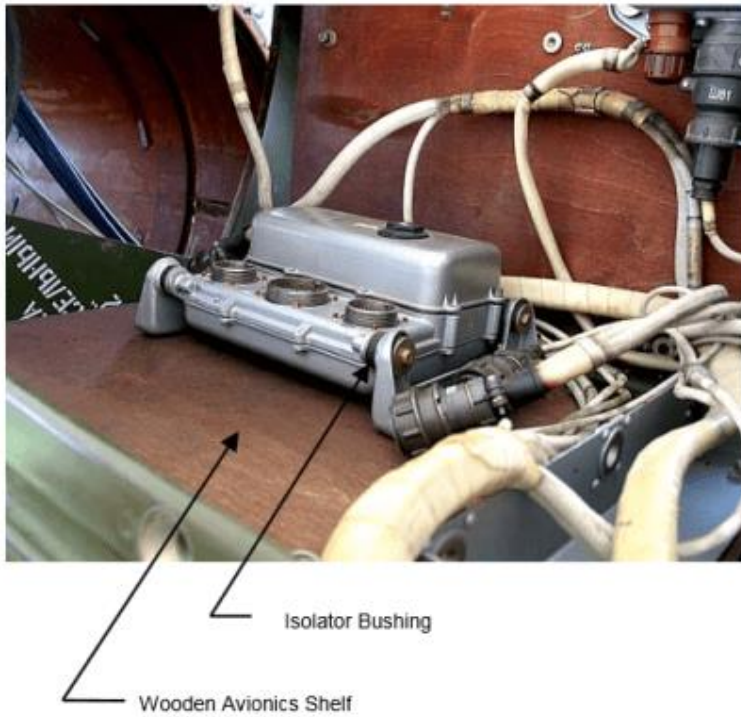
The bushings are made from some type of rubber or elastomeric compound. The bushings provide damping, but their main benefit is to lower the natural frequency of the system. The isolators thus attenuate the shock and vibration energy that flows from the instrument shelf into the avionics component.

Isolator Bushing

Wooden Avionics Shelf

Figure 26.6.  SCUD-B Avionics Component Isolation

Figure 26.7.  iPhone 6 Accidental Drop

The first iPhone 6 was purchased in Perth, Australia on September 19, 2014.  The event was covered by a live TV report.    The buyer mishandled the phone as he unboxed it. The phone survived the drop onto the ground but may have had some fatigue or fracture damage.

Portable electronic devices (PEDs) are expected to survive multiple drops.  Most original equipment suppliers specify between 30 and 50 drops.  Recommended test methods are given in Reference [43].
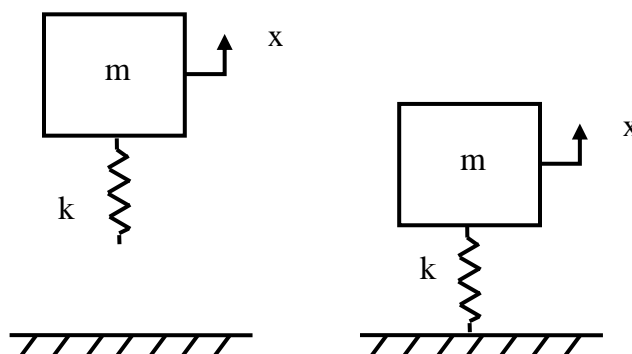


Figure 26.8.  Drop Shock Analytical Model

The accidental drop shock of a component onto a hard surface is difficult to model accurately. The item may undergo rigid-body translation and rotation in each of its six DOF during freefall. The item may have a nonlinear response with plastic deformation during impact. It may or may not bounce. Furthermore, a box-shaped object may strike the ground on any of its corners, edges, or faces.

A very simple method, as a first approximation, is to assume that the object is a linear, undamped, SDOF system subjected to initial velocity excitation as it strikes the ground and remains attached to it via its spring. The object then undergoes free vibration in this configuration. The initial velocity is calculated using a familiar physics formula where the change in kinetic energy is equal to the change in potential energy due to gravity.

Assume that the object is dropped from rest. The initial velocity as it strikes the ground is

$$\dot{x}(0) = \sqrt{2g\Delta h} \qquad\qquad (26.1)$$

The equation of motion is

$$m\ddot{x} + kx = 0 \qquad\qquad (26.2)$$

Or equivalently

$$\ddot{x} + \omega_n^2 x = 0 \qquad\qquad (26.3)$$

The peak displacement is

$$|x(t)| = \frac{\sqrt{2g\Delta h}}{\omega_n} \qquad\qquad (26.4)$$

The peak velocity is equal to the initial velocity in equation (26.1).

The peak acceleration is

$$|\ddot{x}(t)| = \omega_n \sqrt{2g\Delta h} \qquad\qquad (26.5)$$

An example is shown in the following table for three natural frequency cases.

Table 26.1.  Peak Response Values for 36-inch Drop Height

| Natural Freq (Hz) | Displacement (in) | Velocity (in/sec) | Acceleration (G) |
|---|---|---|---|
| 200 | 0.133 | 167 | 543 |
| 600 | 0.044 | 167 | 1630 |
| 1000 | 0.027 | 167 | 2710 |



Figure 26.9.  Herring Gull Dropping Clam

https://palmbeachcountynaturally.wordpress.com/

Examples from biological nature are given in the following table.  Some bird species drop clams and nuts on the ground to open them.   The shell may not break open if dropped on soft sand. Rocks and asphalt are much more effective ground surfaces.

| Table 26.2.   Severe Velocities from Nature, Gaberson [44] | |
|---|---|
| Material | Velocity Threshold |
| Walnut | Crow drops walnut 18 ft onto asphalt, 408 ips |
| Clam | Seagull drops clam 10 ft onto asphalt, 304 ips |
| Egg | Definite Crack at 1 inch drop, 27.8 ips<br>No crack at ½ inch drop, 19.6 ips |

The velocity in the above table is calculated from the drop height per equation (26.1).

## 26.3  CLASSICAL SHOCK
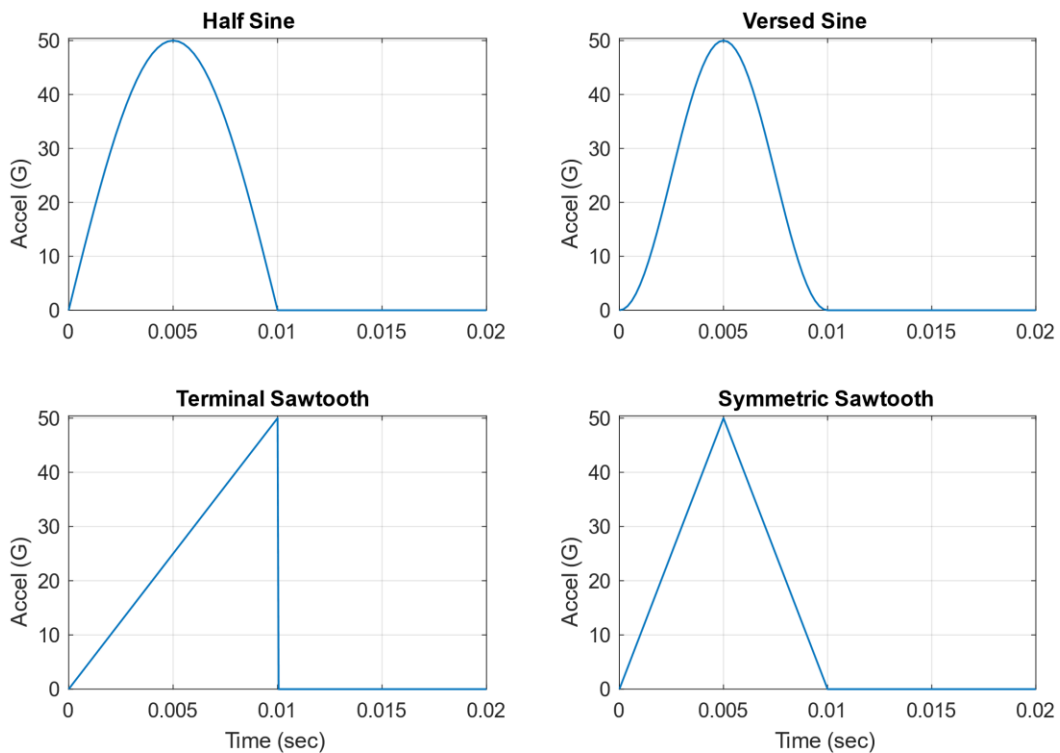


Figure 26.10.  Idealized Classical Pulse Examples

Classical pulses are the simplest base excitation pulses. They are deterministic and can be represented by simple mathematical functions. They are typically one-sided. An SDOF system's response to a classical pulse can be solved exactly using Laplace transforms.

Four classical pulse types are shown in Figure 26.10. Other types include rectangular and trapezoidal pulses. These pulses do not necessarily represent real field environments, but they are still used throughout industry to test equipment ruggedness for convenience.

Shock tests are performed on military equipment [41] to:

a. Provide a degree of confidence that materiel can physically and functionally withstand the relatively infrequent, non-repetitive shocks encountered in handling, transportation, and service environments. This may include an assessment of the overall materiel system integrity for safety purposes in any one or of the handling, transportation, and service environments.
b. Determine the materiel's fragility level, so that packaging may be designed to protect the materiel's physical and functional integrity.
c. Test the strength of devices that attach materiel to platforms that can crash.

Potential equipment failure modes due to shock excitation include:

a. Materiel failure resulting from increased or decreased friction between parts, or general interference between parts.
b. Changes in materiel dielectric strength, loss of insulation resistance, variations in magnetic and electrostatic field strength.
c. Materiel electronic circuit card malfunction, electronic circuit card damage, and electronic connector failure. (On occasion, circuit card contaminants having the potential to cause short circuits may be dislodged under material response to shock.)
d. Permanent mechanical deformation of the material resulting from overstressing of materiel structural and nonstructural members.
e. Collapse of mechanical elements of the materiel resulting from the ultimate strength of the component being exceeded.
f. Accelerated fatiguing of materials (low cycle fatigue).
g. Potential piezoelectric activity of materials, and materiel failure resulting from cracks in fracturing crystals, ceramics, epoxies, or glass envelopes.

Figure 26.11.  Drop Shock Test Machine, Initial Velocity Excitation

Classical pulse shock testing has traditionally been performed on a drop tower.  The component is mounted on a platform that is raised to a certain height. The platform is then released and travels down to the base, which has pneumatic pistons to control the impact of the platform against the base.  In addition, the platform and base both have cushions for the model shown. The pulse type, amplitude, and duration are determined by the initial height, cushions, and pressure in the pistons.  This is a textbook example of a case where the initial potential energy of the raised platform and test item are converted to kinetic energy.  The final velocity of the freefall becomes the initial velocity of the shock excitation.
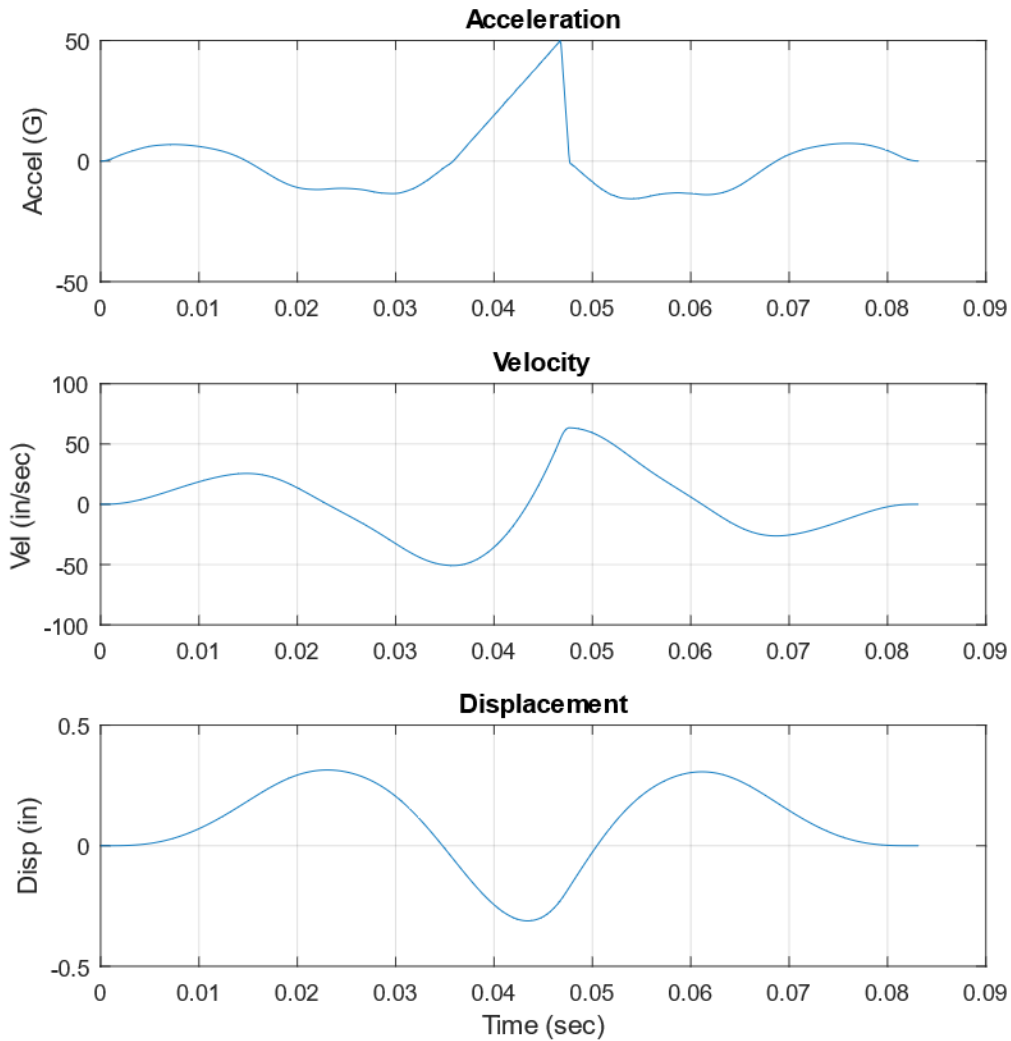
Figure 26.12.  A 50 G, 11 msec, Terminal Sawtooth Pulse for Shaker Shock Test

Classical pulse shock testing can sometimes be performed on shaker tables but with some constraints.  The net velocity and net displacement must each be zero.  Also, the acceleration, velocity, and displacement peaks must each be within the shaker table stroke limits.  Pre and post-pulses are added to classical pulses to meet these requirements.  A hypothetical terminal sawtooth pulse suitable for shaker shock testing is shown in Figure 26.12.

## 26.4  HALF-SINE SHOCK EXAMPLE

Consider a single-of-freedom is subjected to a 50 G, 11 msec half-sine pulse applied as base excitation per Figure 17.14.  Set the amplification factor to Q=10.   Allow the natural frequency to be an independent variable.   Solve for the absolute response acceleration.  The equation of motion for the relative displacement z is

$$\ddot{z} + 2\,\xi\,\omega_n\,\dot{z} + \omega_n^2 z = \begin{cases} A\sin(\pi\,t/T), & \text{for } t \le T \\ 0, & \text{for } t > T \end{cases} \qquad (26.6)$$

The primary response occurs during the half-sine pulse input.  The residual response occurs during the quiet period thereafter.    The total response is the combination of primary and residual.   The exact response for a given time can be calculated via a Laplace transform.  Note that the quiet period solution is free vibration with initial velocity and displacement excitation.
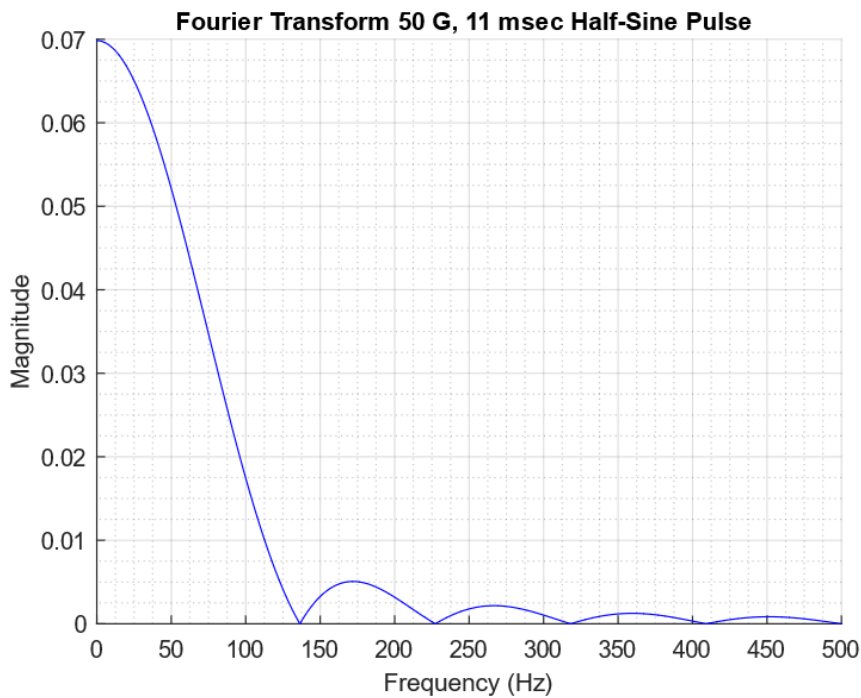


Figure 26.13.  Fourier Transform Half-Sine Shock

A common misunderstanding is to regard the half-sine shock pulse as having a discrete frequency which would be the case if it were extended to a full-sine pulse. The Fourier transform in Figure 26.13 shows that the half-sine pulse has a continuum of spectral content beginning at zero and then rolling off as the frequency increases. There are also certain frequencies where the magnitude drops to zero. The magnitude represents the acceleration, but the absolute magnitude depends on the total duration including the quiet period after the pulse is finished. The post-pulse duration was 10 seconds in the above example, for a total of 10.011 seconds.
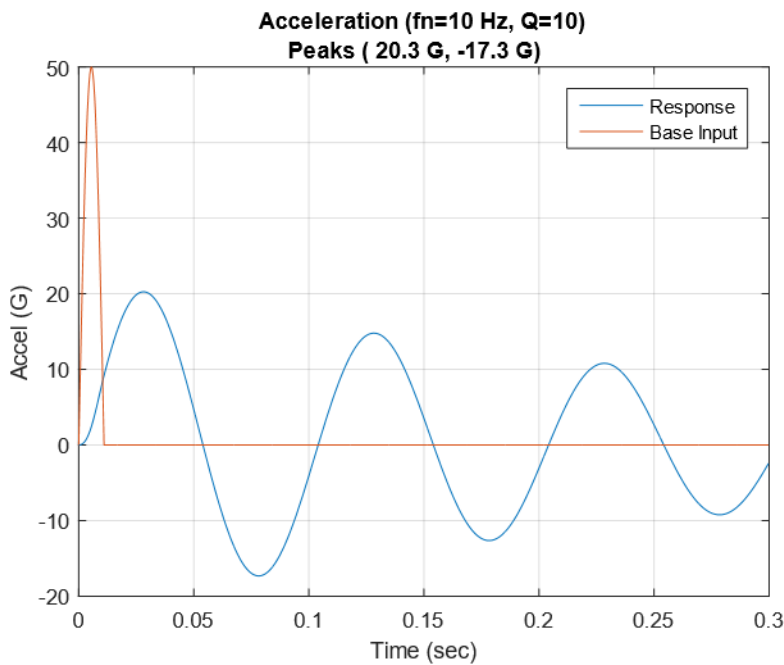


Figure 26.14. SDOF System Response to Half-Sine Shock, 10 Hz

The response in Figure 26.14 has an absolute peak value less than the peak input. This is an isolation case. The response's positive and negative peaks occur after the base input pulse is over.

The base input pulse has the following velocity change

$$\Delta \dot{x} = \frac{2\ddot{x}_{max}t_d}{\pi} = \frac{2(50 \text{ G})(386 \text{ in/sec}^2)(0.011 \text{ sec})}{\pi} = 135 \text{ in/sec} \qquad (26.7)$$

An ideal half-sine pulse is for educational purposes only. Half-sine tests for components must have zero net velocity whether performed on a shaker or drop tower.
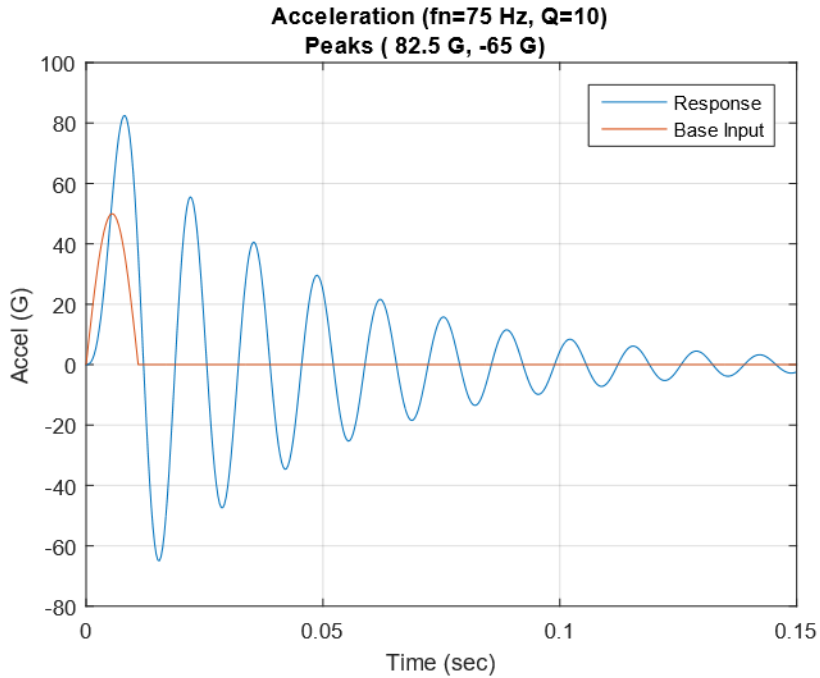
Figure 26.15.  SDOF System Response to Half-Sine Shock, 75 Hz

The response in Figure 26.15 has an absolute peak value that is 1.65 times the peak input.  This is a resonant amplification case.  The absolute peak response occurs during the base input pulse.
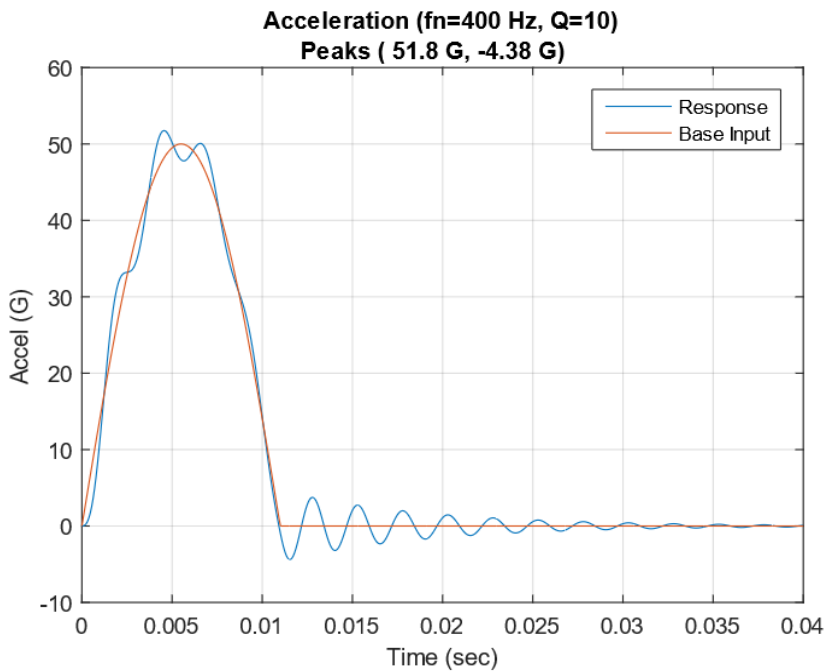


Figure 26.16. SDOF System Response to Half-Sine Shock, 400 Hz

The response converges to the base input as the natural frequency becomes increasingly high. This becomes a unity gain case. The system is considered hard-mounted.

The peak results from the three cases are shown in Table 26.3. The calculation can be repeated for a family of natural frequencies. The peak acceleration results can then be plotted as a shock response spectrum (SRS) as shown in Figure 26.17. The peak relative displacement values can likewise be plotted as an SRS as shown in Figure 26.18.
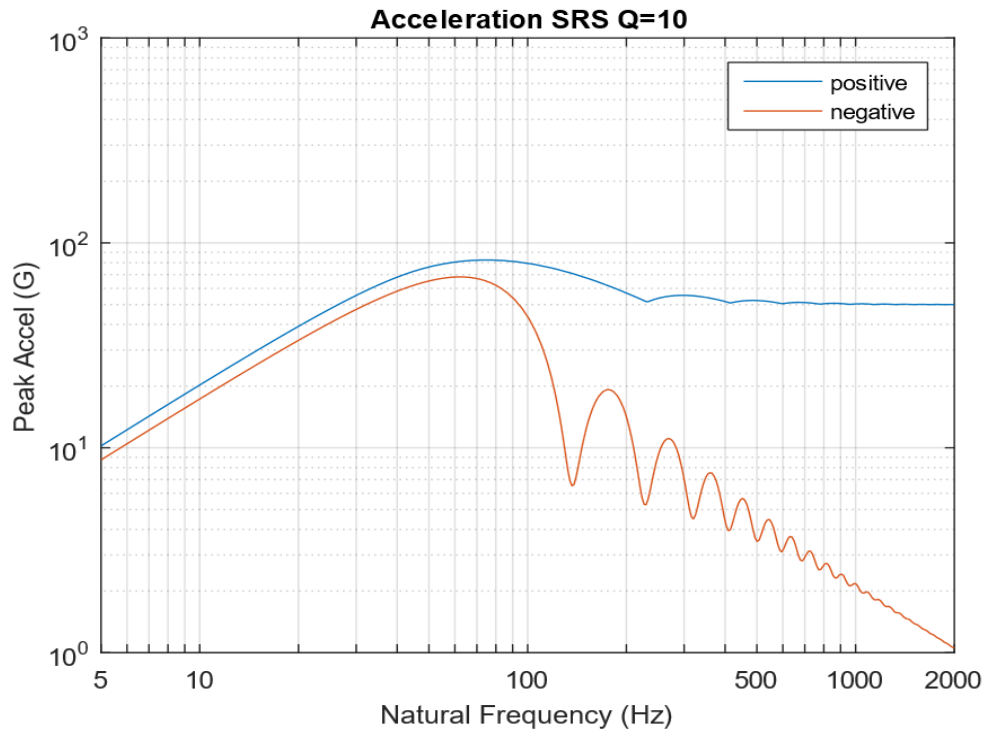


Figure 26.17. Acceleration SRS, 50 G, 11 msec Half-Sine Pulse

The two curves in the above figure contain the coordinates in Table 26.3. The initial slope of each SRS curve is 6 dB/octave indicating a constant velocity line. The curves also show that the peak response can be lowered by decreasing the natural frequency. A low natural frequency could be achieved for a piece of equipment by mounting it via soft, elastomeric isolator bushings or grommets. But a lower natural frequency leads to a higher relative displacement as shown in Figure 26.18.

Table 26.3.  Summary of Peak Response, 50 G, 11 msec, Half-Sine Base Input

| Natural Frequency (Hz) | Peak Positive (G) | Absolute Value of Peak Negative (G) |
|---|---|---|
| 10 | 20.3 | 17.3 |
| 75 | 82.5 | 65 |
| 400 | 51.8 | 4.38 |
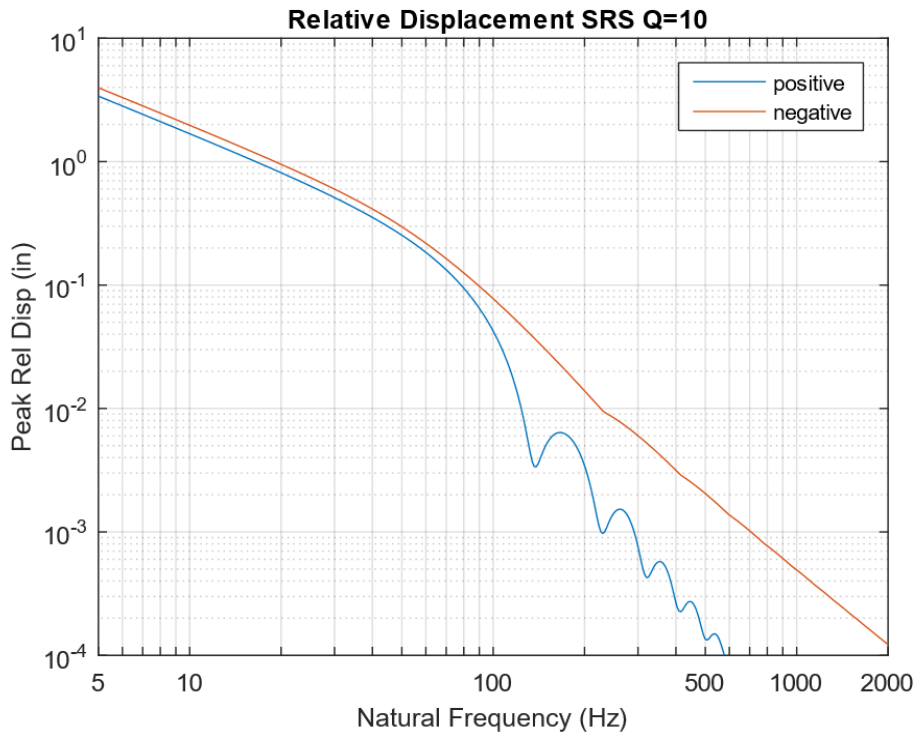


Figure 26.18.  Relative Displacement SRS, 50 G, 11 msec Half-Sine Pulse

The curves in Figure 26.18 could be used for designing isolator mounts for a component.  The isolators must be able to take up the relative displacement without bottoming or topping out.  Also, there must be enough clearance and sway space around the component.
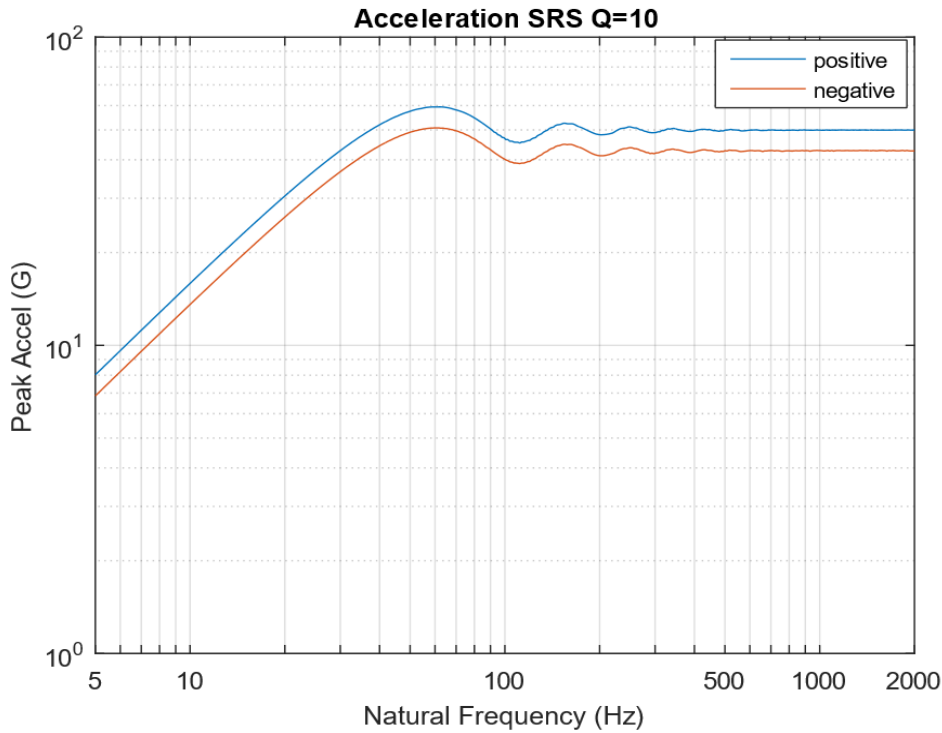
Figure 26.19.  Acceleration SRS, 50 G, 11 msec Terminal Sawtooth Pulse

The positive and negative SRS curves are reasonably close for the terminal sawtooth pulse shown in Figure 26.19.  In contrast, the positive and negative SRS curves for the half-sine pulse in Figure 26.17 diverge as the natural frequency increases above 80 Hz.  The terminal sawtooth pulse is thus usually preferred over the half-sine pulse for classical shock testing.

Another means of visualizing the SRS concept is given in Figure 26.20.
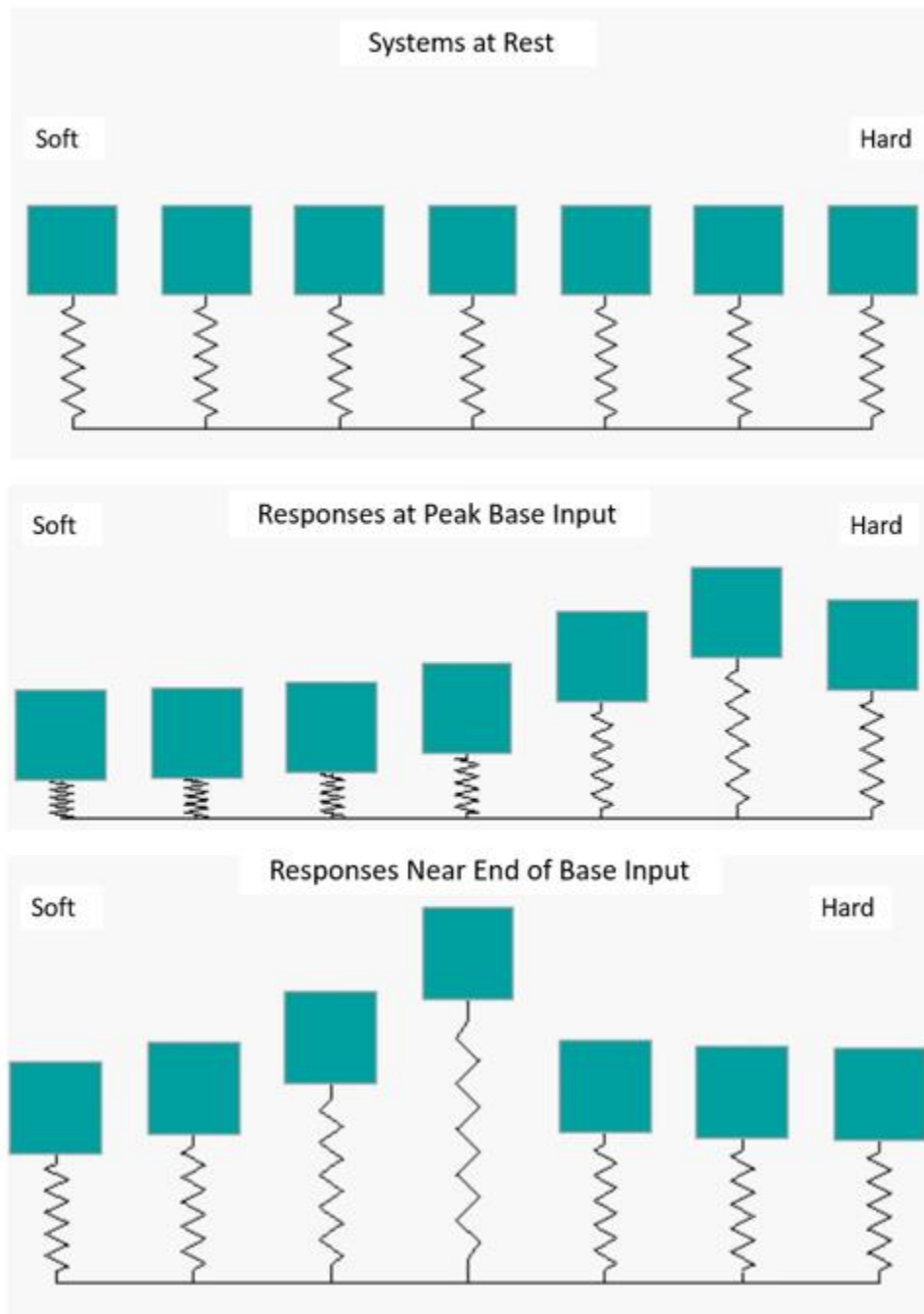
Figure 26.20.   Half-Sine Shock Applied as Base Input to Independent SDOF Systems

The systems are arranged in order of ascending natural frequency from left to right and subjected to a common half-sine base input.  The Soft-mounted system on the left has high spring relative deflection, but its mass remains nearly stationary.  The Hard-mounted system on

the right has low spring relative deflection, and its mass tracks the input with near unity gain. The Middle system ultimately has high deflection for both its mass and spring. The peak positive and negative responses of each system are plotted as a function of natural frequency in the shock response spectrum.

## 26.5 RESPONSE TO ARBITRARY EXCITATION

Recall from Section 17.3 that the response of an SDOF system to base excitation can be expressed in terms of a second-order, ordinary differential equation for the relative displacement z for a base acceleration $\ddot{y}$.

$$\ddot{z} + 2\,\xi\,\omega_n\,\dot{z} + \omega_n{}^2 z = -\ddot{y} \tag{26.8}$$

Equation (26.8) can be solved via Laplace transforms if the base acceleration is deterministic such as a half-sine pulse. A convolution integral is needed if the excitation varies arbitrarily with time. The convolution integral is computationally inefficient, however. An alternative is to use the Smallwood ramp invariant digital recursive filtering relationship [25], [27].

Again, the recursive filtering algorithm is fast and is the numerical engine used in almost all shock response spectrum software. It is also accurate assuming that the data has a sufficiently high sample rate and is free from aliasing. One limitation is that it requires a constant time step.

The equation for the absolute acceleration is

$$\ddot{x}_i = \ 2\exp(-\,\xi\,\omega_n\Delta t)\cos(\omega_d\Delta t)\,\ddot{x}_{i-1}$$

$$-\exp(-\,2\xi\,\omega_n\Delta t)\,\ddot{x}_{i-2}$$

$$+\left\{1 - \left(\frac{1}{\omega_d\Delta t}\right)\exp(-\,\xi\,\omega_n\Delta t)\,\sin(\omega_d\Delta t)\right\}\ddot{y}_i$$

$$+\left\{2\exp(-\,\xi\,\omega_n\Delta t)\left[-\cos(\omega_d\Delta t) + \left(\frac{1}{\omega_d\Delta t}\right)\sin(\omega_d\Delta t)\right]\right\}\ddot{y}_{i-1}$$

$$+\left\{\exp(-2\,\xi\,\omega_n\Delta t) - \left(\frac{1}{\omega_d\Delta t}\right)\exp(-\,\xi\,\omega_n\Delta t)\sin(\omega_d\Delta t)\right\}\ddot{y}_{i-2}$$

$$\tag{26.9}$$

The damped natural frequency is

$$\omega_d = \omega_n \sqrt{1 - \xi^2} \qquad (26.10)$$

The relationship in equation (26.9) is recursive because the response at the current time depends on the two previous responses, which are the first two terms on the righthand side of the equation.  This is a feedback loop in terms of control theory.   The relationship is filtering because the energy at and near the natural frequency is amplified whereas higher frequency energy above √2 times the natural frequency is attenuated.  See Figure 17.17.

Note the similarity between the acceleration response equation (26.9) and the transmitted force equation (17.16).

The equation for the relative displacement [22] is

$$z_i = 2\exp(-\xi\omega_n\Delta t)\cos(\omega_d\Delta t)\,z_{i-1} \quad -\exp(-2\xi\omega_n\Delta t)\,z_{i-2}$$

$$-\frac{\Delta t}{\omega_d}\exp(-\xi\omega_n\Delta t)\sin(\omega_d\Delta t)\,\ddot{y}_{i-1}$$

$$(26.11)$$

A Matlab function for the shock response spectrum (SRS) for base input acceleration is given at:

https://www.mathworks.com/matlabcentral/fileexchange/127269-shock-response-spectrum-for-base-input-acceleration

## 26.5.1 Shock Response Spectrum Test Specification Objective
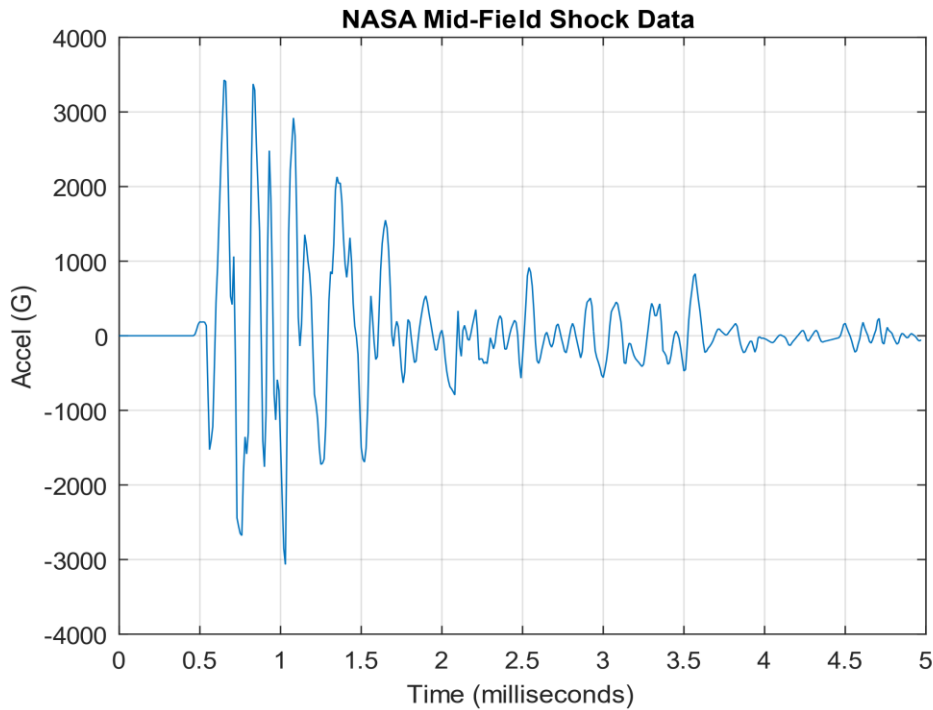


Figure 26.21.  Mid-Field Pyrotechnic Shock Time History

Consider the measured mid-field shock time history in Figure 26.21 as taken from Reference [32].  The time history would be essentially impossible to reproduce in a test lab given that it is a high-frequency, high-amplitude complex, oscillation pulse.  The aerospace practice instead is to derive an SRS to represent the damage potential of the shock event.  The test conductor may then use an alternate pulse to satisfy the SRS specification within reasonable tolerance bands.  This is an indirect method of achieving the test goal.  There are some limitations to this approach.  One is that the test item is assumed to be linear.  Another is that it behaves as an SDOF system.  Nevertheless, this method is used in aerospace, military, and earthquake engineering fields, for both analysis and testing.
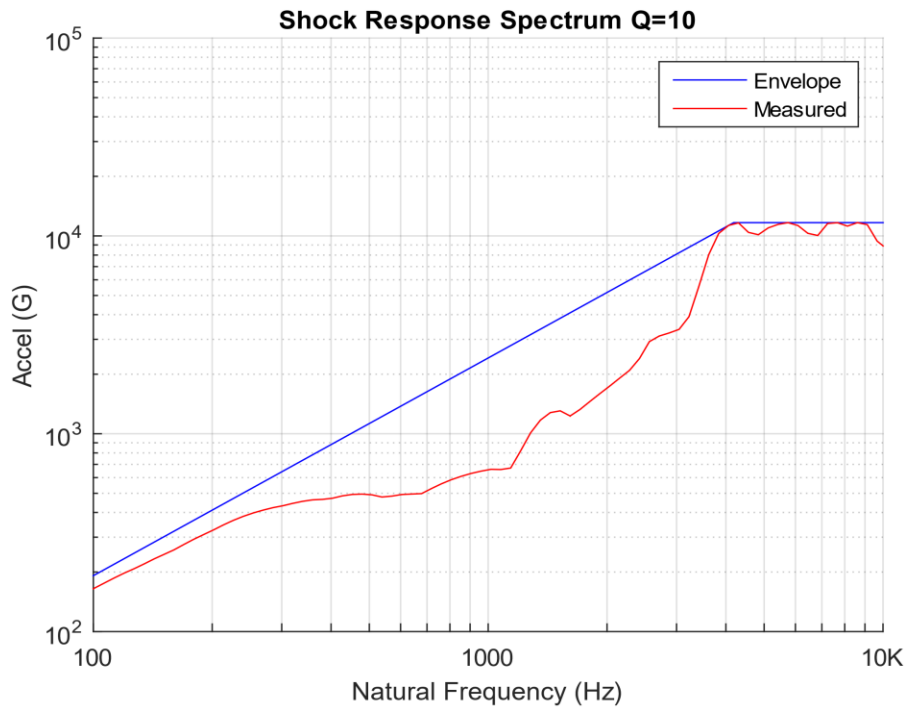
Figure 26.22. Mid-Field Shock Response Spectrum & Envelope

The customary approach is to draw a conservative envelope over the measured SRS. The ramp-plateau format is the most common, although there are variations. The enveloping process shown in the above vibration is very conservative in the mid-frequency domain. An additional dB uncertainty factor may be needed to develop the envelope into a test specification, given that the SRS envelope is derived from a single time history. Industry standards, such as Reference [45], give guidelines for the dB factor.

## 26.6.1  Seismic Waveforms

## P Wave
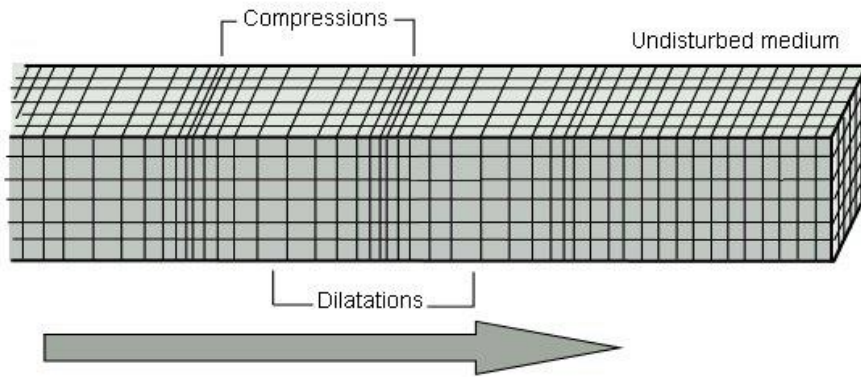
Figure 26.23.  P-Wave

The primary wave, or P-wave, is a body wave that can propagate through the Earth's core.[6] This wave can also travel through water.  The P-wave is also a sound wave with longitudinal motion.  Note that the P-wave is the fastest of the four waveforms.
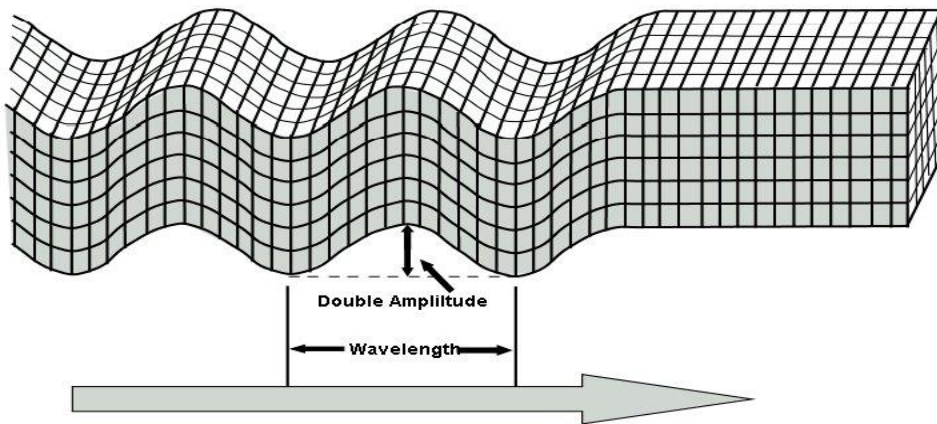
Figure 26.24.  S-Wave

---

[6] Body waves can also manifest at the Earth's surface.

333

The secondary wave, or S-wave, is a shear wave.  It is a type of body wave. The S-wave produces an amplitude disturbance that is at right angles to the direction of propagation. Note that water cannot withstand a shear force.  S-waves thus do not propagate in water.

## Love Wave
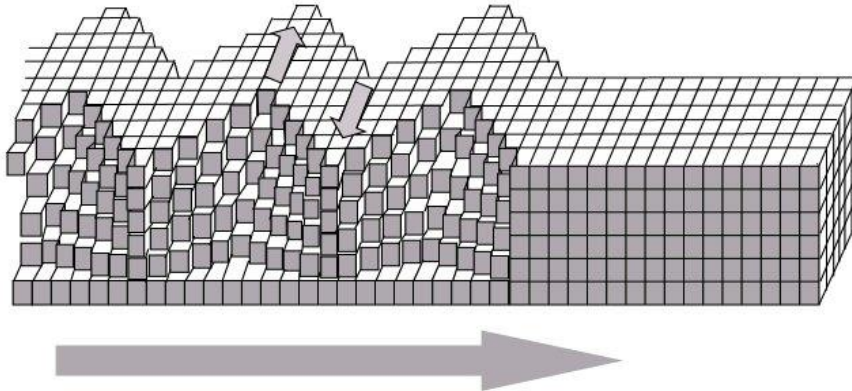


Figure 26.25.  Love Wave

Love waves are shearing horizontal waves.  The motion of a Love wave is similar to the motion of a secondary wave except that a Love wave only travels along the surface of the Earth.  Love waves do not propagate in water.

## Rayleigh Wave
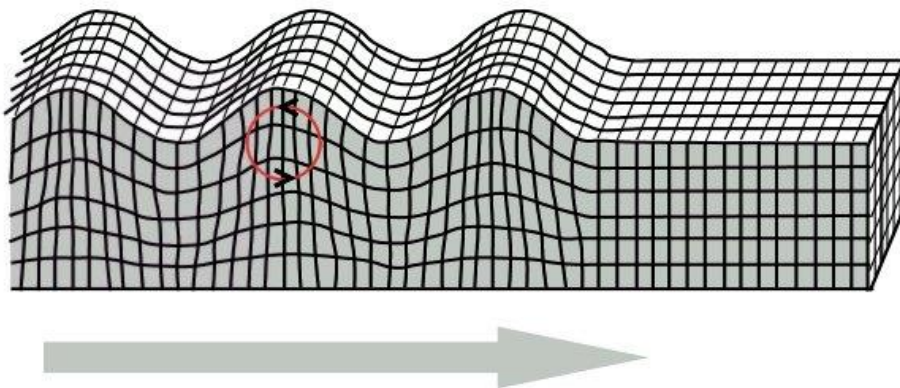


Figure 26.26.  Rayleigh Wave, Retrograde

Rayleigh waves are generated by the interaction of P and S-waves at the surface of the earth, and travel at a slower speed than the other three waveforms.  Rayleigh waves produce retrograde elliptical motion.  The ground motion is thus both horizontal and vertical.  The

motion of Rayleigh waves is similar to the motion of ocean waves in the figure below except that ocean waves are prograde.

Wave Propagation
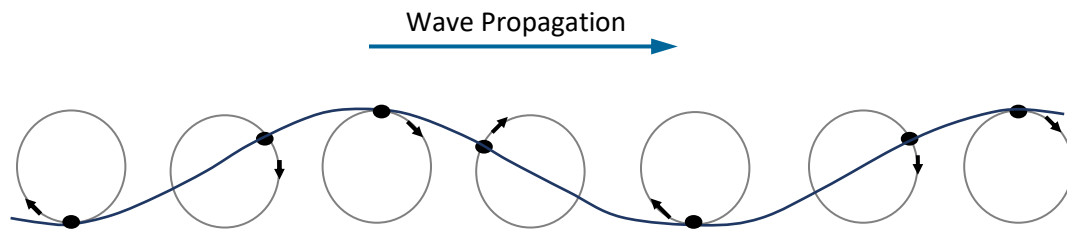
Figure 26.27.  Ocean Surface Wave Particle Motion, Prograde

At greater ground depths, the Rayleigh wave particle motion becomes prograde. In addition, the motion amplitude decays and the eccentricity changes as the depth into the material increases.

Rayleigh waves resulting from airborne acoustical sources may either be prograde or retrograde per Reference [46].  In some cases, the motion may begin as prograde and then switch to retrograde.    Airborne acoustical sources include above-ground explosions and rocket liftoff events.

26.6.2  Seismic Wave Damage Potential

The P and S body waves mainly cause high-frequency (greater than 1 Hz) vibrations which are more efficient than low-frequency waves in causing low buildings to vibrate.

The Rayleigh and Love surface waves mainly cause low-frequency vibrations which are more efficient than high-frequency waves in causing tall buildings to vibrate.

The amplitudes of the low-frequency surface waves have lower decay per distance than the high-frequency wave as distance from the epicenter increases.  Tall buildings located at relatively great distances (60 miles) from a fault may be damaged by surface waves.

P-waves are compressional waves that alternately compress and expand the material through which they pass. The back-and-forth motion produced as compressional waves travel can cause the ground to buckle and fracture and can cause power lines to break.

S-waves cause material to oscillate at right angles relative to the wave propagation direction. They can produce up-and-down and sideways shaking of the ground, as they can travel in any plane.

The Love wave is essentially a sideways S-wave propagating along the surface.

The Rayleigh wave generates a rolling motion.

Figure 26.28.  Damage by Waveform

Structural damage can occur due to the individual or combined effects of the above waveforms. Cumulative damage due to aftershocks is also possible.

## 26.6.3 Ocean T-wave
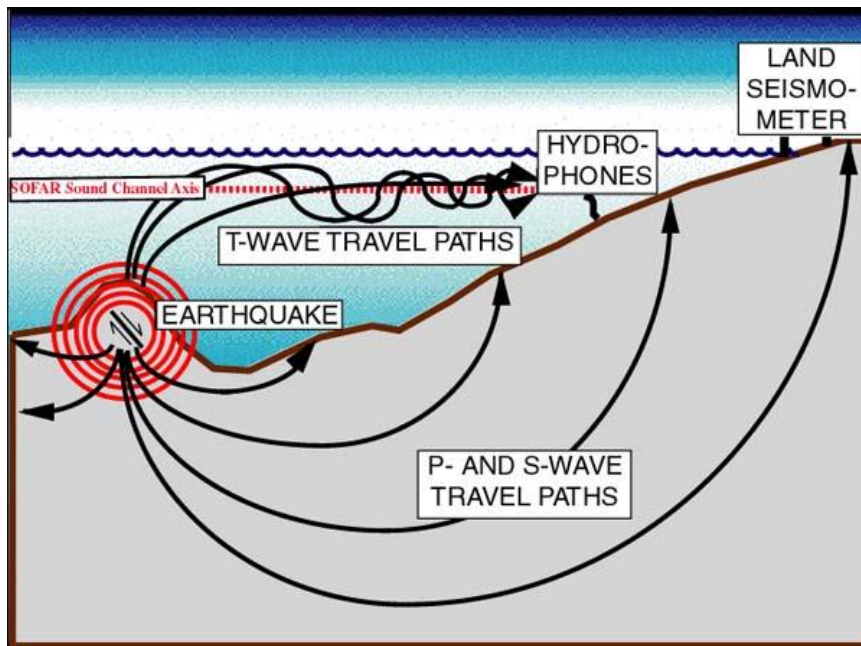


Figure 26.29.  Ocean Floor Earthquake (NOAA Image)

Seismic and volcanic activity at the ocean floor generates a water-borne longitudinal wave called a T-wave, or tertiary wave.   These waves propagate in the ocean's SOFAR channel, which is centered on the depth where the cumulative effect of temperature and water pressure combine to create the region of minimum sound speed in the water column.  SOFAR is short for "Sound Fixing and Ranging Channel."  These T-waves may be converted to ground-borne P or S-waves when they reach the shore.  Acoustic waves travel at 1500 m/s in the ocean whereas seismic P and S-waves travel at velocities from 2000 to 7000 m/s in the crust.

## 26.6.4  Seismic Response Spectrum Method

Professors Theodore von Kármán and Maurice Biot were very active in the early 1930s in the theoretical dynamics aspects of what would later become known as the response spectrum method in earthquake engineering.  Biot proposed that rather than being concerned with the shape of the input time history, engineers should instead use a method describing the *response of systems* to those shock pulses.  The emphasis should instead be on the *effect,* as represented

by the response of a series of single-degree-of-freedom oscillators, similar to that previously shown for the case of a half-sine input in Figure 26.20.

Practical use of the response spectrum method had to wait until the 1970s due to the intricacy of the response calculation for complex, oscillating pulses which required digital computers. Time was also needed to establish and publicize databases of strong motion acceleration time histories.

The response spectrum method was adopted for pyrotechnic shock in the aerospace industry and renamed as shock response spectrum.

## 26.6.5 El Centro Earthquake



Figure 26.30.  El Centro, Imperial Valley Earthquake Damage

Nine people were killed by the May 1940 Imperial Valley earthquake. At Imperial, 80 percent of the buildings were damaged to some degree. In the business district of Brawley, all structures were damaged, and about 50 percent had to be condemned. The shock caused 40 miles of surface faulting on the Imperial Fault, part of the San Andreas system in southern California. Total damage has been estimated at $6 million. The magnitude was 7.1.  This was the first major earthquake for which strong motion acceleration data was obtained that could be used for engineering purposes.
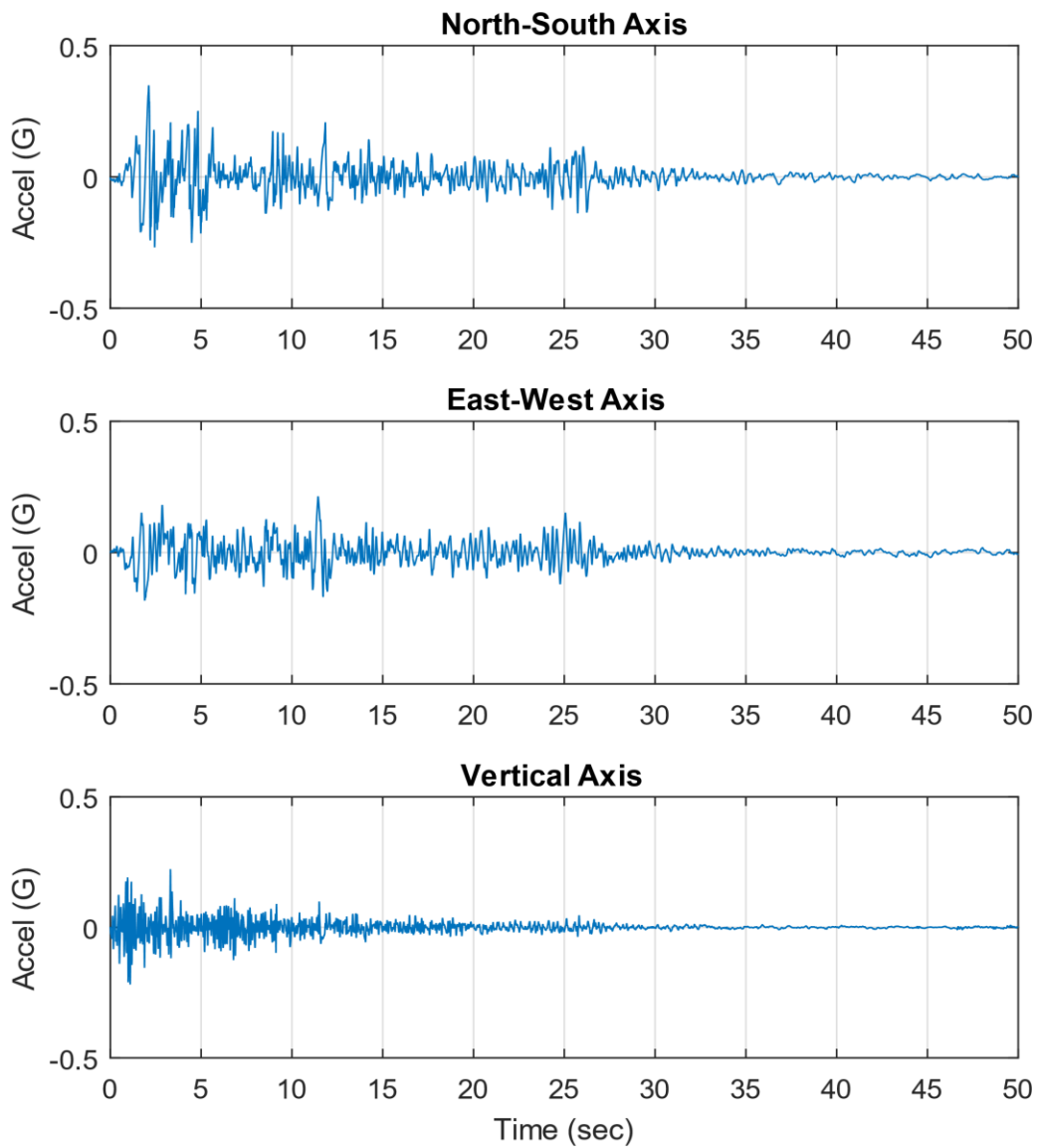
Figure 26.31.  El Centro Earthquake, Triaxial Time History

The highest excitation is in the North-South axis, parallel to the ground.
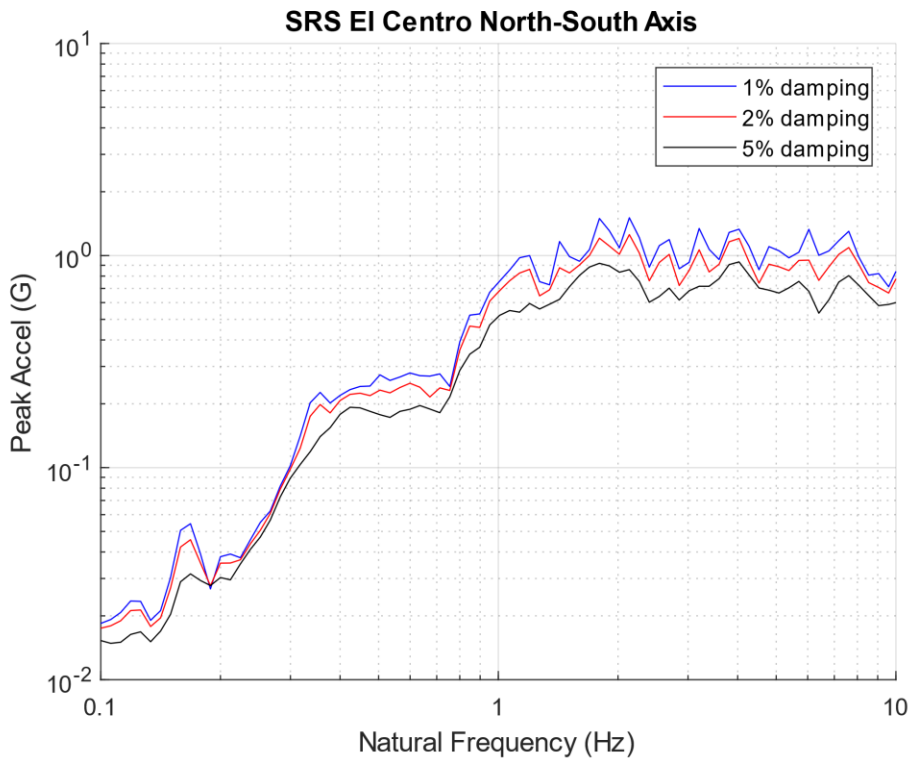
Figure 26.32.  El Centro Earthquake North-South SRS, Three Damping Cases

The acceleration levels reached 1.5 G for the 1% damping curve.  Recall that large civil engineering structures can have nonlinear damping.  The damping values tend to increase as the base excitation levels increase as shown for the Transamerica Title Building in Section 15.9.

**Pseudo Velocity Shock Response Spectrum Q=10**
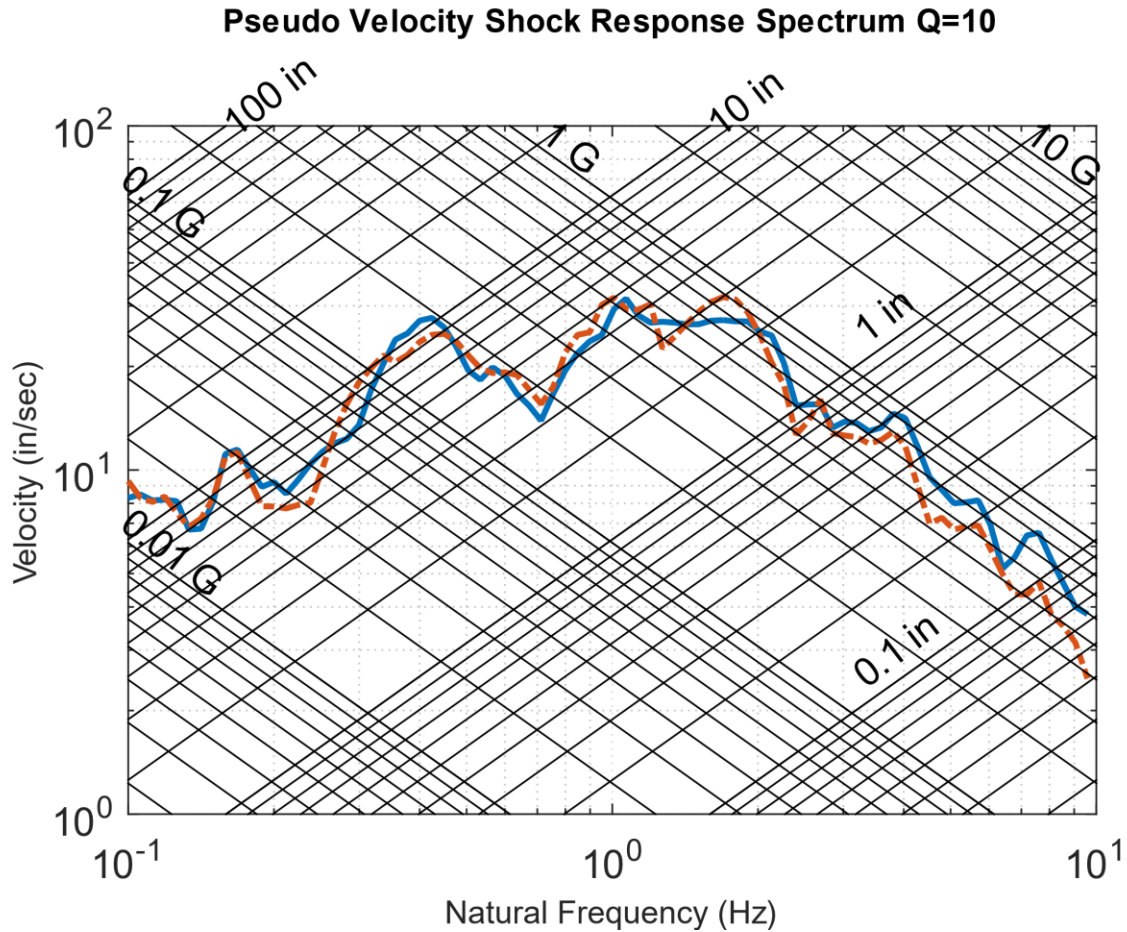
Figure 26.33.  El Centro Earthquake Tripartite SRS

Seismic SRS curves are often plotted in a tripartite format which displays relative displacement, pseudo velocity, and acceleration responses all on the same graph.  The pseudo velocity $\mathbf{PV}$ is calculated from the relative displacement $\mathbf{Z}$ as

$$PV = \omega_n\, Z \qquad\qquad (26.12)$$

Stress can be calculated from pseudo velocity using the methods in Section 0.  The acceleration curve might be the most important design metric for equipment mounted inside a building.  The relative displacement might be the most important concern for analyzing the foundational strength.   The curves also show design tradeoffs.  Lowering the building's natural frequency below 1 Hz reduces the acceleration response but increases the relative displacement. Note that Q=10 is the same as 5% damping.

## 26.6.6 Golden Gate Bridge



Figure 26.34.  Golden Gate Suspension Bridge, San Francisco, California

In addition to traffic loading, the Golden Gate Bridge must withstand the following environments:

1. Earthquakes, primarily originating on the San Andreas and Hayward faults
2. Winds of up to 70 miles per hour
3. Strong ocean currents

The Golden Gate Bridge has performed well in all earthquakes to date, including the 1989 Loma Prieta Earthquake. Several phases of seismic retrofitting have been performed since the initial construction.  The bridge's fundamental mode is a transverse mode with a natural frequency of 0.055 Hz, with a period of 18.2 seconds

Note that California Department of Transportation (CALTRANS) standards require bridges to withstand an equivalent static earthquake force (EQ) of 2.0 G.  This level is plausibly derived as a conservative envelope of the El Centro SRS curves in Figure 26.32.

## 26.6.7 Vandenberg AFB



Figure 26.35.   Rocket Launch from Vandenberg AFB, California


The Vandenberg launch site is near the San Andreas Fault system.  The vehicle is mounted on the pad as a tall cantilever beam.  The vehicle must be analyzed to verify that it can withstand a major seismic event.  The vehicle may be mounted to the pad for only two weeks before launch.  The odds of an earthquake occurring in that time window are minuscule.  But the launch vehicle and payload together may cost well over $1 billion.  The risk thus necessitates the analysis.  Areas of concern are the loads imparted at the launch vehicle's joints and to the payload.
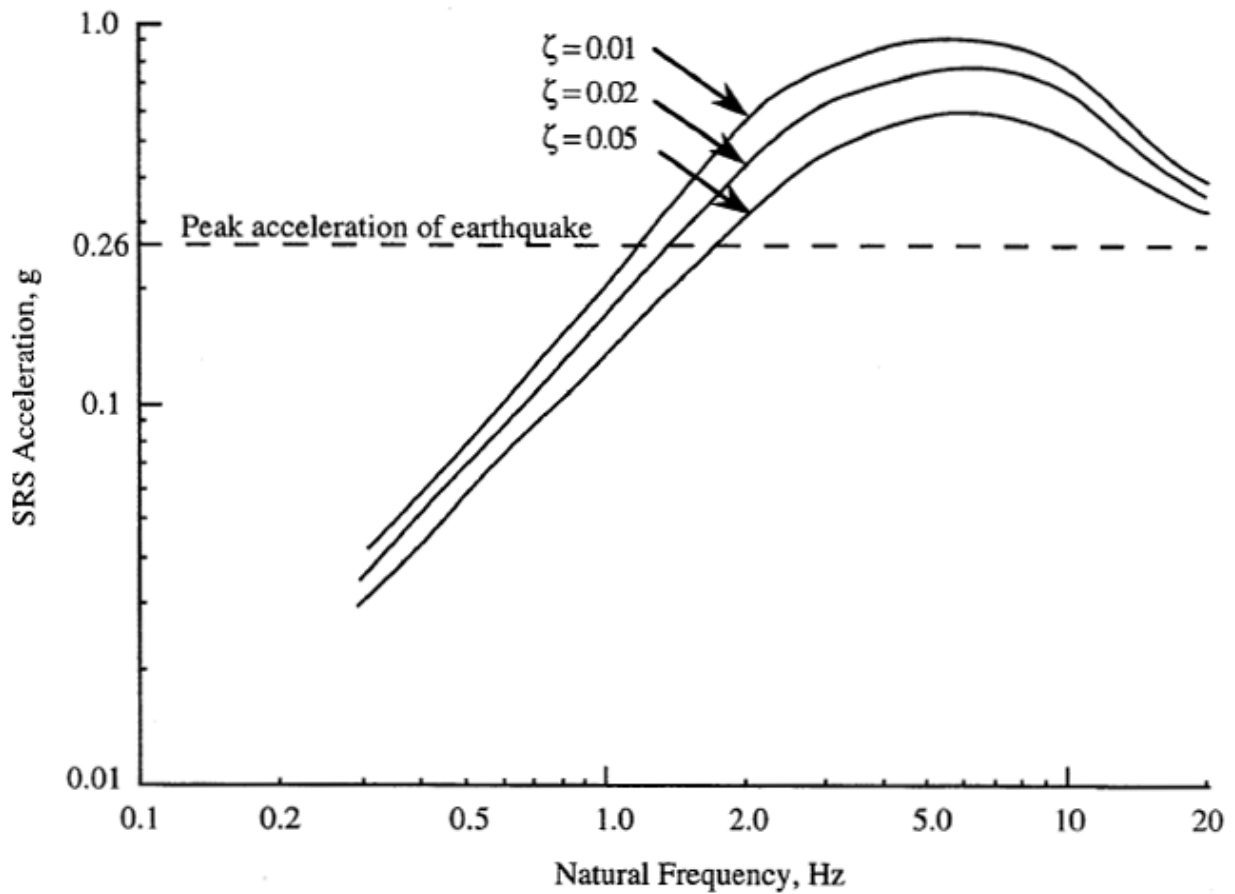
Figure 26.36.   NASA SRS Curves for Launch Vehicles at Vandenberg

SRS curves are given for three damping cases.  The curves are taken from Reference [32].  The vehicle would typically be analyzed as a multi-degree-of-freedom system via a finite element model.  Each SRS curve could be applied to the model using a modal combination method.  An alternative is to synthesize a time history to satisfy a selected SRS curve.  The time history could then be applied to the model via a modal transient analysis.

## 26.6.8 Seismic Testing



Figure 26.37. Electrical Power Generator Seismic Shock Test

The diesel generator is mounted onto a platform at the top of a shaker table which is located below the ground floor. This could be an emergency power generator for a hospital in an active seismic zone. A video clip of the test is available on YouTube at: https://youtu.be/5uSqI7kSYE4

The following Bellcore/Telecordia GR-63-Core SRS levels are used for telecommunication equipment in seismic zones.
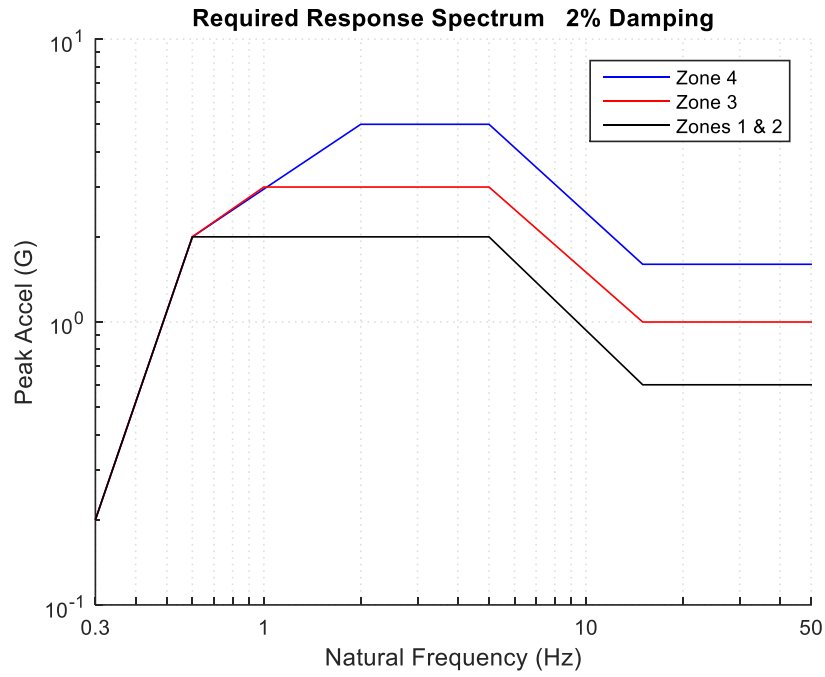
Figure 26.38.  GR-63-Core
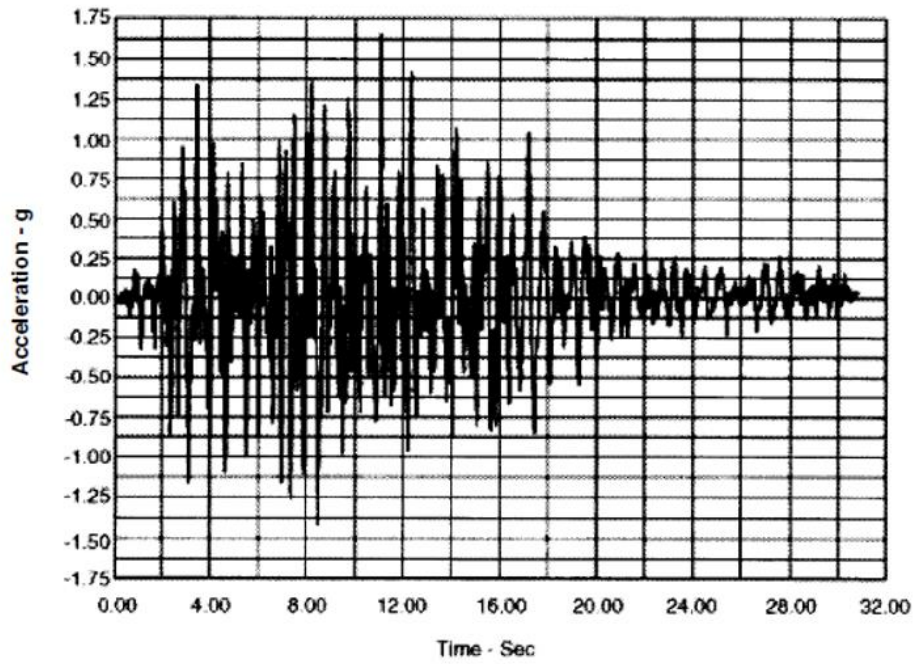


Figure 26.39.  Time History to Satisfy GR-63-Core, Zone 4 (VERTEQII)

Figure 26.40.  Unholtz-Dickie Shaker, Long Stroke

The system performs the vibration tests as specified in Telcordia's GR-63-CORE for all three orthogonal axis.

- Sine Survey: determines the natural frequencies of communications equipment by sweeping 1 to 50 Hz at 0.2 g and 1.0 octave per minute rate.

- Seismic Test: reproduces VERTEQII Zone 4 earthquake time waveform pulse requiring 10 inches (254 mm) of stroke at 40 inches per second (1 m/s) velocity, and 1.65 g max

- Office Vibration: 1.0 g sweep from 5 to 100 Hz and back to 5 Hz using 0.25 octave per minute rate.

- Transportation Vibration: 0.78 grms random from 5 to 200 Hz for 30 minutes

## 26.7 PYROTECHNIC SHOCK

### 26.7.1 Flight Events



Figure 26.41.  Stage Separation Ground Test, Linear Shaped Charge

The gas jet containing metallic particles cuts the metal inducing severe mechanical shock energy, but the smoke and fire would not occur in the near-vacuum of space.

Launch vehicle avionics components must be designed and tested to withstand pyrotechnic shock from various stage, fairing, and payload separation events that are initiated by explosive devices.  Solid rocket motor ignition is another source of pyrotechnic shock.  The source shock energy can reach thousands of acceleration Gs at frequencies up to and beyond 100 kHz.  The corresponding velocities can reach a few hundred in/sec, well above the severity thresholds in the empirical rules-of-thumb in Section 29.4.

Empirical source shock levels for a variety of devices are given in References [32], [47], [48].  These levels are intended only as preliminary estimates for new launch vehicle designs.   The estimates should be replaced by ground test data once the launch vehicle hardware is built and tested.

## 26.7.2 Pyrotechnic Device Photo Gallery
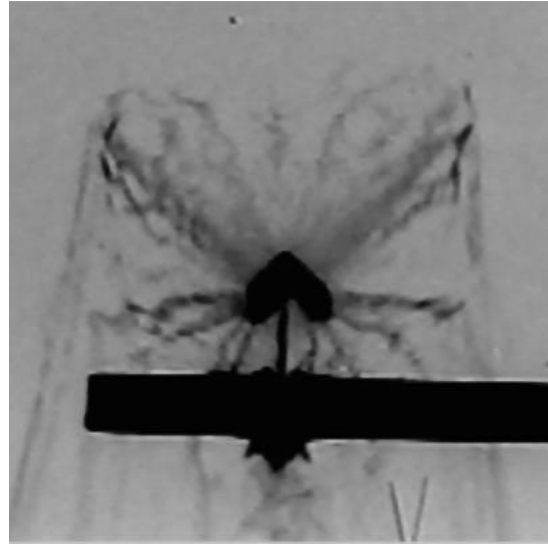


Figure 26.42.  Metal Clad Linear Shaped Charge & Flash X-ray (Ensign-Bickford Aerospace)

The detonation creates a high-temperature, high-pressure gas jet carrying dislodged metallic particles from the inside of the sheath.  The chevron focuses the jet at the launch vehicle's separation plane material causing a fracture.[7]  Severe shock levels are generated as a byproduct.
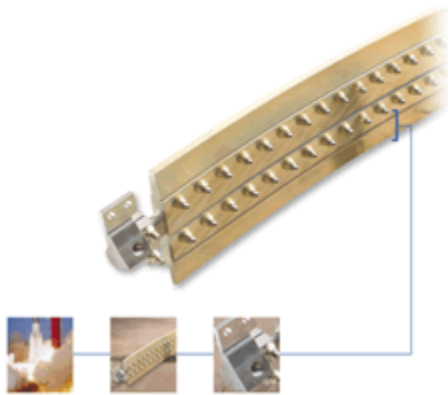


Figure 26.43.  Frangible Joint

A frangible joint may be used for stage or fairing separation.  The key components of a frangible joint:

- Mild Detonating Fuse (MDF)
- Explosive confinement tube
- Separable structural element
- Initiation manifolds
- Attachment hardware

The hot gas pressure from the MDF detonation causes the internal tube to expand and fracture the joint.

---

[7] The Munroe or Neumann effect is the focusing of blast energy by a hollow or void cut on a surface of an explosive.
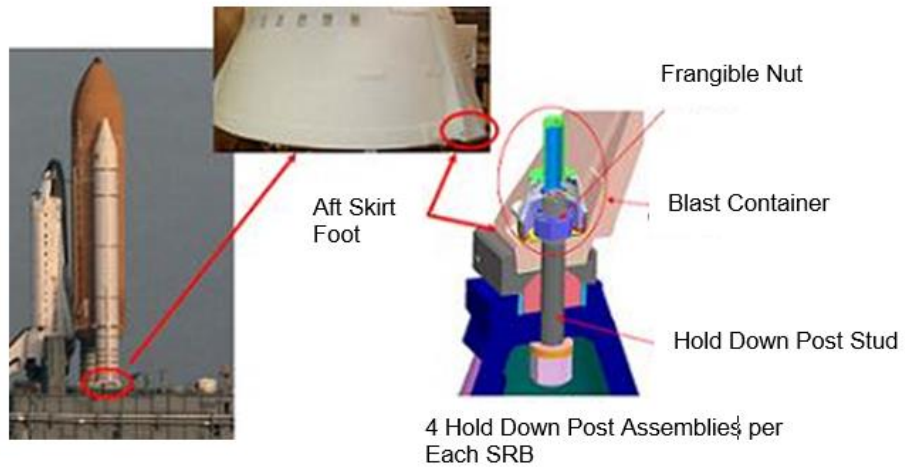
Figure 26.44.  Frangible Nuts, Hold Down Posts

The purpose of the nuts was to hold the SRBs in place against wind and ground-borne excitation.  The nuts were separated just before liftoff.
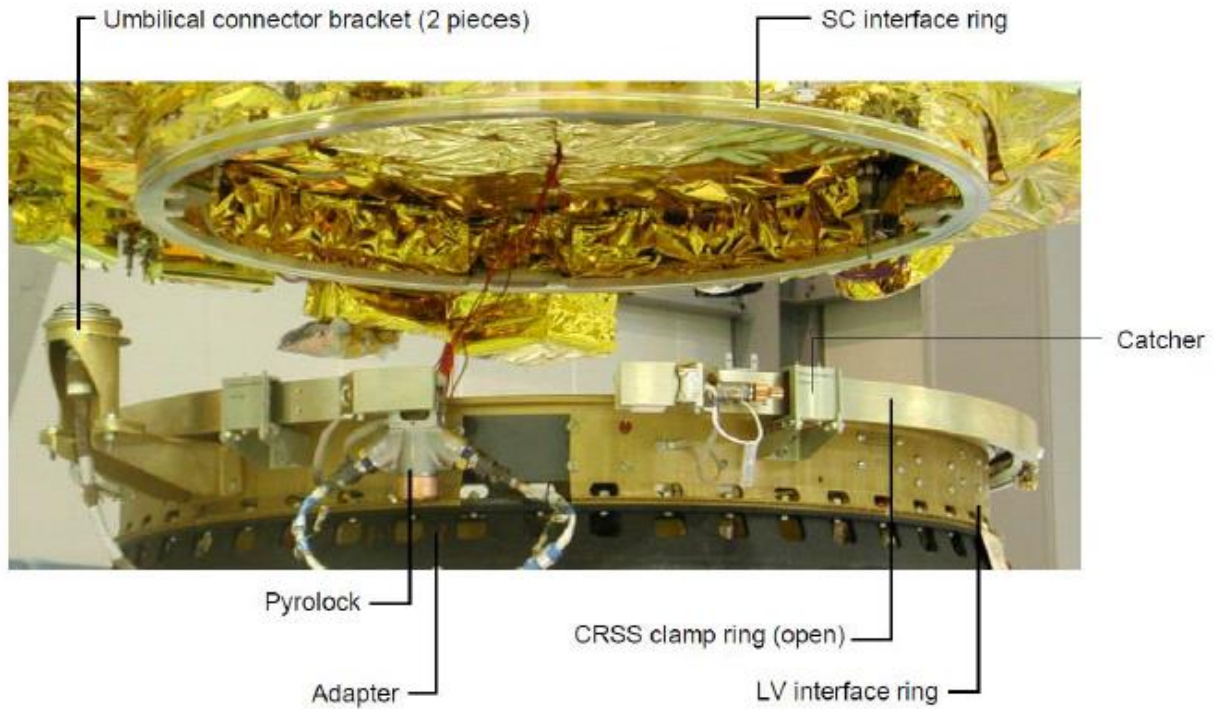
Figure 26.45.  Clamp Band with Pyrotechnic Bolt-Cutters (European Space Agency)

Clamp bands are often used for payload separation from launch vehicle adapters.  They are also commonly used for stage separation in suborbital launch vehicles, similar to the one in Figure 4.2.  A pyrotechnic bolt-cutter uses an explosive charge to drive a chisel blade to cut the band segments' connecting bolt.  The cutters produce some shock energy, but much of the shock is due to the sudden release of strain energy in the preloaded clamp band.   This action can excite a ring mode in the radial axis.  Recall Section 11.3.

The total clamp band release shock is significantly less than linear shaped charge and frangible joint.  Note that an analysis must be performed to verify that no gapping will occur between the band and the joint as the vehicle undergoes bending mode vibration during powered flight.

## 26.8  PYROTECHNIC SHOCK DATA

### 26.8.1 Initial SRS Slopes
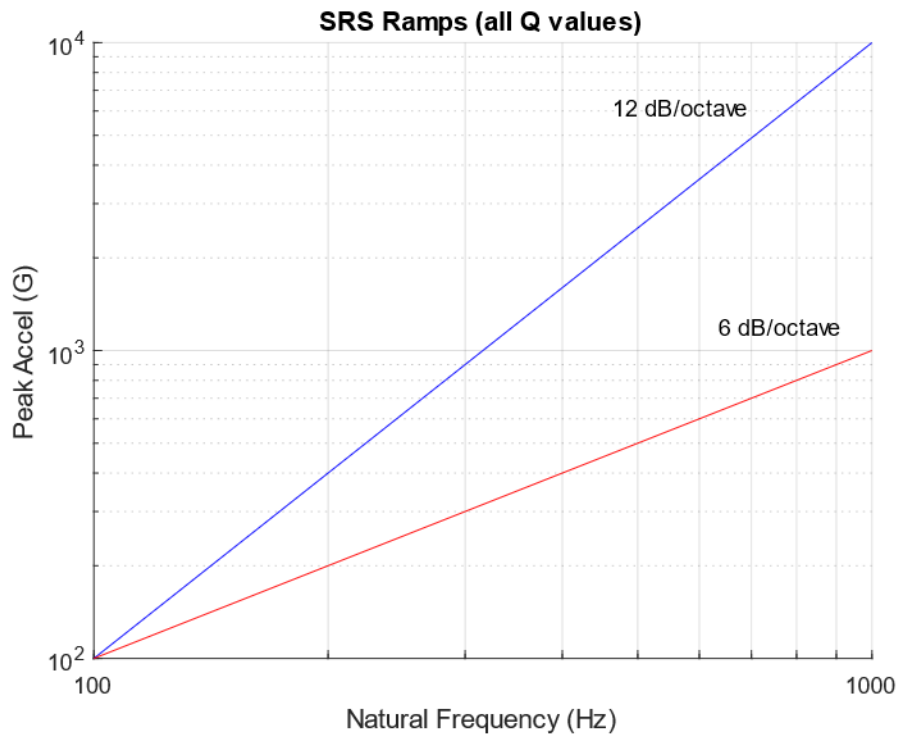


Figure 26.46.  Expected Pyrotechnic SRS Initial Slope Limits

Near-field pyrotechnic shock can be difficult to measure accurately.  The accelerometer data may have a baseline shift or spurious low-frequency transient.  This error could be a result of the accelerometer's own natural frequency being excited or some other problem.   Aerospace pyrotechnic shock SRS specifications usually begin at 100 Hz due to the difficulty of accurately measuring low-amplitude, low-frequency shock, while simultaneously measuring high-amplitude, high-frequency shock.

There are several methods for checking whether the data is acceptable.  One is to check the initial slopes of both the positive and negative SRS curves.  Each should have an overall trend of 6 to 12 dB/octave.  The actual slopes may have local peaks and dips due to low-frequency resonances.  A 12 dB/octave slope represents constant displacement and zero net velocity

change.  A 6 dB/octave slope indicates constant velocity.  Recall the slope formulas in Section 24.1.2.

A second method for checking data accuracy is to verify that the positive and negative SRS curves are within about 3 dB of each other across the entire natural frequency domain.  A third method is to integrate the acceleration time history into velocity.  The velocity time history should oscillate stably about the zero baselines.

These verification goals are challenging to meet with near-field shock measurements of high-energy source shock, such as that from linear shaped charge and frangible joints.  In practice, some high-pass filtering or spurious trend removal may be necessary.  There is no one right way to perform this "data surgery."  It is a matter of engineering judgment.

## 26.8.2 Re-entry Vehicle Separation, Flight Data
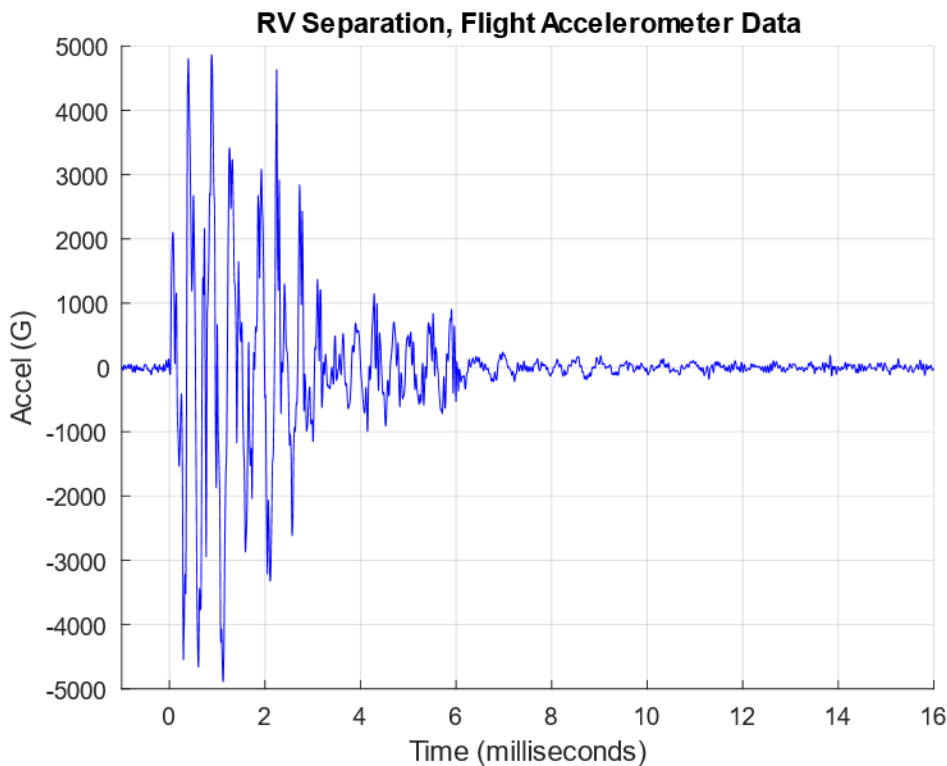


Figure 26.47.  Re-Entry Vehicle, Separation Shock, Near-Field Measurement, Time History

The source device was a linear shaped charge.
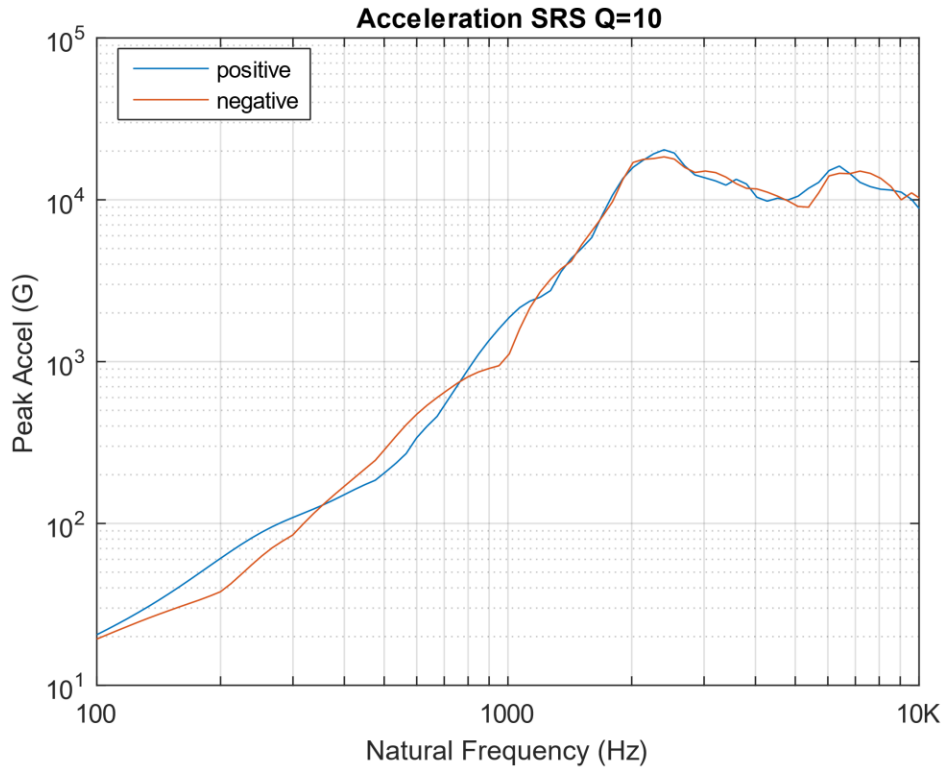
Figure 26.48.  Re-Entry Vehicle, Separation Shock, Near-Field Measurement, SRS

The SRS reached 20,040 G at 2400 Hz, which is an extreme level per the rule-of-thumb Section 29.4.

Each of the two Space Shuttle Boosters was recovered and refurbished after every flight. Each booster contained sensitive avionics components which underwent shock testing for the water impact event.

Figure 26.49. Solid Rocket Booster Water Impact Shock



The data is from the STS-6 Mission.

The accelerometer was mounted at the forward end of the booster adjacent to a large IEA avionics box. This was the worst-case shock event for this component.
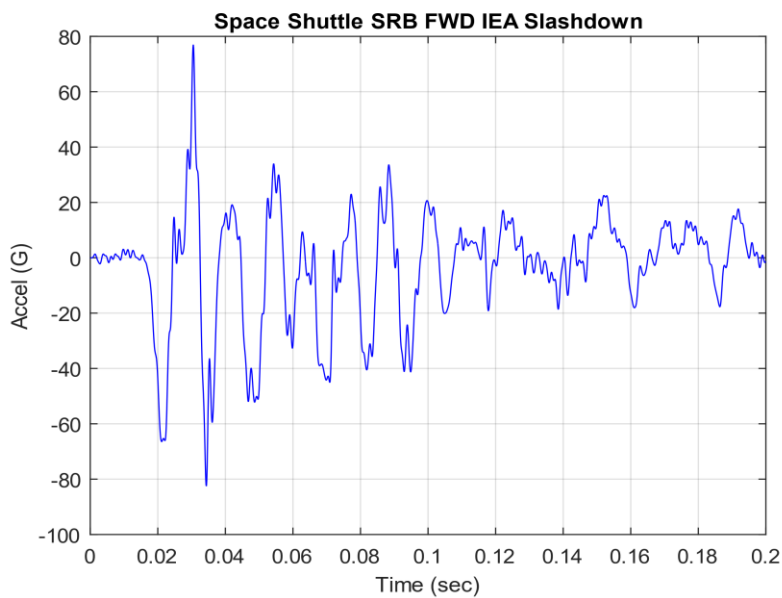
Figure 26.50.  Solid Rocket Booster Water Impact Shock, Time History

**Pseudo Velocity Shock Response Spectrum Q=10**
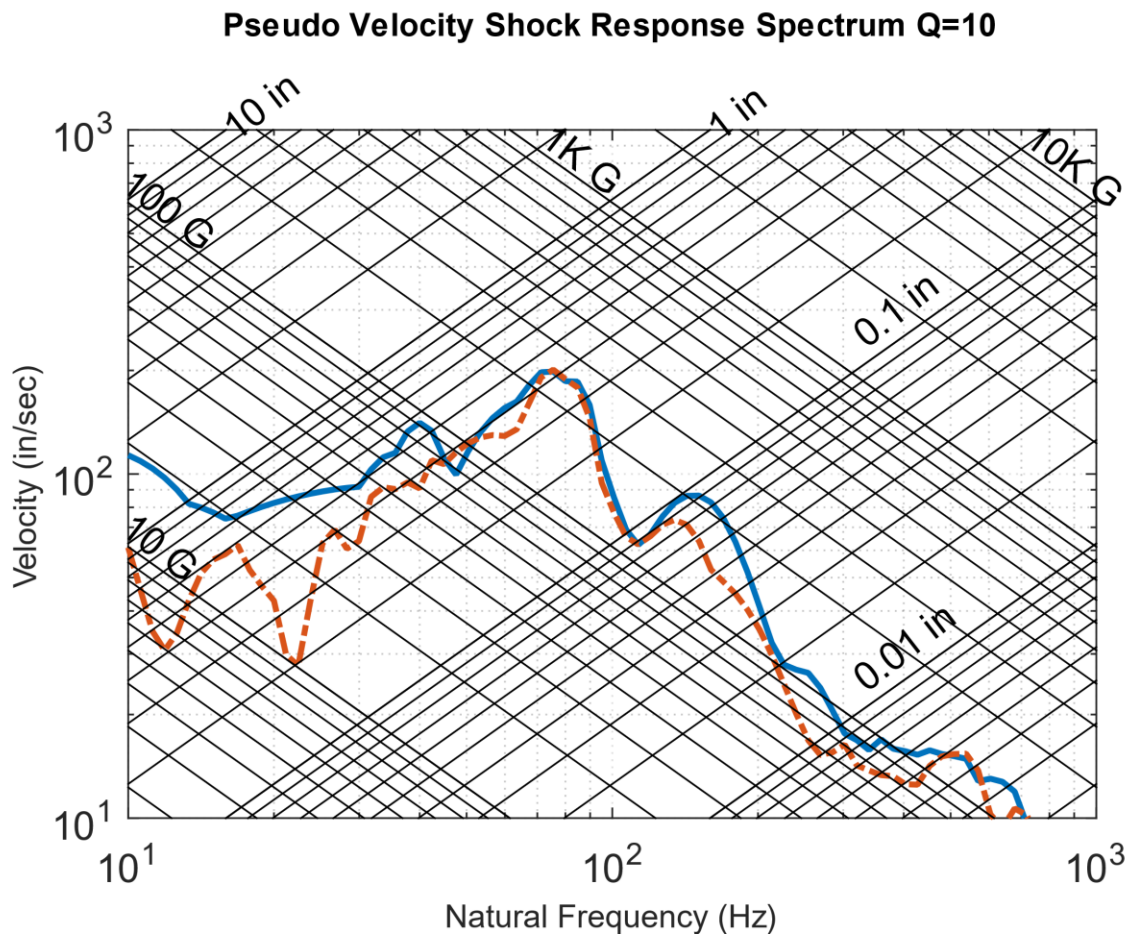
Figure 26.51.  Solid Rocket Booster Water Impact Shock, Tripartite SRS

The maximum acceleration response is 257 G at 85 Hz.  The maximum pseudo velocity response is 201 in/sec at 76 Hz, which is severe per the rule-of-thumb Section 29.4.

### 26.9.1  Shock Fields

#### 26.9.1.1 Near-Field

The near-field environment is dominated by direct stress wave propagation from the source. Peak accelerations above 5000 G occur in the time domain with a frequency content extending beyond 100 kHz.  The near-field usually includes structural locations within approximately 15 cm of the source for severe devices such as linear shaped charge and frangible joint.  No shock-sensitive hardware should be mounted where it would be exposed to a near-field environment.

#### 26.9.1.2 Mid-Field

The mid-field environment is characterized by a combination of wave propagation and structural resonances.  Peak accelerations may occur between 1000 and 5000 G, with substantial spectral content above 10 kHz.  The mid-field for intense sources usually includes structural locations between approximately 15 and 60 cm of the source, unless there are intervening structural discontinuities.

#### 26.9.1.3 Far-Field

The far-field environment is dominated by structural resonances.  The peak accelerations tend to fall below 2000 G, and most of the spectral content is below 10 kHz.  The far-field distances occur outside the mid-field.  The typical far-field SRS has a knee frequency corresponding to the dominant frequency response.  The knee frequency is the frequency at which the initial ramp reaches the plateau in the log-log SRS plot.

#### 26.9.1.4   Joint & Distance Attenuation

The source shock energy is attenuated by intervening material and joints as it propagates from the near-field to the far-field.  Empirical distance and joint attenuation factors for the SRS reduction are given in References [32], [47], [48] .  A typical attenuation curve from [47] is given in Figure 26.52, which assumes an input source shock SRS consisting of a ramp and plateau in log-log format.  Such curves should be used with caution given that the attenuation is highly dependent on damping and structural details.  The curves can be used for preliminary estimates for new launch vehicle designs, but ground separation tests are still needed for the actual

launch vehicle hardware.  These tests are needed to measure the source shock as well as the levels at key component mounting locations.
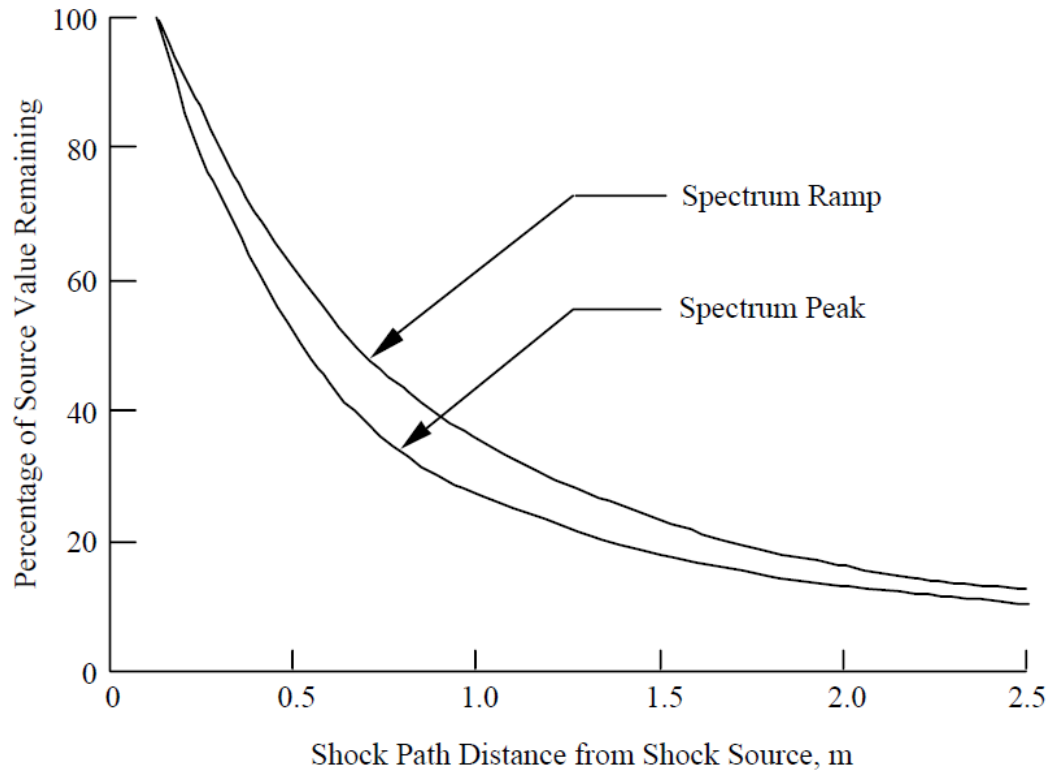


Figure 26.52.  Shock Response Spectrum versus Distance from Pyrotechnic Shock Source

## 26.9.2 Pyrotechnic Shock Testing Methods



Figure 26.53.  Near-Field Shock Simulation using a Plate

The test component is mounted on the other side of the plate. The source device is a textile explosive cord with a core load of 50 grains/ft (PETN explosive).  Up to 50 ft of Detonating Cord has been used for some high G tests.  The maximum frequency of shock energy is unknown so analog anti-aliasing filters are needed for the accelerometer measurements per the guidelines in Section 22.

Note that a component may be mounted in the mid-field shock region of a launch vehicle.  The SRS test level derivation for this zone may include a significant dB factor for uncertainty or as a qualification margin.  This conservatism may require a near-field-type shock test for a component that is actually in a mid-field zone.  This situation can also occur for components mounted in far-fields.
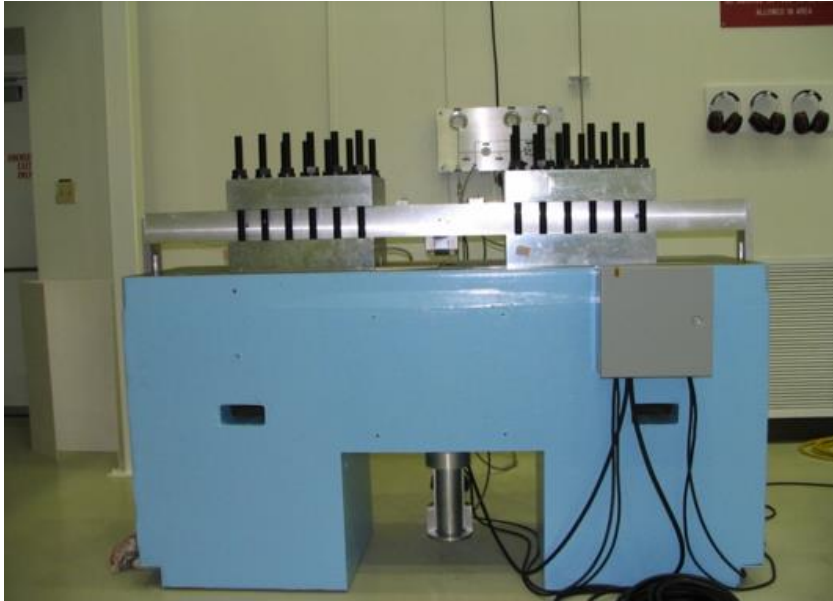
Figure 26.54.  JPL Tunable Shock Beam    (photos courtesy of NASA JPL)

The NASA/JPL Environmental Test Laboratory developed and built a tunable beam shock test bench based on a design from Sandia National Laboratory many years ago. The excitation is provided by a projectile driven by gas pressure.  The beam is used to achieve SRS specifications, typically consisting of a ramp and a plateau in log-log format. The intersection between these two lines is referred to as the "knee frequency." The beam span can be varied to meet a given knee frequency. The high-frequency shock response is controlled by damping material.

Figure 26.55.  Commercial Shock Beam    (photo courtesy of MGA)

https://mgaresearch.com/space-and-defense/

## 26.9.3 Shock Failure Modes



Figure 26.56.  Sensitive Electronic Parts

Pyrotechnic shock can cause crystal oscillators to shatter.  Large components such as DC-DC converters can detach from circuit boards.  In addition, mechanical relays can experience chatter or transfer.



Figure 26.57.  Shock Test Case History, Adhesive & Solder Joint Failure

The image shows adhesive failure and rupture of the solder joint after a stringent shock test.  A large deflection of the PCB resulting from insufficient support/reinforcement of the PCB combined with high shock loads can lead to these failures.  Staking is needed for parts weighing more than 5 grams.
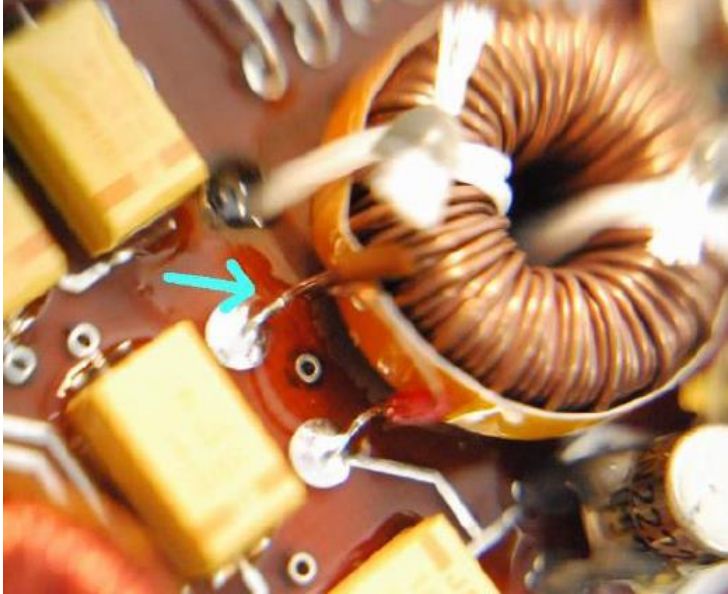
Figure 26.58.  Shock Test Case History, Lead Wire Failure

The image shows a sheared lead between the solder joint and the coil winding.  The lacing cord was insufficient by itself.   The lacing should be augmented by staking with an adhesive.

## 26.9.4 Nonlinear Shock Analysis
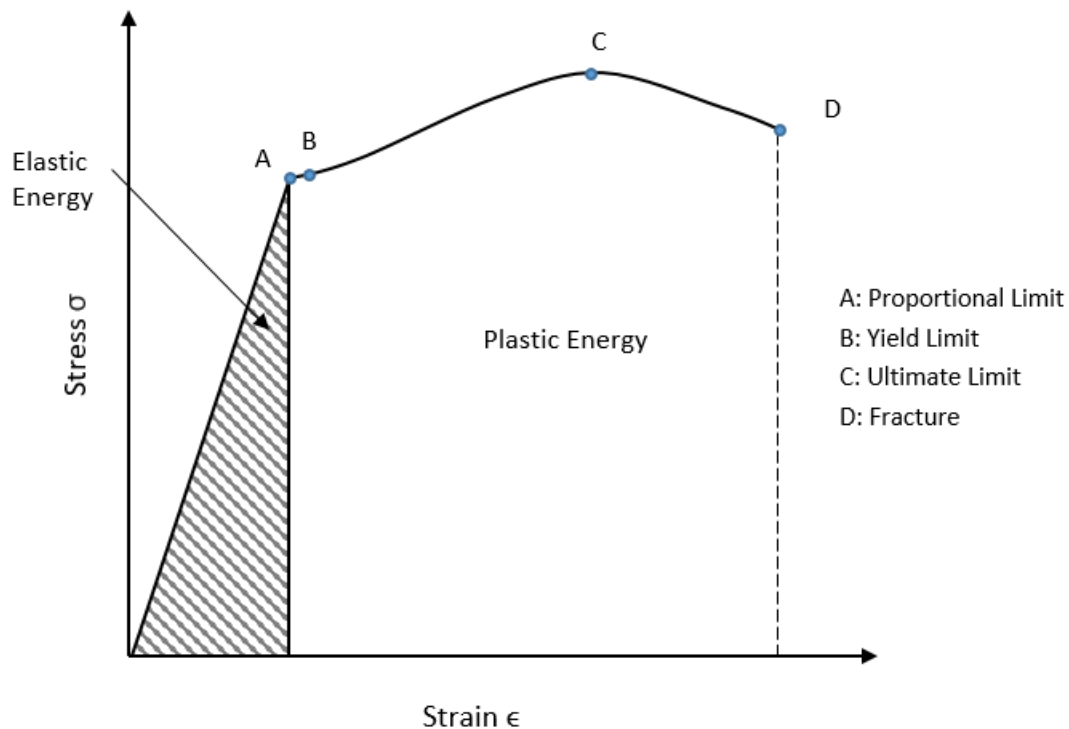


Figure 26.59.  Stress-Strain Curve

The plot shows the applied strain on the horizontal axis and the resisting stress on the vertical axis. The area inside the triangle represents the maximum energy that can be absorbed elastically if the member is strained up to its proportional limit stress. The member will return to its original position when the load is removed. This area is also referred to as resilience or modulus of resilience.

The yield stress, denoted $\sigma_y$, is the stress needed to induce plastic deformation in the specimen. The yield stress is taken to be the stress needed to induce a specified amount of permanent strain, typically 0.2% since it is often difficult to pinpoint the exact stress at which plastic deformation begins.

The remaining area, which is not cross-hatched, represents the plastic (or inelastic) energy if the member is strained up to its fracture point. This area is also referred to as the toughness or modulus of toughness.

A large amount of energy can be absorbed, if permanent, plastic deformation is acceptable.
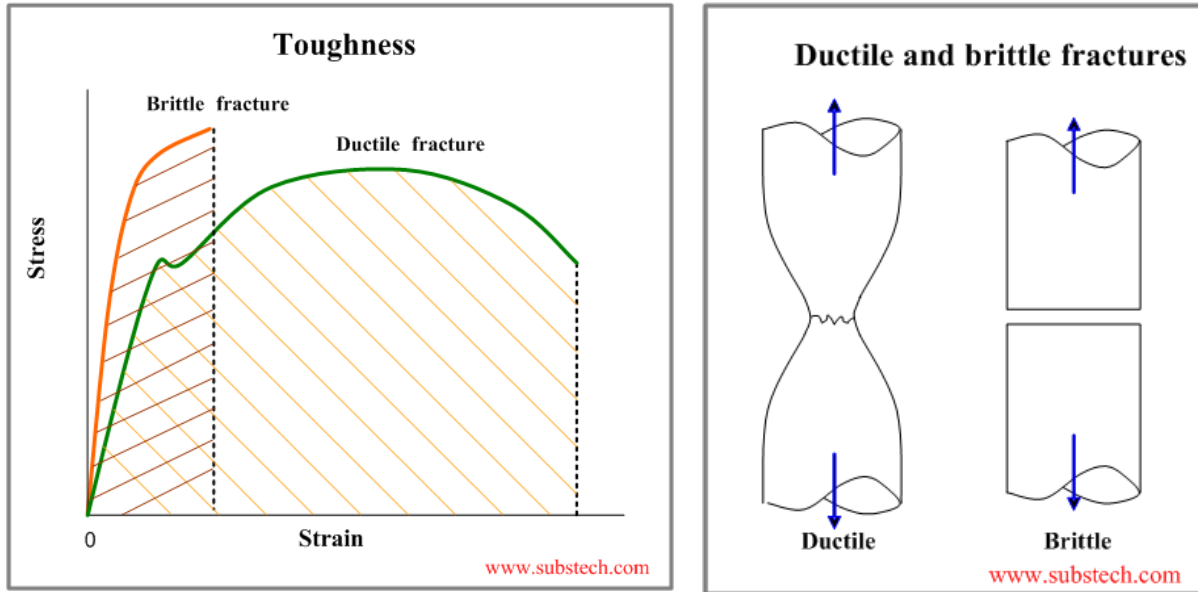
Figure 26.60.  Toughness & Facture

Ductile materials undergo observable plastic deformation and absorb significant energy before fracture. An additional portion of the energy is dissipated as heat during load and unloading cycles.

Brittle fracture is characterized by very low plastic deformation and low energy absorption before breaking.

Toughness is the ability of a material to absorb energy and plastically deform without fracturing. One definition of material toughness is the amount of energy per unit volume that a material can absorb before rupturing. This measure of toughness is different from that used for fracture toughness, which describes load bearing capabilities of materials with flaws.

Toughness requires a balance of strength and ductility. A material should withstand both high stresses and high strains to be tough. Generally, strength indicates how much force the material can support, while toughness indicates how much energy a material can absorb before rupturing.

Toughness (or, deformation energy, UT) is measured in units of joule per cubic meter (J/m$^3$) in the SI system and inch-pound-force per cubic inch (in·lb/in$^3$) in US customary units.
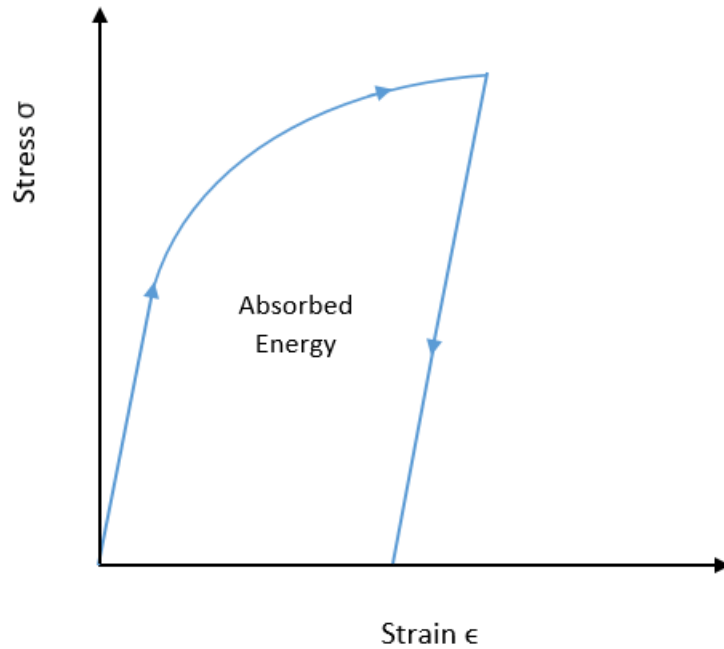
Figure 26.61.   Absorbed Energy in Stress-Strain Curve
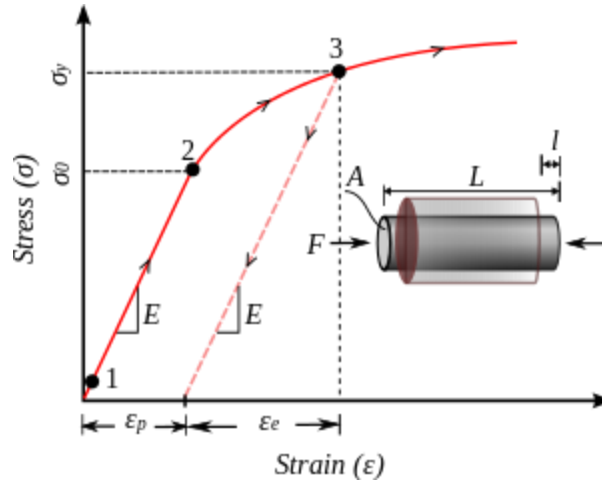


Figure 26.62.   Strain or Work Hardening

The uniaxial stress–strain curve shows typical work hardening plastic behavior of materials in uniaxial compression.  For work hardening materials the yield stress increases with increasing plastic deformation. The strain can be decomposed into a recoverable elastic strain $\varepsilon_p$ and an inelastic strain $\varepsilon_e$.  The stress at initial yield is $\sigma_o$.

26.9.5  Material Response to Shock

A material can sometimes sustain an important dynamic load without damage, whereas the same load, statically, would lead to plastic deformation or to failure. [49]  Many materials subjected to short duration loads have ultimate strengths higher than those observed when they are static.

Hopkinson noted that copper and steel wire can withstand stresses that are higher than their static elastic limit and are well beyond the static ultimate limit without separating proportionality between the stresses and the strains.  This is provided that the length of time during which the stress exceeds the yield stress is of the order of 1 millisecond or less.

Tests carried out on steel (annealed steel with a low percentage of carbon) revealed that the initiation of plastic deformation requires a definite time when stresses greater than the yield stress are applied.  It was observed that this time can vary between 5 milliseconds (under a stress of approximately 352 MPa) and 6 seconds with approximately 255 MPa; with the static yield stress being equal to 214 MPa).  Other tests carried out on five other materials showed that this delay exists only for materials for which the curve of static stress deformation presents a definite yield stress, and the plastic deformation then occurs for the load period.

Table 26.4.  Annealed Steel Test Results

| Parameter | Stress (MPa) | Stress (ksi) |
|---|---|---|
| Static Yield Stress | 214 | 31.1 |
| 5 msec for plastic deformation onset | 352 | 51.1 |
| 6 sec for plastic deformation onset | 255 | 37.0 |

Reference [50] includes the following table where the data was obtained for uniaxial testing using an impact method.

Table 26.5.  Dynamic Strengthening of Materials

| Material | Static Strength (psi) | Dynamic Strength (psi) | Impact Speed (ft/sec) |
|---|---|---|---|
| 2024 Al (annealed) | 65,200 | 68,600 | >200 |
| Magnesium Alloy | 43,800 | 51,400 | >200 |
| Annealed Copper | 29,900 | 36,700 | >200 |
| 302 Stainless Steel | 93,300 | 110,800 | >200 |
| SAE 4140 Steel | 134,800 | 151,000 | 175 |
| SAE 4130 Steel | 80,000 | 440,000 | 235 |
| Brass | 39,000 | 310,000 | 216 |

## 26.10   SHOCK RESPONSE SPECTRUM SYNTHESIS

### 26.10.1        Synthesis Objectives

Consider an SRS specification for a component, subsystem, or large structure.  The article should be tested, if possible, to verify that it can withstand the shock environment.  Certain shock tests can be performed on a shaker table, like the generator test in Figure 26.37.  This requires synthesizing an acceleration time history to satisfy the SRS.  The net velocity and net displacement must each be zero for this test.  These requirements can be met with a certain type of wavelet series, where the individual wavelets may be nonorthogonal.  The resulting wavelet time history should meet the SRS within reasonable tolerance bands, but it may not "resemble" the expected time history which is a limitation of this method.  Another requirement is that the peak acceleration, velocity, and displacement values must be within the shaker table's capabilities.

An innovative method for meeting the SRS with a wavelet series that resembles one or more measured shock time histories is given in Reference [51].

A synthesized time history can also be used for modal transient analysis.  This could be done for articles that are too large or heavy for shaker tables.  This analysis can also be done on small components before shock testing to determine whether they will pass the test.  Or the analysis could be done in support of the isolator mounting design.  There is again a need for the synthesized time history to have net velocity and net displacement which are each zero, to maintain numerical stability in stress calculations from relative displacement values.

Damped-sines can be used for modal transient analysis where the goal is to meet the SRS with a time history that plausibly resembles the expected field shock event.  But damped sines do not meet the desired zero net velocity and displacement goals.  The workaround is to first synthesize a damped-sine series to meet the SRS and then reconstruct it via a wavelet series, in Rube Goldberg fashion.

Wavelet and damped-sine synthesis are shown in the following examples.  The damped-sine section is presented as a historical reference.  The author has since devised a technique for arranging wavelets such that their summation resembles a damped sine series, without using the damped sine series as an intermediate step.

26.10.2 Wavelet Synthesis

26.10.2.1 Wavelet Equation

A wavelet is a sine function modulated by another sine function. The equation for an individual wavelet is

$$
W_m(t) = \begin{cases} 0, & \text{for } t < t_{dm} \\ A_m \sin\left[\dfrac{2\pi f_m}{N_m}(t - t_{dm})\right]\sin[2\pi f_m(t - t_{dm})] , & \text{for } t_{dm} \le t \le \left(t_{dm} + \dfrac{N_m}{2 f_m}\right) \\ 0, & \text{for } t > \left(t_{dm} + \dfrac{N_m}{2 f_m}\right) \end{cases}
$$

(26.13)

where

$W_m(t)$ = acceleration of wavelet m at time t

$A_m$ = wavelet acceleration amplitude

$f_m$ = wavelet frequency

$N_m$ = number of half-sines

$t_{dm}$ = wavelet time delay

Note that $N_m$ must be an odd integer greater than or equal to 3. This is required so that the net velocity and net displacement will each be zero. The total acceleration at time t for a set of n wavelets is

$$
\ddot{x}(t) = \sum_{m=1}^{n} W_m(t)
$$

(26.14)
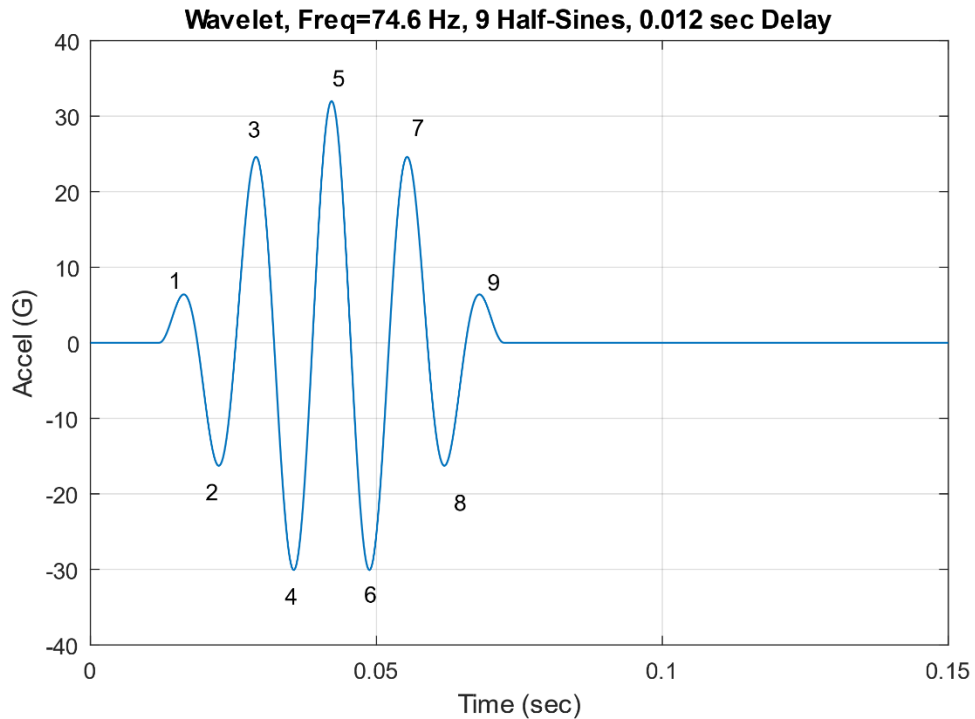
Figure 26.63.  Sample Wavelet

A sample, individual wavelet is shown in Figure 26.63.  This wavelet was a component of a previous analysis for an aerospace project.

26.10.2.2      Wavelet Synthesis Example

Consider the specification:  MIL-STD-810E, Method 516.4, Crash Hazard for Ground Equipment.

Table 26.6.  SRS Q=10, Crash Hazard Specification

| Natural Frequency (Hz) | Peak Accel (G) |
|---|---|
| 10 | 9.4 |
| 80 | 75 |
| 2000 | 75 |

Synthesize a series of wavelets as a base input time history for a shaker shock test to meet the Crash Hazard SRS.  The goals are:

1.  Satisfy the SRS specification
2.  Minimize the displacement, velocity, and acceleration of the base input

The synthesis steps are shown in the following table.

Table 26.7.  Wavelet Synthesis Steps

| Step | Description |
| --- | --- |
| 1 | Form a set of wavelet frequencies.  These may be arbitrary.  But a good choice is to start with the specification's first frequency and proceed in 1/12$^{th}$ octave steps. |
| 2 | Generate a random amplitude, delay, and half-sine number for each wavelet. Constrain the half-sine number to be odd.  These parameters form a wavelet table. |
| 3 | Synthesize an acceleration time history from the wavelet table. |
| 4 | Calculate the shock response spectrum of the synthesis. |
| 5 | Compare the shock response spectrum of the synthesis to the specification. Form a scale factor for each frequency. |
| 6 | Scale the wavelet amplitudes. |
| 7 | Generate a revised acceleration time history. |
| 8 | Repeat steps 3 through 6 until the SRS error is minimized or an iteration limit is reached. |
| 9 | Calculate the final shock response spectrum error. Also calculate the peak acceleration values. Integrate the signal to obtain velocity, and then again to obtain displacement. Calculate the peak velocity and displacement values. |
| 10 | Repeat steps 2 through 9 many times. |
| 11 | Choose the waveform which gives the lowest combination of SRS error, acceleration, velocity, and displacement. |

The resulting time history and SRS are shown in Figure 26.64 and Figure 26.65, respectively.
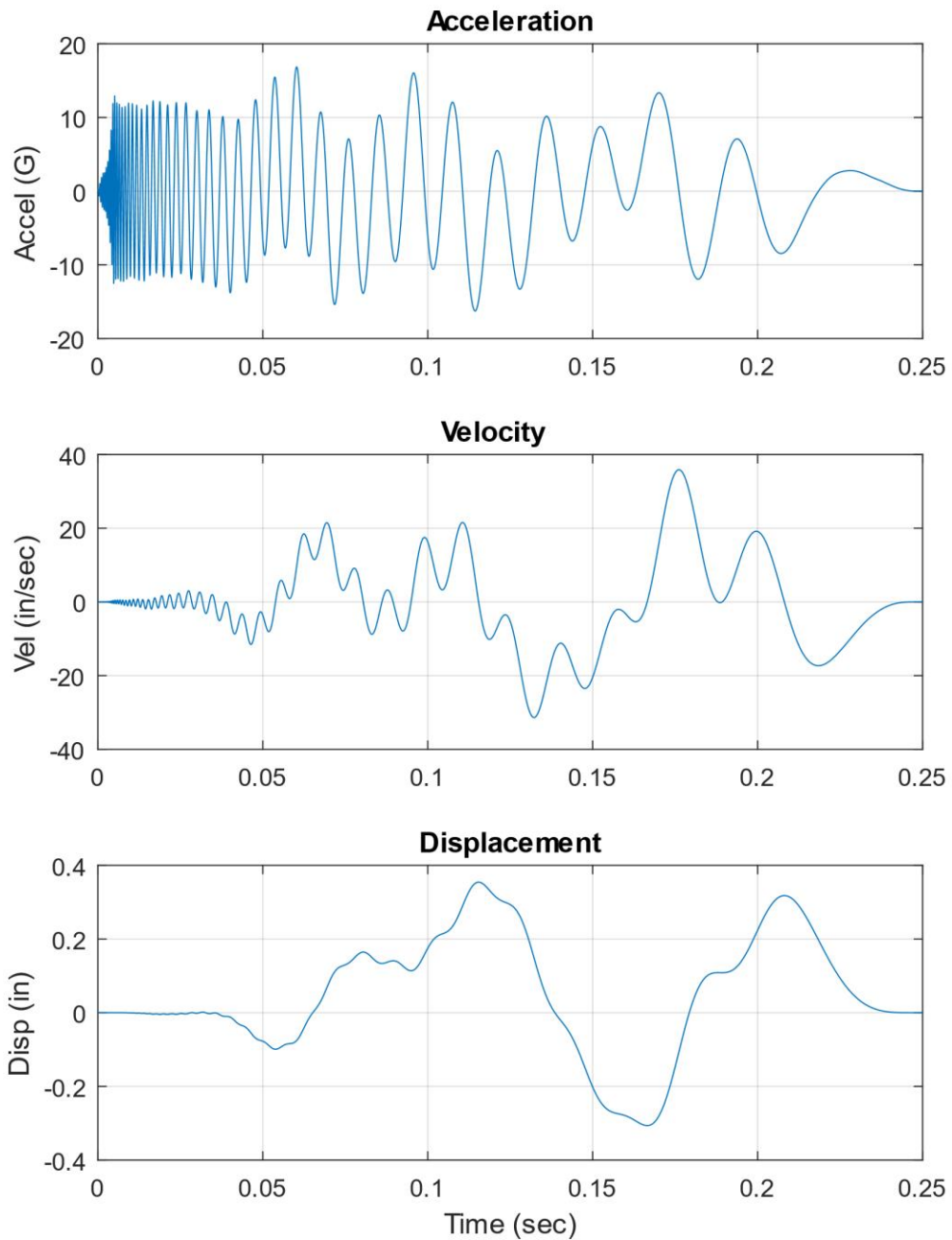
Figure 26.64. Crash Hazard Time History Synthesis

The acceleration time history has a reverse sine sweep character. It is an efficient and optimized waveform for a shaker shock test, and it satisfies the SRS as shown in the next figure. A drawback is that it does not resemble an actual crash shock time history.
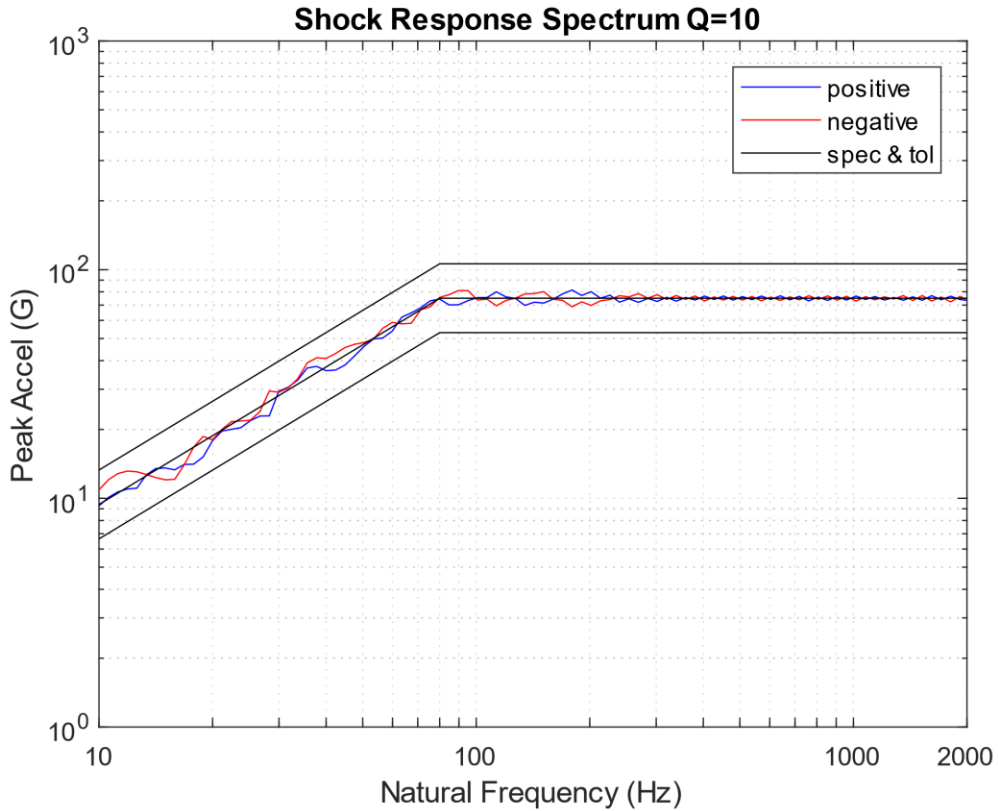
Figure 26.65.  Crash Hazard SRS

The positive and negative curves are from the synthesized waveform.  The tolerance bands are set at ± 3 dB.

## 26.10.3      Damped-Sine Synthesis

*The method in this section is included for historical reasons but is somewhat obsolete.  The author has since discovered a method to skip the damped-sine synthesis and instead perform a wavelet synthesis with the delay times arranged so that the composite waveform resembles a series of damped-sine functions.*

### 26.10.3.1    Damped-Sine Equation

The equation for an individual damped sinusoid is

$$
W_n(t) = \begin{cases} 0, & \text{for } t < t_{dn} \\ A_n \exp[-\xi_n \, \omega_n(t - t_{dn})]\sin[\omega_d(t - t_{dn})] \ , & \text{for } t \geq t_{dn} \end{cases}
$$

(26.15)

where

| | | |
|---|---|---|
| $W_n(t)$ | = | acceleration of damped sinusoid n at time t |
| $A_n$ | = | acceleration amplitude |
| $\omega_n$ | = | angular frequency |
| $\xi_n$ | = | damping value |
| $t_{dn}$ | = | time delay |

The total acceleration at time t for a set of damped sinusoids is

$$
\ddot{x}(t) = \sum_{n=1}^{N} W_n(t)
$$

(26.16)

### 26.10.3.2    Damped-Sine Example

Consider the following specification which could represent a stage separation shock level at some location in a launch vehicle.  A modal transient finite element analysis is to be performed on a component to verify that the component will pass its eventual shock test.  The immediate task is to synthesize a time history to satisfy the SRS.   The time history should "resemble" an actual pyrotechnic shock pulse.

Note that pyrotechnic SRS specifications typically begin at 100 Hz.  The author's rule of thumb is to extrapolate the specification down to 10 Hz in case there are any component modes between 10 and 100 Hz.  This guideline is also to approximate the actual shock event which should have an initial ramp somewhere between 6 and 12 dB/octave.

Table 26.8.  SRS Q=10, Stage Separation Shock

| Natural Frequency (Hz) | Peak Accel (G) |
|---|---|
| 10 | 10 |
| 2000 | 2000 |
| 10,000 | 2000 |

The specification has an initial slope of 6 dB/octave. The synthesis steps are shown in the following table.

Table 26.9.  Damped-Sine Synthesis Steps

| Step | Description |
|---|---|
| 1 | Generate random values for the following for each damped sinusoid: amplitude, damping ratio, and delay.  The natural frequencies are taken in one-twelfth octave steps. |
| 2 | Synthesize an acceleration time history from the randomly generated parameters. |
| 3 | Calculate the shock response spectrum of the synthesis. |
| 4 | Compare the shock response spectrum of the synthesis to the specification. Form a scale factor for each frequency. |
| 5 | Scale the amplitudes of the damped sine components. |
| 6 | Generate a revised acceleration time history. |
| 7 | Repeat steps 3 through 6 as the inner loop until the SRS error diverges. |
| 8 | Repeat steps 1 through 7 as the outer loop until an iteration limit is reached. |
| 9 | Choose the waveform which meets the specified SRS with the least error. |
| 10 | Perform wavelet reconstruction of the acceleration time history so that velocity and displacement will each have net values of zero.  See Reference [51]. |

The resulting time history and SRS are shown in Figure 26.66 and Figure 26.67, respectively.
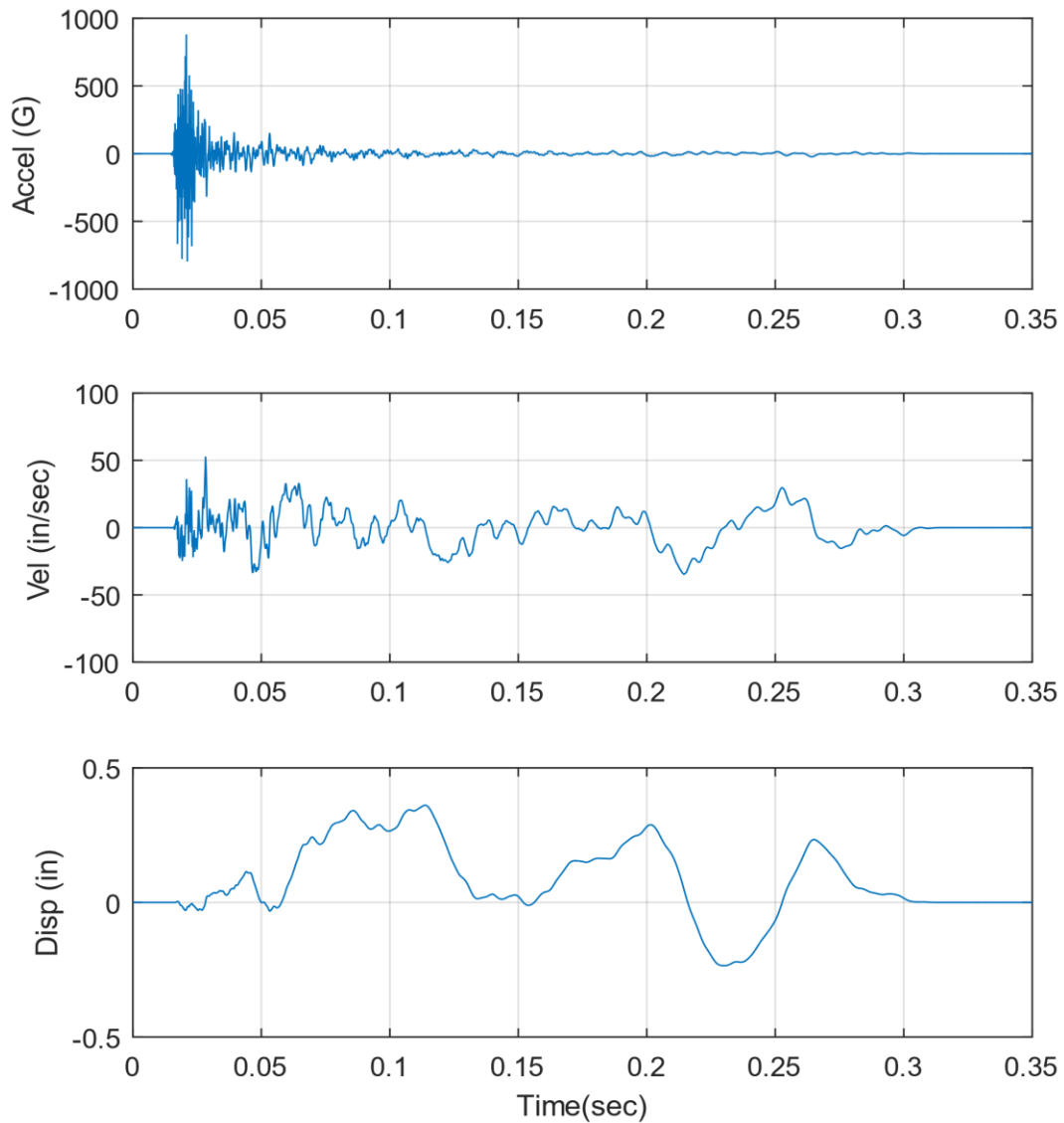
Figure 26.66.  Stage Separation Time History Synthesis

The acceleration time history somewhat resembles a mid or far-field pyrotechnic shock.  The velocity and displacement time histories each have a stable oscillation about their respective baselines.
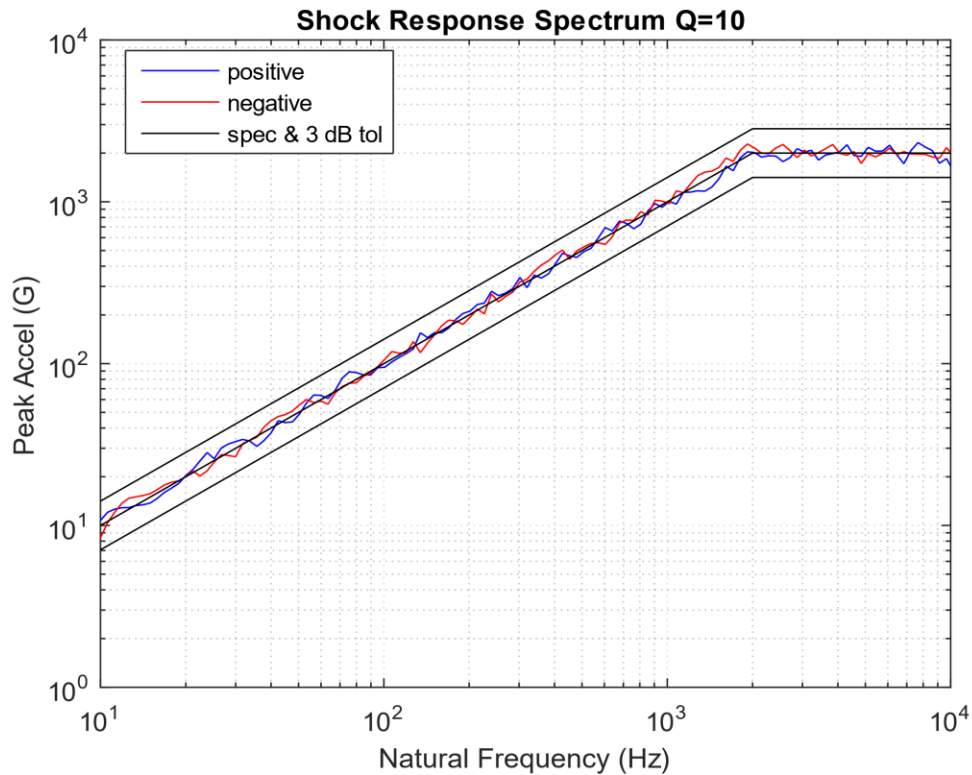
Figure 26.67.  Stage Separation SRS

The positive and negative curves are from the damped-sine synthesis.

## 26.11  MDOF SHOCK

### 26.11.1        MDOF Methods

The SRS is inherently a single-degree-of-freedom concept for calculating peak response for a family of natural frequencies.  But it can be extended to multi-degree-of-freedom (MDOF) systems.  There are two options, each requiring a starting normal modes analysis.  The phase angle is a concern with each option since the SRS does not specify the phase.  Neither method gives the "exact" results.

## 26.11.2    SRS  Synthesis with Modal Transient Analysis

The first method is to synthesize a time history to satisfy the SRS (Section 26.10), followed by a modal transient analysis. This method frees the user from dealing directly with the phase.  But the synthesized time history is not unique.  The user should probably generate multiple time histories to get the response statistical distribution.  This method is well suited for smaller systems but would be very time-consuming for an FEA model with, say, 500,000 degrees of freedom.  Another concern is that the synthesized time history's SRS may be $\pm$ 1.5 dB or so from the nominal SRS at any given natural frequency since shock synthesis is a messy, nonlinear process.

## 26.11.3    Simple Modal Combination

The second method is the modal combination method which has several variants.  The user must make an explicit assumption about the phase, which can have a huge effect on the results. One variant is the absolute sum (ABSSUM) equation which assumes that all modes reach their respective peaks simultaneously, which is a very conservative upper limit.  Another variant is the square-root-of-the-sum-of-the-squares (SRSS) approach which assumes that the overall response is the Euclidean norm of the individual modal responses.  The SRSS variant is not necessarily a lower limit but can be taken as such for conservatively high peak amplitude response estimates.

These modal combination methods are very fast even for large FEA models once the normal modes results are obtained.    But the gap between the ABSSUM and SRSS results can be wide.

The following four equations are given for the case of relative displacement response, but absolute acceleration can be substituted for relative displacement.

The ABSSUM equation for the peak relative displacement $(z_i)_{max}$ at DOF i is

$$(z_i)_{max} \leq \sum_{j=1}^{N} |\hat{q}_{ij}| \left|(\eta_j)_{max}\right| \tag{26.17}$$

where

$\qquad$ j $\qquad$ is the mode index

$\qquad$ N $\qquad$ is the total number of modes

$\qquad$ $\hat{q}_{ij}$ $\qquad$ is the mass-normalized eigenvector coefficient for coordinate i  and mode j

$\left( \eta_j \right)_{max}$ is the peak response for mode j

But equation (26.17) would require the complete modal transient solution, so it will be simplified as follows.

$$(z_i)_{max} \leq \sum_{j=1}^{N} |\Gamma_j| \, |\hat{q}_{ij}| \, \left| (D_j)_{max} \right| \qquad (26.18)$$

where

$\Gamma_j$    is the participation factor for mode j   (Section 9.1.4)

$(D_j)_{max}$    is the Relative Displacement SRS amplitude at the natural frequency for mode j

Equation (26.18) is simple bookkeeping since the $(D_j)_{max}$ values are picked off directly from the SRS curve.

The SRSS equation for the peak relative displacement $(z_i)_{max}$ at DOF i is

$$(z_i)_{max} \approx \sqrt{\sum_{j=1}^{N} \left[ \hat{q}_{ij} \, (\eta_j)_{max} \right]^2} \qquad (26.19)$$

The above equation is simplified into its bookkeeping form

$$(z_i)_{max} \approx \sqrt{\sum_{j=1}^{N} \left[ \Gamma_j \, \hat{q}_{ij} \, (D_j)_{max} \right]^2} \qquad (26.20)$$
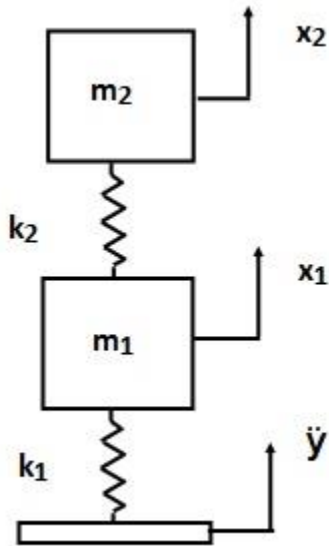
Figure 26.68. Two-DOF System Subjected to Base Excitation

Recall the Two-DOF model from Section 17.3.4 with increased spring stiffness as shown in the following table. Assume 5% damping for each mode.

Table 26.10. Two-DOF System, Parameters

| Variable | Value |
|----------|-------|
| $m_1$ | 2 lbm |
| $m_2$ | 1 lbm |
| $k_1$ | 15,000 lbf/in |
| $k_2$ | 10,000 lbf/in |

Apply the mass and stiffness values from the above table into equation (9.1) to form the following matrices.

$$M = \begin{bmatrix} 2/386 & 0 \\ 0 & 1/386 \end{bmatrix}, \quad K = \begin{bmatrix} 25000 & -10000 \\ -10000 & 10000 \end{bmatrix} \tag{26.21}$$

Table 26.11.  Two-DOF System Modal Parameters

| Mode | Natural Frequency (Hz) | Participation Factor | Modal Mass Ratio |
|------|------------------------|----------------------|------------------|
| 1 | 200 | 0.085 | 0.935 |
| 2 | 425 | -0.022 | 0.065 |

The mass-normalized mode shapes in matrix format are

$$\widehat{Q} = \begin{bmatrix} 8.93 & -10.64 \\ 15.05 & 12.63 \end{bmatrix}$$

(26.22)

Subject the system to the following base input SRS, which could represent a pyrotechnic shock for some component mounted in the mid-field.

Table 26.12.  SRS Q=10

| Natural Frequency (Hz) | Peak Accel (G) |
|------------------------|----------------|
| 10 | 10 |
| 2000 | 2000 |
| 10,000 | 2000 |

The modal combination results are shown in the following three tables. Note that $(D_j)_{max}$ is SRS (G).

Table 26.13.  DOF i=1 Acceleration

| Mode j | fn (Hz) | $\Gamma_j$ | $\hat{q}_{ij}$ | $(D_j)_{max}$ | $\left\| \Gamma_j \right\| \left\| \hat{q}_{ij} \right\| \left\| (D_j)_{max} \right\|$ |
|--------|---------|------------|----------------|---------------|---------------------------------------------------------------------------------------|
| 1 | 200 | 0.085 | 8.93 | 200 | 151.8 |
| 2 | 425 | -0.022 | 10.64 | 425 | 99.5 |

Table 26.14.  DOF i=2 Acceleration

| Mode j | fn (Hz) | $\Gamma_j$ | $\hat{q}_{ij}$ | $(D_j)_{max}$ | $\left|\Gamma_j\right|\left|\hat{q}_{ij}\right|\left|(D_j)_{max}\right|$ |
|--------|---------|------------|----------------|---------------|-------------------------------------------------------------------------|
| 1 | 200 | 0.085 | 15.05 | 200 | 255.9 |
| 2 | 425 | -0.022 | 12.63 | 425 | 118.1 |

Table 26.15.  Acceleration Summary

| DOF i | SRSS (G) | ABSSUM (G) |
|-------|----------|------------|
| 1 | 182 | 251 |
| 2 | 282 | 374 |

The SRSS and ABBSUM results in the above table have a wide difference for each DOF.   The analysis can be considered complete if the Two-DOF system can withstand the ABSSUM results. Otherwise, further consideration is needed for phasing.

Next, the problem was solved using the modal transient method with four synthesized time histories applied individually as base inputs.  The numerical engine for the modal solution is a digital recursive filtering relationship.  See equations (17.12) through (17.15). The input pulses are shown in the next four figures.
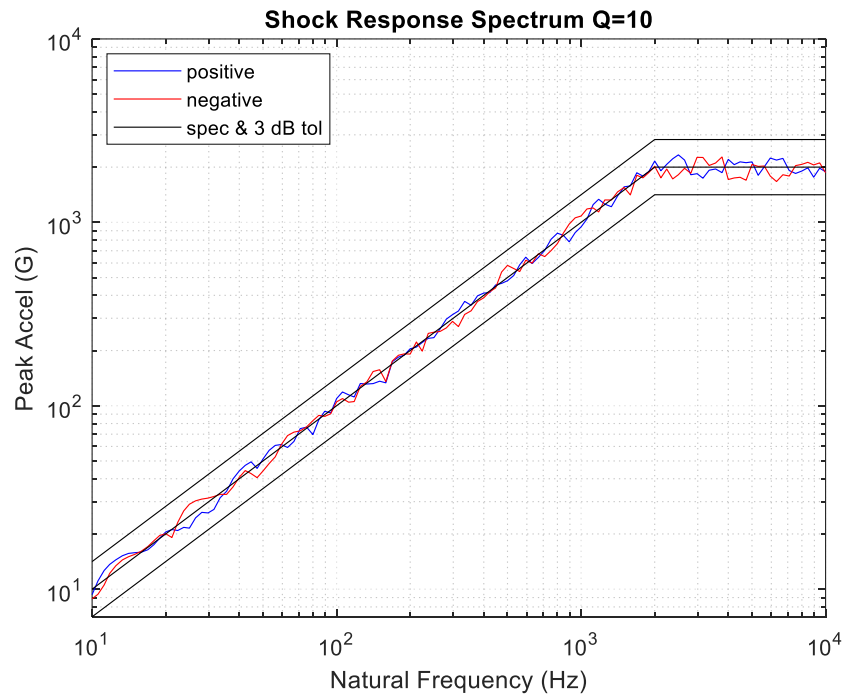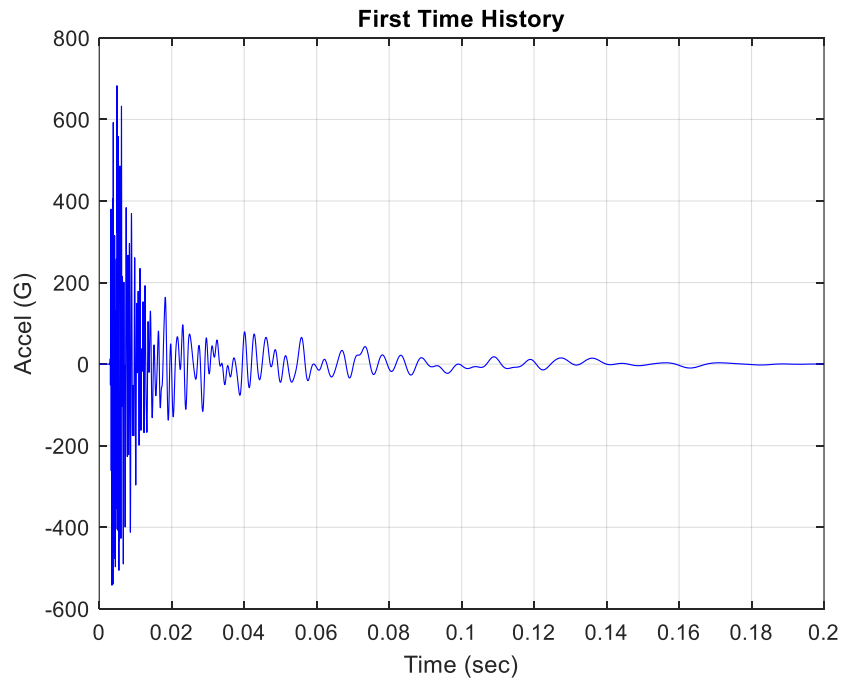
Figure 26.69.  First Synthesized Time History & SRS
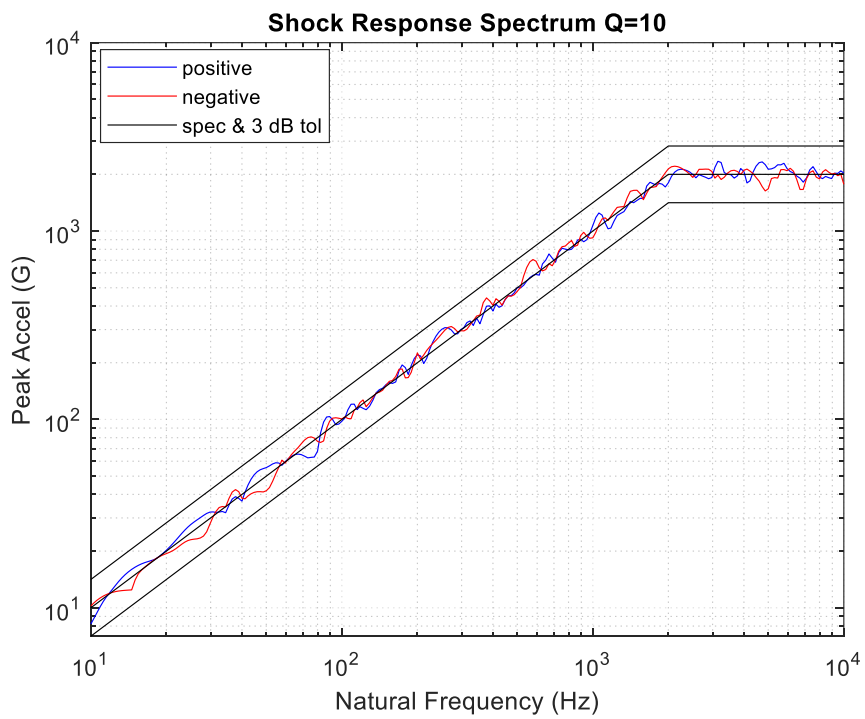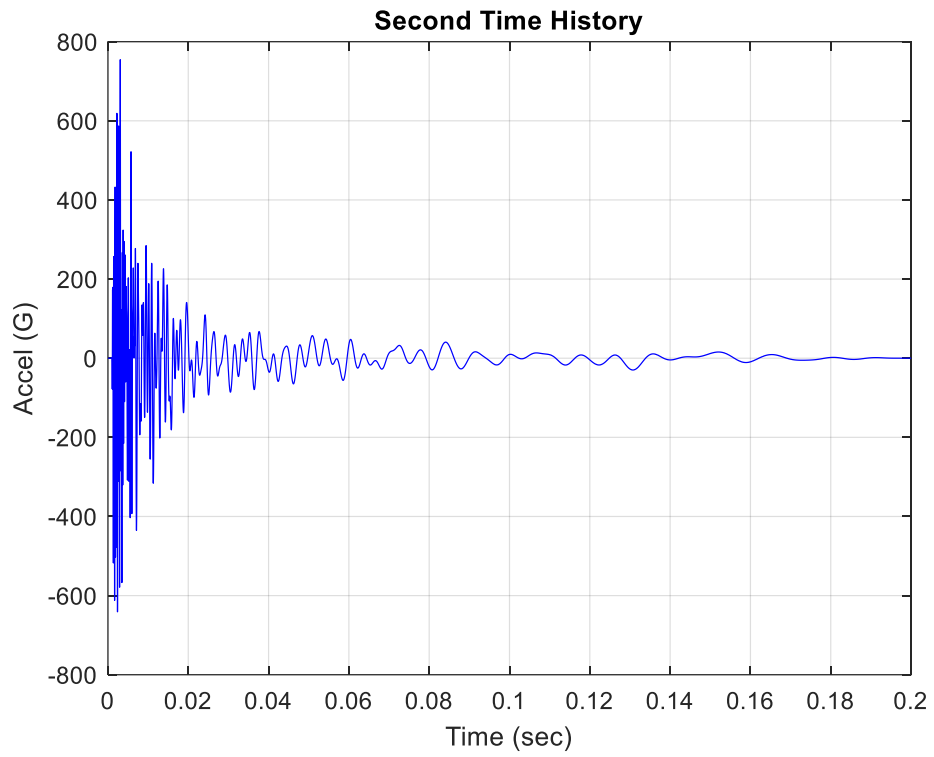
Figure 26.70.   Second Synthesized Time History & SRS
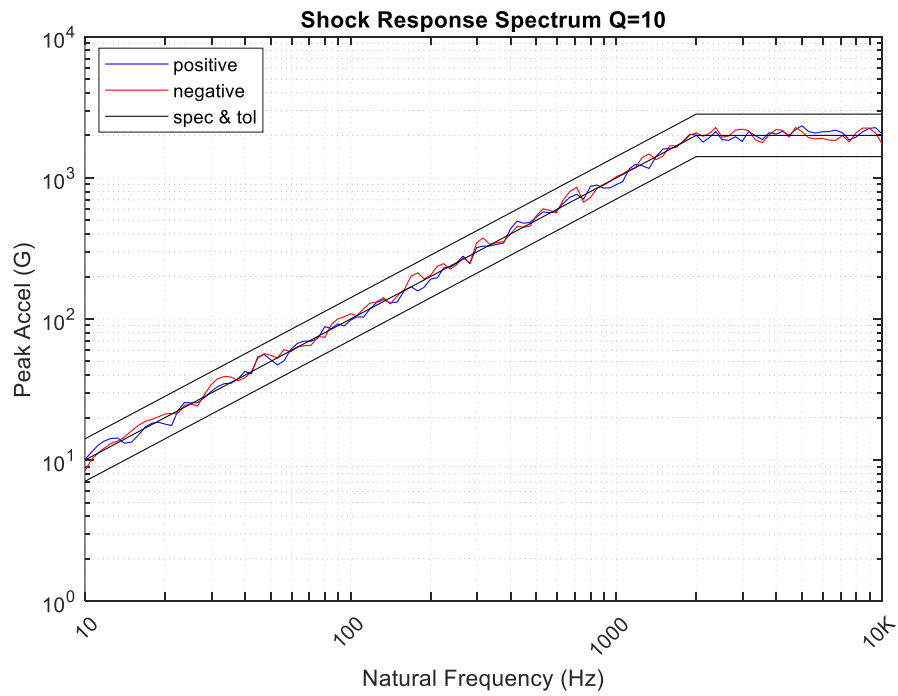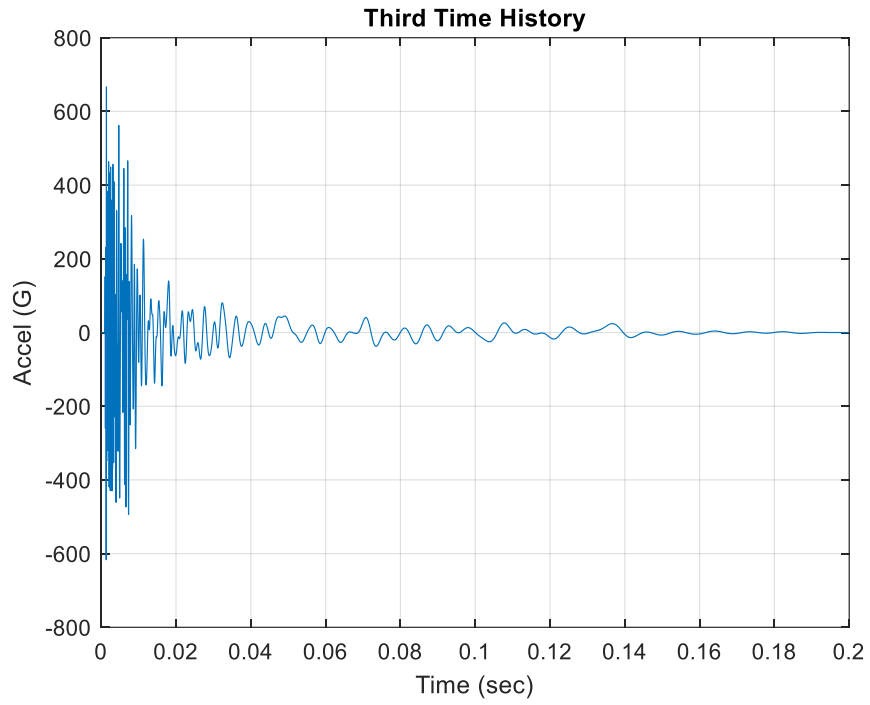
**Figure 26.71.   Third Synthesized Time History & SRS**
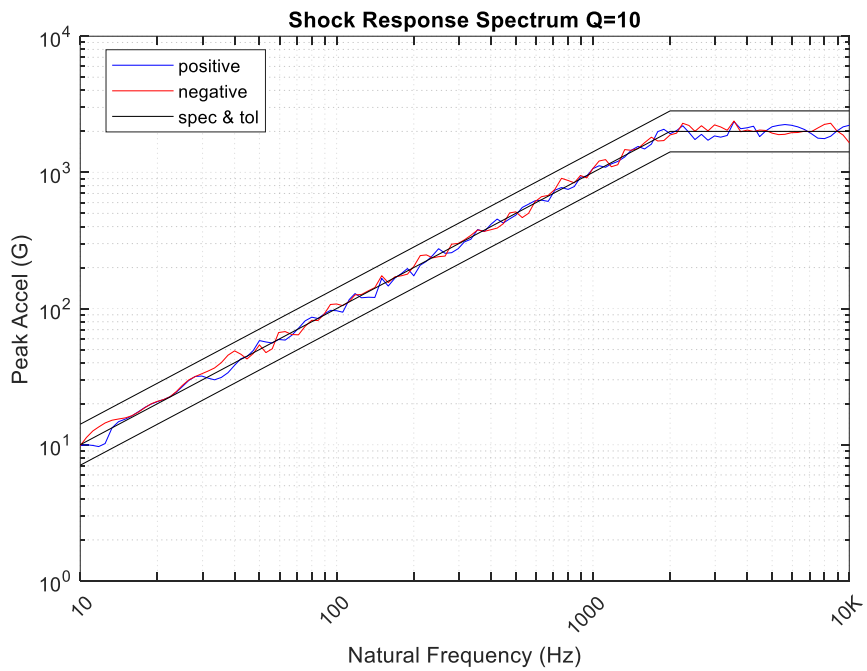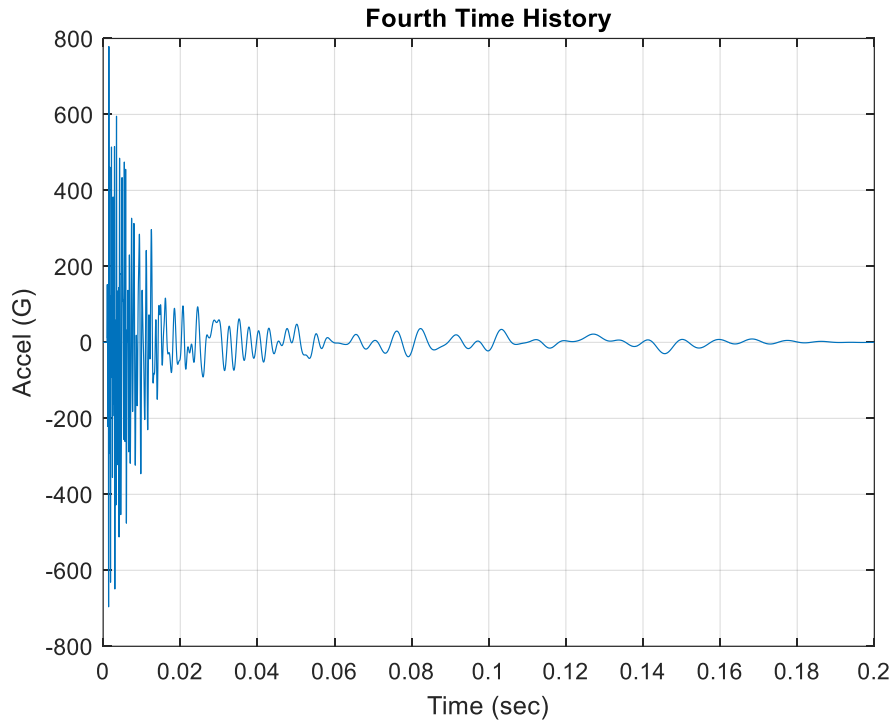
Figure 26.72.   Fourth Synthesized Time History & SRS
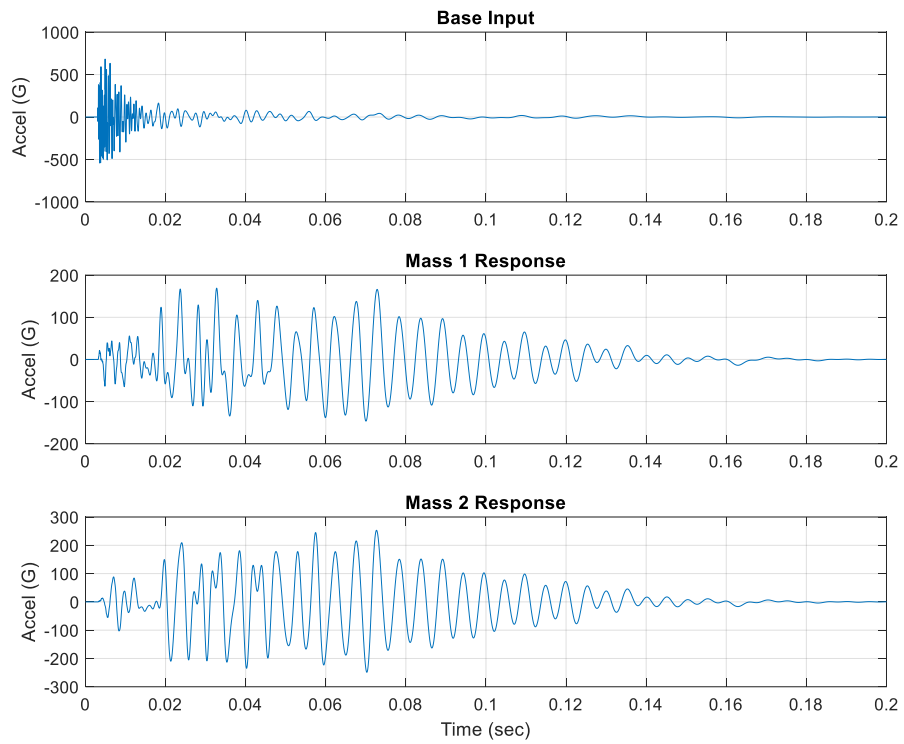
Figure 26.73.   Modal Transient Run 1
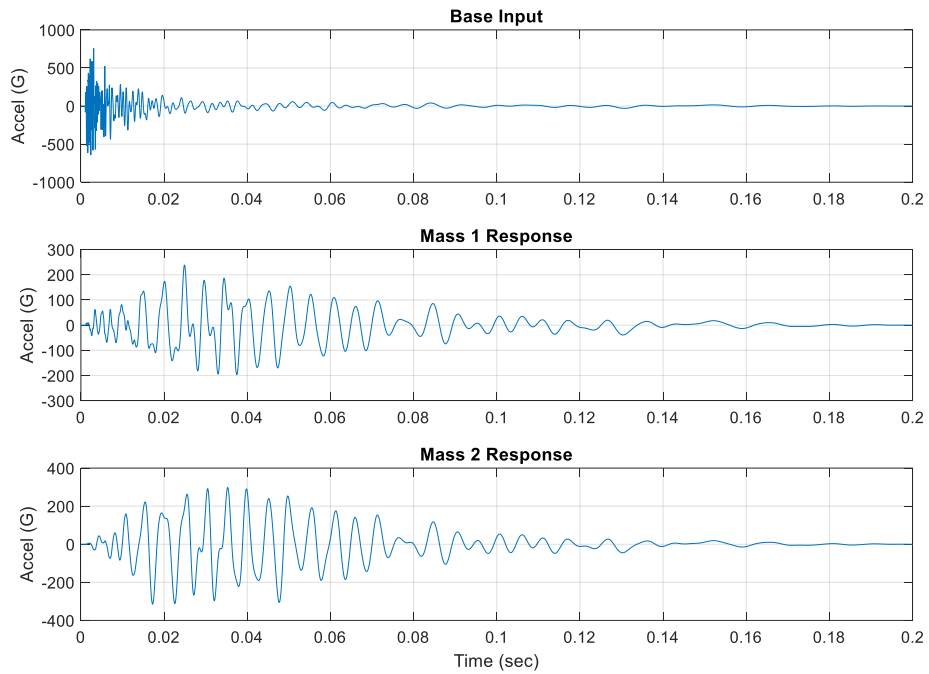


Figure 26.74.   Modal Transient Run 2
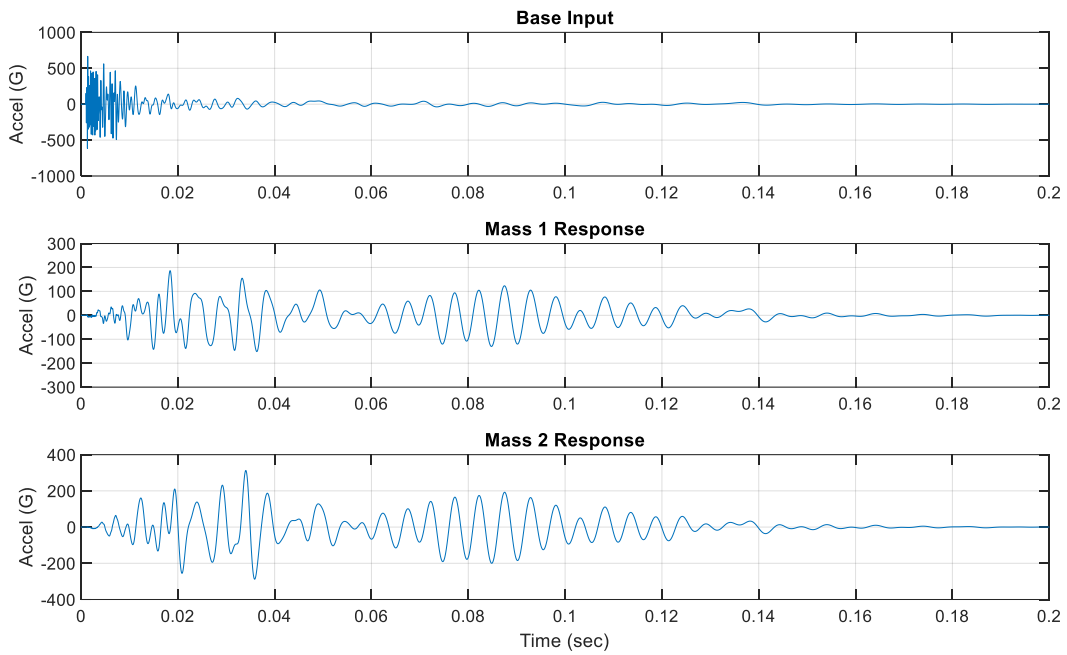
Figure 26.75.   Modal Transient Run 3
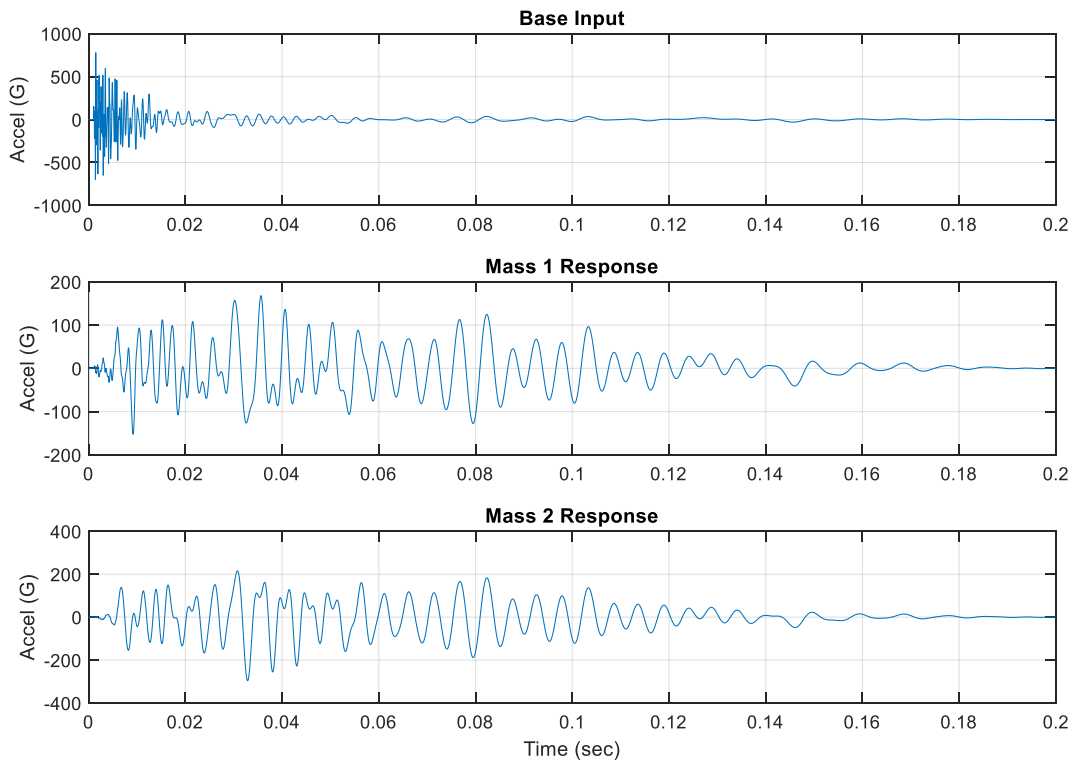


Figure 26.76.   Modal Transient Run 4

Table 26.16.  Acceleration Summary for Synthesis with Modal Transient

| Run | DOF 1 | DOF 2 |
|---|---|---|
| 1 | 169 | 253 |
| 2 | 238 | 315 |
| 3 | 187 | 313 |
| 4 | 168 | 296 |
| Mean | 191 | 294 |
| Max | 238 | 315 |

Table 26.17.  Peak Response Comparison, All Methods

| DOF i | SRSS (G) | ABSSUM (G) | Modal Transient Mean of Four Runs (G) | Modal Transient Max of Four Runs (G) |
|---|---|---|---|---|
| 1 | 182 | 251 | 191 | 238 |
| 2 | 282 | 374 | 294 | 325 |

The comparison in the above table shows that both the mean and the maximum of four modal transient runs for each DOF gave a peak response acceleration somewhere in between the SRSS and ABSSUM values.   This is a topic for further statistical research.   In the meantime, engineering judgment is required to establish the appropriate amount of conservatism for a particular case.

## 26.11.5 MDOF Example, Seismic Mass Method

Repeat the previous modal transient analysis using an equivalent force applied to a seismic mass to indirectly apply the Run 1 waveform from Figure 26.73. This indirect method was introduced in Section 17.3.3. The previous Two-DOF system from Figure 26.68 becomes a Three-DOF system.
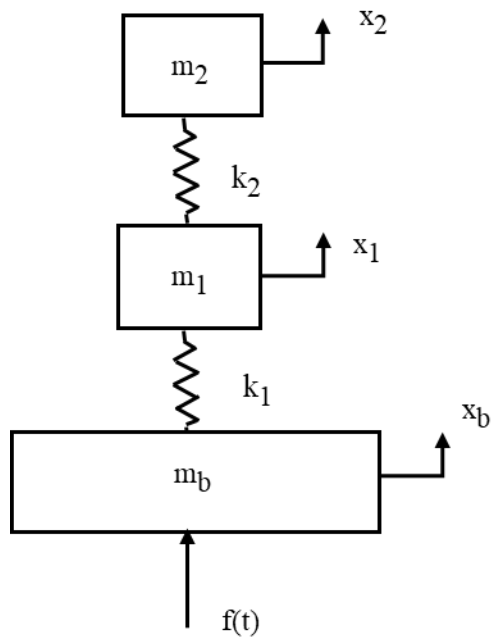


| Variable | Value |
|----------|-------|
| $m_b$ | 10,000 lbm |
| $m_1$ | 2 lbm |
| $m_2$ | 1 lbm |
| $k_1$ | 15,000 lbf/in |
| $k_2$ | 10,000 lbf/in |

5% Damping for all modes

Figure 26.77. Three-DOF System for Base Excitation via Force at Seismic Mass

The equation of motion is

$$\begin{bmatrix} m_b & 0 & 0 \\ 0 & m_1 & 0 \\ 0 & 0 & m_2 \end{bmatrix}\begin{bmatrix} \ddot{x}_b \\ \ddot{x}_1 \\ \ddot{x}_2 \end{bmatrix} + \begin{bmatrix} k_1 & -k_1 & 0 \\ -k_1 & k_1 + k_2 & -k_2 \\ 0 & -k_2 & k_2 \end{bmatrix}\begin{bmatrix} x_b \\ x_1 \\ x_2 \end{bmatrix} = \begin{bmatrix} f(t) \\ 0 \\ 0 \end{bmatrix}$$

(26.23)

The applied force is

$$f(t) = m_b\, \ddot{y}$$

(26.24)

The mass and stiffness matrices for the sample problem are

$$
M = \begin{bmatrix} 1e5/386 & 0 & 0 \\ 0 & 2/386 & 0 \\ 0 & 0 & 1/386 \end{bmatrix}, \qquad K = \begin{bmatrix} 15000 & -15000 & 0 \\ -15000 & 25000 & -10000 \\ 0 & -10000 & 10000 \end{bmatrix}
$$

(26.25)

Damping is added later in the analysis as modal damping.

The numerical engine for the modal solution is a digital recursive filtering relationship. See equations (17.12) through (17.15).

Table 26.18.  Semidefinite Three-DOF System Modal Parameters

| Mode | Natural Frequency (Hz) | Participation Factor | Modal Mass Ratio |
|---|---|---|---|
| 1 | 0 | 5.9 | 1 |
| 2 | 200 | 0 | 0 |
| 3 | 425 | 0 | 0 |

The rigid-body mode at 0 Hz takes up the entire modal mass, but this has no significant effect on the modal transient analysis.

The mass-normalized mode shapes in matrix format are

$$
\widehat{Q} = \begin{bmatrix} 0.196 & 0 & 0 \\ 0.196 & 8.93 & -10.64 \\ 0.196 & 15.05 & 12.63 \end{bmatrix}
$$

(26.26)

The modal transient results from the two approaches are shown in the following figure.  For a given DOF, each modeling method gives nearly identical results.  The seismic method is more versatile since it could be adapted to cases where each of the two masses had up to six DOF (3 translational & 3 rotational) as long as the base input was uniform.
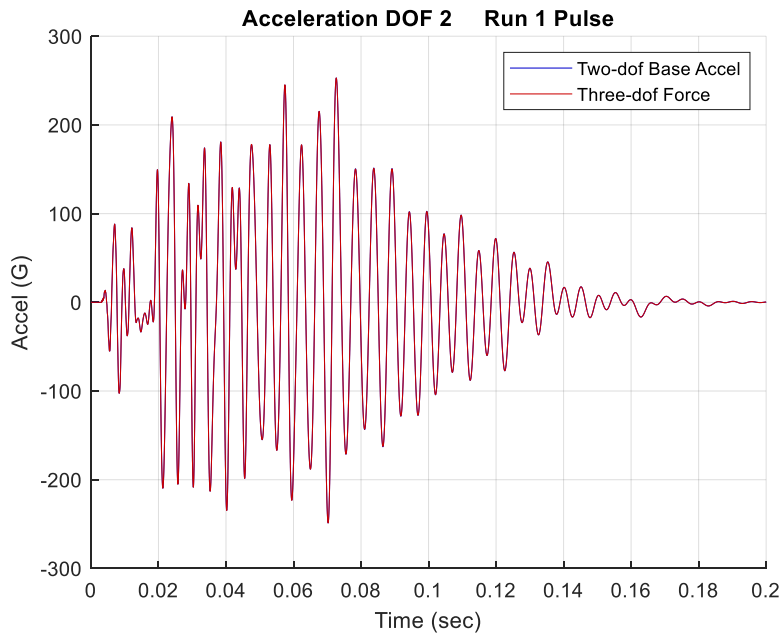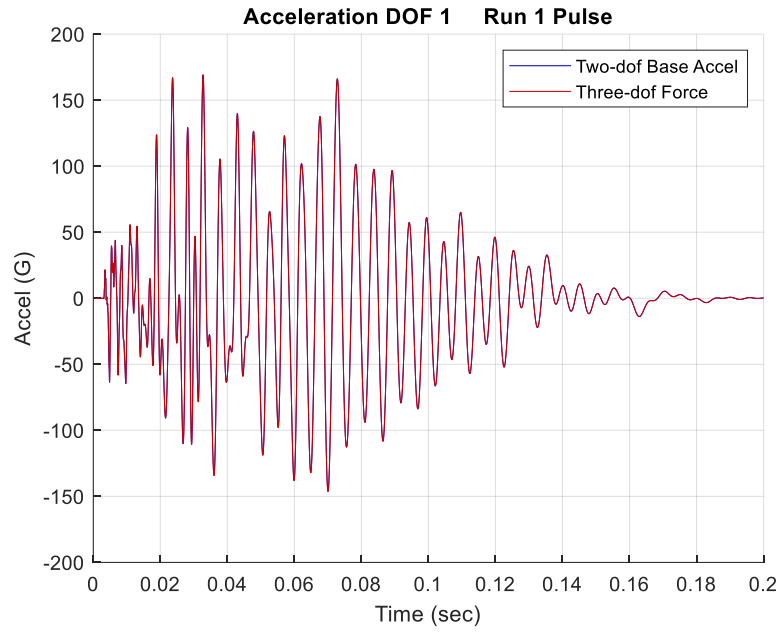
Figure 26.78.   Run 1 Pulse Input, Two Modeling Approaches

# 27 TRANSPORTATION SHOCK AND VIBRATION

## 27.1 VIBRATION

The following figures show typical shock and vibration specifications. Ideally, engineers would take their own accelerometer measurements on the transportation vehicles using mass simulators for their packaged components and systems, but this may be impractical.



Figure 27.1. Data Recorder

Commercial battery-powered recorders are available for transportation measurements. The recorders may be configured with either internal or external accelerometers, as well as other sensor types.

Two key references are ASTM D4728 and MIL-STD-810 Hz. These references have accelerated test levels where higher amplitude, shorter duration test are substituted for the expected environments.

Note that FedEx [52] recommends ASTM D4728 for packages[8] weighing less than 150 lbm with the following durations.

- Express packages-Domestic- 45 minute combination of a 15 min truck profile, 15 min air profile, and 15 min truck profile

- Ground packages-Domestic- 45 minute truck profile

- Express packages-International- 90 minute combination of a 30 min truck profile, 30 min air profile, and 30 min truck profile

---

[8] FedEx recommends these levels for sensitive items such as electronics, medical, and pharmaceutical devices. Non-sensitive items can be tested on a mechanical vibration rotary machine instead, at 1 inch total displacement, 200 cpm and 60 minutes.

A shaker with a minimum 2-inch peak-to-peak stroke limit should be used for the following vibration tests. The highest displacement of following levels is the ASTM D4728 truck at 0.132 inch 1-sigma. But note that 5-sigma peaks are possible in the corresponding time history.
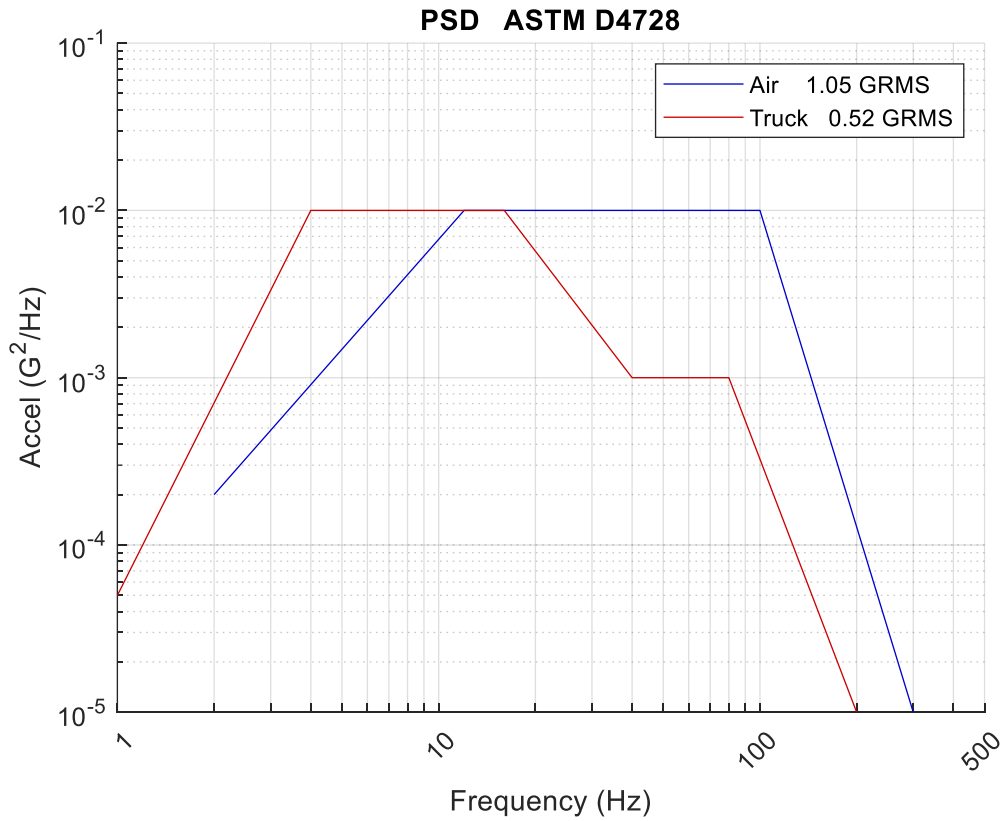


**PSD   ASTM D4728**

Truck

| Freq (Hz) | Accel (G^2/Hz) |
|-----------|----------------|
| 1 | 5e-05 |
| 4 | 0.01 |
| 16 | 0.01 |
| 40 | 0.001 |
| 80 | 0.001 |
| 200 | 1e-05 |

Air

| Freq (Hz) | Accel (G^2/Hz) |
|-----------|----------------|
| 2 | 0.0002 |
| 12 | 0.01 |
| 100 | 0.01 |
| 300 | 1e-05 |

Figure 27.2.   ASTM D4728 Transportation Random Vibration Levels

**PSD  MIL-STD-810H Common Carrier**

Legend:
- Vertical 1.08 GRMS
- Transverse 0.21 GRMS
- Longitudinal 0.76 GRMS
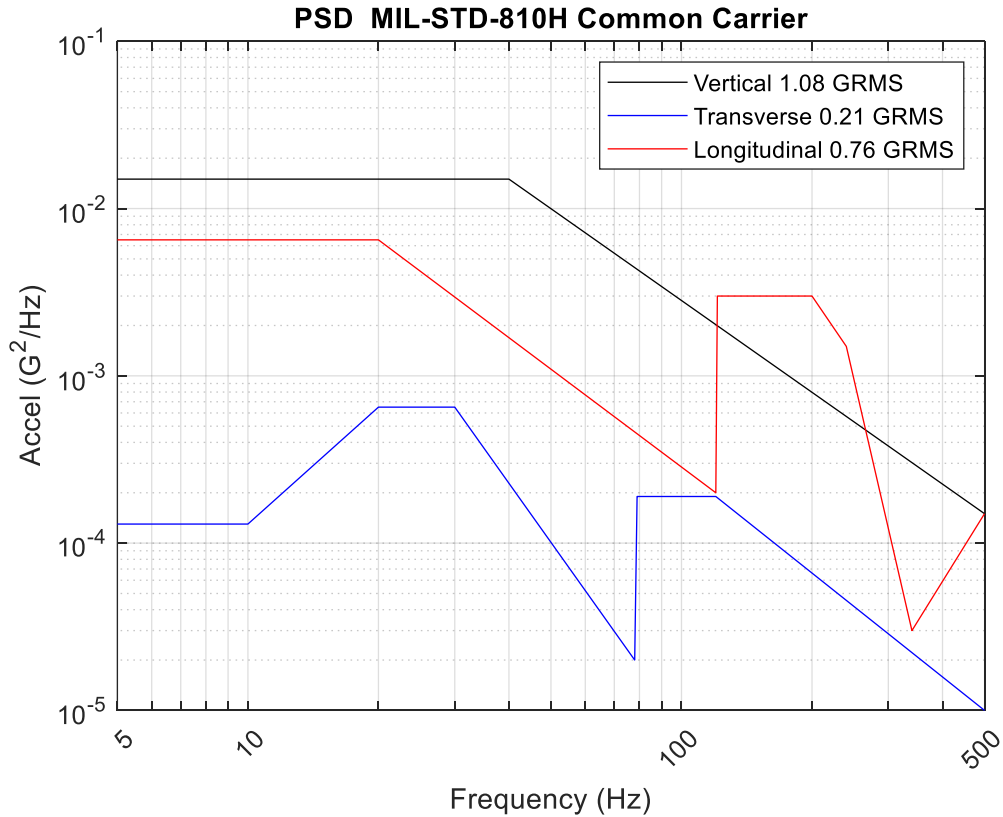
| Vertical | | Transverse | | Longitudinal | |
|---|---|---|---|---|---|
| Freq (Hz) | Accel (G^2/Hz) | Freq (Hz) | Accel (G^2/Hz) | Freq (Hz) | Accel (G^2/Hz) |
| 5 | 1.5e-02 | 5 | 1.3e-04 | 5 | 6.5e-03 |
| 40 | 1.5e-02 | 10 | 1.3e-04 | 20 | 6.5e-03 |
| 500 | 1.5e-04 | 20 | 6.5e-04 | 120 | 2.0e-04 |
| | | 30 | 6.5e-04 | 121 | 3.0e-03 |
| | | 78 | 2.0e-05 | 200 | 3.0e-03 |
| | | 79 | 1.9e-04 | 240 | 1.5e-03 |
| | | 120 | 1.9e-04 | 340 | 3.0e-05 |
| | | 500 | 1.0e-05 | 500 | 1.5e-04 |

Figure 27.3.    US Highway Truck Vibration Levels

The duration is 60 minutes per 1000 miles.    See MIL-STD-810H, Figure 514.8C-2 and Table 514.8C-I.

## 27.2  SHOCK

**Impact Tests Using Free Fall Drop Tester**
Drop Heights: 18-30"
Drop Count: 10-20 individual drops
Equipment Used: Lansmont PDT-80 Drop tester or Lansmont PDT-300 or similar
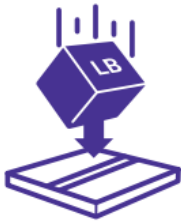
**Hazard Impact for Flat Packages**
Drop Height: 30" to package surface
Drop Count: 1 on the largest face
Equipment Used: Wooden Hazard Box
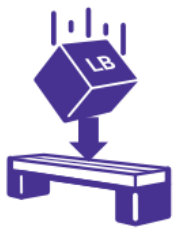
**Bridge Impact for Elongated Packages**
Drop Heights: 30" to package surface
Drop Count: 1 drop in center of package
Equipment Used: Wooden Hazard Box

Figure 27.4.    Drop Shock Tests

FedEx recommends a series of drop tests to cover transportation and handling shock.
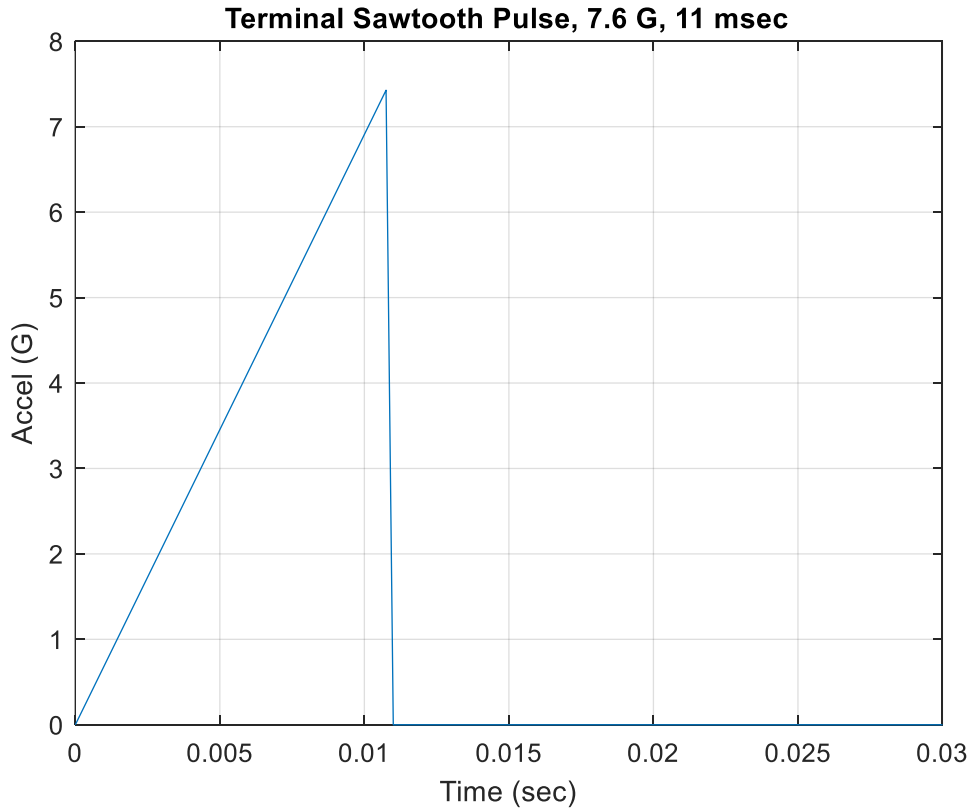
Figure 27.5.    Typical Terminal Sawtooth Pulse

Table 27.1.  MIL-STD-810H, Procedure II – Transportation Shock Test Sequence

| On Road (5000 km) Terminal Peak Sawtooth Pulse Duration:  11 msec | | | Off Road (5000 km) Terminal Peak Sawtooth Pulse Duration:  5 msec | |
|---|---|---|---|---|
| Amplitude (G-pk) | Number of Shocks | | Amplitude (G-pk) | Number of Shocks |
| 5.1 | 42 | | 10.2 | 42 |
| 6.4 | 21 | | 12.8 | 21 |
| 7.6 | 3 | | 15.2 | 3 |

MIL-STD-810H allows an equivalent shock response spectrum to be substituted for the time history pulse.

The above table is referenced as Table 516.8-VII in MIL-STD-810H.

The following method requires a double, nested transformation for the solution of the physical displacements and accelerations. User-specified DOF are constrained to have a specified motion. An advantage of this method is that it can account for multipoint base excitation. A disadvantage is that it requires extra bookkeeping and taking the inverse of matrices. Caution must be exercised when taking inverses of matrices due to potential numerical stability issues.

The variables for this section are:

| | |
|---|---|
| $M$ | Mass matrix |
| $K$ | Stiffness matrix |
| $F$ | Applied force |
| $F_d$ | Forces at driven DOF |
| $F_f$ | Forces at free DOF |
| $I$ | Identity matrix |
| $\Pi$ | Transformation matrix |
| $u$ | Displacement vector |
| $u_d$ | Displacements at driven DOF |
| $u_f$ | Displacements at free DOF |

The equation of motion for an undamped multi-degree-of-freedom system is

$$M\,\ddot{\bar{u}} + K\,\bar{u} = \bar{F} \tag{28.1}$$

The displacement vector is

$$\bar{u} = \begin{bmatrix} u_d & u_f \end{bmatrix}^T \tag{28.2}$$

Again, subscript d indicates the DOF driven by enforced displacement, and f represents the free or undriven DOF.

Partition the matrices and vectors as follows.

$$\begin{bmatrix} M_{dd} & M_{df} \\ M_{fd} & M_{ff} \end{bmatrix} \begin{bmatrix} \ddot{u}_d \\ \ddot{u}_f \end{bmatrix} + \begin{bmatrix} K_{dd} & K_{df} \\ K_{fd} & K_{ff} \end{bmatrix} \begin{bmatrix} u_d \\ u_f \end{bmatrix} = \begin{bmatrix} F_d \\ F_f \end{bmatrix} \qquad (28.3)$$

Create a transformation matrix such that

$$\begin{bmatrix} u_d \\ u_f \end{bmatrix} = \Pi \begin{bmatrix} u_d \\ u_w \end{bmatrix} \qquad (28.4)$$

$$\Pi = \begin{bmatrix} I & 0 \\ T_1 & T_2 \end{bmatrix} \qquad (28.5)$$

Substitute the transformation into the partitioned equation of motion.

$$\begin{bmatrix} M_{dd} & M_{df} \\ M_{fd} & M_{ff} \end{bmatrix} \Pi \begin{bmatrix} \ddot{u}_d \\ \ddot{u}_w \end{bmatrix} + \begin{bmatrix} K_{dd} & K_{df} \\ K_{fd} & K_{ff} \end{bmatrix} \Pi \begin{bmatrix} u_d \\ u_w \end{bmatrix} = \begin{bmatrix} F_d \\ F_f \end{bmatrix} \qquad (28.6)$$

Premultiply by $\Pi^T$,

$$\Pi^T \begin{bmatrix} M_{dd} & M_{df} \\ M_{fd} & M_{ff} \end{bmatrix} \Pi \begin{bmatrix} \ddot{u}_d \\ \ddot{u}_w \end{bmatrix} + \Pi^T \begin{bmatrix} K_{dd} & K_{df} \\ K_{fd} & K_{ff} \end{bmatrix} \Pi \begin{bmatrix} u_d \\ u_w \end{bmatrix} = \Pi^T \begin{bmatrix} F_d \\ F_f \end{bmatrix} \qquad (28.7)$$

28.1.1 MDOF Enforced Displacement

Transform the equation of motion (28.7) to uncouple the mass matrix so that the resulting mass matrix is

$$\begin{bmatrix} \hat{M}_{dd} & 0 \\ 0 & \hat{M}_{ww} \end{bmatrix} = \Pi^T \begin{bmatrix} M_{dd} & M_{df} \\ M_{fd} & M_{ff} \end{bmatrix} \Pi \qquad (28.8)$$

Apply the transformation to the mass matrix

$$\Pi^T M \Pi = \begin{bmatrix} I & T_1^T \\ 0 & T_2^T \end{bmatrix} \begin{bmatrix} M_{dd} & M_{df} \\ M_{fd} & M_{ff} \end{bmatrix} \begin{bmatrix} I & 0 \\ T_1 & T_2 \end{bmatrix} \qquad (28.9)$$

$$\Pi^T M \Pi = \begin{bmatrix} I & T_1^T \\ 0 & T_2^T \end{bmatrix} \begin{bmatrix} M_{dd} + M_{df} T_1 & M_{df} T_2 \\ M_{fd} + M_{ff} T_1 & M_{ff} T_2 \end{bmatrix} \qquad (28.10)$$

$$\Pi^T M \Pi = \begin{bmatrix} M_{dd} + M_{df} T_1 + T_1^T(M_{fd} + M_{ff} T_1) & (M_{df} + T_1^T M_{ff})T_2 \\ T_2^T(M_{fd} + M_{ff} T_1) & T_2^T M_{ff} T_2 \end{bmatrix}$$

$$(28.11)$$

$$\Pi^T M \Pi = \begin{bmatrix} M_{dd} + T_1^T M_{fd} + (M_{df} + T_1^T M_{ff})T_1 & (M_{df} + T_1^T M_{ff})T_2 \\ T_2^T(M_{fd} + M_{ff} T_1) & T_2^T M_{ff} T_2 \end{bmatrix}$$

$$(28.12)$$

Let

$$T_2 = I \qquad (28.13)$$

$$\Pi^T M \Pi =$$

$$\begin{bmatrix} M_{dd} + T_1^T M_{fd} + (M_{df} + T_1^T M_{ff})T_1 & M_{df} + T_1^T M_{ff} \\ M_{fd} + M_{ff} T_1 & M_{ff} \end{bmatrix} = \begin{bmatrix} \hat{M}_{dd} & 0 \\ 0 & \hat{M}_{ww} \end{bmatrix}$$

$$(28.14)$$

Set

$$M_{df} + T_1^T M_{ff} = 0 \qquad (28.15)$$

$$T_1^T = -M_{df} M_{ff}^{-1} \qquad (28.16)$$

$$T_1 = -M_{ff}^{-1} M_{fd} \tag{28.17}$$

The transformation matrix is

$$\Pi = \begin{bmatrix} I_{dd} & 0 \\ T_1 & I_{ff} \end{bmatrix} \tag{28.18}$$

$$\hat{M}_{dd} = M_{dd} + T_1{}^T M_{fd} + \left( M_{df} + T_1{}^T M_{ff} \right) T_1 \tag{28.19}$$

$$\hat{M}_{ww} = M_{ff} \tag{28.20}$$

$$\Pi^T K \Pi = \begin{bmatrix} I_{dd} & T_1{}^T \\ 0 & I_{ff} \end{bmatrix} \begin{bmatrix} K_{dd} & K_{df} \\ K_{fd} & K_{ff} \end{bmatrix} \begin{bmatrix} I_{dd} & 0 \\ T_1 & I_{ff} \end{bmatrix} \tag{28.21}$$

By similarity, the transformed stiffness matrix is

$$\begin{bmatrix} \hat{k}_{dd} & \hat{k}_{dw} \\ \hat{k}_{wd} & \hat{k}_{ww} \end{bmatrix} = \begin{bmatrix} K_{dd} + T_1{}^T K_{fd} + \left( K_{df} + T_1{}^T K_{ff} \right) T_1 & K_{df} + T_1{}^T K_{ff} \\ K_{fd} + K_{ff} T_1 & K_{ff} \end{bmatrix}$$

$$\tag{28.22}$$

$$\begin{bmatrix} \hat{F}_d \\ \hat{F}_w \end{bmatrix} = \begin{bmatrix} I_{dd} & T_1 \\ 0 & I_{ff} \end{bmatrix} \begin{bmatrix} F_d \\ F_f \end{bmatrix} \tag{28.23}$$

$$\begin{bmatrix} \hat{F}_d \\ \hat{F}_w \end{bmatrix} = \begin{bmatrix} I_{dd} F_d + T_1 F_f \\ I_{ff} F_f \end{bmatrix} \tag{28.24}$$

$$\begin{bmatrix} \hat{F}_d \\ \hat{F}_w \end{bmatrix} = \begin{bmatrix} F_d + T_1 F_f \\ F_f \end{bmatrix} \tag{28.25}$$

$$\begin{bmatrix} \hat{M}_{dd} & 0 \\ 0 & \hat{M}_{ww} \end{bmatrix} \begin{bmatrix} \ddot{u}_d \\ \ddot{u}_w \end{bmatrix} + \begin{bmatrix} \hat{k}_{dd} & \hat{k}_{dw} \\ \hat{k}_{wd} & \hat{k}_{ww} \end{bmatrix} \begin{bmatrix} u_d \\ u_w \end{bmatrix} = \begin{bmatrix} \hat{F}_d \\ \hat{F}_w \end{bmatrix} \tag{28.26}$$

$$\hat{M}_{ww}\, \ddot{u}_w + \hat{k}_{wd}\, u_d + \hat{k}_{ww}\, u_w = \hat{F}_w \tag{28.27}$$

The equation of motion is thus

$$\hat{M}_{ww}\, \ddot{u}_w + \hat{k}_{ww}\, u_w = \hat{F}_w - \hat{k}_{wd}\, u_d \tag{28.28}$$

The previous equation can be solved using modal analysis. The decoupled, modal equation set can then be solved using a digital recursive relationship for the case of a transient analysis. See equations (17.12) through (17.15). The final displacements are found via

$$\begin{bmatrix} u_d \\ u_f \end{bmatrix} = \Pi \begin{bmatrix} u_d \\ u_w \end{bmatrix} = \begin{bmatrix} I_{dd} & 0 \\ -M_{ff}^{-1} M_{fd} & I_{ff} \end{bmatrix} \begin{bmatrix} u_d \\ u_w \end{bmatrix} \tag{28.29}$$

### 28.1.2 MDOF Enforced Acceleration

Transform the equation of motion (28.7) to uncouple the mass matrix so that the resulting mass matrix is

$$\begin{bmatrix} \hat{K}_{dd} & 0 \\ 0 & \hat{K}_{ww} \end{bmatrix} = \Pi^T K \Pi \tag{28.30}$$

Apply the transformation to the stiffness matrix.

$$\Pi^T K \Pi = \begin{bmatrix} I & T_1^T \\ 0 & T_2^T \end{bmatrix} \begin{bmatrix} K_{dd} & K_{df} \\ K_{fd} & K_{ff} \end{bmatrix} \begin{bmatrix} I & 0 \\ T_1 & T_2 \end{bmatrix} \tag{28.31}$$

$$\Pi^T K \Pi = \begin{bmatrix} I & T_1^T \\ 0 & T_2^T \end{bmatrix} \begin{bmatrix} K_{dd} + K_{df} T_1 & K_{df} T_2 \\ K_{fd} + K_{ff} T_1 & K_{ff} T_2 \end{bmatrix} \tag{28.32}$$

$$\Pi^T K \Pi = \begin{bmatrix} K_{dd} + K_{df} T_1 + T_1{}^T (K_{fd} + K_{ff} T_1) & (K_{df} + T_1{}^T K_{ff}) T_2 \\ T_2{}^T (K_{fd} + K_{ff} T_1) & T_2{}^T K_{ff} T_2 \end{bmatrix}$$

(28.33)

$$\Pi^T K \Pi = \begin{bmatrix} K_{dd} + T_1{}^T K_{fd} + (K_{df} + T_1{}^T K_{ff}) T_1 & (K_{df} + T_1{}^T K_{ff}) T_2 \\ T_2{}^T (K_{fd} + K_{ff} T_1) & T_2{}^T K_{ff} T_2 \end{bmatrix}$$

(28.34)

Let

$$T_2 = I$$

(28.35)

$$\Pi^T K \Pi =$$

$$\begin{bmatrix} K_{dd} + T_1{}^T K_{fd} + (K_{df} + T_1{}^T K_{ff}) T_1 & K_{df} + T_1{}^T K_{ff} \\ K_{fd} + K_{ff} T_1 & K_{ff} \end{bmatrix} = \begin{bmatrix} \widehat{K}_{dd} & 0 \\ 0 & \widehat{K}_{ww} \end{bmatrix}$$

(28.36)

Set

$$K_{df} + T_1{}^T K_{ff} = 0$$

(28.37)

$$T_1{}^T = -K_{df} K_{ff}{}^{-1}$$

(28.38)

$$T_1 = -K_{ff}{}^{-1} K_{fd}$$

(28.39)

The transformation matrix is

$$\Pi = \begin{bmatrix} I_{dd} & 0 \\ T_1 & I_{ff} \end{bmatrix}$$

(28.40)

$$\hat{K}_{dd} = K_{dd} + T_1{}^T K_{fd} + (K_{df} + T_1{}^T K_{ff})T_1 \tag{28.41}$$

$$\hat{K}_{ww} = K_{ff} \tag{28.42}$$

By similarity, the transformed mass matrix is

$$\Pi^T M \Pi = \begin{bmatrix} I_{dd} & T_1{}^T \\ 0 & I_{ff} \end{bmatrix} \begin{bmatrix} M_{dd} & M_{df} \\ M_{fd} & M_{ff} \end{bmatrix} \begin{bmatrix} I_{dd} & 0 \\ T_1 & I_{ff} \end{bmatrix} \tag{28.43}$$

$$\begin{bmatrix} \hat{m}_{dd} & \hat{m}_{dw} \\ \hat{m}_{wd} & \hat{m}_{ww} \end{bmatrix} = \begin{bmatrix} M_{dd} + T_1{}^T M_{fd} + (M_{df} + T_1{}^T M_{ff})T_1 & M_{df} + T_1{}^T M_{ff} \\ M_{fd} + M_{ff} T_1 & M_{ff} \end{bmatrix}$$

$$\tag{28.44}$$

$$\begin{bmatrix} \hat{F}_d \\ \hat{F}_w \end{bmatrix} = \begin{bmatrix} I_{dd} & T_1 \\ 0 & I_{ff} \end{bmatrix} \begin{bmatrix} F_d \\ F_f \end{bmatrix} \tag{28.45}$$

$$\begin{bmatrix} \hat{F}_d \\ \hat{F}_w \end{bmatrix} = \begin{bmatrix} I_{dd}F_d + T_1 F_f \\ I_{ff} F_f \end{bmatrix} \tag{28.46}$$

$$\begin{bmatrix} \hat{F}_d \\ \hat{F}_w \end{bmatrix} = \begin{bmatrix} F_d + T_1 F_f \\ F_f \end{bmatrix} \tag{28.47}$$

$$\begin{bmatrix} \hat{m}_{dd} & \hat{m}_{dw} \\ \hat{m}_{wd} & \hat{m}_{ww} \end{bmatrix} \begin{bmatrix} \ddot{u}_d \\ \ddot{u}_w \end{bmatrix} + \begin{bmatrix} \hat{K}_{dd} & 0 \\ 0 & \hat{K}_{ww} \end{bmatrix} \begin{bmatrix} u_d \\ u_w \end{bmatrix} = \begin{bmatrix} \hat{F}_d \\ \hat{F}_w \end{bmatrix} \tag{28.48}$$

$$\hat{m}_{wd} \ddot{u}_d + \hat{m}_{ww} \ddot{u}_w + \hat{K}_{ww} u_w = \hat{F}_w \tag{28.49}$$

The equation of motion is thus

$$\hat{m}_{ww}\ddot{u}_w + \hat{K}_{ww}u_w = \hat{F}_w - \hat{m}_{wd}\ddot{u}_d \tag{28.50}$$

The previous equation can be solved using modal analysis. The decoupled, modal equation set can then be solved using a digital recursive relationship for the case of a transient analysis.

The final displacements are found via

$$\begin{bmatrix} u_d \\ u_f \end{bmatrix} = \Pi \begin{bmatrix} u_d \\ u_w \end{bmatrix} = \begin{bmatrix} I_{dd} & 0 \\ -K_{ff}^{-1}K_{fd} & I_{ff} \end{bmatrix} \begin{bmatrix} u_d \\ u_w \end{bmatrix} \tag{28.51}$$

## 28.1.3 MDOF Enforced Acceleration Example
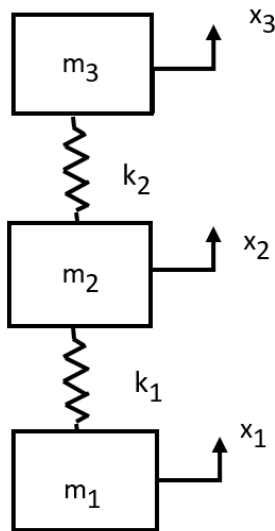


| Variable | Value |
|----------|-------|
| $m_1$ | 1 lbm |
| $m_2$ | 2 lbm |
| $m_3$ | 1 lbm |
| $k_1$ | 15,000 lbf/in |
| $k_2$ | 10,000 lbf/in |

5% Damping for all modes

Figure 28.1. Three-DOF System for Enforced Acceleration

The following is effectively a repeat of the Three-DOF seismic example in Section 26.11.5 with some adaptations for enforced motion. The value of the base mass $m_1$ in the above figure is arbitrary given that the acceleration $\ddot{x}_1$ will be specified. There are no external forces for this example. The equation of motion is

$$\begin{bmatrix} m_1 & 0 & 0 \\ 0 & m_2 & 0 \\ 0 & 0 & m_3 \end{bmatrix}\begin{bmatrix} \ddot{x}_1 \\ \ddot{x}_2 \\ \ddot{x}_3 \end{bmatrix} + \begin{bmatrix} k_1 & -k_1 & 0 \\ -k_1 & k_1+k_2 & -k_2 \\ 0 & -k_2 & k_2 \end{bmatrix}\begin{bmatrix} x_1 \\ x_2 \\ x_3 \end{bmatrix} = \begin{bmatrix} 0 \\ 0 \\ 0 \end{bmatrix} \tag{28.52}$$

The partitioning results in the following matrices.

$$M_{dd} = m_1 \tag{28.53}$$

$$M_{ff} = \begin{bmatrix} m_2 & 0 \\ 0 & m_3 \end{bmatrix} \tag{28.54}$$

$$M_{df} = M_{df}{}^T = [0 \quad 0] \tag{28.55}$$

$$K_{dd} = k_1 \tag{28.56}$$

$$K_{ff} = \begin{bmatrix} k_1 + k_2 & -k_2 \\ -k_2 & k_2 \end{bmatrix} \tag{28.57}$$

$$K_{df} = K_{df}{}^T = [-k_1 \quad 0] \tag{28.58}$$

$$K_{ff}{}^{-1} = \begin{bmatrix} \dfrac{1}{k_1} & \dfrac{1}{k_1} \\ \dfrac{1}{k_1} & \dfrac{k_1+k_2}{k_1 k_2} \end{bmatrix} \tag{28.59}$$

$$T_1 = -K_{ff}{}^{-1} K_{fd} = -\begin{bmatrix} \dfrac{1}{k_1} & \dfrac{1}{k_1} \\ \dfrac{1}{k_1} & \dfrac{k_1+k_2}{k_1 k_2} \end{bmatrix} \begin{bmatrix} -k_1 \\ 0 \end{bmatrix} = \begin{bmatrix} 1 \\ 1 \end{bmatrix} \tag{28.60}$$

The transformation matrix is

$$\Pi = \begin{bmatrix} I_{dd} & 0 \\ T_1 & I_{ff} \end{bmatrix} = \begin{bmatrix} 1 & 0 & 0 \\ 1 & 1 & 0 \\ 1 & 0 & 1 \end{bmatrix} \tag{28.61}$$

The transformed mass matrix is

$$\begin{bmatrix} \widehat{m}_{dd} & \widehat{m}_{dw} \\ \widehat{m}_{wd} & \widehat{m}_{ww} \end{bmatrix} = \begin{bmatrix} m_1 + m_2 + m_3 & m_2 & m_3 \\ m_2 & m_2 & 0 \\ m_3 & 0 & m_3 \end{bmatrix} \tag{28.62}$$

$$\widehat{m}_{dd} = m_1 + m_2 + m_3 \tag{28.63}$$

$$\widehat{m}_{ww} = \begin{bmatrix} m_2 & 0 \\ 0 & m_3 \end{bmatrix} \tag{28.64}$$

$$\widehat{m}_{dw} = \widehat{m}_{wd}{}^T = [m_2 \quad m_3] \tag{28.65}$$

The transformed stiffness matrix is

$$\begin{bmatrix} \hat{K}_{dd} & 0 \\ 0 & \hat{K}_{ww} \end{bmatrix} = \begin{bmatrix} 0 & 0 & 0 \\ 0 & k_1+k_2 & -k_2 \\ 0 & -k_2 & k_2 \end{bmatrix} \tag{28.66}$$

$$\hat{k}_{dd} = 0 \tag{28.67}$$

$$\hat{k}_{ww} = \begin{bmatrix} k_1+k_2 & -k_2 \\ -k_2 & k_2 \end{bmatrix} \tag{28.68}$$

$$\hat{k}_{dw} = \hat{k}_{wd}{}^T = \begin{bmatrix} 0 & 0 \end{bmatrix} \tag{28.69}$$

The resulting transformed undamped equation of motion is

$$\begin{bmatrix} m_2 & 0 \\ 0 & m_3 \end{bmatrix} \begin{bmatrix} \ddot{u}_{w,1} \\ \ddot{u}_{w,2} \end{bmatrix} + \begin{bmatrix} k_1+k_2 & -k_2 \\ -k_2 & k_2 \end{bmatrix} \begin{bmatrix} u_{w,1} \\ u_{w,2} \end{bmatrix} = \begin{bmatrix} m_2 \\ m_3 \end{bmatrix} \ddot{u}_d \tag{28.70}$$

Solve the previous equation using modal analysis. The physical displacements are then

$$\begin{bmatrix} x_1 \\ x_2 \\ x_3 \end{bmatrix} = \begin{bmatrix} 1 & 0 & 0 \\ 1 & 1 & 0 \\ 1 & 0 & 1 \end{bmatrix} \begin{bmatrix} u_d \\ u_{w,1} \\ u_{w,2} \end{bmatrix} \tag{28.71}$$

The physical velocities and accelerations can be calculated similarly.

Now substitute the values from Figure 28.1 into the previous equation set. Apply the Run 1 time history from Figure 26.73 to $m_1$ as an enforced acceleration. Solve the previous equation using a modal analysis with digital recursive filtering. The results are shown in the following figure along with those of two previous methods. The three curves are nearly identical for a given DOF.

Again, the enforced motion method is more versatile because it can accommodate up to six DOF per node as well as multipoint displacement or acceleration inputs.
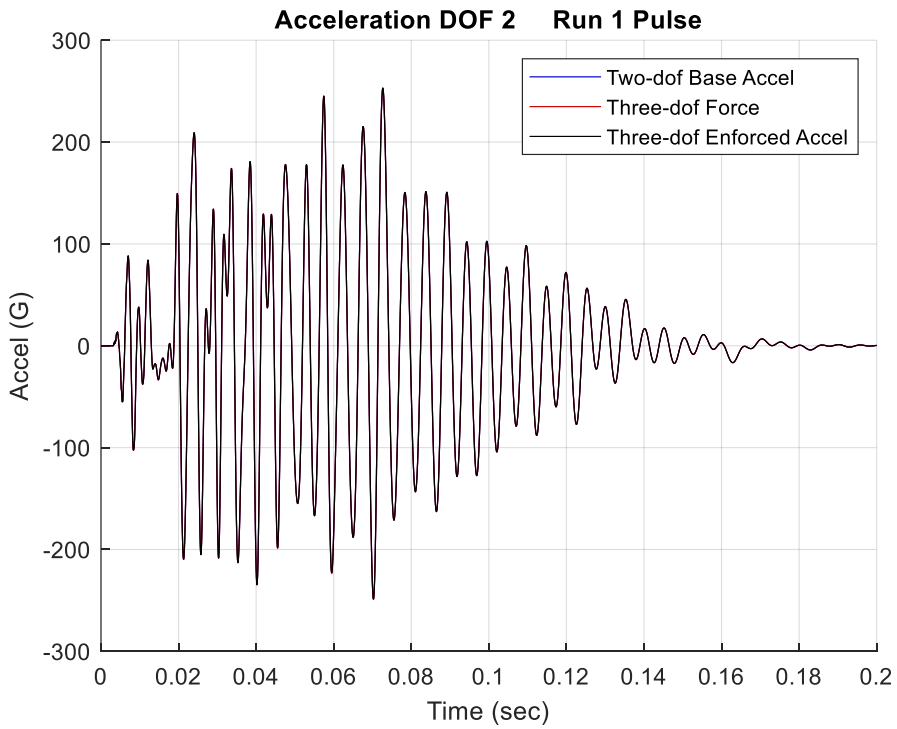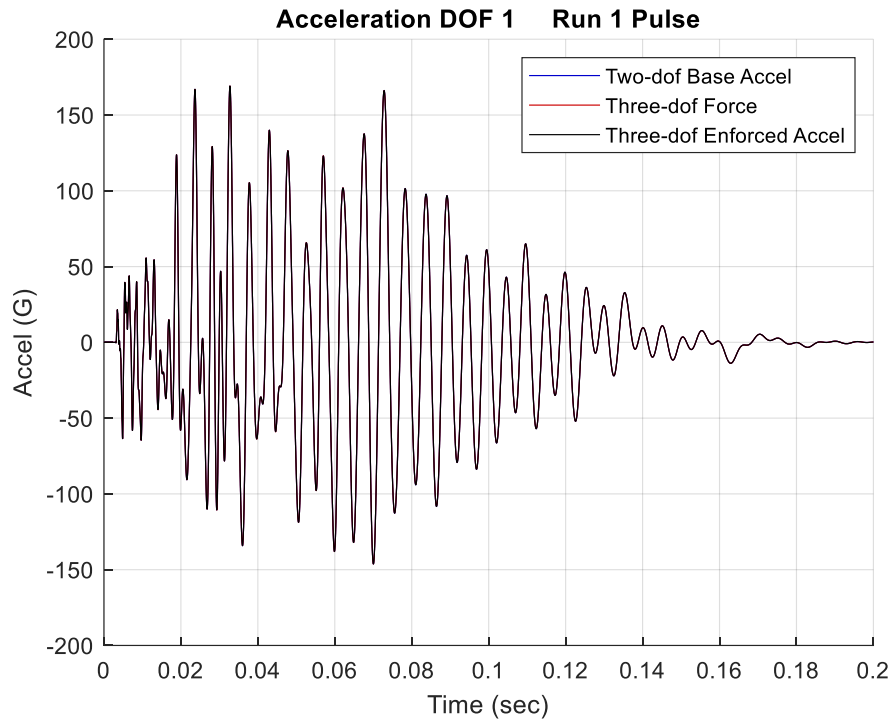
Figure 28.2.  Run 1 Pulse Input, Three Modeling Approaches

# 29 PSEUDO VELOCITY & THE STRESS-VELOCITY RELATIONSHIP

## 29.1  PSEUDO VELOCITY

The Shock Response Spectrum (SRS) models the peak response of a single-degree-of-freedom (SDOF) system to a base acceleration, where the system's natural frequency is an independent variable.   The absolute acceleration and the relative displacement of the SDOF system can be readily calculated. The relative velocity can also be calculated, but the common practice is to approximate the relative velocity in terms of the "pseudo velocity."

The preferred method for calculating the peak pseudo velocity is to multiply the peak relative displacement by the angular natural frequency as shown in equation (26.12).   An alternate method is to divide the peak acceleration by this frequency.

## 29.2 STRESS-VELOCITY RELATIONSHIP



Howard A. Gaberson (1931-2013) championed the idea that dynamic stress correlated better with pseudo velocity than with either acceleration or relative displacement. Gaberson was a shock and vibration specialist who was with the U.S. Navy Civil Engineering Laboratory and later the Facilities Engineering Service Center from 1968 to 2000, mostly conducting dynamics research. He specialized in shock and vibration signal analysis and published more than 100 papers and articles. Gaberson pointed out that the kinetic energy in a mechanical system is proportional to velocity squared.  The pseudo velocity is thus a measure of the stored peak energy in the system at a particular frequency and has a direct relationship to the survival or failure of the system.   The following equations are taken from Reference [53].

Consider the stress-velocity relationship for a traveling wave in an infinite rod.

Compression zone          Rarefaction zone

Direction of travel $\longrightarrow$
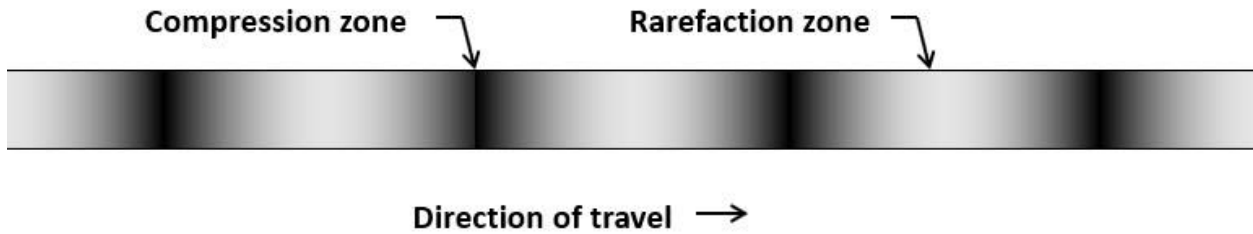
Figure 29.1.  Propagating Wave in an Infinite Rod

The stress $\sigma$ is proportional to the velocity as

$$\sigma(x, t) = -\rho\, c\, v(x, t) \qquad\qquad (29.1)$$

The velocity depends on natural frequency, but the stress-velocity relationship does not.  The lack of a frequency term in equation (29.1) was another reason that Gaberson promoted the stress-velocity relationship.

$\longleftarrow$  Direction of travel $\longrightarrow$
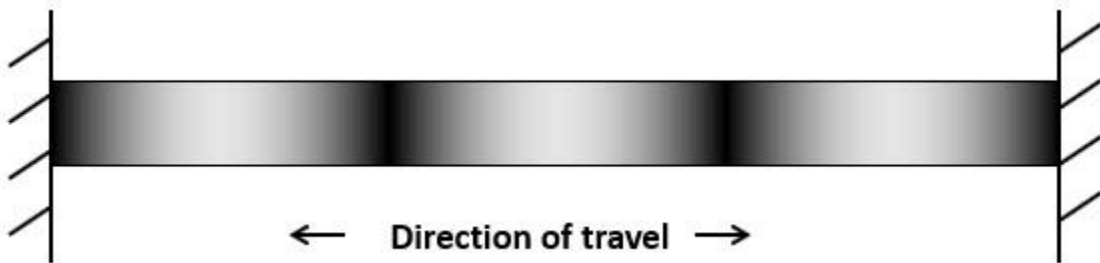
Figure 29.2.  Propagating Wave in a Finite Rod

The principle can be extended to a finite rod with common boundary conditions where the peak modal stress $[\sigma_n]_{max}$ is

$$[\sigma_n]_{max} = \rho c\, [v_n]_{max} \qquad\qquad (29.2)$$

The index $n$ represents the mode number. The peak stress is mainly due to the fundamental mode in most cases. But higher modes can contribute significant stress in certain cases, such as pyrotechnic shock response.

## 29.3  BEAM STRESS

Consider the bending vibration of a simply-supported beam. The modal stress due to bending is proportional to the modal velocity as follows

$$[\sigma_n]_{max} = \hat{c}\sqrt{EA\rho/I}\ [v_n]_{max} \tag{29.3}$$

The distance from the beam's neutral axis to the outer fiber is $\hat{c}$.

Note this equation applies to other boundary condition cases per Reference [54].

Equation (29.3) can be simplified as follows:

$$[\sigma_n]_{max} = \hat{k}\,\rho c\,[v_n]_{max} \tag{29.4}$$

Values for the $\hat{k}$ constant for typical cross-sections are:

| Cross-section | $\hat{k}$ |
|---------------|-----------|
| Solid Circular | 2 |
| Thin Wall Pipe | $\sqrt{2}$ |
| Rectangular | $\sqrt{3}$ |

The method can also be used for complex structures but with some uncertainty.

The general stress-velocity formula is

$$[\sigma_n]_{max} = K\,\rho c\,[v_n]_{max} \qquad (29.5)$$

The constant of proportionality $K$ depends on geometry, etc.

Bateman [55] claimed the following range for complex equipment  $4 < K < 8$.  Gaberson [56] gave a larger range with $1 < K < 10$.

Equation (29.5) could thus be used to "bound the problem" by assuming a high and low $K$ value.

Note that the stress-velocity equations do not require that peak stress and peak velocity occur at the same location.  Any stress concentration factor must be applied separately.  The equations are useful as quick estimates before any advanced modeling such as finite element analysis.  The equations can also be used to "sanity check" any finite element results.

## 29.4  SHOCK VELOCITY THRESHOLD RULE-OF-THUMB

An empirical rule-of-thumb in MIL-STD-810E [41] and SMC-TR-06-11 [57] states that a shock response spectrum is considered severe only if one of its components exceeds the level

Threshold = [ 0.8 (G/Hz) * Natural Frequency (Hz) ] $\qquad (29.6)$

For example, the severity threshold at 100 Hz would be 80 G.

This rule is effectively a velocity criterion.  MIL-STD-810E states that it is based on unpublished observations that military-quality equipment does not tend to exhibit shock failures below a shock response spectrum velocity of 100 inches/sec (254 cm/sec).

Equation (29.6) actually corresponds to 50 inches/sec.  It thus has a built-in 6 dB margin of conservatism.

The 100 inches/sec threshold is defined in part by the observation that the severe velocities which cause yield point stresses in mild steel beams turn out to be about 130 inches/sec.

## 29.5  VELOCITY THRESHOLD FROM YIELD STRESS

The velocity threshold $V_{th}$ can be calculated from the yield stress as follows for a beam with a rectangular cross-section.

$$V_{th} = \frac{\sigma_{yield}}{K \, \rho c} \tag{29.7}$$

The parameters for mild steel are

| $\sigma_{yield}$ | 33 ksi |
|---|---|
| $\rho$ | 0.00075 lbf sec^2/in^4 |
| c | 199,000 inches/sec |

$$V_{th} = \frac{33,000 \; \text{lbf/in}^2}{\sqrt{3}\,(0.00075 \; \text{lbf sec}^2/\text{in}^4)(199,000 \; \text{in/sec})} = 128 \; \text{in/sec} \tag{29.8}$$

Gaberson [56] gave the limits in Table 29.1.  Severe Velocities, Fundamental Limits to Modal Velocities in Structures.

Table 29.1.  Severe Velocities, Fundamental Limits to Modal Velocities in Structures

| Material | E (psi) | $\sigma_{yield}$ (psi) | $\rho$ (lbm/in³) | Rod $V_{max}$ (ips) | Beam $V_{max}$ (ips) | Plate $V_{max}$ (ips) |
|---|---|---|---|---|---|---|
| Douglas Fir | 1.92e+06 | 6450 | 0.021 | 633 | 366 | 316 |
| Aluminum 6061-T6 | 10.0e+06 | 35,000 | 0.098 | 695 | 402 | 347 |
| Aluminum 7075-T6 | 10e+06 | 66,000 | 0.1 | 1300 | 751 | 650 |
| Magnesium AZ80A-T5 | 6.5e+06 | 38,000 | 0.065 | 1015 | 586 | 507 |
| Structural Steel, High Strength | 29e+06 | 33,000 | 0.283 | 226 | 130 | 113 |
| | | 100,000 | | 685 | 394 | 342 |
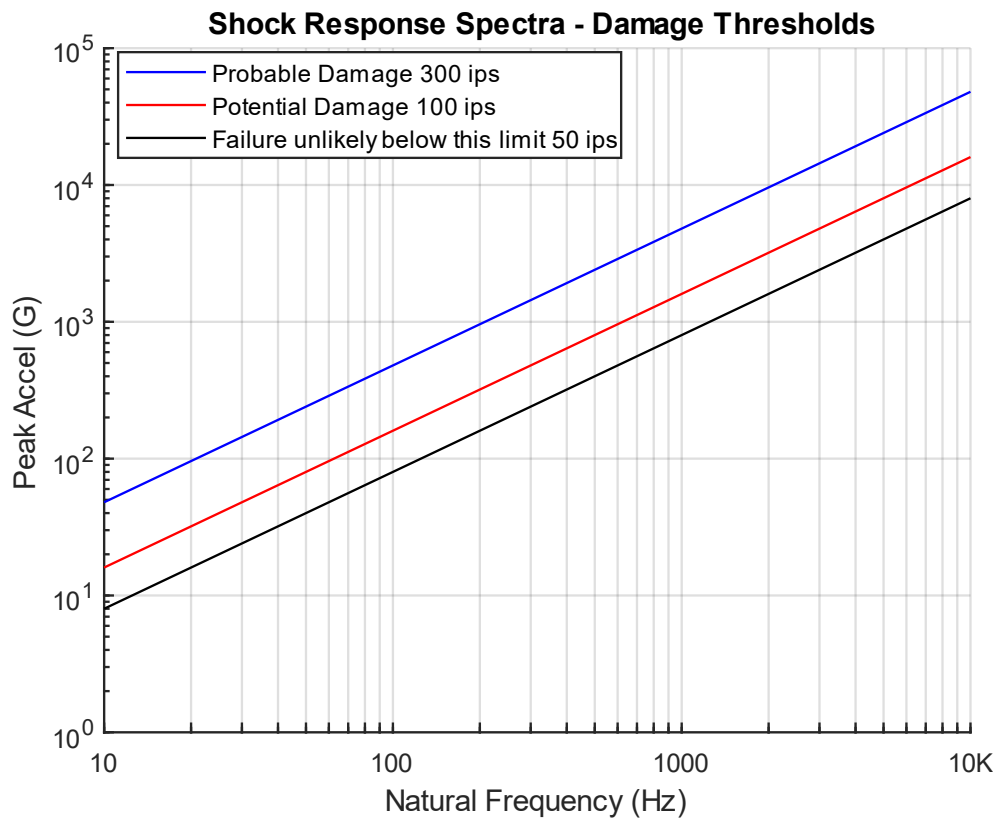
Figure 29.3.  Morse Chart, Shock Response Spectra, Damage Thresholds

The Morse Chart in **Figure 29.3** was derived for aerospace components subjected to shock environments [58]. The curves are defined by the following formulas.

Table 29.2.  Morse Chart Severity Thresholds

| Threshold | Formula |
|-----------|---------|
| 300 ips | [ 4.8 (G/Hz) * Natural Frequency (Hz) ] |
| 100 ips | [ 1.6 (G/Hz) * Natural Frequency (Hz) ] |
| 50 ips | [ 0.8 (G/Hz) * Natural Frequency (Hz) ] |

# 30 DIGITAL FILTERING

## 30.1 FILTERING INTRODUCTION

Filtering is a tool for resolving signals. It can be performed on either analog or digital signals. Analog anti-aliasing filtering was covered in Section 22.5. The present section is limited to digital filtering with an emphasis on the Butterworth filter, which is implemented in the time domain as a digital recursive filtering relationship.

## 30.2 HIGH-PASS & LOW-PASS FILTERS

A high-pass filter is a filter that allows the high-frequency energy to pass through. It is thus used to remove low-frequency energy from a signal.

A low-pass filter is a filter that allows the low-frequency energy to pass through. It is thus used to remove high-frequency energy from a signal.

A band-pass filter may be constructed by using a high-pass filter and low-pass filter in series

## 30.3  BUTTERWORTH FILTER CHARACTERISTICS

**BUTTERWORTH LOWPASS FILTER  L=ORDER    $\Omega_c = 1$ rad/sec**
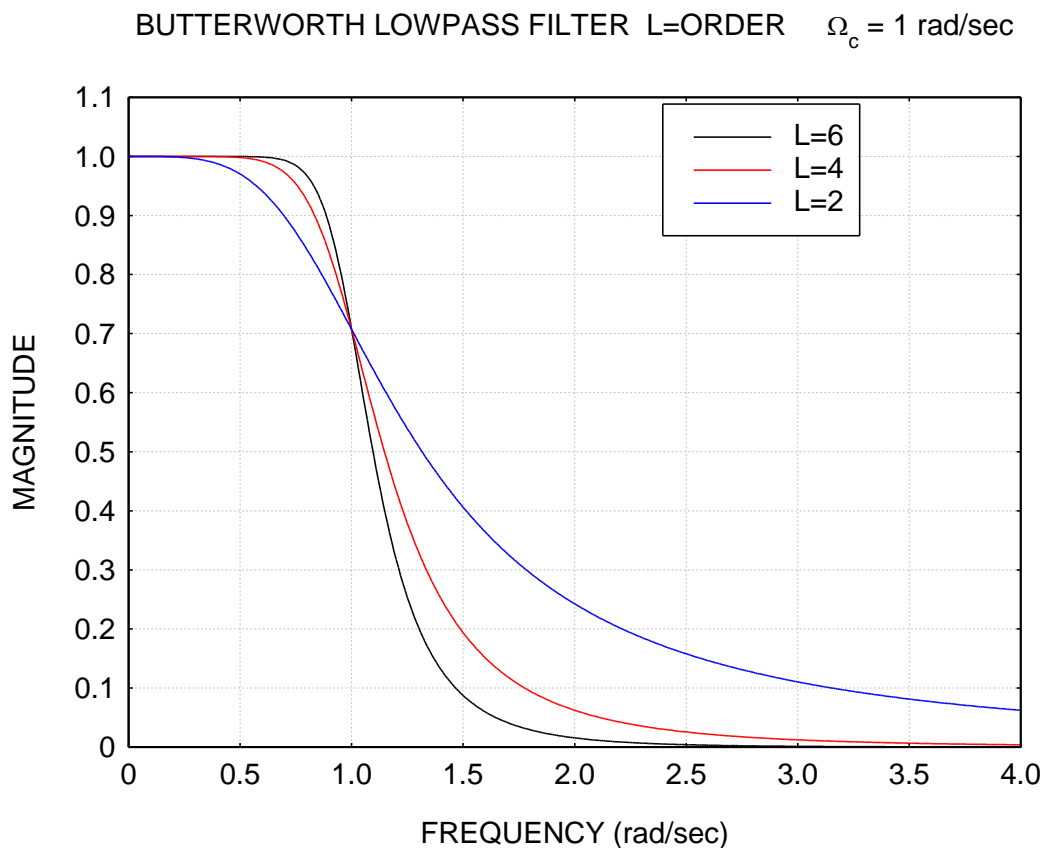


Figure 30.1.  Butterworth Filter, Three Orders, Transfer Function Magnitudes

A Butterworth filter is one of several common infinite impulse response (IIR) filters.  Other filters in this group include Bessel and Chebyshev filters.  These filters are classified as feedback filters.  The Butterworth filter can be used either for high-pass, low-pass, or band-pass filtering.  It is characterized by its cut-off frequency.  The cut-off frequency is the frequency at which the corresponding transfer function magnitude is –3 dB, equivalent to 0.707.  The transfer function curves in Figure 30.1 each pass through the same cut-off frequency point.

A Butterworth filter is also characterized by its order, with the sixth-order preferred in this document.  A property of Butterworth filters is that the transfer magnitude is –3 dB at the cut-off frequency regardless of the order.  Other filter types, such as Bessel, do not share this characteristic.

Consider a low-pass, sixth-order Butterworth filter with a cut-off frequency of 100 Hz. The corresponding transfer function magnitude is given in the figure below.
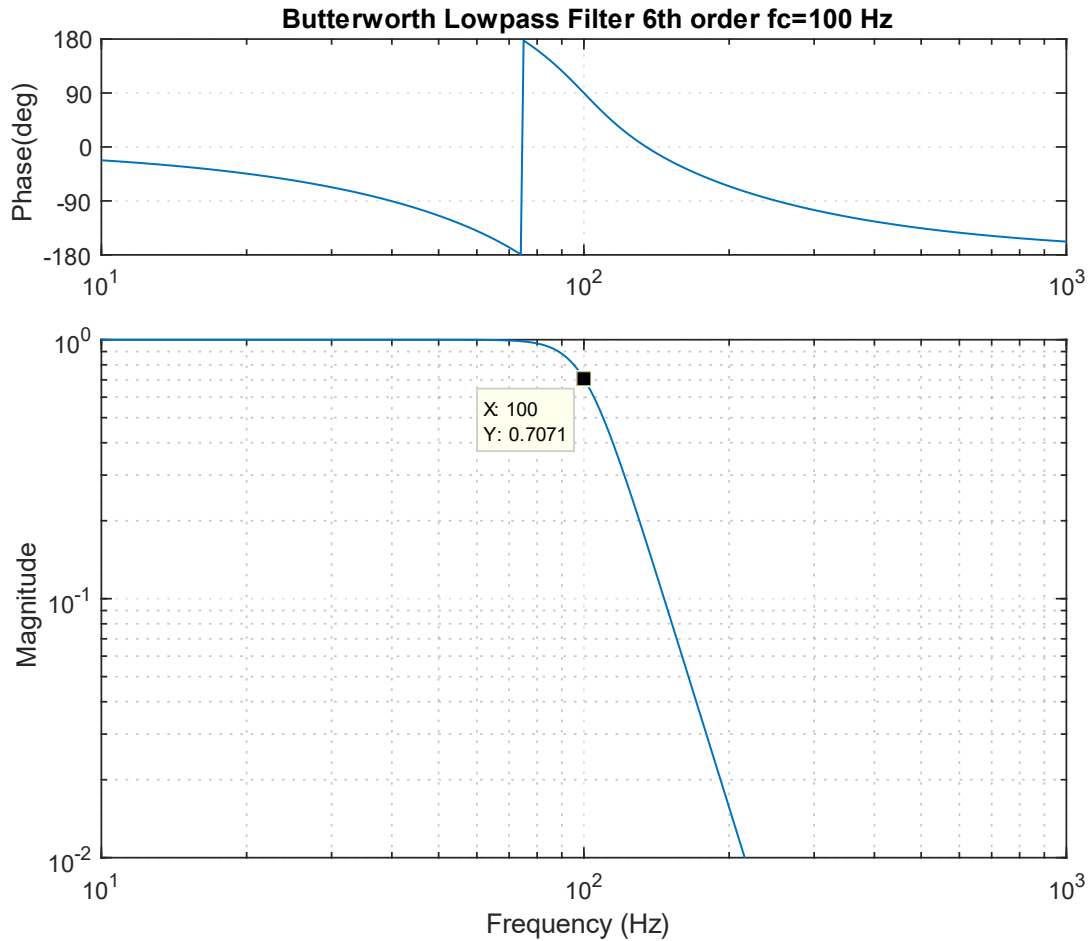


Figure 30.2. Butterworth Low-Pass Filter, 100 Hz, Transfer Function

Note that the curve has a gradual roll-off beginning at about 70 Hz. Ideally, the transfer function would have a rectangular shape, with a corner at (100 Hz, 1). This ideal is never realized in practice due to stability concerns in the time domain. Thus, a compromise is usually required to select the cut-off frequency. The transfer function could also be represented in terms of a complex function, with real and imaginary components. A transfer function magnitude plot for a sixth-order Butterworth filter with a cut-off frequency of 100 Hz as shown in Figure 30.3.
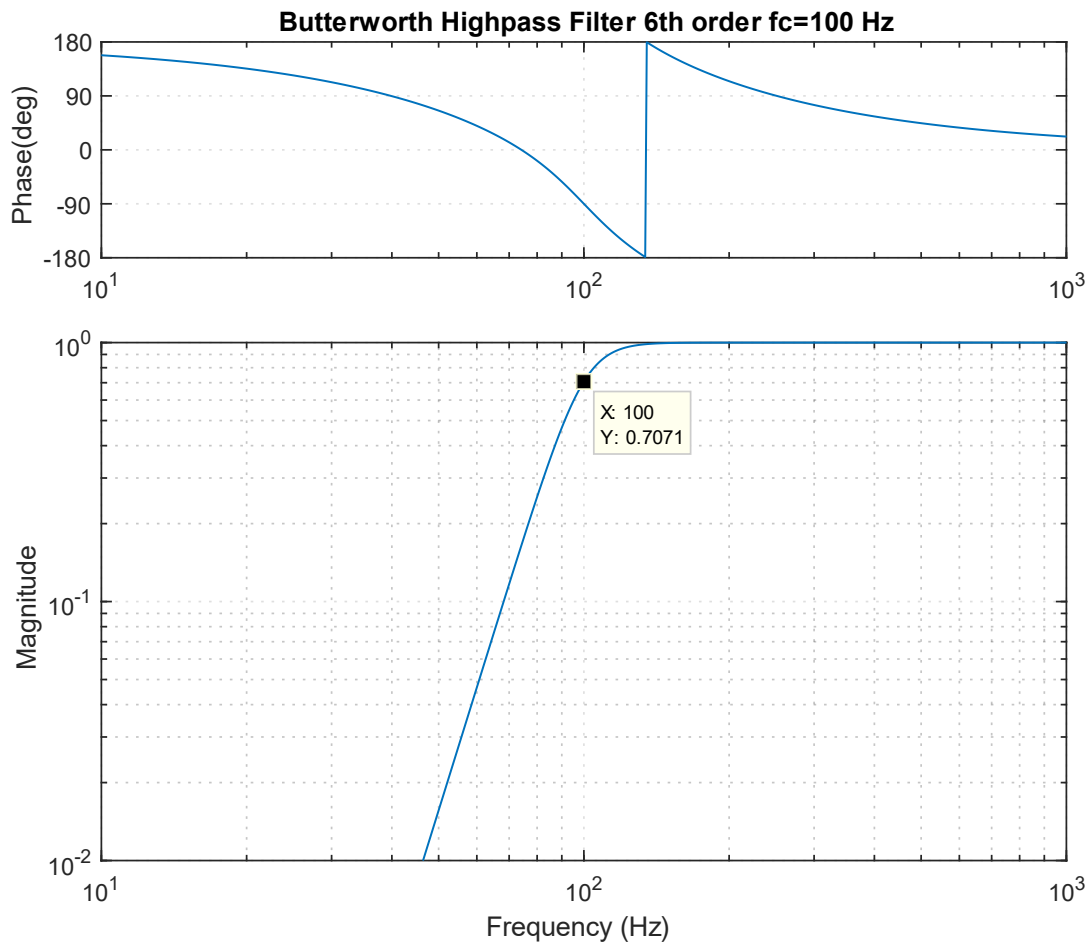
Figure 30.3.  Butterworth High-Pass Filter, 100 Hz, Transfer Function


The curves in the previous figures suggest that filtering could be achieved as follows:

1. Take the Fourier transform of the input time history
2. Multiply the Fourier transform by the filter transfer function, in complex form
3. Take the inverse Fourier transform of the product

The above frequency domain method is valid.  Nevertheless, the filtering algorithm is usually implemented in the time domain for computational efficiency, maintaining stability, avoiding leakage errors, etc.
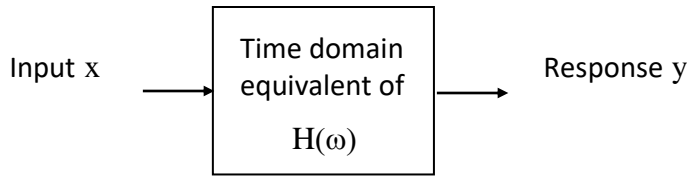
Figure 30.4.   Filter Block Diagram

The filter transfer function can be represented by $H(\omega)$ as shown in Figure 30.4. The filtering transfer function is implemented as a digital recursive filtering relationship in the time domain. The response $y_k$ at time index $k$ is

$$
y_k = \left\{ \sum_{n=0}^{L} b_n \, x_{k-n} \right\} - \left\{ \sum_{n=1}^{L} a_n \, y_{k-n} \right\}
\tag{30.1}
$$

The filter order is $L$. The filter coefficients $a_n$ and $b_n$ can be derived using the method in Reference [59]. The equation is recursive because the output at any time depends on the output at previous times.

## 30.4   PHASE CORRECTION
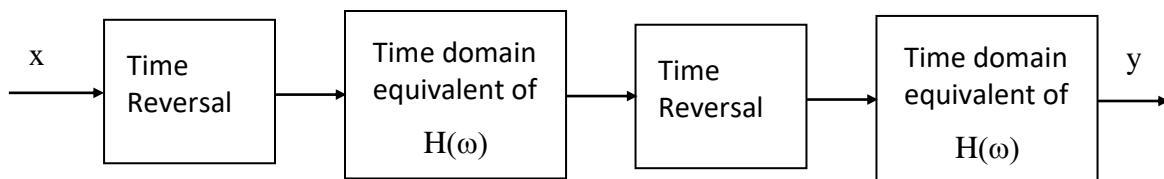


Figure 30.5.   Refiltering for Phase Correction

An ideal filter should provide a linear phase response.  This is particularly desirable if shock response spectra calculations are required.   Butterworth filters, however, do not have a linear phase response.   Other IIR filters share this problem.  Several methods are available, however, to correct the phase response.  One is the refiltering method in Reference [59].  An important note about refiltering is that it reduces the transfer function magnitude at the cut-off frequency to −6 dB, as shown in the example in Figure 30.6.

420
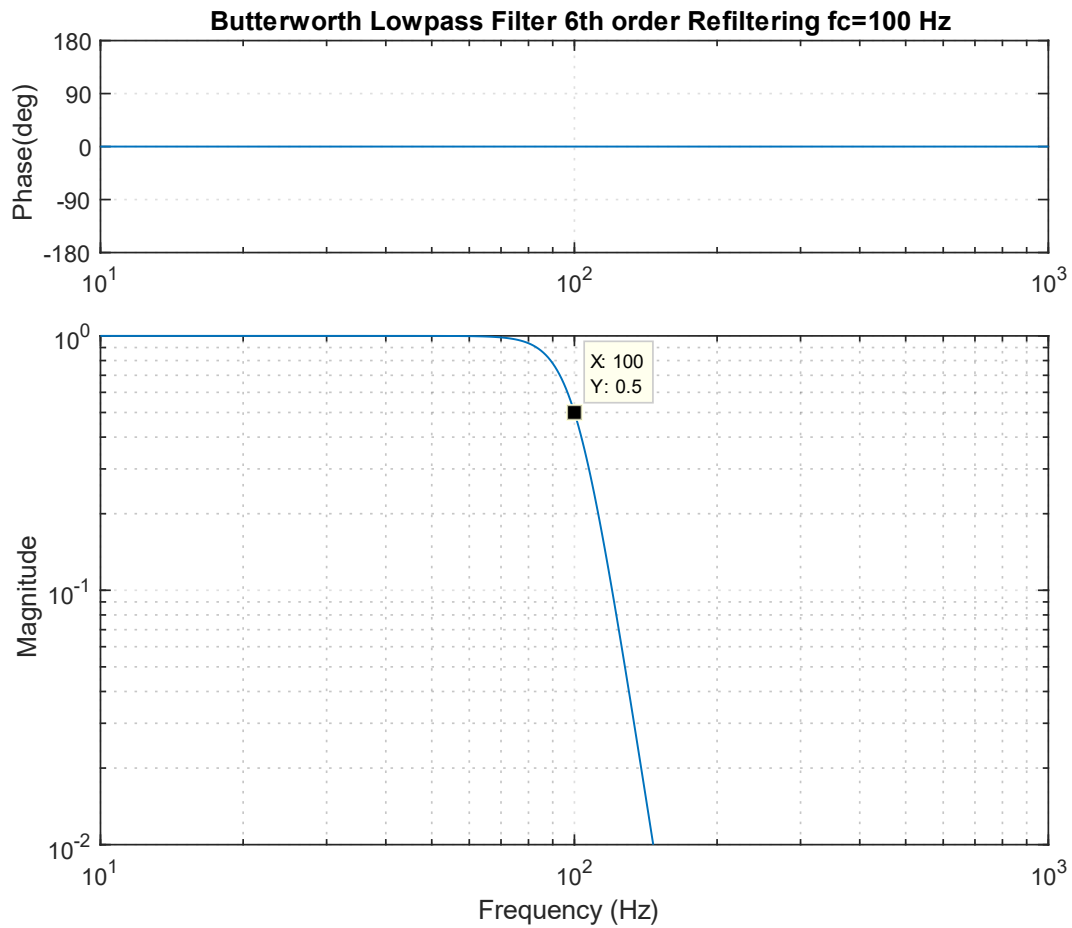
**Figure 30.6.** Butterworth Filter 6$^{th}$ Order Low-Pass Filter with Refiltering, Transfer Function

## 30.5  PSD CALCULATION VIA DIGITAL FILTER

Recall the synthesized time history from Figure 24.11 which satisfied the Navmat P-9492 PSD specification.   Calculate the power spectral density by applying band-pass filtering over successive bands.   This method is useful as a means of better understanding the PSD function. The filtering is performed using a Butterworth sixth-order filter without refiltering for phase correction.  The bands are full octaves. The results are shown in Table 30.1.

Table 30.1. Band-pass Filter Results, Octave Bands

| fl (Hz) | fc (Hz) | fu (Hz) | Δf (Hz) | GRMS | GRMS^2 | GRMS^2/Hz |
|---------|---------|---------|---------|------|--------|-----------|
| 14 | 20 | 28 | 14 | 0.36 | 0.13 | 0.0091 |
| 28 | 40 | 57 | 29 | 0.80 | 0.64 | 0.0226 |
| 57 | 80 | 113 | 56 | 1.47 | 2.17 | 0.0384 |
| 113 | 160 | 226 | 113 | 2.16 | 4.67 | 0.0413 |
| 226 | 320 | 453 | 227 | 2.92 | 8.54 | 0.0377 |
| 453 | 640 | 905 | 452 | 3.11 | 9.70 | 0.0214 |
| 905 | 1280 | 1810 | 905 | 3.02 | 9.15 | 0.0101 |
| 1810 | 2560 | 3620 | 1810 | 1.31 | 1.71 | 0.0009 |

The band center frequency is fc. The lower and upper band limits are fl and fc, respectively. The bandwidth is Δf which is the difference between the band limits. A GRMS value is calculated for each band. Then the GRMS value is squared and divided by the bandwidth. The last column is the PSD in GRMS^2/Hz. The time histories for the two rows in the table are shown in Figure 30.7. The GRMS^2/Hz points are plotted along with Navmat PSD in Figure 30.8. Recall that GRMS^2/Hz is abbreviated as G^2/Hz.
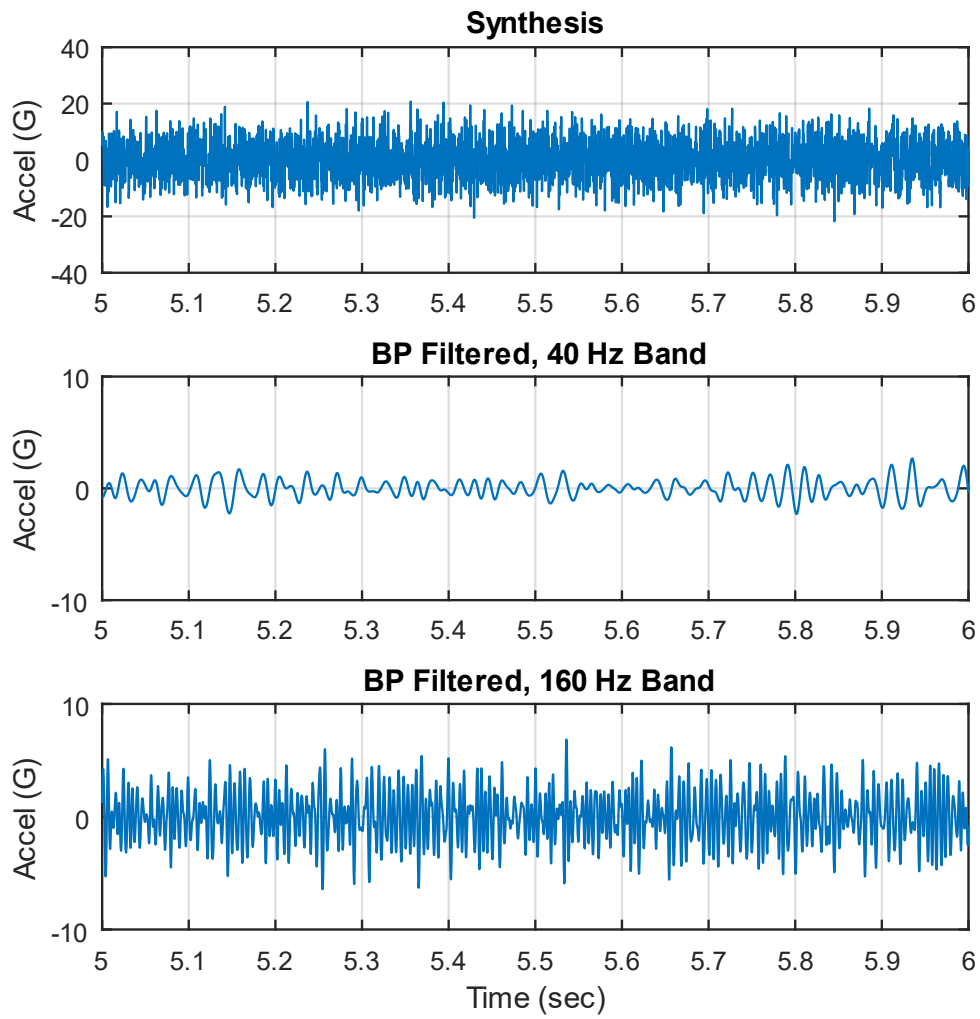
Figure 30.7.  Synthesized Time History with Two Filtering Cases, Close-up View

The bands are in full octave format.
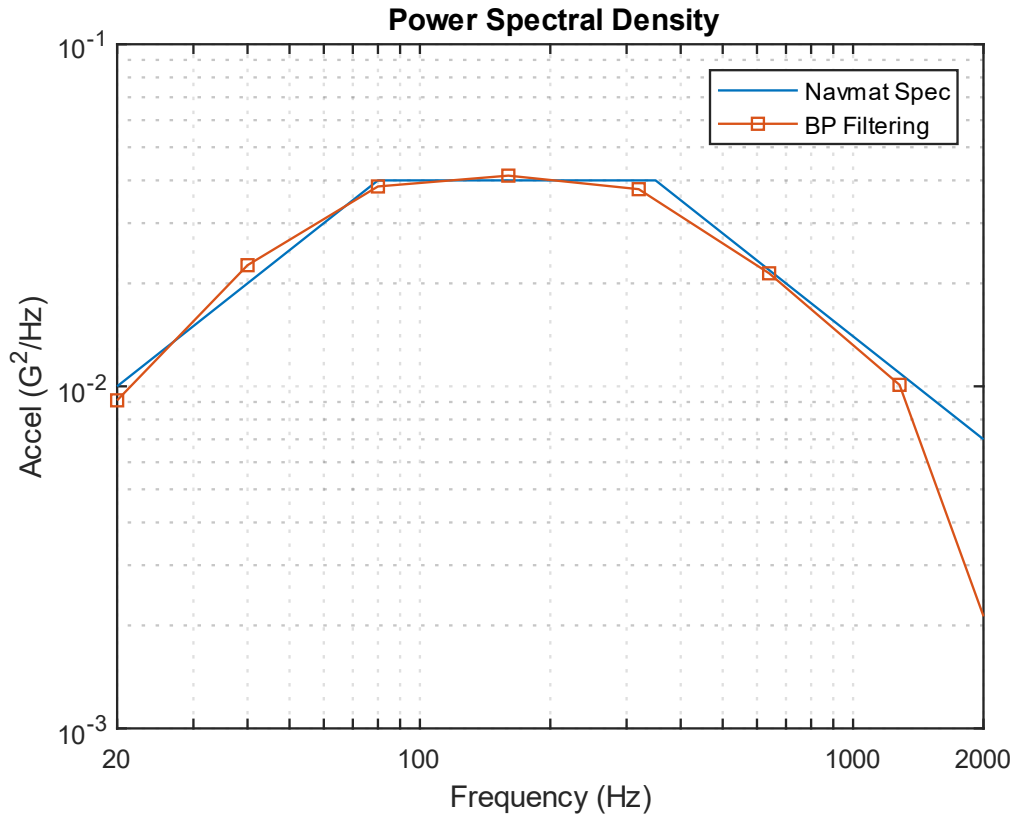
Figure 30.8.  PSD Comparison

The PSD points calculated via band-pass filtering track the specification fairly well.  The dropout for the last point is not a concern because the bandwidth extended from 1810 to 3620 Hz, but the specification stopped at 2000 Hz.

The following example shows how filtering can aid in analyzing seismic data from a seismometer.  Filtering is used to find the onset of P-wave in seismic time history from the Solomon Island earthquake, Magnitude 6.8, October 8, 2004.  The measured data is from a homemade seismometer in Mesa, Arizona.



Figure 30.9.  Author's Homemade Lehman Seismometer

The boom is a horizontal pendulum. It has a period of 14.2 seconds, equivalent to a natural frequency of 0.071 Hz. A sensor at the free end measures the displacement. The boom length is 64 inches. The total frame height is 35 inches. The boom has a knife edge that pivots against a bolt head in the lower cross-beam of the frame.

The boom is suspended from the frame by a wire cable. The cable is attached to the top cross-beam of the frame. The other end of the cable is attached to the boom, about two-thirds of the

distance from the pivot to the free end of the boom. The pivot point is offset from the top cable attachment point.  Thus, the boom oscillates as if it were a "swinging gate."

The plate supporting the frame has three adjustable mounting feet. The feet can be adjusted to tune the pendulum to the desired natural frequency.  Furthermore, the wire cable has a turnbuckle which is used to adjust the height of the free end of the boom. The detached frame in the center of the figure is used for assembly and to limit the displacement during tuning.



Figure 30.10.  Non-contact Relative Displacement Sensor

The classic sensor for Lehman seismometers is a magnetic coil attached to the boom.  The coil moves between the poles of a magnet, thus inducing a voltage proportional to the velocity. The signal requires tremendous amplification.   The author had better success with the inductive displacement sensor.

Figure 30.11.  Ballast Mass Partially Submerged in Oil

The damping method is shown in this figure.



Figure 30.12.   Pivot at the End of the Boom

The chisel blade butted up against a chrome-plated bolt head.
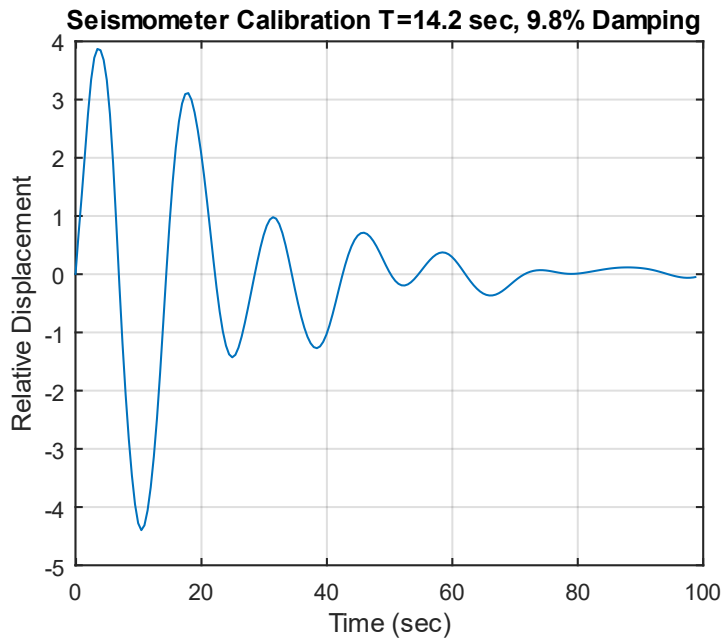
Figure 30.13.   Seismometer Free Vibration Response

The seismometer was given an initial displacement and then allowed to vibrate freely.     The period was 14.2 seconds, with 9.8% damping.   The corresponding frequency is 0.0705 Hz.

The trace in Figure 30.14 is the displacement time history of the Solomon Islands earthquake on October 8, 2004, as measured by the Lehman seismometer via the inductive sensor. The seismometer was located at home in Mesa, Arizona.  The data was acquired by a Nicolet Vision system. The Nicolet sample rate was set to 50 samples per second with its low pass filter set to 5 Hz.

**LEHMAN SEISMOMETER HORIZONTAL RESPONSE TO SOLOMON ISLAND EARTHQUAKE    UTC 2004/10/08 08:27:53**
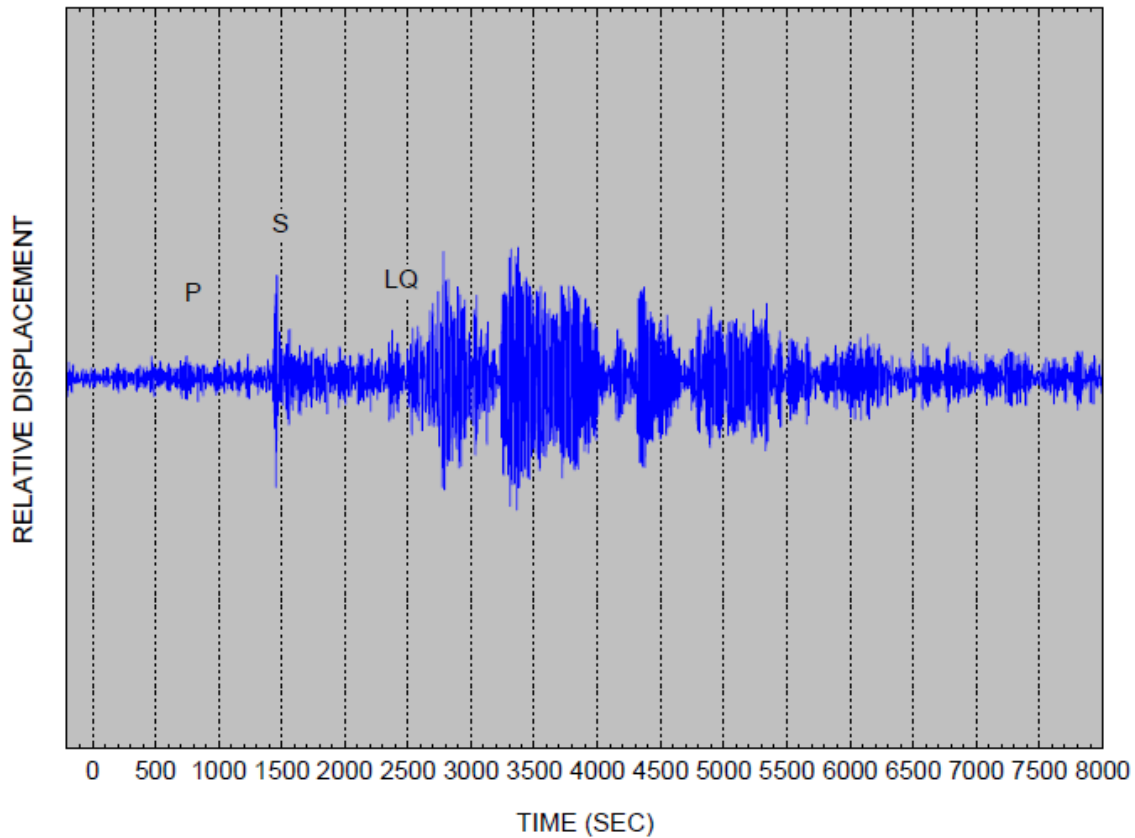
Figure 30.14.   Measured Solomon Earthquake Time History, Lehman Seismometer

A Krohn-Hite filter, model 3343, was used to high-pass filter the analog displacement signal at 0.03 Hz before its input to the Nicolet system. It also provided a 20 dB gain.

The time is referenced to the earthquake occurrence using the USGS data. The plot's Y-axis is labeled as relative displacement because it is the response of the boom relative to the ground. Further calculation would be required to estimate the true ground motion. The time history shows that the Earth is remarkably reverberant. The oscillations last well over one hour.  The phase components are the P primary wave, S secondary or shear wave, and LQ Love wave. Recall the seismic wave diagrams in Section 26.6.1.

The P-wave is indiscernible against the background microseismic noise. Nevertheless, it can be extracted by additional filtering, as shown in the next figure.

**High-Pass Filtered Time History 0.2 Hz**
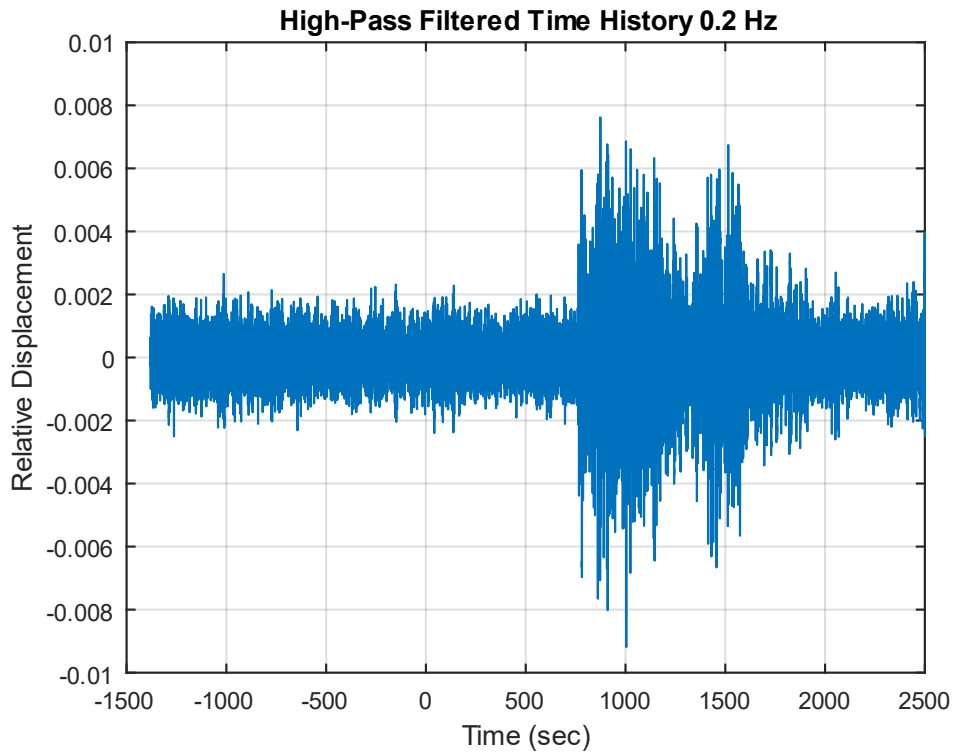
Figure 30.15.  High-pass Filtered Seismic Waveform Showing Onset of P-wave

The P-wave arrives in Mesa, Arizona about 760 seconds after it was generated near the Solomon Islands.    The S-wave arrives around 1400 seconds.   Some intermediate waveforms begin as P-waves and transform into other types through reflection and refraction.   Both the P and S-waves are body waves that travel faster than surface waves.   The frequency content of body and surface waves is shown in the following table, as taken from Reference [1].

Table 30.2.  Seismic Waveform Periods and Frequencies

| Wave Type | Period (sec) | Natural Frequency (Hz) |
|---|---|---|
| Body | 0.01 to 50 | 0.02 to 100 |
| Surface | 10 to 350 | 0.003 to 0.1 |

## 30.7 INTEGRATION AND DIFFERENTIATION OF ACCELEROMETER SIGNALS

There are occasional needs to integrate accelerometer time histories into velocity. This may be done to evaluate the accuracy of pyrotechnic shock data where the velocity is expected to have a stable oscillation about its zero baseline. Accelerometer data may also be double-integrated to displacement, but the accuracy depends on the frequency response of the accelerometers. Some accelerometer types such as variable capacitance and servo motor designs can accurately measure acceleration down to zero frequency. The common piezoelectric accelerometer may have a practical lower limit of a few Hertz, however. Some type of high-pass filter is needed in this case. The high-pass filtering may be performed using an analog filter in the accelerometer's signal conditioner. Or the filtering may be performed digitally as a post-processing step.

Another integration scenario is the case where an acceleration time history is synthesized for use in a modal transient analysis. The corresponding velocity and displacements should each be stable, especially if dynamic stresses are to be calculated. Consider the simple case of the synthesized white noise acceleration time history in Figure 30.16.

The integration steps are performed using the trapezoidal method which has sufficient accuracy. The resulting velocity displacement each has a drift. These effects arise in part because the integration does not account for initial velocity and initial displacement, each of which is either unknown or unspecified. The next task is to correct the acceleration time history so that its velocity and displacement will each be stable. There is no one right way to do this, but an example is shown in Figure 30.17. The correction steps were:

1. Remove mean from acceleration
2. High-pass filter acceleration at 6 Hz, Butterworth 6th order with refiltering for phase correction
3. Apply fade in and out to acceleration using 2% of the total duration at each end
4. Integrate to velocity
5. Remove mean from velocity
6. Apply fade in and out to velocity using 2% of the total duration at each end
7. Integrate to displacement
8. Perform first-order trend removal on displacement
9. Apply fade in and out to displacement using 2% of the total duration at each end
10. Differentiate displacement to velocity
11. Differentiate velocity to acceleration Integrate corrected acceleration to velocity
12. Integrate velocity to displacement
13. Verify that the resulting velocity and displacement each have stable oscillations about their respective zero baselines and that each begins and ends at zero
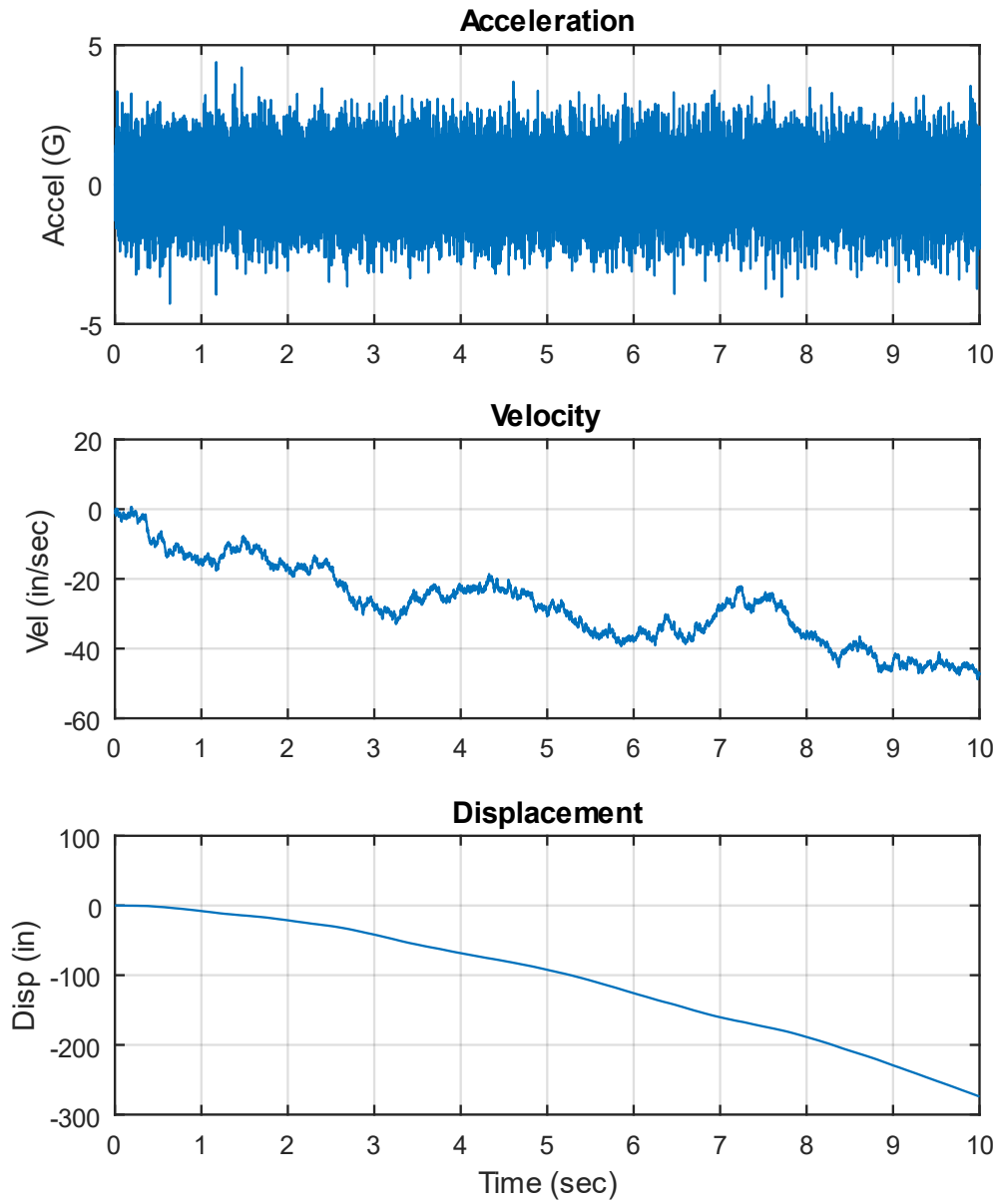
Figure 30.16.  White Noise Acceleration Time History with Corresponding Velocity and Displacement
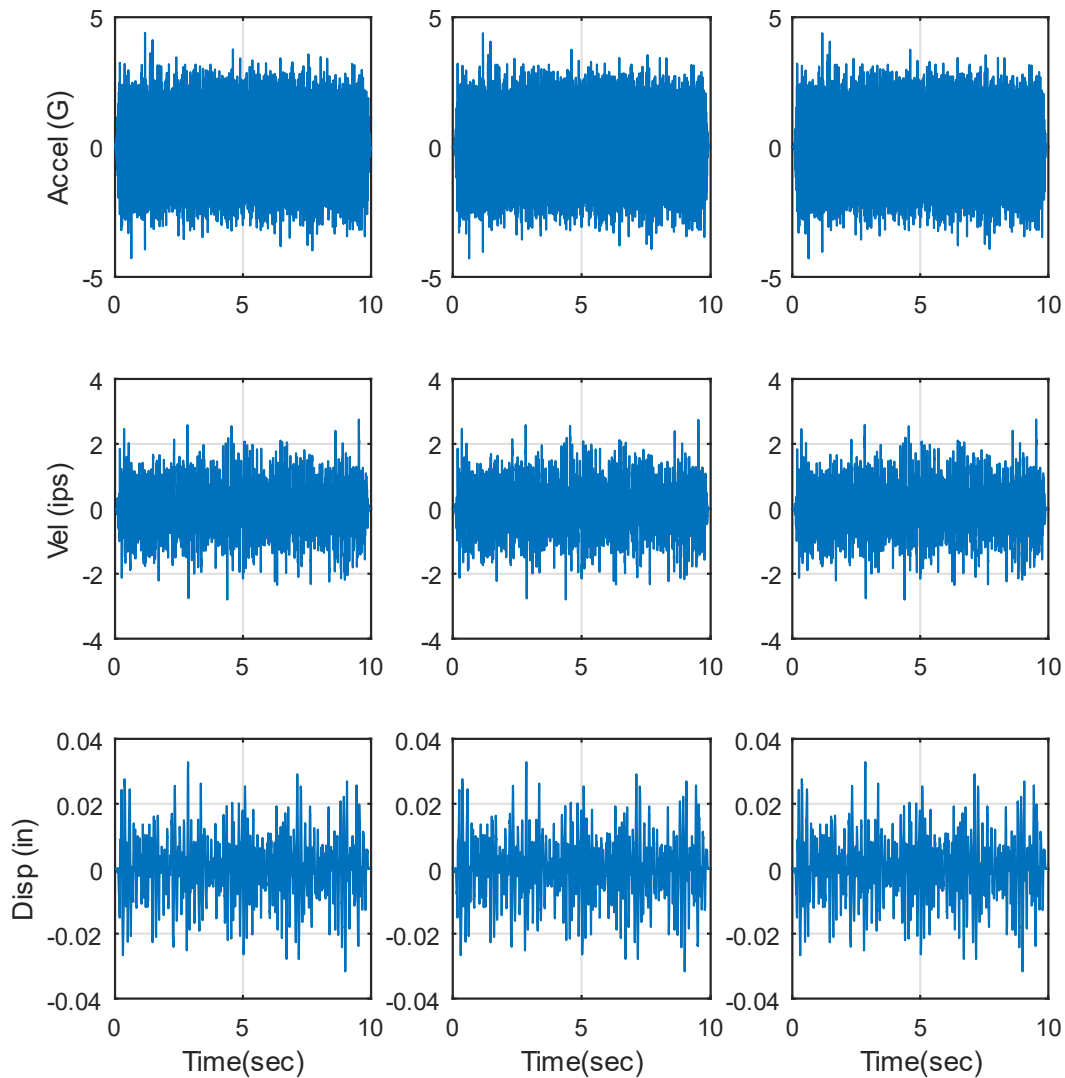
Figure 30.17.   Acceleration Time History Correction and Verification

Nine subplots appear as follows:

Row 1, Col 1 - processed acceleration before integration
Row 2, Col 1 - integrated velocity
Row 3, Col 1 - double integrated displacement

Row 3, Col 2 - double integrated displacement (repeated)
Row 2, Col 2 - differentiated velocity from double integrated displacement
Row 1, Col 2 - double differentiated acceleration from double integrated displacement

Row 1, Col 3 - double differentiated acceleration (repeated)

Row 2, Col 3 - integrated velocity from double differentiated acceleration

Row 3, Col 3 - double integrated displacement from double differentiated acceleration

The corrected acceleration is the time history shown in Row 1, Col 2 and repeated in Row 1, Col 3.
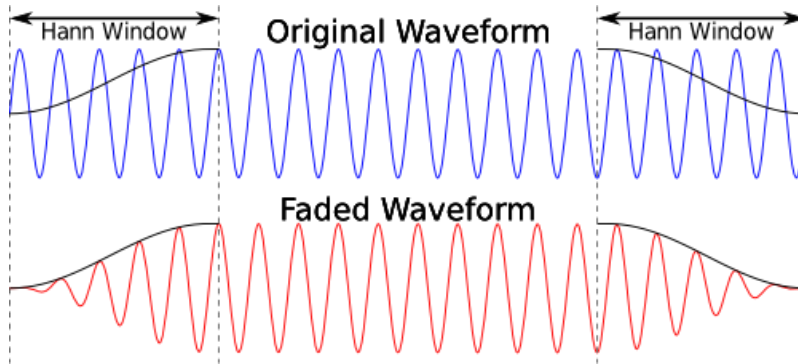


Figure 30.18. Fade In and Out Windows

Note that the fade-in and out windows are similar to those shown in Figure 30.19.
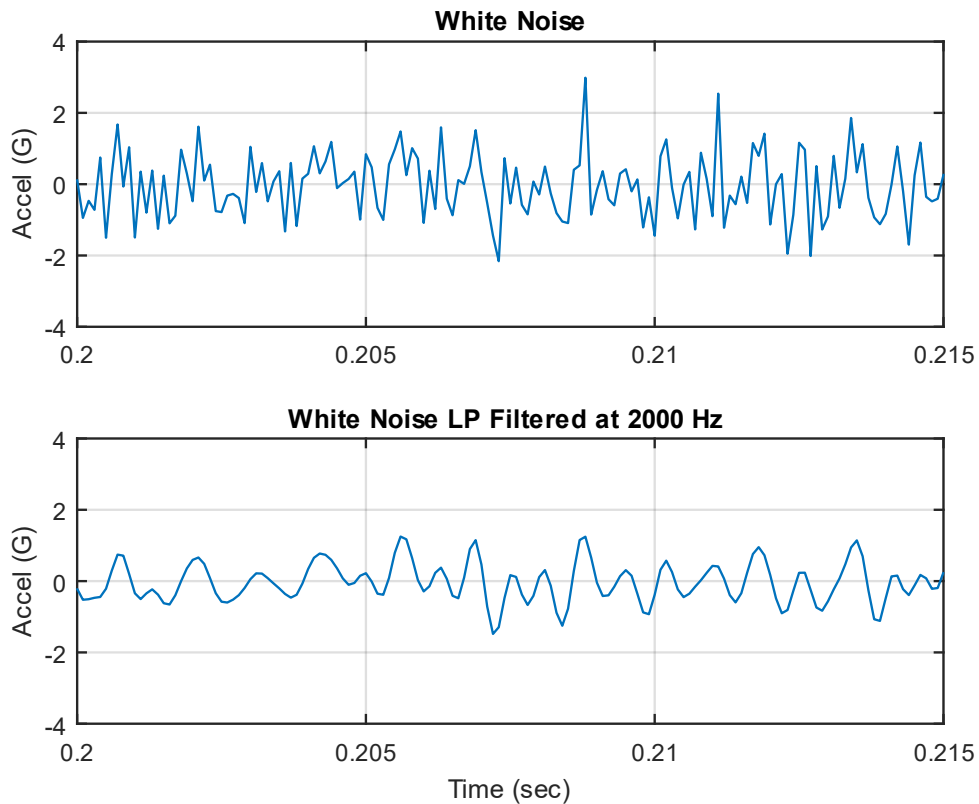
Figure 30.20.  White Noise Segment Before and After Low-Pass Filtering

White noise is an idealized concept.  True white noise would have a flat PSD level from zero to infinity frequency units.  Digital white noise is inherently frequency limited by its sample rate. Furthermore, white noise may be subject to low-pass filtering to smooth it before its use as an excitation function, as shown in the above figure.

The top subplot is a white noise sampled at 10,000 samples/sec and has a choppy appearance. Aliasing would be suspected if the top plot were measured data.

The bottom subplot is the same time history low-pass filtered at 2000 Hz which smooths the data.  Either time history should be suitable for either applied force or base excitation of an SDOF system with a natural frequency of 200 Hz, for example.  Recall that the SDOF system itself behaves as a mechanical filter.  But the low-pass filtered version could have some

potential numerical accuracy benefits, although an investigation of this hypothesis is left as future work.


## 30.9  LAUNCH VEHICLE COUPLED-LOADS ANALYSIS FILTERING
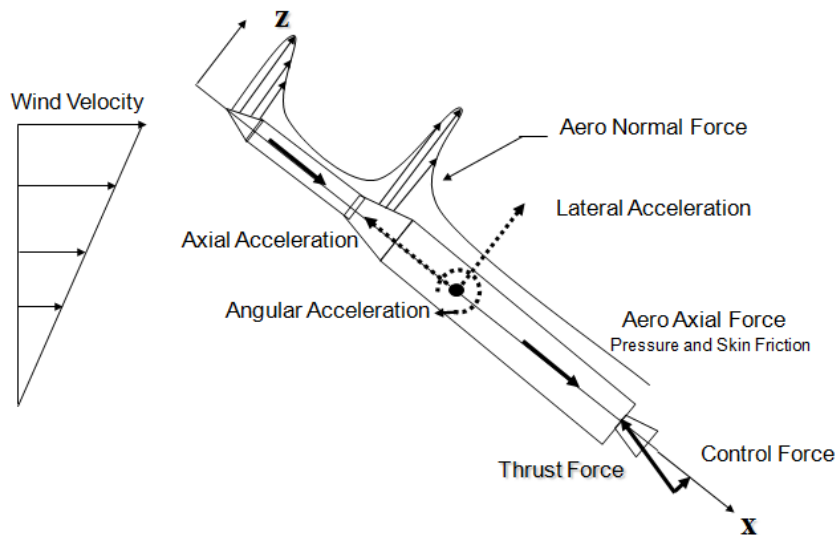


Figure 30.21.  Sources of Aero-Mechanical Loads


Coupled Loads Analysis (CLA) predicts payload & launch vehicle responses due to major dynamic and quasi-static loading events.  This analysis is performed before launch.  It can also be performed as post-flight data reconstruction using flight accelerometer data.   Flight accelerometer data is low-pass filtered for coupled-loads analyses. The cut-off frequency varies by the launch vehicle, payload, key events, etc.  The primary sources of these low-frequency loads are:

1.  Pre-launch events: ground winds, seismic loads
2.  Liftoff: engine/motor thrust build-up, ignition overpressure, pad release
3.  Air-loads: buffet, gust, static-elastic, maneuvers
4.  Liquid engine ignitions and shutdowns


Reference [60] gives the following frequency guidelines for CLA.  The low-frequency dynamic response of the launch vehicle/payload system to transient flight events is typically analyzed from 0 Hz to 100 Hz.  The response frequency domain can be up to 150 Hz for some small launch vehicles.   See also Section 36.

# 31 RELATIVE FATIGUE ANALYSIS

## 31.1 INTRODUCTION

### 31.1.1 Purpose and Scope

Flight accelerometer time histories are inherently nonstationary, meaning the vibration levels change as the vehicle undergoes various flight events. These changes include shifts in both the overall level and the amplitude distribution with respect to frequency. The skewness, kurtosis, and histogram may likewise change.

There is a need to derive a PSD envelope for nonstationary acceleration time histories, such as launch vehicle data so that components can be designed and tested accordingly. Note that component vibration shaker table tests are almost always performed with stationary vibration and with a normal distribution.

The traditional method divides the accelerometer data into segments that are idealized as "piecewise stationary" in terms of their respective PSDs. A maximum envelope is then drawn for the superposition of segment PSDs. This method requires no assumptions about the response characteristics of the test item, but it can be overly conservative.

An alternate method is the FDS which applies the time history as a base input to an SDOF system with variable natural frequency and amplification factors. The response of each system is then calculated. Upper and lower estimates of the amplification factor can be used to cover uncertainty. A rainflow cycle count is then performed on the response time histories. The rainflow cycles are then fed into a Miners-type cumulative damage summation with an assumed fatigue exponent. Upper and lower estimates of the fatigue exponent can be used to cover uncertainty.

The resulting damage index does not predict whether the component will pass or fail. Rather it is a relative index that allows for the comparison between different vibration environments. The final FDS plot gives the relative damage as a function of natural frequency with the amplification factor and fatigue exponent duly noted. Furthermore, an FDS may be calculated from a base input PSD using the Dirlik method as an intermediate step.

The FDS method can be used to derive a PSD to cover a nonstationary time history, using trial-and-error with random number generation along with convergence. The envelope is then justified using a comparison of candidate PSD spectra with the measured time history spectra.

The PSD envelope can be optimized by choosing the one with the least overall level which still envelops the accelerometer data spectra, or minimizes the response spectra error.

The FDS enveloping method has the potential of yielding a less conservative PSD than the traditional piecewise stationary method, i.e. pencil sharpening.

The purpose of this section is to present and explain the FDS enveloping method.

Note that the FDS method can be used to evaluate the severity of two different shock or vibration environments, which will also be covered in a future revision.

## 31.2 SDOF MODEL
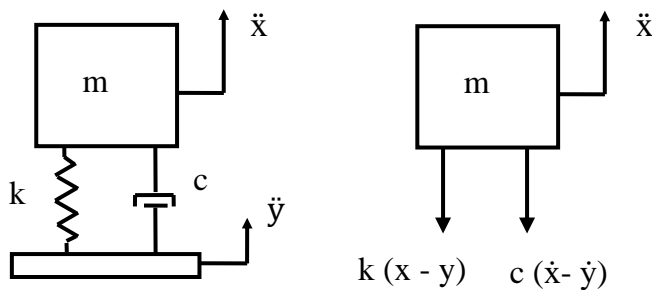


Figure 31.1.   SDOF System Subjected to Base Excitation

Please review Sections 17.3 & 26.5 for the equation of motion and time domain solution method.  The response time history can then be fed into the rainflow cycle counting algorithm as given later in this chapter.

Please also review the shock & vibration response spectra functions in Sections 25 & 26.   The fatigue damage spectrum is in the same family as these functions.  Each of the three response spectra functions has natural frequency as its X-axis label, and each is referenced to an amplification factor Q.  The fatigue damage spectrum is additionally referenced to a fatigue exponent b.

## 31.3 FATIGUE IN THE TIME DOMAIN

### 31.3.1 Rainflow Cycle Counting



Figure 31.2.   Goju-no-to Pagoda, Miyajima Island, Japan

Endo & Matsuishi 1968 developed the Rainflow Counting method by relating stress reversal cycles to streams of rainwater flowing down a Pagoda.  The method is implemented in ASTM E1049–85, section 5.4.4.

STRESS TIME HISTORY
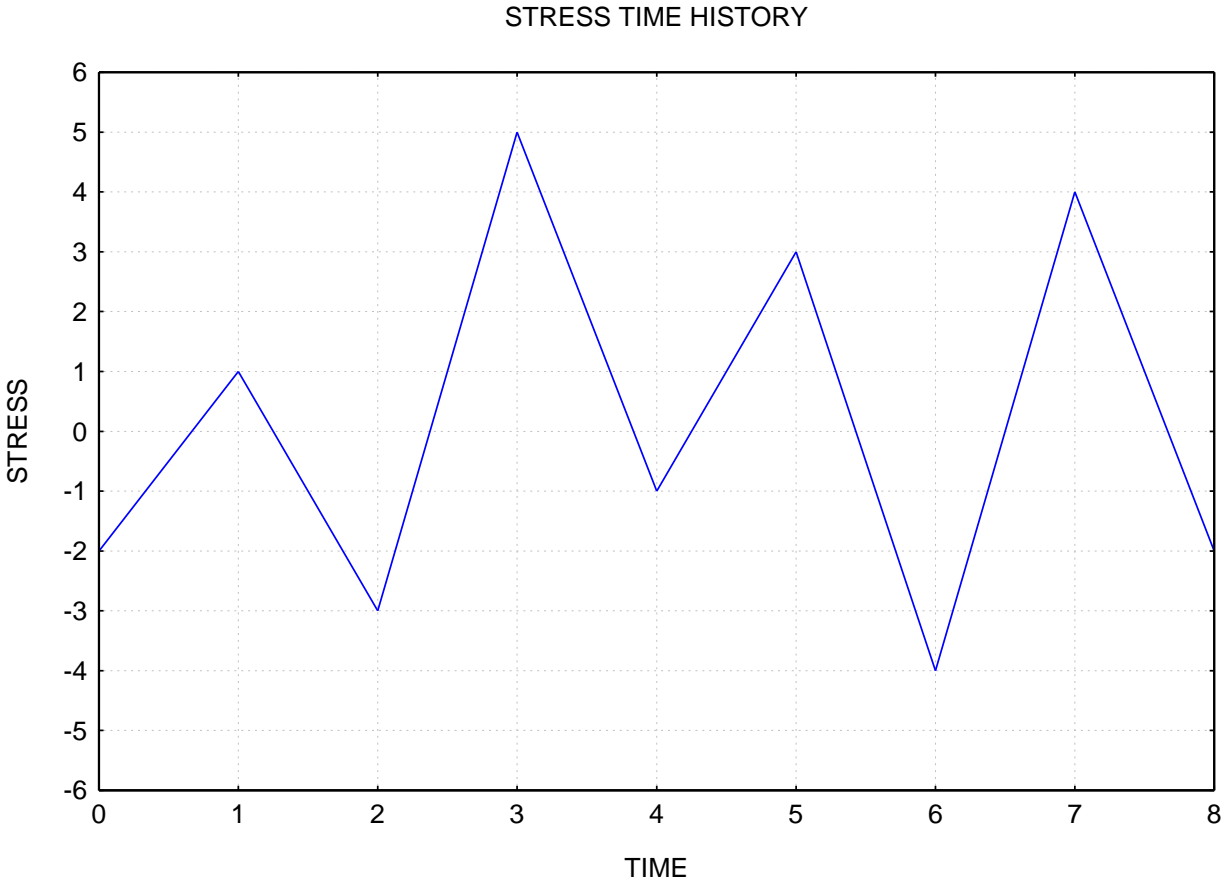


Figure 31.3.  Sample Time History

Rainflow cycle counting can be performed on sine, random, sine-on-random, transient, steady-state, stationary, nonstationary, or any oscillating response signal whatsoever.  The counting methods ignore the time unit, because it is only concerned with the order of the coordinates.  Stress is used in the sample time history in the above figure, but the amplitude metric could be acceleration, velocity, displacement, etc.

The time history is rotated 90 degrees clockwise in the next figure.  The black lines in this figure represent the rainflow streams down the "roof" sections.  ASTM E1049–85, section 5.4.4 has rules for stream junctions in terms of which stream may continue and which must end.   The streams are counted either as one-half or one whole cycle accordingly.   Note that the amplitude is one-half of the range.

## RAINFLOW PLOT
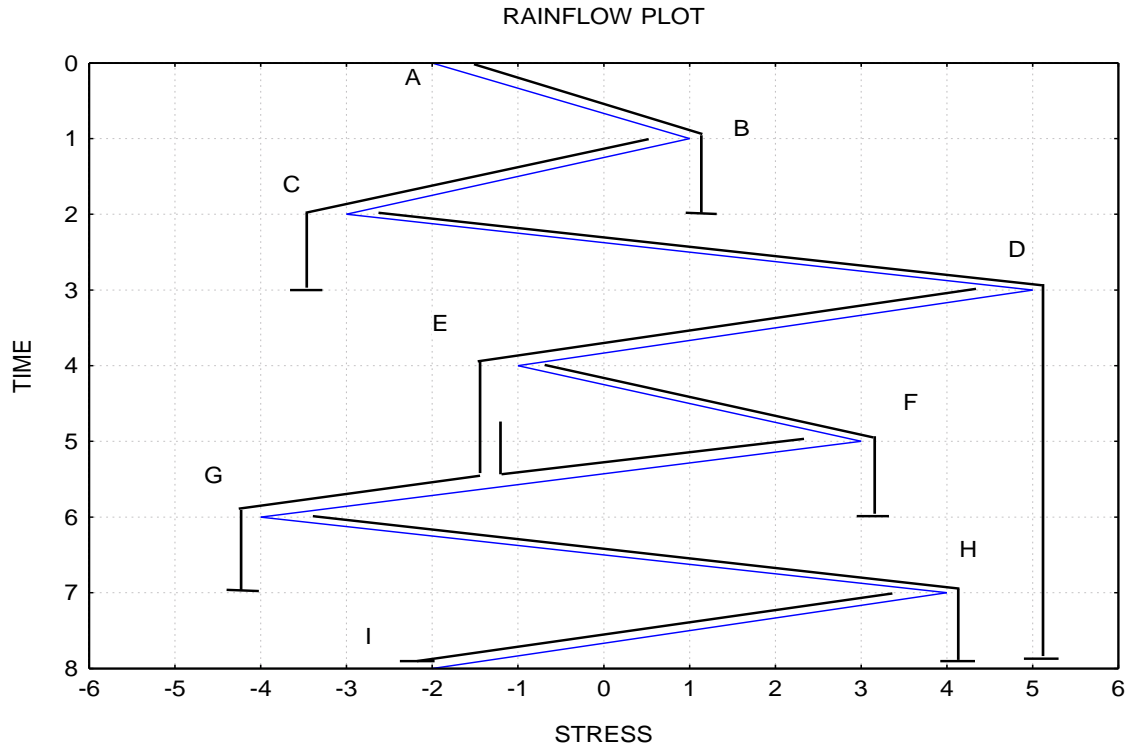


| Stream | Stream Description | Cycles | Range |
|--------|--------------------|--------|-------|
| A to B | The A to B stream ends when it encounters the C to D stream which began to the left of A. | 0.5 | 3 |
| B to C | The B to C stream ends when it encounters the B to G stream which began to the right of B. | 0.5 | 4 |
| C to D | The C to D stream ends at the ground. | 0.5 | 8 |
| D to G | The D to E to G stream ends at the ground. | 0.5 | 9 |
| E to F | The E to F half-cycle stream ends when it encounters the G to H stream which began to the left of E.  It picks up an additional half-cycle from the leftward flow starting from F which yields to the D to G stream | 1.0 | 4 |
| G to H | The G to H stream ends at the ground. | 0.5 | 8 |
| H to I | The H to I stream ends at the ground. | 0.5 | 6 |

Figure 31.4. Sample Time History Rotated 90 degrees Clockwise

### 31.3.2 Relative Fatigue Damage

The cycle counting results are typically sorted into bins by range per industry practice to simplify the damage summation calculation.   But this step is unnecessary because each coordinate pair can be fed directly into the relative damage summation.  Furthermore, direct input is more accurate for the damage summation since binning requires rounding the ranges.

The relative fatigue summation is similar to the Palmgren-Miner rule.

$$D = \sum_{i=1}^{m} A_i{}^b \, n_i \tag{31.1}$$

The damage index D is only intended as a comparison metric for a given response rainflow cycle data set.  It is not used to predict absolute failure.  The amplitude A is a response metric.  It is typically the absolute acceleration response in this document, but the pseudo velocity could be used instead.

The approach in the above damage equation is Basquin-like because it assumes an S/N curve that is a straight line in log-log format.

### 31.4  MATLAB RAINFLOW CYCLE COUNTING

The Matlab Signal Processing Toolbox has a rainflow function that was introduced in R2017b. The function is based on ASTM E1049−85.

See:   https://www.mathworks.com/help/signal/ref/rainflow.html

Let x be a set of amplitude points from a response time history.  The Matlab command is:

    c=rainflow(x);

The output array c has five columns:   Count, Range, Mean, Start, and End

Only the first two columns are needed for the damage calculation.  The relative damage d can then be calculated for a fatigue exponent b by the following code snippet. Again, the amplitude is one-half of the range.

    cycles=c(:,1);
    amp=c(:,2)/2;
    d=sum( cycles.*amp.^b )

A Matlab function for implementing the rainflow and relative damage equations is given at: https://www.mathworks.com/matlabcentral/fileexchange/127224-rainflow-fatigue-relative-damage

A Matlab function that combines the SDOF response to an acceleration base input, rainflow cycle counting, and the damage calculation is given at:

https://www.mathworks.com/matlabcentral/fileexchange/127229-sdof-response-to-acceleration-base-input-with-rainflow

## 31.5  FREQUENCY DOMAIN

### 31.5.1  Spectral Moments

$j^{th}$ spectral moment for a PSD:

$$m_j = \int_0^\infty f^j \, G(f) df \qquad (31.2)$$

Expected peak rate:

$$\nu_p = \sqrt{m_4/m_2} \qquad (31.3)$$

Estimated rate of zero up crossings:

$$\nu_0^+ = \sqrt{m_2/m_0} \qquad (31.4)$$

### 31.5.2  Dirlik Method

Several methods have been derived for performing rainflow cycle counting for a response PSD [61].  Note that they tend to be conservative.  The Dirlik method [62], [63] is an example of a semi-empirical method for cycle identification and is widely used in industry.  The Dirlik equation is based on the weighted sum of the exponential and two Rayleigh distributions.

The immediate output of the Dirlik method is a "Cumulative Histogram of Range (peak-valley)." This can readily be converted into individual cycles with their respective amplitudes. Again, note that the amplitude is one-half of the range. The continuous probability function before normalization is:

$$p_{dk}(Z(s)) = \left\{ \frac{D_1}{\widehat{Q}} \exp\left(-\frac{Z}{\widehat{Q}}\right) + \frac{D_2 Z}{R^2} \exp\left(\frac{-Z^2}{2R^2}\right) + D_3 Z \exp\left(\frac{-Z^2}{2}\right) \right\} \frac{1}{2\sqrt{m_0}} \tag{31.5}$$

$$D_1 = \frac{2(x_m - \gamma^2)}{1 + \gamma^2} \tag{31.6}$$

$$D_2 = \frac{1 - \gamma - D_1 + D_1^2}{1 - R} \tag{31.7}$$

$$D_3 = 1 - D_1 - D_2 \tag{31.8}$$

$$\widehat{Q} = \frac{1.25(\gamma - D_3 - D_2 R)}{D_1} \tag{31.9}$$

$$R = \frac{\gamma - x_m - D_1^2}{1 - \gamma - D_1 + D_1^2} \tag{31.10}$$

$$\gamma = \frac{m_2}{\sqrt{m_0 m_4}} \tag{31.11}$$

$$x_m = \frac{m_1}{m_0} \sqrt{\frac{m_2}{m_4}} \tag{31.12}$$

444

Dirlik Damage Index:

$$D_{dk} = \frac{\nu_p\, T}{\hat{A}}\, m_0{}^{b/2} \left[ D_1\, \hat{Q}^{\,b}\Gamma(1+b) + \left(\sqrt{2}\right)^b \Gamma\left(1 + \frac{b}{2}\right)\left(D_2|R|^b + D_3\,\right)\right] \qquad (31.13)$$

The Dirlik index becomes a relative index for $\hat{A} = 1$. The Palmgren-Miner summation is effectively embedded in equation (31.13).

A Matlab Dirlik function for a response PSD is given at:

https://www.mathworks.com/matlabcentral/fileexchange/127239-dirlik-relative-damage-for-response-psd

A Matlab Dirlik function for an SDOF response to a base input PSD is given at:

https://www.mathworks.com/matlabcentral/fileexchange/127244-dirlik-relative-damage-for-sdof-response-to-base-input-psd

## 31.6  FATIGUE DAMAGE SPECTRUM

The FDS function uses the SDOF system model in Figure 25.1   The base input for an FDS can be either a time history or a PSD.  The SRS and VRS calculations have two independent variables, fn & Q, in addition to a base input function.  The FDS has these same variables plus the fatigue exponent b.  The calculation in equation (31.1) is repeated for each fn, Q & b combination of interest.  The FDS is plotted as a function of natural frequency with the Q & b values noted in the plot's title.  The Y-axis label is damage raised to exponent b.

Table 31.1.  Fatigue Damage Spectrum Calculation, Time History & PSD Methods

| Step | Time Domain | Frequency Domain |
|------|-------------|------------------|
| 1 | Base Input Acceleration Time History | Base Input Acceleration PSD |
| 2 | SDOF Response Acceleration Time History via Digital Recursive Filtering Relationship for given fn & Q, Equation (26.9) | SDOF Response Acceleration PSD via Power Transmissibility for given fn & Q, Equation (24.22) |
| 3 | Rainflow Cycle Count, ASTM E1049–85 | Spectral Moments Calculation, Section 31.5.1 |
| 4 | Relative Damage Summation for each Fatigue Exponent b, Equation (31.1) | Relative Damage Calculation via Dirlik Method for each Fatigue Exponent b, Equation (31.13) |

A Matlab function for the FDS time domain is given at:

https://www.mathworks.com/matlabcentral/fileexchange/127254-fds-for-a-base-input-acceleration-time-history

A Matlab function for the FDS frequency domain method is given at:

https://www.mathworks.com/matlabcentral/fileexchange/127264-fds-of-base-input-acceleration-psd-via-the-dirlik-method

Each of these FDS functions allows for multiple Q & b combinations.

## 31.7  SAMPLE CASES

### 31.7.1 Time & Frequency Domain FDS Comparison
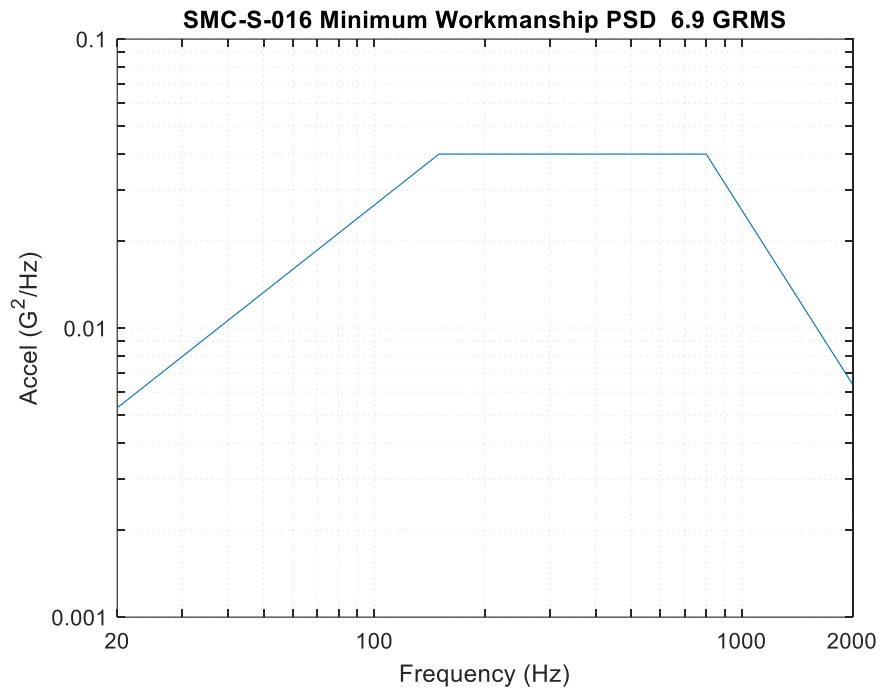


Figure 31.5.   SMC-S-016 Minimum Workmanship PSD

A sample PSD is shown in the above figure.  The corresponding duration is 60 seconds.  A time history [9] is synthesized to satisfy the PSD as shown in Figure 31.6 with verification that it meets the PSD in Figure 31.7.   The fatigue damage spectrum is calculated both from the direct PSD and from the indirect time history, for Q=10 and b=4.  The two FDS curves have excellent agreement as shown in Figure 31.8.

---

[9] The  synthesized  time  history  is  not  unique  because  the  PSD  does  not  specify  phase.   The resulting FDS will likewise not be unique.  The FDS statistical distribution is a topic for future research.
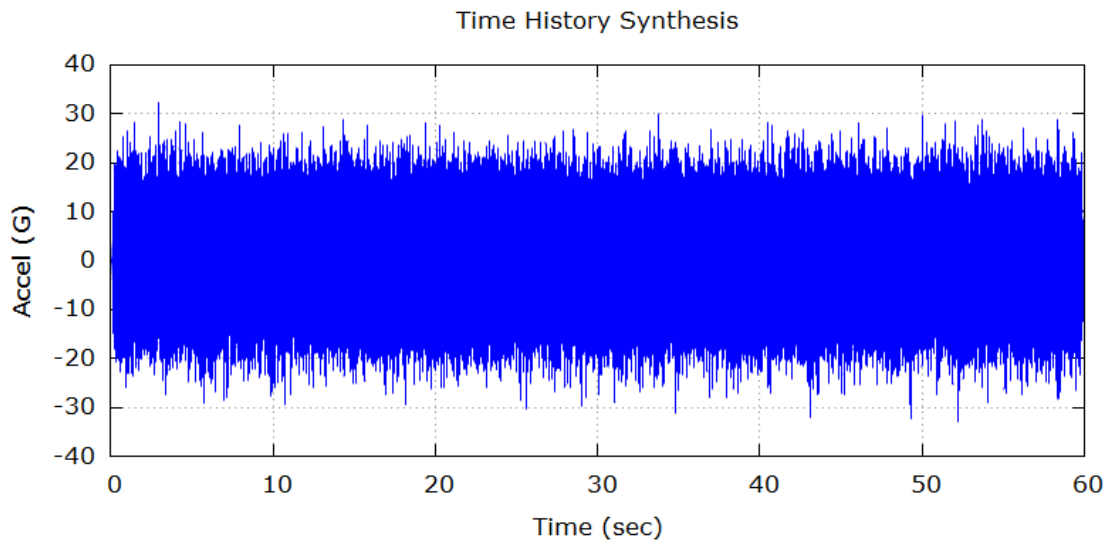
Figure 31.6.   SMC-S-016 Time History Synthesis for PSD
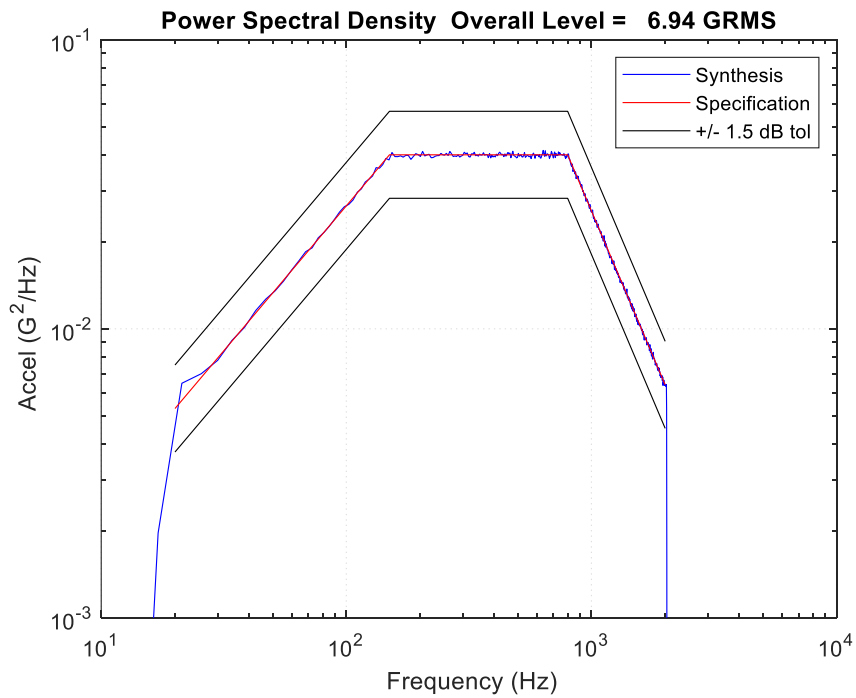


Figure 31.7.   SMC-S-016 Synthesis Verification
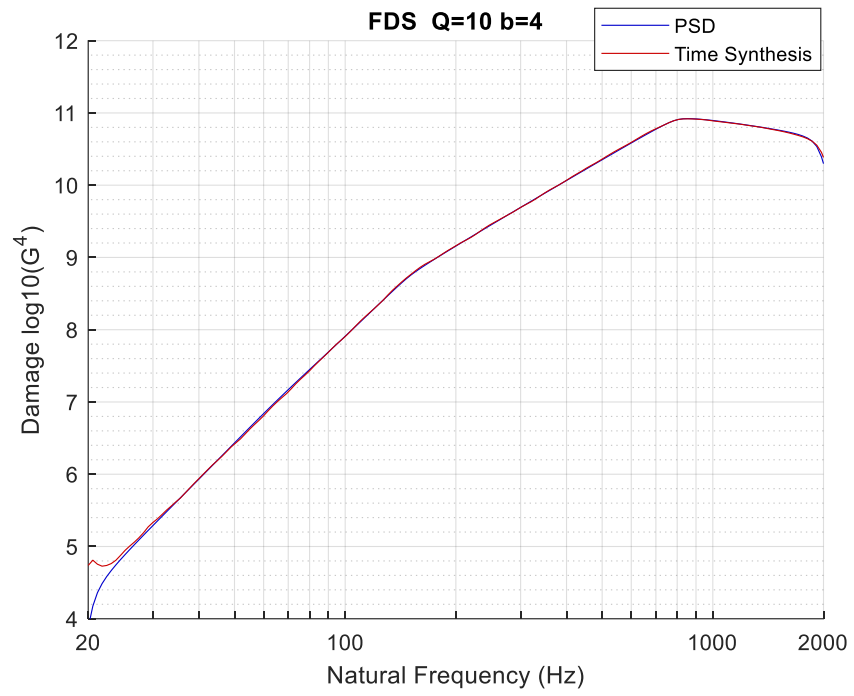
Figure 31.8.   FDS Comparison

## 31.7.2 Nonstationary Acceleration Enveloping to Derive a PSD via FDS
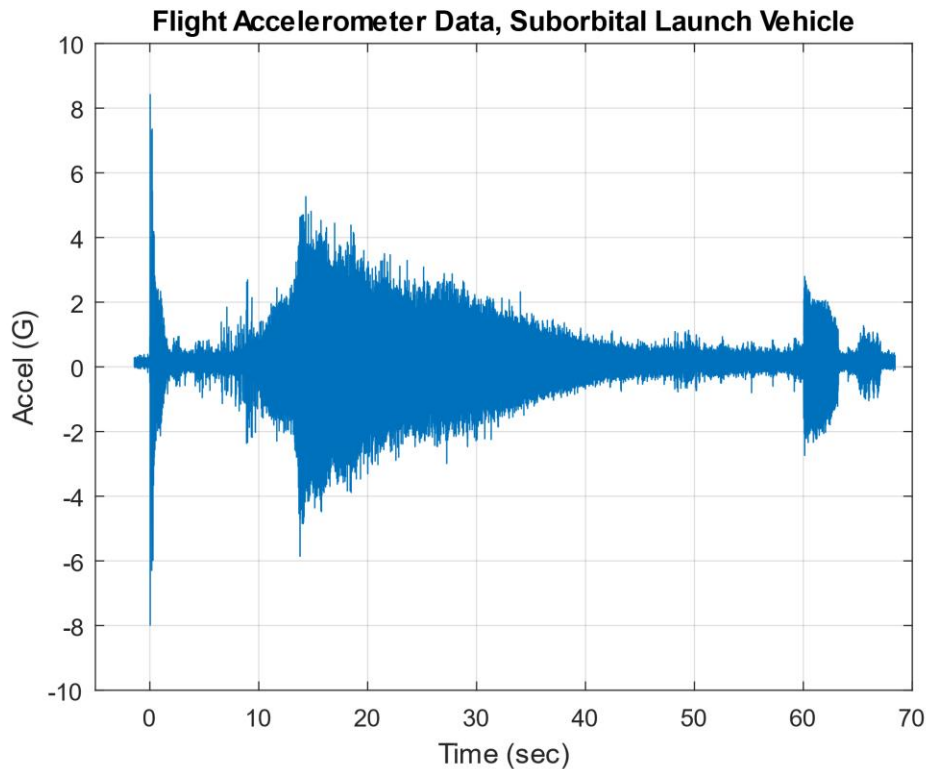


Figure 31.9.   Nonstationary Time History

The time history in the above figure was previously shown in Figure 21.1.  Now assume that a PSD must be derived to cover the flight data.  PSD specifications imply that the corresponding time history is stationary and Gaussian for analysis and test purposes regardless of the source time history characteristics.  The historical approach assumes "piecewise stationary" segments, with one-second windows and 50% overlap or some variation.  A PSD is then calculated for each segment, perhaps in one-twelfth octave format.  The final PSD is the maximum envelope of the individual PSDs.  A simplified PSD is then derived from the PSD envelope.  Obviously, this method can be overly-conservative for nonstationary data.

A more realistic envelope PSD can be derived via fatigue damage spectrum justification. [37] This method is demonstrated for the nonstationary time history in Figure 31.9 in the following plots.
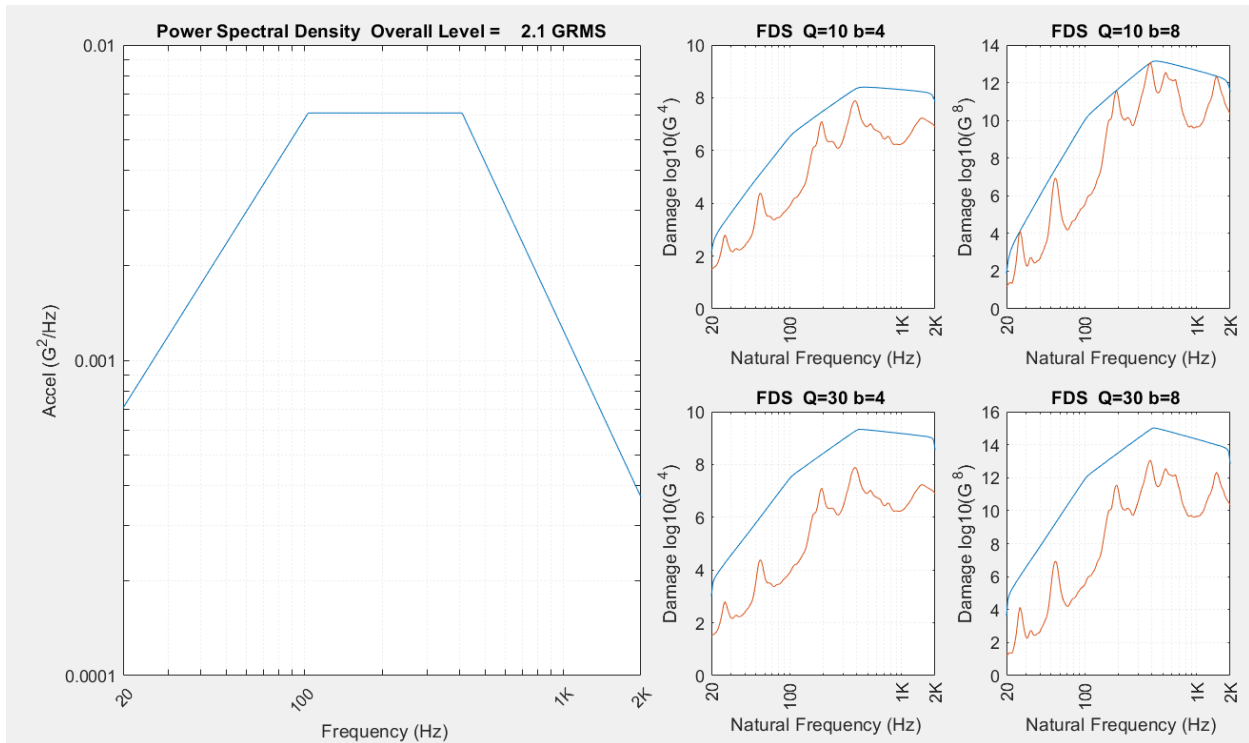
Red FDS curves are from flight data.  Blue curves are from the envelope.

| Freq (Hz) | Accel (G^2/Hz) |
|-----------|----------------|
| 20        | 7.1E-04        |
| 104       | 6.1E-03        |
| 408       | 6.1E-03        |
| 2000      | 3.7E-04        |

Figure 31.10.   Nonstationary Time History Envelope PSD

The method shown here uses trial-and-error with convergence.   Several simplified candidate PSDs are generated.  A set of FDS functions is calculated for each candidate PSD as well as for the nonstationary time history.   Four combinations are used for the Q and b parameters. Each candidate PSD is scaled so that its FDS functions envelop the corresponding flight data FDS.  The winning candidate is the "optimized PSD" which has the lowest combination of overall acceleration, velocity, and displacement or some other goal.   A general purpose ramp-plateau-ramp shape was chosen for this PSD example, but other shapes could have been used.
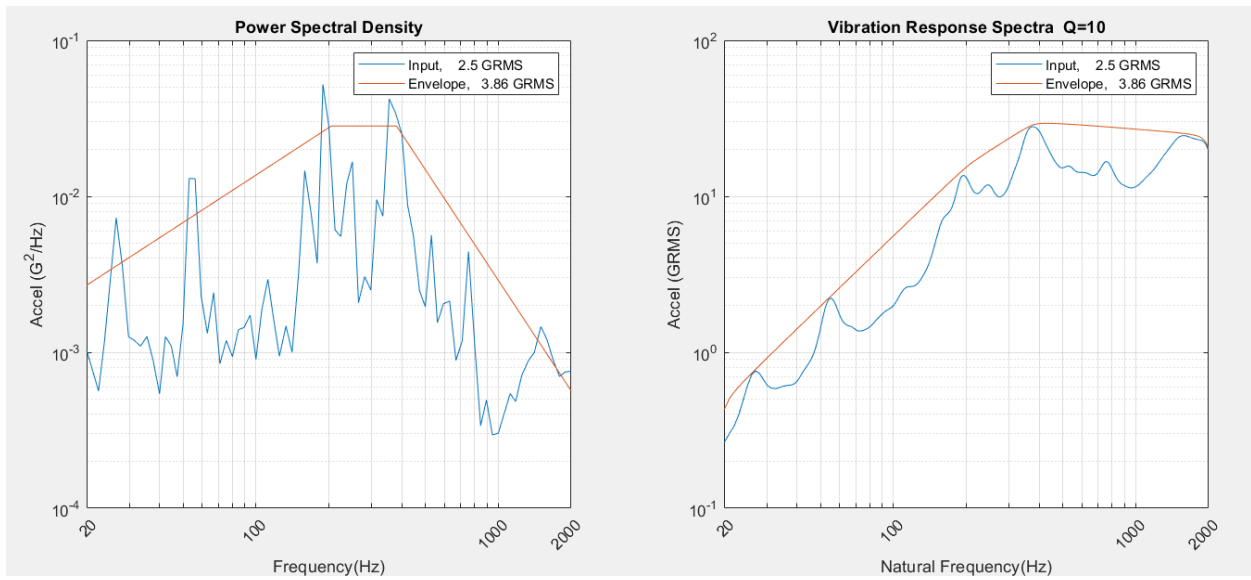
Figure 31.11.   Piecewise Stationary Method with Peak Clipping via VRS Justification

The red PSD curve is the maximum envelope of the individual PSDs over one-second segments with 50% overlap.

There are industry rules of thumb for allowable peak clipping margins.  But the VRS method is more sensible, as previously shown in Section 25.4.

452
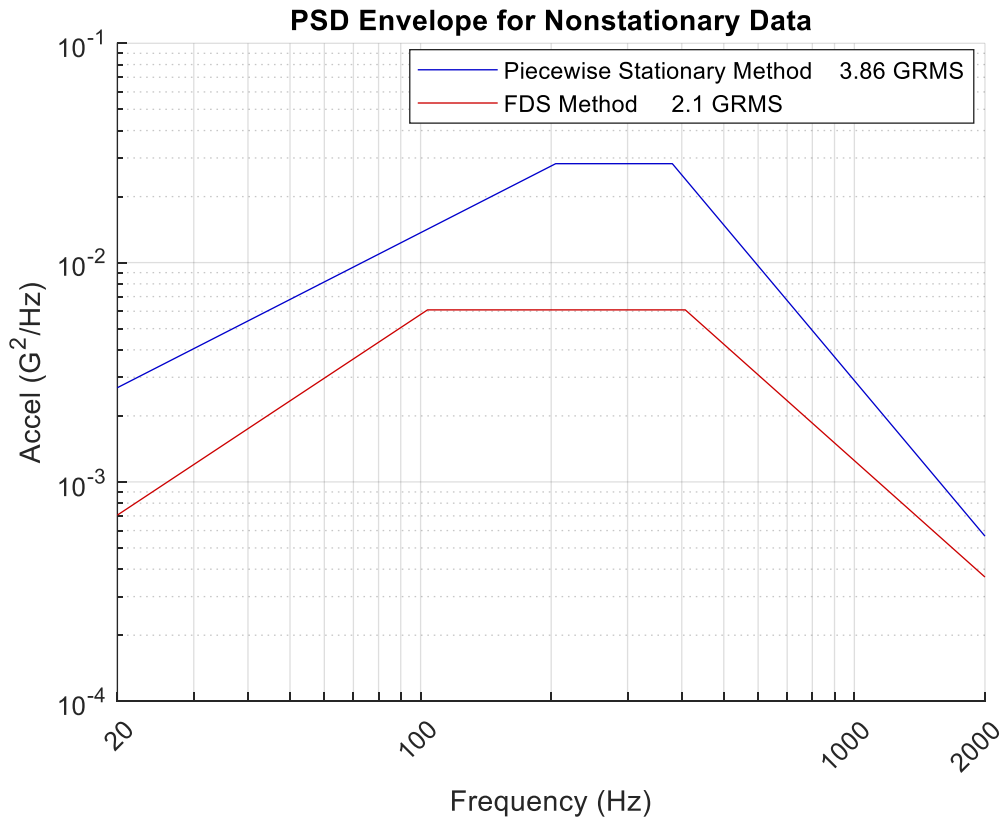
Figure 31.12.   Enveloping Method Comparison

The FDS method yields a PSD that is 5.3 dB less than the traditional piecewise stationary method in terms of the overall level.

# 32  SHAKER TABLE VIBRATION TESTING

## 32.1  SHAKER CONTROL
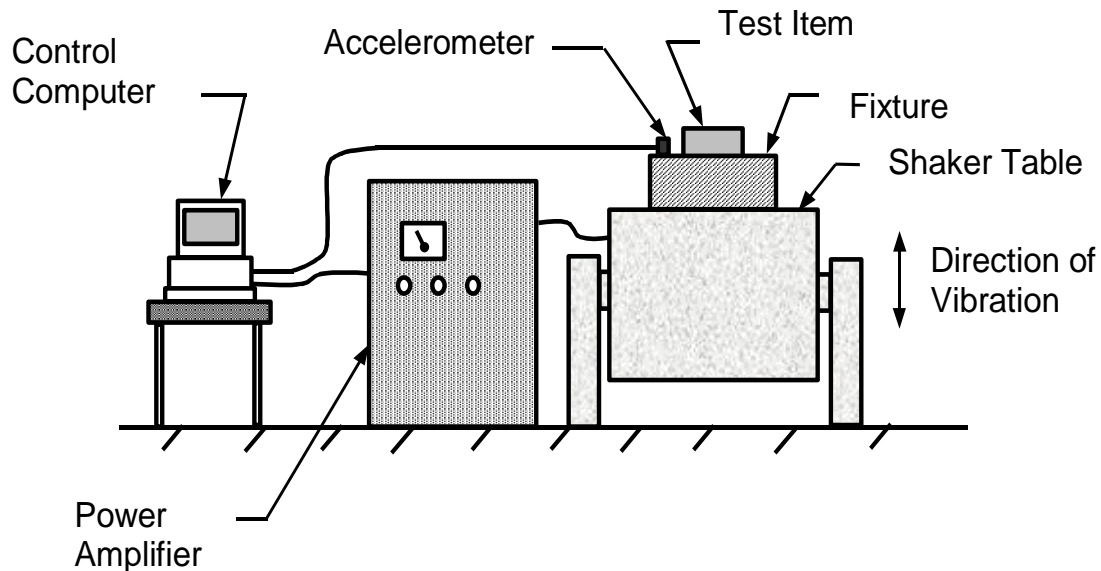


Figure 32.1.   Shaker System

### 32.1.1 Test Overview

An electromagnetic shaker is conceptually similar to an audio speaker, with a field coil and armature. Consider a PSD base input test.   The test article is mounted to the shaker via a fixture.   The control computer applies a very low voltage signal to the shaker via the power amplifier.   The control accelerometer on top of the fixture returns a voltage signal to the computer, forming a feedback loop.  This is called a "loop check."

The computer converts the return voltage signal to acceleration via the accelerometer's sensitivity factor and calculates a frequency-dependent gain factor for the system.

The computer synthesizes an acceleration time history to satisfy the PSD, which must be converted to a voltage time history accounting for the gain factor.   The computer outputs this signal to the power amplifier and shaker.

The test proceeds at -12 dB relative to the nominal specification and dwells for 30 seconds or so, depending on control stability.   The gain will be repeatedly recalculated during the test given potential nonlinearities, fixture resonances, etc.   The voltage drive signal is updated accordingly.   The computer will need to "notch" the voltage signal at any shaker head or fixture resonant frequencies within the specification bandwidth.   Ideally, there would be no test equipment resonances in the bandwidth, but they tend to occur in practice for specifications up to 2000 Hz.

The test proceeds at 3 dB increments with a dwell at each level.   This process is called "equalization."  Finally, the full-level test is performed for the specified duration.

### 32.1.2  Control Strategies

The diagram in Figure 32.1 is simplified.  At least two control accelerometers should be present for stability due to potential spatial variation in the vibration level across the top of the fixture. This variation could be due to shaker rocking modes, fixture resonances, etc.   The most common control method is to take the average PSD value from the control accelerometers at each frequency.  Another method is "maximum line" or "extremal" control where the peak PSD value is taken for the set of accelerometers at each frequency.

Some test items and fixtures are so unwieldy that control accelerometers may be needed on the test item itself with maximum line control.

In addition, reference accelerometers may be mounted on the item to measure transmissibility functions, from which natural frequencies and damping ratios can be extracted.  This applies to both PSD and sine sweep base inputs.

### 32.1.3  Electronic Test Items

Electronic components should be powered and monitored before, during, and after the vibration test.   Note that some failure or malfunction modes such as relay chatter may only be present during vibration, as discussed in Section 4.3.5.  Monitoring is also important because the test should be stopped immediately if a failure occurs.

### 32.1.4  PSD Bandsplitting

Some PSD test specifications are too high in amplitude for a given shaker system.  Bandsplitting can be cautiously used in these cases.

Here is an excerpt from Reference [64]:

When the test level cannot be achieved, apply Band-Splitting to the spectrum which cannot be tested. The preferred test method for the selection of the band separation shall be to start at the lowest test frequency and extend the first Split Band to the highest energy/frequency level attainable. Start Band 2 at the end of Band 1, etc. No more than 4 Bands are allowed. The resultant band selection shall be evaluated to assure reasonability, avoid splitting at known resonances, etc. Efforts should be made to minimize the number of bands and to make the actual test bands approximately of equal energy content.

The following is a numerical experiment to assess whether bandsplitting is valid for fatigue. The results are affirmative except near the split frequency.
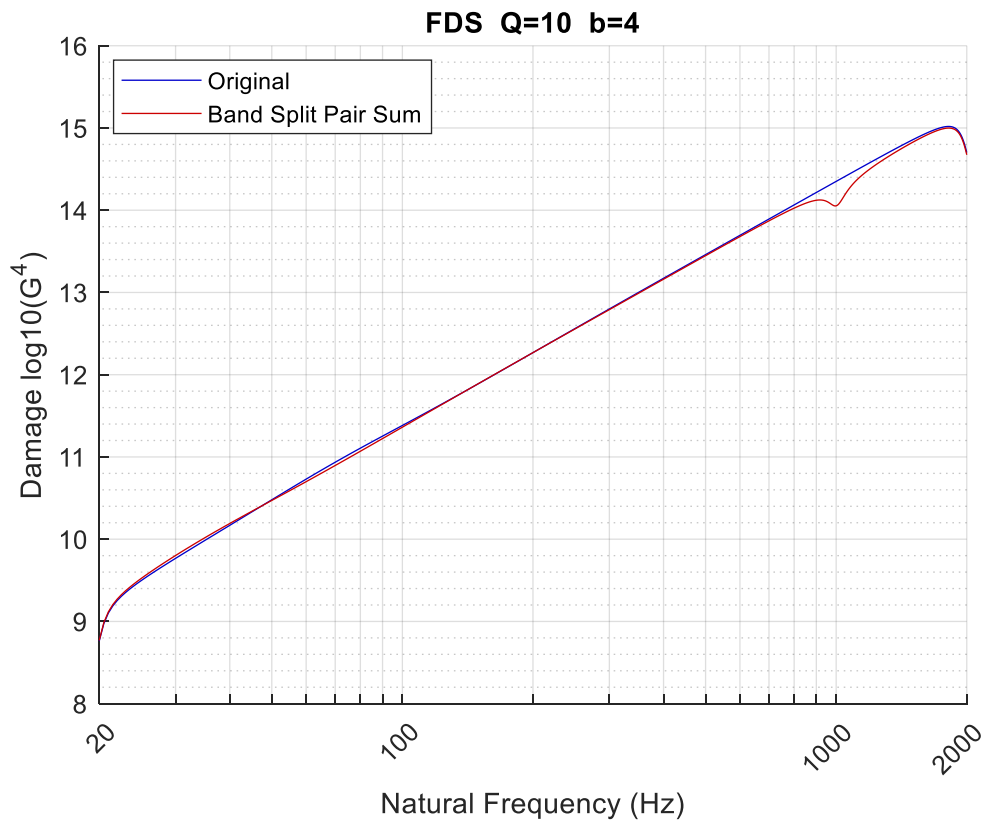


Figure 32.2.   FDS Comparison

The input PSD was band-limited white noise with an amplitude of 1 G^2/Hz over 20 to 2000 Hz. The duration was 120 seconds. The fatigue damage spectrum (FDS) of this input PSD is shown as the Original curve in Figure 32.2. The FDS represents the response of single-degree-of-freedom spring-mass systems.

Next, the original PSD was split into two PSDs, one from 20 to 1000 Hz and the other from 1000 to 2000 Hz, with a duration of 120 seconds each. An FDS was calculated for each of these two split PSDs. Fatigue damage accumulates linearly with time, so the two FDS functions were added together as shown in the red curve. The Original and Band Split FDS are very close except that the Split FDS is lower at the 1000 Hz dividing frequency. The band split frequency should be chosen so that it is well separated from the test item's natural frequency. Another approach would be to allocate a small amount of overlap between the bands near 1000 Hz to bring the two FDS curves together at this frequency.

## 32.1.5 Time-Level Equivalence

There is a practice within vibration testing that allows a either higher or lower PSD level to be substituted for the nominal level with an appropriate change in duration. A higher level would have a lower duration and vice-versa with respect to the nominal specification. The goal is to maintain constant relative fatigue damage, as discussed in Section 31.

The approach assumes that the test item has a linear response and that its potential failure mode would be the same for the new level and duration.

Here is another excerpt from Reference [64]:

> When levels are not attainable by Band-Splitting, impose a time/level trade. Split the spectrum into 4 Bands of equal energy content, and run each at the maximum level attainable by the test equipment. Run the bands for an extended time in accordance with the method of calculation which follows:

$$T_{Test} = ( Grms_{Specified} / Grms_{Attainable})^Y \times T_{Specified}$$

where:

$T_{Test}$ = New Test Duration (seconds)

$Grms_{Specified}$ = Required Overall Test Level (Grms)

$Grms_{Attainable}$ = Actual Overall Test Level Attainable by Test Equipment (Grms)

$Y$ = Exponent Determined by characteristics of Test Article

$T_{Specified}$ = Required Test Duration Corresponding to Full Vibration Levels (seconds)

The value of Y must be chosen to best characterize the construction and materials specific to each test item. This must be a case-by-case evaluation coordinated with the contracting organization and/or the technical representative. Examples of exponents (Y) and corresponding previous use values are:

| Item | Y |
|---|---|
| Electrical Black Boxes | 4.0 |
| Stainless Steel Feed Lines and Bellows | 5.3 |
| Hydraulic Actuators | 5.3 |
| Electrical Connectors | 5.0 |
| Ordnance | 5.3 |

## 32.1.6 Generalized Time-Level Equivalence

Steinberg [18] gives the following equivalence formula.

$$T_1 G_1{}^b = T_2 G_2{}^b \qquad\qquad (32.1)$$

where each $G$ value is in terms of GRMS

The fatigue exponent b is taken as 6.4 for PCB-component lead wires.

A good approach for time scaling is to take upper and lower fatigue exponent estimates to bound the problem. A smaller b is more conservative for scaling to a higher level at a shorter duration.

## 32.2  TEST FIXTURES
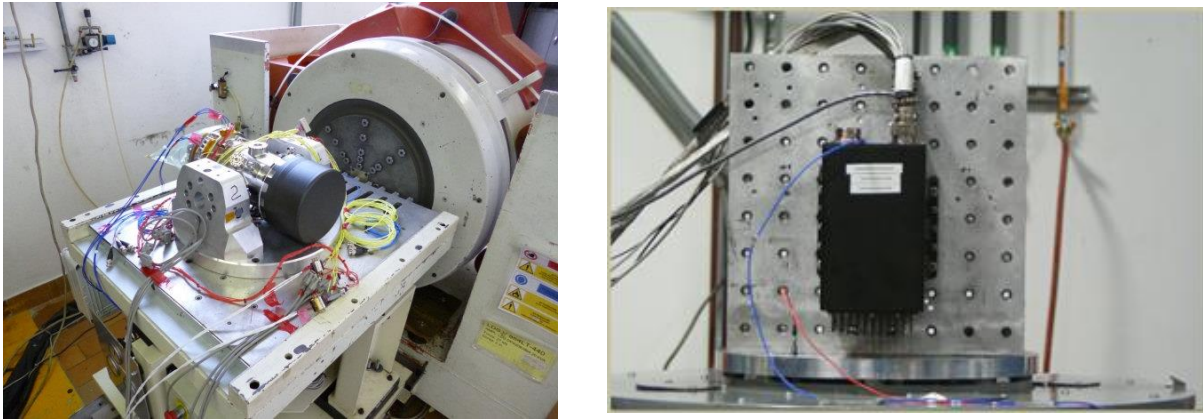


Figure 32.3.   Typical Vibration Test Fixtures

### 32.2.1 Materials

The fixture transfers the mechanical vibration from the shaker table to the test article.

The best vibration fixtures are simple, rigid, and lightweight with the minimum number of features.  Shaker and power amplifier systems are limited in terms of voltage, current, and force pounds.  Lighter fixtures are needed to achieve higher acceleration levels.

Aluminum alloy is a good choice for small to medium fixtures because it is cheaper than other materials such as magnesium.  Aluminum 6061-T6/T651 & 7075-T6 are suitable alloys. Aluminum 6061 is weldable.  Aluminum 7075 is not suitable for welding, however, since the heat-affected zones of the weld in this alloy are very prone to fatigue cracking and stress-corrosion cracking while in service.

Magnesium is a better choice than aluminum in terms of weight-to-stiffness ratio and can provide higher damping.  Magnesium Zirconium K1A alloy in cast form has excellent hysteresis damping. Magnesium Alloy AZ31B-Tool Plate also has very good damping.  It is a free-machining material with good weldability properties.

Fixtures should have high damping to limit their resonant response.   Higher damping also provides a transmissibility ratio relatively closer to unity gain across the entire frequency spectrum.

32.2.2 Joints

Some fixtures require joints. Bolted joints have more damping than welded ones. But welded joints have more rigidity if they are continuous.

Welded joints can be used with caution. They may have material distortion and high residual stress from thermal expansion and contraction during the welding process. After welding and before machining, the fixture should be left overnight in an oven at 250 °C to reduce warping and residual stress.

Welded joints may also have porosity, inclusions, and microcracks. Some amount of microcracking is inevitable but needs to be managed via inspection and fracture calculations. The quality of the weld is paramount. The weld joints should be continuous and smooth, with two or even three passes if possible.

32.2.3 Helical Coil & Key Inserts

Fixtures and adapter plates require mounting holes to accommodate the test article. Helical Coils and Key Inserts are two ways to strengthen a connection between soft materials such as aluminum and magnesium.

Figure 32.4.  Keenserts (useful photo but not a test fixture)

# 33 Maximum Prediction Environment

## 33.1 INTRODUCTION

Shock and vibration test levels are typically derived from maximum predicted environment (MPE) levels.[10] MPEs are preferably derived from measured accelerometer data on a vehicle or system in a test or field application. The MPEs include some uncertainty margin over the reference data due to potential variation, such as flight-to-flight variation in a launch vehicle. This section contains industry guidelines for deriving MPEs.

## 33.2 SMC-S-016 EXCERPT

The following is from SMC-S-016, 3.51 Statistical Estimates of Vibration, Acoustic, and Shock Environments

Qualification and acceptance tests for vibration, acoustic, and shock environments are based upon statistically expected spectral levels. The level of the extreme expected environment used for qualification testing is that level not exceeded on at least 99% of flights, and estimated with 90% confidence (P99/90 level). The level of the maximum expected environment used for acceptance testing is that not exceeded on at least 95% of flights, and estimated with 50% confidence (P95/50 level). These statistical estimates are made assuming a lognormal flight-to-flight variability having a standard deviation of 3 dB, unless a different assumption can be justified. As a result, the P95/50 level estimate is 4.9 dB above the estimated mean (namely, the average of the logarithmic values of the spectral levels of data from all available flights).

When data from N flights are used for the estimate, the P99/90 estimate in dB is 2.0 + 3.9/N^(1/2) above the P95/50 estimate. When data from only one flight are available, those data are assumed to represent the mean, and so the P95/50 is 4.9 dB higher and the P99/90 level is 6 dB higher than the P95/50 level. When ground testing produces the realistic flight environment (e.g., engine operation or activation of explosive ordnance), the statistical distribution can be determined using the test data, provided data from a sufficient number of tests are available.

---

[10] Maximum Expected Flight Level (MEFL) is an equivalent term for aerospace vehicles.

## 33.3 COMMENTARY

P95/50 means that there is a 50% chance of 1 exceedance in 20 flights.

SMC-S-016 defines the MPE for vibration, shock, and acoustic environments at a P95/50 statistical level.  The P95/50 MPE is defined as 4.9 dB above the log-mean of the available flight data set to account for flight-to-flight variability.  This approach is based on measurements of 24 static firings and over 40 flight tests which define a standard deviation sigma of 3 dB.   From the normal tolerance limit table, the statistical factor Z at P95/50 with a large number of samples is 1.64.  Therefore, the 4.9 dB is calculated from 3 dB x 1.64.  As a result, the P95/50 level is defined as 4.9 dB above the log-mean level.

The log-mean is just the average of the logarithmic of the spectral values at each frequency of all the available flight data sets.  The reason for calculating the log-mean is that each spectral value of each data set is considered as log-normally distributed.  That is the normal distribution of the logarithmic value of the spectral values at each frequency.

## 33.4  TYPICAL AEROSPACE INDUSTRY PRACTICE

A data point could be a value from a PSD, SRS, or SPL at a given frequency from measured flight or test data.

If only one data point is available, add 4.9 dB to derive the P95/50 level MPE.

If two data points are available, add 4.9 dB to the log-mean to derive P95/50 level MPE.

If three or more data points are available, calculate the true P95/50 MPE.

## 33.5  NORMAL TOLERANCE LIMIT

The normal tolerance method assumes

1.  The population has either a normal or log-normal distribution.
2.  The samples are selected at random.

The problem is to find a tolerance factor $K$ that will yield an upper limit that covers at least $100\beta$ percent of the population with a confidence of $100\gamma$ percent as expressed by

$$P[F(\text{ mean} + K(\text{std dev}) ) \geq \beta] = \gamma \qquad (33.1)$$

where  $F$ is a cumulative distribution function.

The normal tolerance limit is calculated from the mean and standard deviation of a sample set of data points.

$$\text{Limit} = \text{mean} + K \,(\text{std dev}) \tag{33.2}$$

The K factor depends on the number of samples and needed conservatism.

## 33.6  LOG-NORMAL OPTION

The data samples are converted to base ten logarithms.  The mean and standard deviation of the log data are then inserted into equation (33.2).  The limit is then the anti-log as follows:

$$\text{Limit} = 10^{\wedge}[\,\log\text{ mean} + K \,(\log\text{ std dev})\,] \tag{33.3}$$

## 33.7  K-FACTORS, ONE-SIDED

Table 33.1.  Normal Distribution Tolerance K Factors for Upper Tolerance Limit (Ref [65])

| n | $\gamma$=0.50 | | | $\gamma$=0.75 | | | $\gamma$=0.90 | | |
|---|---|---|---|---|---|---|---|---|---|
| | $\beta$=0.90 | $\beta$=0.95 | $\beta$=0.99 | $\beta$=0.90 | $\beta$=0.95 | $\beta$=0.99 | $\beta$=0.90 | $\beta$=0.95 | $\beta$=0.99 |
| 3 | 1.50 | 1.94 | 2.76 | 2.50 | 3.15 | 4.40 | 4.26 | 5.31 | 7.34 |
| 4 | 1.42 | 1.83 | 2.60 | 2.13 | 2.68 | 3.73 | 3.19 | 3.96 | 5.44 |
| 5 | 1.38 | 1.78 | 2.53 | 1.96 | 2.46 | 3.42 | 2.74 | 3.40 | 4.67 |
| 7 | 1.35 | 1.73 | 2.46 | 1.79 | 2.25 | 3.13 | 2.33 | 2.89 | 3.97 |
| 10 | 1.33 | 1.71 | 2.42 | 1.67 | 2.10 | 2.93 | 2.06 | 2.57 | 3.53 |
| 15 | 1.31 | 1.68 | 2.39 | 1.58 | 1.99 | 2.78 | 1.87 | 2.33 | 3.21 |
| 20 | 1.30 | 1.67 | 2.37 | 1.53 | 1.93 | 2.70 | 1.76 | 2.21 | 3.05 |
| 30 | 1.29 | 1.66 | 2.35 | 1.48 | 1.87 | 2.61 | 1.66 | 2.08 | 2.88 |
| 50 | 1.29 | 1.65 | 2.34 | 1.43 | 1.81 | 2.54 | 1.56 | 1.96 | 2.74 |
| $\infty$ | 1.28 | 1.64 | 2.33 | 1.28 | 1.64 | 2.33 | 1.28 | 1.64 | 2.33 |

# 34 THE GREAT SPACECRAFT BASE INPUT VIBRATION TEST DEBATE

## 34.1 DEBATE INTRODUCTION



Figure 34.1.  Shaker Table Vibration Test

Engineers prepare the MESSENGER spacecraft for a vibration test on a shaker table at The Johns Hopkins University Applied Physics Laboratory, Laurel, Maryland.  The purpose of this test is to verify that the spacecraft can withstand the launch vehicle environment during liftoff and ascent.

Flight-configured spacecraft are subjected to base input vibration tests for certain programs. The spacecraft are often one-of-a-kind, so the vibration test is effectively a proto-qualification test covering both design and workmanship verification. The tests may be sinusoidal or random. The sine vibration is typically at low frequencies, below 100 Hz. The author's colleagues are divided on whether these spacecraft system-level tests are prudent and effective.

## 34.2 ARGUMENTS AGAINST SPACECRAFT VIBRATION TESTING

The following assertions are made by A.M. Kabe and E. Perl from The Aerospace Corporation in informal working group meetings.

1. Vibration tables cannot replicate the impedance of the launch vehicle interface, nor the interaction that occurs between the launch vehicle and spacecraft when they are a coupled system; hence, the modes of vibration will not be the same as in flight.

2. Only translational motions are applied at the base, one axis at a time, whereas during flight, the launch vehicle/spacecraft system will vibrate simultaneously in all six degrees of freedom at each mass point and each interface point between the launch vehicle and spacecraft.

3. The total acceleration load during powered flight also depends on the spacecraft's rigid-body acceleration which a shaker cannot replicate.

4. Derivation of a "base input" environment from a few accelerometer locations at the launch vehicle/spacecraft interface will generally lead to an over-prediction of the motions at the interface since local deformations are mapped on the assumption that the interface acts as a rigid plane.

5. The use of (response)/(base motion) ratios to extract damping, a common practice, is not a valid approach for multi-degree-of-freedom systems it fails to account for the mode participation factor.

6. The test article may not include the actual spacecraft launch vehicle adapter or the propellant mass in the tanks because of safety and contamination concerns.

7. The test requirement forces the spacecraft organization to design its system to not only survive the launch environment but also to survive an artificial test that more often than not produces overly conservative loads in many parts of the structure while not adequately testing others.

8. The test can pose an unnecessary risk of damaging flight hardware late in the program.

Note that A.M. Kabe advocates acoustic reverberant chamber testing of spacecraft as a workmanship screen, as an alternative to base shake testing. He also favors shaker table vibration testing on a component or subsystem level.


## 34.3 ARGUMENTS FOR SPACECRAFT VIBRATION TESTING

The following justification points are made by NASA engineers Daniel Kaufman, Scott Gordon, Steve Hendricks, and Dennis Kern.

1. Essentially all current launch vehicle organizations (Delta, Atlas, Taurus, Pegasus, Ariane, HII, Proton, Long March, Falcon, etc.) specify and require or strongly recommend a spacecraft sine or random vibration test.

2. Testing is also required by NASA documents, such as References [66] and [67].

3. Insurance companies require vibration tests on all commercial communications satellites.

4. Some test facilities have the capability to perform simultaneous multi-axis vibration testing, as needed.

5. The vibration test provides qualification for tertiary/ancillary hardware that would not otherwise be tested. This includes: Cable harnesses, bellows, connectors, actuators, plumbing lines, waveguides, brackets, dampers, shades and shields, articulation & deployment mechanisms, shunt heaters, louvers, purge equipment, hinges, and restraints, blankets & supports.

6. The test provides an opportunity to determine the structural linearity in the operational vibration range of response. Note that linearity is typically assumed in coupled loads analysis (CLA).

7. Force limiting reasonably accounts for the interaction with the base motion and has been effectively employed in spacecraft vibration testing, thus reducing the potential for an over-test at the spacecraft's natural frequencies in the test configuration. The force limiting takes into account the CLA response levels.

8. Force gauges under the spacecraft provide a very accurate method of measuring and limiting to the CLA loads during the vibration test for mid to high apparent mass modes.

9. Numerous case histories have shown that vibration testing is effective for uncovering design or workmanship flaws that would have otherwise caused mission degradation or failure.

## 34.4 SPACECRAFT TESTING EXPERIENCES

Note that NASA/GSFC typically uses sine vibration testing, whereas JPL tends to use random. A few examples from sine testing at GSFC are:

- TRMM: During Observatory sine testing, found that the NASDA-supplied PAF clamp band had insufficient tension and gapped during the test. As a result, the clamp band tension was increased for flight.

- GOES had a workmanship problem involving a missing or loose bolt which caused the structural failure of a mission-critical antenna. It was detected during the lateral sine test.

- NOAA-K experienced inertial measurement unit (IMU) saturation during sine sweep testing. Because the spacecraft IMU provides guidance information for the Titan II launch vehicle during ascent, IMU saturation during launch would have resulted in a mission failure. Changes were made and launch vehicle restraints were implemented to resolve the problem, including wind restrictions at launch and a commanded first-stage shutdown vs. fuel depletion.

- TDRS-H: During the sine vibration test, the first two modes for the Space Ground Link (SGL) antenna were lower than predicted by the model. The first mode dropped from 15 Hz to 11 Hz and the second mode dropped from 33 Hz to 25 Hz. It turned out that the mathematical model of this "simple" antenna was wrong and therefore the Verification Loads Cycle had to be rerun.

A few examples from random vibration testing at JPL are:

- Cassini: Experienced an RTG electrical short to its spacecraft mount in a system random vibration test. Significant degradation in spacecraft electrical power could have resulted. The spacecraft mount was redesigned.

- CloudSat: Cloud Profiling Radar waveguide failure in spacecraft random vibration test due to apparent poor workmanship of adhesive bonding. Possible loss of science data averted.

- MER 1: Fundamental modes of the Rover in spacecraft random vibration test were 20% greater than predicted in all three axes. (Fixed base modal test had been performed on Rover, Lander, and Cruise Stage separately; FE models were then combined. The estimated stiffness of the Lander attachment to Rover was too low.) FE model was updated just in time for the verification CLA cycle. The vibration test also revealed improper torque of bolts on some tanks in low-level runs. Bolts were properly torqued and the test was completed successfully.

- MSL Rover: experienced several motor encoder screws backed out of at least one of the Rover actuators during the Rover random vibration test. The actuators are used throughout Rover and the issue was unlikely to have otherwise been found before launch, which could have been a serious threat to the mission.

JPL prefers random vibration because it is easier to control, particularly for force limiting.

Note that JPL tested the SMAP spacecraft to the following workmanship PSD:

> 20 Hz to 250 Hz, 0.01 G^2/Hz

The overall level was 1.5 GRMS. The duration was one minute. The vibration was applied in the vertical axis and in one "45-degree" lateral axis.

## 34.5 SINE SWEEP CONTROL

Sine sweep vibration (Section 20) is more difficult to control than random, especially in the case of lightly-damped modes. The sweep rate, compression factor, and tracking filter must be selected with great care.

INVAP experienced control issues during sine vibration testing of the ARSAT-1 structural test model. But note that dynamic simulators were used for the test, which can have much less damping than the actual flight hardware.

# 35 LOW-FREQUENCY STRUCTURAL LOADS FOR LAUNCH VEHICLE & SPACECRAFT SECONDARY STRUCTURES & COMPONENTS

## 35.1 MASS ACCELERATION CURVE
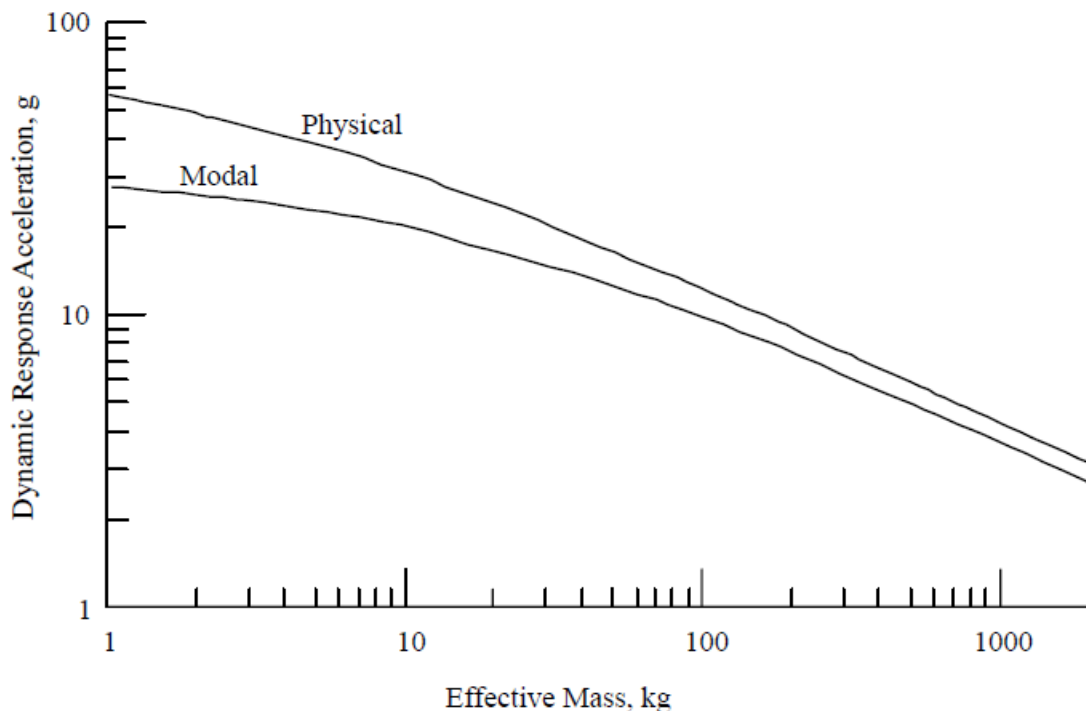


Figure 35.1.   Physical and Modal MAC for the Galileo Spacecraft Launched on Shuttle and Inertial Upper Stage from NASA-HDBK-7005

Payloads, secondary structures, and component loads can be specified in the form of a Mass-Acceleration Curve (MAC) as shown in the example in the above figure.  The lighter the mass, the higher the corresponding acceleration. This observation is true for both transient and random dynamic loads.  This method effectively assumes that the component's fundamental frequency is much higher than any excitation frequency. The resulting analysis becomes a rigid-body analysis.

The MAC can be derived from measured flight or test data, or analytical loads. Care must be taken to avoid "double dipping," if two or more sources are used.

The MAC is intended for very preliminary and reasonably conservative load estimates so that the stress engineer can quickly size structural members.  For payloads, a coupled loads analysis can be later performed to refine the load and stress predictions.  See Section 36.

## 35.2  VIBRATION RESPONSE SPECTRUM

Component loads can be expressed as a Vibration Response Spectrum (VRS) as described in Section 25.  This assumes that the component responds as a single-degree-of-freedom (SDOF) system subjected to base acceleration.

The Y-axis for this function is peak response acceleration. The X-axis is the natural frequency (Hz). The amplification factor Q must also be noted. A family of curves for various Q factors can be included in a single plot.

The VRS curve(s) can be derived from measured flight or test data, or analytical loads. Again, care must be taken to avoid "double dipping," if two or more sources are used.

The resulting VRS can then be used for design purposes by picking off the peak response acceleration value for a given natural frequency and Q.

A similar VRS can be derived for relative displacement. This is important for cases where clearance, sway space, alignment, or isolator deflection are concerns.

# 36 HURTY-CRAIG-BAMPTON METHOD, FIXED INTERFACE MODEL

## 36.1 INTRODUCTION
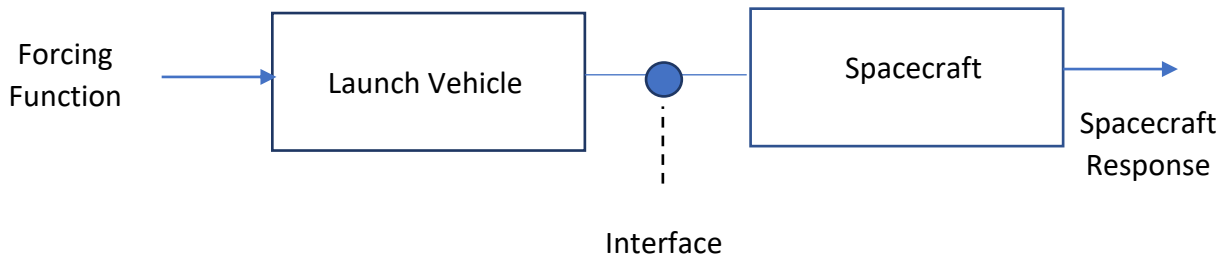


Figure 36.1.   Launch Vehicle & Spacecraft Diagram

The forcing function and response are multi-dimensional.

The Hurty-Craig-Bampton (Craig-Bampton for short) method [68], [69], [70] is used for reducing the size of a finite element model, particularly where two or more subsystems are connected. It combines the motion of boundary points with modes of the subsystem assuming the boundary points are held fixed.   It is commonly used to prepare models for coupled loads analysis (CLA).

As an example, consider a spacecraft dynamic model with 10,000 DOF.  The resulting mass and stiffness matrices will be (10,000 x 10,000) in size.  Also, assume a single attachment node between the spacecraft and launch vehicle interface with six DOF at the connecting node.

Assume that the CLA is to be performed out to 50 Hz and that the spacecraft has ten modes up to 50 Hz.  The spacecraft model could be reduced to 16 DOF, with ten for these modes and another six for the interface DOF.   The spacecraft mass and stiffness matrices could thus be reduced to (16 x 16).

The fixed interface approach is justified because the launch vehicle's mounting structure interface is relatively stiff.

## 36.2 FREQUENCY DOMAIN OF INTEREST

The upper frequency should be at least 1.5 times higher than the highest excitation frequency as a rule of thumb.   Here are some guidelines from standard references with some minor editing.

NASA-STD-5002, Load Analyses of Spacecraft and Payloads, 1996

5.3.2 Transient load analysis (excerpt)

Statistical variation of parameters governing the forcing functions is accommodated by generating multiple cases of forcing functions for a single flight event. After all cases are analyzed, the maximum transient load is taken as the largest load from any of the cases. The frequency range of transient load analysis is limited by the accuracy of both the model and the forcing functions. For Shuttle liftoff and landing, the transient analysis generally accounts only for frequencies from 0 to 35 Hz. For some expendable launch vehicles, significant axial loads are generated at higher frequencies during engine cutoff events, and transient analyses must be run to 60 Hz or higher. For other events such as docking, robotics berthing, plume impingement, and spacecraft landing, the modal content must be selected to adequately capture the dynamic response.

* * *

NASA-HDBK-7005, Dynamic Environmental Criteria, 2001

5.1 Low-Frequency Vibration and Transient Responses. Low-frequency vibration and transient responses of payloads and spacecraft result in loads and motions that must be determined analytically to evaluate structural integrity and functionality. From the Sections referenced in Table 5.1, the primary sources of these low-frequency loads are pre-launch events (ground winds and possible seismic loads), liftoff (engine/motor thrust buildup, ignition overpressure, and pad release), air loads (buffet, gust, and static-elastic), and liquid engine ignitions and shutdowns. These events have an upper-frequency limit that is dependent on the launch vehicle and the stage of its operation, e.g., 35 Hz for the Shuttle, and 50-60 Hz in most cases for expendables. Major load events due to spacecraft operation are deployments and transients peculiar to the mission, such as docking and landing. Most cases involve linear system response, but nonlinear responses occur in certain cases. Examples are the account of trunnion sliding for Shuttle payloads, the liftoff release mechanism for Atlas, and the response of spacecraft deployment and docking mechanisms.

* * *

SMC-TR-06-11, Test Requirements for Launch, Upper-Stage, and Space Vehicles, AEROSPACE REPORT NO. TR-2004(8583)-1 REV. A

3.24 Maximum Predicted Acceleration

The maximum predicted acceleration, defined for structural loads analysis and test purposes, is the highest acceleration determined from the combined effects of quasi-steady acceleration, vibration and acoustics, and transient flight events (liftoff, engine ignitions, and shutdowns, flight through transonic and maximum dynamic pressure, gust, and vehicle separation). The frequency range of concern is usually limited to below 70 Hz for structural loads resulting from the noted transient events, and to below 300 Hz for secondary structural loads resulting from the vibration and acoustic environments. Maximum accelerations are predicted for each of three mutually perpendicular axes in both positive and negative directions. When a statistical estimate is applicable, the maximum predicted acceleration is at least the acceleration that is not expected to be exceeded on 99 percent of flights, estimated with 90 percent confidence (P99/90).

* * *

European Cooperation for Spacecraft Standardization (ECSS), Spacecraft Mechanical Loads Analysis Handbook:

ECSS-E-HB-32-26A_19February2013

4.6.1 Spacecraft flight environments and dynamic loads

The launch consists of a series of events, each of which has several independent sources of load for the launch vehicle and payload. The flight environments that generate static and dynamic loads on spaceflight hardware are normally categorized as follows:

- The static acceleration, generated by constant external forces or which change slowly with time so that the dynamic response of the structure is not significant (also called quasi-static acceleration associated to a quasi-static event).
- The low-frequency dynamic response, typically from 0 Hz to 100 Hz, of the launch vehicle/payload system to transient flight events. However, for some small launch vehicles, the range of low-frequency dynamic response can be up to 150 Hz.
- The high-frequency random vibration environment, which typically has significant energy in the frequency range from 20 Hz to 2000 Hz, is transmitted from the launch vehicle to the payload at the launch vehicle/payload interfaces.
- The high-frequency acoustic pressure environment, typically from 20 Hz to 8000 Hz, is inside the payload compartment. The payload compartment acoustic pressure environment generates dynamic loads on components in two ways: (1)

by direct impingement on the surfaces of exposed components, and (2) by the acoustic pressure impingement upon the component mounting structures, which induces random vibrations that are mechanically transmitted to the components.

- Shock events. The energy spectrum is usually concentrated at or above 500 Hz and is measured in a frequency range of 100 Hz to 10 KHz.

### 4.6.6 Spacecraft-launcher Coupled Loads Analysis

The structural response of the spacecraft to transient flight events (low-frequency mechanical environment) is simulated by spacecraft-launcher coupled dynamic analysis, which is a key task of the loads' cycle process. The coupled loads analysis is a transient (or harmonic) analysis performed by using the mathematical models of the spacecraft and launcher, merged together, and by applying the forcing functions for the different launch events.

The main objective of the CLA is to calculate the loads on the spacecraft, where the term "loads" refers to the set of internal forces, displacements, and accelerations that characterize the structural response to the applied forces. The spacecraft loads derived from the analysis are taken as a basis to verify the dimensioning of the spacecraft itself.

The low-frequency domain typically ranges from 0 to up 100 Hz and corresponds to the frequency content of the forcing functions used in the CLA. The excitation may be of aerodynamic origin (wind, gust, buffeting at transonic velocity) or may be induced by the propulsion system (e.g. thrust build-up or tail-off transient, acoustic loads in the combustion chambers). Of primary interest are the spacecraft interface accelerations and interface forces. The interface accelerations can be used to derive an equivalent sine spectrum at the spacecraft interface. The interface forces can be employed to calculate the "equivalent accelerations" at the spacecraft's center of gravity (quasi-static accelerations). Of large interest is also the recovery of the internal responses which are used to verify the structural integrity of the spacecraft and its components. The computed responses and their deduced minimum and maximum levels can be employed within the design, verification, and test phases of the spacecraft. For example, secondary structures and flexible components such as solar arrays, booms, instruments, and propellant tanks are also designed (and test verified) to withstand the dynamic environment induced at the base of the spacecraft. The dynamic loads (e.g. accelerations, forces, stresses) on these components can be verified directly by means of the CLA (apart from acoustic loads under the fairing which are analyzed separately).

In the test verification phase of the spacecraft, the equivalent sine spectrum computed using the CLA is often used to assess and justify the reduction, at specific resonant

frequencies, of the spectrum specified by the launcher authority. This might be required to avoid possible damage to the spacecraft structure itself or its components (e.g. solar arrays, booms).

## 36.3  GOVERNING EQUATION OF MOTION

The dynamic response of a system is modeled as

$$M\ddot{u} + Ku = F \tag{36.1}$$

where
| | |
|---|---|
| $M$ | is the mass matrix |
| $K$ | is the stiffness matrix |
| $F$ | is the force vector |
| $u$ | is the displacement vector |

Damping is not included in the above equation but can be added later as modal damping.

## 36.4  MATRIX PARTITIONING

The partitioned mass and stiffness matrices for each subsystem or component are respectively

$$\begin{bmatrix} M_{ii} & M_{ib} \\ M_{bi} & M_{bb} \end{bmatrix} \text{ and } \begin{bmatrix} K_{ii} & K_{ib} \\ K_{bi} & K_{bb} \end{bmatrix}$$

The subscript i denotes an interior DOF.
The subscript b denotes an interface boundary DOF.
The undamped equation of motion is

$$\begin{bmatrix} M_{ii} & M_{ib} \\ M_{bi} & M_{bb} \end{bmatrix} \begin{bmatrix} \ddot{u}_i \\ \ddot{u}_b \end{bmatrix} + \begin{bmatrix} K_{ii} & K_{ib} \\ K_{bi} & K_{bb} \end{bmatrix} \begin{bmatrix} u_i \\ u_b \end{bmatrix} = \begin{bmatrix} F_i \\ F_b \end{bmatrix} \tag{36.2}$$

where

$u_i$  =  interior DOF physical displacement (independent elastic DOF)

$u_b$  =  boundary DOF physical displacement

## 36.5 NORMAL MODES

The physical properties are transformed into modal properties as follows.

$$[K_{ii} - \omega_j^2 M_{ii}]\{\varphi_i\}_j = 0 \tag{36.3}$$

The complete set of $N_i$ fixed-interface (flexible) normal modes is $\Phi_{ii}$. The assembled modal matrix is

$$\Phi_i \equiv \begin{bmatrix} \Phi_{ii} \\ 0_{bi} \end{bmatrix} \tag{36.4}$$

The matrix $\Phi_i$ has a size of $N_u$ x $N_i$, where $N_u$ is the total number of DOF. Next, the modes are mass-normalized so that

$$\Phi_{ii}{}^T M_{ii} \Phi_{ii} = I_{ii} \tag{36.5}$$

$$\Phi_{ii}{}^T K_{ii} \Phi_{ii} = \Lambda_{ii} = \text{diag}(\omega_j^2) \tag{36.6}$$

$\Lambda_{ii}$ is the diagonal matrix of eigenvalues.

The mass-normalized eigenvector matrix $\Phi_{ii}$ relates the modal coordinate displacements to the physical displacements for the fixed-interface or grounded model. The number of columns may be truncated depending on the maximum angular frequency $\omega_i$ of interest.

## 36.6 CONSTRAINT MODES

A constraint mode is defined as the static deformation of a structure when a unit displacement is applied to one coordinate of a specified set of constraint coordinates, C, while the remaining coordinates of that set are restrained, and the remaining DOF of the structure are force-free. The interface constraint mode matrix is calculated via the following static relationship.

$$\begin{bmatrix} K_{ii} & K_{ib} \\ K_{bi} & K_{bb} \end{bmatrix} \begin{bmatrix} \Psi_{ib} \\ I_{bb} \end{bmatrix} = \begin{bmatrix} 0_{ib} \\ R_{bb} \end{bmatrix} \tag{36.7}$$

where

$\Psi_{ib}$    is the interior partition of the constraint mode matrix

$R$    contains the reaction forces on the component due to its connection to adjacent components at boundary degrees-of-freedom

The columns of the constraint matrix $\Psi_{ib}$ are rigid body displacements at the interior DOF due to a unit motion at one of the boundary DOF. Note that for a structure with a statically determinant boundary (exactly six DOF), $\Psi_{ib}$ is just the matrix of six rigid body modes at the boundary points.

The interface constraint mode matrix $\Psi_c$ is

$$\Psi_c \equiv \begin{bmatrix} \Psi_{ib} \\ I_{bb} \end{bmatrix} = \begin{bmatrix} -\left[ K_{ii}^{-1} K_{ib} \right] \\ I_{bb} \end{bmatrix} \tag{36.8}$$

The matrix $\Psi_c$ has a row number equal to the total DOF and a column number equal to the boundary DOF.

The interface constraint mode matrix is essentially the same one used in the Guyan reduction transformation matrix. Guyan reduction is also known as static condensation. See also the similarities to the MDOF enforced acceleration method in Section 28.1.2.

Note that the constraint modes are stiffness-orthogonal to all of the fixed-interface normal modes, that is

$$\Phi_i^T K \Psi_c = 0 \tag{36.9}$$

The displacement transformation of the Craig-Bampton method uses both fixed-interface normal modes and interface constraint modes.

The physical coordinates $u^{(s)}$ can be represented as

$$u^{(s)} \equiv \begin{Bmatrix} u_i \\ u_b \end{Bmatrix}^{(s)} = \begin{bmatrix} \Phi_{ik} & \Psi_{ib} \\ 0 & I_{bb} \end{bmatrix}^{(s)} \begin{Bmatrix} p_k \\ p_b \end{Bmatrix}^{(s)} = \begin{bmatrix} \Phi_{ik} & -\left[ K_{ii}^{-1} K_{ib} \right] \\ 0 & I_{bb} \end{bmatrix}^{(s)} \begin{Bmatrix} p_k \\ p_b \end{Bmatrix}^{(s)} \tag{36.10}$$

where

$p_k$   =   interior modal displacements

$p_b$   =   boundary modal displacements (equal to the boundary physical displacements)

$$\Phi_{ik} \quad = \quad \text{interior partition of the matrix of kept fixed-interface modes} \\ \text{(after modal truncation)}$$

$$\Psi_{ib} \quad = \quad \text{interior partition of the constraint mode matrix or boundary} \\ \text{modes (rigid-body vectors)}$$

$$u_i \quad = \quad \text{interior DOF physical displacement (independent elastic DOF)}$$

$$u_b \quad = \quad \text{boundary dof physical displacement}$$

Note that Nastran uses a different convention with subscript R representing the boundary DOF and L representing the modal DOF.

The Craig-Bampton transformation matrix $\Psi_{CB}^{(s)}$ is

$$\Psi_{CB}^{(s)} = \begin{bmatrix} \Phi_{ik} & \Psi_{ib} \\ 0 & I_{bb} \end{bmatrix}^{(s)} = \begin{bmatrix} \Phi_{ik} & -\left[K_{ii}^{-1}K_{ib}\right] \\ 0 & I_{bb} \end{bmatrix}^{(s)} \tag{36.11}$$

Thus

$$u^{(s)} \equiv \begin{Bmatrix} u_i \\ u_b \end{Bmatrix}^{(s)} = \begin{bmatrix} \Phi_{ik} & \Psi_{ib} \\ 0 & I_{bb} \end{bmatrix}^{(s)} \begin{Bmatrix} p_k \\ p_b \end{Bmatrix}^{(s)} = \Psi_{CB}^{(s)} \begin{Bmatrix} p_k \\ p_b \end{Bmatrix}^{(s)} \tag{36.12}$$

The total physical displacements of the interior DOF are

$$u_i = \Phi_{ik}p_k + \Psi_{ib}p_b \tag{36.13}$$

where

$\Psi_{ib}p_b$ are the rigid-body boundary displacements

$\Phi_{ik}p_k$ are the physical displacements relative to the boundary rigid-body displacement

Substitute equation (36.12) into equation (36.2).

$$\left\{M^{(s)}\right\}\left\{\Psi_{CB}^{(s)}\right\} \begin{Bmatrix} p_k \\ p_b \end{Bmatrix}^{(s)} + \left\{K^{(s)}\right\}\left\{\Psi_{CB}^{(s)}\right\} \begin{Bmatrix} p_k \\ p_b \end{Bmatrix}^{(s)} = \begin{bmatrix} F_i \\ F_b \end{bmatrix} \tag{36.14}$$

where

$$M^{(s)} = \begin{bmatrix} M_{ii} & M_{ib} \\ M_{bi} & M_{bb} \end{bmatrix} \quad \text{and} \quad K^{(s)} = \begin{bmatrix} K_{ii} & K_{ib} \\ K_{bi} & K_{bb} \end{bmatrix}$$

Premultiply by $\left\{\Psi_{CB}^{(s)}\right\}^T$.

$$\left\{\Psi_{CB}^{(s)}\right\}^T\left\{M^{(s)}\right\}\left\{\Psi_{CB}^{(s)}\right\}\begin{Bmatrix}p_k\\p_b\end{Bmatrix}^{(s)} + \left\{\Psi_{CB}^{(s)}\right\}^T\left\{K^{(s)}\right\}\left\{\Psi_{CB}^{(s)}\right\}\begin{Bmatrix}p_k\\p_b\end{Bmatrix}^{(s)} = \left\{\Psi_{CB}^{(s)}\right\}^T\begin{bmatrix}F_i\\F_b\end{bmatrix} \tag{36.15}$$

## 36.7 REDUCED COMPONENT MATRICES

The reduced component mass matrix for system s is

$$\widehat{M}_{CB}^{(s)} = \left\{\Psi_{CB}^{(s)}\right\}^T\left\{M^{(s)}\right\}\left\{\Psi_{CB}^{(s)}\right\} \tag{36.16}$$

$$\widehat{M}_{CB}^{(s)} = \begin{bmatrix}\Phi_{ik} & 0\\\Psi_{ib} & I_{bb}\end{bmatrix}^{(s)}\begin{bmatrix}M_{ii} & M_{ib}\\M_{bi} & M_{bb}\end{bmatrix}^{(s)}\begin{bmatrix}\Phi_{ik} & \Psi_{ib}\\0 & I_{bb}\end{bmatrix}^{(s)} \tag{36.17}$$

$$\widehat{M}_{CB}^{(s)} = \begin{bmatrix}\Phi_{ik}^T & 0\\\Psi_{ib}^T & I_{bb}\end{bmatrix}^{(s)}\begin{bmatrix}M_{ii}\Phi_{ik} & M_{ii}\Psi_{ib}+I_{bb}M_{ib}\\M_{bi}\Phi_{ik} & M_{bi}\Psi_{ib}+I_{bb}M_{bb}\end{bmatrix}^{(s)} \tag{36.18}$$

$$\widehat{M}_{CB}^{(s)} = \begin{bmatrix}\Phi_{ik}^TM_{ii}\Phi_{ik} & \Phi_{ik}^T(M_{ii}\Psi_{ib}+I_{bb}M_{ib})\\(\Psi_{ib}^TM_{ii}+I_{bb}M_{bi})\Phi_{ik} & I_{bb}(M_{bi}\Psi_{ib}+I_{bb}M_{bb})\end{bmatrix}^{(s)} \tag{36.19}$$

$$\widehat{M}_{CB}^{(s)} = \begin{bmatrix}\hat{I}_{kk} & \widehat{M}_{kb}\\\widehat{M}_{bk} & \widehat{M}_{bb}\end{bmatrix}^{(s)} \tag{36.20}$$

$\widehat{M}_{bb}$ represents the total mass properties translated to the boundary points in the above equation.

The reduced stiffness matrix for system s is

$$\widehat{K}_{CB}^{(s)} = \left\{\Psi_{CB}^{(s)}\right\}^T\left\{K^{(s)}\right\}\left\{\Psi_{CB}^{(s)}\right\} \tag{36.21}$$

$$\widehat{K}_{CB}^{(s)} = \begin{bmatrix}\Phi_{ik} & 0\\\Psi_{ib} & I_{bb}\end{bmatrix}^{(s)}\begin{bmatrix}K_{ii} & K_{ib}\\K_{bi} & K_{bb}\end{bmatrix}^{(s)}\begin{bmatrix}\Phi_{ik} & \Psi_{ib}\\0 & I_{bb}\end{bmatrix}^{(s)} \tag{36.22}$$

$$\widehat{K}_{CB}^{(s)} = \begin{bmatrix} {\Phi_{ik}}^T & 0 \\ {\Psi_{ib}}^T & I_{bb} \end{bmatrix}^{(s)} \begin{bmatrix} K_{ii}\Phi_{ik} & K_{ii}\Psi_{ib} + I_{bb}K_{ib} \\ K_{bi}\Phi_{ik} & K_{bi}\Psi_{ib} + I_{bb}K_{bb} \end{bmatrix}^{(s)} \tag{36.23}$$

$$\widehat{K}_{CB}^{(s)} = \begin{bmatrix} {\Phi_{ik}}^T K_{ii}\Phi_{ik} & {\Phi_{ik}}^T(K_{ii}\Psi_{ib} + I_{bb}K_{ib}) \\ ({\Psi_{ib}}^T K_{ii} + I_{bb}K_{bi})\Phi_{ik} & I_{bb}(K_{bi}\Psi_{ib} + I_{bb}K_{bb}) \end{bmatrix}^{(s)} \tag{36.24}$$

Again,

$$\Psi_{ib} = -K_{ii}^{-1}K_{ib} \tag{36.25}$$

Thus, the off-diagonal terms are each zero.

$$\widehat{K}_{CB}^{(s)} = \begin{bmatrix} \Lambda_{kk} & 0_{kb} \\ 0_{bk} & \widehat{K}_{bb} \end{bmatrix}^{(s)} \tag{36.26}$$

$\widehat{K}_{bb}$ is the Interface stiffness matrix, the stiffness associated with displacing one boundary DOF while the others are held fixed. $\widehat{K}_{bb} = 0$ if the interface is a statically determinant single node.

The reduced force vector for system s is

$$\widehat{F}_{CB}^{(s)} = \left\{\Psi_{CB}^{(s)}\right\}^T \{F^{(s)}\} = \left\{\Psi_{CB}^{(s)}\right\}^T \begin{bmatrix} F_i \\ F_b \end{bmatrix}^{(s)} \tag{36.27}$$

$F_i = 0$  if the only forces are at the boundary.

The Craig-Bampton undamped modal equation of motion for system s is

$$\begin{bmatrix} \widehat{I}_{kk} & \widehat{M}_{kb} \\ \widehat{M}_{bk} & \widehat{M}_{bb} \end{bmatrix}^{(s)} \begin{Bmatrix} \ddot{p}_k \\ \ddot{p}_b \end{Bmatrix}^{(s)} + \begin{bmatrix} \Lambda_{kk} & 0_{kb} \\ 0_{bk} & \widehat{K}_{bb} \end{bmatrix}^{(s)} \begin{Bmatrix} p_k \\ p_b \end{Bmatrix}^{(s)} = \left\{\Psi_{CB}^{(s)}\right\}^T \begin{bmatrix} F_i \\ F_b \end{bmatrix}^{(s)} \tag{36.28}$$

$$\widehat{M}_{CB}^{(s)} \begin{Bmatrix} \ddot{p}_k \\ \ddot{p}_b \end{Bmatrix}^{(s)} + \widehat{K}_{CB}^{(s)} \begin{Bmatrix} p_k \\ p_b \end{Bmatrix}^{(s)} = \widehat{F}_{CB}^{(s)} \tag{36.29}$$

The version with modal damping is

$$\begin{bmatrix} \hat{I}_{kk} & \hat{M}_{kb} \\ \hat{M}_{bk} & \hat{M}_{bb} \end{bmatrix}^{(s)} \begin{Bmatrix} \ddot{p}_k \\ \ddot{p}_b \end{Bmatrix}^{(s)} + \begin{bmatrix} 2\xi_k\omega_k & 0_{kb} \\ 0_{bk} & 0_{bb} \end{bmatrix}^{(s)} \begin{Bmatrix} \dot{p}_k \\ \dot{p}_b \end{Bmatrix}^{(s)} + \begin{bmatrix} \Lambda_{kk} & 0_{kb} \\ 0_{bk} & \hat{K}_{bb} \end{bmatrix}^{(s)} \begin{Bmatrix} p_k \\ p_b \end{Bmatrix}^{(s)}$$

$$= \left\{\Psi_{CB}^{(s)}\right\}^T \begin{bmatrix} F_i \\ F_b \end{bmatrix}^{(s)}$$

(36.30)

Note that the term $2\xi_k\omega_k$ represents a diagonal submatrix.

A modal damping value of 1% is commonly used in launch vehicle and spacecraft analysis. The damping value may be chosen to vary with the mode number. Modal testing can be used to experimentally determine the damping value.

The transformation in the previous equation set is successful because the modes become uncoupled from each other, greatly reducing the manipulation required to solve the equations. Typically, modal displacements and accelerations are computed by numerical integration for a given set of initial conditions and forcing function time histories. Physical accelerations and displacements follow from the Craig-Bampton transformation matrix per equation (36.12).

Typically, in the analysis of spacecraft payloads, all forces applied to the structure come through the boundary points and there are no applied loads to the non-boundary points, i.e., only $F_b$ is of concern and $F_i$ is zero. However, in the combined coupled loads analysis of the payload and launch vehicle, applied loads do act at non-boundary points in the launch vehicle and must be considered.

## 36.8 CRAIG-BAMPTON MODEL CHECKS

### 36.8.1 Introduction

The following checks assume six degrees-of-freedom per node but can be adapted for other cases.

36.8.2  Rigid Body Check

Test the equations o£ motion by enforcing rigid body displacements at the boundary degrees-of-freedom, $u_b$ , and observing that the non-boundary or elastic freedoms displace appropriately.  Construct the matrix of six rigid body modes, $[R]$, for the boundary DOF that satisfy the equation:

$$[u_b] = [R][q_{\text{rigid body}}] \tag{36.31}$$

where

$[q_{\text{rigid body}}]$ is the 6 x 1 vector of pure rigid body displacements and rotations for x, y, z, Rx, Ry, and Rz motion at some convenient point and in global coordinates

As a common example, the matrix of rigid body modes for a simple six-degree-of-freedom interface at point A relative to some arbitrary point B is:

$$[R] = \begin{bmatrix} 1 & 0 & 0 & 0 & \Delta Z & -\Delta Y \\ 0 & 1 & 0 & -\Delta Z & 0 & \Delta X \\ 0 & 0 & 1 & \Delta Y & -\Delta X & 0 \\ 0 & 0 & 0 & 1 & 0 & 0 \\ 0 & 0 & 0 & 0 & 1 & 0 \\ 0 & 0 & 0 & 0 & 0 & 1 \end{bmatrix} \tag{36.32}$$

where
$$\Delta X = X_B - X_A$$
$$\Delta Y = Y_B - Y_A$$
$$\Delta Z = Z_B - Z_A$$

Assume no elastic motion such that $\ddot{p}_k = 0$ and $p_k = 0$.  Apply a set of unit displacements, translational and rotational, as

$$[q_{\text{rigid body}}] = [\,I\,] \tag{36.33}$$

$$[u_b] = [R][I] \tag{36.34}$$

Next, apply a set of unit accelerations, translational and rotational, as

$$[\ddot{u}_b] = [R][I] \tag{36.35}$$

### 36.8.3 Rigid Body Mass Matrix

The Craig-Bampton equation of motion (Eq. 2.5.2) provides the 6 x 6 rigid body mass matrix

$$[R]^T \left[\widehat{M}_{CB}^{(s)}\right][R] = \begin{bmatrix} m & 0 & 0 & 0 & -mz & -my \\ 0 & m & 0 & -mz & 0 & mx \\ 0 & 0 & m & my & -mx & 0 \\ 0 & -mz & my & I_{xx} & I_{xy} & I_{xz} \\ mz & 0 & -mx & I_{yx} & I_{yy} & I_{yz} \\ -my & mx & 0 & I_{zx} & I_{zy} & I_{zz} \end{bmatrix} \tag{36.36}$$

where

m is the total mass of the finite element model; x, y, and z are the distances from the rigid body point to the center of mass; and the I terms are the mass moments of inertia and products of inertia at the rigid body point.

### 36.8.4 Free EigenValue Problem

The Craig-Bampton equation of motion represents a free, unconstrained structure. Check that it yields the natural frequencies and mode shapes for this condition from the original finite element model.

$$\left\{\widehat{K}_{CB}^{(s)} - \lambda^2 \widehat{M}_{CB}^{(s)}\right\}\{\Phi\} = 0 \tag{36.37}$$

Note that the rigid body modes are zero by definition if the boundary is statically determinate.

### 36.9 QUASI-STATIC ANALYSIS

Boundary forces and internal displacements in a structure can be calculated for rigid-body acceleration. This can be done to check design load cases or to uncover possible modeling errors. The Craig-Bampton model is well suited for this.

The $\ddot{u}_b$ variable is set equal to the rigid-body acceleration, which is commonly called the quasi-static acceleration (oxymoron). Let G be the rigid-body acceleration.

$$\ddot{u}_b = \ddot{p}_b = G \tag{36.38}$$

The velocity $\dot{u}_b$ is ignored. Recall that this velocity is the same as $\dot{p}_b$.

For pure rigid-body acceleration,

$$\ddot{p}_k = 0 \quad \text{and} \quad \dot{p}_k = 0 \tag{36.39}$$

Substitute the previous two equations into equation (36.30).

$$\begin{bmatrix} \hat{I}_{kk} & \hat{M}_{kb} \\ \hat{M}_{bk} & \hat{M}_{bb} \end{bmatrix}^{(s)} \begin{Bmatrix} 0 \\ G \end{Bmatrix}^{(s)} + \begin{bmatrix} \Lambda_{kk} & 0_{kb} \\ 0_{bk} & \hat{K}_{bb} \end{bmatrix}^{(s)} \begin{Bmatrix} p_k \\ p_b \end{Bmatrix}^{(s)} = \begin{bmatrix} \Phi_{ik} & 0 \\ \Psi_{ib} & I_{bb} \end{bmatrix}^{(s)} \begin{bmatrix} 0 \\ F_b \end{bmatrix}^{(s)} \tag{36.40}$$

The bottom row of the above equation yields

$$\hat{M}_{bb}G + \hat{K}_{bb}p_b = F_b \tag{36.41}$$

In the case of rigid-body motion,

$$\hat{K}_{bb}p_b = [K_{bi}\Psi_{ib} + I_{bb}K_{bb}]p_b = 0 \tag{36.42}$$

The rigid-body acceleration and force relationship is

$$\hat{M}_{bb}G = F_b \tag{36.43}$$

The top row of the equation (36.40) yields

$$\Lambda_{kk} p_k = -\hat{M}_{kb} G \tag{36.44}$$

$$p_k = -\Lambda_{kk}^{-1} \hat{M}_{kb} G \tag{36.45}$$

484

## 36.10 BASE ACCELERATION ANALYSIS AND TESTING

Base acceleration input analyses are very common in structural dynamics and are ideally suited to the Craig-Bampton formulation. Transient inputs are often derived from a large CLA involving the launch vehicle and one or more payloads. Then, as payload models are refined, the interface transients are applied to the component models rather than repeating the long and costly coupled loads analysis.

The forces $F_b$ are the forces of constraint that are required to produce the desired base motion.

The top row of equation (36.30) is

$$\ddot{p}_k + \widehat{M}_{kb}\ddot{p}_b + 2\xi_k\omega_k\dot{p}_k + \Lambda_{kk}p_k = \Phi_{ik}F_i \tag{36.46}$$

$$\ddot{p}_k + 2\xi_k\omega_k\dot{p}_k + \Lambda_{kk}p_k = -\widehat{M}_{kb}\ddot{p}_b + \Phi_{ik}F_i \tag{36.47}$$

Assume no internal forces and simplify the previous equation.

$$\ddot{p}_k + 2\xi_k\omega_k\dot{p}_k + \Lambda_{kk}p_k = -\widehat{M}_{kb}\ddot{u}_b \tag{36.48}$$

The boundary forcing function is

$$F_b = -\widehat{M}_{kb}\ddot{u}_b \tag{36.49}$$

The reactions at the boundary ignoring damping and assuming no internal forces are

$$F_b = \widehat{M}_{bk}\ddot{p}_k + \widehat{M}_{bb}\ddot{p}_b + \widehat{K}_{bb}p_b \tag{36.50}$$

$$F_b = \widehat{M}_{bk}\ddot{p}_k + \widehat{M}_{bb}\ddot{u}_b + \widehat{K}_{bb}u_b \tag{36.51}$$

Again, $\widehat{K}_{bb} = 0$ for statically determinant systems. The uncoupled equation set for this case with modal damping is

$$\begin{bmatrix} 1 & 0 \\ 0 & 1 \end{bmatrix}\begin{Bmatrix} \ddot{p}_k \\ \ddot{u}_b \end{Bmatrix} + \begin{bmatrix} 2\xi_k\omega_k & 0 \\ 0 & 0 \end{bmatrix}\begin{Bmatrix} \dot{p}_k \\ \dot{u}_b \end{Bmatrix} + \begin{bmatrix} \Lambda_{kk} & 0 \\ 0 & 0 \end{bmatrix}\begin{Bmatrix} p_k \\ u_b \end{Bmatrix} = \begin{bmatrix} -\widehat{M}_{kb} \\ 1 \end{bmatrix}\ddot{u}_b \tag{36.52}$$

The physical acceleration response is calculated from

$$\left\{ \begin{array}{c} \ddot{u}_i \\ \ddot{u}_b \end{array} \right\} = \begin{bmatrix} \Phi_{ik} & \Psi_{ib} \\ 0 & I_{bb} \end{bmatrix} \left\{ \begin{array}{c} \ddot{p}_k \\ \ddot{u}_b \end{array} \right\} = \Psi_{CB} \left\{ \begin{array}{c} \ddot{p}_k \\ \ddot{u}_b \end{array} \right\} \tag{36.53}$$

## 36.11  LOAD TRANSFORMATION MATRIX

### 36.11.1    Introduction

The Load Transformation Matrix (LTM) is used to recover physical parameters such as accelerations, displacements, forces, and stresses from the original finite element model using the generalized accelerations and, for redundant interfaces, the physical displacements of the boundaries.   There are various types of LTMs.

### 36.11.2    Displacement from Acceleration LTM

Assume no internal force, $F_i = 0$, and substituted into equation (36.2).

The resulting undamped partitioned equation of motion is

$$\begin{bmatrix} M_{ii} & M_{ib} \\ M_{bi} & M_{bb} \end{bmatrix} \begin{bmatrix} \ddot{u}_i \\ \ddot{u}_b \end{bmatrix} + \begin{bmatrix} K_{ii} & K_{ib} \\ K_{bi} & K_{bb} \end{bmatrix} \begin{bmatrix} u_i \\ u_b \end{bmatrix} = \begin{bmatrix} 0 \\ F_b \end{bmatrix} \tag{36.54}$$

The top row is

$$M_{ii}\ddot{u}_i + M_{ib}\ddot{u}_b + K_{ii}u_i + K_{ib}u_b = 0 \tag{36.55}$$

Solve for the internal displacements.

$$K_{ii}u_i = -[M_{ii}\ddot{u}_i + M_{ib}\ddot{u}_b + K_{ib}u_b] \tag{36.56}$$

$$u_i = -K_{ii}^{-1}[M_{ii}\ddot{u}_i + M_{ib}\ddot{u}_b] - K_{ii}^{-1}K_{ib}u_b \tag{36.57}$$

Recall from equation (36.12) that the internal acceleration can be expressed as

$$\ddot{u}_i = \Phi_{ik}\ddot{p}_k + \Psi_{ib}\ddot{u}_b \tag{36.58}$$

By substitution,

$$u_i = -K_{ii}^{-1}[M_{ii}(\Phi_{ik}\ddot{p}_k + \Psi_{ib}\ddot{u}_b) + M_{ib}\ddot{u}_b] - K_{ii}^{-1}K_{ib}u_b \tag{36.59}$$

$$u_i = -K_{ii}^{-1}[M_{ii}\Phi_{ik}\ddot{p}_k + (M_{ib} + M_{ii}\Psi_{ib})\ddot{u}_b] - K_{ii}^{-1}K_{ib}u_b \tag{36.60}$$

Recall

$$\Psi_{ib} = -\left[K_{ii}^{-1}K_{ib}\right] \tag{36.61}$$

By substitution,

$$u_i = -K_{ii}^{-1}[M_{ii}\Phi_{ik}\ddot{p}_k + (M_{ib} + M_{ii}\Psi_{ib})\ddot{u}_b] + \Psi_{ib}u_b \tag{36.62}$$

The LTM is the first matrix on the right-hand side.

$$\begin{bmatrix} u_b \\ u_i \end{bmatrix} = \begin{bmatrix} 0 & 0 & 1 \\ -K_{ii}^{-1}(M_{ib} + M_{ii}\Psi_{ib}) & -K_{ii}^{-1}M_{ii}\Phi_{ik} & \Psi_{ib} \end{bmatrix} \begin{bmatrix} \ddot{u}_b \\ \ddot{p}_k \\ u_b \end{bmatrix} \tag{36.63}$$

### 36.11.3    Interface Force LTM

Sometimes only the interface forces and net center of gravity forces are of interest.

The bottom row of equation (36.30) for the case of no internal forces is

$$[\widehat{M}_{bk} \quad \widehat{M}_{bb}]\begin{Bmatrix} \ddot{p}_k \\ \ddot{p}_b \end{Bmatrix} + \widehat{K}_{bb}p_b = F_b \tag{36.64}$$

$$[\widehat{M}_{bk} \quad \widehat{M}_{bb}]\begin{Bmatrix} \ddot{p}_k \\ \ddot{u}_b \end{Bmatrix} + \widehat{K}_{bb}u_b = F_b \tag{36.65}$$

$$[\widehat{M}_{bk} \quad \widehat{M}_{bb} \quad \widehat{K}_{bb}]\begin{bmatrix} \ddot{u}_b \\ \ddot{p}_k \\ u_b \end{bmatrix} = F_b \tag{36.66}$$

The matrix $[\widehat{M}_{bk} \quad \widehat{M}_{bb} \quad \widehat{K}_{bb}]$ is the LTM that relates Craig-Bampton accelerations and boundary displacements to the interface forces.

The forces at the spacecraft net center-of-gravity (CG) can be calculated from the interface forces through an additional transformation as described in Reference [69].

## 36.12 CRAIG-BAMPTON EXAMPLE



English units:
mass (lbf sec^2/in)

| | |
|---|---|
| m1 | 10 |
| m2 | 8 |
| m3 | 6 |
| m4 | 5 |

stiffness (lbf/in)

| | |
|---|---|
| k1 | 100,000 |
| k2 | 90,000 |
| k3 | 80,000 |

Assume 5% damping for all modes
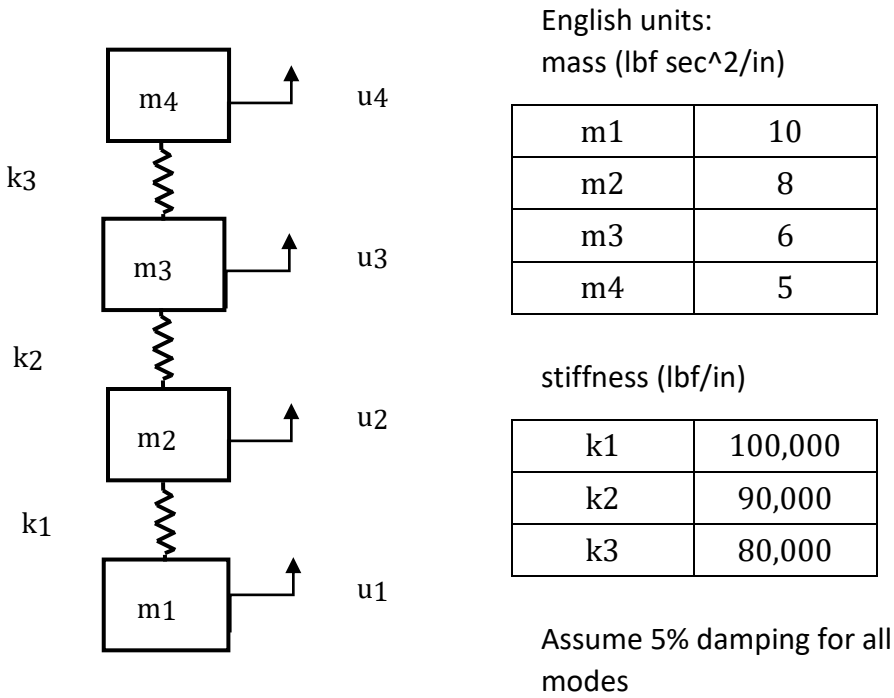
Figure 36.2.  Four-DOF System

Create a Craig-Bampton model with the boundary DOF set to $u_1$.

The unconstrained mass matrix with its displacement vector is

$$
M = \begin{bmatrix} 10 & 0 & 0 & 0 \\ 0 & 8 & 0 & 0 \\ 0 & 0 & 6 & 0 \\ 0 & 0 & 0 & 5 \end{bmatrix} \quad \text{with} \quad \begin{bmatrix} u_1 \\ u_2 \\ u_3 \\ u_4 \end{bmatrix}
$$

Reordering to put the boundary DOF last,

$$M = \begin{bmatrix} M_{ii} & M_{ib} \\ M_{bi} & M_{bb} \end{bmatrix} = \begin{bmatrix} 8 & 0 & 0 & 0 \\ 0 & 6 & 0 & 0 \\ 0 & 0 & 5 & 0 \\ 0 & 0 & 0 & 10 \end{bmatrix} \quad \text{with} \quad \begin{bmatrix} u_2 \\ u_3 \\ u_4 \\ u_1 \end{bmatrix}$$

The partitioned mass submatrices are

$$M_{ii} = \begin{bmatrix} 8 & 0 & 0 \\ 0 & 6 & 0 \\ 0 & 0 & 5 \end{bmatrix}$$

$$M_{bi} = M_{ib}{}^T = [0 \quad 0 \quad 0]$$

$$M_{bb} = 10$$

The unconstrained stiffness matrix is

$$K = \begin{bmatrix} 100{,}000 & -100{,}000 & 0 & 0 \\ -100{,}000 & 190{,}000 & -90{,}000 & 0 \\ 0 & -90{,}000 & 170{,}000 & -80{,}000 \\ 0 & 0 & -80{,}000 & 80{,}000 \end{bmatrix} \quad \text{with} \quad \begin{bmatrix} u_1 \\ u_2 \\ u_3 \\ u_4 \end{bmatrix}$$

Reordering to put the boundary DOF last,

$$K = \begin{bmatrix} K_{ii} & K_{ib} \\ K_{bi} & K_{bb} \end{bmatrix} = \begin{bmatrix} 190{,}000 & -90{,}000 & 0 & -100{,}000 \\ -90{,}000 & 170{,}000 & -80{,}000 & 0 \\ 0 & -80{,}000 & 80{,}000 & 0 \\ -100{,}000 & 0 & 0 & 100{,}000 \end{bmatrix} \quad \text{with} \quad \begin{bmatrix} u_2 \\ u_3 \\ u_4 \\ u_1 \end{bmatrix}$$

The partitioned stiffness submatrices are

$$K_{ii} = \begin{bmatrix} 190{,}000 & -90{,}000 & 0 \\ -90{,}000 & 170{,}000 & -80{,}000 \\ 0 & -80{,}000 & 80{,}000 \end{bmatrix}$$

$$K_{bi} = K_{ib}{}^T = [-100{,}000 \quad 0 \quad 0]$$

$$K_{bb} = 100{,}000$$

Again, the component fixed-interface normal modes are obtained by restraining all boundary DOF and solving the generalized eigenvalue problem.

$$\left[K_{ii} - \omega_j^2 M_{ii}\right]\{\varphi_i\}_j = 0 \tag{36.67}$$

The fixed-interface natural frequencies are

| n | fn (Hz) | ωn (rad/sec) |
|---|---------|--------------|
| 1 | 9.1 | 57.4 |
| 2 | 22.9 | 143.6 |
| 3 | 33.4 | 210.2 |

The diagonal eigenvector matrix is

$$\Lambda_{ii} = \begin{bmatrix} 3294 & 0 & 0 \\ 0 & 20619 & 0 \\ 0 & 0 & 44170 \end{bmatrix}$$

The fixed-interface mass-normalized modes with all three kept are

$$\Phi_{ik} = \begin{bmatrix} 0.1360 & 0.2762 & 0.1739 \\ 0.2473 & 0.0769 & -0.3156 \\ 0.3114 & -0.2662 & 0.1792 \end{bmatrix}$$

The stiffness submatrix multiplication is

$$-\left[K_{ii}^{-1}K_{ib}\right] = \begin{bmatrix} 190{,}000 & -90{,}000 & 0 \\ -90{,}000 & 170{,}000 & -80{,}000 \\ 0 & -80{,}000 & 80{,}000 \end{bmatrix}^{-1} \begin{bmatrix} -100{,}000 \\ 0 \\ 0 \end{bmatrix} = \begin{bmatrix} 1 \\ 1 \\ 1 \end{bmatrix}$$

The interface constraint mode matrix $\Psi_c$ is

$$\Psi_c \equiv \begin{bmatrix} \Psi_{ib} \\ I_{bb} \end{bmatrix} = \begin{bmatrix} -[K_{ii}^{-1}K_{ib}] \\ I_{bb} \end{bmatrix} = \begin{bmatrix} 1 \\ 1 \\ 1 \\ 1 \end{bmatrix}$$

The Craig-Bampton transformation matrix is

$$\Psi_{CB} = \begin{bmatrix} \Phi_{ik} & \Psi_{ib} \\ 0 & I_{bb} \end{bmatrix} = \begin{bmatrix} 0.1360 & 0.2762 & 0.1739 & 1 \\ 0.2473 & 0.0769 & -0.3156 & 1 \\ 0.3114 & -0.2662 & 0.1792 & 1 \\ 0 & 0 & 0 & 1 \end{bmatrix}$$

The transformed mass and stiffness matrices (reduced component matrices) are

$$\widehat{M}_{CB} = \Psi_{CB}{}^T \begin{bmatrix} M_{ii} & M_{ib} \\ M_{bi} & M_{bb} \end{bmatrix} \Psi_{CB} = \begin{bmatrix} \widehat{I}_{kk} & \widehat{M}_{kb} \\ \widehat{M}_{bk} & \widehat{M}_{bb} \end{bmatrix} = \begin{bmatrix} 1 & 0 & 0 & 4.129 \\ 0 & 1 & 0 & 1.339 \\ 0 & 0 & 1 & 0.3936 \\ 4.129 & 1.339 & 0.3936 & 29.0 \end{bmatrix}$$

$$\widehat{M}_{kb} = \begin{bmatrix} 4.129 \\ 1.339 \\ 0.3936 \end{bmatrix}$$

$$\widehat{K}_{CB} = \Psi_{CB}{}^T \begin{bmatrix} K_{ii} & K_{ib} \\ K_{bi} & K_{bb} \end{bmatrix} \Psi_{CB} = \begin{bmatrix} 3294 & 0 & 0 & 0 \\ 0 & 20{,}619 & 0 & 0 \\ 0 & 0 & 44{,}170 & 0 \\ 0 & 0 & 0 & 0 \end{bmatrix}$$

Recall the equation of motion for the modal coordinates for the case of base excitation.

$$\ddot{p}_k + 2\xi_k\omega_k\dot{p}_k + \Lambda_{kk}p_k = -\widehat{M}_{kb}\ddot{u}_b \tag{36.68}$$

The resulting equation for the example with uniform 5% damping is

$$
\begin{bmatrix} 1 & 0 & 0 \\ 0 & 1 & 0 \\ 0 & 0 & 1 \end{bmatrix} \begin{bmatrix} \ddot{p}_1 \\ \ddot{p}_2 \\ \ddot{p}_3 \end{bmatrix} + \begin{bmatrix} 5.74 & 0 & 0 \\ 0 & 14.36 & 0 \\ 0 & 0 & 21.02 \end{bmatrix} \begin{bmatrix} \dot{p}_1 \\ \dot{p}_2 \\ \dot{p}_3 \end{bmatrix} + \begin{bmatrix} 3294 & 0 & 0 \\ 0 & 20619 & 0 \\ 0 & 0 & 44170 \end{bmatrix} \begin{bmatrix} p_1 \\ p_2 \\ p_3 \end{bmatrix}
$$

$$
= - \begin{bmatrix} 4.129 \\ 1.339 \\ 0.3936 \end{bmatrix} \ddot{u}_b
$$

Now let $\ddot{u}_b$ be a 1 G sine sweep from 5 to 50 Hz at one octave/min. Solve for the modal acceleration using the digital recursive filtering relationship in equation (17.15). Recall from equation (36.12) that the internal acceleration can be expressed as

$$
\ddot{u}_i = \Phi_{ik}\ddot{p}_k + \Psi_{ib}\ddot{u}_b
$$

(36.69)

$$
\begin{bmatrix} \ddot{u}_2 \\ \ddot{u}_3 \\ \ddot{u}_4 \end{bmatrix} = \begin{bmatrix} 0.1360 & 0.2762 & 0.1739 \\ 0.2473 & 0.0769 & -0.3156 \\ 0.3114 & -0.2662 & 0.1792 \end{bmatrix} \begin{bmatrix} \ddot{p}_1 \\ \ddot{p}_2 \\ \ddot{p}_3 \end{bmatrix} + \begin{bmatrix} 1 \\ 1 \\ 1 \end{bmatrix} \ddot{u}_b
$$

The physical acceleration results are shown in the next figure. Note that $\ddot{u}_1 = \ddot{u}_b$.
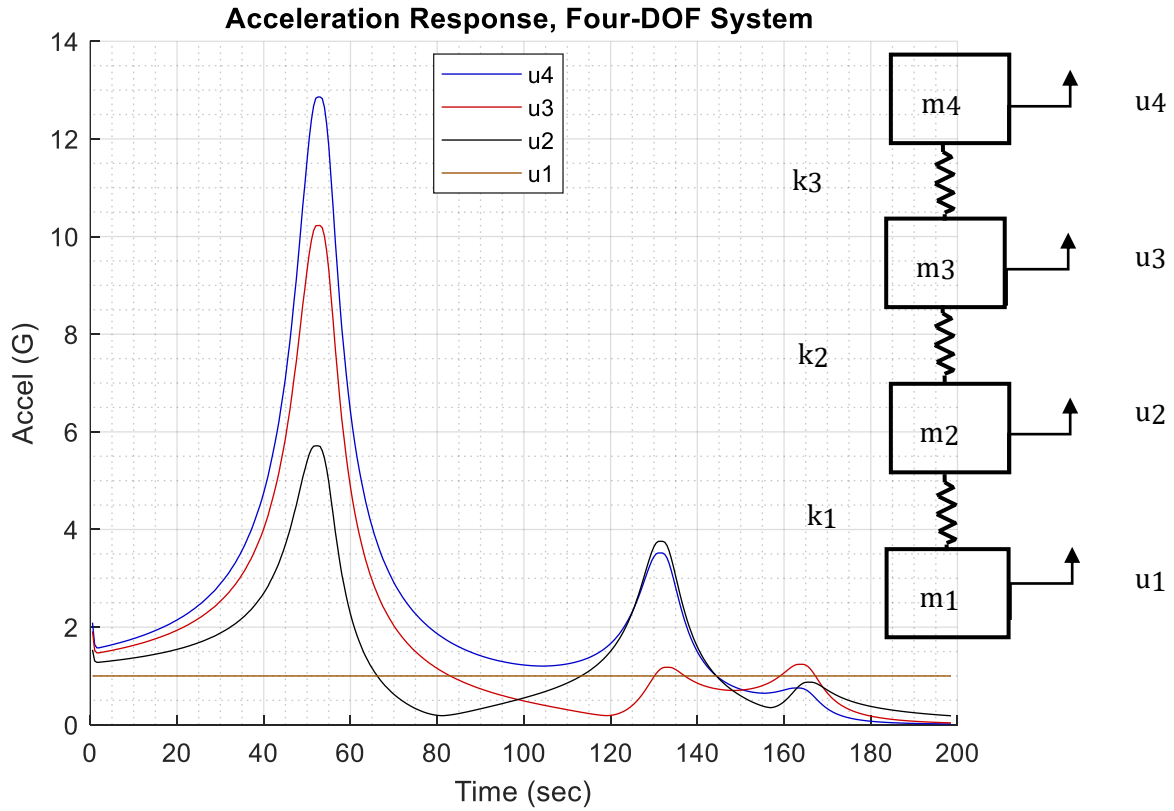
Figure 36.3.   Four-DOF System, Physical Acceleration Responses

The peak value for each one-second window is shown with 50% overlap.

## 36.13  ASSEMBLED GLOBAL MATRICES FOR TWO CONNECTED SYSTEMS

The following assembled mass matrix is formed.

$$\widehat{M}_{CB} = \begin{bmatrix} \hat{I}_{k_1 k_1} & 0_{k_1 k_2} & \widehat{M}_{k_1 b}^{(1)} \\ 0_{k_2 k_1} & \hat{I}_{k_2 k_2} & \widehat{M}_{k_2 b}^{(2)} \\ \widehat{M}_{bk_1}^{(1)} & \widehat{M}_{bk_2}^{(2)} & \widehat{M}_{bb}^{(1)} + \widehat{M}_{bb}^{(2)} \end{bmatrix}$$

(36.70)

Again, the subscript b denotes an interface boundary degrees-of-freedom.

The numerical subscripts denote non-interface degrees-of-freedom.

The following assembled stiffness matrix is formed.

$$\widehat{K}_{CB} = \begin{bmatrix} \Lambda_{k_1 k_1}^{(1)} & 0_{k_1 k_2} & 0_{k_1 b} \\ 0_{k_2 k_1} & \Lambda_{k_2 k_2}^{(2)} & 0_{k_2 b} \\ 0_{bk_1} & 0_{bk_2} & \widehat{K}_{bb}^{(1)} + \widehat{K}_{bb}^{(2)} \end{bmatrix}$$

(36.71)

The combined undamped system equation of motion is thus

$$\widehat{M}_{CB} \begin{Bmatrix} \ddot{p}_k \\ \ddot{p}_b \end{Bmatrix} + \widehat{K}_{CB} \begin{Bmatrix} p_k \\ p_b \end{Bmatrix} = \hat{F}_{CB}$$

(36.72)

This coupling is called modal synthesis.

An example will be included in the next revision.

*This section is a placeholder for a future revision. Each of the spring-mass systems in the previous sections can be considered as a simple finite element model. But FEA usually refers to modeling beams, plates, shells, machined parts, assemblies, etc.*

The following two examples use an FEA model of a rectangular plate, but any MDOF model could be substituted.

Consider a plate mounted to a base at each of its four corners. The plate is to be subject to uniform seismic excitation. There are two methods to apply the base excitation in an FEA, as shown in Figure 37.1 and Figure 37.2.



$$\ddot{U}_1 = \ddot{U}_2 = \ddot{U}_3 = \ddot{U}_4$$
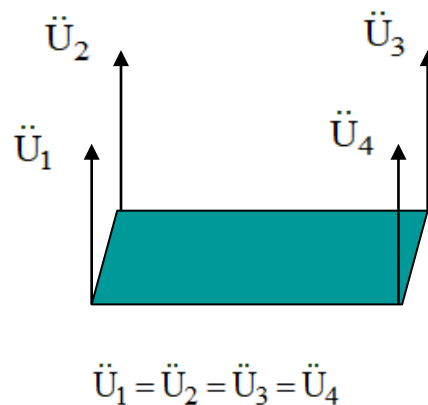
Figure 37.1.  Direct Enforce Acceleration Method

The direct enforcement method is computationally intensive, requiring matrix transformations and a matrix inversion as shown in Reference [71].
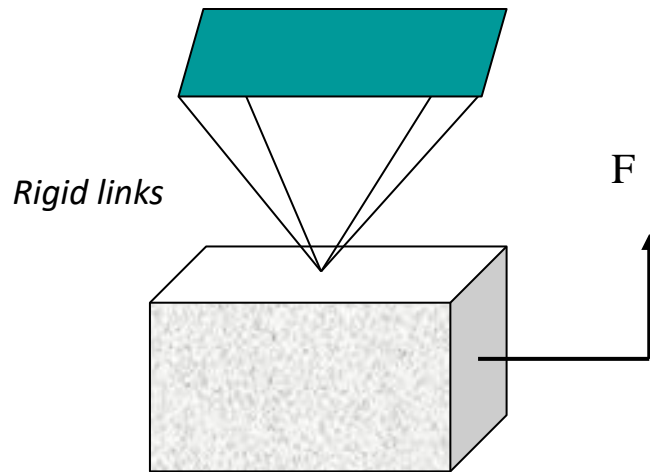
Figure 37.2.   Seismic Mass Method

The seismic mass is chosen to be several orders of magnitude higher in mass than the plate.  An equivalent force is calculated and applied to the seismic mass to excite the desired acceleration at each of the plate's corners.  This method adds a DOF to the plate system resulting in a rigid-body mode at zero frequency.  But the remaining natural frequencies and mode shapes should be the same as if the plate were mounted normally to its joining structure.   The author's experience is that the seismic mass method is faster and more accurate and more reliable than the direct enforced method.  This method was introduced in Section 17.3.3.

Colin Gordon [72] has derived generic criterion curves, with an emphasis on semiconductor facilities, as shown in the following table and figure. The velocity is measured in one-third octave bands over the frequency range from 8 Hz to 100 Hz.  The limits are for floor measurements.

| Table 38.1. Generic Vibration Criterion Curves | | | |
|---|---|---|---|
| Criterion Curve | Max Level Velocity RMS (micrometers/sec) | Detail Size (microns) | Description of Use |
| Workshop (ISO) | 800 | N/A | Distinctly feelable vibration. Appropriate to workshops and nonsensitive areas. |
| Office (ISO) | 400 | N/A | Feelable vibration. Appropriate to offices and nonsensitive areas. |
| Residential Day (ISO) | 200 | 75 | Barely feelable vibration. Appropriate to sleep areas in most instances. Probably adequate for computer equipment, probe test equipment and low-power (to 20X) microscopes. |
| Theater (ISO) | 100 | 25 | Vibration not feelable. Suitable for sensitive sleep areas. Suitable in most instances for microscopes to 100X and for other equipment of low sensitivity. |
| VC-A | 50 | 8 | Adequate in most instances for optical microscopes to 400X, microbalances, optical balances, proximity and projection aligners, etc. |
| VC-B | 25 | 3 | An appropriate standard for optical microscopes to 1000X, inspection and lithography equipment (including steppers) to 3 micron line widths. |
| VC-C | 12.5 | 1 | A good standard for most lithography and inspection equipment to 1 micron detail size. |

| Criterion Curve | Max Level Velocity RMS (micrometers/sec) | Detail Size (microns) | Description of Use |
|---|---|---|---|
| VC-D | 6 | 0.3 | Suitable in most instances for the most demanding equipment including electron microscopes (TEMs and SEMs) and E-Beam systems, operating to the limits of their capability. |
| VC-E | 3 | 0.1 | A difficult criterion to achieve in most instances. Assumed to be adequate for the most demanding of sensitive systems including long path, laser-based, small target systems and other systems requiring extraordinary dynamic stability. |
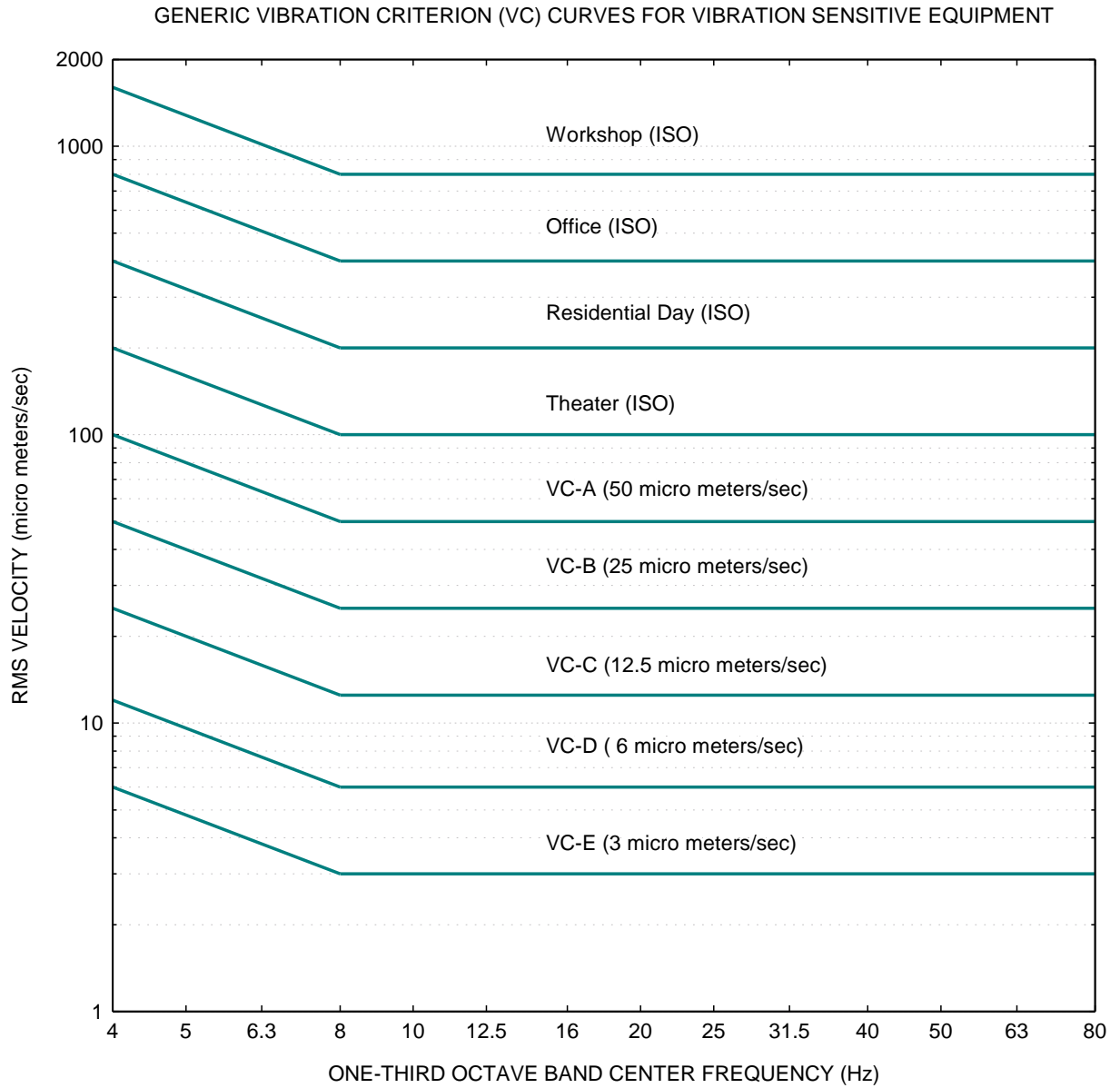
Figure 38.1.   Generic Vibration Criterion Curves

# 39 MATLAB SCRIPTS

The following scripts are posted on the Mathworks File Exchange.

FFT – One-sided, Full Amplitude, Discrete Fourier Transform
https://www.mathworks.com/matlabcentral/fileexchange/127334-fft-one-sided-full-amplitude-discrete-fourier-transform

Power Spectral Density of a Time History
https://www.mathworks.com/matlabcentral/fileexchange/127339-power-spectral-density-psd-of-a-time-history

SDOF Response to Base Input PSD
https://www.mathworks.com/matlabcentral/fileexchange/127793-sdof-response-to-base-input-psd

Synthesize a Time History for an Acceleration PSD
https://www.mathworks.com/matlabcentral/fileexchange/127399-synthesize-a-time-history-for-an-acceleration-psd

SDOF Response to Base Input Acceleration Time History for Given Natural Frequency
https://www.mathworks.com/matlabcentral/fileexchange/127589-sdof-response-to-base-input-for-given-natural-frequency

Shock Response Spectrum (SRS) for base input acceleration
https://www.mathworks.com/matlabcentral/fileexchange/127269-shock-response-spectrum-for-base-input-acceleration

A Matlab function for implementing the rainflow and relative damage equations
https://www.mathworks.com/matlabcentral/fileexchange/127224-rainflow-fatigue-relative-damage

A Matlab function that combines the SDOF response to an acceleration base input, rainflow cycle counting, and the damage calculation
https://www.mathworks.com/matlabcentral/fileexchange/127229-sdof-response-to-acceleration-base-input-with-rainflow

A Matlab Dirlik function for a response PSD is given at
https://www.mathworks.com/matlabcentral/fileexchange/127239-dirlik-relative-damage-for-response-psd

A Matlab Dirlik function for an SDOF response to a base input PSD is given at
https://www.mathworks.com/matlabcentral/fileexchange/127244-dirlik-relative-damage-for-sdof-response-to-base-input-psd

A Matlab function for the FDS time domain
https://www.mathworks.com/matlabcentral/fileexchange/127254-fds-for-a-base-input-acceleration-time-history

A Matlab function for the FDS frequency domain method
https://www.mathworks.com/matlabcentral/fileexchange/127264-fds-of-base-input-acceleration-psd-via-the-dirlik-method

This script calculates the Dirlik fatigue damage from a stress PSD using S/N Coefficients from MIL-HDBK-5J, MMPDS or NASGRO
https://www.mathworks.com/matlabcentral/fileexchange/127294-dirlik-stress-psd-fatigue

# 40 BIBLIOGRAPHY

[1]  T. Lay and T. Wallace, Modern Global Seismology, New York: Academic Press, 1995.

[2]  ISO 2631-1, *Evaluation of human exposure to whole-body vibration, Part 1: General requirements,* International Organization for Standardization, 1997.

[3]  M. Griffin, Handbook of Human Vibration, London: Academic Press, 1990.

[4]  S. G. Siuru W., *Science and Technology Perspectives Laser Gyroscopes - The Revolution in Guidance and Control,* Air University Review, 1985.

[5]  J. Koughan, *The Collapse of the Tacoma Narrows Bridge, Evaluation of Competing Theories of its Demise, and the Effects of the Disaster of Succeeding Bridge Designs,* The University of Texas at Austin, 1996.

[6]  D. Hartog, Mechanical Vibrations, New York: McGraw-Hill, 1940.

[7]  M. Levy and M. Salvadori, Why Buildings Fall Down, New York: Norton, 1992.

[8]  H. Bachmann, Vibration Problems in Structures, Berlin: Birkhauser Verlag, 1995.

[9]  K. Billah and R. Scanlan, "Resonance, Tacoma Narrows Bridge Failure, and Undergraduate Physics, Textbooks," *American Journal of Physics,* 1991.

[10] T. Irvine, "Free Vibration of a Single-Degree-of-Freedom System, Revision B," Vibrationdata, 2005.

[11] T. Irvine, "Free Vibration of a Two-Degree-of-Freedom System Subjected to Initial Velocity and Displacement, Revision C," Vibrationdata, 2011.

[12] T. Irvine, "Longitudinal Natural Frequencies of Rods and Response to Initial Conditions, Revision D," Vibrationdata, 2010.

[13] M. Bai and W. Thatcher, *High G Pyrotechnic Shock Simulation using Metal-to-Metal Impact,* Washington DC: The Shock and Vibration Bulletin, Naval Research Laboratory, September 1979.

[14] R. Blevins, Formulas for Natural Frequency and Mode Shapes, Malabar, Florida: R. Krieger, 1979.

[15] T. Irvine, "Bending Frequencies of Beams, Rods and Pipes, Revision T," Vibrationdata, 2018.

[16] A. Leissa, Vibration of Plates, NASA SP-160, Washington D.C.: National Aeronautics and Space Administration, 1969.

[17] E. Baker, Structural Analysis of Shells, Malabar, Florida: Krieger, 1972.

[18] D. S. Steinberg, Vibration Analysis for Electronic Equipment, Third Edition, New York: Wiley, 2000.

[19] R. Marshall, L. Phan and M. Celebi, "Full-Scale Measurement of Building Response to Ambient Vibration and the Loma Prieta Earthquake," *Fifth U.S. National Conference on Earthquake Engineering, Earthquake Awareness and Mitigation Across the Nation,* vol. 11, 1994.

[20] M. Collins, Liftoff: The Story of America's Adventure in Space, New York City: Grove Press, 1989.

[21] T. Irvine, "Modal Transient Analysis of a System Subjected to an Applied Force, Revision L," Vibrationdata, 2013.

[22] T. Irvine, *An Introduction to the Shock Response Spectrum, Revision S,* Vibrationdata, 2012.

[23] J. Emmerson, "On Shaky Ground," Letters, Smithsonian Air & Space, May 2001.

[24] T. Irvine, "The Generalized Coordinate Method for Discrete Systems, Revision F," Vibrationdata, 2012.

[25] D. O. Smallwood, "An Improved Recursive Formula for Calculating Shock Response Spectra," *Shock and Vibration Bulletin, No. 51,* May 1981.

[26] T. Irvine, " Two-Stage Isolation for Harmonic Base Excitation, Revision C," Vibrationdata, 2015.

[27] T. Irvine, "Derivation of the Filter Coefficients for the Ramp Invariant Method as Applied to Base Excitation of a Single-degree-of-Freedom System, Revision D," Vibrationdata, 2018.

[28] V. Wowk, *Machinery Vibration Measurement and Analysis,* New York: McGraw-Hill, 1991.

[29] T. Irvine, "Modal Transient Vibration Response of a Cantilever Beam Subjected to Base Excitation," Vibrationdata, 2016.

[30] T. Scharton and D. Pankow, "Extreme Peaks in Random Vibration Testing," in *Aerospace/JPL, Spacecraft and Launch Vehicle Dynamic Environments Workshop*, Hawthorne, California, 2006.

[31] K. Ahlin, "Comparison of Test Specifications and Measured Field Data," *Sound & Vibration,* September 2006.

[32] Himelblau et al, NASA-HDBK-7005, *Dynamic Environmental Criteria,* Washington DC: National Aeronautics and Space Administration, 2001.

[33] W. Fackler, *Equivalence Techniques for Vibration Testing, SVM-9,* Washington D.C.: The Shock and Vibration Information Center, Naval Research Laboratory, US Department of Defense, 1972.

[34] H. Luhrs, *Random Vibration Effects on Piece Part Applications,* Los Angeles, California: Proceedings of the Institute of Environmental Sciences, 1982.

[35] *General Environmental Verification Specification for STS & ELV Payloads, Subsystems, and Components,* NASA Goddard Space Flight Center, 1996.

[36] *Vibration, Shock, and Acoustics,* McDonnell Douglas Astronautics Company, Western Division, 1971.

[37] S. DiMaggio, B. Sako and S. Rubin, *Analysis of Nonstationary Vibroacoustic Flight Data Using a Damage-Potential Basis,* 2003: AIAA Dynamic Specialists Conference.

[38] H. Himelblau, A. Piersol and e. al, *IES Handbook for Dynamic Data Acquisition and Analysis,* Mount Prospect, Illinois, 1994.

[39] R. Randall, Frequency Analysis, 3rd edition, Bruel & Kjaer, 1987.

[40] F. Harris, Trigonometric Transforms, Technical Publication DSP-005, San Diego, CA: Scientific-Atlanta.

[41] MIL-STD-810E, *Environmental Engineering Considerations and Laboratory Tests,* United States Department of Defense, 1989.

[42] NAVMAT P-9492, *Navy Manufacturing Screening Program,* Washington D.C.: Department of the Navy, Naval Material Command, 1979.

[43] JEDEC JESD22-B111A, *Board Level Drop Test Method of Components for Handheld Electronic Products Standard,* JEDEC Solid State Technology Association, 2016.

[44] H. Gaberson, *Pseudo Velocity Shock Analysis, Short Course Slides,* SAVIAC.

[45] "Mechanical Shock Design and Verification Handbook, ECSS-E-HB-32-25A," European Cooperation for Space Standardization, Noordwijk, The Netherlands, July 2015.

[46] D. Albert and J. Orcutt, "Observations of Low-frequency Acoustic-to-seismic Coupling in the Summer and Winter," *Journal of the Acoustical Society of America ,* vol. (86), July 1989.

[47] W. Kacena, M. McGrath and A. Rader, "Aerospace Systems Pyrotechnic Shock Data, Vol. VI., NASA CR 116406," Goddard Space Flight Center, Maryland, 1970.

[48] European Cooperation for Space Standardization, "Mechanical Shock Design and Verification Handbook," Noordwijk, The Netherlands, July 2015.

[49] C. Lalanne, Sinusoidal Vibration (Mechanical Vibration and Shock), New York: Taylor & Francis, 1999.

[50] R. Huston and H. Josephs, Practical Stress Analysis in Engineering Design, Dekker, CRC Press, 2008.

[51] R. Ferebee and T. Irvine, NASA/TM-2008-215253, An Alternative Method of Specifying Shock Test Criteria, 2008.

[52] FedEx, *Testing Packages for FedEx, Small Parcel Networks,* 2022.

[53] R. Chalmers and H. Gaberson, "Modal Velocity as a Criterion of Shock Severity," *Shock and Vibration*

*Bulletin, Naval Research Lab,* December 1969.

[54] T. Irvine, "Shock and Vibration Stress as a Function of Velocity, Revision G," Vibrationdata, 2013.

[55] A. Piersol and T. Paez, Harris' Shock and Vibration Handbook, 6th Edition; V. Bateman, Shock Testing Machines, Chapter 27, New York City: McGraw-Hill, 2010.

[56] H. Gaberson, "Shock Severity Estimation," *Sound & Vibration,* January 2012.

[57] SMC-TR-06-11 AEROSPACE REPORT NO. TR-2004(8583)-1 Rev. A, *Test Requirements for Launch, Upper-Stage, and Space Vehicles,* El Segundo, CA: Aerospace Corporation.

[58] R. Morse, *Presentation at Spacecraft & Launch Vehicle Dynamics Environments Workshop Program,* Aerospace Corp., El Segundo, CA, June 2000.

[59] S. Sterns and R. David, Signal Processing Algorithms in Fortran and C, New Jersey: Prentice-Hall, 1993.

[60] ECSS-E-HB-32-26A, *Spacecraft Mechanical Loads Analysis Handbook,* Noordwijk, The Netherlands: European Cooperation for Spacecraft Standardization (ECSS), 2013.

[61] M. Mrsnik, J. Slavic and M. Boltezar, *Frequency-domain Methods for a Vibration-fatigue-life Estimation - Application to Real Data,* International Journal of Fatigue, Vol 47., 2013.

[62] A. Halfpenny and F. Kihm, *Rainflow Cycle Counting and Acoustic Fatigue Analysis Techniques for Random Loading,* Southampton, UK: RASD Conference, 2010.

[63] A. Halfpenny, *A Frequency Domain Approach for Fatigue Life Estimation from Finite Element Analysis,* Dublin: International Conference on Damage Assessment of Structures, 1999.

[64] Martin-Marietta, *Test Methods and Control, V,* Denver, 1989.

[65] C. Harris, *Shock and Vibration Handbook, 4th edition (Chapter 20),* New York: McGraw-Hil, 1995.

[66] NASA-STD-7002B, *Payload Test Requirements,* Washington D.C.: National Aeronautics and Space Administration, 2018.

[67] GSFC-STD-7000 REV A, *General Environmental Verification Standard (GEVS),* Greenbelt, MD: NASA Goddard Space Flight Center, 2013.

[68] C. R and K. A, *Fundamentals of Structural Dynamics, Second Edition,* New Jersey: 2006, 2006.

[69] J. Young and W. Haile, *Primer on the Craig-Bampton Method,* 2000.

[70] S. Gordon, *The Craig-Bampton Method,* FEMCI Presentation, 1999.

[71] T. Irvine, "Modal Transient Analysis of a Multi-degree-of-freedom System with Enforced Motion,

Revision C," Vibrationdata, 2011.

[72] G. C., *Generic Vibration Criteria for Vibration-Sensitive Equipment,* SPIE Proceedings Volume 1619, 1991.